

**Experimental study of polarisation
observables T , P and H in π^0 and η
photoproduction off quasifree nucleons
with the Crystal Barrel/TAPS setup**

Inauguraldissertation

zur

Erlangen der Würde eines Doktors der Philosophie

vorgelegt der

Philosophisch-Naturwissenschaftlichen Fakultät

der Universität Basel

von

Nicolas Martin Jermann

2023

Genehmigt von der Philosophisch-Naturwissenschaftlichen Fakultät
auf Antrag von

Erstbetreuung: Prof. Dr. B. Krusche, Prof. Dr. U. Thoma

Zweitbetreuung: Prof. Dr. C. Bruder

Externer Experte: Prof. Dr. V. Crede

Basel, den 21. Februar 2023

Prof. Dr. M. Mayor
Dekan

Abstract

All visible matter is made up of elementary particles and their interactions. The four fundamental interactions are gravitational, electromagnetic, weak and strong interaction. On the level of nucleons, i.e. protons and neutrons, the strong interaction acting on their constituents, the quarks and gluons, dominates. The goal of this work is a small contribution to a better understanding of this strong interaction.

Quantum chromodynamics (QCD) is the underlying gauge theory describing that interaction within the Standard Model of particle physics (SM). In contrast to the high-energy regime, the low-energy regime cannot be treated perturbatively, which makes theoretical calculations very difficult. Excitation spectra of nucleons are a vital testing ground for comparing experimental findings with theoretical predictions.

During the last two decades, much progress has been made on the theory side, e.g. lattice gauge methods, and in experiments. In particular, energy-tagged photon beams at electron accelerators have become important. They have reached a state where asymmetries measured with polarised photons and polarised targets allow for detailed partial wave analyses (PWA). However, the predicted excited states are not in agreement with experimental observations.

The present experiment was conducted at the Electron Stretcher Accelerator (ELSA) in Bonn, Germany, in 2018 and 2021 with the (almost) 4π covering Crystal Barrel/TAPS detector setup. The incident electron beam of $E_\gamma = 3.2$ GeV energy impinges on a diamond radiator, where it produces coherent bremsstrahlung photons with a linear polarisation at a coherent edge of $E_\gamma = 1.2$ GeV. The photons again impinge on a transversely polarised, deuterated butanol target. This allows the simultaneous measurement of the beam asymmetry Σ_{but} , target asymmetry T , recoil asymmetry P and the beam-target double polarisation observable H . Analysed are the final states $\pi^0 p$, $\pi^0 n$, ηp

and ηn in exclusive reactions. The mesons are reconstructed from photons by the decay channels $\pi^0 \rightarrow 2\gamma$, $\eta \rightarrow 2\gamma$ and $\eta \rightarrow 3\pi^0 \rightarrow 6\gamma$.

It is the first time that results for the observables T , P and H are shown for $\pi^0 n$ and ηn , which improves the quality, contributions and understanding of partial waves in the centre of mass energy range from $W = 1.5 \text{ GeV}$ to 2.5 GeV . The reactions on the proton and the beam asymmetry of butanol show an excellent agreement with existing data and improve the quality of the world data.

Of special interest is the previously observed narrow structure in ηn around $W = 1.68 \text{ GeV}$ that has not been observed in ηp , which has led to many speculations about its origin. The results from this experiment strongly prefer an interpretation as interference of two S waves as its origin and, thus, no new resonance.

Acknowledgements

This work is dedicated to my mentor, friend and role model Prof. Dr Bernd Krusche. I have been thankful for your enormous support in experimental, technical, methodical and physical expertise, the exciting discussions and mentoring over countless years. In loving memories.

Furthermore, this work would not have been possible without the tremendous support of many other people. A special thank you goes to:

Ulrike Thoma, for short notice stand in as first supervisor, all the assistance and discussions about the experiment, analysis and results, as well as the excellent collaboration between Bonn and Basel.

Christoph Bruder, for short notice stand in as second supervisor, all the help with administrative questions, the discussions in the doctoral committee meetings and mentoring the last months at the University of Basel.

Volker Crede, for serving as external expert.

Michael Erzer, Christian Meier, Debdeep Ghosal, Alexander Käser and Sebastian Lutterer for insightful discussions and help at countless group meetings, coffee breaks and conference meetings.

Jan Hartmann, for technical support with EXPLORA, the enormous help during the beam times, the help in the most different steps of the data analysis and the discussions.

Farah Afzal, for providing the linear beam polarisation degrees and constructive discussions about the results and their interpretation.

Annika Thiel and Stefan Runkel, for providing beam and target NMR polarisation degrees, as well as the discussions in several meetings.

Volker Metag, Tobias Seifen and all other participants at the analysis meetings of CBELSA/TAPS, for constructive inputs and discussions.

Victor Kashevarov, Andrey Sarantsev and Kirill Nikonov, for providing partial wave analysis solutions.

Jürg Jourdan, for the discussions at the doctoral committee meeting.

Everybody in the CBELSA/TAPS collaboration, for making the beam times possible and for the taken shifts.

All my family and friends, for unconditional support over all these years.

Contents

1	Introduction	1
1.1	Historical overview	2
1.2	Standard Model of particle physics	4
1.2.1	Quantum chromodynamics	5
1.2.2	Quantum electrodynamics	7
1.2.3	Electroweak interaction and Higgs mechanism	7
1.3	Quark model	9
1.3.1	Hadrons	9
1.3.2	Flavour quantum numbers	12
1.4	Nucleon resonances	15
1.4.1	Notation	15
1.4.2	Experimental spectrum of nucleon resonances	15
1.4.3	Theoretical description through constituent quark model and lattice quantum chromodynamics	15
1.5	Meson photoproduction	19
1.5.1	Reaction types	20
1.5.2	Kinematics	21
1.5.3	Electromagnetic multipole expansion	23
1.5.4	Chew-Goldberg-Nambu-Low amplitudes	24
1.5.5	Helicity amplitudes	26
1.5.6	Isospin amplitudes	27
1.6	Polarisation observables	29
1.6.1	Unpolarised cross section	29
1.6.2	Polarised cross section	30
1.6.3	Electromagnetic multipole expansion of polarisation ob- servables	33
1.6.4	Polarisation observables within this experiment	34

1.7	Current status of theory and experiment	39
1.7.1	Theoretical description with partial wave analyses	39
1.7.2	Observed narrow structure in ηn around 1.68 GeV	43
1.7.3	Experimental data situation	44
2	Experimental setup	51
2.1	Electron Stretcher Accelerator	52
2.2	Crystal Barrel/TAPS detector setup	54
2.2.1	Tagging system	54
2.2.2	Goniometer	56
2.2.3	Crystal Barrel	57
2.2.4	Forward Plug	59
2.2.5	Inner Detector	59
2.2.6	MiniTAPS	60
2.2.7	Gamma Intensity Monitor and Flux Monitor	62
2.2.8	Cherenkov detector	63
2.3	Targets	65
2.3.1	Polarised deuterated butanol target	65
2.3.2	Carbon foam target	68
2.4	Trigger conditions	69
2.5	Beam times and data sets	71
3	Event reconstruction	73
3.1	Software	74
3.1.1	ROOT	74
3.1.2	Data analysing software	74
3.1.3	Monte Carlo simulation software	75
3.2	Particle reconstruction	78
3.2.1	Tagging system	78
3.2.2	Crystal Barrel and Forward Plug detector setup	79
3.2.3	MiniTAPS detector system	83
3.2.4	Gamma Intensity Monitor and Flux Monitor	86
3.3	Calibration	87
3.3.1	Time calibration	87
3.3.2	Energy calibration	88

4	Event selection	97
4.1	Multiplicity	98
4.2	Meson reconstruction	100
4.2.1	Invariant mass reconstruction	100
4.2.2	Constraining the meson mass	101
4.2.3	χ^2 anticut on background mesons	101
4.3	Coincidence time	103
4.4	Random background subtraction	107
4.5	Background suppression	110
4.5.1	Invariant mass	111
4.5.2	Coplanarity	115
4.5.3	Missing mass	119
4.5.4	Polar angle difference	122
4.5.5	Fermi momentum	125
4.5.6	Summary of kinematic cut positions and number of total events	129
4.5.7	Effect of kinematic cut positions	132
4.6	Remaining background contamination	139
5	Data analysis	145
5.1	Target surface density	146
5.2	Photon flux	149
5.2.1	Electron flux	149
5.2.2	Tagging efficiency	151
5.3	Polarisation degrees	156
5.3.1	Target nucleon polarisation	156
5.3.2	Beam photon polarisation	157
5.4	Dilution factor	160
5.4.1	Carbon scaling factor	162
5.4.2	Monte Carlo simulation	165
5.4.3	Dependence on the Fermi momentum cut position	167
5.4.4	Experimentally determined dilution factor	168
5.5	Background correction	170
5.6	Reconstruction of the centre of mass energy from the final state	171
5.6.1	Kinematic reconstruction	171

5.6.2	Flux reconstruction	174
5.7	Data merging methods	176
5.7.1	Arithmetic Average	176
5.7.2	Inverse-variance weighted average	176
5.7.3	Linear weighted average	177
5.7.4	Average of overlapping bins	177
6	Extraction of polarisation observables	179
6.1	Binned asymmetry fitting method	180
6.2	Unbinned maximum likelihood estimation method	186
6.2.1	Probability density function	186
6.2.2	Likelihood function	188
6.3	Comparison between the extraction methods	193
6.3.1	Polarisation observables	193
6.3.2	Statistical methods for comparison	193
6.3.3	Statistical uncertainty	200
6.4	Systematic uncertainty	203
6.4.1	Polarisation degrees	203
6.4.2	Dilution factor	204
6.4.3	Background contamination	206
6.4.4	Total systematic uncertainty	206
7	Results	211
7.1	Comparison of η decay channels	212
7.2	Comparison of beam times	214
7.3	Beam asymmetry Σ_{but}	217
7.4	Target asymmetry T	224
7.5	Recoil asymmetry P	231
7.6	Beam-target double polarisation observable H	236
7.7	Partial wave contributions	242
7.8	Narrow structure in ηn around $W = 1.68$ GeV	247
8	Conclusion and outlook	251
	Appendices	253

A Kinematic cut positions	255
A.1 Invariant mass cut positions	256
A.2 Coplanarity cut positions	262
A.3 Missing mass cut positions	267
A.4 Fermi momentum cut positions	272
A.5 Polar angle difference cut positions	278
B Data analysis	283
B.1 Cherenkov radiation for CO ₂	283
B.2 Linear beam photon polarisation degrees	285
B.3 Carbon scaling factor	289
C Extraction of polarisation observables	291
C.1 Integrated asymmetries in Dec2021	292
C.2 Asymmetry Fitting	293
C.2.1 Beam asymmetry $A_{\Sigma_{but}}$	294
C.2.2 Target asymmetry A_T	298
C.2.3 Beam-target asymmetry A_{PH}	302
C.3 Detector acceptance from the maximum likelihood estimation in ηN	306
C.4 Comparison between extraction methods	307
C.4.1 Simple difference	307
C.4.2 Error normalised difference with maximum correlation .	308
C.4.3 Systematic and statistical uncertainty in merged beam time data	309
C.5 Systematic uncertainty of the dilution factor in Dec2021	310
D Results	311
D.1 Preliminary results from Dec2021	311
D.1.1 Comparison of beam times with preliminary data	312
D.1.2 Results with merged preliminary data	315
D.2 Target asymmetry T from Oct2018	318
D.3 χ^2/ndf from Legendre polynomial fits	320
D.4 Legendre coefficients	325
D.4.1 $\gamma p \rightarrow \pi^0 p$	325
D.4.2 $\gamma n \rightarrow \pi^0 n$	330

Contents

D.4.3	$\gamma p \rightarrow \eta p$	335
D.4.4	$\gamma n \rightarrow \eta n$	340
D.5	BnGa 2022-02 predictions in ηn	345
D.6	Data tables (Oct2018 data)	346
D.6.1	$\gamma p \rightarrow \pi^0 p$	346
D.6.2	$\gamma n \rightarrow \pi^0 n$	352
D.6.3	$\gamma p \rightarrow \eta p$	358
D.6.4	$\gamma n \rightarrow \eta n$	363
D.7	Data tables (T in merged full data)	369
D.7.1	$\gamma p \rightarrow \pi^0 p$	369
D.7.2	$\gamma n \rightarrow \pi^0 n$	371
D.7.3	$\gamma p \rightarrow \eta p$	373
D.7.4	$\gamma n \rightarrow \eta n$	375
References		376

1 | Introduction

This chapter gives a rough overview of the underlying theories, physical concepts and mathematical descriptions in which this thesis is done. The topics discussed focus on the latter used reactions and phenomena.

The chapter starts with an overview of the most important events in the history of particle physics in Section 1.1, followed by the different theories that build the Standard Model of particle physics (SM) in Section 1.2.

Section 1.3 explains the quark model that brings light into the whole *particle zoo* by classifying hadrons in terms of valence quarks. The inner structure of the nucleon with its resonances is discussed in Section 1.4.

Section 1.5 describes the process of pseudoscalar photoproduction in more detail. Especially the multipole expansion and the different types of representations are discussed. Section 1.6 gives an overview of polarisation observables in single pseudoscalar photoproduction experiments in general and within this experiment.

The last part, Section 1.7, shows the current state of the theory, i.e. partial wave analyses (PWA), and the experimental data situation.

If not mentioned otherwise, $\cos(\theta) \equiv \cos(\theta_{meson}^{CM})$, where CM indicates the centre of mass frame, for better readability. This simplification holds for the whole work.

1.1 Historical overview

4th c. BC First idea of atoms as uncuttable units that build up matter [1–3]

18th c. First evidence for the existence of atoms from reactions of elements in a certain ratio [4] and the Brownian motion [5]

1815 Idea that all elements contain hydrogen [6]

1897 Discovery of the electron [7]

1905 Einstein developed the theory of special relativity, i.e. invariance of physical laws for all inertial frames of reference and the same speed of light in vacuum for all observers [8]

1913 Discovery of the positive charged nucleus with the scattering of α particles on a gold foil [9]

1913 Bohr model for describing atoms, i.e. the atom is a small, dense and positively charged nucleus with negatively charged electrons orbiting around the nucleus [10]

1913 Discovery of isotopes [11]

1919 Discovery of the proton [12]

1920 Rutherford postulates a neutral particle in the nucleus - the neutron - to keep it stable [13]

1932 Discovery of the neutron [14]

1935 Explaining the interaction of protons and neutrons with the exchange of mesons [15]

1937 Discovery of the muon [16]

1947 Discovery of the pion [17, 18] and the kaon [19]

1953 Development of quantum chromodynamics (QCD) [20]

1955 Discovery of the antiproton [21]

- 1956** Discovery of the electron neutrino [22]
- 1965** Nobel Prize for Tomonaga, Schwinger and Feynman for the development of quantum electrodynamics (QED) [23], one of the most accurate theories today [24, 25]
- 1964** Development of the quark model by introducing a $SU(3)$ flavour symmetry [26, 27]
- 1964** Development of the Higgs mechanism [28–30]
- 1967** Development of the electroweak theory (EW) [31, 32]
- 1969** Discovery of quarks at the Stanford Linear Accelerator Center (SLAC) in California, USA [33]
- 1973** Discovery of the Z^0 boson at the European Council for Nuclear Research (French: Conseil Européen pour la Recherche Nucléaire, CERN) in Geneva, Switzerland [34, 35]
- 1975** First use of the term *Standard Model of particle physics* (SM) as a combination of theories for the electromagnetic, weak and strong interaction [36]
- 2012** Discovery of the Higgs boson at CERN [37, 38]

1.2 Standard Model of particle physics

Matter is made up of visible, baryonic matter, dark matter and dark energy, as known from cosmological observations [39]. The standard model of Big Bang cosmology - the Λ CDM theory - is the most straightforward theory that can explain crucial cosmological phenomena such as the cosmic microwave background and the accelerating expansion of the universe. The theory suggests that dark energy accounts for 68.5% [40] of the total energy in the universe, whereas dark matter accounts for 26.5% [40] and baryonic matter for 4.9% [40].

Baryonic matter, from now on called matter, can be described by elementary particles and their interactions through the four fundamental forces: gravity, electromagnetic, weak and strong interaction. All but gravity can be combined with the elementary particles to form the Standard Model of particle physics (SM).

The SM consists of different theories: quantum electrodynamics (QED), which can be extended to the electroweak theory (EW), quantum chromodynamics (QCD) and the Higgs mechanism. The SM is formulated as a quantum field theory (QFT), where particles are excitations of a field, and interactions can be visualised by Feynman diagrams formulated by Lagrangian densities. An overview of the elementary particles in the SM can be found in Figure 1.1.

Depending on the statistics - Fermi-Dirac or Bose-Einstein - that the particle obeys, they are called fermions or bosons. After the spin-statistics theorem [41–43], the former are spin-1/2 particles whereas the latter have integer spin.

Fermions are categorised into three families, also called generations. The first one with the electron, electron neutrino, up and down quark build up long-living particles like protons and neutrons, that again build up matter as we know it. The second and third families are made of particles with similar properties. However, they are heavier and decay too fast to form stable matter.

Quarks cannot be found as free particles due to the confinement of the QCD that bounds them to hadrons. They carry a colour charge: red, green and blue. The gluon, the force carrier of the strong interaction, exists in eight types, each carrying a colour and an anticolour.

		generations			force carriers	Goldstone bosons	
		I	II	III			
leptons		$< 1.1 \text{ eV}$ 0 $1/2$ ν_e electron neutrino	$< 0.19 \text{ MeV}$ 0 $1/2$ ν_μ muon neutrino	$< 18.2 \text{ MeV}$ 0 $1/2$ ν_τ tau neutrino	91.19 GeV 0 1 Z^0 Z^0 boson	125.25 GeV 0 0 0 H^0 Higgs boson	← mass ← charge ← spin ← symbol ← name
		511.00 keV -1 $1/2$ e electron	105.66 MeV -1 $1/2$ μ muon	1.78 GeV -1 $1/2$ τ tau	80.38 GeV 0 ± 1 W^\pm W^\pm boson	gauge bosons	
quarks		2.16 MeV $2/3$ $1/2$ u up	1.27 GeV $2/3$ $1/2$ c charm	172.76 GeV $2/3$ $1/2$ t top	0 0 1 γ photon		
		4.67 MeV $-1/3$ $1/2$ d down	93 MeV $-1/3$ $1/2$ s strange	4.18 GeV $-1/3$ $1/2$ b bottom	0 0 1 g gluon		

Figure 1.1: Standard Model of particle physics with its three generations of fermions, the force carrier bosons and the Higgs boson. Gluons g interact with quarks (strong interaction), photons γ with quarks and charged leptons (electromagnetic interaction) and Z^0 and W^\pm bosons with all fermions (weak interaction). The Higgs boson is responsible for the physical masses of the elementary particles.

Furthermore, all particles shown in Figure 1.1 have a corresponding antiparticle, i.e. antiup \bar{u} , positron \bar{e} (e^+), etc. The electric neutrally bosons, i.e. gluon, photon, Z^0 and Higgs boson, are their own antiparticle.

Although the SM is a very successful model with many proven experimental predictions - the latest example is the discovery of the Higgs boson in 2012 [37,38] - there are important phenomena that cannot be explained by it, e.g. neutrino oscillation, matter-antimatter asymmetry, dark matter or gravity.

1.2.1 Quantum chromodynamics

Quantum chromodynamics (QCD) describes the strong interaction with six quarks and eight gluons as force carriers. Quarks carry a colour charge,

whereas gluons carry an additional anticolour charge.

More formally, QCD is a nonabelian gauge theory based on the local symmetry of the $SU(3)$ colour group. The Lagrangian density that describes this is given by [44]:

$$\mathcal{L}_{QCD} = \sum_q \bar{\psi}_{q,i} (i\gamma^\mu (D_\mu)_{ij} - m_q \delta_{ij}) \psi_{q,j} - \frac{1}{4} G_{\mu\nu}^a G_a^{\mu\nu}, \quad (1.1)$$

where $\psi_{q,i}$ are the quark field spinors for a quark of flavour q , γ^μ are the Dirac matrices, D_μ the gauge covariant derivative containing the coupling constant α_s , m_q the mass of a quark, δ the Kronecker delta and $G_{\mu\nu}^a$ the gauge invariant gluon field strength tensor. Furthermore, the Einstein sum convention [45] is used, where one sums over repeated indices.

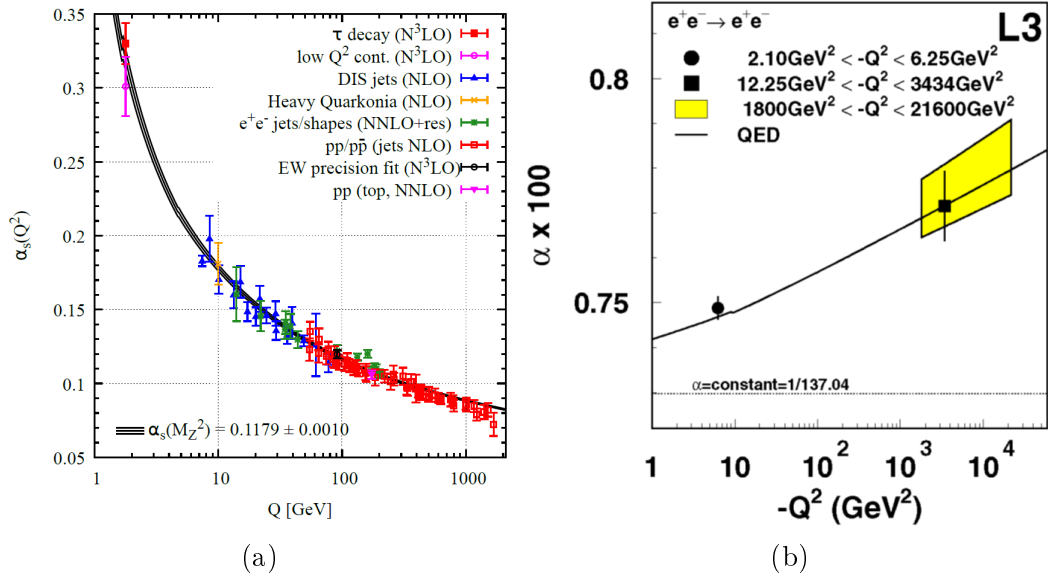


Figure 1.2: Coupling constant of the strong interaction in quantum chromodynamics α_s (a) and the electromagnetic interaction in quantum electrodynamics α as a function of the momentum transfer Q^2 . Figure (a) taken from [44]. Figure (b) taken from [46].

The coupling constant of QCD has two interesting properties: confinement (not yet proven analytically) for low energies and asymptotic freedom for high energies [47, 48]. The first says that there are no free quarks in nature. This is due to the increase of the coupling constant α_s (Figure 1.2a) towards lower energies, meaning there will be a new quark-antiquark pair before two quarks can be separated from one another. The second says that quarks can be seen

as free if the distance between the quarks is small since the coupling constant α_s becomes small. Therefore, perturbation theory is applicable.

1.2.2 Quantum electrodynamics

Quantum electrodynamics (QED) describes the electromagnetic interaction with the photon as force carrier. It is one of the most accurate theories available today [24, 25]. In contrast to QCD, the coupling constant α increases towards higher energies (Figure 1.2b). Thus, perturbation theory can only be applied if the energies are not too large. The coupling constant α is around $1/137 \approx 0.0073$ at the mass of the Z^0 boson, i.e. $m_{Z^0} = 91.2 \text{ MeV}$.

QED is an abelian gauge theory based on the local symmetry group $U(1)$. The Lagrangian density that describes the QED is given by [25]:

$$\mathcal{L}_{QED} = \bar{\psi} (i\gamma^\mu D_\mu - m) \psi - \frac{1}{4} F_{\mu\nu} F^{\mu\nu}, \quad (1.2)$$

where ψ are the electromagnetic field spinors for a fermion, γ^μ are the Dirac matrices, D_μ the gauge covariant derivative containing the coupling constant α , m the mass of the particle and $F^{\mu\nu}$ the electromagnetic field tensor. By explicitly calculating the equations of motion, the Maxwell equations result [25].

1.2.3 Electroweak interaction and Higgs mechanism

QED can be combined with the weak interaction to form the electroweak theory (EW) [31, 32, 49]. This is based on the local symmetry group $SU(2) \times U(1)$ that results in a rather complex Lagrangian density made of a kinematic term for fermions, a Yukawa interaction term for fermions, an interaction term between W and B vector bosons and a Higgs term [44]. The W and B vector bosons result in the physical photon, Z^0 and W^\pm bosons. The Higgs mechanism breaks the electroweak symmetry leading to the physical masses of the gauge bosons [29].

EW does not describe all leptons the same way. Charged ones, i.e. electron, muon and tauon, are described as left- and right-handed particles, similar to quarks. Neutral ones, i.e. neutrinos, on the other side, are described as left-handed particles only. Most theories beyond the SM introduce right-handed

neutrinos (not yet observed) to build a Grand Unified Theory (GUT), which could explain some phenomena that cannot be explained by the SM alone.

1.3 Quark model

The quark model was proposed by Gell-Mann [26] and Zweig [27] in 1964 as an independent theory for the description of hadrons. Nowadays, it is mainly absorbed in the SM.

Hadrons are built of *main* quarks - the valence quarks - and a sea of quark-antiquark pairs - the sea quarks - as well as gluons. Usually, the sea quarks and gluons are absorbed into to the valence quarks, which then define the properties of the hadrons. These quarks are called constituent quark. Flavour quantum numbers (Section 1.3.2) like strangeness, baryon number or isospin are defined by them. However, some essential properties like mass cannot be explained.

1.3.1 Hadrons

The confinement in QCD (Section 1.2.1) ensures that quarks do not occur as single particles in nature but as bound ones: hadrons. Since bound structures must be colour neutral, a hadron in a most simple quark model can be made of a quark-antiquark pair (meson) or three quarks (baryon). More complex objects with two quark-antiquark pairs - tetraquarks - or three quarks and a quark-antiquark pair combined - pentaquarks - (also baryon) can also exist. After first evidence in 2003 [50], the latter two were finally proven to exist in the last 10 years [51–55].

Nearly all hadrons decay very quickly ($\tau < 1 \mu\text{s}$ [44]) to other particles except proton and neutron. The latter has a mean lifetime of $\tau = (879.4 \pm 0.6)\text{s}$ [44] and decays to a proton, electron and electron neutrino, whereas the former can be seen as stable with a mean lifetime of more than 10^{29} years [44].

If a hadron is made only of up and down quarks, it is called unflavoured.

Mesons

Mesons are bosons made of two *main* quarks (or two antiquarks). The valence quarks can have their spin either aligned or in opposite directions, resulting in a meson spin of 1 or 0. In the first case, three spin projections form a spin-1 triplet, whereas in the second case, only one spin projection is

possible with a spin-0 singlet.

Of particular interest are mesons in the ground state with angular momentum $l = 0$, resulting in pseudoscalar mesons with $J^P = 0^-$ and vector mesons with $J^P = 1^-$. Here, J is the total angular momentum and P is the parity.

The three lightest quarks - u , d , s - with their antiquarks can form nine different mesons. Figure 1.3 shows the pseudoscalar and vector meson nonets. They are shown in a $S - I_3$ plane, where S is the strangeness and I_3 is the third component of the isospin.

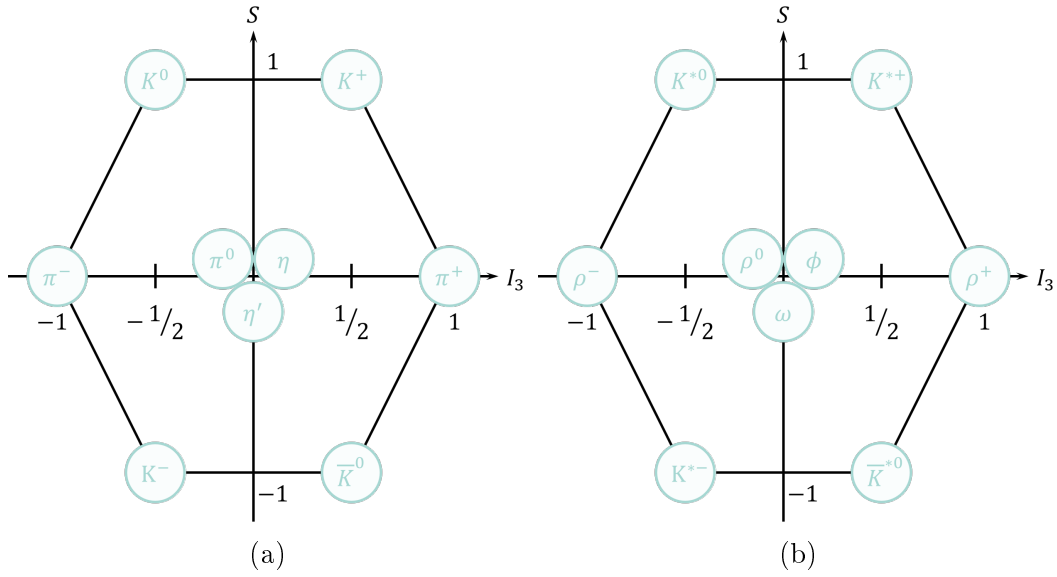


Figure 1.3: Pseudoscalar meson nonet with $J^P = 0^-$ (a) and vector meson nonet with $J^P = 1^-$ (b). The nonets are drawn in a $S - I_3$ system, where S is the strangeness and I_3 is the third component of the isospin.

The (valence) quark configuration of the pseudoscalar and vector mesons can be found in Table 1.1. The configuration of the physical η and η' mesons are thereby approximations, given indirectly through a mixing of the $SU(3)$ states η_1 and η_8 . They can be described by:

$$|\eta\rangle = |\eta_8\rangle \cos \theta - |\eta_1\rangle \sin \theta \quad |\eta'\rangle = |\eta_8\rangle \sin \theta + |\eta_1\rangle \cos \theta, \quad (1.3)$$

where $\theta = (-14.1 \pm 2.8)^\circ$ [56] is the mixing angle. The same description can be used for the physical ϕ and ω mesons, which are given through the ϕ_1 and ϕ_8 states in the same way as the η and η' mesons, but with a mixing angle of 36.4° [44]. Attention, the mixing angles are model dependent such that they

may differ in literature [44].

Meson	Quark content	Mass [MeV/c ²]	Main decay modes (\mathcal{BR} [%])
π^-	$d\bar{u}$	139.57039 ± 0.00017	$\mu^+\nu_\mu$ (99.98770 ± 0.00004)
π^+	$u\bar{d}$	139.57039 ± 0.00017	$\mu^-\bar{\nu}_\mu$ (99.98770 ± 0.00004)
π^0	$\frac{u\bar{u} - d\bar{d}}{\sqrt{2}}$	134.9768 ± 0.0005	2γ (98.823 ± 0.034)
η	$\frac{u\bar{u} + d\bar{d} - s\bar{s}}{\sqrt{3}}$	547.862 ± 0.017	2γ (39.41 ± 0.20) $3\pi^0$ (32.68 ± 0.23) $\pi^+\pi^-\pi^0$ (22.92 ± 0.28)
η'	$\frac{u\bar{u} + d\bar{d} + 2s\bar{s}}{\sqrt{6}}$	957.78 ± 0.06	$\pi^+\pi^-\eta$ (42.5 ± 0.5) $\rho^0\gamma$ (29.5 ± 0.4) $\pi^0\pi^0\gamma$ (22.4 ± 0.5)
ρ^-	$u\bar{d}$	775.11 ± 0.34	$\pi^+\pi^0$ (~ 100)
ρ^+	$d\bar{u}$	775.11 ± 0.34	$\pi^-\pi^0$ (~ 100)
ρ^0	$\frac{u\bar{u} - d\bar{d}}{\sqrt{2}}$	775.26 ± 0.25	$2\pi^0$ (~ 100)
ω	$\frac{u\bar{u} + d\bar{d}}{\sqrt{2}}$	786.65 ± 0.12	$\pi^+\pi^-\pi^0$ (89.3 ± 0.6)
ϕ	$s\bar{s}$	1019.461 ± 0.016	K^+K^- (49.2 ± 0.5) $K_L^0K_S^0$ (34.0 ± 0.4) $\rho^0\pi^0/\pi^+\pi^-\pi^0$ (15.24 ± 0.33)

Table 1.1: Quark configuration, mass and main decay modes with branching ratio (\mathcal{BR}) above 10 % for the lightest unflavoured pseudoscalar mesons (upper range) and vector mesons (lower range). Values taken from [44].

Baryons

Baryons are fermions made of three *main* quarks (or antiquarks). The valence quarks can have all their spins aligned or one spin in the opposite direction, resulting in a baryon spin of 3/2 or 1/2 in the ground state. The first has four spin projections and forms a spin-3/2 decuplet. The latter has two spin projections and forms a spin-1/2 octet.

Again, baryons in the ground state with angular momentum $l = 0$ and positive parity P are of particular interest.

The three lightest quarks - u , d , s - with their antiquarks build up an octet ($J^P = 1/2^+$) and a decuplet ($J^P = 3/2^+$). Due to the symmetry of the wave function, no ninth spin-1/2 particle exists in the ground state. The multiplets can be seen in Figure 1.4 in the $S - I_3$ plane, where S is the strangeness and I_3 is the third component of the isospin.

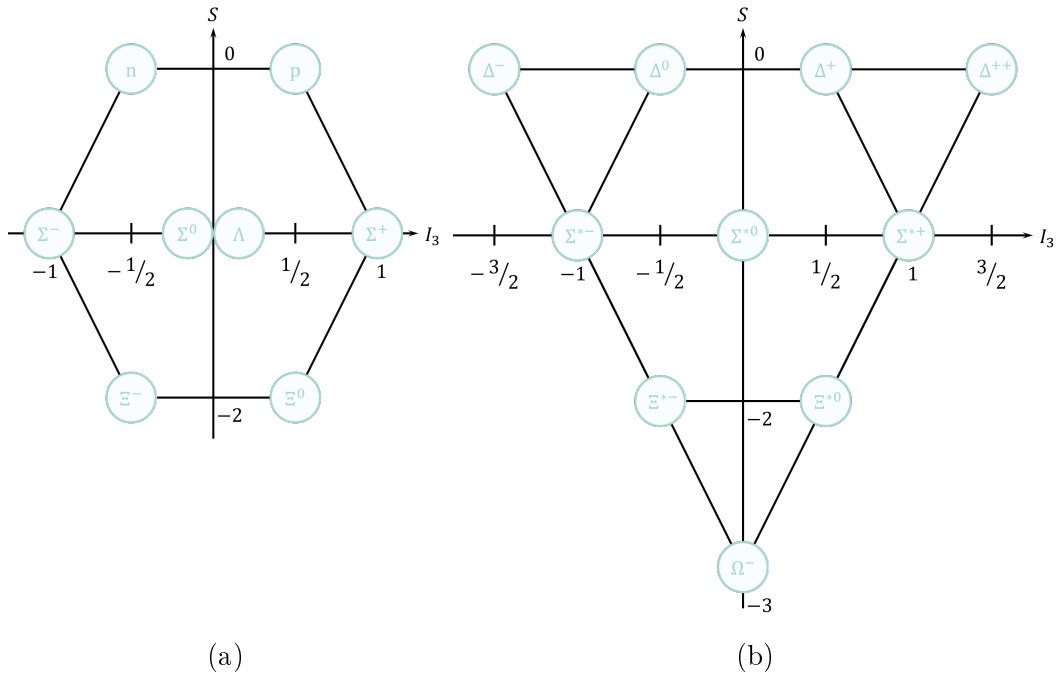


Figure 1.4: Baryon octet with $J^P = 1/2^+$ (a) and baryon decuplet with $J^P = 3/2^+$ (b). The multiplets are drawn in the $S - I_3$ system, where S is the strangeness and I_3 is the third component of the isospin.

The quark configuration of the lightest unflavoured ($S = C = B = T = 0$, Section 1.3.2) baryons in the ground state can be found in Table 1.2.

1.3.2 Flavour quantum numbers

Within the quark model and SM flavour is the species or type, respectively, of the elementary particles: quarks and leptons. Each one has six flavours. Similar to the quantum numbers of an electron, the state of quarks can be described by flavour quantum numbers.

Baryon	Quark content	Mass [MeV/c ²]	Main decay modes (\mathcal{BR} [%])
p	uud	$938.272\,081 \pm 0.000\,006$	stable
n	udd	$939.565\,413 \pm 0.000\,006$	$p e^- \bar{\nu}_e$ (~ 100)
Δ^-	ddd	1232 ± 2	$n\pi^-$ (99.4)
Δ^0	udd	1232 ± 2	$n\pi^0/p\pi^-$ (99.4)
Δ^+	uud	1232 ± 2	$n\pi^+/p\pi^0$ (99.4)
Δ^{++}	uuu	1232 ± 2	$p\pi^+$ (99.4)

Table 1.2: Quark configuration, mass and main decay modes with the branching ratio (\mathcal{BR}) for the lightest unflavoured baryons in the ground state. The proton (p) and neutron (n) have isospin $I = 1/2$, where the Δ baryons have $I = 3/2$. Values taken from [44].

Strangeness, charm, bottomness and topness

The strangeness S is equal to the difference between antistrange quarks $N_{\bar{s}}$ and strange quarks N_s :

$$S = -N_s + N_{\bar{s}}. \quad (1.4)$$

Similarly, the quantum numbers charm C , bottomness B' and topness T are given. Since the sign of a quark in the corresponding quantum number is defined to be equal to the sign of its electric charge Q , C and T subtract the antiquarks from the quarks, where B' does it the other way around - analogue to the strangeness.

Baryon number and lepton number

The baryon number B is equal to the number of baryons, which leads to the formula

$$B = \frac{1}{3} (N_q - N_{\bar{q}}), \quad (1.5)$$

where N_q is the number of quarks and $N_{\bar{q}}$ is the number of antiquarks inside a hadron. In a very similar way, the lepton number L and the lepton flavour numbers - L_e, L_μ, L_τ - are given as the difference between leptons and antileptons in total and as the difference in the corresponding flavours, respectively.

Isospin

The concept of isospin I was introduced by Werner Heisenberg in 1932 [57] to explain likewise behaviours of protons and neutrons. Thereby, $I = 1/2$ is equal for the proton and neutron, where the third component is $I_3 = +1/2$ for the proton and $I_3 = -1/2$ for the neutron. The name itself was first mentioned by Eugene Wigner in 1937 [58] to point out the similar behaviour to the spin. The third component of the isospin I_3 is given by:

$$I_3 = \frac{1}{2} (N_u - N_d - N_{\bar{u}} + N_{\bar{d}}), \quad (1.6)$$

where N_q are the number of corresponding up and down (anti)quarks. All other quarks have $I = I_3 = 0$.

Gell-Mann-Nishijima formula

Nakano and Nishijima [59], as well as Gell-Mann [60], found a connection between the electric charge Q of a hadron and the flavour quantum numbers for the light quarks (u, d, s), nowadays called Gell-Mann-Nishijima formula:

$$Q = I_3 + \frac{1}{2} (B + S). \quad (1.7)$$

This connection can also be seen in the hadron multiplets (Figures 1.3 and 1.4). If the hadron contains heavier quarks as well, Equation 1.7 can be generalised to

$$Q = I_3 + \frac{1}{2} (B + S + C + B' + T). \quad (1.8)$$

The strong interaction conserves all flavour quantum numbers, whereas the electroweak interaction only conserves baryon number, lepton number and lepton flavour numbers within the SM.

1.4 Nucleon resonances

Similar to the excitation of electrons in an atom, baryons can be excited, too. The proton and neutron are the most studied and interesting baryons, called nucleons.

1.4.1 Notation

Nucleons are the ground states ($l = 0$) of unflavoured baryons with isospin $I = 1/2$. Two types of excitations are thereby distinguished: N^* resonances with $I = 1/2$ and Δ resonances with $I = 3/2$.

The notation is given as $R(W)J^P$, $R_{JP}(W)$ or $R(W)$. Thereby, R is N^* or Δ , J^P is the total angular momentum J with parity P and W is the mass in MeV/c^2 of the resonance in the centre of mass (CM) frame. Excited states are also commonly given as $l_{2I2J}(W)$ or even $l_{2I2J}(W)J^P$, where l is the angular momentum and I the isospin. Prominent examples are $P_{33}(1232) = \Delta(1232)$ and $S_{11}(1535) = N(1535)$ the dominant resonances in π^0 and η photoproduction, respectively.

1.4.2 Experimental spectrum of nucleon resonances

The $\Delta(1232)$ and $N(1535)$ resonances are visible in the electron-proton scattering spectrum that can be seen in Figure 1.5a, whereas towards higher energies, it is tough to distinguish between the resonances as they begin to overlap. Therefore, other experiments, e.g. meson photoproduction, are better suited. Figure 1.5b shows the spectrum of photoproduction experiments on the proton with different final states, where in different final states, different resonances are visible.

1.4.3 Theoretical description through constituent quark model and lattice quantum chromodynamics

As mentioned, a perturbative treatment of the QCD theory is not applicable in the low-energy regime as the coupling constant α_s becomes very large, e.g. $\alpha_s \approx 0.3$ at $Q \approx 2 \text{ GeV}$ (Figure 1.2a). Effective theories, i.e. constituent quark

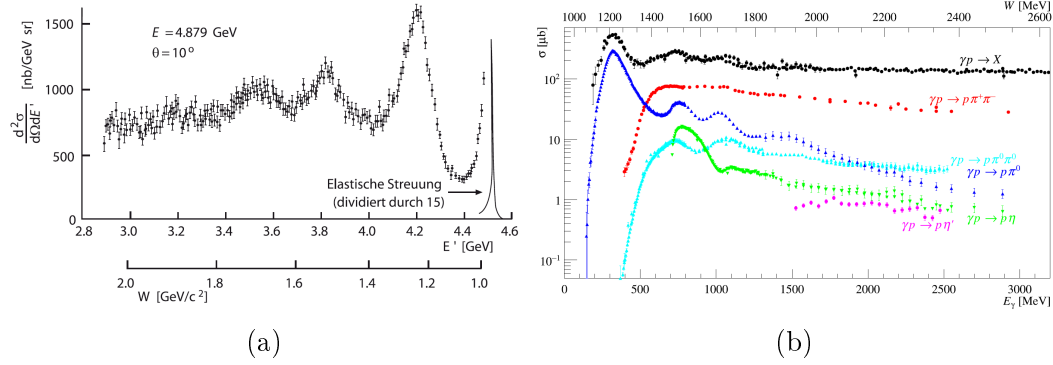


Figure 1.5: (a) Cross section of electron-proton scattering with a beam energy of 4.9 GeV at a scattering angle of 10° . (b) Cross section from photon-proton scattering with different final states. Figure (a) taken from [61] with data from the DESY experiment in 1968 [62]. Figure (b) taken from [63] with data from [64–74].

models, or theories with discretised spacetime, i.e. lattice QCD, are possible approximate solutions for this problem. Other approaches would be chiral perturbation theory [75], the Dyson-Schwinger and Bethe-Salpeter equation approach [76], or the holographic QCD [77]. See [63] for an overview.

Constituent quark model

The nucleon is built of three valence quarks and a sea of sea quarks and gluons. The latter two can be absorbed in the first and build constituent quarks, giving the nucleon its quantum numbers.

The mass of the u , d and s constituent quarks lies around $m_{u,d} \approx 330$ MeV and $m_s \approx 550$ MeV respectively [78–81], whereas their current masses, also called naked, *real* or permanent masses, are about $m_u = 2.16^{+0.49}_{-0.26}$ MeV, $m_d = 4.67^{+0.48}_{-0.17}$ MeV and $m_s = 93^{+11}_{-5}$ MeV [44]. The difference can be explained by taking the limit to massless quarks in the spontaneous chiral symmetry breaking in QCD [82, 83].

Interactions between sea quarks, gluons and valence quarks are all absorbed in the potential built by the three constituent quarks, which reduces the number of degrees of freedom (ndf). For large distances of ~ 2 fm [84] between the quarks, the potential usually increases linearly to ensure confinement. However, the potential may differ for shorter distances depending on the model. In the early days, a Coulomb-like potential $\sim 1/r$ with one gluon exchange was

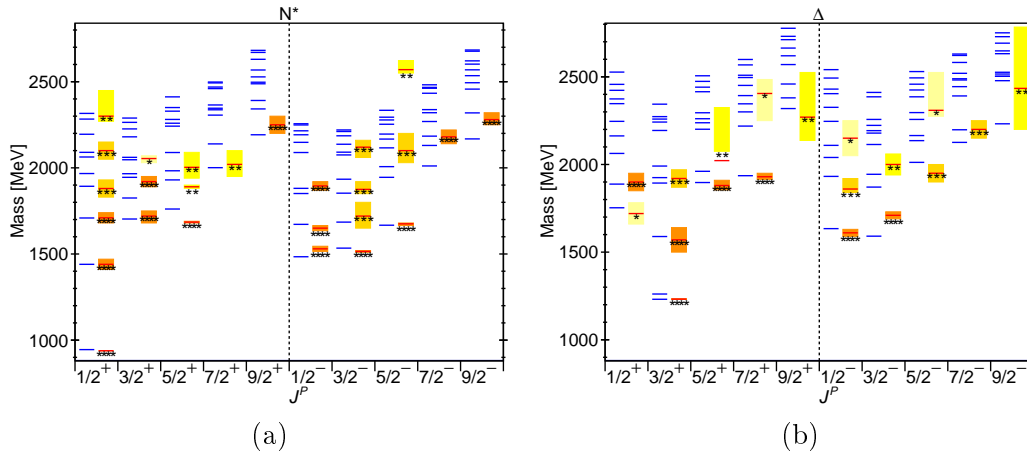


Figure 1.6: Experimentally observed N^* (a) and Δ (b) resonances listed by the Particle Data Group (PDG) [44] with the uncertainty given as coloured band compared to the relativistic constituent quark model of Ronniger and Metsch [81]. The number of stars (and darkness of colour) corresponds to the certainty of existence based on experimental findings: * * * existence certain and properties at least fairly well explored, * * * existence very likely certain but further confirmation and more research desirable, ** evidence of existence fair, * evidence of existence poor.

chosen [78], whereas more modern models [80,81] use chiral dynamics [85,86] with instanton interactions [87]. The models of Löring, Metsch and Petry [80], as well as of Ronniger and Metsch [81], use the relativistic covariant Bethe-Salpeter equation for calculating predictions.

Figure 1.6 shows the experimentally found N^* and Δ resonances listed by the Particle Data Group (PDG) [44] compared to the relativistic constituent quark model of Ronniger and Metsch [81]. The number of proposed resonances is much higher in the model than observed in experiments. This problem is referred to as *missing resonance problem*. This is even more astonishing as the model only has ten model parameters. In models with even fewer parameters, e.g. the one of Löring, Metsch and Petry [80] with seven, this problem still remains. The models can describe most low-lying states, whereas for higher-lying states, not even the order can be produced correctly.

It is unclear whether the *missing resonance problem* comes from the experimental or theoretical side. On the one hand, most of the identified resonances are from πN scattering, where many are predicted to have vanishing decay amplitudes [88]. On the other hand, the right ndf has not been found yet and

the quark model needs other interactions to describe nature.

Lattice quantum chromodynamics and further approaches

Another theoretical approach to calculating nucleon resonances is the discretisation of spacetime, where it is possible to solve QCD numerically. These lattice QCD models have another significant disadvantage (today): the extremely high computational power that is needed, even for calculating the lowest laying states [89].

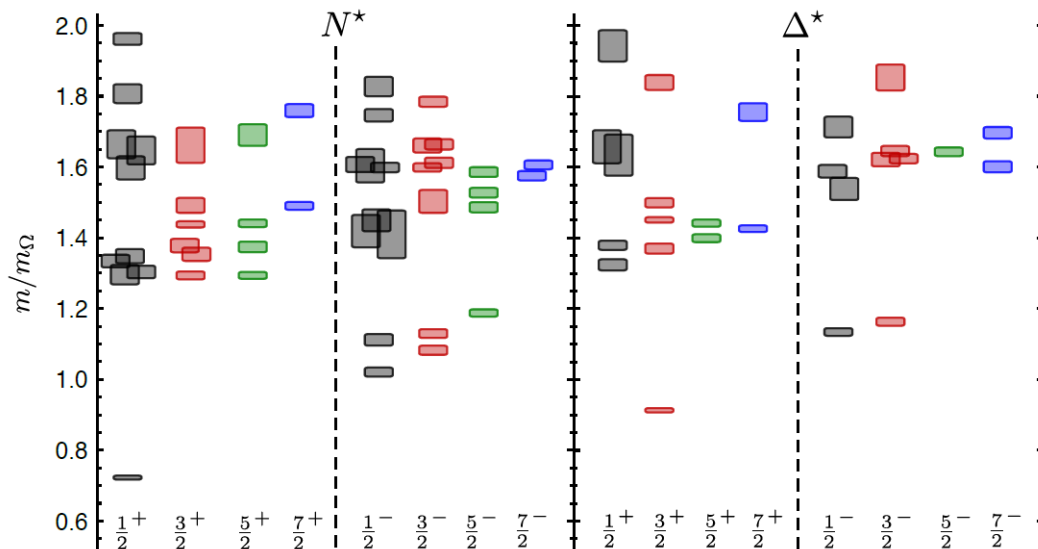


Figure 1.7: Predicted nucleon resonances from a lattice quantum chromodynamics calculation with a pion mass $m_\pi = 396$ MeV. Figure taken from [90].

A lattice QCD model with a pion mass of $m_\pi = 396$ MeV [90], which is more than twice as much as the real mass of about 139.6 MeV [44], can be seen in Figure 1.7. As for constituent quark models, there are more predicted states than experimentally observed. More recent calculations [91] use smaller pion masses of $m_\pi = 358$ MeV and $m_\pi = 278$ MeV. However, the predicted states are very similar compared to modern constituent quark models [80, 81] and disagree with the experimentally found ones. Moreover, naturally emerging hybrid states increase the resonance numbers even more [91].

1.5 Meson photoproduction

Photoproduction is the creation of particles in reactions with a photon in the initial state. Usually, photons are generated by the bremsstrahlung's process in electron accelerators and led onto a fixed target. Examples of such accelerator facilities include ELSA [92] in Bonn, Germany, MAMI [93] in Mainz, Germany and CEBAF [94] at the Jefferson Lab in Newport News, USA.

In contrast to meson scattering experiments, photoproduction has two major advantages: it is more sensitive in the search for missing resonances, i.e. some resonances couple very weakly to the πN channel [95], and it gives access to electromagnetic transition amplitudes. The drawback of photoproduction is the production of additional background terms like vector meson exchange, Kroll-Rudeman or Born terms. Neutral decay modes suppress some background terms and are of particular interest.

In the photoproduction of a single uncharged meson m on nucleon N , the initial and final states are given by γN and mN , respectively. The reaction can be described by:

$$\gamma N \rightarrow mN. \quad (1.9)$$

Because only exclusive photoproduction reactions are investigated within this work, the final state explicitly defines the complete reaction, e.g. ηn represents the reaction $\gamma n \rightarrow \eta n$.

π^0 and η differ by a crucial quantity: the isospin. The former has isospin 1 and the latter isospin 0. This results in very different couplings with isospin-1/2 particles like nucleons. π^0 couple to N^* and Δ resonances, whereas isospin conservation in the strong interaction only allows N^* resonances in η couplings. Thus, η serves as an isospin filter.

An example of a Feynman diagram for π^0 and η photoproduction on a nucleon can be found in Figure 1.8. The most dominant nucleon resonances - Δ (1232) for π^0 and N^* (1535) for η - are shown as intermediate states. Additionally, the angular momenta l or total angular momenta J , respectively, are given together with the parity P . The first vertex with the photon interaction is the electromagnetic vertex. The second one, where a meson is produced, is the strong vertex. They are called that way due to their dominant interactions.

For better readability and if not mentioned otherwise, N^* will be used as

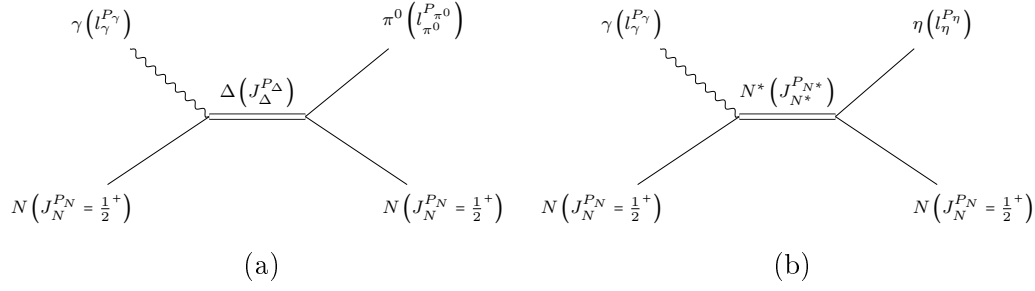


Figure 1.8: First order Feynman diagram for π^0 (a) and η (b) photoproduction on a nucleon N with their most dominant resonances $\Delta = \Delta(1232)$ and $N^* = N^*(1535)$ as their intermediate states. The angular momenta l or total angular momenta J , respectively, together with the parity P are given in brackets.

an abbreviation for both possible nucleon resonances, N^* and Δ , from now on. Furthermore, m is a general placeholder for π^0 , η or any neutral pseudoscalar meson.

Important for the description are the angular momenta of the particles. Nucleons have $J^P = 1/2^+$ in the ground state, whereas the initial photon can have different angular momenta and parities written as l_γ^P . The total angular momenta J and parity P of the resonance are therefore given by:

$$J_{N^*}^{P_{N^*}} = \left(l_\gamma \pm \frac{1}{2} \right)^{P_\gamma}. \quad (1.10)$$

1.5.1 Reaction types

Three types of reactions can be distinguished in meson photoproduction experiments off nuclei: quasifree, coherent and incoherent.

Coherent reactions off a nucleus A can be described by the reaction:

$$\gamma A \rightarrow mA. \quad (1.11)$$

Here, notice that the target nucleus stays unchanged in the ground state.

Incoherent reactions produce a meson together with the excitation of the nucleus to a state A^* , which then decays into the ground state by emitting a photon:

$$\gamma A \rightarrow mA^* \rightarrow mA\gamma. \quad (1.12)$$

The quasifree reaction, also called break-up reaction, happens on a nucleon

inside the nuclei while keeping the other nucleons unchanged. One speaks of the participant nucleon and the spectator nucleus. It can be described by:

$$\gamma N(A) \rightarrow mNA', \quad (1.13)$$

where A' is the remaining nucleus with a nucleon N less. For example, quasifree meson photoproduction on bound nucleons inside deuterium can be described by:

$$\gamma N(A) \rightarrow mnp, \quad (1.14)$$

where the reaction either happens on the proton and the neutron stays unchanged or vice versa. For better readability, the indicated deuterium nucleus in brackets is ignored from here on. If not mentioned otherwise, it is assumed that the reaction happens quasifree on a nucleon inside deuterium.

1.5.2 Kinematics

General four-vectors

A four-vector in natural units with $c = \hbar = 1$ is given by the energy E and the momentum $\vec{p} = (p_x, p_y, p_z)$:

$$p = (E, \vec{p}) = (E, p_x, p_y, p_z). \quad (1.15)$$

Here, the Minkowski metric [96] with the time component at the 0^{th} position is assumed to be generally valid.

An important property is energy-momentum conservation for real particles:

$$E^2 = m^2 + \vec{p}^2, \quad (1.16)$$

where m is the mass of the particle. Massless particles like the photon have an energy equal to the momentum, whereas particles at rest ($\vec{p} = 0$) have an energy equal to their mass.

Threshold energy

Reactions within this experiment can be described with Equation 1.14 and must fulfil energy-momentum conservation, also called four-momentum con-

servation:

$$p_\gamma + p_{N_t} = p_m + p_{N_r}. \quad (1.17)$$

Here, p is the four-momentum of the corresponding particle (from left to right): beam photon, target nucleon, measured meson, measured recoil nucleon. The second target nucleon inside deuterium - the spectator - is assumed to stay at rest with no interaction whatsoever.

The beam photon hits the target along the z -axis, such that its four-momentum is given by:

$$p_\gamma = (E_\gamma, 0, 0, E_\gamma). \quad (1.18)$$

If it is further assumed that the target nucleon is at rest, its four-momentum is given by:

$$p_{N_t} = (m_N, 0, 0, 0). \quad (1.19)$$

However, the nucleons in this experiment are bound in deuterium and experience Fermi momentum \vec{p}_F , such that the four-momentum of the target nucleon is given by:

$$p_{N_t} = \left(\sqrt{m_N^2 + \vec{p}_F^2}, \vec{p}_F \right). \quad (1.20)$$

Rearranging Equation 1.17, the Fermi momentum of the target nucleon is given by:

$$\vec{p}_F = \vec{p}_m + \vec{p}_{N_r} - \vec{p}_\gamma. \quad (1.21)$$

Squaring Equation 1.17 results in the Lorentz-invariant Mandelstam variable

$$s = W^2 = (p_\gamma + p_{N_t})^2 = (p_m + p_{N_r})^2, \quad (1.22)$$

where W is the CM energy. Assuming a target at rest, the CM energy is given by:

$$W = \sqrt{s} = \sqrt{m_N^2 + 2m_N E_\gamma}. \quad (1.23)$$

This equation also gives the threshold energy of η and π^0 photoproduction on free nucleons. Therefore, Equation 1.23 can be set equal to the minimal CM energy in the final state - $m_m + m_N$ - which results in

$$E_\gamma^{thr} = \frac{(m_m + m_N)^2 - m_N^2}{2m_N} = m_m + \frac{m_m^2}{2m_N}. \quad (1.24)$$

Since the experiment is performed on quasifree nucleons bound in deuterium,

Equation 1.24 is slightly modified:

$$E_\gamma^{thr} = \frac{(m_m + m_n + m_p)^2 - m_D^2}{2m_D} = \begin{cases} 630.75 \text{ MeV,} & \text{for } \eta \\ 142.22 \text{ MeV,} & \text{for } \pi^0 \end{cases}, \quad (1.25)$$

where $m_D = (1875.61294357 \pm 0.00000057) \text{ MeV}$ [97] is the mass of the deuterium nuclei. The nucleon masses can be found in Table 1.2.

1.5.3 Electromagnetic multipole expansion

The differential cross section (DCS) for meson photoproduction can be decomposed into a series of electromagnetic multipole amplitudes. Therefore, the angular momentum of the initial and final states must be decomposed. Real (on-shell) nucleons have a total angular momentum $J_N = 1/2$ and a positive parity $P_N = +1$. The beam photon γ carries the angular momentum l_γ relative to the target nucleon, whereas the parity depends on the multipole:

$$P_\gamma = \begin{cases} (-1)^{l_\gamma} & \text{for EL} \\ (-1)^{l_\gamma+1} & \text{for ML} \end{cases}. \quad (1.26)$$

EL and ML stand for electric and magnetic multipole, respectively.

The angular momentum and parity of the intermediate state N^* are constrained by the initial and final states:

$$\begin{aligned} |l_\gamma - J_N| \leq J_{N^*} \leq |l_\gamma + J_N| & \quad P_{N^*} = P_\gamma \cdot P_N \\ |l_m - J_N| \leq J_{N^*} \leq |l_m + J_N| & \quad P_{N^*} = P_m \cdot P_N. \end{aligned} \quad (1.27)$$

Together with the known momenta and parities of the nucleons, the conditions for the resonance are given by:

$$J_{N^*} = \left| l_\gamma \pm \frac{1}{2} \right| = \left| l_m \pm \frac{1}{2} \right| \quad P_{N^*} = P_\gamma = P_m. \quad (1.28)$$

Conservation of angular momentum and parity directly define EL and ML with the relation:

$$l_\gamma = \begin{cases} l_m \pm 1 & \text{for EL} \\ l_m & \text{for ML} \end{cases}. \quad (1.29)$$

l_γ	γ -MP	l_γ^P	$J_{N_i}^P$	$J_{N^*}^P$	l_m^P	$J_{N_f}^P$	MP	$p_\gamma^*/p_m^* d\sigma/d\Omega$
1	E1	1^-	$1/2^+$	$1/2^-$	0^-	$1/2^+$	E_{0+}	$ E_{0+} ^2$
				$3/2^-$	2^-	$1/2^+$	E_{2-}	$\frac{1}{2} E_{2-} ^2(5-3x^2)$
	M1	1^+	$1/2^+$	$1/2^+$	1^+	$1/2^+$	M_{1-}	$ M_{1-} ^2$
				$3/2^+$			M_{1+}	$\frac{1}{2} M_{1+} ^2(5-3x^2)$
2	E2	2^+	$1/2^+$	$3/2^+$	1^+	$1/2^+$	E_{1+}	$\frac{9}{2} E_{1+} ^2(1+x^2)$
				$5/2^+$	3^+	$1/2^+$	E_{3-}	$\frac{1}{9} E_{3-} ^2(1+6x^2-5x^4)$
	M2	2^-	$1/2^+$	$3/2^-$	2^-	$1/2^+$	M_{2-}	$\frac{9}{2} M_{2-} ^2(1+x^2)$
				$5/2^-$			M_{2+}	$\frac{1}{9} M_{2+} ^2(1+6x^2-5x^4)$

Table 1.3: Lowest lying electromagnetic multipoles (MP) for the reaction $\gamma N \rightarrow mN$. Thereby, m is a neutral pseudoscalar meson and N a nucleon, i.e. proton or neutron. The angular momenta J/l and parity P are given for the initial and final states. The differential cross section $d\sigma/d\Omega$ is given in terms of CGLN amplitudes [98,99] (Section 1.5.4). The $x = \cos(\theta)$ denotes the angular dependence, p_γ and p_m the four momenta of the photon and meson, respectively, and the star indicates the quantity in the centre of mass frame. As always, $\theta = \theta_m^*$ is the polar angle of the meson in the centre of mass frame.

The notation for multipoles is $E_{l_{m\pm}}$ and $M_{l_{m\pm}}$ depending on the multipole itself. The coupling between the final state nucleon and the meson defines the sign. For $J_{N^*} > 1/2$, always two multipoles - an EL and a ML - have the same angular distribution. This phenomenon is called the *Minami ambiguity* [100].

The lowest lying states with the information about the initial and final state configurations, the multipoles and the CGLN amplitudes representation can be found in Table 1.3. For example, the $N(1535)$ resonance has $J^P = 1/2^-$ such that it is a E_{0+} multipole with positive coupling in the final state.

1.5.4 Chew-Goldberg-Nambu-Low amplitudes

The transition probability in a scattering process like the ones shown in Figure 1.8 can be calculated by the scattering matrix S , which again can be expressed in terms of invariant matrix elements M_{fi} that describe the DCS [101]:

$$\frac{p_\gamma^*}{p_m^*} \frac{d\sigma}{d\Omega} = \frac{1}{2} \sum_{\text{spins}} |M_{fi}|^2, \quad (1.30)$$

where p_γ and p_m are the four momenta of the incident beam photon and the scattered meson, respectively, and * denotes the CM frame.

Using two-component spinors and Pauli matrices [102], the matrix elements can be expressed by the CM energy W , the nucleon mass m_N , the spinors of the initial and final states χ_i and χ_f and the matrix \mathcal{F} :

$$M_{fi} = \frac{4\pi W}{m_N} \cdot \chi_f^\dagger \mathcal{F} \chi_i. \quad (1.31)$$

Since the initial and final spin states are $\pm 1/2$, the spinors are given by:

$$\chi_{1/2} = \begin{pmatrix} 1 \\ 0 \end{pmatrix} \quad \chi_{-1/2} = \begin{pmatrix} 0 \\ 1 \end{pmatrix}. \quad (1.32)$$

One of the most common parametrisations of \mathcal{F} is the Chew-Goldberg-Nambu-Low (CGLN) one, which for photoproduction is given by [103]:

$$\begin{aligned} \mathcal{F}_{CGLN} = & iF_1 \vec{\sigma} \cdot \vec{\epsilon} + F_2 (\vec{\sigma} \cdot \hat{p}_m) (\vec{\sigma} \cdot (\hat{p}_\gamma \times \vec{\epsilon})) \\ & + iF_3 (\vec{\sigma} \cdot \hat{p}_\gamma) (\hat{p}_m \cdot \vec{\epsilon}) + iF_4 (\vec{\sigma} \cdot \hat{p}_m) (\hat{p}_m \cdot \vec{\epsilon}). \end{aligned} \quad (1.33)$$

Here, $\vec{\sigma}$ are the nucleon spin matrices, $\vec{\epsilon}$ the polarisation vector and F_i the four complex CGLN amplitudes. The latter depend on the CM energy W and the polar angle θ .

The CGLN amplitudes can be written as a series of magnetic and electric multipoles $M_{l\pm}$ and $E_{l\pm}$, respectively, and Legendre polynomials P_l :

$$\begin{aligned} F_1 &= \sum_{l=0}^{\infty} [(lM_{l+} + E_{l+})P'_{l+1} + ((l+1)M_{l-} + E_{l-})P'_{l-1}], \\ F_2 &= \sum_{l=0}^{\infty} [((l+1)M_{l+} + lM_{l-})P'_l], \\ F_3 &= \sum_{l=0}^{\infty} [(E_{l+} - M_{l+})P''_{l+1} + (E_{l-} + M_{l-})P''_{l-1}], \\ F_4 &= \sum_{l=0}^{\infty} [(M_{l+} - E_{l+} - M_{l-} - E_{l-})P''_l]. \end{aligned} \quad (1.34)$$

The Legendre polynomials are given by:

$$P_l = P_l(x) = \frac{1}{2^l l!} \frac{d^l}{dx^l} (x^2 - 1)^l, \quad (1.35)$$

where $x = \cos(\theta)$.

It can be seen that the CGLN amplitudes are directly connected with the parity, spin and angular momentum of a resonance. Taking Equations 1.30, 1.31 and 1.33, one obtains the DCS in terms of the CGLN amplitudes and angular distribution series in $x = \cos(\theta)$:

$$\begin{aligned} \frac{p_\gamma^*}{p_m^*} \frac{d\sigma}{d\Omega} = & \left(|F_1|^2 + |F_2|^2 + \frac{1}{2}|F_3|^3 + \frac{1}{2}|F_4|^3 + \text{Re}(F_1 F_3^*) \right) \\ & + (\text{Re}(F_3 F_4^*) - 2\text{Re}(F_1 F_2^*)) \cdot x \\ & - \left(\frac{1}{2}|F_3|^3 + \frac{1}{2}|F_4|^3 + \text{Re}(F_1 F_4^*) + \text{Re}(F_2 F_3^*) \right) \cdot x^2 \\ & - \text{Re}(F_3 F_4^*) \cdot x^3. \end{aligned} \quad (1.36)$$

1.5.5 Helicity amplitudes

Helicity amplitudes are a different approach to describing a reaction. Helicity λ is defined as [25]:

$$\lambda = \frac{\vec{s} \cdot \vec{p}}{|\vec{p}|}, \quad (1.37)$$

where \vec{s} is the spin vector and \vec{p} is the momentum vector. Photons have $\lambda_\gamma = \pm 1$ if they are transversely polarised and 0 if they are longitudinally polarised. Nucleons have $\lambda_N = \pm 1/2$ and pseudoscalar mesons like π^0 and η have $\lambda_m = 0$. The helicity matrix elements are given by [101]:

$$H_{N_f, \lambda_{\gamma N_i}} = \langle \lambda_{N_f} | T | \lambda_{\gamma N_i} \rangle, \quad (1.38)$$

where T is the transition matrix. Twelve elements exist, whereas only eight contribute to reactions with real photons. This number is further decreased to four due to parity conservation, resulting in:

$$\begin{aligned} H_1 & := H_{1/2, 3/2} = H_{-1/2, -3/2}, \\ H_2 & := H_{1/2, 1/2} = H_{-1/2, -1/2}, \\ H_3 & := H_{-1/2, 3/2} = H_{1/2, -3/2}, \\ H_4 & := H_{1/2, -1/2} = H_{-1/2, 1/2}, \end{aligned} \quad (1.39)$$

which are explicitly given by [101]:

$$\begin{aligned}
 H_1 &= \frac{1}{\sqrt{2}} e^{i\phi} \sin(\theta) \cos\left(\frac{\theta}{2}\right) \sum_{l \geq 0} [(B_{l+} - B_{(l+1)-})(P_l'' - P_{l+1}'')], \\
 H_2 &= \sqrt{2} \cos\left(\frac{\theta}{2}\right) \sum_{l \geq 0} [(A_{l+} - A_{(l+1)-})(P_l' - P_{l+1}')], \\
 H_3 &= \frac{1}{\sqrt{2}} e^{i\phi} \sin(\theta) \sin\left(\frac{\theta}{2}\right) \sum_{l \geq 0} [(B_{l+} - B_{(l+1)-})(P_l'' - P_{l+1}'')], \\
 H_4 &= \sqrt{2} \sin\left(\frac{\theta}{2}\right) \sum_{l \geq 0} [(A_{l+} - A_{(l+1)-})(P_l' - P_{l+1}')]. \tag{1.40}
 \end{aligned}$$

P_l are again the Legendre polynomials (Equation 1.35), θ the polar angle of the meson in the CM frame, ϕ the azimuthal angle and l is the nucleon-meson relative orbital angular momentum defining the total angular momentum in the final state $J = l \pm 1/2$. $A_{l\pm}$ and $B_{l\pm}$ are the helicity elements corresponding to $\lambda_{\gamma N_i} = 1/2$ and $\lambda_{\gamma N_i} = 3/2$ and are given by: [95]

$$\begin{aligned}
 A_{l\pm} &= \frac{1}{2} ((l+2)E_{l+} + M_{l+}), \\
 A_{(l+1)-} &= \frac{1}{2} (-lE_{(l+1)-} + (l+2)M_{(l+1)-}), \\
 B_{l+} &= E_{l+} - M_{l+}, \\
 B_{(l+1)-} &= E_{(l+1)-} + M_{(l+1)-}. \tag{1.41}
 \end{aligned}$$

These helicity elements are directly connected to the electromagnetic couplings from γN to N^* with $A_{1/2}$ and $A_{3/2}$ [95]. Nucleon resonances with $J = 1/2$ have only an $A_{1/2}$ component, whereas nucleon resonances with $J \geq 3/2$ also have an $A_{3/2}$ one. The DCS is given by:

$$\frac{p_\gamma^*}{p_m^*} \frac{d\sigma}{d\Omega} = \frac{1}{2} (H_1^2 + H_2^2 + H_3^2 + H_4^2). \tag{1.42}$$

1.5.6 Isospin amplitudes

Multipole amplitudes, e.g. CGLN or helicity amplitudes, can be decomposed into isospin amplitudes. As seen in Section 1.4 and the introduction of this section, N^* resonances can be produced in pseudoscalar photoproduction like $\pi^0 N$ and ηN final states, where Δ resonances can only be produced by isospin-1 particles like π^0 . Whether a vertex is affected by the strong or

the electromagnetic interaction is essential. The strong interaction conserves isospin and the third component of the isospin I_3 , whereas the electromagnetic interaction only conserves the latter.

Isospin amplitudes can be expressed in terms of an isoscalar component \hat{S} with $\Delta I = 0$, that is independent of I_3 , and an isovector component \hat{V} with $\Delta I = 0, \pm 1$ [104], that depends on I_3 . Together they result in the electromagnetic observable:

$$\hat{A}_{em} = \hat{S} + \hat{V}. \quad (1.43)$$

Generally, the matrix elements can be written as:

$$A = \langle I_f, I_{3,f} | \hat{A} | I_i, I_{3,i} \rangle, \quad (1.44)$$

which, for the $\pi^0 N$ final state, leads to the three independent elements [104]:

$$\begin{aligned} A^{IS} &= \left\langle \frac{1}{2}, \pm \frac{1}{2} \left| \hat{S} \right| \frac{1}{2}, \pm \frac{1}{2} \right\rangle, \\ A^{IV} &= \left\langle \frac{1}{2}, \pm \frac{1}{2} \left| \hat{V} \right| \frac{1}{2}, \pm \frac{1}{2} \right\rangle, \\ A^{V3} &= \left\langle \frac{3}{2}, \pm \frac{1}{2} \left| \hat{V} \right| \frac{3}{2}, \pm \frac{1}{2} \right\rangle. \end{aligned} \quad (1.45)$$

In case of the ηN final state, no A^{V3} term occurs. Taking the corresponding eigenstates, the amplitudes for π^0 and η photoproduction on nucleons are given by [101]

$$\begin{aligned} A(\gamma p \rightarrow \pi^0 p) &= \sqrt{\frac{2}{3}} \cdot A^{V3} + \sqrt{\frac{1}{3}} \cdot (A^{IV} - A^{IS}), \\ A(\gamma n \rightarrow \pi^0 n) &= \sqrt{\frac{2}{3}} \cdot A^{V3} + \sqrt{\frac{1}{3}} \cdot (A^{IV} + A^{IS}), \\ A(\gamma p \rightarrow \eta p) &= A^{IS} + A^{IV}, \\ A(\gamma n \rightarrow \eta n) &= A^{IS} - A^{IV}. \end{aligned} \quad (1.46)$$

The isospin amplitudes A become the same for Δ resonances in $\pi^0 p$ and $\pi^0 n$ final states if only A^{V3} contributes. However, for N^* resonances they are very different in π^0 and η photoproduction on nucleons.

1.6 Polarisation observables

Polarisation observables are an excellent tool to compare PWA with experimental findings. One of the most essential measurable quantities in nuclear and particle physics is the DCS $d\sigma/d\Omega$. Here, the DCS of a reaction can be seen as the probability that this reaction occurs at a specific energy and spatial angle. The total cross section (CS) σ can be found by integrating the DCS over the solid angle. Furthermore, the DCS can be split into polarisation observables and trigonometrical functions. In the following, all DCS could also be given as a function of the CM energy W instead of the incoming photon energy E_γ .

1.6.1 Unpolarised cross section

The unpolarised CS, marked with a 0 as index, is one of the 16 polarisation observables occurring in the general CS on pseudoscalar photoproduction. For the pure determination of polarisation observables, the unpolarised CS is not required to be known, whereas it always has to be known for absolute values, e.g. Legendre coefficients in $\mu\text{b sr}^{-1}$.

Total cross section

The CS can be seen as an energy-dependent event rate. In experiments, it can be found in two different ways.

The straightforward one is the integration of the DCS over the complete solid angle:

$$\sigma_0(E_\gamma) = \int_{\Omega} \left(\frac{d\sigma}{d\Omega} \right)_0(E_\gamma, x) d\Omega, \quad (1.47)$$

where $x = \cos(\theta)$. A sum can approximate the DCS over the angular bins:

$$\sigma_0(E_\gamma) \simeq \frac{4\pi}{N_{CT}} \cdot \sum_{i=1}^{N_{CT}} \left(\frac{d\sigma}{d\Omega} \right)_0. \quad (1.48)$$

In the second approach, the CS is given by the integral of Legendre fitting functions $f_l(E_\gamma, x)$ over x . This results in the Legendre coefficient A_0 , which

corresponds to the angular momentum $l = 0$:

$$\sigma_0(E_\gamma) = \int_{-1}^1 f_l(E_\gamma, x) dx = 4\pi \frac{p_\gamma^*}{p_m^*} A_0(E_\gamma). \quad (1.49)$$

Here, $p_{\gamma,m}^*$ are the four momenta of the photon γ and the meson m in the CM frame. The Legendre fitting functions are given by the Legendre coefficients $A_l(E_\gamma)$ and the Legendre Polynomials P_l (Equation 1.35):

$$f_l(E_\gamma, x) = \frac{p_\gamma^*}{p_m^*} \sum_{l=0}^N A_l(E_\gamma) P_l(x). \quad (1.50)$$

Differential cross section

The DCS can be split into an unpolarised DCS multiplied with terms containing polarisation observables (Section 1.6.2). Experimentally, the unpolarised DCS can be given as a normalised rate:

$$\left(\frac{d\sigma}{d\Omega}\right)_0(E_\gamma, x) = \frac{N(E_\gamma, x)}{N_\gamma(E_\gamma) \cdot \epsilon_{det}(E_\gamma, x) \cdot n_t \cdot \Gamma_i/\Gamma \cdot \Delta\Omega}, \quad (1.51)$$

where N is the yield, N_γ is the photon flux, ϵ_{det} is the detection efficiency, n_t is the target surface density, Γ_i/Γ is the branching ratio \mathcal{BR} and $\Delta\Omega = 4\pi/N_{CT}$ is the solid angle that is covered by the x bins. Furthermore, E_γ is the energy of the incident beam photon and $x = \cos(\theta)$ is the cosine of the polar angle θ of the measured meson in the CM frame.

1.6.2 Polarised cross section

General cross section

The CS can be written in terms of four complex amplitudes, e.g. CGLN (Section 1.5.4) or helicity (Section 1.5.5) amplitudes, which again can be decomposed in terms of electromagnetic multipoles or isospin amplitudes (Section 1.5.6).

The determination of the unpolarised DCS is insufficient for the unambiguous determination of the amplitudes and, thus, the multipole decomposition. Therefore, further observables are needed.

Observables can be categorised as single and double polarisation observ-

beam		target			recoil			target + recoil			
		x	y	z	-	-	-	x	x	z	z
		-	-	-	x'	y'	z'	x'	z'	x'	z'
-	σ_0	-	T	-	-	P	-	$T_{x'}$	$T_{z'}$	$L_{x'}$	$L_{z'}$
linear	$-\Sigma$	H	$(-P)$	G	$O_{x'}$	$(-T)$	$O_{z'}$	$(-L_{z'})$	$(L_{x'})$	$(T_{z'})$	$(-T_{x'})$
circular	-	F	-	$-E$	$C_{x'}$	-	$C_{z'}$	-	-	-	-

Table 1.4: The 16 polarisation observables that can be measured in pseudoscalar meson photoproduction: four of single type (σ_0 , Σ , T , P), four of beam-target type (H , G , F , E), four of beam-recoil type ($O_{x'}$, $O_{z'}$, $C_{x'}$, $C_{z'}$) and four of target-recoil type ($T_{x'}$, $T_{z'}$, $L_{x'}$, $L_{z'}$). The observables shown in brackets indicate another possibility for its measurement. The combinations containing y and y' for target + recoil are not shown since they do not contain additional information. All 16 polarisation observables could also be measured with triple polarisation measurements.

ables. The unpolarised DCS σ_0 forms together with the beam asymmetry Σ , the target asymmetry T and the recoil polarisation P the group of the single polarisation observables (\mathcal{S} -type).

Double polarisation observables are again categorised into three groups: beam-target (\mathcal{BT} -type), beam-recoil (\mathcal{BR} -type) and target-recoil (\mathcal{TR} -type). Photons can be polarised linearly or circularly, whereas the target and recoil nucleons can be polarised in the three spatial directions x , y , z and x' , y' , z' , respectively. Six combinations do not give additional information such that twelve double polarisation observables result in 16 polarisation observables in total (Table 1.4).

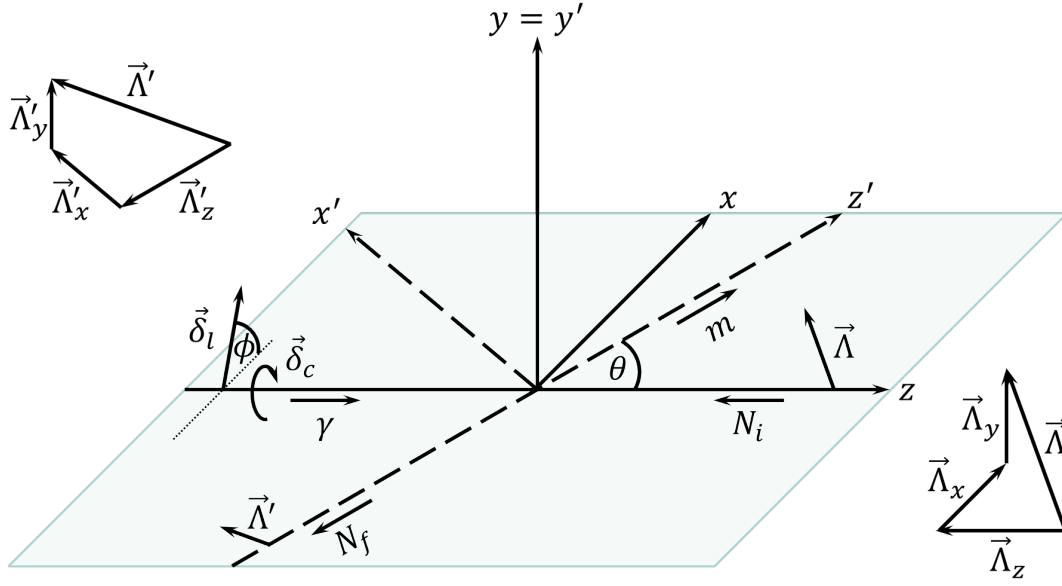


Figure 1.9: Coordinate systems in the centre of mass frame describing the general differential cross section in Equation 1.52. The reaction plane $x - z$ together with y define the initial state system, whereas the recoil plane $x' - z'$, shifted by θ with respect to the reaction plane, together with y' define the final state system. The general photon γ has a linear polarisation $\vec{\delta}_l$, including the angle ϕ with the reaction plane, and a circular polarisation $\vec{\delta}_c$. The initial state target nucleon N_i and final state recoil nucleon N_f have a polarisation vector $\vec{\Lambda}$ and $\vec{\Lambda}'$, respectively, that can be split into their spatial components.

Summarised, the general DCS is given by:

$$\begin{aligned}
 \frac{d\sigma}{d\Omega} = & \left(\frac{d\sigma}{d\Omega} \right)_0 \cdot \left\{ 1 \cdot [1 - \delta_l \Lambda_y \Lambda'_{y'}] - \Sigma \cdot [\delta_l \cos(2\phi) - \Lambda_y \Lambda'_{y'}] \right. \\
 & + T \cdot [\Lambda_y - \delta_l \Lambda'_{y'} \cos(2\phi)] + P \cdot [\Lambda'_{y'} - \delta_l \Lambda_y \cos(2\phi)] \\
 & - E \cdot [\delta_c \Lambda_z - \delta_l \Lambda_x \Lambda'_{y'} \sin(2\phi)] + F \cdot [\delta_c \Lambda_x + \delta_l \Lambda_z \Lambda'_{y'} \sin(2\phi)] \\
 & + G \cdot [\delta_l \Lambda_z \sin(2\phi) \delta_c \Lambda_x \Lambda'_{y'}] - H \cdot [\delta_l \Lambda_x \sin(2\phi) - \delta_c \Lambda_z \Lambda'_{y'}] \\
 & - C_{x'} \cdot [\delta_c \Lambda'_{x'} - \delta_l \Lambda_y \Lambda'_{z'} \sin(2\phi)] - C_{z'} \cdot [\delta_c \Lambda'_{z'} + \delta_l \Lambda_y \Lambda'_{x'} \sin(2\phi)] \\
 & - O_{x'} \cdot [\delta_l \Lambda'_{x'} \sin(2\phi) \delta_c \Lambda_y \Lambda'_{z'}] - O_{z'} \cdot [\delta_l \Lambda'_{z'} \sin(2\phi) - \delta_c \Lambda_y \Lambda'_{x'}] \\
 & + L_{x'} \cdot [\Lambda_z \Lambda'_{x'} + \delta_l \Lambda_x \Lambda'_{z'} \cos(2\phi)] + L_{z'} \cdot [\Lambda_z \Lambda'_{z'} - \delta_l \Lambda_x \Lambda'_{x'} \cos(2\phi)] \\
 & \left. + T_{x'} \cdot [\Lambda_x \Lambda'_{x'} - \delta_l \Lambda_z \Lambda'_{z'} \cos(2\phi)] + T_{z'} \cdot [\Lambda_x \Lambda'_{z'} + \delta_l \Lambda_z \Lambda'_{x'} \cos(2\phi)] \right\}, \tag{1.52}
 \end{aligned}$$

where the polarisation observables are written in front of the square brackets, $\delta_{l,c}$ are the degrees of the linearly (l) or circularly (c) polarised photon,

$\Lambda_{x,y,z}$ are the polarisation degrees of the target nucleon along the corresponding axis, $\Lambda'_{x',y',z'}$ are the polarisation degrees of the recoil nucleon along the corresponding axis and ϕ is the angle between the photon polarisation plane and the reaction plan. A detailed overview of the reaction within the defined coordinate systems can be found in Figure 1.9.

Complete experiment

Not all 16 polarisation observables are needed to unambiguously determine the four complex CGLN amplitudes. In 1975, the *BDS rule* derived by Barker, Donnachie and Storrow [105] claimed that nine suitable chosen observables - all \mathcal{S} -type observables and at least one \mathcal{BT} -, \mathcal{BR} - and \mathcal{TR} -type observable - are sufficient for the unambiguous determination of all amplitudes except a global phase. This is nowadays known as *complete experiment*.

In 1996, Keaton and Workman found that the BDS rule is not sufficient [106]. A year later, Chiang and Tabakin [107] showed that eight polarisation observables are sufficient for the unambiguous determination of the amplitudes: the four \mathcal{S} -type observables and four carefully chosen double polarisation observables.

In 2014, Wunderlich, Beck and Tiator [108] stated that only the four \mathcal{S} -type observables and one of \mathcal{BR} - or \mathcal{TR} -type are needed for a truncated partial wave analysis (PWA) with a truncation at $l_{max} = 4$ (ignoring H waves and higher ones). Nevertheless, one can also make statements about the contributions of specific resonances without knowing the complete experiment.

1.6.3 Electromagnetic multipole expansion of polarisation observables

As for the DCS, polarisation observables can also be expressed in terms of multipoles.

For simplification *profile functions* are introduced, where the observable itself is multiplied by the unpolarised CS:

$$\check{O} = O \cdot \left(\frac{d\sigma}{d\Omega} \right)_0. \quad (1.53)$$

The observables can then be written in terms of partial waves as a sum of

energy- and angular-dependent Legendre coefficients and Legendre polynomials:

$$P_l^m(x) = (1-x^2)^{m/2} \frac{d^m}{dx^m} P_l(x), \quad (1.54)$$

where $P_l(x)$ are the Legendre polynomials defined in Equation 1.35 and $x = \cos(\theta)$. The expansion has a cut-off l_{max} defining the highest order of included partial waves. In a truncated partial wave analysis, the observables are given by [109]:

$$\check{O} = \frac{p_\gamma^*}{p_m^*} \sum_{l=\beta}^{2l_{max}+\beta+\gamma} (A_{l_{max}})_l^{\check{O}}(W) P_l^\beta(x), \quad (1.55)$$

where p_γ^*/p_m^* is the phase space factor given by the four momenta of the photon and meson in the CM frame, W is the CM energy, $(A_{l_{max}})_l^{\check{O}}$ are the Legendre coefficients and β and γ are observable-dependent constants (Table 1.5).

Constant	σ	$\check{\Sigma}$	\check{T}	\check{P}	\check{H}	\check{G}	\check{E}	\check{F}
β	0	2	1	1	1	2	0	1
γ	0	-2	-1	-1	-1	-2	0	-1

Table 1.5: Constants β and γ for polarisation observables of single and beam-target type used in a truncated partial wave analysis. Values taken from [109].

For all polarisation observables of \mathcal{S} - and \mathcal{BT} -type the summation goes up to l_{max} since $\beta = -\gamma$. However, this is not the case for the other double polarisation types.

The Legendre coefficients can be interpreted in terms of multipoles by [109]:

$$(A_{l_{max}})_l^{\check{O}}(W) = \left\langle \mathcal{M}_{l_{max}}(W) \left| \mathcal{C}_l^{\check{O}} \right| \mathcal{M}_{l_{max}}(W) \right\rangle, \quad (1.56)$$

where $\mathcal{M}_{l_{max}}(W)$ contains the multipoles $E_{l\pm}$ and $M_{l\pm}$ and $\mathcal{C}_l^{\check{O}}$ is a Hermitian matrix. See [109] for more information.

Depending on the cut-off l_{max} , only certain partial waves can contribute, i.e. $l = 0$ corresponds to S waves, $l = 1$ to P waves, $l = 2$ to D waves and so on. See Table 1.6 for an overview.

1.6.4 Polarisation observables within this experiment

This experiment is performed with linearly polarised photons and transversely polarised nucleons in the initial state such that besides the unpolarised

l	P	MP	partial wave states
0 (S)	-	E_{0+}	$N1/2^-, \Delta1/2^-$ $S_{11}(1535)1/2^-$
1 (P)	+	$E_{1+}, M_{1\pm}$	$N1/2^+, N3/2^+, \Delta1/2^+, \Delta3/2^+$ $P_{11}(1440)1/2^+, P_{33}(1232)3/2^+$
2 (D)	-	$E_{2\pm}, M_{2\pm}$	$N3/2^-, N5/2^-, \Delta3/2^-, \Delta5/2^-$ $D_{13}(1520)3/2^-, D_{33}(1700)3/2^-$
3 (F)	+	$E_{3\pm}, M_{3\pm}$	$N5/2^+, N7/2^+, \Delta5/2^+, \Delta7/2^+$ $F_{15}(1680)5/2^+, F_{35}(1905)5/2^+$
4 (G)	-	$E_{4\pm}, M_{4\pm}$	$N7/2^-, N9/2^-, \Delta7/2^-, \Delta9/2^-$ $G_{17}(2190)7/2^-$
5 (H)	+	$E_{5\pm}, M_{5\pm}$	$N9/2^+, N11/2^+, \Delta9/2^+, \Delta11/2^+$ $H_{19}(2220)9/2^+, H_{311}(2420)11/2^+$

Table 1.6: Overview of partial waves and electromagnetic multipoles (MP) with their parity P and their dominant resonances listed by the Particle Data Group [44]. The notation is $l_{2I2J}(W)J^P$, i.e. l_{1x} are N^* resonances and l_{3x} are Δ resonances. Values taken from [109].

DCS, only the four polarisation observables Σ , T , P and H remain from Equation 1.52:

$$\frac{d\sigma}{d\Omega} = \left(\frac{d\sigma}{d\Omega} \right)_0 \cdot \{1 - \delta_l \Sigma \cos(2\phi) + \Lambda_y [T - \delta_l P \cos(2\phi)] - \delta_l \Lambda_x H \sin(2\phi)\}. \quad (1.57)$$

Taking CGLN amplitudes (Section 1.5.4) the polarisation observables can be described by [110]:

$$\begin{aligned} \check{\Sigma} &= -\frac{p_\gamma^*}{p_m^*} \sin^2(\theta) \cdot \text{Re} \left((F_3^* F_3 + F_4^* F_4) / 2 + F_2^* F_3 + F_1^* F_4 + F_3^* F_3 \cos(\theta) \right), \\ \check{T} &= \frac{p_\gamma^*}{p_m^*} \sin(\theta) \cdot \text{Im} \left(F_1^* F_3 - F_2^* F_4 + (F_1^* F_4 - F_2^* F_3) \cos(\theta) - F_3^* F_4 \sin^2(\theta) \right), \\ \check{P} &= -\frac{p_\gamma^*}{p_m^*} \sin(\theta) \cdot \text{Im} \left(2F_1^* F_2 + F_1^* F_3 - F_2^* F_4 - (F_2^* F_3 - F_1^* F_4) \cos(\theta) \right. \\ &\quad \left. - F_3^* F_4 \sin^2(\theta) \right), \\ \check{H} &= -\frac{p_\gamma^*}{p_m^*} \sin(\theta) \cdot \text{Im} \left(2F_1^* F_2 + F_1^* F_3 - F_2^* F_4 + (F_1^* F_4 - F_2^* F_3) \cos(\theta) \right). \end{aligned} \quad (1.58)$$

As with CGLN amplitudes, the polarisation observables can also be expressed with helicity amplitudes (Section 1.5.5) [105]:

$$\begin{aligned}
 \check{\Sigma} &= 2 \operatorname{Re} (H_1^* H_2 - H_3^* H_4), \\
 \check{T} &= 2 \operatorname{Im} (H_4^* H_1 - H_3^* H_2), \\
 \check{P} &= 2 \operatorname{Im} (H_4^* H_2 - H_3^* H_1), \\
 \check{H} &= -2 \operatorname{Im} (H_3^* H_1 - H_4^* H_2).
 \end{aligned} \tag{1.59}$$

Polarisation observables in a truncated partial wave analysis

As seen in Section 1.6.3, polarisation observables can be expressed in terms of Legendre polynomials. Inserting the constants β and γ and taking out the $(1-x^2)^{m/2}$ factor in $P_l^m(x)$, the investigated observables in this experiment can be written as:

$$\begin{aligned}
 \check{\Sigma} &= \frac{p_\gamma^*}{p_m^*} \sin^2(x) \sum_{l=2}^{2l_{max}} (A_{l_{max}})_l^{\check{\Sigma}}(W) P_l''(x), \\
 \check{T} &= \frac{p_\gamma^*}{p_m^*} \sin(x) \sum_{l=1}^{2l_{max}} (A_{l_{max}})_l^{\check{T}}(W) P_l'(x), \\
 \check{P} &= \frac{p_\gamma^*}{p_m^*} \sin(x) \sum_{l=1}^{2l_{max}} (A_{l_{max}})_l^{\check{P}}(W) P_l'(x), \\
 \check{H} &= \frac{p_\gamma^*}{p_m^*} \sin(x) \sum_{l=1}^{2l_{max}} (A_{l_{max}})_l^{\check{H}}(W) P_l'(x).
 \end{aligned} \tag{1.60}$$

It can be seen that $\check{\Sigma}$ has $(2l_{max} - 1)$ Legendre coefficients, whereas \check{T} , \check{P} and \check{H} have $2l_{max}$. The derivatives of the Legendre polynomials P_l'' and P_l' are done with respect to x .

Polarisation observables in the detector system

A coordinate system describing the detector system of the experiment is better suited for describing the particles and their polarisation degrees. Therefore, the reaction coordinate system is rotated around the beam axis, i.e. z -axis. The meson is rotated by $\phi' = \alpha - \phi$, the photon polarisation plane is rotated by α and the nucleon polarisation plane is rotated by β . The polarisation degree of the photon is given by δ , whereas the nucleon polarisation degree is Λ . See Figure 1.10 for more details.

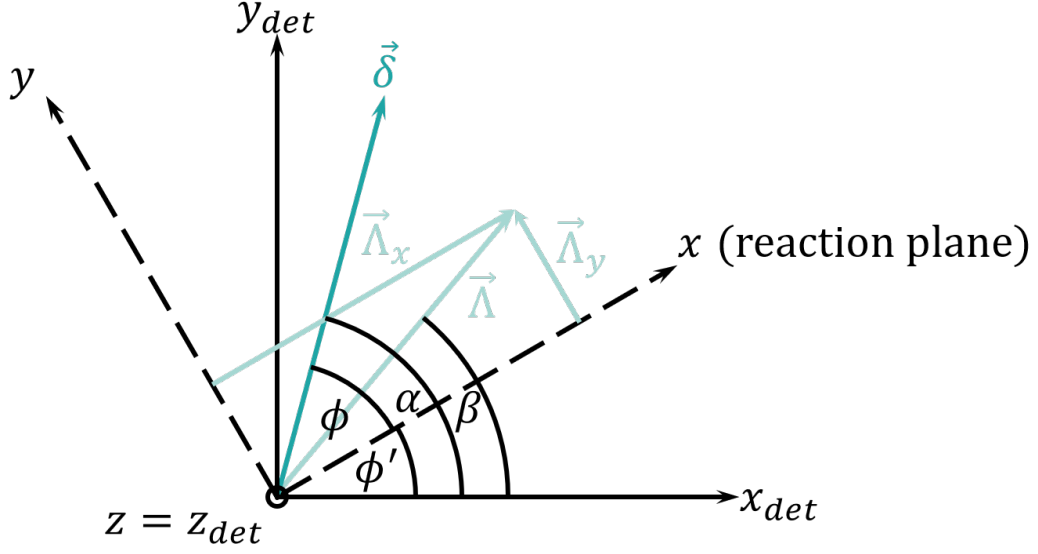


Figure 1.10: Relation between the coordinate systems used in Equation 1.57 (x, y, z) and the detector coordinate system used in Equation 1.61 ($x_{det}, y_{det}, z_{det}$). The latter is rotated by $-\phi'$ around the z -axis. The photon polarisation degree is given by $\delta = |\vec{\delta}|$, the nucleon polarisation degree by $\Lambda = |\vec{\Lambda}|$. The z -axis points out of the paper.

Thus, the DCS in the detector coordinate system is given by:

$$\begin{aligned} \frac{d\sigma}{d\Omega} = \left(\frac{d\sigma}{d\Omega} \right)_0 \cdot \{ & 1 - \delta\Sigma \cos(2(\alpha - \phi')) + \Lambda T \sin(\beta - \phi') \\ & - \delta\Lambda P \cos(2(\alpha - \phi')) \sin(\beta - \phi') \\ & - \delta\Lambda H \sin(2(\alpha - \phi')) \cos(\beta - \phi') \}. \end{aligned} \quad (1.61)$$

For simplicity, the angle ϕ' is redefined to $\phi := \phi'$ from now on.

Asymmetries in the detector system

The different polarisation terms in Equation 1.61 can be defined as asymmetries, which can be connected to the DCS of the corresponding polarisation planes. For easier readability, the DCS $d\sigma/d\Omega$ is replaced by the CS σ in the

following equations:

$$A_{\Sigma}(\phi) = \frac{1}{\delta} \frac{\sigma^{\perp} - \sigma^{\parallel}}{\sigma^{\perp} + \sigma^{\parallel}} = \Sigma \cos(2(\alpha - \phi)), \quad (1.62)$$

$$A_T(\phi) = \frac{1}{\Lambda} \frac{\sigma_{\uparrow} - \sigma_{\downarrow}}{\sigma_{\uparrow} + \sigma_{\downarrow}} = T \sin(\beta - \phi), \quad (1.63)$$

$$A_{PH}(\phi) = \frac{1}{\delta\Lambda} \frac{\sigma_{\uparrow}^{\perp} - \sigma_{\downarrow}^{\perp} - \sigma_{\uparrow}^{\parallel} + \sigma_{\downarrow}^{\parallel}}{\sigma_{\uparrow}^{\perp} + \sigma_{\downarrow}^{\perp} + \sigma_{\uparrow}^{\parallel} + \sigma_{\downarrow}^{\parallel}} = P \cos(2(\alpha - \phi)) \sin(\beta - \phi) + H \sin(2(\alpha - \phi)) \cos(\beta - \phi), \quad (1.64)$$

where σ^{\parallel} and σ^{\perp} are the DCS belonging to the beam polarisation angles α^{\parallel} and $\alpha^{\perp} = \alpha^{\parallel} + 90^{\circ}$, i.e. $\pm 45^{\circ}$, and σ_{\uparrow} and σ_{\downarrow} are the DCS belonging to the target polarisation angles β_{\uparrow} and $\beta_{\downarrow} = \beta_{\uparrow} + 180^{\circ}$, i.e. 90° and 270° .

1.7 Current status of theory and experiment

1.7.1 Theoretical description with partial wave analyses

Multiple theoretical models describe the experimental data adequately. Proper partial wave analyses (PWA) make theoretical assumptions and fit the experimental data to get resonances. They are therefore the connection point between theory and experiment. The most common PWA are either proper partial wave analyses (PWA) like the Scattering Analysis Interactive Dial-in (SAID) [111] or isobar models like the Bonn-Gatchina (BnGa) [112] and Mainz Unitary Isobar Model (MAID) [113]. PWA decomposes observables in terms of partial waves with $E_{l\pm}$ and $M_{l\pm}$ multipoles containing resonant and background terms. They usually get the parameters from fitting the resonances with a Breit-Wigner function. Isobar models, on the other hand, fit the data with already parametrised resonant and background terms.

Besides the here discussed models, there exist other PWA approaches, e.g. Jülich-Bonn (JüBo) with a dynamical coupled-channel model using the S -matrix [114] or the Giessen Model using a coupled-channel unitary Lagrangian approach [115].

The most common description of a resonance is with a Breit-Wigner function [116]. The amplitude is given by [44]:

$$A(W) = \frac{\tilde{\alpha}}{W_R^2 - W^2 - iW\Gamma_R}, \quad (1.65)$$

where $\tilde{\alpha}$ contains the resonance coupling in the initial and final states, W_R is the mass of the resonance, $W = \sqrt{s}$ is the CM energy and Γ_R is the width of the resonance. However, this parametrisation only results in the resonance's correct mass and width if it does not overlap with other resonances, e.g. $\Delta(1232) 3/2^+$. Otherwise, the K -matrix approach, directly connected to the scattering matrix S , results in more reasonable resonances [117].

The following subsections briefly describe the SAID, BnGa and MAID models. The CS from their predictions can be seen in Figure 1.11. The different models have only minor differences in the CS, whereas they may differ quite strongly in certain polarisation observable predictions. A more detailed dis-

cussion and comparison of different PWA models can be found in [63].

$R(W[\text{MeV}])$	J^P	Total	πN	ηN	PWA
$p(938)$	$1/2^+$	****	****	****	♠♥♣◇
$n(939)$	$1/2^+$	****	****	****	♠♥♣◇
$N(1440)$	$1/2^+$	****	****	****	♠♥♣◇
$N(1520)$	$3/2^-$	****	****	****	♠♥♣◇
$N(1535)$	$1/2^-$	****	****	****	♠♥♣◇
$N(1650)$	$1/2^-$	****	****	****	♠♥♣◇
$N(1675)$	$5/2^-$	****	****	*	♠♥♣◇
$N(1680)$	$5/2^+$	****	****	*	♠♥♣◇
$N(1700)$	$3/2^-$	***	**	*	♠♥◇
$N(1710)$	$1/2^+$	****	****	**	♠♥◇
$N(1720)$	$3/2^+$	****	****	*	♠♥♣◇
$N(1860)$	$5/2^+$	**	**	*	♠◇
$N(1875)$	$3/2^-$	**	**	*	♠♥◇
$N(1880)$	$1/2^+$	**	*	*	♠♥◇
$N(1895)$	$1/2^-$	****	*	****	♠♥◇
$N(1900)$	$3/2^+$	****	**	*	♠♥◇
$N(1990)$	$7/2^+$	**	**	*	♠♥◇
$N(2000)$	$5/2^+$	**	*	*	♠♥♣◇
$N(2040)$	$3/2^+$	*	*		
$N(2060)$	$5/2^-$	**	**	**	♠♥◇
$N(2100)$	$1/2^+$	**	**	*	♠♥◇
$N(2120)$	$3/2^-$	**	**		♠♥◇
$N(2190)$	$7/2^-$	****	****	*	♠♥♣◇
$N(2220)$	$9/2^+$	****	****	*	♥♣◇
$N(2250)$	$9/2^-$	****	****	*	♠♥♣◇
$N(2300)$	$1/2^+$	**	**		
$N(2570)$	$5/2^-$	**	**		
$N(2600)$	$11/2^-$	**	**		♣
$N(2700)$	$13/2^+$	**	**		♠

Table 1.7: N^* resonances listed by the Particle Data Group [44] with the certainty of their existence: **** existence certain and properties at least fairly well explored, *** existence very likely certain but further confirmation and more research desirable, ** evidence of existence fair, * evidence of existence poor. πN and ηN indicate the observed certainty in photoproduction experiments and the corresponding final state. The last column indicates the partial wave analyses (PWA) that include the specific resonance in its model: ♠ Eta-MAID 2018, ♥ BnGa 2019 and BnGa 2022, ♣ SAID MA19, ◇ MAID 2021.

Tables 1.7 and 1.8 show the resonances from the PDG [44] and their certainty of existence. Different PWA include different resonances in their models,

$R(W[\text{MeV}])$	J^P	Total	πN	PWA
$\Delta(1232)$	$3/2^+$	***	***	♥♣◇
$\Delta(1600)$	$3/2^+$	***	**	♥♣◇
$\Delta(1620)$	$1/2^-$	***	***	♥♣◇
$\Delta(1700)$	$3/2^-$	***	***	♥♣◇
$\Delta(1750)$	$1/2^+$	*	*	
$\Delta(1900)$	$1/2^-$	**	**	♥◇
$\Delta(1905)$	$5/2^+$	***	***	♥♣◇
$\Delta(1910)$	$1/2^+$	***	***	♥♣◇
$\Delta(1920)$	$3/2^+$	**	**	♥◇
$\Delta(1930)$	$5/2^-$	**	**	♣◇
$\Delta(1940)$	$3/2^-$	**	**	♥
$\Delta(1950)$	$7/2^+$	***	***	♥◇
$\Delta(2000)$	$5/2^+$	**	**	♥◇
$\Delta(2150)$	$1/2^-$	*	*	
$\Delta(2200)$	$7/2^-$	**	**	♥◇
$\Delta(2300)$	$9/2^+$	**	**	◇
$\Delta(2350)$	$5/2^-$	*	*	
$\Delta(2390)$	$7/2^+$	*	*	
$\Delta(2400)$	$9/2^-$	**	**	♣◇
$\Delta(2420)$	$11/2^+$	***	***	♣
$\Delta(2750)$	$13/2^-$	**	**	
$\Delta(2950)$	$15/2^+$	**	**	

Table 1.8: Δ resonances listed by the Particle Data Group [44] with the certainty of their existence: *** existence certain and properties at least fairly well explored, ** existence very likely certain but further confirmation and more research desirable, * evidence of existence fair, * evidence of existence poor. πN and ηN indicate the observed certainty in photoproduction experiments and the corresponding final state. The last column indicates the partial wave analyses (PWA) that include the specific resonance in its model: ♥ BnGa 2019 and BnGa 2022, ♣ SAID MA19, ◇ MAID 2021.

which is indicated as well. The two models BnGa 2019 and BnGa 2022 do include the exactly same resonances.

Scattering Analysis Interactive Dial-in

Scattering Analysis Interactive Dial-in (SAID) is a proper PWA fitting a large database of pion-nucleon scattering, electro- and photoproduction data [111]. It has been developed by the George Washington University in Washington DC, USA.

The resonance parameters are found from a fit to elastic pion scattering, where the multipole contributions are found from a fit to all data with the K -matrix formalism [118]. Thereby, the matrix elements are energy-dependent polynomials of order 5.

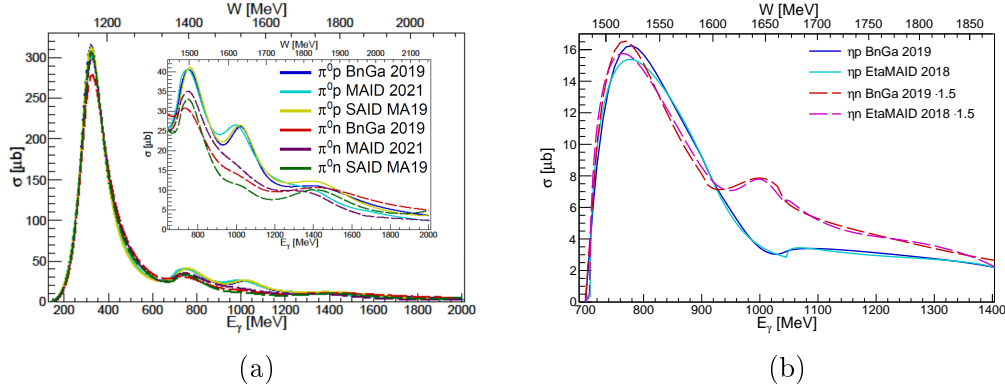


Figure 1.11: Total cross section σ as a function of the incident photon energy E_γ and centre of mass energy W for the partial wave analyses models BnGa 2019 [119], MAID 2021 [120], SAID MA19 [121] and EtaMAID 2018 [122] in π^0 (a) and η (b) photoproduction on the proton and the neutron.

Most data are only available for photoproduction on the proton and only used to determine the couplings in γN such that they do not provide new resonances [123, 124]. However, the most recent model - SAID MA19 - is available for both $\pi^0 p$ and $\pi^0 n$ final states [121].

Bonn-Gatchina

Bonn-Gatchina (BnGa) is a coupled channel PWA that fits pion scattering data together with photoproduction data [112]. It has been developed by the Rheinische Friedrich-Wilhelms-Universität Bonn in Bonn, Germany, and the Petersburg Nuclear Physics Institute (PNPI) in Gatchina, Russia.

In the low-energy region, the K -matrix approach is applied, whereas some high-energy resonances ($W > 2.2$ GeV) are parametrised with relativistic multi-channel Breit-Wigner amplitudes [125]. Besides the unpolarised CS, polarisation observable data are included as well. Data are taken from pion-induced reactions $\pi N \rightarrow \pi N$, $\pi^- p \rightarrow \eta n, K^0 \Lambda, K^0 \Sigma^0, \pi^0 \pi^0 n$, $\pi^+ p \rightarrow K^+ \Sigma^+$ and photon induced reactions $\gamma p \rightarrow \eta p, \pi^0 p, \pi^+ n, K^+ \Lambda, K^+ \Sigma, K^0 \Sigma^+, \pi^0 \pi^0 p, \pi^0 \eta p$ [125]. Background terms, i.e. Born terms, t -channel and u -channel processes, are also included in the fit.

The most recent model available for all observables in the final states $\pi^0 N$ and ηN is the BnGa 2019 [119]. An even more recent one, BnGa 2022-02, is on the way [126].

Mainz Isobar Model

The Mainz Isobar Model (MAID) is a unitary isobar model developed by the Johannes Gutenberg Universität in Mainz, Germany [93].

The T -matrix approach is used and resonances are expressed as multi-channel Breit-Wigner functions [127]. The MAID 2007 model includes the photoproduction $\gamma p \rightarrow \pi^0 p, \pi^+ n, \eta p$, whereas the updated EtaMAID 2018 model also includes the reactions $\gamma p \rightarrow \eta'$ and $\gamma n \rightarrow \eta n, \eta' n$ [122]. Background terms, i.e. Born terms, s -channel, t -channel and u -channel processes, are also included in the fit.

The most recent model for the final state ηN is the EtaMAID 2018 [122], whereas the most recent one for the $\pi^0 N$ final state is the MAID 2021 [120]. However, MAID 2021 has yet to be finalised. The total CS is shown in Figure 1.11 anyway, as it will not change much any more and results in a good description. On the other hand, polarisation observables are much more sensitive to the fitted data and show a discrepancy if the model is not finalised.

1.7.2 Observed narrow structure in ηn around 1.68 GeV

One of the primary motivations for η photoproduction on the neutron with a coherent edge at $E_\gamma = 1200$ MeV - corresponding to $W \approx 1770$ MeV - is the investigation of the observed narrow structure in the differential and total CS [128–132] and in the helicity-dependent CS [133] (Figure 1.12).

Different explanations try to explain the narrow structure visible in the CS of ηn but not in ηp . It might originate from an intrinsic resonance [134, 135], strangeness loops [136], coupled channel effects [137, 138] or interferences of already known resonances [122, 133, 139, 140].

A helicity-dependent experiment [133] led to a further interesting behaviour of the narrow structure: it is not visible in the helicity-3/2 CS but very prominent in the helicity-1/2 one, indicating a direct relation to the S_{11} or P_{11} partial waves. However, since the structure can be described with interference effects (Figure 1.13a) [122, 140] and with a narrow $N(1685)1/2^+$ resonance (Figure

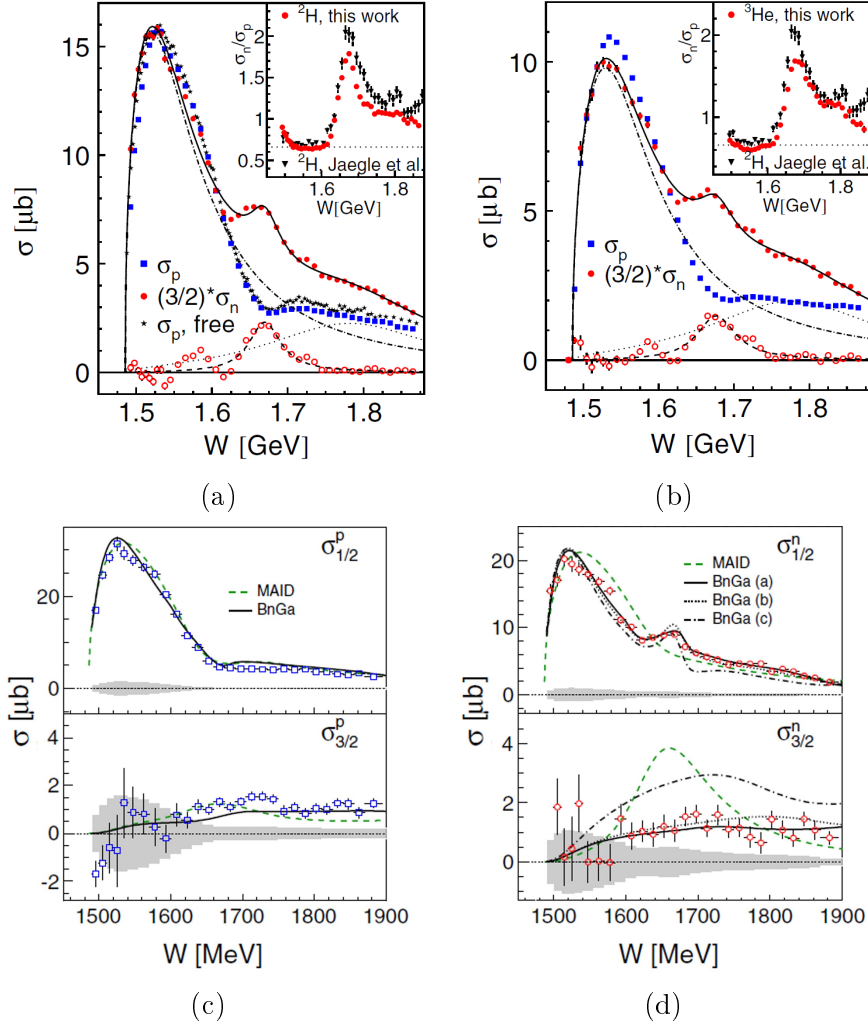


Figure 1.12: Total cross section of ηp and ηn final states in exclusive photoproduction reactions on nucleons bound in deuterium (a) and He-3 (b) as well as helicity-dependent cross sections for ηp (c) and ηn (d). Figures (a) and (b) taken from [132]. Figures (c) and (d) adapted from [133].

1.13b) [141] the puzzle is not yet solved.

In conclusion, whether the narrow structure in the ηn CS is caused by interference effects, a new resonance, or even something else cannot be said. If the origin is an interference effect, it should be clarified which one.

1.7.3 Experimental data situation

Numerous experiments have already been performed investigating most of the different polarisation observables in π^0 and η photoproduction [111].

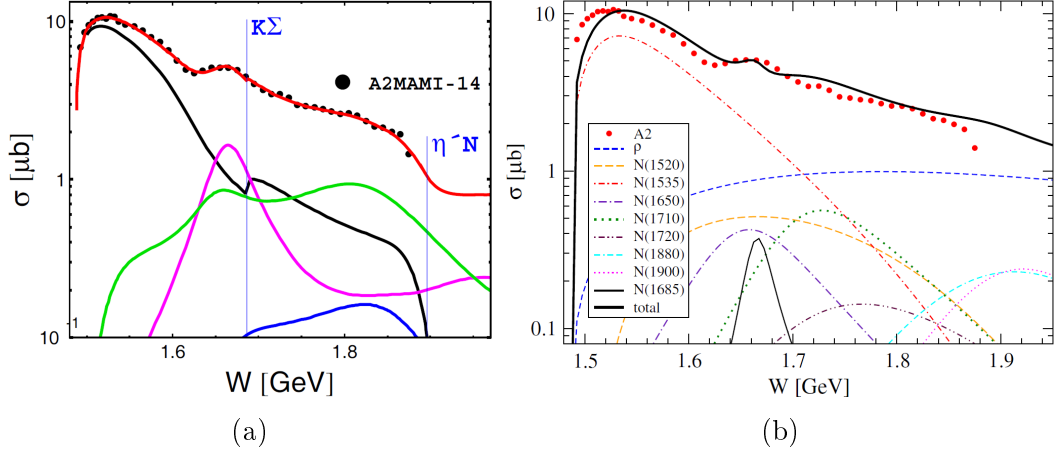


Figure 1.13: Two models that fit the cross section of ηn : (a) without additional resonance, (b) with one. Figure (a) adapted from [122]. Figure (b) taken from [141].

However, most of the observables are only available in a certain kinematic region and mainly for π^0 photoproduction on protons or π^\pm photoproduction on nucleons.

The current data situation for the polarisation observables Σ , T , P and H in π^0 and η photoproduction can be seen in Figures 1.14-1.17. The kinematic range covered by this experiment can be seen as light grey boxes.

Previous experiments studied the reaction $\pi^0 p$ the most, such that high statistical data exist for all four observables. The same is true for the beam asymmetries in the here studied reactions and the target asymmetry in ηp . These data are perfectly suited for cross-checking the correctness of the analysis in this work. Σ in $\pi^0 n$ as well as P and H in ηp can kinematically be extended for higher energies. Most interesting are the observables T , P and H in $\pi^0 n$ and ηn , which is determined with this experiment for the first time.

The data that is marked with a *, i.e. Stausberg 2019, is not finalised but *good* preliminary ones.

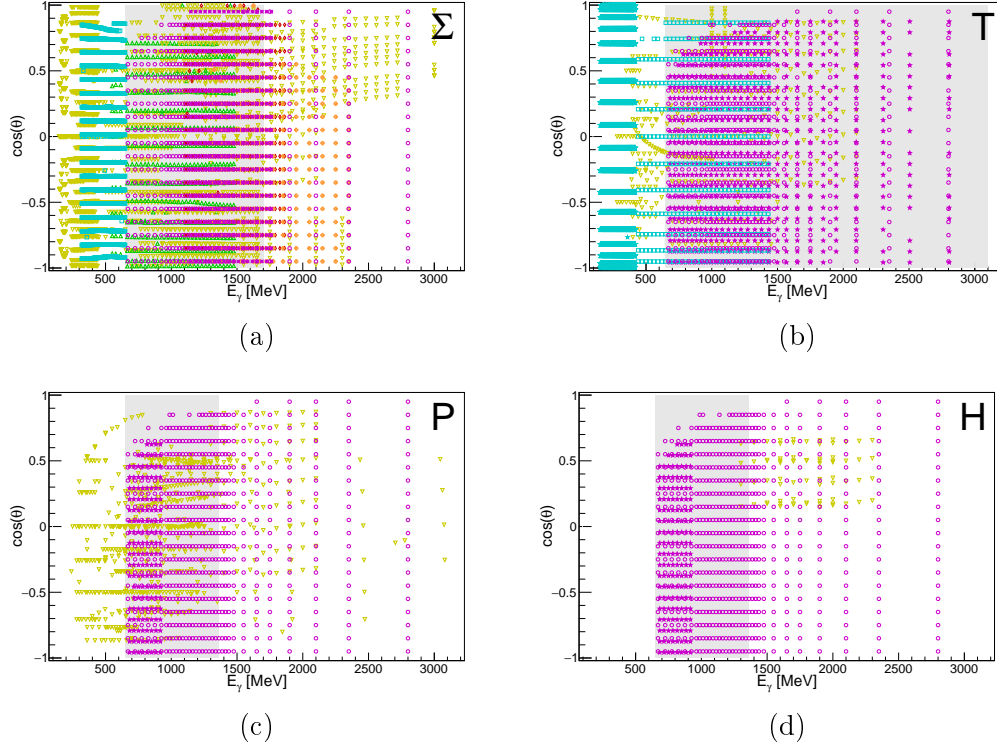


Figure 1.14: Current data situation for the observables Σ , T , P and H in π^0 photoproduction on the proton. The light grey box indicates the kinematically accessible ranges in this experiment. The most recent data with high statistics from the CBELSA/TAPS experiment at ELSA in Bonn, Germany, are shown as magenta circles, crossed x and stars [142–144], those from the LEPS2/BGOegg experiment at SPring-8 in Sayo Town, Japan, are shown as orange crosses [145], those from the A2 experiment at MAMI in Mainz, Germany, are shown as cyan squares and stars [146–148], those from the CLAS experiment at CEBAF/JLab in Newport News (VA), USA, are shown as red diamonds [149] and those from the GRAAL experiment at ESRF in Grenoble, France, as green triangles [150]. All other data, shown as yellow inverted triangles, are from multiple older experiments [151–183] for Σ , [179–190] for T , [179–183, 189–229] for P and [230, 231] for H . Most of the data can be found summarised on the SAID homepage [111].

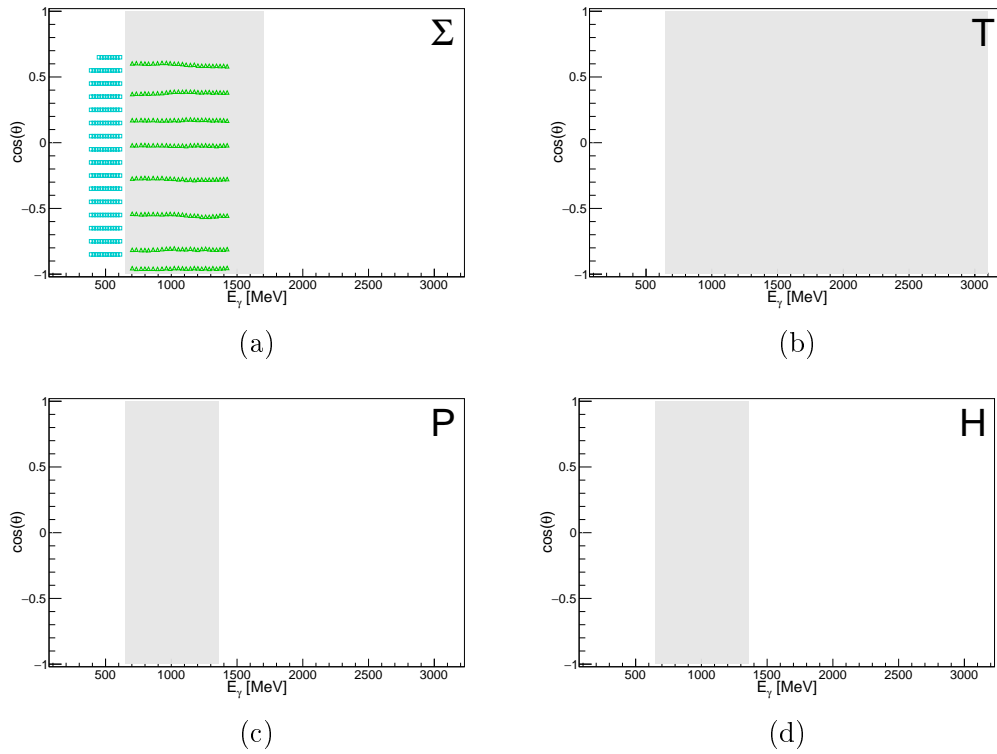


Figure 1.15: Current data situation for the observables Σ , T , P and H in π^0 photoproduction on the neutron. The light grey box indicates the kinematically accessible ranges in this experiment. The most recent data with high statistics from the GRAAL experiment at ESRF in Grenoble, France, are shown as green triangles [232], those from the A2 experiment at MAMI in Mainz, Germany, are shown as cyan squares [233].

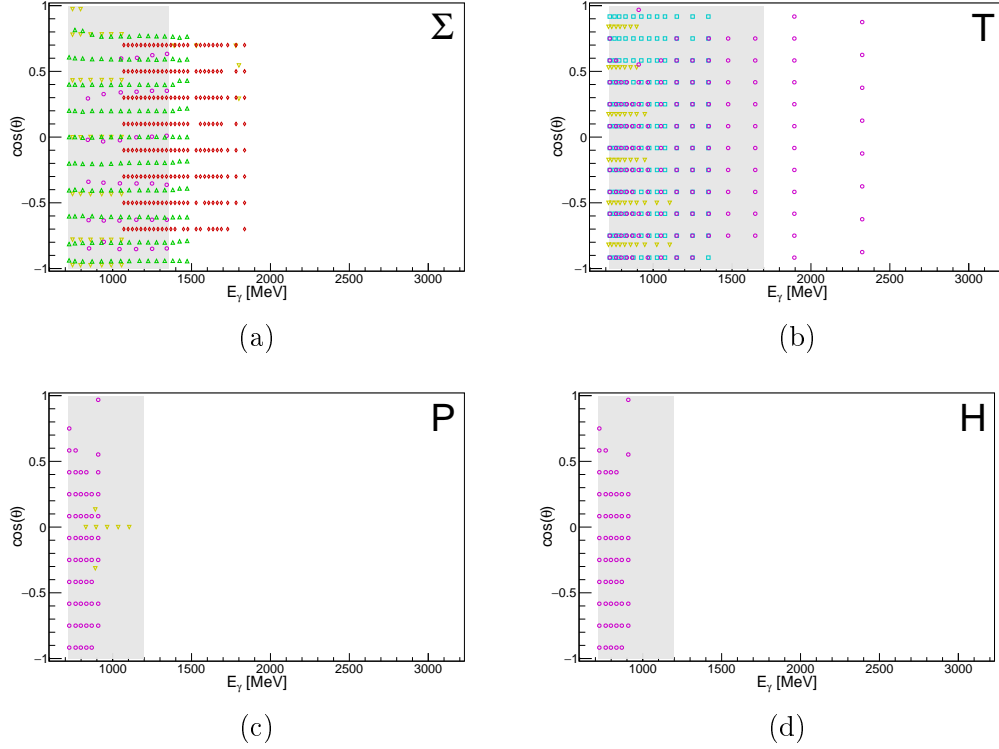


Figure 1.16: Current data situation for the observables Σ , T , P and H in η photoproduction on the proton. The light grey box indicates the kinematically accessible ranges in this experiment. The most recent data with high statistics from the CBELSA/TAPS experiment at ELSA in Bonn, Germany, are shown as magenta circles [119, 234, 235], those from the A2 experiment at MAMI in Mainz, Germany, are shown as cyan squares [236], those from the CLAS experiment at CEBAF/JLab in Newport News (VA), USA, are shown as red diamonds [237] and those from the GRAAL experiment at ESRF in Grenoble, France, as green triangles [238]. All other data, shown as yellow inverted triangles, are from multiple older experiments [239, 240] for Σ , [184] for T and [241, 242] for P . Most of the data can be found summarised on the SAID homepage [111].

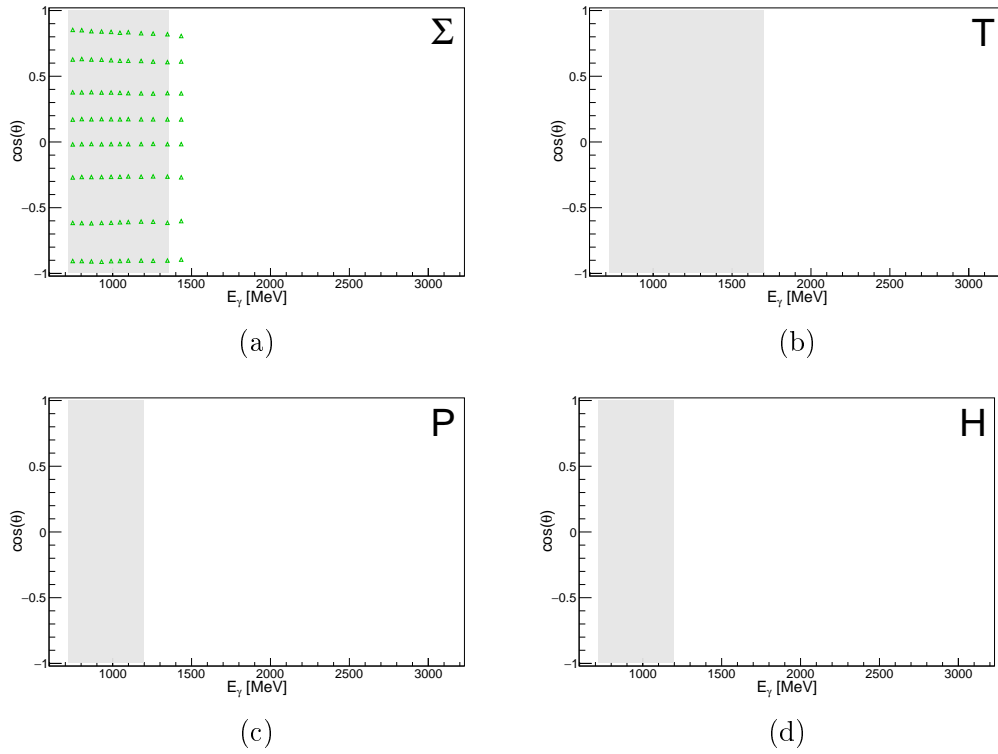


Figure 1.17: Current data situation for the observables Σ , T , P and H in η photoproduction on the neutron. The light grey box indicates the kinematically accessible ranges in this experiment. The most recent data with high statistics from the GRAAL experiment at ESRF in Grenoble, France, are shown as green triangles [243].

2 | Experimental setup

The CBELSA/TAPS experiment with the Crystal Barrel/TAPS detector setup takes place at the Electron Stretcher Accelerator (ELSA) facility in Bonn, Germany. The experiments for this work took place in October/November 2018 (Oct2018) and November/December 2021 (Dec2021).

Section 2.1 starts with an overview of the electron accelerator facility ELSA, where the experiment is situated.

Section 2.2 is about the different detector parts building up the setup. It explains what they are made of, their properties and how they work.

The transversely polarised deuterated butanol (dButanol) target and how nucleons can be polarised is explained in Section 2.3, whereas Section 2.4 shows the used trigger conditions in the experiment. Due to the used beam current, not all events can be stored such that *good* conditions must be set to store the interesting ones.

The chapter is concluded with Section 2.5, where the beam times and the resulting data sets are explained.

2.1 Electron Stretcher Accelerator

The Electron Stretcher Accelerator (ELSA) [92] is located at the Physics Institute of the Rheinische Friedrich-Wilhelms-Universität in Bonn, Germany. It accelerates polarised and unpolarised electrons up to 3.2 GeV in three stages: linear accelerator (LINAC), booster synchrotron and stretcher ring [92].

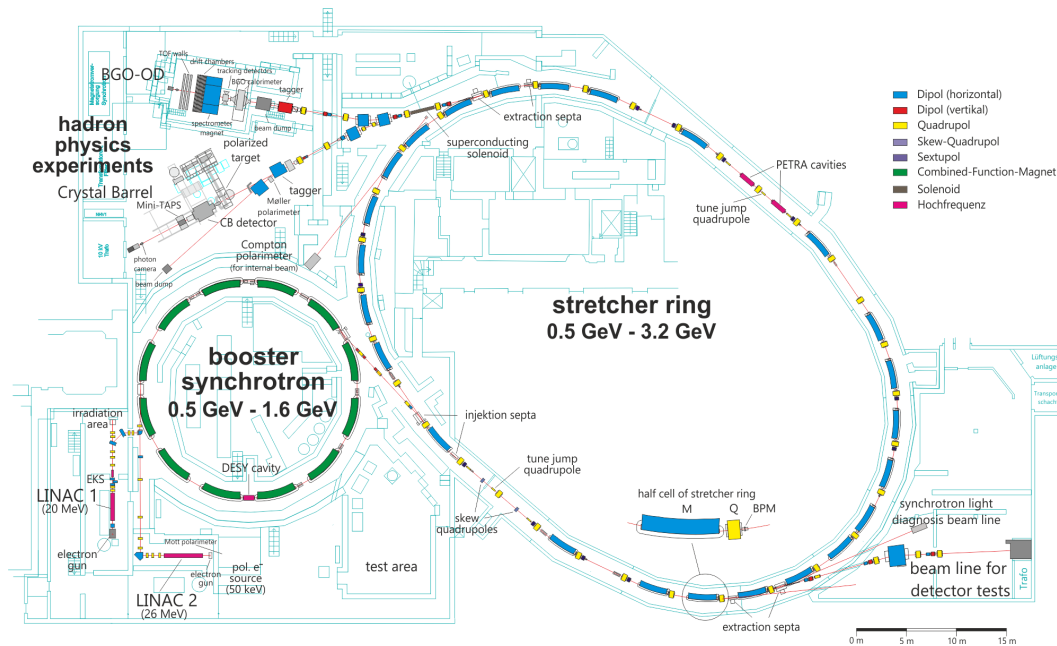


Figure 2.1: Schematic representation of the Electron Stretcher Accelerator (ELSA) in Bonn, Germany, with its three steps: linear accelerator (LINAC), booster synchrotron and stretcher ring. Figure taken from [244].

Here, LINAC 2 is used with unpolarised electrons. They are produced by a thermal gun and accelerated up to 26 MeV before being led into the booster synchrotron. LINAC 2 could also be used with polarised electrons that are produced on a GaAs photo-cathode by circularly polarised laser light [245]. Their polarisation can reach up to more than 80% [245]. The other linear accelerator, LINAC 1, that produces unpolarised electrons by a thermal gun and accelerates them up to 20 MeV, is not available at the moment.

The booster synchrotron accelerates electrons up to 1.6 GeV at a frequency of 50 Hz before they are led into the stretcher ring. Due to different circumferences of the booster synchrotron and the stretcher ring, at least seven injections must be performed to fill the stretcher ring. They are further accelerated to

3.2 GeV. To increase the beam current and have a more stable extraction a multiple of seven can also be injected into the ring, i.e. 21 or 28 injections, as done in this experiment. Besides a stretcher and an acceleration mode, the stretcher ring can also store the beam for quite some time to provide a continuous beam.

A second collaboration also uses ELSA for its experiments: BGO-OD [246]. Their setup is designed for unpolarised targets with complex final states to search for strangeness and vector mesons.

2.2 Crystal Barrel/TAPS detector setup

The detector setup is perfectly suited for looking at reactions with photons in the final state, as they deposit nearly all their energy in the two main spectrometers: Crystal Barrel (CB) with Forward Plug (FP) and MiniTAPS (MT). Together, they cover 94.6% of the 4π solid angle making angle-dependent determination possible.

Furthermore, several charge-sensitive detectors are used for distinguishing protons from neutrons and photons.

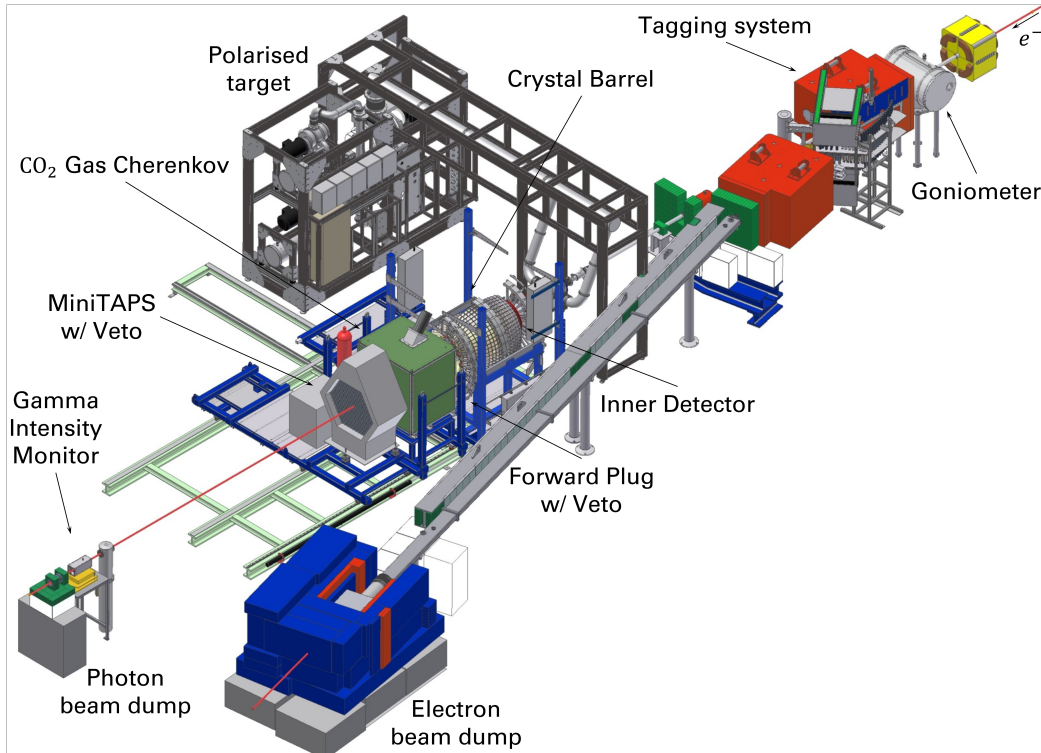


Figure 2.2: Schematic representation of the Crystal Barrel/TAPS experiment since 2005. Figure adapted from [63].

2.2.1 Tagging system

Electrons from ELSA are converted to photons with a thin radiation foil through the bremsstrahlung process. The photons fly through a 4 mm lead collimator towards the target. On the other hand, the scattered electrons get

deflected by a dipole magnet towards the tagging system (Tagger, Figure 2.3a). Since the energy of the beam electrons E_0 and the one of the detected one in the Tagger E_{e^-} are known, the energy of the photon is directly given by:

$$E_\gamma = E_0 - E_{e^-}. \quad (2.1)$$

Undelected beam electrons, which do not produce photons impinging the target, are deflected by 9 deg towards the electron beam dump by an additional dipole magnet.

The Tagger is made of two different detectors: a bar hodoscope and a fibre detector. Scattered electrons within an energy range of $(0.021 - 0.825) E_0$ [247] are registered by the first. The bar hodoscope is made of 96 overlapping organic scintillators with attached photomultiplier tube (PMT) [247]. Their signal is thereby digitalised by leading edge discriminators (LED) and time-to-digital converters (TDC). The scintillators overlap such that an electron hits two, which helps to reduce the background. The relative energy resolution is 0.1 to 6 % [247] (Figure 2.3b).

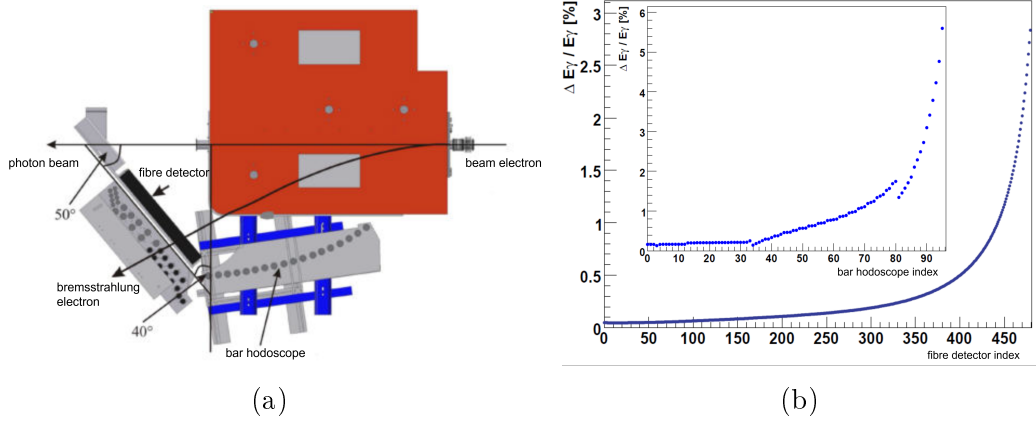


Figure 2.3: (a) Schematic representation of the tagging system with its two detector components: bar hodoscope and fibre detector. (b) Energy resolution of the bars and fibres as a function of the incident photon energy E_γ . Figure (a) adapted from [248]. Figure (b) adapted from [247].

Additionally to the bar hodoscope, the fibre detector covers the energy range of $(0.116 - 0.871) E_0$ [247] enhancing the detection range in the high-energy range. It consists of 480 scintillators with multi-anode PMT readout. They are built to 30 modules, each consisting 16 fibres, with an energy resolution of 0.1 to 0.4 % of E_0 [247] (Figure 2.3b).

2.2.2 Goniometer

The goniometer [163] is situated in a vacuum chamber in front of the Tagger. It consists of a Møller radiator, four copper radiators of different thicknesses, diagnostic instruments and a diamond radiator (Figure 2.4).

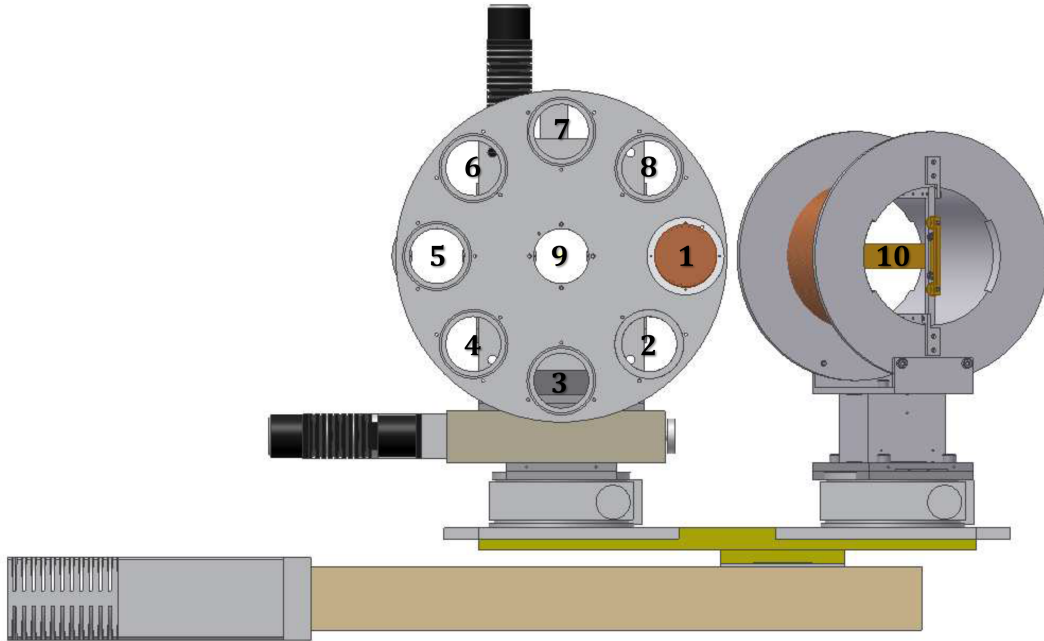


Figure 2.4: Schematic representation of the goniometer with its different radiators: (1) luminescent screen, (2) 300 μm copper radiator, (3) horizontal wire, (4) vertical wire, (5) 150 μm copper radiator, (6) 50 μm copper radiator, (7) 12 μm copper radiator, (8) empty, (9) diamond radiator, (10) Møller radiator. Figure adapted from [249].

The Møller radiator, made of a 20 μm thick ferromagnetic foil surrounded by a solenoid [250], is for measuring polarisation degrees of circularly polarised photons.

The amorphous copper radiators with a thickness of 12 μm to 300 μm - corresponding to 0.00084 – 0.021 radiation lengths X_0 [250] - are used to generate an unpolarised photon beam. They are situated in the slots of the aluminium wheel.

As diagnostic instruments, a luminescent screen and a horizontal and vertical wire can be used to visualise the beam and scan the beam profile.

The diamond radiator, which is a 500 μm thick diamond crystal - corresponding to $4.1 \cdot 10^{-3} X_0$ - is glued to a 12.5 μm thick kapton foil [249]. It is

situated in the centre of the aluminium wheel and used for polarising photons linearly, like in this experiment. It thereby must be aligned specifically to produce coherent bremsstrahlung. The whole process was developed by Ken Livingston [251] and is called Stonehenge technique. The polarisation direction and the coherent edge can be adjusted. The coherent edge is the position of the steepest drop just after the highest polarisation values. Here, the polarisation degree orientations are set to $\pm 45^\circ$ with a coherent edge at 1200 MeV.

2.2.3 Crystal Barrel

The Crystal Barrel calorimeter (CB) covers 89% of 4π and is made of 1230 CsI(Tl) crystals (Figure 2.5). It is excellent for detecting photons, i.e. 2 GeV photons deposit 99% of their energy in it [252].

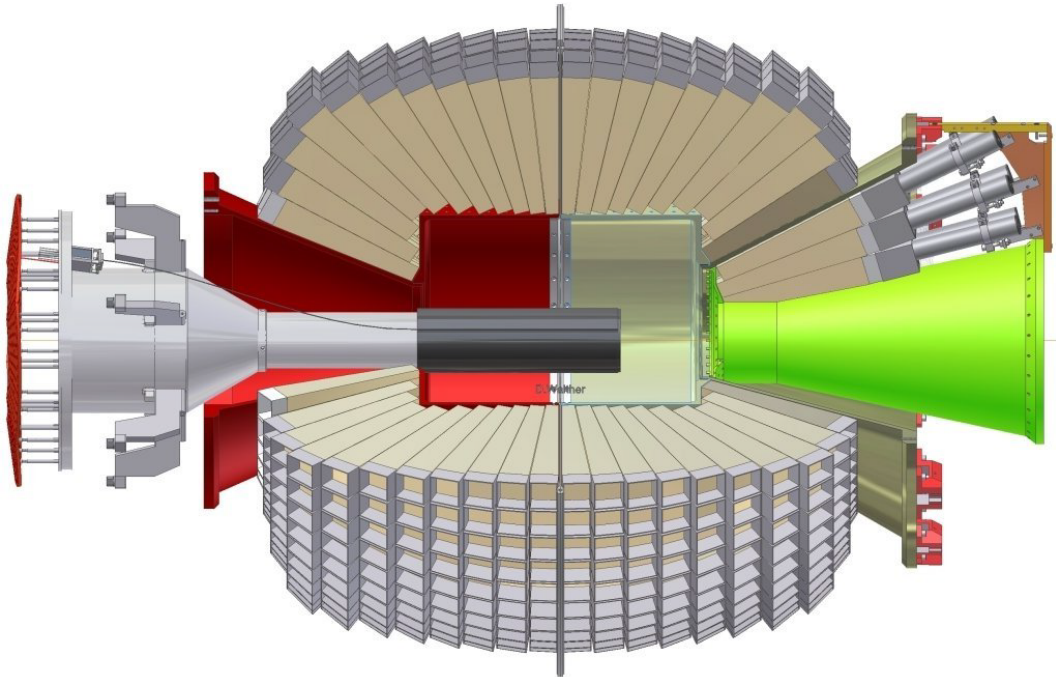


Figure 2.5: Schematic representation of the Crystal Barrel spectrometer with the Forward Plug detector (right) and the charge sensitive Inner Detector (left). The photon beam enters from the left-hand side. Figure taken from [253].

CB was built at CERN, where it was used in the low-energy antiproton ring (LEAR) facility starting in 1989 [254] and was moved to ELSA in 2000. It has the shape of a barrel and surrounds the Inner Detector (Section 2.2.5), which again surrounds the target (Section 2.3). The crystals have a length

of 30 cm - corresponding to 16 radiation lengths X_0 [254] - that are arranged in 21 rings. CB covers the polar angles from $\theta = 30^\circ$ to $\theta = 156^\circ$ with the resolution of $\Delta\theta = 6^\circ$ and the full azimuthal angle ϕ with the resolution of $\Delta\phi = 6^\circ$. However, the last ring starting at $\theta = 150^\circ$ has a azimuthal resolution of $\Delta\phi = 12^\circ$ [254]. Since most photons produce an electromagnetic shower, which is spread over multiple crystals, a resolution of 1.5° can be achieved for energies of more than 50 MeV [254].

The relative energy resolution is given by [254]:

$$\frac{\sigma_E}{E} = \frac{2.5\%}{\sqrt[4]{E[\text{GeV}]}}. \quad (2.2)$$

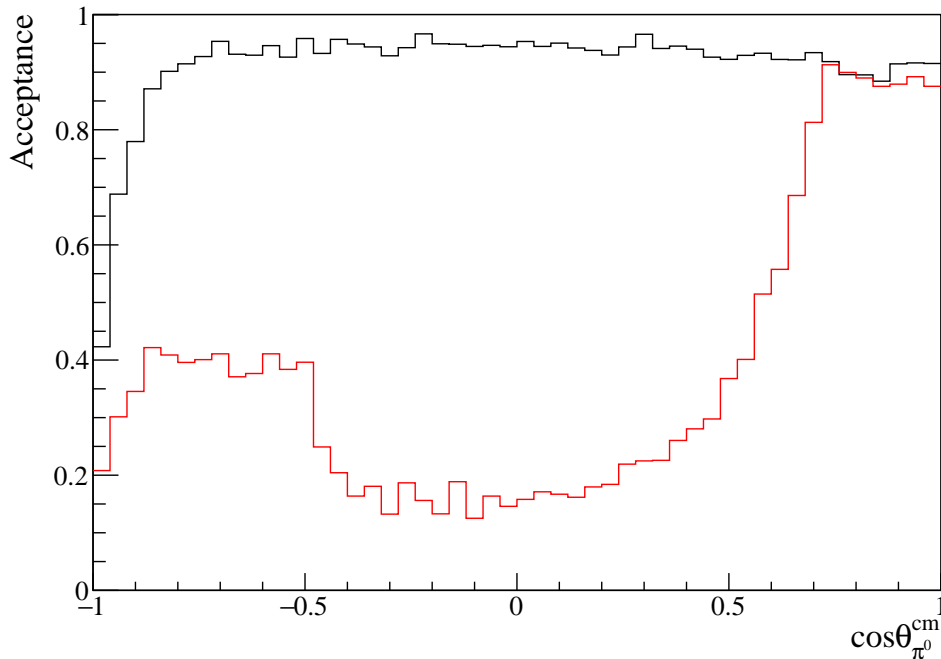


Figure 2.6: Monte Carlo simulation of the trigger acceptance in the reaction $\gamma n \rightarrow \pi^0 n$ as a function of $\cos(\theta)$ before (red) and after (black) the hardware upgrade of Crystal Barrel. Figure taken from [255].

In 2018 an upgrade of the readout electronic from PIN photodiodes to avalanche photodiodes CB was finished and CB can also be used in the first level cluster trigger system with its timing information [255–257]. Figure 2.6 shows a comparison between the old and the new trigger from a MC simulation of the reaction $\gamma n \rightarrow \pi^0 n$ as a function of the meson angle in the CM frame.

As expected, in the forward direction, the acceptances are very similar due to the primary influence of FP and MT. However, going towards more backward angles, a significant deviation of more than a factor of 5 is visible. This upgrade was crucial for this experiment as a dButanol target is used and the reaction can occur on protons and neutrons. The analysis is therefore done exclusively, i.e. the recoil nucleon must be detected too, where the number of detected events on neutrons would be minimal with the old trigger. The new trigger solves this problem and makes nearly the whole solid angle accessible for the analysis.

Another upgrade not completed in the 2018 beam time but in the 2021 one was the replacement of charge-to-digital-converters (QDC) readout with custom-made FPGA-based sampling analogue-to-digital-converters, the SADC [258]. They can handle information much faster and an increase of more than a factor of 2 was archived in the data taking rate.

2.2.4 Forward Plug

At the photon beam leaving side of CB, three rings with 90 CsI(Tl) crystals build the Forward Plug detector (FP). It is made of the same crystals as CB and covers the polar angles from 11.2° to 27.5° and the whole azimuthal angle [259] (Figure 2.5). Because of the holding structure, the detector is shifted by 3 cm towards the photon beam dump.

The charge-sensitive Inner Detector (Section 2.2.5) does not cover all angles for the FP such that two layers of 90 organic scintillators - the Forward Plug Veto detector (FP Veto, FPV) - are arranged in front of the FP to identify charged particles [260]. The first layer covers the same solid angles as the FP crystals, whereas the second layer is shifted by 6° around the beam axis [260].

The readout is done with lightguides and PMT. The analogue signal is converted to a digital one with LED and multi-hit TDC. Signals from FP are used in the trigger system too.

2.2.5 Inner Detector

Before particles hit the CB, they propagate through three 2 mm thick layers of cylindrical scintillating fibres, the Inner Detector (ID) [248, 261]. ID is made of 513 fibres. Sometimes this detector is also called Charged Particle

Identification detector (ChaPI) since it is used to identify charged particles (Figure 2.5).



Figure 2.7: Schematic representation of the Inner Detector (ID, a) and the three scintillating fibres (b) that build up the active area of the detector. Figures taken from [262]

The outer layer is aligned parallel with the photon beam direction. The central layer is turned by an angle of 25.7° and the inner layer by -24.5° [261]. The number of fibres - 191, 165, 157 - decreases with the radius of the layers - 6.4 cm, 6.13 cm, 5.81 cm - from the outer to the inner layer [261].

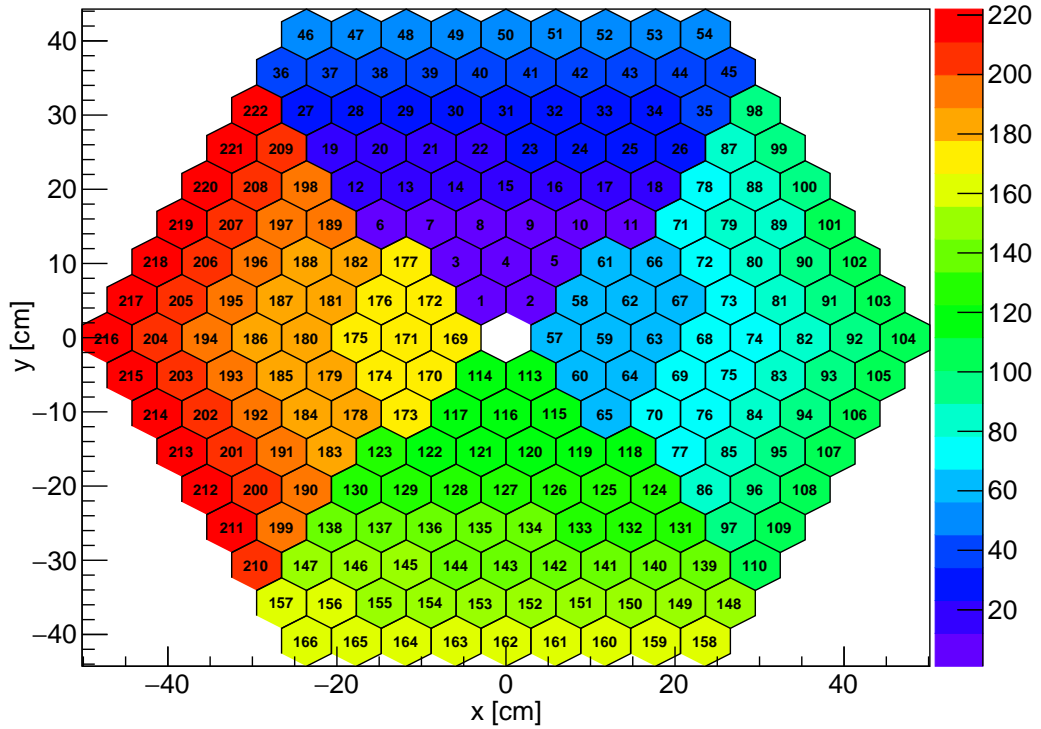
The centre of the ID is shifted by 5.1 cm toward the incoming beam compared to the CB/target centre [263]. It covers the polar angles from $\theta = 23.1^\circ$ to $\theta = 166^\circ$ [143] and has a length of 40 cm [261]. The angular resolutions are $\Delta\theta = 0.4^\circ$ and $\Delta\phi = 0.1^\circ$ [264].

The readout is done with multi-anode PMT and digitalised with LED and multi-hit TDC. Therefore, it does not give any energy information [261].

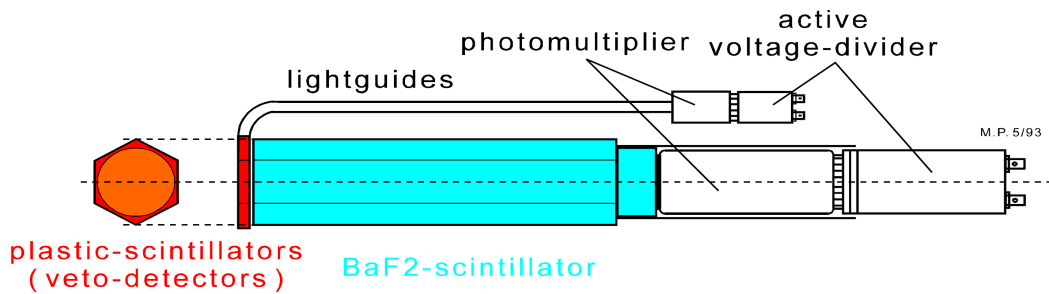
2.2.6 MiniTAPS

The MiniTAPS (MT) [265, 266] - originally TAPS stands for Two-Arm-Photon-Spectrometer - covers the most forward angles from $\theta = 1^\circ$ to $\theta = 12^\circ$ and is made of 216 hexagonal BaF_2 crystals. The elements were originally used in the TAPS experiments at the MAMI accelerator facility in Mainz, Germany [265].

Since MT is situated 210 cm behind the target centre and BaF_2 crystals have an excellent time resolution of 0.87 ns [268], it could be used as time-of-



(a)



(b)

Figure 2.8: (a) Schematic representation of the MiniTAPS with its four logical sectors and element numbering. (b) A single element. Figure (b) taken from [267].

flight (TOF) detector like TAPS in the A2 experiments at MAMI in Mainz, Germany [132, 269]. However, since it only detects a small part of all events and gives no additional information, the TOF method is not used in this setup.

The crystals have the dimension $5.9 \text{ cm} \times 5.9 \text{ cm} \times 25 \text{ cm}$ - corresponding

to 12 radiation lengths X_0 [265].

The energy resolution is given by [266]:

$$\frac{\sigma_E}{E} = 1.91\% + \frac{0.59\%}{\sqrt{E[\text{GeV}]}}. \quad (2.3)$$

Another property of the crystals is the decay over two scintillation components: a fast one called short gate (SG) and a slow one called long gate (LG). This property could also be used to identify different particles in reactions using the pulse-shape-analysis (PSA), which again is regularly used within A2 experiments at MAMI [270–272]. As for the TOF method, the number of events is too low for a broad application of the PSA method.

The readout is done with PMT and custom-built readout modules [267] that include ADC for the energy information and TDC for the timing information. In front of TDC, CDF are installed and two different LED - LEDHigh and LEDLow - are used to provide trigger conditions.

The detector is split into four logical sectors for the trigger (Figure 2.8a). If one hit in a sector is above LEDHigh, or two hits in two different sectors are above LEDLow, the trigger condition will be fulfilled. In the two most inner rings, LEDHigh is switched off to suppress background events from e^-e^+ events. In more recent experiments - including this one - only one LED trigger condition (LEDHigh) is used.

The MT Veto detector (MTV) is placed in front of MT to identify charged particles. MTV is made of 5 mm thick organic scintillators. The elements have the identical shape as the BaF_2 crystals such that one Veto element covers exactly one MT element. The readout is done with multi-anode PMT that are digitalised by LED and TDC. Therefore, MTV does not provide any energy information.

2.2.7 Gamma Intensity Monitor and Flux Monitor

At the end of the photon beamline, the Gamma Intensity Monitor (GIM) is situated, which is made of 4×4 PbF_2 crystals [273]. Due to the high density of the crystals [44], GIM can work with high rates. Incoming photons mainly produce e^+e^- pairs, which generate Cherenkov light detected by the connected PMT readout system.

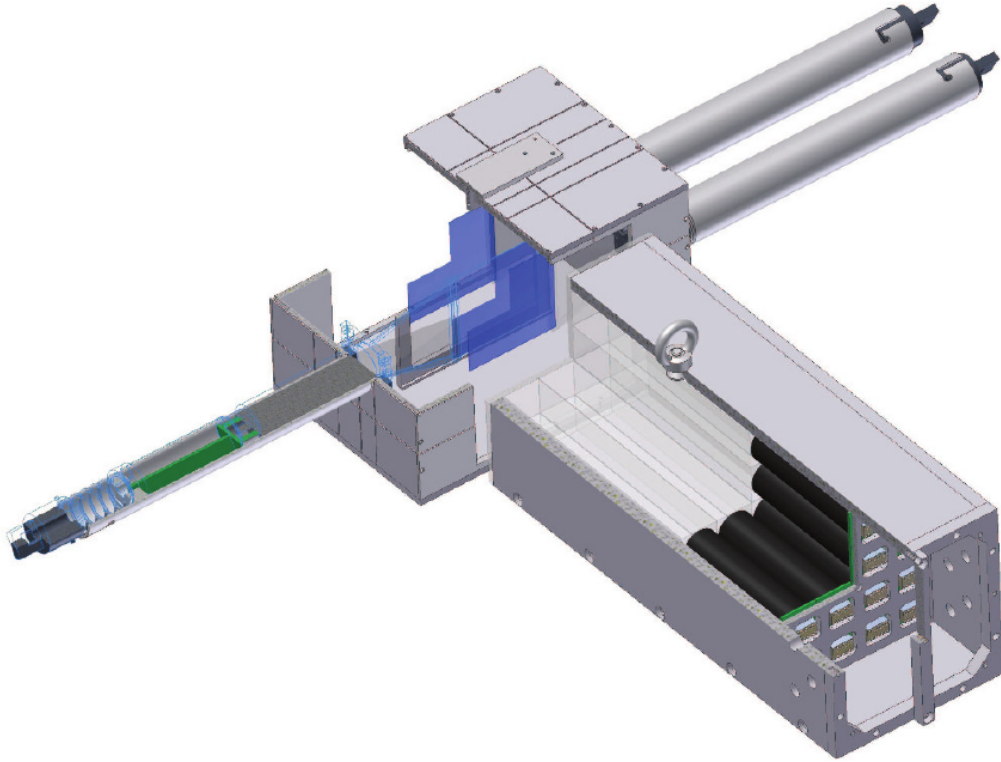


Figure 2.9: Schematic representation of the Gamma Intensity Monitor with the Flux Monitor behind it. Figure taken from [262].

GIM is used to precisely monitor the photon flux during the experiment. Since (Tagger) rates of more than 5 MHz are used during the experiment, dead times of the GIM readout system become important and the efficiency drops [268]. Therefore, an additional detector - the Flux Monitor (FluMo) [274] - is installed in front of the GIM (Figure 2.10). FluMo produces only a fraction of e^+e^- pairs compared to GIM, so it does not get saturated. Two organic scintillators detect hits. A third veto scintillator is present in front of the FluMo. It shows a constant fraction of the total flux and can be used to determine the GIM detection efficiency, which again is needed for the photon flux determination.

2.2.8 Cherenkov detector

To suppress electromagnetic background, i.e. e^+e^- pair production, a CO_2 gas Cherenkov detector is placed as a veto between FP and MT [275]. It has the dimensions $1.2\text{ m} \times 1.2\text{ m} \times 1.0\text{ m}$ and is made of aluminium with an

entrance and exit window.

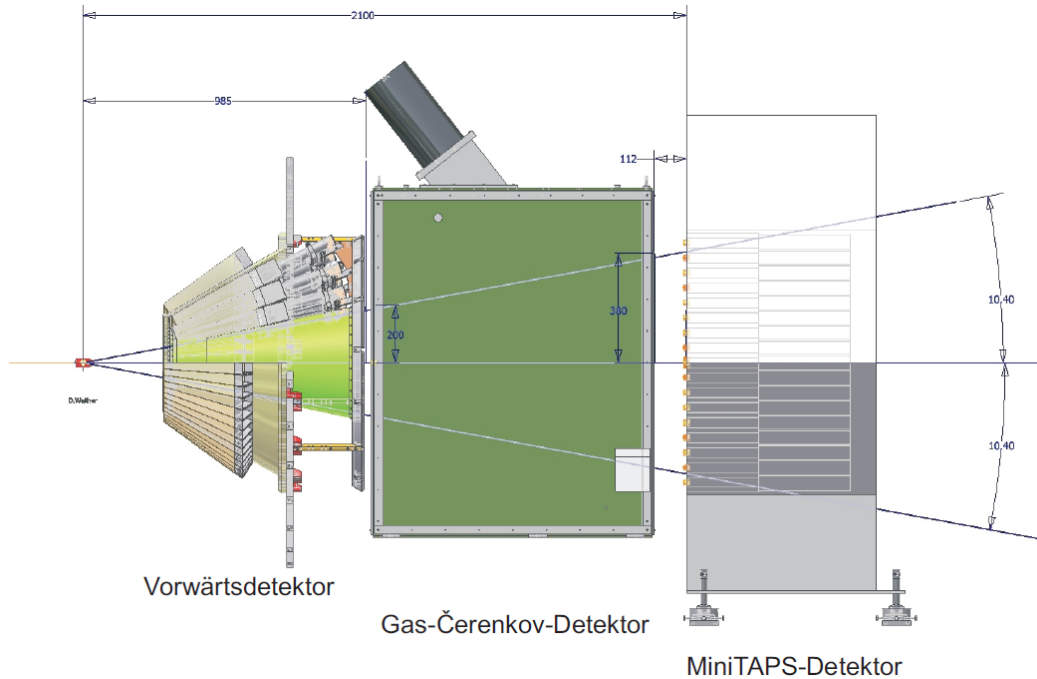


Figure 2.10: Schematic representation of the CO_2 gas Cherenkov detector ("Gas-Čerenkov-Detektor") situated between Forward Plug ("Vorwärtsdetektor") and MiniTAPS ("MiniTAPS-Detektor"). Figure taken from [275].

The produced light is focused towards the top, where a PMT is installed. Since the refractive index of CO_2 is $n = 1.00045$ [276, 277] under standard conditions, the threshold energy for electrons is 17.4 MeV (Appendix B.1). This is even below the 20.0 MeV threshold energy from the reconstruction. Other particles do not produce Cherenkov radiation with the maximum provided energy of 3.2 GeV from ELSA.

Reducing e^+e^- pair production is essential since the production yield is proportional to the atomic number Z^2 . Thus, much electromagnetic background is suppressed with a dButanol target, which also consists of carbon and oxygen atoms with $Z = 6$ and $Z = 8$. Some Compton effects that scale with Z are further suppressed.

The detection efficiency is 90 % for 19 MeV and (99.7 ± 4.5) % for energies above 100 MeV [275] making the Cherenkov detector very suitable as a veto for electromagnetic showers.

2.3 Targets

2.3.1 Polarised deuterated butanol target

This work aims to determine polarisation observables for π^0 and η photo-production on transversely polarised nucleons. Therefore, two complications occur. First, free neutrons have a mean lifetime of 879.4 ± 0.6 seconds [44] such that they can only be investigated in bound systems like deuterium (D). Second, deuterium cannot be polarised easily since it would require very high magnetic fields of around 20 T and very low temperatures of the order of mK [278]. The solution is a frozen spin target with many deuterium molecules and a long relaxation time that is easy to handle, i.e. deuterated butanol (dButanol). The chemical structure of dButanol is C_4D_9OD , meaning it has ten bound protons and neutrons within D per molecule and 32 protons and neutrons bound in carbon and oxygen.

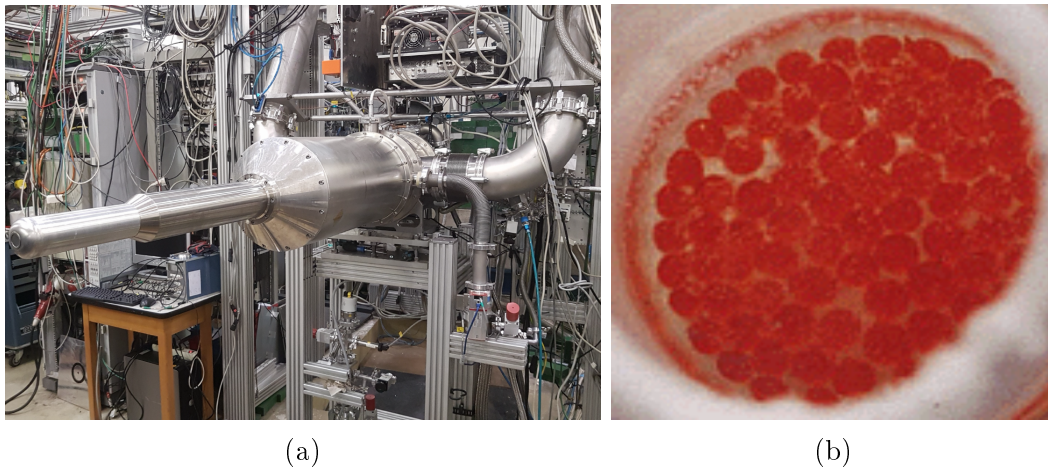


Figure 2.11: (a) Dubna-Mainz Frozen Spin Target inside the Crystal Barrel/TAPS detector setup. (b) Frozen deuterated butanol beads. Figure (a) taken from [279]. Figure (b) taken from [271].

The energy level of particles with a non-vanishing dipole moment in an external magnetic field B split into $2s + 1$ Zeeman levels with the magnetic quantum number $m = -s, \dots, s$, which increases in integer steps. Thus, nucleons split into two levels ($m = \pm 1/2$), whereas deuterium nuclei split into three ($m = -1, 0, 1$). In thermal equilibrium (TE), the occupation number ratio is

given by [278]:

$$\frac{N(E + \Delta E)}{N(E)} = \exp\left(-\frac{\Delta E}{k_B T}\right) \quad \text{with} \quad \Delta E = g\mu B \Delta m = h\nu_{e^-}, \quad (2.4)$$

where N is the occupation number, E the energy, ΔE the energy difference between the levels, $k_B = 1.3806 \cdot 10^{-23} \text{ J K}^{-1}$ [44] the Boltzmann constant, T the temperature, g the Landé factor, $\mu = \mu_B = 9.2740 \cdot 10^{-24} \text{ J T}^{-1}$ [44] the Bohr magneton for electrons, $\mu = \mu_N = 5.0508 \cdot 10^{-27} \text{ J T}^{-1}$ [44] the nuclear magneton for nucleons and nuclei, Δm the difference between the magnetic quantum number of energy levels, $h = 6.6261 \cdot 10^{-34} \text{ J s}$ [97] the Plank constant and ν_{e^-} the microwave radiation of the electron. The Landé factor is 2.0023 for electrons [97], 5.5857 for protons [97], -3.8261 for neutrons [97] and 0.8574 for deuterium [97]. The polarisation in TE is given by the Brillouin function [280]:

$$P = \frac{\langle I_z \rangle}{I} = \frac{N(I) - N(-I)}{\sum_{m=-1}^{m=+1} N(m)} = \mathcal{B}_I\left(\frac{\mu B}{2k_B T}\right). \quad (2.5)$$

The sum of the magnetic moments of the proton and neutron is $0.8798\mu_N$, which differs from the deuteron by about 2.5%. The deuteron is, therefore, not a pure S state with $l = 0$ but has D state contributions with $l = 2$. This reduces the magnetic moment and, therefore, the nucleon polarisation by approximately 7.4% [281] (Section 5.3.1). This value is found with Clebsch-Gordan coefficients from the average D wave admixture of $(4.90 \pm 1.04)\%$ [281]. A possible P state admixture with $l = 1$ is excluded by parity conservation.

Looking at Equation 2.5, it is visible that a *good* polarisation degree of deuterium with its relatively small Landé factor is only achievable for very low temperatures and very high magnetic fields, as mentioned before. Therefore, deuterium cannot be used as target material and the polarisation of the nucleons must be obtained in another way.

This experiment uses the Dubna-Mainz Frozen Spin Target [283,284]. The polarisation of deuterium in dButanol is done by the dynamic nuclear polarisation (DNP) technique [280] and can be described by the spin temperature theory [278]. The dButanol target is doped with 2.7% Finland D36 radicals [279], a paramagnetic material that provides free electrons for the DNP procedure.

The target is cooled down to 300 mK. An external solenoid magnet pro-

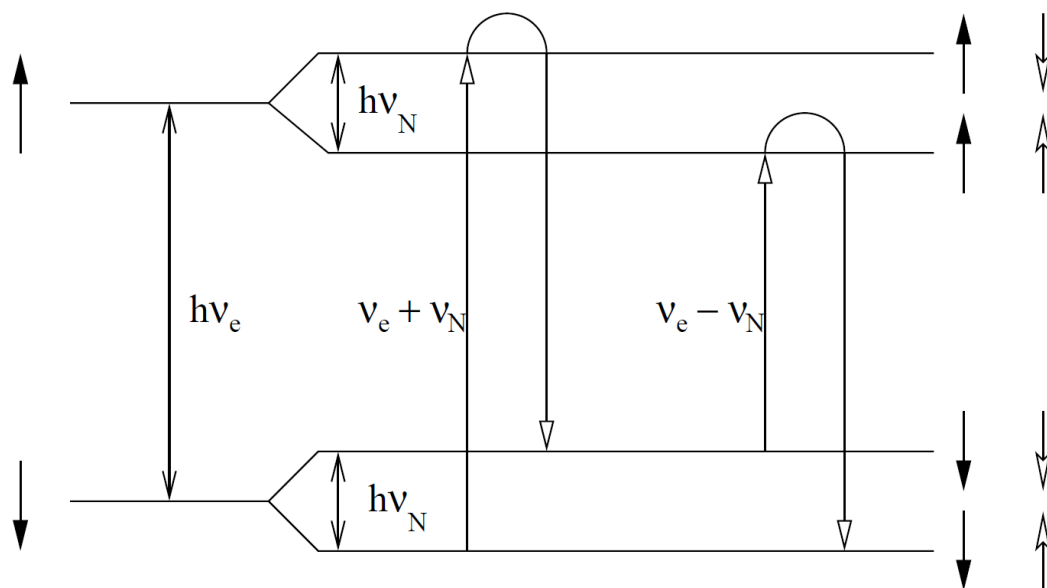


Figure 2.12: Schematic representation of the dynamic nuclear polarisation (DNP) process. Figure taken from [282].

duces a 2.5 T magnetic field that polarises the electrons to nearly 100% [283]. The polarisation of the electrons is transferred to the nucleons by microwave irradiation. The electrons and nucleons interact causing four energy levels according to the Zeeman splitting, i.e. hyperfine structure. The microwave irradiation spin flips the electrons and nucleons simultaneously. The relaxation time, where the spins return to the ground state, is several orders of magnitude lower for electrons than for nucleons. Therefore, electrons are quickly available for further spin flipping. The polarisation is dynamically transferred from the electrons to the nucleons (Figure 2.12), giving this technique its name.

The applied microwave frequency can provide parallel or antiparallel spin in the nucleons. The best frequency is found by scanning a specific range and maximising the polarisation increase.

After reaching the maximum polarisation degree of up to 80% the magnet is removed and replaced by a 0.6 T holding magnet. Additionally, the helium dilution refrigerator cools down the target to around 27 mK, which with the magnet provides relaxation times of more than 1000 h [279]. After some days, the whole procedure is repeated.

At the beginning and end of the data taking with the transverse magnetic field, the target polarisation is measured using the nuclear magnetic resonance

(NMR) technique [285, 286].

The dButanol molecules are frozen in portions of small beads (Figure 2.11b), which do not fill out the entire space inside the target cell. Therefore, an additional filling factor needs to be considered in the later calculations of the target surface density.

2.3.2 Carbon foam target

In addition to the dButanol target, a carbon target is used. That target has a similar target surface density and is used to investigate the contribution of carbon (and oxygen) in the later analysis.



Figure 2.13: Carbon foam target. Figure taken from [287].

Figure 2.13 shows the carbon foam target. It has a length of about 2 cm and has been used in several experiments before [262, 271, 287, 288].

2.4 Trigger conditions

Detectors need some time to detect events due to dead time effects of the readout electronics. Furthermore, the digitalisation of signals takes some time. Therefore, it is impossible to store every event with the used electron beam current and trigger conditions are needed to select exciting events.

These trigger conditions are implemented with FPGA modules [289, 290]. The conditions are chosen so that the events of interest are taken while dismissing as much background as possible. They come from the detector electronics and mainly check for multiplicity.

The information available within 300 ns is used. The trigger signal is taken as reference time by the TDC. It starts the ADC conversion and the `ClusterFinder`. The latter decides if the event is taken, i.e. the correct detector elements have triggered or rejected by sending a reset signal to all detector components, avoiding long readout time.

Due to the upgrade in the readout of the photodiodes in CB [256, 257], this is one of the first experiments where CB is taken as direct/first-level trigger. In previous experiments, the trigger was split into a two-level trigger system because CB had no available time information and could not be used in the first-level trigger system. See [262] for more information.

The experiment uses the `vme_trig_42i` and `vme_trig_42k` triggers for normal data taking runs in the Oct2018 and Dec2021 beam time, respectively. The only difference between them is the light pulser during spill breaks, which is included in the latter. The `vme_tagger_coinc` trigger is used for tagging efficiency and amorphous copper runs. They are required to determine the photon flux and the linear polarisation. This `vme_tagger_coinc` trigger is a coincident hit in two neighbouring tagger scintillator bars. The trigger conditions of the `vme_trig_42` triggers can be written as:

$$(\text{taps1} \wedge \text{cf1} \wedge \neg \text{chkv}) \vee \text{cf2} \vee (\text{taps2} \wedge \neg \text{chkv}). \quad (2.6)$$

The exact conditions for the fulfilment of the separate conditions are given in Table 2.1

Moreover, additional conditions are required to reconstruct particles to reduce background. For MT, threshold values of 17 MeV are required for the

trigger	detector	requirements
taps1	MT	at least one hit above a threshold of 80 MeV
taps2	MT	at least two hits above a threshold of 80 MeV or 500 MeV, latter only for the two most inner rings
cf1	CB incl. FP	at least one hit above a threshold of 45 MeV for ring 1, 32 MeV for ring 2, 27 MeV for ring 3, 31 MeV for ring 4, 30 MeV for the last ring and around 16 MeV for the other rings
cf2	CB incl. FP	at least two hits above the same thresholds as for cf1
-chkv	Cherenkov	no hit in the Cherenkov detector

Table 2.1: Trigger conditions for the different detector parts that are used for the *vme_trig_42* trigger (see Equation 2.6).

crystals in the first two rings and 13 MeV for the other rings. A particle event deposit (PED) centre crystal must further have an energy of at least 20 MeV and a cluster one of at least 25 MeV.

For the CB (including FP), an energy of 1 MeV is required in a crystal and 20 MeV is required for the central PED crystal and a cluster. See Chapter 3 for more details.

2.5 Beam times and data sets

The data for the analysis come from two beam times, each using a dButanol target for the main experimental data and a carbon target for the determination of carbon dilution in the target later on (Section 5.4). The first dButanol beam time took place in October 2018 followed by a carbon beam time in November 2018. The second dButanol one took place in December 2021 after the carbon beam time in November 2021. The both beam times are abbreviated with Oct2018 and Dec2021, respectively.

	Oct2018	Nov2018	Nov2021	Dec2021
Start	15.10.2018	17.11.2018	08.11.2021	17.11.2021
End	17.11.2018	26.11.2018	12.11.2021	12.12.2021
Data taking [h]	596	108	64	283
Data taking* [h]	513	101	274	60
Beam current* [nA]	0.45	0.45	0.77	0.77
# Data events* [$\cdot 10^9$]	2.156	0.416	0.520	2.327
Max. events/run [$\cdot 10^6$]	2	2	5	5
Av. event rate* [Hz]	1167	1149	2319	2360
# Raw π^0 * [$\cdot 10^6$]	401	80	432	95
Max. target pol. [%]	75.3	-	-	69.4
Av. target pol. [%]	69.9	-	-	65.1

Table 2.2: Information about the beam times. The * indicates that only usable runs with the *vme_trig_42* trigger are considered, e.g. no low-rate runs. The raw number of π^0 is automatically calculated within the data acquisition software and is only a rough estimation.

Table 2.2 provides an overview of the beam times with some basic information. Low-rate and copper runs are usually done once per day. The tagging rate is around 8 MHz for normal data taking runs. For low-rate runs, this rate is decreases to $\lesssim 300$ kHz, which then is similar to the GIM rate. This rate corresponds to one of $\lesssim 15$ kHz for the first 32 Tagger bars (highest photon energies), which is taken as a reference for ELSA.

Generally, the beam was much more stable in Oct2018, such that the event

rate or beam current was not fluctuating much. Moreover, the coherent edge of the photon beam polarisation at 1200 MeV was sometimes walking or jumping up to ± 100 MeV shifts in Dec2021. This needed to be adjusted every time, decreasing data taking time and making determining the linear polarisation degree more difficult.

The main difference between the two beam times lies in the CB readout. The Oct2018 beam time used the slower QDC readout, whereas the Dec2021 beam time was done with the SADC readout [258]. This led to a doubling of the event rate. In Oct2018, the SADC were also in use most of the time for testing and comparing reasons. However, the SADC readout still had some major problems in the Oct2018 beam time, such that they were only fully operative in the Dec2021 one.

The electrons in ELSA are accelerated up to 3.2 GeV with a beam current of ~ 0.45 nA and ~ 0.77 nA in Oct2018 and Dec2021, respectively. A 4 mm collimator focuses the beam on the target for both beam times.

3 | Event reconstruction

This chapter discusses how the investigated reactions $\gamma N \rightarrow \pi^0 N$ and $\gamma N \rightarrow \eta N$ can be identified with the available Crystal Barrel/TAPS setup.

The first Section 3.1 provides an overview of the used software that is based on ROOT, which again is primarily based on C++.

The reconstruction of particles and assigning physical information, e.g. energy, time, angle or charge, within the single detector components and their interplay is discussed in Section 3.2.

Section 3.3 shows how the reconstructed energy and time information is calibrated in the different detector parts. The calibration *converts* raw detector signals like voltage to valid physical values like energy.

If not denoted otherwise, all figures within this chapter are taken from the Oct2018 beam time. As the setup was identical in the Dec2021 beam time, their figures look the same. The only difference between the experimental setup is the SADC readout in CB that replaced the QDC one in Dec2021.

3.1 Software

The calculations and data analyses are done with the help of software. It is therefore crucial, that the used programmes are adjusted and further developed to suit the experiments done within the framework of this work.

Nearly all used software is based on ROOT (Section 3.1.1), which again is primarily based on C++. Therefore, the reconstruction is performed using different programmes and libraries (Section 3.1.2). Also, Monte Carlo simulated events (Section 3.1.3) are used to compare experimental data and simulated predictions.

3.1.1 ROOT

ROOT [291, 292] is an open-source data analysis framework developed by CERN for analysing large data sets from high-energy particle physics experiments. It is mainly written in C++ but also consists of some parts in Fortran and Python. It can make complicated calculations, fit data with the most complicated fit functions, make nice graphical outputs of data and many more. Important classes are, for example, TH1 that stores data as histograms, TLorentzVector that is a general four vector defined by the position and time or momentum and energy and TTree that represents a columnar dataset. The standard ending of ROOT files is `.root`.

3.1.2 Data analysing software

Extended Plugable Objectoriented Root Analysis

Extended Plugable Objectoriented Root Analysis (EXPLORA) is a software package based on ROOT that fully reconstructs the detected particles in the Crystal Ball/TAPS experimental setup. It can also be used to analyse data or simulate reactions. The configuration files given to EXPLORA are written in Extensible Markup Language (XML). They define all needed information for the reconstruction by setting flags. The programme is mainly written by Schmidt [293], Hartmann [262], Piontek [294], Schmitz [295] and Kalischewski [296]. However, (nearly) all CBELSA/TAPS collaborators contribute sooner or later.

EXPLOSCAR

The analysis is done in `OSCAR` instead of `EXPLORA` itself. For connecting both programmes, an additional software package or interface, respectively, is written in the framework of this work: `EXPLOSCAR`.

`EXPLOSCAR` has three main features: First, it processes the raw `EXPLORA` data to `OSCAR` readable ones. Second, it combines the detected particles into a physical reaction. Third, it makes some basic cuts such that it serves as presort programme, i.e. coincidence time cuts.

This software is developed to dismiss a significant part of background reactions and, thus, to speed up the later analysis with `OSCAR`.

`EXPLOSCAR` is based on `ROOT` and written in `C++`.

OSCAR Simplifies Coding and Analyzing with ROOT

`OSCAR Simplifies Coding and Analyzing with ROOT` `OSCAR` is a software package based on `ROOT` that analyses the reaction by computing physical properties and making cuts on them. Originally, `OSCAR` was designed for the A2 experiment at MAMI in Mainz, Germany. It was mainly developed by Werthmüller [270]. `OSCAR` can, for example, fully reconstruct the true centre of mass energy W from the final state in single meson photoproduction reactions off quasifree nucleons.

However, it has been extended with the `libTOCB` that fits the situation of the Crystal Barrel/TAPS experimental setup at ELSA in Bonn, Germany. It was developed by Witthauer [271]. Within this work, this library has been developed further to read the data from `EXPLOSCAR` and to fit the investigated reactions.

3.1.3 Monte Carlo simulation software

In addition to the analysis of experimental data, Monte Carlo (MC) simulations are performed for comparisons. However, no MC simulations are needed for the final results and no MC-generated data is used.

Virtual Monte Carlo (VMC) [296] is part of `EXPLORA` and generates pseudo detector data with the help of the CERN software `Geant3` or `Geant4`. `Geant` simulates the passage of particles through matter [297, 298]. Here, `Geant3` is

used due to its confirmation with this detector setup in the past [262, 271, 272]. However, no MC data are used to determine the polarisation observables themselves, in contrast to the determination of the DCS. The simulation of photons works quite well, where there are some differences between simulated and experimental data for the nucleons.

VMC can also handle Fermi momentum distributions for quasifree nucleons. Therefore, nucleons inside a nucleus with $A \geq 2$ are distributed by a probability density function (PDF). For nucleons inside deuterium, the PDF is given by [299]:

$$f_{pdf}^D(p_F^2) = \frac{2p_F^2}{\pi} \cdot \left(\sum_{i=1}^{13} \frac{c_i + d_i}{p_F^2 + m_i^2} \right) \quad \text{with} \quad p_F^2 = \frac{p_F^2}{\hbar^2}, \quad (3.1)$$

where the mass parameters m_i are given by

$$m_i = 0.23162461 + (i - 1) \cdot m_0 \quad \text{with} \quad m_0 = 1 \text{ fm}^{-1}, \quad (3.2)$$

and the coefficients c_i and d_i can be found in Table 3.1. The coefficients c_{13} , d_{11} , d_{12} and d_{13} are defined by the other coefficients [299].

i	c_i [fm ^{-1/2}]	d_i [fm ^{-1/2}]
1	8.868 807 6 · 10 ⁻¹	2.313 519 3 · 10 ⁻²
2	-3.471 709 3 · 10 ⁻¹	-8.560 457 2 · 10 ⁻¹
3	-3.050 238 0	5.606 819 3
4	5.620 776 6 · 10 ¹	-6.946 292 2 · 10 ¹
5	-7.495 733 4 · 10 ²	4.163 111 8 · 10 ²
6	5.336 527 9 · 10 ³	-1.254 662 1 · 10 ³
7	-2.270 686 3 · 10 ⁴	1.238 783 0 · 10 ³
8	6.043 446 6 · 10 ⁴	3.373 917 2 · 10 ³
9	-1.029 205 8 · 10 ⁵	-1.304 115 1 · 10 ⁴
10	1.122 335 7 · 10 ⁵	1.951 252 4 · 10 ⁴
11	-7.592 522 6 · 10 ⁴	-1.563 432 372 1 · 10 ⁴
12	2.905 971 5 · 10 ⁴	6.623 108 923 · 10 ³
13	-4.815 736 798 · 10 ³	-1.169 818 469 · 10 ³

Table 3.1: Coefficients for the probability density function (PDF) describing the Fermi momentum distribution of nucleons in deuterium (Equation 3.1).

The PDF describing the Fermi momentum distribution of nucleons inside

^{12}C can be described by [300]:

$$f_{pdf}^C(p_F) = \frac{0.004 \cdot a^{3/2}}{\sqrt{\pi}} \cdot p_F'^2 \cdot (e^{-ap_F'^2} + c \cdot e^{-bp_F'}) \quad \text{with } p_F' = 0.005 \cdot p_F, \quad (3.3)$$

where $a = 1/0.416$, $b = 1/0.23$ and $c = 0.04$. This distribution could also be used for heavier nuclei like ^{16}O or ^{40}Ca due to their tiny differences [272].

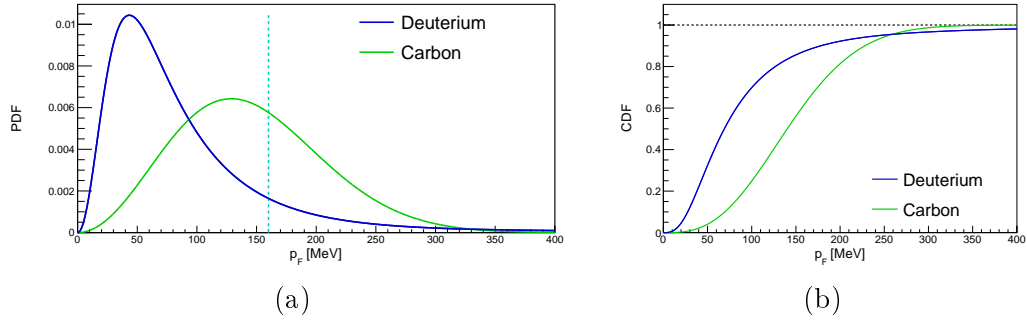


Figure 3.1: Probability density function (PDF, a) and cumulative distribution function (CDF, b) of the Fermi momentum of nucleons inside deuterium (blue) and carbon (green). The explicit PDF can be found in Equations 3.1 and 3.3.

The cumulative distribution function (CDF) is the probability that a random variable X will be less than or equal to x . It is connected to the PDF by the integral:

$$f_{CDF}(x) = P(X \leq x) = \int_0^x f_{PDF}(x') dx', \quad (3.4)$$

where in general, the lower integration limit would be $-\infty$. However, the PDF of the Fermi momentum distribution is positively definite such that its integral can start at 0 without loss of generality.

Figure 3.1b shows the CDF of the Fermi momentum distributions of D and C. It is visible that the most significant difference between the CDFs is around 93 MeV and that they have a point of intersection around 259 MeV.

3.2 Particle reconstruction

The reconstruction of particles in the calorimeters is performed using energy, time, angle and charge information from the detected clusters. The latter occurs because particles do not always deposit all their energy in one crystal alone but spread it over several. Therefore, it is said that the cluster is spread over different particle energy deposits (PED). These PED are found with the `ClusterFinder` algorithm in `EXPLORA`, which subdivides a cluster into different PED if more than one local maximum is found. This subdetector reconstruction is discussed in the following.

3.2.1 Tagging system

The tagging system is made up of overlapping bars and fibres. Clusters are built when at least two overlapping elements get a hit [247]. Figure 3.2 shows an example of a hitting electron. The time difference between the signals is set to 6 ns for the bars and 7 ns for the fibres. Due to inefficiencies in the fibres, single hits are taken as well. To be combined, the time difference between bar and fibre clusters must be less than 4 ns.

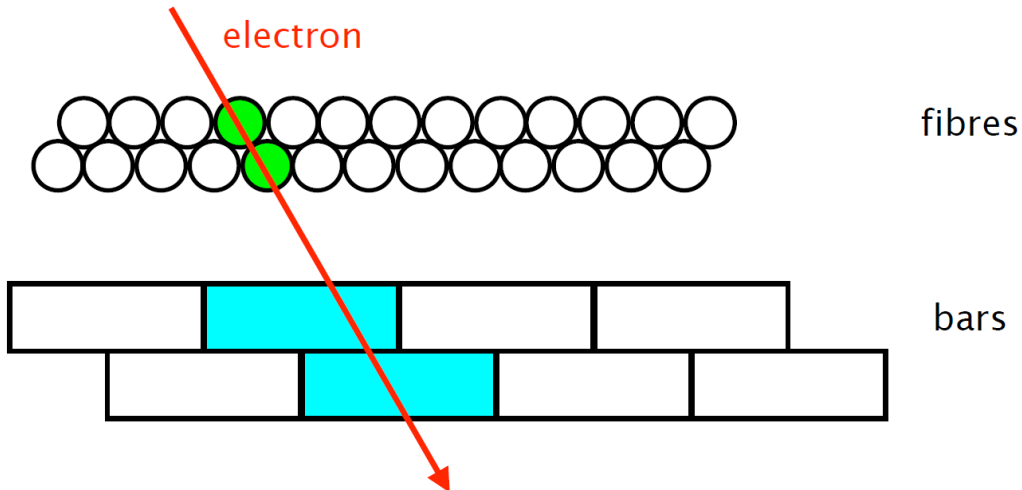


Figure 3.2: Schematic representation of a valid Tagger hit with two firing fibres and two firing bars. Figure taken from [253, 271].

The energy for a reconstructed beam photon E_γ is given by the normalised

sum of the fibre hits whenever possible:

$$E_\gamma = \frac{1}{n_f} \cdot \sum_{i=1}^{n_f} E_i. \quad (3.5)$$

Here, n_f is the number of fibre hits. Calibrated polynomials then give the energy values E_i [247]. If no fibre is available, the energy is taken from the bars. The reason for this lies in the better resolution for the fibres.

The time for a reconstructed beam photon is calculated using a weighted sum over the times of tagging bars and fibres:

$$t_\gamma = \frac{w_f \cdot \sum_{i=1}^{n_f} t_i + w_b \cdot \sum_{i=1}^{n_b} t_i}{w_f \cdot n_f + w_b \cdot n_b}. \quad (3.6)$$

Here, n_f and n_b are the number of fired hits in the fibres and bars. The weights w_f and w_b are given by the resolution of the inverse square of the corresponding detector's full width half max (FWHM). They were calculated by [247, 268]:

$$w_f = \frac{1}{(\text{FWHM}_f)^2}, \quad w_b = \frac{1}{(\text{FWHM}_b)^2}. \quad (3.7)$$

The ratio between the two FWHM is around 2, meaning the bars have a better time resolution.

3.2.2 Crystal Barrel and Forward Plug detector setup

Crystal Barrel and Forward Plug

If a cluster consists of one-PED, only the energies of the different crystals E_i are summed up:

$$E_{PED} = E_{cluster} = \sum_{i=0}^n E_i. \quad (3.8)$$

A single crystal threshold of 1 MeV must be surpassed. The centre of a PED and a cluster must exceed an energy threshold of 20 MeV. The crystal hits for an event must be within the time range of 100 ns (Figure 3.3a).

If more than one-PED is found, some part of the detected energy comes from other PED. Since two-PED events are strongly dominant in such cases, their energy reconstruction will be explained in the following.

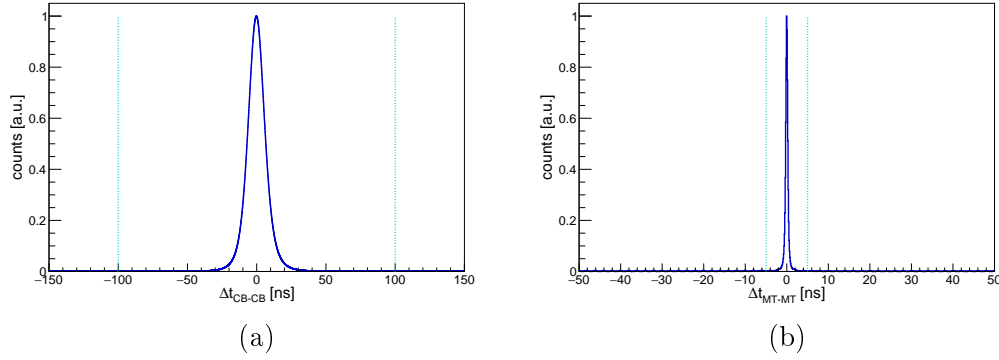


Figure 3.3: Time difference between coincidence hits in Crystal Barrel-Crystal Barrel (CB-CB, a) and MiniTAPS-MiniTAPS (MT-MT, b) with its cut positions at 100 ns and 5 ns. The Forward Plug is included in CB.

Crystals from PED are weighted with [301]:

$$w_{12} = E_2^{max} \cdot e^{-|r_1 - r_2|/r_M}, \quad (3.9)$$

where E_2^{max} is the maximum crystal energy of the second PED, $|r_1 - r_2|$ is the distance between the crystals in the second PED and a specific crystal in the first one and $r_M = 3.57$ cm is the Molière radius [301]. The distances $r_{1,2}$ are further corrected by the depth of the shower d . The entire energy reconstruction is pretty elaborated and can be found in detail in [301].

The photon energy resolution of CB is given in Equation 2.2. A weighted sum reconstructs the position of the detected particles over all contributing crystals such that a PED is defined by its radius r_{PED} and the two angles θ_{PED} and ϕ_{PED} :

$$r_{PED} = \frac{\sum_{i=1}^n w_i r_i}{\sum_{i=1}^n w_i}, \quad \theta_{PED} = \frac{\sum_{i=1}^n w_i \theta_i}{\sum_{i=1}^n w_i}, \quad \phi_{PED} = \frac{\sum_{i=1}^n w_i \phi_i}{\sum_{i=1}^n w_i}. \quad (3.10)$$

The weights w_i are given by:

$$w_i = \max \left\{ 0, w_0 + \ln \left(\frac{E_i}{\sum_{i=1}^n E_i} \right) \right\}, \quad (3.11)$$

where $w_0 = 4.25$ is the cutoff parameter found with a MC simulation [302].

Due to energy loss, an additional energy correction function is applied [303], which was again found by a MC simulation and its comparison to π^0

measurements.

As a result, an angular resolution of less than 2° is achieved for photons [304], which is more than three times better than the angular coverage of a crystal (Section 2.2.3). The logarithmic weighting in Equation 3.11 improves the angular resolution by weighting outside crystals more.

Inner Detector

ID is made of three layers of organic scintillators to identify charged particles (Section 2.2.5). The reconstruction of ID is done in multiple steps before spacial and time information are compared with CB hits.

In the first step, clusters are determined in each layer separately with the condition that neighbouring fibres must fire within a 14 ns time window (Figure 3.4c). A threshold of 150 keV is requested for a hit. Afterwards, the clusters in the two layers are compared to each other. The two clusters are merged if their time difference is again less than 14 ns and the intersection point satisfies the geometry.

In the second step, two-layer hits are compared and three-layer hits are built. For one three-layer hit, three two-layer hits are detected (1 + 2, 1 + 3, 2 + 3), which again must be within a time window of 14 ns. Furthermore, their spatial coherence is checked by applying a cut on the three points in the $\phi - z$ -plane. The centre of that triangle is taken as the direction point for the particle. See [262] for more details and some visualisations.

In the last step, clusters in ID are compared to the ones in CB and FP. Their coincidence time signal must be smaller than 50 ns and the difference between their two angles $\Delta\theta$ and $\Delta\phi$ must be smaller than 12° (Figure 3.4). The overlap between ID and FP is only around the most outer ring in FP.

Because of the different number of coincidence layer hits **EXPLORA** assigns a reconstruction quality to a PED, called **ChargedQuality**. Suppose all three layers register a hit, the value is set to 1. If only two hit, the value is $2/3$ and if only one layer hits, the event is dismissed due to unusable angle information. However, a particle is assigned as charged if the **ChargedQuality** is at least $2/3$, i.e. if at least two layers registered a hit. See Figure 3.8a for the distribution of the charge quality.

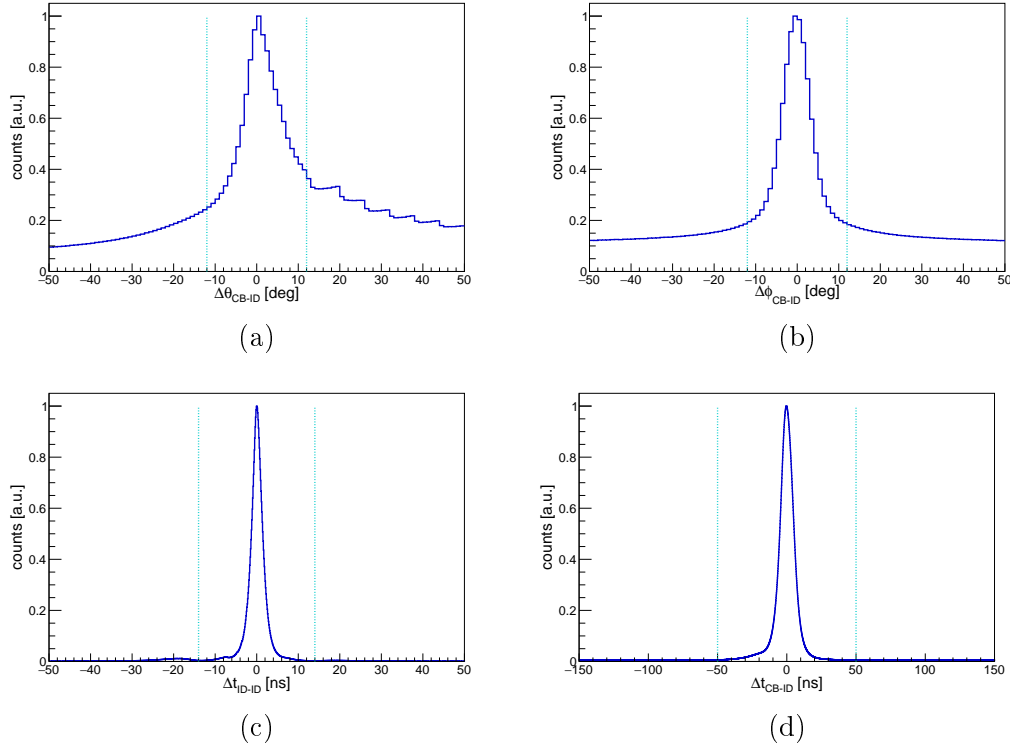


Figure 3.4: Angle difference between coincidence hits in Crystal Barrel with Forward Plug (CB) and Inner Detector (ID) for the polar angle θ (a) and the azimuthal angle ϕ (b) with its cut positions at $\pm 12^\circ$. The time difference between coincidence hits in ID (c) and between hits in CB and ID (d) with its cut positions at 14 ns and 50 ns, respectively, can be seen as well.

Forward Plug Veto

FPV is a charge-sensitive detector. It is made of two layers of organic scintillator material and situated directly in front of FP (Section 2.2.4). The two overlapping layers must fire within a time window of 20 ns (Figure 3.5c). The polar resolution is doubled to $\Delta\theta = 6^\circ$.

To assign a hit in FPV with a hit in FP, a coincidence time of 50 ns and angular resolutions of $\Delta\theta \leq 8^\circ$ and $\Delta\phi \leq 14^\circ$ are required (Figure 3.5).

As for the ID *EXPLORA*, assigns a `ChargedQuality` to a PED depending on the number of FPV hits per cluster. For 1 hit, it is 0.45. For 2, it is 1. For 3, it is 0.75. For more than 3, it is set to 0.5. However, a particle is assigned as charged if the `ChargedQuality` is at least 0.45, i.e. if at least one layer registered a hit. See Figure 3.8a for the distribution of the charge quality.

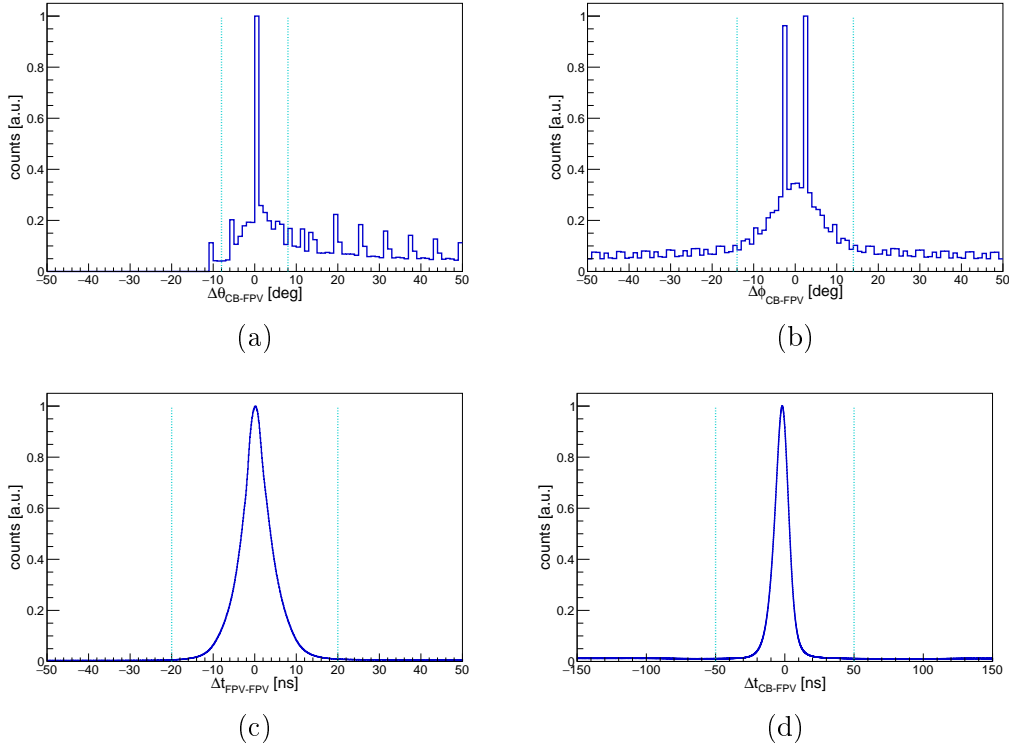


Figure 3.5: Angle difference between coincidence hits in Crystal Barrel with Forward Plug (CB) and Forward Plug Veto (FPV) for the polar angle θ (a) and the azimuthal angle ϕ (b) with its cut positions at $\pm 8^\circ$ for first and $\pm 14^\circ$ for latter. Figures (c) and (d) show the time difference between coincidence hits in FPV and CB and FPV, respectively. The cut positions are set at ± 20 ns and ± 50 ns.

3.2.3 MiniTAPS detector system

MiniTAPS

The reconstruction of particles detected in MT is done similarly to CB, with some vital differences.

Because of more background in the forward direction, the thresholds are chosen slightly higher. The crystal threshold is chosen to be 17 MeV for the two most inner rings and 13 MeV for the other ones. A central PED crystal must have at least 20 MeV and a cluster must exceed 25 MeV. The time difference between two hits in the same cluster must be smaller than 5 ns (Figure 3.3b).

For one-PED events, the energy is calculated with Equation 3.8. For two-PED events, the energies are weighted with a ratio of the two-PED energies.

Since MT has a much better angular resolution, more than one-PED events are very rare.

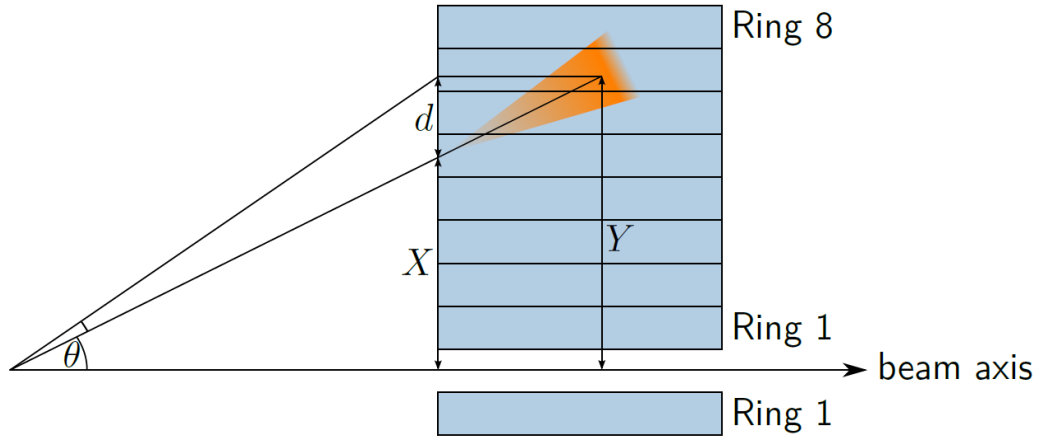


Figure 3.6: Schematic representation of a part of MiniTAPS (MT) shown from the side. The orange cone represents the cluster shower, where the position in the upward direction needs to be corrected by the offset d . Figure taken from [262].

MT is a vertical detector that shows towards the target. The position that is calculated with Equation 3.10, where $w_0 = 4.0$ in Equation 3.11 [305], needs to be corrected by its penetration depth. Therefore, an offset value d is introduced.

As well as for CB, some elaborated algorithm is used to reconstruct the true energy and position. The energy is corrected by a linear function from a MC simulation [306]. The hexagonal shape of MT crystals leads to some further, smaller corrections and shower losses that are corrected too [306].

MiniTAPS Veto

MTV is charge sensitive, situated in front of MT and is made of non-overlapping organic scintillators. Thus, all hits are traded separately and the element's centre is taken as the impact point.

Hits in MTV are compared to hits in MT and chosen to be coincident if their time difference is less than 15 ns. The distance between the impact point of the MTV and the one on the surface of MT must be less than the excircle diameter of a MiniTAPS element, i.e. 6.51 cm [265] (Figure 3.7).

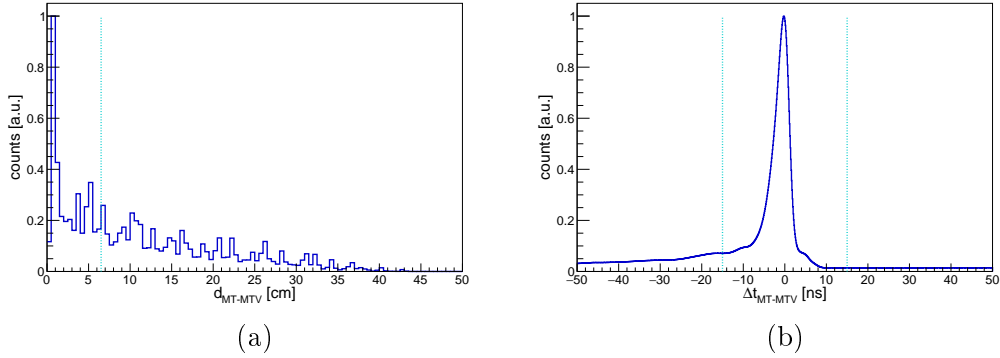


Figure 3.7: (a) Distance between a coincidence hit in MiniTAPS (MT) and MiniTAPS Veto (MTV) with its cut position at 6.51 cm. (b) Time difference between coincidence hits in MTV and MT with its cut positions at ± 15 ns.

Since one MTV element covers exactly one MT element, the most probable charged hit is registered if only one MTV element fires. The **ChargedQuality** is therefore set to the inverse number of fired MTV elements (Figure 3.8b). The relative distribution of charged hits is around 65 % for 1 MTV hits, 24 % for 2, 8 % for 3, 2 % for 4 and less than 1 % for more. All events up to 6 fired MTV elements are set as charged for the event selection.

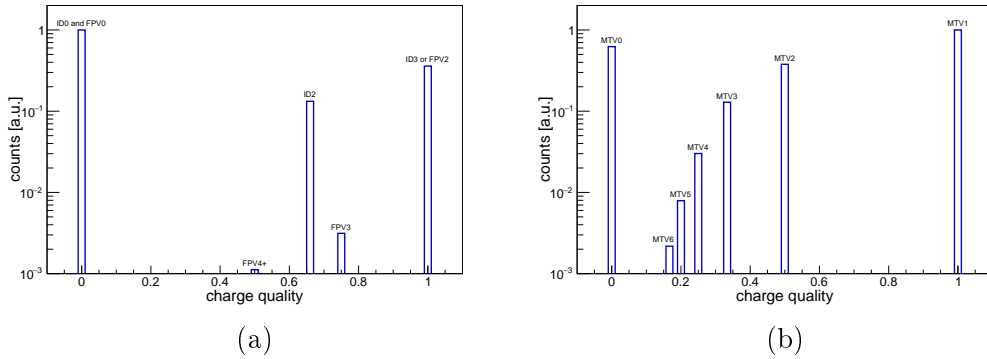


Figure 3.8: Charge quality of reconstructed particles in Inner Detector (ID, a) and Forward Plug Veto (FPV, a) and the MiniTAPS Veto (MTV, b). The number behind the shortcut of the detectors stands for the number of registered hits in the corresponding veto detector. See text for more details.

3.2.4 Gamma Intensity Monitor and Flux Monitor

GIM and FluMo have the purpose of determining the photon flux. Therefore, they only need the timing information.

After a hit is measured in GIM, no events are taken for the next 12 ns to avoid double counting. In the FluMo, a coincidence time of 10 ns is required for hits in the two scintillator layers with no simultaneous hit in the veto layer.

3.3 Calibration

Before data from the detectors in a scattering experiment can be used and reliable statements about physical processes can be made, the raw digital data must be converted into a physically meaningful one. The different readout data from digital converters, mainly Time-to-Digital Converters (TDC) for time and Analogue-to-Digital Converters (ADC and SADC) for energy, need to be calibrated.

Scintillators have their own readout electronics that may be very sensitive to different environmental influences. To treat this correctly, different time depending run sets are commonly used in the calibration.

All calibrations within the framework of this work but the MT cosmics one (Section 3.3.2) are done by collaboration colleagues. However, a brief overview of the working principles is given here.

3.3.1 Time calibration

The time calibration converts raw TDC channel numbers to a physical time, typically given in ns.

All detectors have an output to Single-Hit TDC (MT) or Multi-Hit TDC (all other detectors) to register a signal given as channel numbers between two timing signals. The start is given by the trigger, the stop by the detector, except for MT, where it is vice versa.

The connection between a TDC channel c_{TDC} and a physical time t is linearly connected by a gain factor g and an offset o :

$$t = g \cdot c_{TDC} + o. \quad (3.12)$$

The offset ensures that coincidence detector hits have the same time.

For every detector, coincidence times are plotted and the peak is moved to 0, which removes jitter effects from the trigger and results in a better time resolution. The time difference is given by:

$$\Delta t = t_1 - t_2 = (t_1^{det} - t_{trigg}) - (t_2^{det} - t_{trigg}), \quad (3.13)$$

where $t_{1,2}^{det}$ are the times from two different detector modules and t_{trigg} is the trigger time.

The Tagger bars time is taken as a reference for timing coincidences between different detectors.

Detector	FWHM [ns]
Tagger-Tagger	0.8592 ± 0.0002
Tagger (fibres)-Tagger	1.4384 ± 0.0004
CB-Tagger	7.591 ± 0.008
ID-Tagger	2.188 ± 0.001
FP-Tagger	4.70 ± 0.01
FPV-Tagger	4.93 ± 0.01
MT-Tagger	0.85 ± 0.01
MTV-Tagger	3.34 ± 0.02
CHKV-Tagger	1.231 ± 0.002
GIM-Tagger	3.0775 ± 0.0006

Table 3.2: Typical time resolutions for different coincidence times with Tagger bars (Tagger) as reference time. Numbers are taken from [144].

See Table 3.2 for an overview of typical coincidence time resolutions in different detectors. FWHM is the full width half maximum determined by a Gaussian fit to the time spectra given by:

$$\text{FWHM} = 2\sqrt{2\ln(2)}\sigma \approx 2.355\sigma. \quad (3.14)$$

More details about the time calibration can be found in [268] and [144].

3.3.2 Energy calibration

The energy calibration converts the voltage from raw ADC channel numbers to physical energy, typically given in MeV.

Particles hit the detector material and interact with its scintillation material such that light is emitted. At the end of every scintillator material, a PMT is mounted to absorb the emitted light. The PMT converts photons to electrons, multiplies them to measurable voltages and guides the signal to an ADC.

The connection between an ADC channel c_{ADC} and a physical energy E is linearly connected by a gain factor g and a pedestal offset p :

$$E = g \cdot (c_{ADC} - p). \quad (3.15)$$

The pedestal is the ADC channel where no energy is deposited.

Depending on the detector and its scintillator material, the energy calibration is performed in different ways, described in the following sections.

Tagger

The Tagger energy E_{e^-} must be calibrated to calculate the energy of the photons E_γ that impinge the target (Equation 2.1).

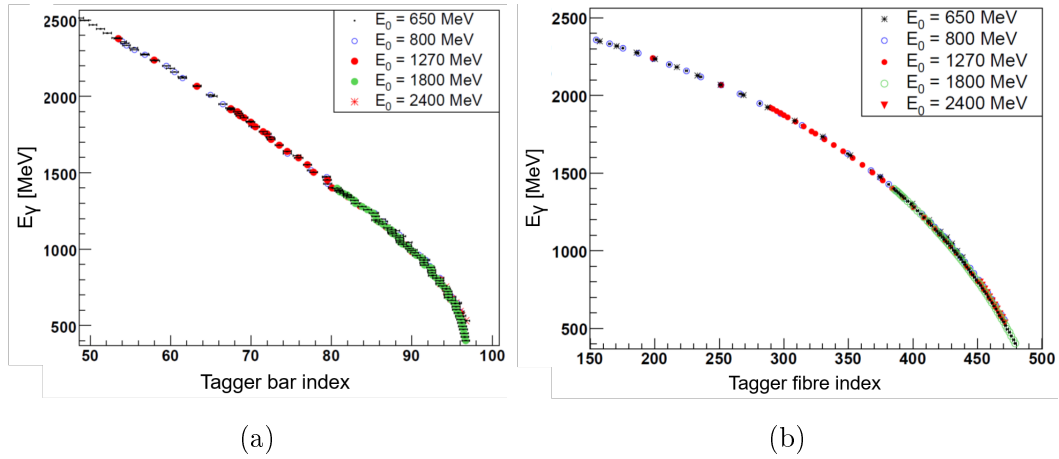


Figure 3.9: Incident beam photon energy E_γ as a function of the Tagger bar (a) and Tagger fibre (b) for different ELSA beam electron energies E_0 . Figures taken from [247].

Electrons with well-known ELSA electron energies E_0 are deflected towards the Tagger without a radiator. The magnetic field is varied to get multiple data points (Figure 3.9). The data points are fitted with a polynomial function of degree 4 and 5, respectively, to get a well-defined photon energy for every measured electron energy [247].

More details about the Tagger energy calibration can be found in [247].

Crystal Barrel with Forward Plug

Dual-range ADC provide a good energy resolution for the low energy range up to 125 MeV and the high energy range up to 2 GeV for the FP elements and 1.1 GeV for the others. The signal is therefore divided by 8 for the high-range.

Light pulser calibration First, the pedestal p and gain g for both ranges are determined by LED light [257]. The light is damped with different filters so that ADC values can be found as a function of the transmission T . The y -intersect is equal to the pedestal, whereas the slope is connected to the gain by:

$$E_{low} = g \cdot (c_{ADC,low} - p_{low}), \quad (3.16)$$

$$E_{high} = g \cdot g_{LP} \cdot (c_{ADC,high} - p_{high}) \quad \text{with} \quad g_{LP} = g_{high}/g_{low}. \quad (3.17)$$

The gain ratio g_{LP} is approximately 1/8 and is monitored during data-taking runs with special LP runs (Figure 3.10b).

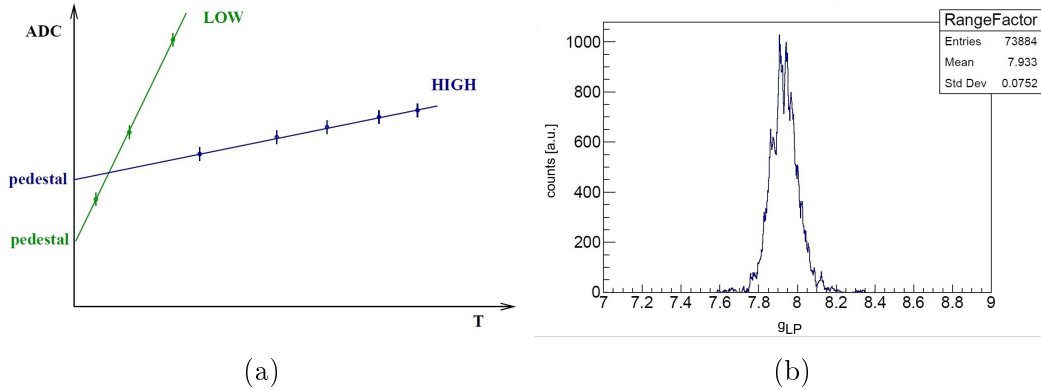


Figure 3.10: (a) Typical transmission measurement of the dual-range Analogue-to-Digital Converter (ADC, low and high) with the light-pulser system. (b) Gain ratio factor $1/g_{LP} \approx 8$ during the beam time and for all Crystal Barrel (CB) crystals. Figure (a) taken from [307]. Figure (b) taken from [308].

Invariant mass calibration The fine calibration is performed by looking at the invariant mass in inclusive π^0 photoproduction. Two neutral PED are required and their invariant mass squared $m_{\gamma\gamma}^2$ is calculated by:

$$m_{\gamma\gamma}^2 = E_{\gamma_1} E_{\gamma_2} (1 - \cos(\phi_{\gamma_1\gamma_2})), \quad (3.18)$$

where E_{γ_1, γ_2} is the energy of the first and second photon, respectively, and

$$\begin{aligned} \phi_{\gamma_1 \gamma_2} &= \frac{\vec{p}_{\gamma_1} \cdot \vec{p}_{\gamma_2}}{|\vec{p}_{\gamma_1}| \cdot |\vec{p}_{\gamma_2}|} = \sin(\theta_{\gamma_1}) \sin(\theta_{\gamma_2}) \cos(\phi_{\gamma_1}) \cos(\phi_{\gamma_2}) \\ &\quad + \sin(\theta_{\gamma_1}) \sin(\theta_{\gamma_2}) \sin(\phi_{\gamma_1}) \sin(\phi_{\gamma_2}) \\ &\quad + \cos(\theta_{\gamma_1}) \cos(\theta_{\gamma_2}) \end{aligned} \quad (3.19)$$

is the opening angle between them, defined by their momenta $\vec{p}_{\gamma_{1,2}}$. Here, $\theta_{\gamma_{1,2}}$ and $\phi_{\gamma_{1,2}}$ are the polar and azimuthal angles of the corresponding photon.

Gaussian error propagation of the individual uncertainties gives the uncertainty of the invariant mass:

$$\Delta m_{\gamma\gamma} = \frac{m_{\gamma\gamma}}{2} \cdot \sqrt{\left(\frac{\Delta E_{\gamma_1}}{E_{\gamma_1}}\right)^2 + \left(\frac{\Delta E_{\gamma_2}}{E_{\gamma_2}}\right)^2 + \left(\frac{\Delta \cos(\phi_{\gamma_1 \gamma_2})}{1 - \cos(\phi_{\gamma_1 \gamma_2})}\right)^2}, \quad (3.20)$$

where the uncertainty of the opening angle is given by [270]:

$$\begin{aligned} \Delta \cos(\phi_{\gamma_1 \gamma_2}) &= \\ &\quad \{ (-\sin(\theta_{\gamma_1}) \sin(\theta_{\gamma_2}) \sin(\phi_{\gamma_1} - \phi_{\gamma_2}) \Delta \phi_{\gamma_1})^2 \\ &\quad + (-\sin(\theta_{\gamma_1}) \sin(\theta_{\gamma_2}) \sin(\phi_{\gamma_2} - \phi_{\gamma_1}) \Delta \phi_{\gamma_2})^2 \\ &\quad + ([\cos(\theta_{\gamma_1}) \sin(\theta_{\gamma_2}) \cos(\phi_{\gamma_1} - \phi_{\gamma_2}) - \sin(\theta_{\gamma_1}) \cos(\theta_{\gamma_2})] \Delta \theta_{\gamma_1})^2 \\ &\quad + ([\sin(\theta_{\gamma_1}) \cos(\theta_{\gamma_2}) \cos(\phi_{\gamma_2} - \phi_{\gamma_1}) - \cos(\theta_{\gamma_1}) \sin(\theta_{\gamma_2})] \Delta \theta_{\gamma_2})^2 \}^{1/2}. \end{aligned} \quad (3.21)$$

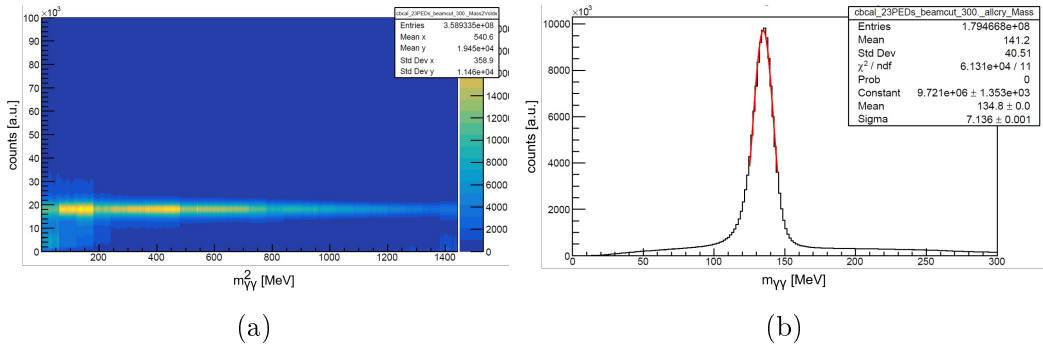


Figure 3.11: Crystal Barrel (CB) energy calibration overviews. (a) Squared invariant mass of two photons as a function of the CB elements. Elements 1 to 180 are part of the Forward Plug (FP). (b) Invariant mass of two photons with the fitted Gaussian function (red). Figures taken from [309].

The calibration moves the $m_{\gamma\gamma}$ peak belonging to the π^0 decay towards its nominal PDG mass of $m_{\pi^0} = 134.977 \text{ MeV}$ [44]. A cluster mostly consists of multiple crystal hits, such that the energy of one crystal depends on the others. The calibration is done iteratively and the new gain value g_{new} is calculated for every crystal separately by:

$$g_{new} = g_{old} \cdot \left(\frac{m_{\pi^0}^2}{m_{\gamma\gamma}^2} \cdot (1 - d) + d \right). \quad (3.22)$$

If all gain factors are systematically shifted towards one direction, which mostly happens, an additional damping factor $d = 0.3$ must be used [304] as already given in Equation 3.22. In the end, the average π^0 peak position is found at its nominal mass with an overall FWHM of $(16.805 \pm 0.002) \text{ MeV}$ (Figure 3.11b).

More details about the CB energy calibration can be found in [302] and [304].

MiniTAPS

Cosmics calibration Before an experiment, a raw MT energy calibration is performed with minimal ionising cosmical particles, i.e. muons. When charged particles pass through matter, they lose energy due to ionisation, which can be described by the Bethe-Bloch formula [61, 310, 311]:

$$-\frac{dE}{dx} = \frac{4\pi}{m_e c^2} \frac{nz^2}{\beta^2} \left(\frac{e^2}{4\pi\epsilon_0} \right)^2 \left[\ln \left(\frac{2m_e c^2 \beta^2}{I(1-\beta^2)} \right) - \beta^2 - \frac{\delta}{2} - \frac{U}{2} \right], \quad (3.23)$$

where m_e is the mass of the electron, c the speed of light, n the electron density, ze the charge of the particle, $\beta = v/c$, v the velocity, ϵ_0 the vacuum permittivity, I the average ionisation potential of the atoms, δ a density effect correction and U a shell effect correction.

The density correction gets important for high energies where the real media gets polarised. The shell effect correction is important for low energies, where the atomic binding is important. However, the latter is around 1% for a pion with a kinetic energy of $T = 6 \text{ MeV}$ [44]. Additional corrections can be applied in Equation 3.23 for treating the low energy region as it is based on the first order Born approximation [44].

BaF₂ has minimum ionisation of $1.303 \text{ MeV cm}^2 \text{ g}^{-1} = 6.374 \text{ MeV cm}^{-1}$ [312,

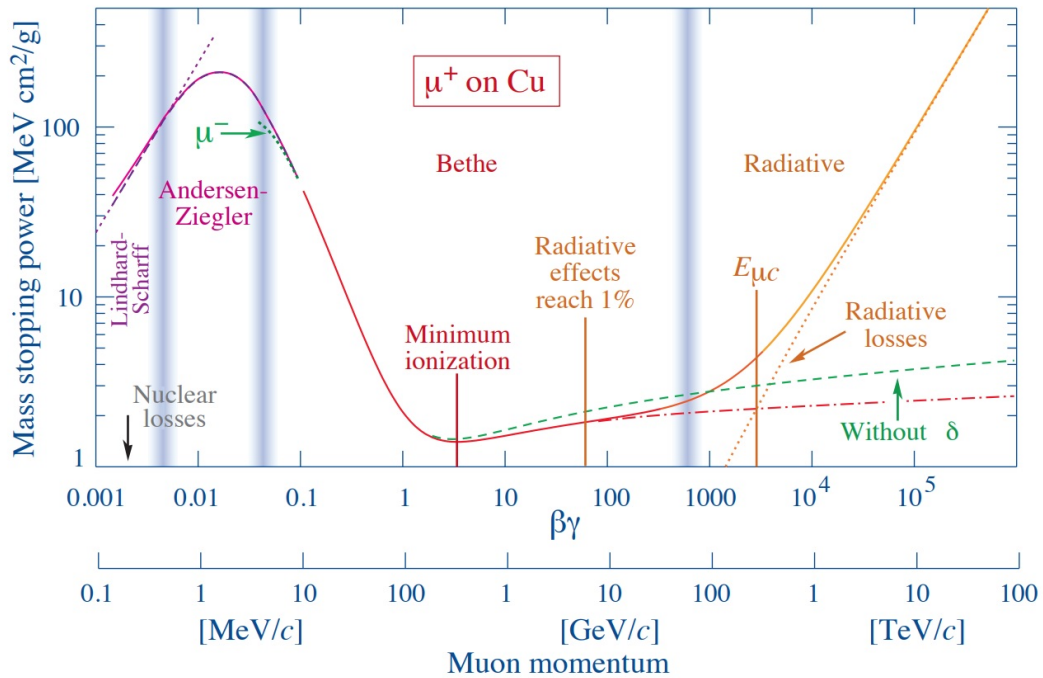


Figure 3.12: Energy loss per range $-dE/dx$ (Mass stopping power) as a function of $\beta\gamma$ for muons in copper. γ is the Lorentz factor given as $(1 - \beta^2)^{-1/2}$ with $\beta = v/c$. Figure taken from [44].

313]. One BaF_2 crystal has a height of around 5.9 cm [265] leading to a minimum ionising energy of around 37.6 MeV for cosmic muons crossing MT elements. This property can be used to pre-calibrate MT for the experiment. Therefore, the MT data acquisition is started in the standalone mode with no beam to take cosmic data. The number of events is plotted for every MT element separately as a function of the ADC channel. The pedestal is found by fitting a simple Gaussian function to the first rising peak. In contrast, the minimum ionising peak is found by a fit function consisting of a Gaussian signal and an exponential background term. Figure 3.13 shows an example of such a fit.

Furthermore, voltages (HV) and Leading-Edge-Discriminators (LED) are calibrated with cosmics before an experiment. The HV calibration adjusts the voltage value of the elements such that the gain factor lies around $g_{ideal} = 0.48 \pm 0.05$. It was empirically found that this value results in a good energy resolution. The LED calibration uses the linear dependence between the given voltage value in mV and a resulting MeV value. Therefore, the LED calibration

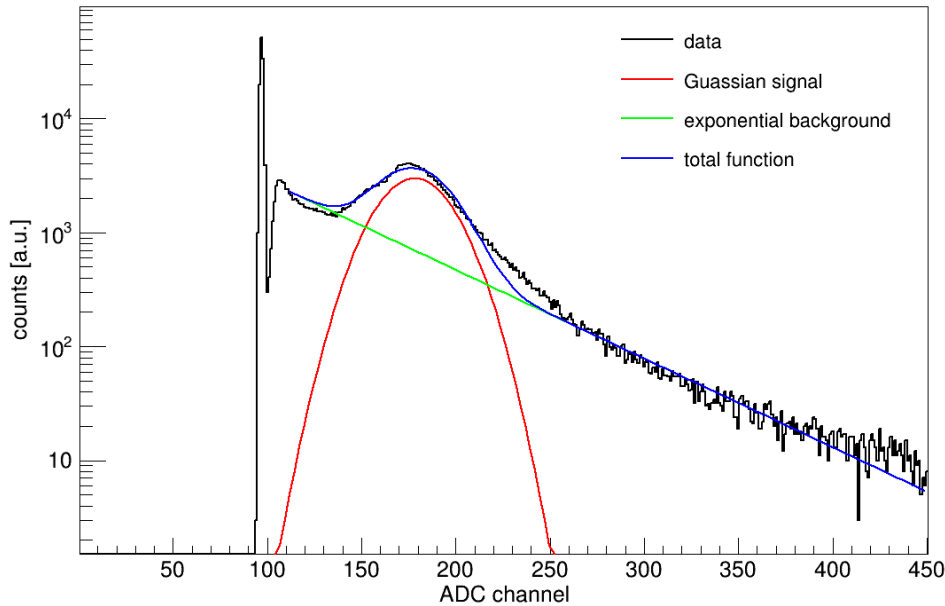


Figure 3.13: Raw Analogue-to-Digital Converter (ADC) spectrum of Mini-TAPS (MT) element 93 for cosmical data. The first and highest peak corresponds to the pedestal. The second and fitted peak is the minimal ionising peak of the BaF_2 material. The fit function (blue) consists of a Gaussian signal (red) and an exponential background (green).

is performed after the cosmics energy calibration. Four different mV values are set, typically 30, 50, 80, 100. This calibration needs to be performed due to the slightly different hardware response and readout. Within the experiments in this work, a LED value of 80 MeV is set.

Invariant mass calibration The BaF_2 crystals that MT is made of have two decay modes: short and long gate. Since the PSA method is not used here, the short gate is not calibrated specifically. The long gate energy calibration, which takes the full integration time for the signals, is the MT energy calibration.

The energy calibration for MT crystals is similar to the CB one except for the taken events. Both photons from the π^0 decay rarely end up in MT such that its statistics would need to be better for an element-based energy calibration. Instead, events with one photon in MT and one in CB are taken. Therefore, the MT energy calibration is performed once the CB energy calibration is finished.

The pedestal is found by fitting the pulser signal from a 1 Hz pulser frequency with a Gaussian function. The invariant mass of the photons from the π^0 decay is shifted iteratively towards the nominal mass (Equation 3.22).

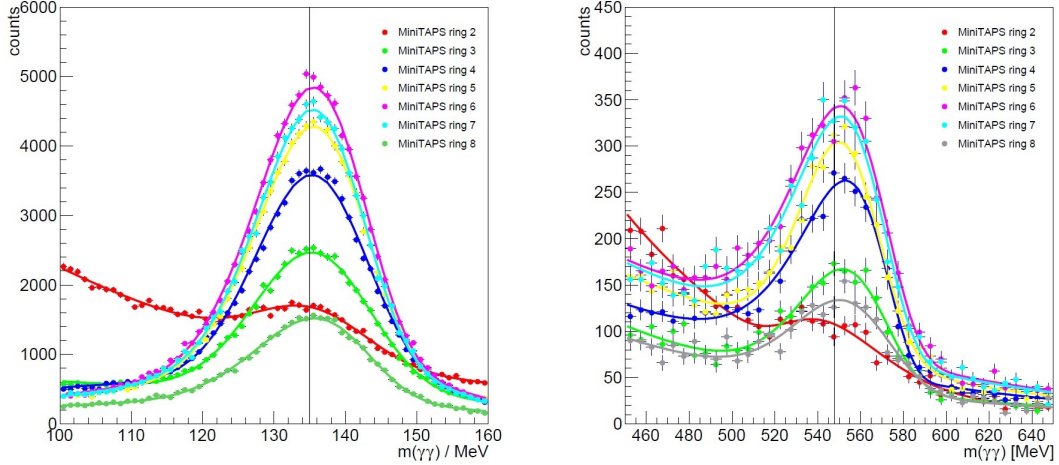


Figure 3.14: Ring dependent invariant mass fits of π^0 (left) and η (right) in Oct2018. Figure taken from [314].

In the end, an average π^0 position is found at its nominal mass with a FWHM of (19.97 ± 0.02) MeV for the π^0 and (49.6 ± 0.5) MeV for the η [314]. Because the π^0 mass is used for the energy calibration and shower losses increase with increasing energy, the peak position of more massive mesons, especially η , is lying slightly too high. The η mass is found at 555.2 MeV in Oct2018 and 551.4 MeV in Dec2021. Because the meson peaks are fitted to find the mean and FWHM positions for kinematical cut positions in the invariant mass spectrum, later on, this discrepancy has no effect.

However, the width of the meson peaks are ring dependent such that it mostly increases towards the outer rings. An overview of the different peak structures is performed as a final step to check the calibration quality (Figure 3.14).

More information about the MiniTAPS energy calibration can be found in [143] and [314].

4 | Event selection

The previous chapter explained how raw detector information is processed to obtain physically meaningful quantities. PED are built and assigned to particles with charge, angle, energy and time information. The next step is the identification of reactions and the reduction of unwanted background. To save computational time, this is done in two steps.

The particles are combined to reactions and presorted in `EXPLOSCAR`. The correct number of neutral and charged particles must be detected to get the right event candidate, which is explained in Section 4.1.

The π^0 and η are short-living mesons that mainly decay to photons. The mesons must be reconstructed from the photons, including a raw invariant mass check, constraining the meson mass and a χ^2 anticut on background mesons, all explained in Section 4.2.

As a last step in the presort, the coincidence time between the detected photons and between the meson and the recoil nucleon must match. Section 4.3 discusses these coincidence times, whereas Section 4.4 shows how random time hits in the tagging systems can be corrected rightfully.

After the presort, `OSCAR` with its extension `libTOCB` analysis the reactions and their participating particles in more detail. Most different kinematic properties are investigated to throw away background reaction events. Many of these properties underlie the energy-momentum conservation of the reactions. Therefore, Section 4.5 describes the background suppression and the number of resulting events.

The last Section 4.6 discusses the remaining background contamination.

If not mentioned otherwise, the figures within this chapter are taken from the October 2018 beam time.

4.1 Multiplicity

Reaction events are built from the reconstructed PED within EXPLOSCAR. π^0 and η photoproduction on the proton and the neutron are investigated, resulting in four reactions:

$$\gamma p \rightarrow \pi^0 p, \quad (4.1)$$

$$\gamma n \rightarrow \pi^0 n, \quad (4.2)$$

$$\gamma p \rightarrow \eta p, \quad (4.3)$$

$$\gamma n \rightarrow \eta n. \quad (4.4)$$

Both mesons are short-lived particles with a mean lifetime of less than 1 fs [44]. Only their decay products, the photons, can be detected such that the mesons are reconstructed from them. The investigated decay channels are:

$$\pi^0 \rightarrow 2\gamma, \quad (4.5)$$

$$\eta \rightarrow 2\gamma, \quad (4.6)$$

$$\eta \rightarrow 3\pi^0 \rightarrow 6\gamma. \quad (4.7)$$

In the end, six different reactions are examined.

The correct number of detected PED is required as a first step: multiplicity. If three particles are in the final state, e.g. $\pi^0 p$ with $\pi^0 \rightarrow 2\gamma$, three PED are required: one charged and two neutral.

As a second step, the correct number of charged and uncharged multiplicities are required in the final state. Protons are charged, whereas neutrons and photons are neutral. Half PED events are taken to increase statistics for reactions with a charged particle in the final state. If charged particles such as protons have a small kinematic energy, they may get stuck in one of the veto detectors. Therefore, no regular PED event can be detected in the main spectrometers CB (with FP) or MT. Since the veto detectors do not have an ADC readout, no kinetic energy information is known about these particles and they are called half PED events instead. However, the kinetic energy is reconstructed from the final state for getting the right centre of mass energy W (Section 5.6) such that these events are well defined.

Reaction	PED	Multiplicity
$\gamma p \rightarrow \pi^0 p \rightarrow 2\gamma p$	2.5 – 3	$1c + 2n$
$\gamma n \rightarrow \pi^0 n \rightarrow 2\gamma n$	3	$0c + 3n$
$\gamma p \rightarrow \eta p \rightarrow 2\gamma p$	2.5 – 3	$1c + 2n$
$\gamma n \rightarrow \eta n \rightarrow 2\gamma n$	3	$0c + 3n$
$\gamma p \rightarrow \eta p \rightarrow 3\pi^0 p \rightarrow 6\gamma p$	6.5 – 7	$1c + 6n$
$\gamma n \rightarrow \eta n \rightarrow 3\pi^0 n \rightarrow 6\gamma n$	7	$0c + 7n$

Table 4.1: Investigated reactions with their required number of total, charged (c) and neutral (n) particle energy deposit (PED), i.e. clusters. 0.5 PED means that the proton is measured in a veto detector but not in one of the main spectrometers.

An overview of the PED number and the multiplicities can be found in Table 4.1.

4.2 Meson reconstruction

After the multiplicity preselection, the decay products from the mesons are combined to reconstruct the meson itself.

4.2.1 Invariant mass reconstruction

The first check is done by calculating the invariant mass (IM). For the meson decays $\pi^0 \rightarrow 2\gamma$ and $\eta \rightarrow 2\gamma$ Equation 3.18 is used. For the decay $\eta \rightarrow 3\pi^2 \rightarrow 6\gamma$ the IM is given by:

$$m_{6\gamma} = \sqrt{\left(\sum_{i=1}^3 E_{\pi_i^0}\right)^2 - \left(\sum_{i=1}^3 \vec{p}_{\pi_i^0}\right)^2} = \sqrt{\left(\sum_{i=1}^6 E_{\gamma_i}\right)^2 - \left(\sum_{i=1}^6 \vec{p}_{\gamma_i}\right)^2}, \quad (4.8)$$

where $E_{\pi_i^0}/E_{\gamma_i}$ and $\vec{p}_{\pi_i^0}/\vec{p}_{\gamma_i}$ are the energy and momentum of the three neutral pions and six decay photons, respectively.

Within the presort in **EXPLOSCAR** very conservative cut positions are chosen, i.e. $50 \text{ MeV} < m_{\gamma\gamma} < 250 \text{ MeV}$ for π^0 and $350 \text{ MeV} < m_{\gamma\gamma} < 750 \text{ MeV}$ for η . The IM is investigated in more detail in the section about background suppression, Section 4.5.1.

For the reactions $\gamma p \rightarrow \pi^0 p \rightarrow 2\gamma p$ and $\gamma p \rightarrow \eta p \rightarrow 2\gamma p$ the two neutral particles are assigned to photons, the charged one is assumed to be the proton. Three neutral particles are detected in the same meson decay channels on the neutron, which must be assigned to two photons and one neutron. This is done by a χ^2 -test to the IM, where the best combination for building a meson is assigned to the two photons. The third neutral particle is the neutron candidate. χ_{ij}^2 for the particle combination $i \neq j$ is given by:

$$\chi_{ij}^2 = \left(\frac{m_{\gamma_i\gamma_j} - m_m}{\Delta m_{\gamma_i\gamma_j}}\right)^2, \quad (4.9)$$

where m_m is the nominal π^0 mass, $m_{\gamma_i\gamma_j}$ is the calculated IM with photon candidates i and j and $\Delta m_{\gamma_i\gamma_j}$ is their IM error (Equation 3.20).

A further complication occurs for the $\eta \rightarrow 3\pi^2 \rightarrow 6\gamma$ decay modes, where six photons have 15 possibilities of being combined to three pions. Once again, a

χ^2 -test is applied for each π^0 to find the best overall combination with its sum:

$$\chi_{ijklmn}^2 = \chi_{ij}^2 + \chi_{kl}^2 + \chi_{mn}^2, \quad (4.10)$$

where each χ_{ij}^2 is calculated using Equation 4.9 and the nominal PDG pion mass.

4.2.2 Constraining the meson mass

The angular resolution of the detected photons is better than the energy resolution. Therefore, the reconstructed energy of the mesons E_m is corrected by the nominal mass m_m :

$$E'_m = \frac{m_m}{m_{\gamma\gamma}} \cdot E_m. \quad (4.11)$$

Generally, this correction is only accurate for photons with the same energy. However, possible deviations were investigated in the past [272], where no significant changes were observed. The working principle was developed by Volker Hejny [315] and confirmed several times before [270–272, 316]. Except for the IM spectrum, this correction is always applied, significantly improving the resolution of coplanarity or missing mass.

4.2.3 χ^2 anticut on background mesons

The main physical background in π^0 photoproduction occurs from η photoproduction and vice versa. Therefore, a χ^2 anticut can be applied for reactions on the neutron—the additional neutral particle results in more possibilities of building a meson.

The best χ^2 value is calculated using the π^0 and η mass and their values are compared. If $\chi_{\pi^0}^2 < \chi_{\eta}^2$ in ηn , it is more likely that the two photons occur from a π^0 decay than from a η decay and the event is dismissed. The same is performed in $\pi^0 n$, where events are dismissed if $\chi_{\eta}^2 < \chi_{\pi^0}^2$.

For ηn with the $\eta \rightarrow 3\pi^0 \rightarrow 6\gamma$ the χ^2 anticut is applied on the single π^0 IM.

As shown in Figure 4.1, the χ^2 anticut has only a minor effect in $\pi^0 n$ photoproduction, whereas it is especially effective for ηn . Much of the background can be thrown away while the signal strength stays nearly unchanged.

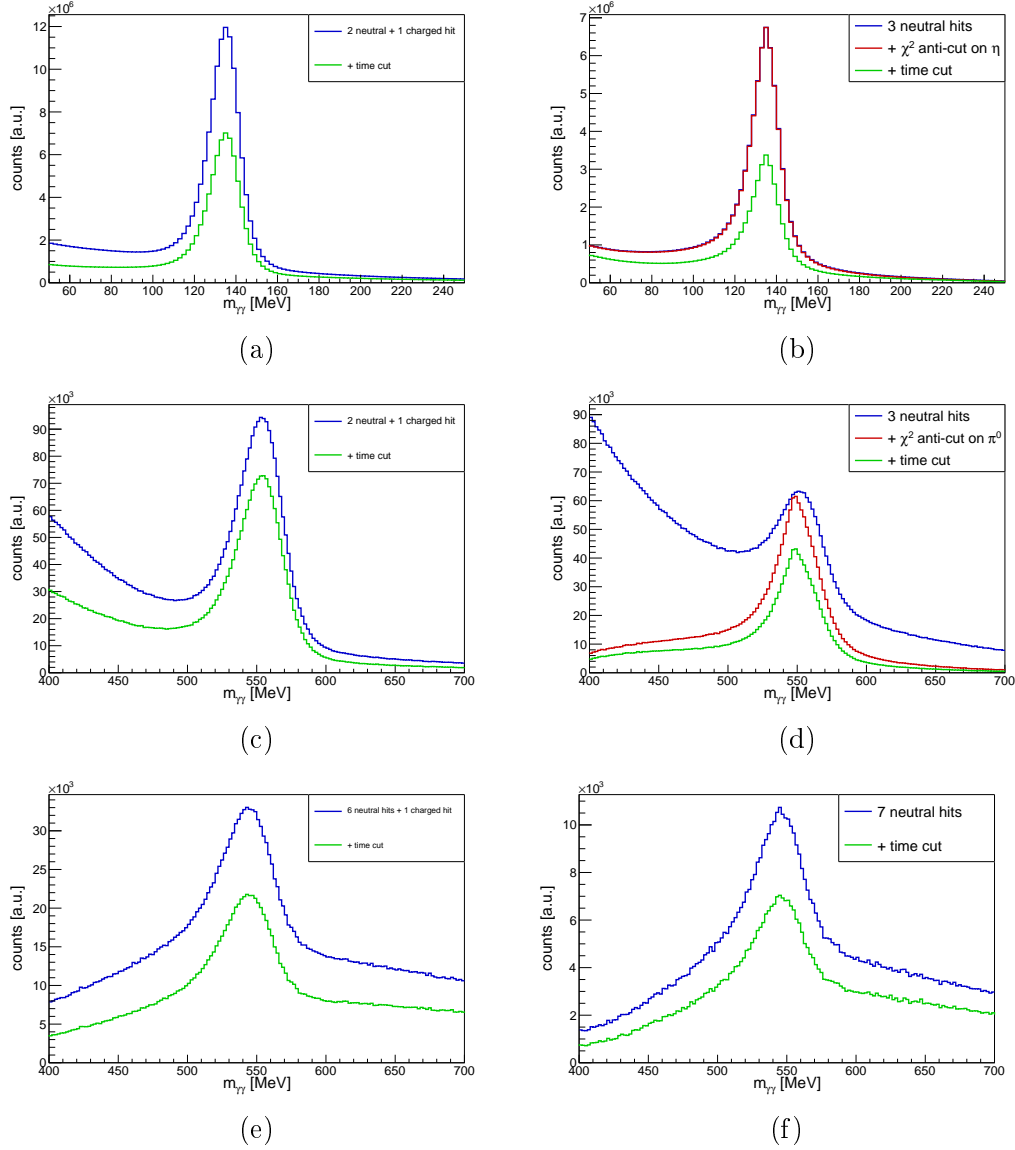


Figure 4.1: Invariant mass with different presort cuts in π^0 (a-b) and η (c-f) photoproduction on the proton (left column) and the neutron (right column). (c-d) show the $\eta \rightarrow 2\gamma$ decay channel, (e-f) the $\eta \rightarrow 6\gamma$ decay channel. The blue line indicates a multiplicity cut (Section 4.1), the red line indicates an additional χ^2 anticut on $2\gamma n$ final states (Section 4.2.3) and the green line indicates an additional time cut (Section 4.3).

4.3 Coincidence time

All detected final state particles must occur from the same reaction. Therefore, the coincidence time between decay photons from meson decays and the coincidence time between the meson and recoil nucleon must be as small as possible, i.e. distributed around 0. However, due to resolution and dead time effects, the time is not precisely 0 but distributed around that value.

Reconstructed PED from EXPLORA are sorted into three main tree containers of type `CBTParticle`:

- `BeamPhotons`: Reconstructed electrons in the Tagger system
- `CBGammas`: Reconstructed particles in the CB (with FP) detector system
- `MiniTapsGammas`: Reconstructed particles in the MT detector system

They contain all available detector information like time, deposited energy, detected angles or cluster size.

The time difference between two registered particles is given as their simple difference:

$$\Delta t = t_1 - t_2, \quad (4.12)$$

where $t_{1,2}$ is the time of particle 1 and 2 in no preferred order. All combinations for the coincidence time between two photons from a meson decay are calculated and filled in a histogram (Figure 4.2). In the $\eta \rightarrow 3\pi^0 \rightarrow 6\gamma$ decay channel, multiple differences are calculated, whereas in the other decay channels only one time difference between photons exists.

As clearly visible in Figure 4.2, the time differences between photons do not depend on the nucleon. Due to a larger opening angle between photons coming from the η decay, there are very few events where both photons are detected in MT, explaining its low statistics.

The time difference between the meson and the nucleon is again calculated from their simple difference:

$$\Delta t = t_m - t_N \quad \text{with} \quad t_m = \frac{1}{N} \sum_{i=1}^N t_{\gamma_i}, \quad (4.13)$$

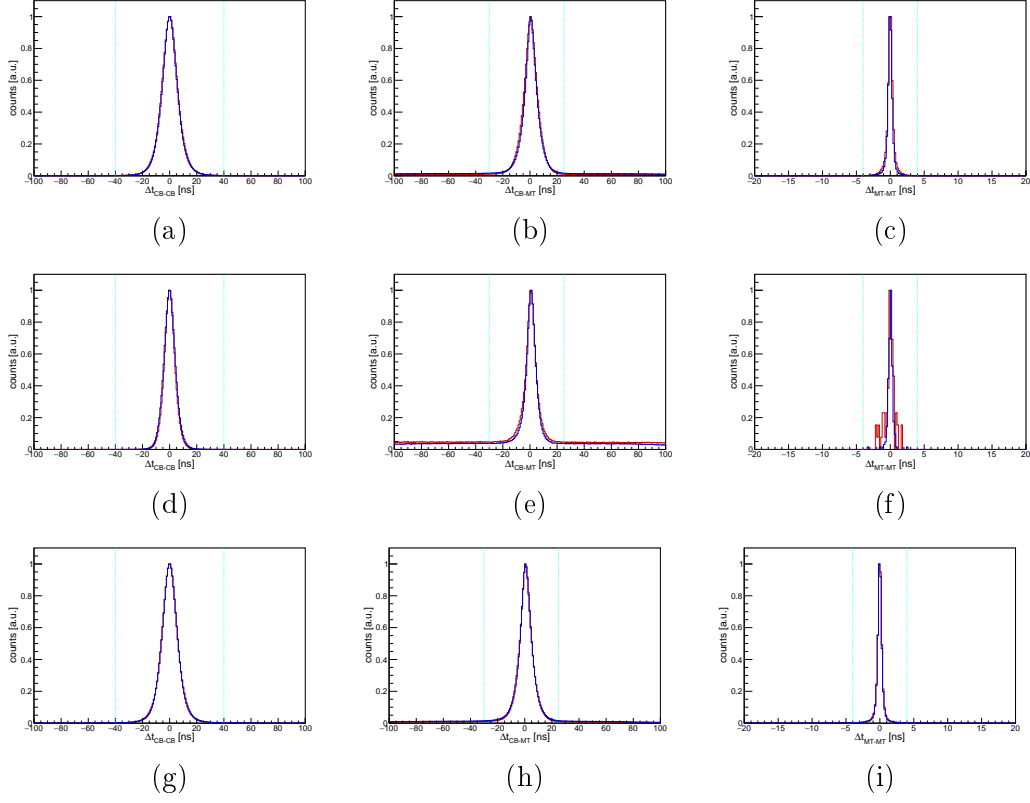


Figure 4.2: Coincidence time difference between decay photons from $\pi^0 \rightarrow 2\gamma$ (a-c), $\eta \rightarrow 2\gamma$ (d-f) and $\eta \rightarrow 6\gamma$ (g-i) decay channel. The left column shows Crystal Barrel-Crystal Barrel (CB-CB) hits, the middle column shows Crystal Barrel-MiniTAPS (CB-MT) hits and the right column shows MiniTAPS-MiniTAPS (MT-MT) hits for reactions on the proton (blue) and neutron (red). The cut positions are shown as a dotted cyan line.

where the nucleon time t_N is subtracted from the meson time t_m . The time of the meson is calculated by the mean of the photon times where MT hits are preferred. If a decay photon is detected in MT, its time information is used and the CB one is ignored. The reason lies in the better time resolution of <1 ns (Section 3.3.1).

The meson time is later taken as the reaction time for the random background subtraction in Section 4.4.

Figure 4.3 shows the time differences between meson and nucleon. It is clearly more background visible in the CB-MT times for the reaction on the proton, where the meson decays in two photons. This mainly comes from random electromagnetic background in the forward direction with an

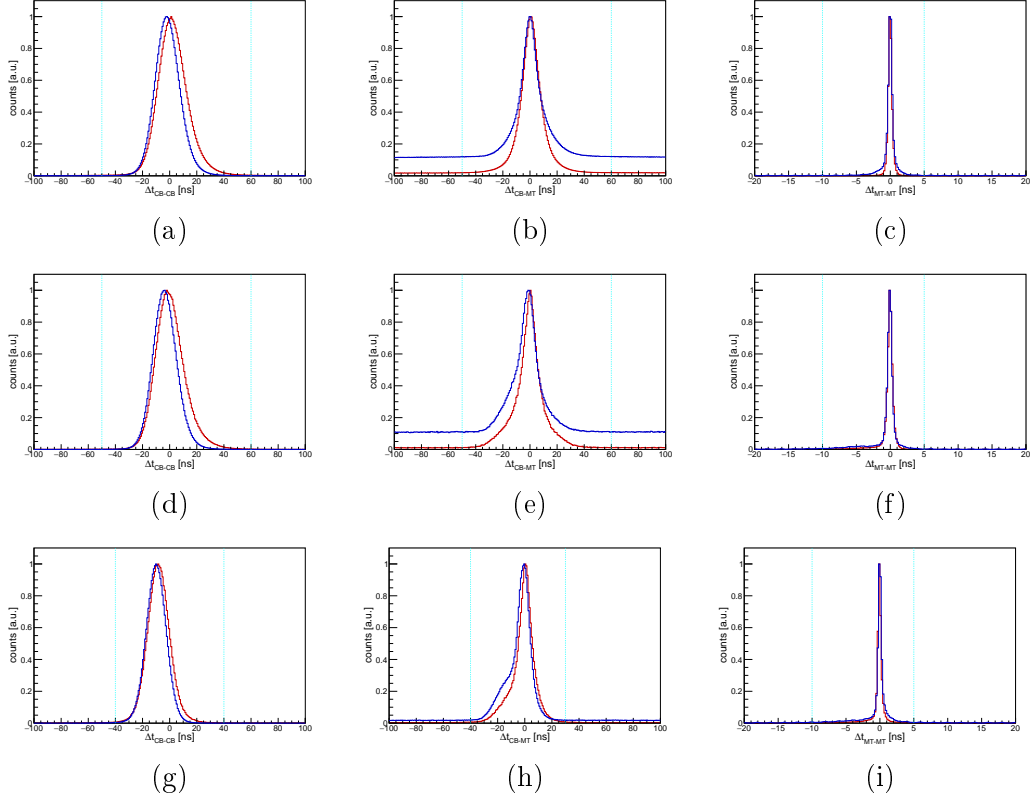


Figure 4.3: Coincidence times between the meson and the nucleon for $\pi^0 \rightarrow 2\gamma$ (a-c), $\eta \rightarrow 2\gamma$ (d-f) and $\eta \rightarrow 6\gamma$ (g-i) decay channels. The left column shows Crystal Barrel-Crystal Barrel (CB-CB) hits, the middle column shows Crystal Barrel-MiniTAPS (CB-MT) hits and the right column shows MiniTAPS-MiniTAPS (MT-MT) hits for reactions on the proton (blue) and neutron (red). The cut positions are shown as a dotted cyan line.

undetected second electron or positron.

The coincidence Tagger-meson time is given by the simple difference between their times. However, due to multiple Tagger electrons, random hits have to be subtracted as discussed in the following Section 4.4.

Table 4.2 shows the different time cuts. For coincidence meson-nucleon times in the 6γ decay channel, a narrower cut position is chosen for CB-CB and CB-MT times. Due to the large number of photons for defining the time of the meson, its time is known more precisely with fewer random background events. The latter case is further dominated by MT times from photons.

Detectors	Particles	Final states	Time cut interval [ns]
CB-CB	$\gamma - \gamma$	$2\gamma N, 6\gamma N$	$[-40, +40]$
CB-MT	$\gamma - \gamma$	$2\gamma N, 6\gamma N$	$[-30, +25]$
MT-MT	$\gamma - \gamma$	$2\gamma N, 6\gamma N$	$[-4, +4]$
CB-CB	$m - N$	$2\gamma N$	$[-50, +60]$
CB-CB	$m - N$	$6\gamma N$	$[-40, +40]$
CB-MT	$m - N$	$2\gamma N$	$[-50, +60]$
CB-MT	$m - N$	$6\gamma N$	$[-40, +40]$
MT-MT	$m - N$	$2\gamma N, 6\gamma N$	$[-10, +5]$
Tagger-CB	$m - e^-$	$2\gamma N, 6\gamma N$	$[-15, +15]$
Tagger-MT	$m - e^-$	$2\gamma N, 6\gamma N$	$[-2, +3]$

Table 4.2: Coincidence time cuts between photons from meson decays and between meson and nucleon for the different detectors. Time information from the MiniTAPS is preferred for the meson time (see text).

4.4 Random background subtraction

This experiment uses a high current of up to 1 nA, resulting in multiple electrons in the Tagger per event. Figure 4.4 shows the number of Tagger hits per event in $\pi^0 p$ where the mean is around 26 hits per event in Oct2018 and around 41 hits per event in Dec2021. The difference is due to the higher current in Dec2021.

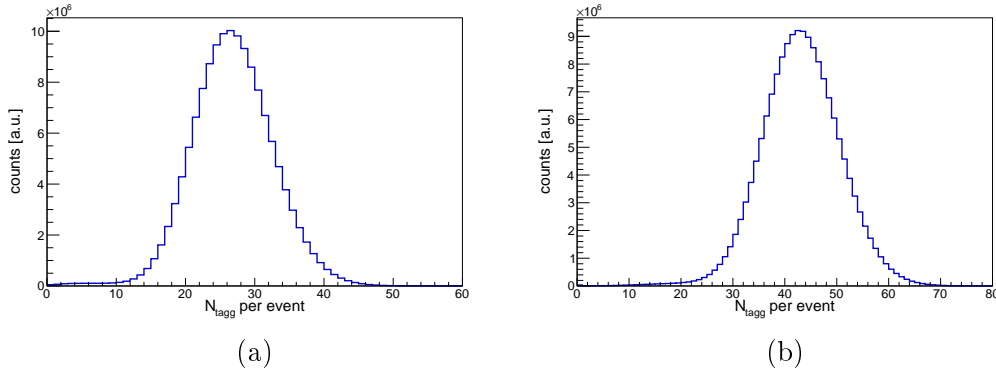


Figure 4.4: Number of Tagger hits per event in $\pi^0 p$ in Oct2018 (a) and Dec2021 (b).

These random background electrons would result in a wrong photon energy and, thus, in non-physical events. Therefore, the difference between Tagger time and reaction time is filled in a histogram for all electron hits in the Tagger. Three ranges are defined: The first lies around the actual signal peak - the prompt peak - and is set to $[-25 \text{ ns}, 15 \text{ ns}]$ for CB and $[-2 \text{ ns}, 3 \text{ ns}]$ for MT. The second and third are sideband ranges set to $[-250 \text{ ns}, -50 \text{ ns}]$ and $[50 \text{ ns}, 250 \text{ ns}]$.

All events are weighted to subtract the random background from the signal peak events correctly. Prompt events get the weight $w_P = 1$, sideband events are weighted by:

$$w_{SB} = -\frac{\Delta t_P}{\Delta t_{SB1} + \Delta t_{SB2}} = \begin{cases} -0.075, & \text{CB} \\ -0.0125, & \text{MT} \end{cases}, \quad (4.14)$$

where Δt_P is the time range of the prompt window and $\Delta t_{SB1,SB2}$ are the ones of the two sideband windows.

The number of real events N is thus given as the number of prompt events N_P plus the weighted sideband events N_{SB} :

$$N = N_P + w_{SB} \cdot N_{SB}. \quad (4.15)$$

Since w_{SB} is negative, sideband events are subtracted from prompt events, giving this method its name.

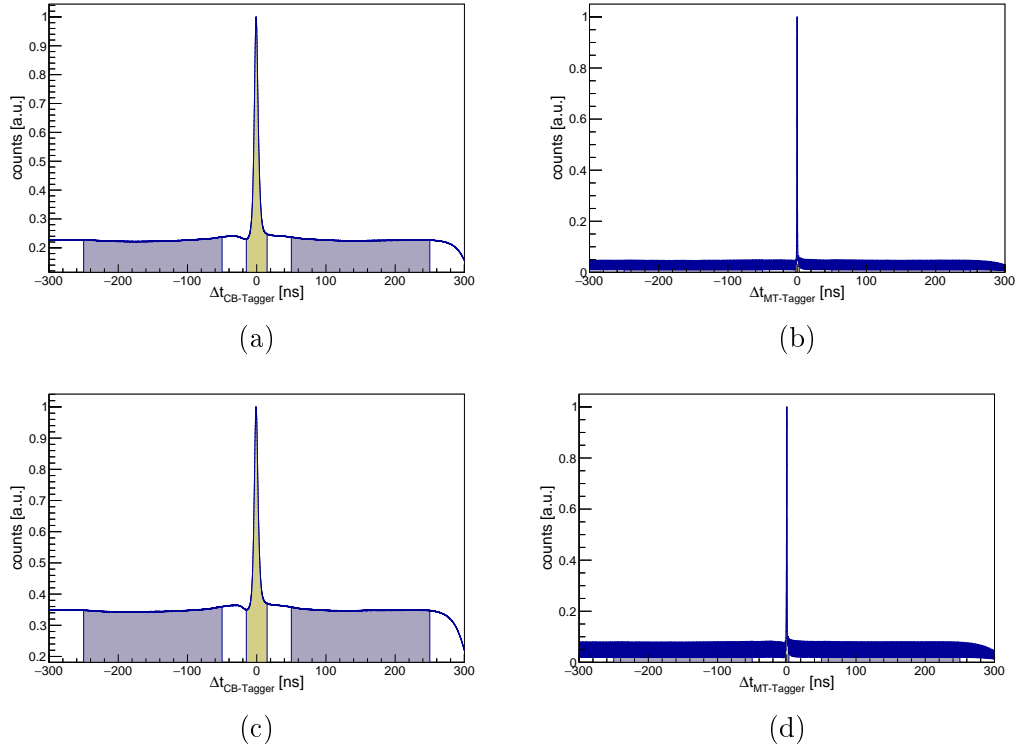


Figure 4.5: Time difference in $\pi^0 p$ between Crystal Barrel (CB) and Tagger (left column) and MiniTAPS (MT) and Tagger (right column) for the random background subtraction in Oct2018 (first row) and Dec2021 (second row). The prompt event band is shown in yellow the sideband is in blue (see text).

Figure 4.5 shows the random background subtraction in $\pi^0 p$. A 2 ns structure is visible in the Tagger-MT spectra, which is caused by the injection frequency of ELSA. In Dec2021, there are more random background hits compared to Oct2018. The reason for this is the higher beam current during the second beam time, which results in a higher probability of random hits. However, this difference does not affect the results because the random background hits are subtracted in the analysis and the calculation of the polarisation ob-

servables.

4.5 Background suppression

After the presort with **EXPLOSCAR**, only events that fit the minimal conditions remain. However, many background events, which come from random hits, different reactions and final state interactions, survive. To extract polarisation observables in scattering experiments, the background needs to be strongly suppressed, so that relatively small systematic uncertainties remain. The goal is to throw away as many background events as possible while keeping as many good ones.

Five kinematic cut positions, i.e. invariant mass, coplanarity, missing mass, polar angle difference and Fermi momentum, are determined to achieve the best signal to background ratio with the smallest systematic uncertainty possible. The number of total events depends strongly on the investigated reaction leading to different approaches for defining cut positions.

If there are many events, the cut positions are determined energy- and angle-dependent. Generally, there are made 12 $\cos(\theta)$ bins. If the statistics decreases, this number is halved, as for some ηN cut positions. The energy binning depends on the reaction as well as on the linear polarisation degrees and the photon flux and can be found in Table 4.3. The polarisation observables are determined by the same energy binning.

Due to the Fermi motion of the nucleons in deuterium and carbon/oxygen nuclei, the cut positions are found more sophisticated than in the presort, e.g. raw invariant mass cut in Section 4.2.1.

First, the carbon data is subtracted from the dButanol data to get the deuterium signal. Carbon and dButanol data are therefore normalised by the photon flux (Section 5.2) and the carbon data is additionally scaled by a factor that takes the differences in the target densities into account (Section 5.4).

Second, the different spectra have much less background if the cut positions of the other cuts are applied, i.e. a coplanarity, missing mass, polar angle difference and Fermi momentum cut is applied for the invariant mass. Therefore, the cut positions are determined iteratively, starting with static cut positions. Four iterations are performed until the cut positions do not change anymore.

E_γ bin	E_γ [MeV]	ΔE_γ [MeV]	E_γ^{low} [MeV]	E_γ^{high} [MeV]
1	685	35	650	720
2	760	40	720	800
3	840	40	800	880
4	920	40	880	960
5	1000	40	960	1040
6	1080	40	1040	1120
7	1160	40	1120	1200
8	1280	80	1200	1360
9	1530	170	1360	1700
10	2000	300	1700	2300
11	2700	400	2300	3100

Table 4.3: Energy binning for determining the background suppression cut positions. E_γ stands for the average value of the corresponding energy bin. The reactions with an η meson in the final state only use E_γ bins 2 – 9 due to its threshold energy and strongly decreasing event yields towards higher energies.

4.5.1 Invariant mass

π^0 and η have a mean decay time of less than a femtosecond [44]. Thus, only their decay products - the photons - can be detected. The invariant mass (IM) for a meson that decays into two photons is given by Equation 3.18, for mesons decaying into six photons over three neutral pions by Equation 4.8.

After the raw IM cuts in the preselection (Section 4.2), more sophisticated cut positions must be determined to remove the remaining background. The IM spectra are therefore fitted with a modified Gaussian function that has an additional exponential decay part in the energy region below the mean value [317]:

$$f(x) = \begin{cases} N \cdot G, & x \geq \mu \\ N \cdot (G + (1 - G) \cdot \exp(\frac{x - \mu}{\lambda})), & x < \mu \end{cases}, \quad (4.16)$$

where G is the normalised Gaussian function

$$G = \exp\left(-\frac{(x - \mu)^2}{2\sigma^2}\right). \quad (4.17)$$

Here, N is the height, μ the mean and σ^2 the variance. The advantage compared to a classical Gaussian function is a better description of the low-energy range in the IM spectra, which is especially important for the η meson. This function is motivated by the shape of the experimental and MC simulation data. Furthermore, this function describes the shape of deposited energy in crystals like BaF_2 [266].

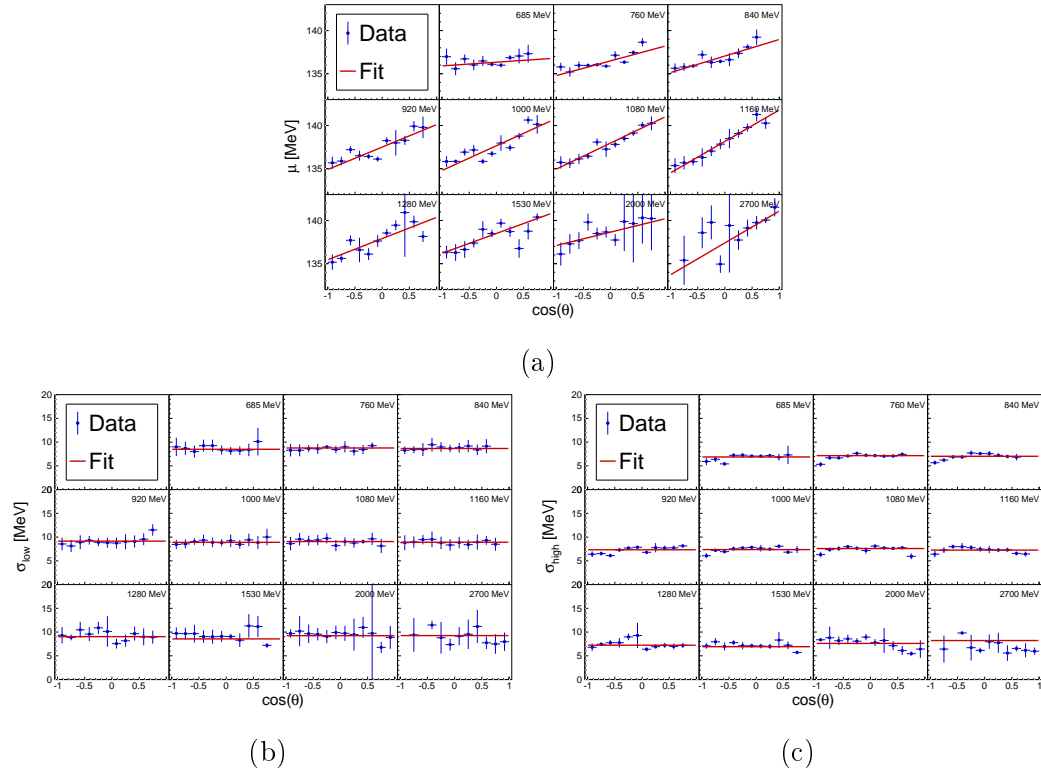


Figure 4.6: E_γ and $\cos(\theta)$ dependent mean (a), sigma low (b) and sigma high (c) cut positions with their linear (mean) and constant (sigma) fitting functions from the invariant mass spectra in $\pi^0 p$.

The fit function is asymmetric, so the σ values are also asymmetric. The distance between the curve and the mean value at FWHM is taken. The FWHM of the lower and higher parts are converted to σ_{low} and σ_{high} with Equation 3.14. If there is no asymmetry at all, i.e. $\lambda \rightarrow 0$, the two σ values would be the same and the function would become a simple Gaussian.

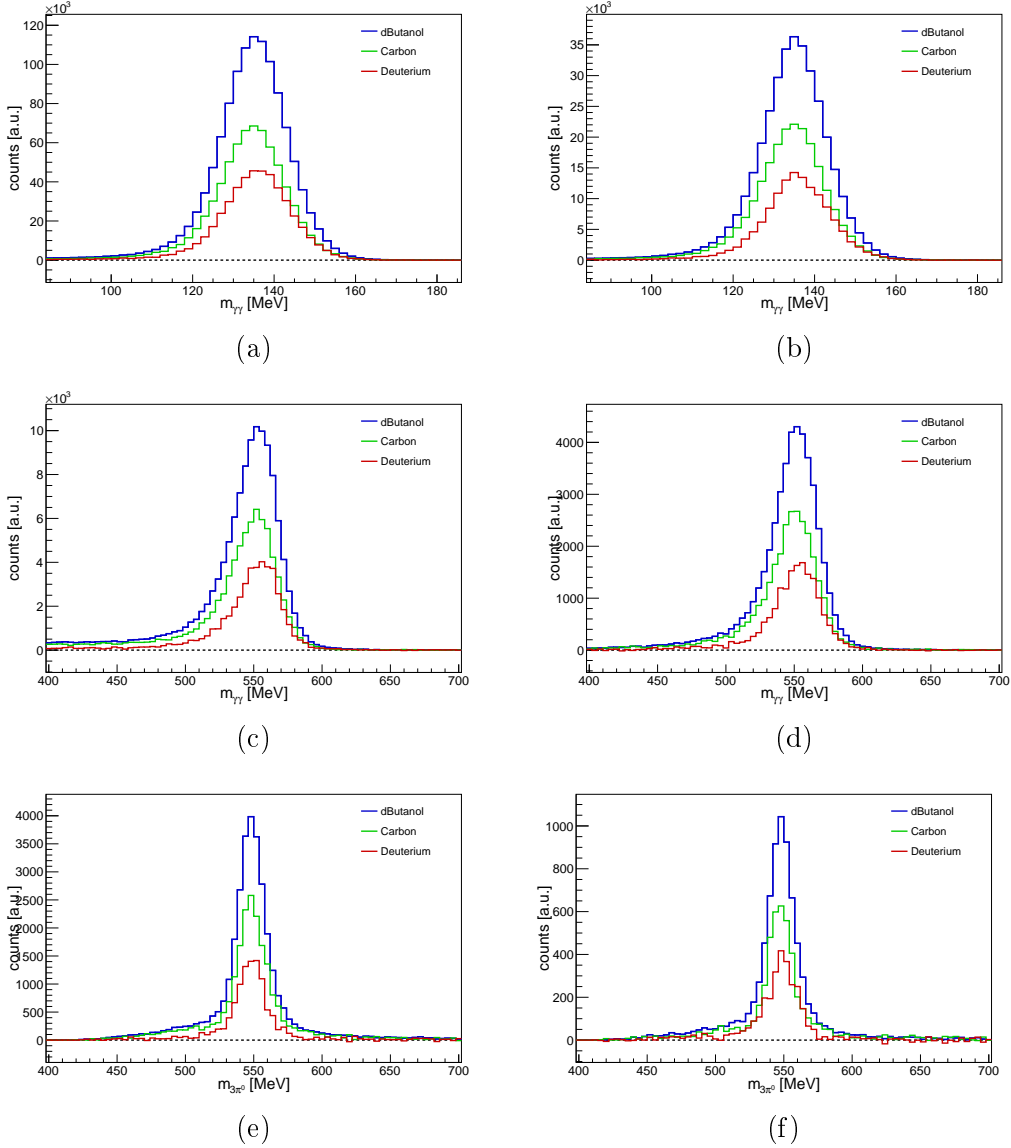


Figure 4.7: Energy and angular integrated invariant mass of deuterated butanol (blue), carbon (green) and deuterium (red) in $\pi^0 p$ (a), $\pi^0 n$ (b), ηp with $\eta \rightarrow 2\gamma$ (c), ηn with $\eta \rightarrow 2\gamma$ (d), ηp with $\eta \rightarrow 6\gamma$ (e) and ηn with $\eta \rightarrow 6\gamma$ (f).

After the determination of the mean and width values, they are separately plotted as a function of $\cos(\theta)$ for fixed E_γ , where they are fitted with a linear (mean) or constant function (widths). The fit functions are chosen for phenomenological reasons and do not have a straightforward theoretical motivation. At least three points are required for the fit. If only fewer points are available, the shape of the next higher or lower-lying energy bin is taken

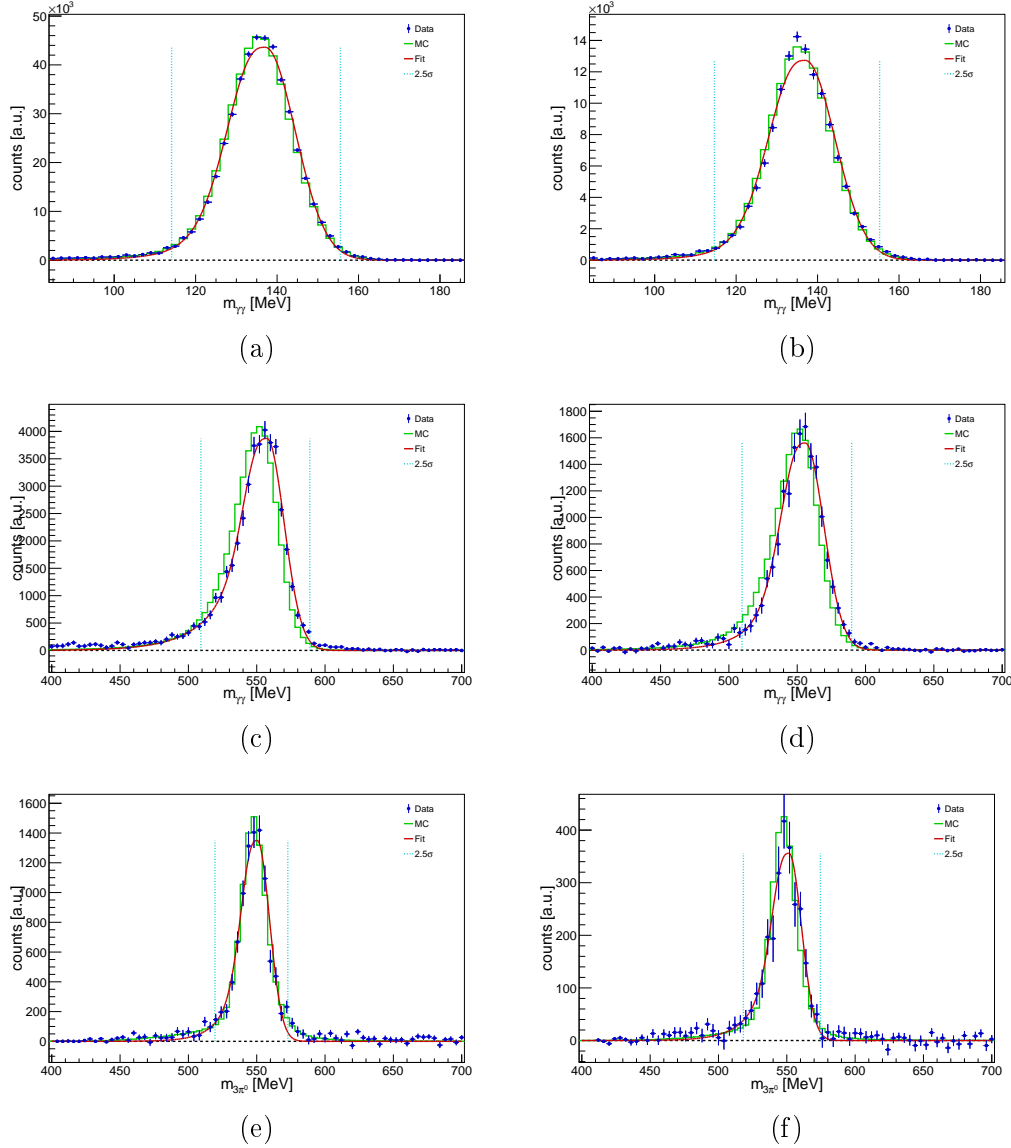


Figure 4.8: Energy and angular integrated invariant mass of deuteron data (blue points), Monte Carlo simulation (green line) and the fit function (red, Equation 4.16) with 2.5σ cut widths (dotted cyan line) in $\pi^0 p$ (a), $\pi^0 n$ (b), ηp with $\eta \rightarrow 2\gamma$ (c), ηn with $\eta \rightarrow 2\gamma$ (d), ηp with $\eta \rightarrow 6\gamma$ (e) and ηn with $\eta \rightarrow 6\gamma$ (f).

and scaled by the value extracted from the angular-integrated spectra. An additional 10% is added for the widths. In the end $\pm 2.5\sigma$ width cut positions are taken, keeping the events within $[\mu - 2.5\sigma_{low}, \mu + 2.5\sigma_{high}]$.

Figure 4.6 shows the energy- and angular-dependent mean (Figure 4.6a), sigma low (Figure 4.6b) and sigma high (Figure 4.6c) values with the corre-

sponding fit functions in $\pi^0 p$. The same figures for the other reactions can be found in Appendix A.1.

12 $\cos(\theta)$ bins are taken for $\pi^0 N$ and 6 for ηN . Only ηn with $\eta \rightarrow 6\gamma$ has too few events to determine angular-dependent cut positions. In all other reactions, almost no angular dependence was found such that only energy-dependent cut positions are taken for ηn with $\eta \rightarrow 6\gamma$. The energy dependence was found to be small.

It should be clear that for determining polarisation observables later on, such low statistic bins, i.e. less than 50 events, will not give useful results and will be ignored.

Figure 4.7 and 4.8 show the IM spectra for all reactions. All available cut positions, i.e. coplanarity (Section 4.5.2), missing mass (Section 4.5.3), Fermi momentum (Section 4.5.5) and polar angle difference (Section 4.5.4), are applied to all data in the figures. Figure 4.7 shows the dButanol, carbon and deuterium data. The carbon data are scaled to the photon flux (Section 5.2) and the target nucleon density (Section 5.4.1). The deuterium data is the difference between dButanol and carbon data. Figure 4.8 shows the deuterium data compared to a MC simulation, the fit function (Equation 4.16) and the $\pm 2.5\sigma$ cut position.

For the $\eta \rightarrow 6\gamma$ decay channel on both nucleons, an additional static ± 20 MeV cut position is applied around the nominal π^0 mass for all three candidates. This cut position corresponds to a confidence level of $> 2.6\sigma$ ($> 99.2\%$). However, this cut has a minor effect. Figure 4.25h and 4.26h show the π^0 invariant mass from reactions on the proton and neutron. It is visible that very few events occur outside that cut band.

4.5.2 Coplanarity

Due to momentum conservation, the azimuthal angle difference $\Delta\phi$ between the meson ϕ_m and the recoil nucleon ϕ_N , called coplanarity, must be at 180° . This is valid in the CM and laboratory systems since the two systems are connected by a Lorentz boost in the z -direction only. The coplanarity is smeared out because of the angular resolution and Fermi motion. The latter's effect is especially visible in extreme regions, i.e. near the threshold.

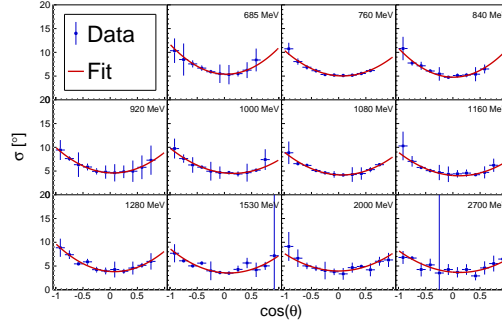


Figure 4.9: E_γ and $\cos(\theta)$ dependent sigma cut positions with their quadratic fitting functions from the coplanarity spectra in $\pi^0 p$.

The formal definition of the coplanarity is given by:

$$\Delta\phi = \begin{cases} \phi_m - \phi_N, & \text{if } \phi_m - \phi_N \geq 0 \\ 2\pi - |\phi_m - \phi_N|, & \text{if } \phi_m - \phi_N < 0 \end{cases}. \quad (4.18)$$

A Gaussian function with an additional exponential term is used as a proper fitting function, given by:

$$f(x) = N \cdot \left(G + (1 - G) \cdot \exp\left(-\frac{|x - \mu|}{\lambda}\right) \right). \quad (4.19)$$

The exponential term is implemented to describe the low and high-laying regions better. The data could also be approximated in a narrow window around the peak by a simple Gaussian function.

The parameters are described in Equation 4.16 where the Gaussian function G is given with Equation 4.17. The mean position is fixed at 180° . The sigma value is again calculated from the FWHM.

Since the mean position is fixed, only the widths are of interest. Except for ηn with $\eta \rightarrow 6\gamma$, the same binning and the same handling of bad $\cos(\theta)$ bins as for the invariant mass (Section 4.5.1) is applied. The only difference lies in the determination of the sigma values. First, only one sigma value is determined since function 4.19 is symmetric around the peak position. Second, the fit function of the sigma data is chosen to be a quadratic function. Figure 4.9 shows the determined sigma values with the fit function in $\rightarrow \pi^0 p$. The same figures for the other reactions can be found in Appendix A.2.

The sigma values of ηn and ηp with $\eta \rightarrow 2\gamma$ are very similar and agree

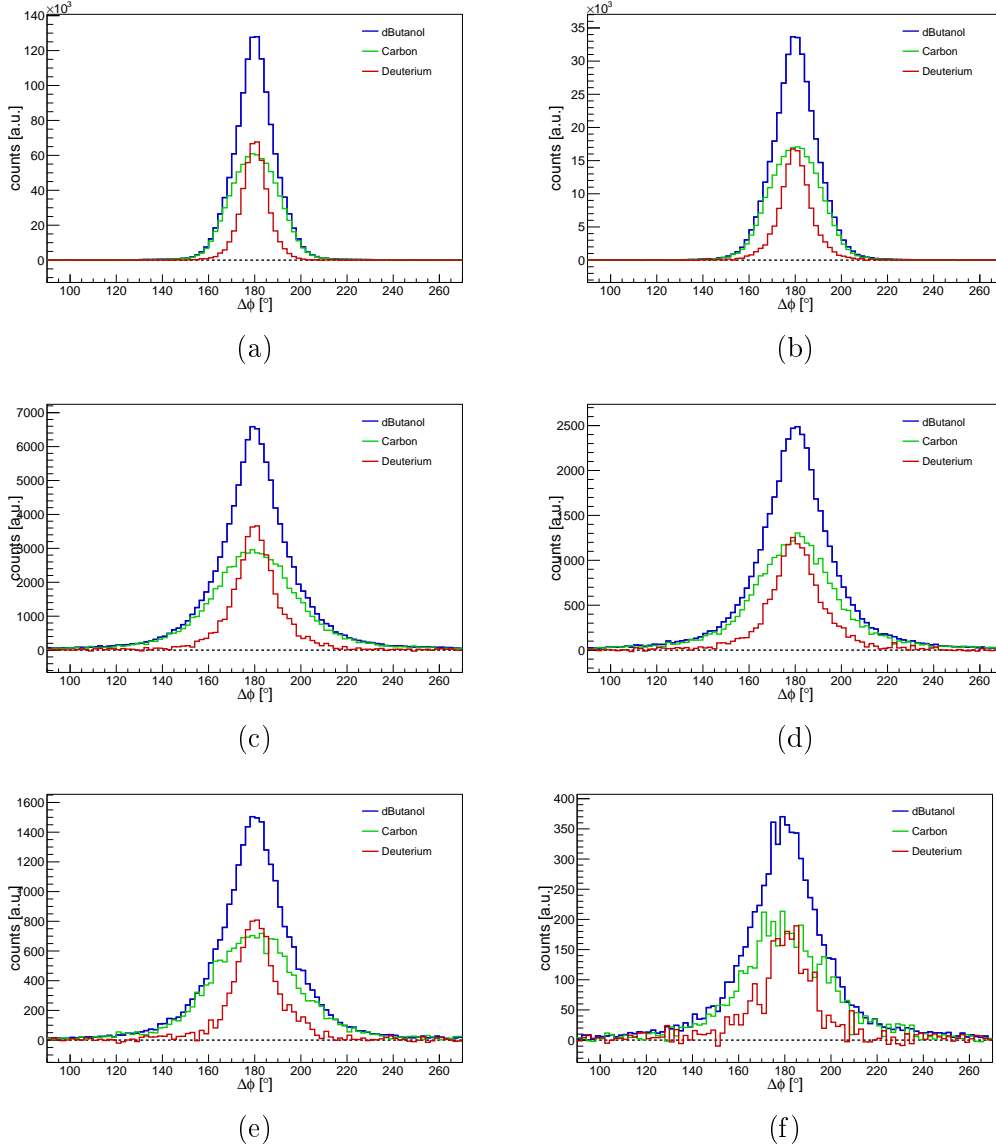


Figure 4.10: Energy and angular integrated coplanarity of deuterated butanol (blue), carbon (green) and deuterium (red) in $\pi^0 p$ (a), $\pi^0 n$ (b), ηp with $\eta \rightarrow 2\gamma$ (c), ηn with $\eta \rightarrow 2\gamma$ (d), ηp with $\eta \rightarrow 6\gamma$ (e) and ηn with $\eta \rightarrow 6\gamma$ (f).

within the statistical uncertainty. The same applies to the energy or angular integrated data in $\eta \rightarrow 6\gamma$. Furthermore, a strong energy and angular dependence is found for the coplanarity, such that for ηn with $\eta \rightarrow 6\gamma$ no integrated spectra can be taken and the cut positions from ηp with $\eta \rightarrow 6\gamma$ are used instead. An additional systematic uncertainty of around 3% is determined. Because only a small part of the total ηn events are coming from the

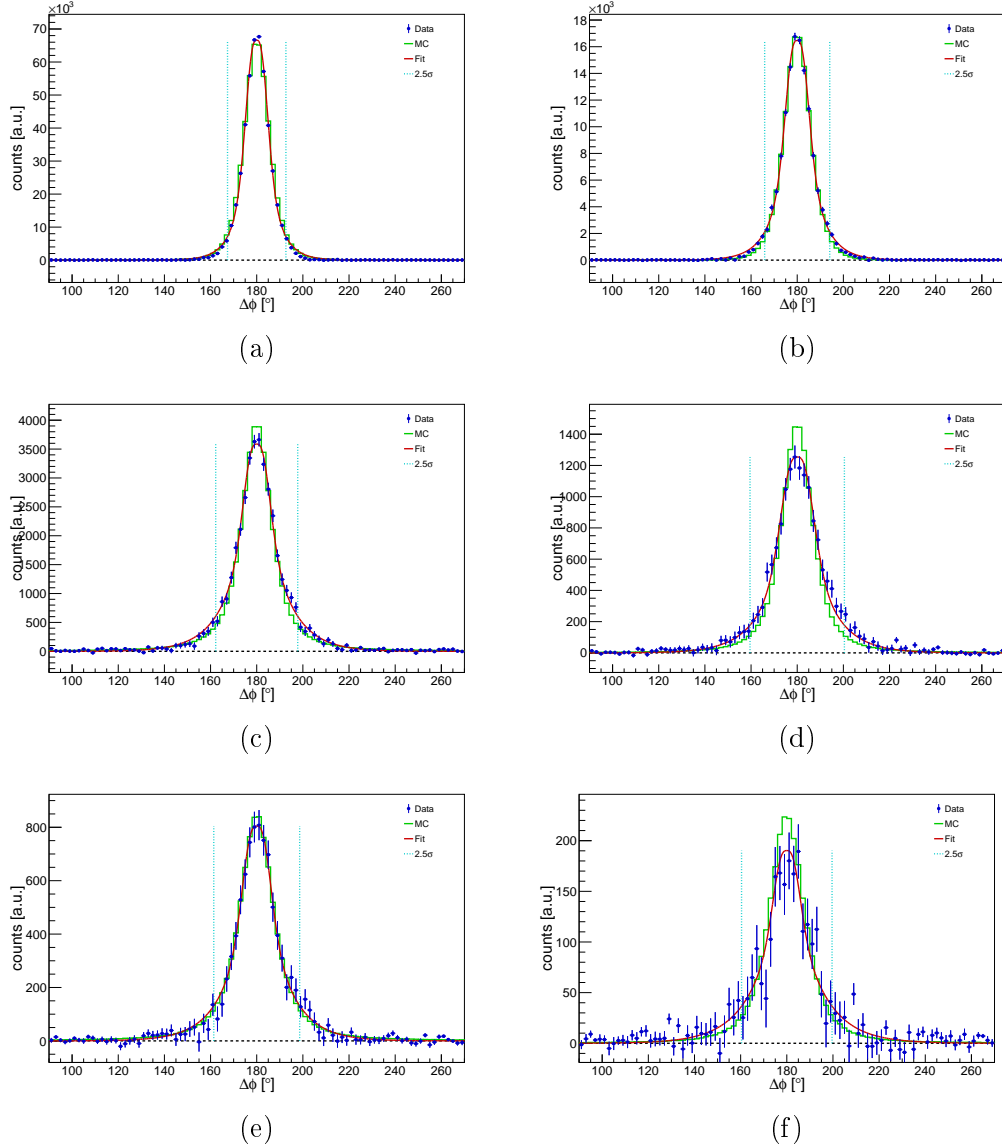


Figure 4.11: Energy and angular integrated coplanarity of deuterium data (blue points), Monte Carlo simulation (green line) and the fit function (red, Equation 4.19) with 2.5σ cut widths (dotted cyan line) in $\pi^0 p$ (a), $\pi^0 n$ (b), ηp with $\eta \rightarrow 2\gamma$ (c), ηn with $\eta \rightarrow 2\gamma$ (d), ηp with $\eta \rightarrow 6\gamma$ (e) and ηn with $\eta \rightarrow 6\gamma$ (f).

$\eta \rightarrow 6\gamma$ decay channel (Table 4.4), this uncertainty is below 0.5% in the end and therefore negligible. Again $\pm 2.5\sigma$ width cut positions are chosen.

Figures 4.10 and 4.11 show the coplanarity spectra for all reactions. The colour code and method are the same as for the IM (Section 4.5.1), i.e. all available cut positions are applied and the carbon data are scaled to account

for the photon flux and the different target densities.

4.5.3 Missing mass

Missing mass Δm refers to ignoring the information about the detected recoil nucleon and treating it as a missing particle. Assuming an initial nucleon at rest, the missing mass is given by the nominal mass of the nucleon m_N , the four-vector of the initial photon $p_\gamma = (E_\gamma, 0, 0, E_\gamma)$ and the four-vector of the detected meson $p_m = (E_m, \vec{p}_m)$:

$$\Delta m = \sqrt{(E_\gamma + m_N - E_m)^2 - (\vec{p}_\gamma - \vec{p}_m)^2}. \quad (4.20)$$

A Gaussian function (Equation 4.17) with a normalisation factor is used to fit the missing mass spectra, where mean and sigma are the parameters of interest. As for the invariant mass (Section 4.5.1) and coplanarity (Section 4.5.2), these parameters are plotted as a function of $\cos(\theta)$ for fixed E_γ bins and fitted with a phenomenological function to extrapolate the cut positions. A linear function is chosen for both here.

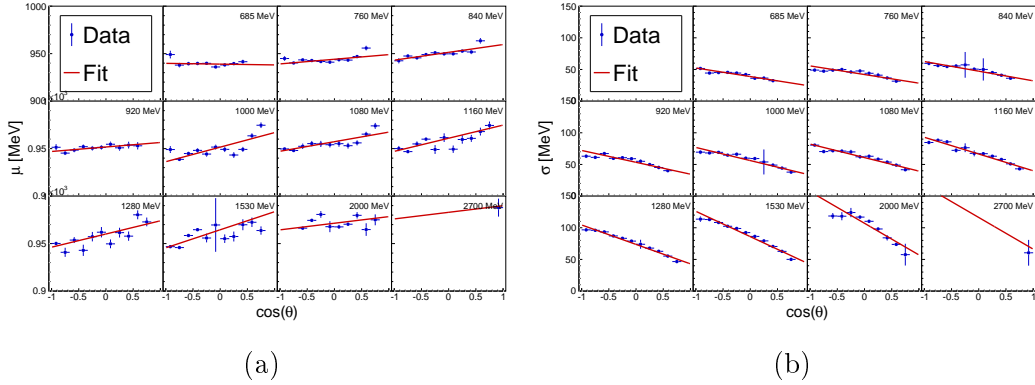


Figure 4.12: E_γ and $\cos(\theta)$ dependent mean (a) and sigma (b) cut positions with their linear fitting functions from the missing mass spectra in $\pi^0 p$.

Figure 4.12 shows the mean and sigma cut positions with their linear fit functions in $\pi^0 p$. The same figures for the other reactions can be found in Appendix A.3.

As for the coplanarity, the integrated spectra look very similar for the reactions on the proton and neutron such that the reaction ηn with $\eta \rightarrow 6\gamma$

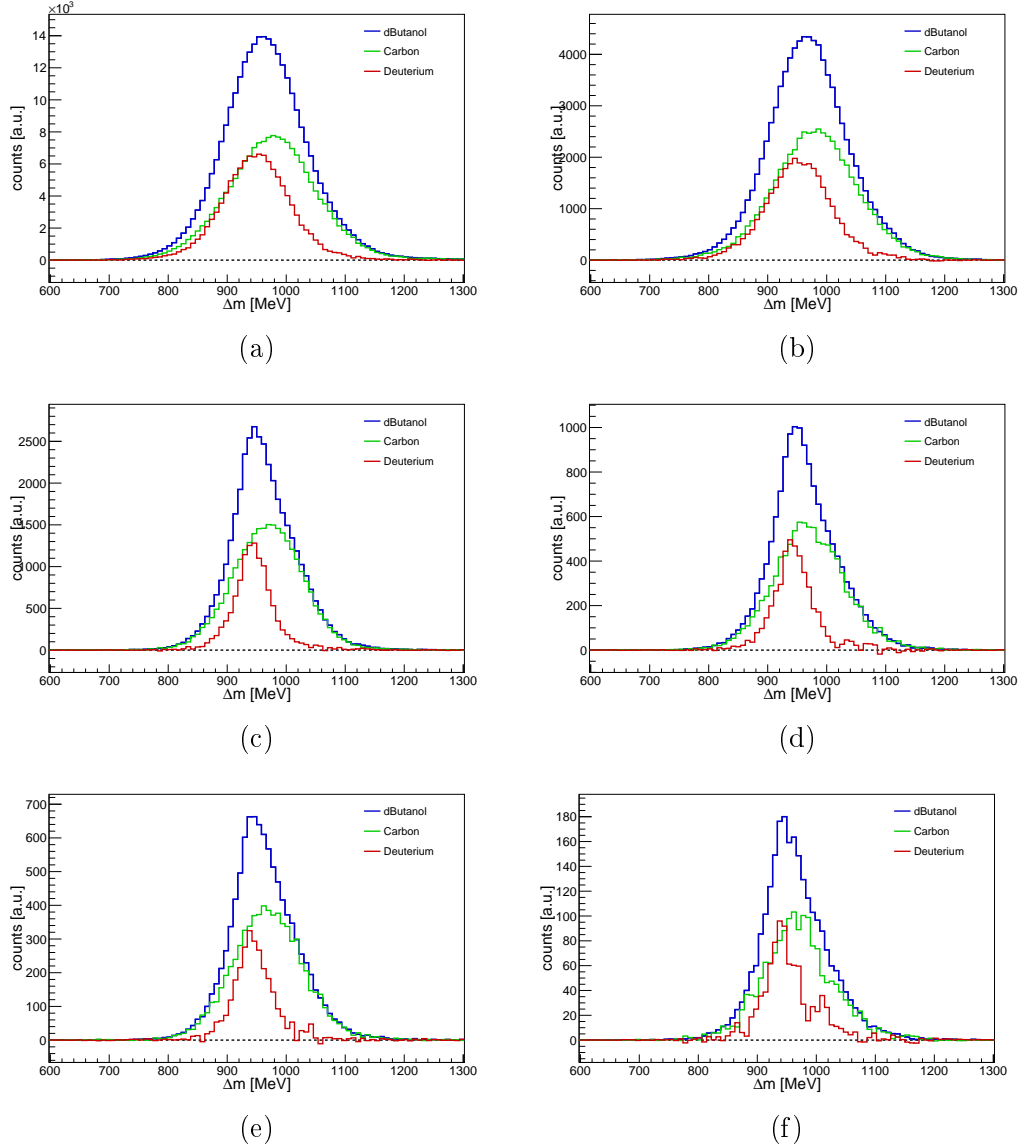


Figure 4.13: Energy and angular integrated missing mass of deuterated butanol (blue), carbon (green) and deuterium (red) in $\pi^0 p$ (a), $\pi^0 n$ (b), ηp with $\eta \rightarrow 2\gamma$ (c), ηn with $\eta \rightarrow 2\gamma$ (d), ηp with $\eta \rightarrow 6\gamma$ (e) and ηn with $\eta \rightarrow 6\gamma$ (f).

uses the cut positions found in the same reaction on the proton. Again, $\pm 2.5\sigma$ width cut positions around the mean value are chosen.

As mentioned at the beginning of this section, the missing mass should lie around the nominal mass of the recoil nucleon. The assumption of an initial nucleon at rest is wrong due to the Fermi motion. However, one can still clearly see a (smeared out) missing mass peak. Near the threshold, Fermi momenta

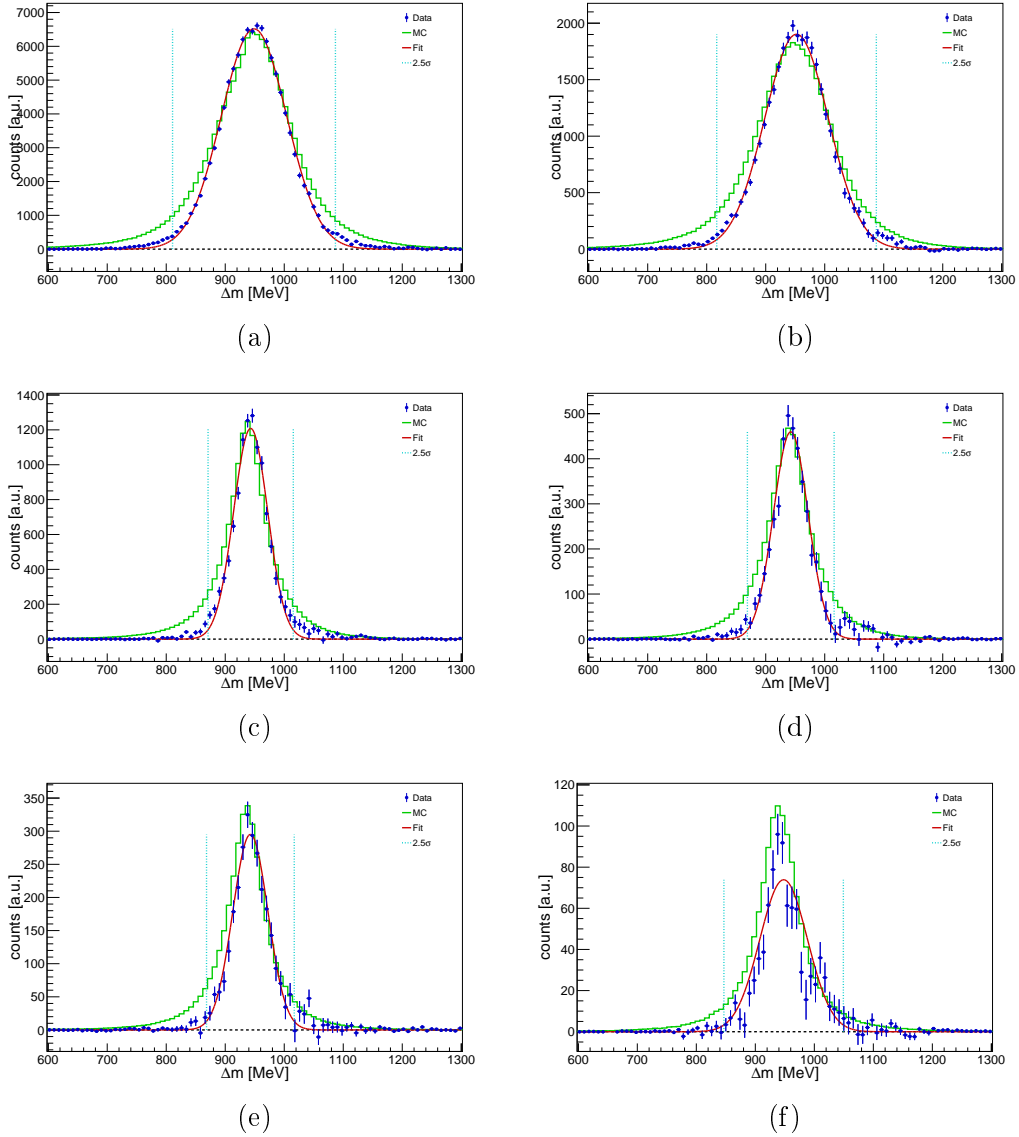


Figure 4.14: Energy and angular integrated missing mass of deuterium data (blue points), Monte Carlo simulation (green line) and the fit function (red, Equation 4.17) with 2.5σ cut widths (dotted cyan line) in $\pi^0 p$ (a), $\pi^0 n$ (b), ηp with $\eta \rightarrow 2\gamma$ (c), ηn with $\eta \rightarrow 2\gamma$ (d), ηp with $\eta \rightarrow 6\gamma$ (e) and ηn with $\eta \rightarrow 6\gamma$ (f).

strongly influence the missing mass with negative values in z -direction. This results in a more asymmetric shape of the missing mass in this region.

Figures 4.13 and 4.14 show the missing mass spectra for $\gamma N \rightarrow \pi^0 N$, $\gamma N \rightarrow \eta N$ with $\eta \rightarrow 2\gamma$ and $\gamma N \rightarrow \eta N$ with $\eta \rightarrow 6\gamma$. The colour code and method are the same as for the IM (Section 4.5.1), i.e. all available cut positions are

applied and the carbon data are scaled to account for the photon flux and the different target densities.

In contrast to the IM and coplanarity, the agreement between MC and data could be better for the missing mass. The Fermi momentum of the incident nucleons is implemented for the first time in VMC. It is visible in the following Section 4.5.5, that the Fermi momentum is lying at slightly higher values, which causes the broader structure of the missing mass in the MC simulation compared to the data. The position of the peak seems to be correct, whereas the shape looks too wide. However, no direct values are used from any MC simulated data such that their line shapes are shown only for comparison. Nevertheless, future experiments should investigate the VMC with Fermi momentum smearing more.

4.5.4 Polar angle difference

The polar angle difference $\Delta\theta$ between the measured and the missing recoil nucleon should be 0. As for the missing mass (Section 4.5.3), the recoil nucleon can be treated as a missing particle when assuming the initial nucleon is at rest, i.e. ignoring Fermi motion.

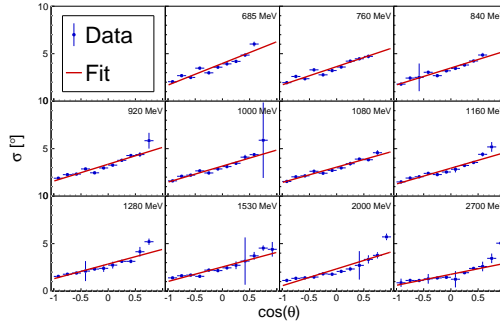


Figure 4.15: E_γ and $\cos(\theta)$ dependent sigma cut positions with their linear fitting functions from the polar angle difference spectra in π^0p .

Again, momentum conservation holds such that the polar angle of the missing recoil nucleon is given by:

$$\theta_{miss} = \arctan\left(\frac{\sqrt{(p_m^x)^2 + (p_m^y)^2}}{E_\gamma - p_m^z}\right), \quad (4.21)$$

where p_m^i is the i -component of the meson momentum and E_γ is the incoming photon energy. The resulting polar angle difference is given by:

$$\Delta\theta = \theta_{meas} - \theta_{miss}, \quad (4.22)$$

where θ_{meas} is the measured recoil nucleon polar angle.

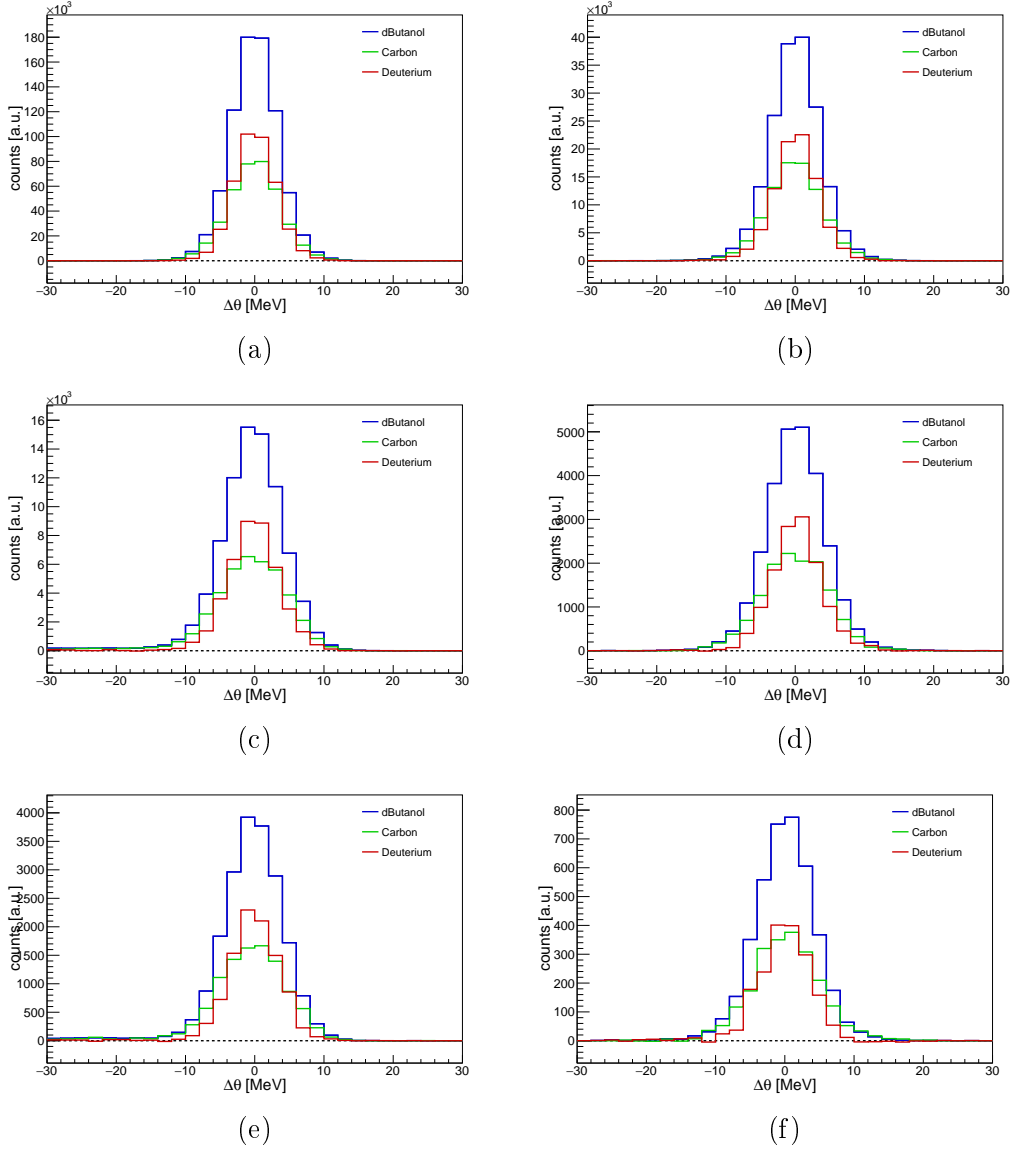


Figure 4.16: Energy and angular integrated polar angle difference of deuterated butanol (blue), carbon (green) and deuterium (red) in $\pi^0 p$ (a), $\pi^0 n$ (b), ηp with $\eta \rightarrow 2\gamma$ (c), ηn with $\eta \rightarrow 2\gamma$ (d), ηp with $\eta \rightarrow 6\gamma$ (e) and ηn with $\eta \rightarrow 6\gamma$ (f).

Figure 4.15 shows the energy- and angular-dependent sigma cut positions

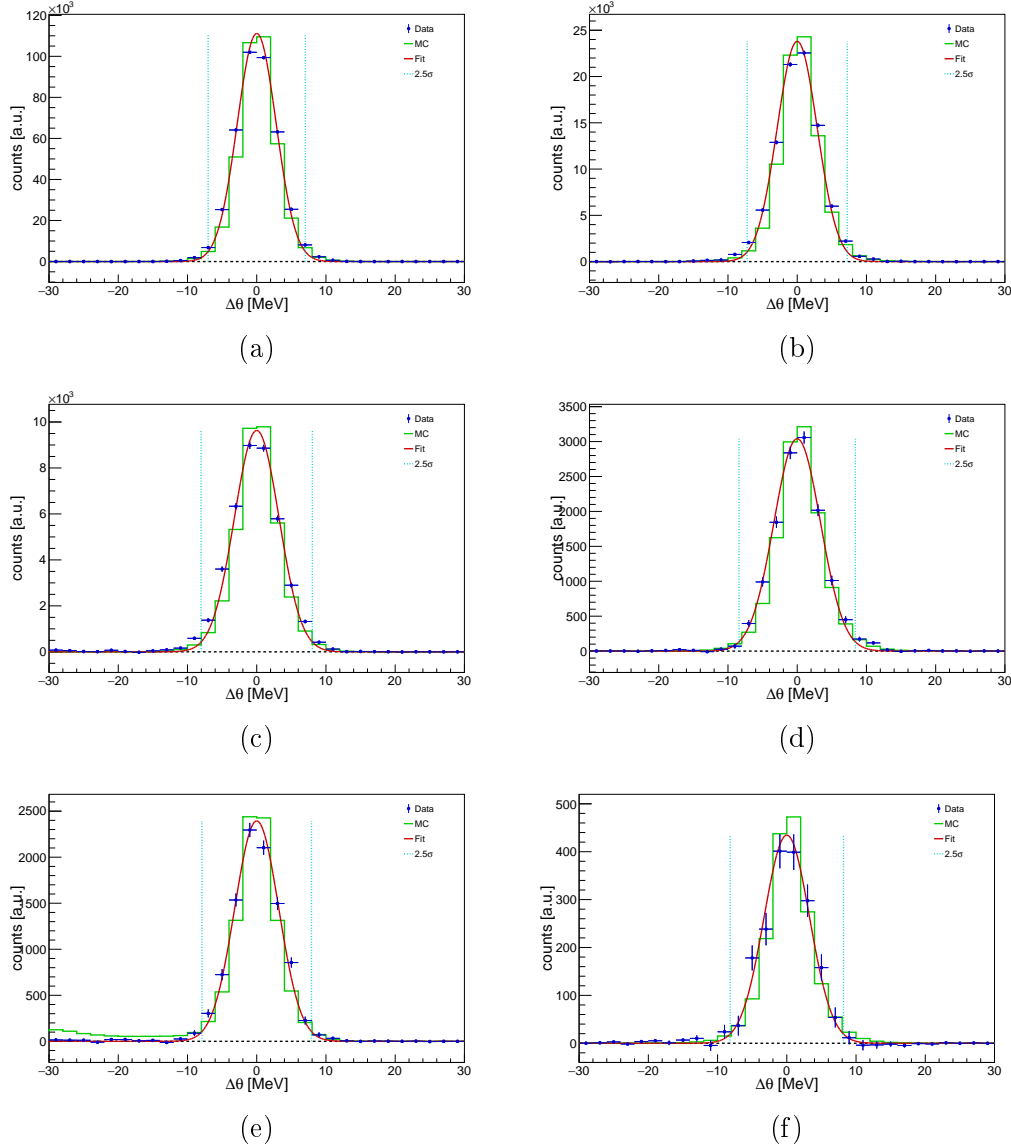


Figure 4.17: Energy and angular integrated polar angle difference of deuterium data (blue points), Monte Carlo simulation (green line) and the fit function (red, Equation 4.17) with 2.5σ cut widths (dotted cyan line) in $\pi^0 p$ (a), $\pi^0 n$ (b), ηp with $\eta \rightarrow 2\gamma$ (c), ηn with $\eta \rightarrow 2\gamma$ (d), ηp with $\eta \rightarrow 6\gamma$ (e) and ηn with $\eta \rightarrow 6\gamma$ (f).

with its linear fit function in $\pi^0 p$. The same figures for the other reactions can be found in Appendix A.5.

The strategy of finding $\pm 2.5\sigma$ width cut positions around $\Delta\theta = 0^\circ$ is very similar to those in the previous sections. A Gaussian function (Equation 4.17) with a fixed mean at 0 is fit to the carbon-subtracted dButanol data as a

function of $\cos(\theta)$ bins and E_γ , except for the $\eta \rightarrow 6\gamma$ decay channel. Due to the lower event number and the highly similar spectra with $\eta \rightarrow 2\gamma$, the cut positions from the $\eta \rightarrow 2\gamma$ decay channels are applied for the $\eta \rightarrow 6\gamma$ one in ηn . The σ values as a function of $\cos(\theta)$ are fitted with a linear function for every E_γ bin. A minimum of $\sigma = 1^\circ$ is required for all positions.

Figures 4.16 and 4.17 show the polar angle difference spectra for all reactions. The colour code and method are the same as for the IM (Section 4.5.1), i.e. all available cut positions are applied and the carbon data are scaled to account for the photon flux and the different target densities.

4.5.5 Fermi momentum

Deuterated butanol is the target material, consisting of polarised and unpolarised nucleons. The first are bound inside deuterium, the latter in carbon (and oxygen) that produce unwanted background. The bounding of nucleons inside nuclei results in relative momenta of nucleons to each other: Fermi momentum motion.

Depending on the nuclei, these momenta can differ. Section 3.1.3 showed theoretical models describing this motion of nucleons inside deuterium and carbon. Oxygen is (nearly) identical to carbon. The one of the deuterium-bound nucleons peaks at lower momenta compared to carbon-bound nucleons.

In the threshold region, Fermi momentum motion can make a significant difference because events are accepted or rejected only due to their Fermi momentum.

The shown reactions in Equations 4.1-4.4 assume a free nucleon as a target. In the quasifree case, the photoproduction of mesons can be described well by:

$$\gamma N(A) \rightarrow mNA', \quad (4.23)$$

where γ stands for the photon, A is the nucleus, where the nucleon is bound and A' is the nucleus with one N less. The investigated reactions in this work can be written as:

$$\gamma n(D) \rightarrow mnp, \quad (4.24)$$

$$\gamma p(D) \rightarrow mpn. \quad (4.25)$$

A carbon target is used to determine the carbon contribution in the dButanol data. The reactions can be written as:

$$\gamma n(^{12}\text{C}) \rightarrow mn^{11}\text{C}, \quad (4.26)$$

$$\gamma p(^{12}\text{C}) \rightarrow mp^{11}\text{B}. \quad (4.27)$$

Equation 4.23 can be transformed into a kinematic equation:

$$p_\gamma + p_N = p_m + p_{N'}, \quad (4.28)$$

where $p = (E, \vec{p})$ are the four-vectors of the particles and the spectator nucleus/nucleon A' is assumed to be unaffected in the reaction. Rearranging Equation 4.28 one finds the Fermi momentum of the target (and spectator) nucleon:

$$\vec{p}_F = \vec{p}_N = \vec{p}_m + \vec{p}_{N'} - \vec{p}_\gamma. \quad (4.29)$$

The Fermi momentum cut position is statically chosen to be $p_F = |\vec{p}_F| < 160 \text{ MeV}$ such that the background can be rejected and not too much signal is cut away. Looking at the theoretical model describing the Fermi momentum of deuterium in 3.1, this cut position should include around 87.5% ($\sim 1.53\sigma$) of the deuterium data but only around 62.0% ($\sim 0.88\sigma$) of the carbon data. A lower cut position would suppress the ratio even more and decrease the systematic uncertainty and the number of events significantly, increasing the statistical uncertainty. Because the statistics in this experiment mainly drive the uncertainty, a further decrease in the cut position would increase the uncertainty even more.

The determination of the Fermi momentum cut position has one of the most significant effects on rejecting carbon and oxygen dilution, i.e. the dilution factor and its systematic uncertainty (Section 5.4.3). Decreasing the cut position to lower values would increase the dilution factor and therefore reduce the systematic uncertainty but significantly increase the statistical uncertainty. Since the latter is the dominant uncertainty, a very low cut position would be contra-productive. On the other hand, the Fermi momentum cut position reduces additional background, e.g. from final state interactions, quite well such that it should not be chosen too high. Together, these lead to the chosen value of 160 MeV.

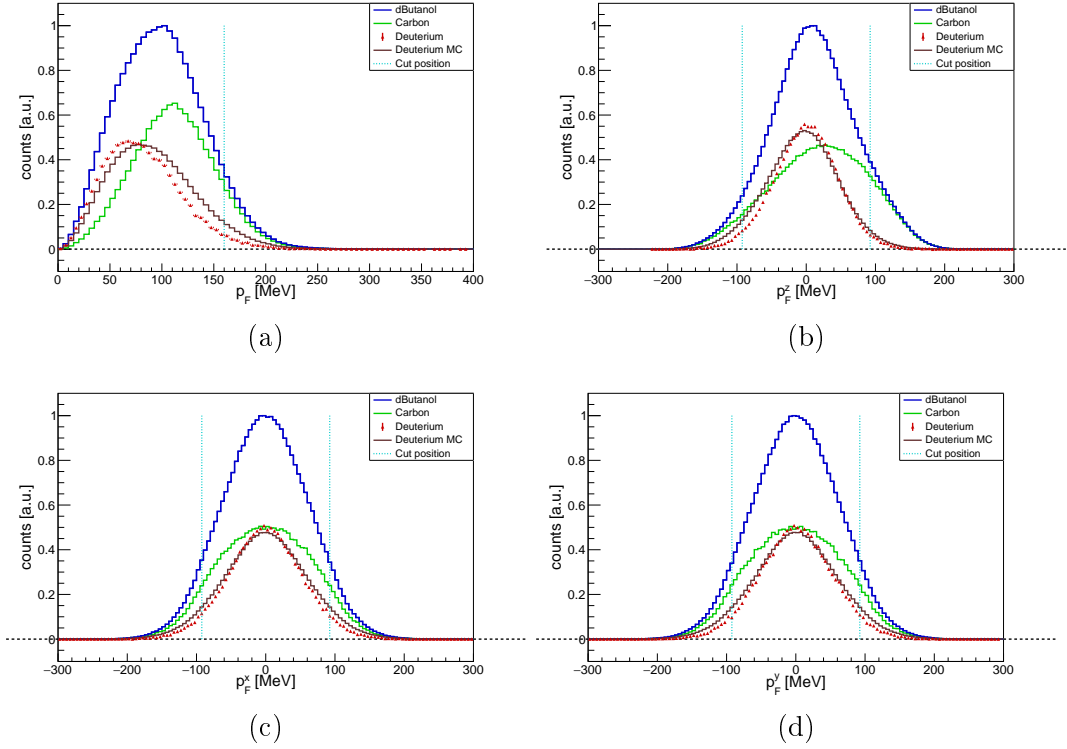


Figure 4.18: Total (a) and component (b-d) Fermi momentum in $\pi^0 p$. (b) shows the Fermi momentum component in z -direction, (c) in x -direction and (d) in y -direction.

The deuterium MC simulation shows subtle energy and angular dependence of the Fermi momentum such that the momenta get more spread for higher energies and very backward angles ($\cos(\theta) \rightarrow -1$), where the nucleon goes towards MT. However, with a static Fermi momentum cut of 160 MeV, it is ensured to take more than 80% of all deuterium data in all kinematic regions.

An additional Fermi momentum component cut is applied to suppress random events further. The Fermi momentum is random in the three spatial directions, resulting in:

$$p_x = p_y = p_z = \frac{p_F}{\sqrt{3}} \approx 92.4 \text{ MeV}. \quad (4.30)$$

Figure 4.18 shows the total and component-wise Fermi momentum spectra of dButanol, scaled carbon, deuterium, MC deuterium data and the cut positions. The total Fermi momentum spectra of the other reactions can be found in Figure 4.19 and the components are given in Appendix A.4. Also,

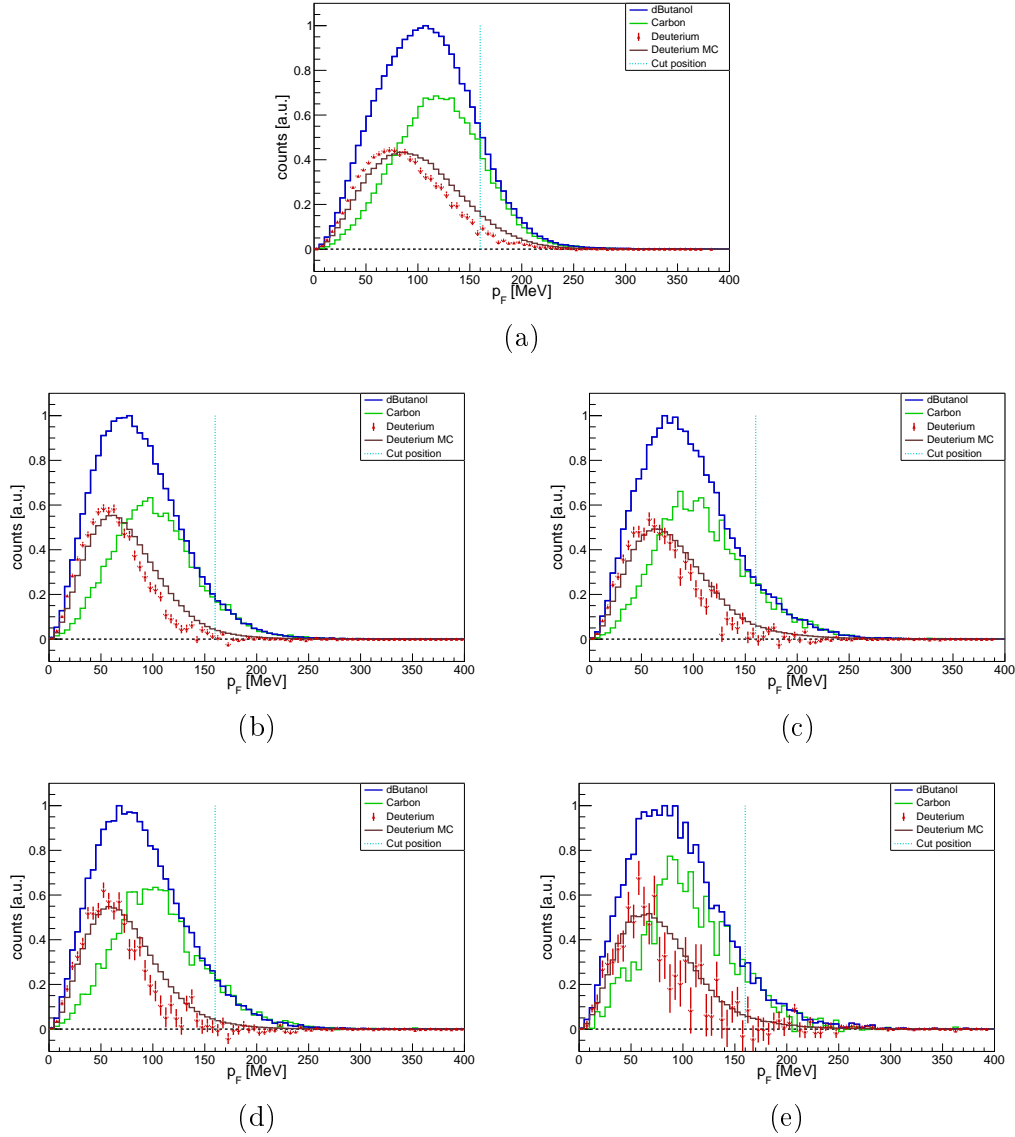


Figure 4.19: Total Fermi momentum in $\pi^0 n$ (a), ηp (b,d) and ηn (c,e) with $\eta \rightarrow 2\gamma$ (b-c), $\eta \rightarrow 6\gamma$ (d-e). The spectra in $\pi^0 p$ can be found in Figure 4.18.

an overview of energy or angular-dependent Fermi momentum spectra can be found there for all reactions.

The situation for the spectra is the same as for IM, i.e. all cuts are applied and the carbon data are correctly scaled.

As mentioned in the previous section, implementing the Fermi momentum needs more investigation. The MC values are shifted towards higher values compared to the data. As always, all cuts that are applied for the data are

also applied for the MC simulation.

4.5.6 Summary of kinematic cut positions and number of total events

The in detail described raw cut positions in the presort (Section 4.1-4.4) and kinematic cut positions (Section 4.5) can briefly be summarised as:

- Multiplicity: all final state particles must be detected (Section 4.1)
- Time: $4 - 5\sigma$ ($>99.9\%$) width cuts (Section 4.3)
- χ^2 anticut: for $2\gamma n$ final states on invariant mass (Section 4.2.3)
- Invariant mass: 2.5σ ($\approx 98.8\%$) width cuts (Section 4.5.1)
- Invariant mass on π^0 for $\eta \rightarrow 6\gamma$ decay channel: $\sim 2.6\sigma$ ($\approx 99.1\%$) around nominal π^0 mass
- Coplanarity: 2.5σ ($\approx 98.8\%$) width cuts (Section 4.5.2)
- Missing mass: 2.5σ ($\approx 98.8\%$) width cuts (Section 4.5.3)
- Fermi momentum: $\sim 1.5\sigma$ ($\approx 87.5\%$) width cuts (Section 4.5.5)
- Polar angle difference: 2.5σ ($\approx 98.8\%$) width cuts (Section 4.5.4)

Assuming that the iterative background suppressing cut positions - invariant mass, coplanarity, missing mass, Fermi momentum, polar angle difference - are all independent, an overall event acceptance of $0.988^4 \cdot 0.875 = 83.4\%$ results. For the $\eta \rightarrow 6\gamma$ decay channel, this value must be multiplied by 0.991^3 due to the additional IM cut on the single π^0 , resulting in 81.1% . Due to some correlations between the kinematic properties, mainly missing mass and Fermi momentum, this can be seen as a lower bound, i.e. less than 20% of all good events are cut away due to the applied cut positions.

The number of events in the different reactions and on different targets can be found in Table 4.4. Given is the number of events after the complete reconstruction process with all applied background rejection cuts. It can be seen that there are more than 3 times fewer events on reactions on neutrons than there are on protons. As was shown [130], the detection efficiency for

Target	BT	$\gamma p \rightarrow \pi^0 p$	$\gamma n \rightarrow \pi^0 n$	$\gamma p \rightarrow \eta p$		$\gamma n \rightarrow \eta n$	
		$\pi^0 \rightarrow 2\gamma$		$\eta \rightarrow 2\gamma$	$\eta \rightarrow 6\gamma$	$\eta \rightarrow 2\gamma$	$\eta \rightarrow 6\gamma$
dButanol	Oct2018	1455 ± 14	340 ± 7	122 ± 4	29 ± 2	45 ± 2	6 ± 1
	Dec2021	1427 ± 15	332 ± 7	122 ± 4	27 ± 2	46 ± 2	6 ± 1
	All	2883 ± 28	672 ± 14	244 ± 7	56 ± 3	91 ± 5	13 ± 2
carbon	Oct2018	142 ± 5	36 ± 2	13 ± 1	3 ± 1	5 ± 1	1 ± 1
	Dec2021	180 ± 5	45 ± 3	15 ± 1	3 ± 1	6 ± 1	1 ± 1
	All	3321 ± 9	80 ± 5	28 ± 3	6 ± 1	11 ± 2	2 ± 1
deuterium	Oct2018	758 ± 26	173 ± 13	64 ± 7	15 ± 3	23 ± 4	3 ± 2
	Dec2021	742 ± 26	167 ± 13	64 ± 7	14 ± 3	24 ± 4	3 ± 2
	All	1500 ± 53	340 ± 25	129 ± 13	30 ± 3	47 ± 8	6 ± 3

Table 4.4: Number of events (in thousand) after the reconstruction and all background rejection cut positions. BT is an abbreviation for beam time. Deuterium events are deuterated butanol events minus flux and target density-corrected carbon events. The uncertainty is mainly due to some uncertainty coming from the random background subtraction and the target density constant in the normalisation of the carbon data.

neutrons is less than 0.3 times the one for protons with decreasing neutron detection efficiencies towards lower photon energies.

The photon detection efficiency is around 90% in the Crystal Ball/TAPS detector setup [262]. Reactions with many photons in the final state, e.g. $\gamma N \rightarrow \eta N$ with $\eta \rightarrow 6\gamma$, are therefore suppressed. The complete photon detection efficiency decreases even more for reactions with many final state photons due to an increase in overlapping PED. An additional suppression of the $\eta \rightarrow 6\gamma$ decay channel is the 20% lower branching ratio and the additional π^0 cuts. All together leads to a significantly lower event yield of less than 25% for the $\eta \rightarrow 6\gamma$ decay channel compared to the $\eta \rightarrow 2\gamma$ one, which has been observed before [262].

Figure 4.20 shows the absolute number of *good* deuterium events that passed all criteria described in this chapter. The events are shown energy- and angular-dependent for all reactions. For obtaining the deuterium events, the carbon data are scaled to account for the photon flux and the different target densities and subtracted from the dButanol data, i.e. normalised by the photon flux (Section 5.2) and the relative target surface densities (Section 5.4). In all reactions, the number of events decreases towards higher energies. The

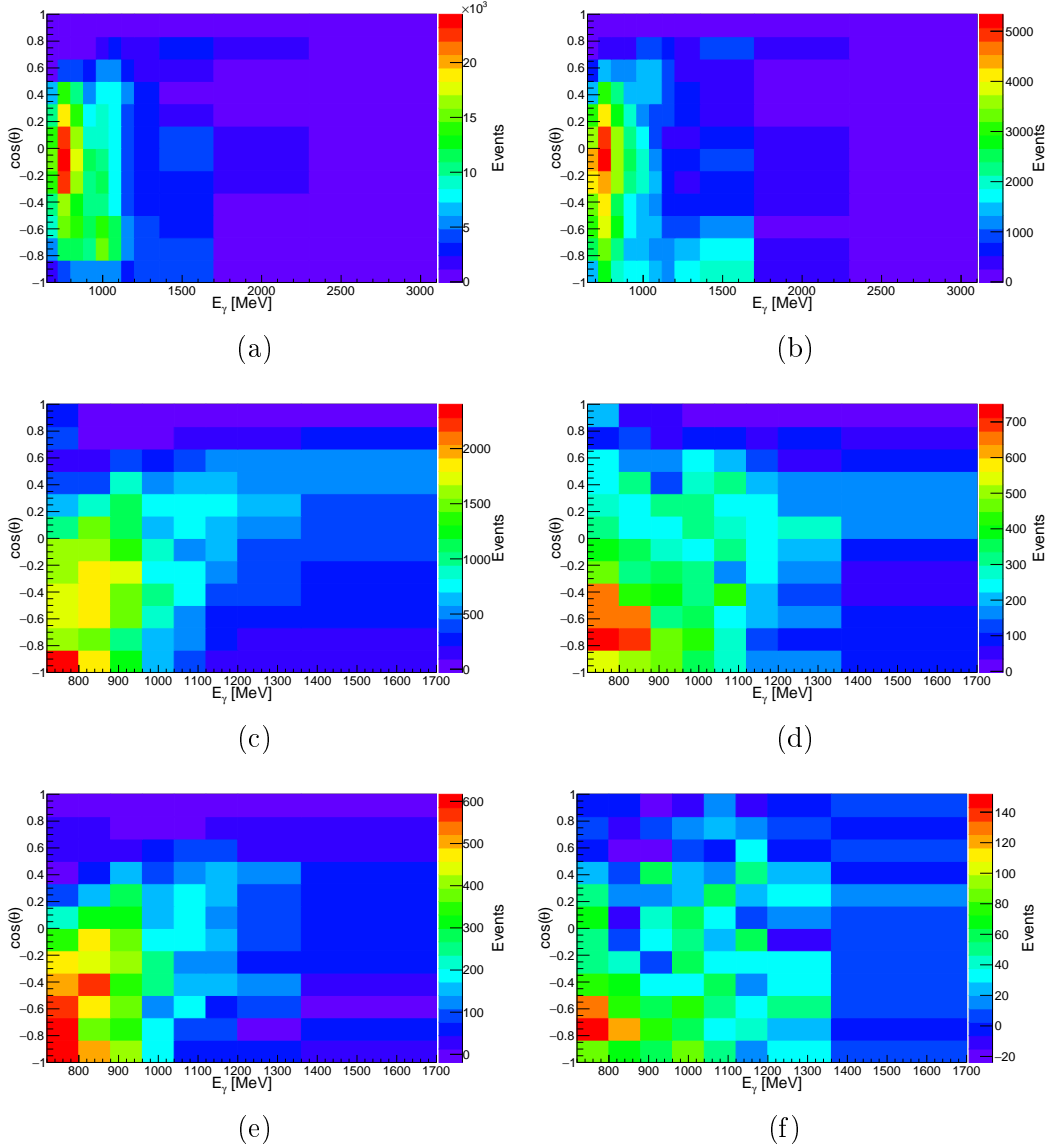


Figure 4.20: E_γ and $\cos(\theta)$ dependent absolute deuteron events that passed all selection and background suppression criteria. Shown are all reactions: (a) $\pi^0 p$, (b) $\pi^0 n$, (c) ηp with $\eta \rightarrow 2\gamma$, (d) ηp with $\eta \rightarrow 2\gamma$, (e) ηp with $\eta \rightarrow 6\gamma$ and (f) ηp with $\eta \rightarrow 6\gamma$.

reason for this lies in the bremsstrahlung process that is proportional to $1/E_\gamma$. Both η decay channels result in very similar spectra, whereas the ones from π^0 look quite different. In the first case, the meson prefers backward angles, where the nucleon is going in the forward direction. In the second case, the meson is centred around the vertical experimental axis, i.e. 90° .

4.5.7 Effect of kinematic cut positions

The figures in this section provide an overview of the impact of the kinematic cuts applied for suppressing background, as described in Section 4.5. In contrast to the cut finding procedure, the raw dButanol data are shown here. Although, the photon flux and target-density-normalised carbon-subtracted data can be seen as well as *last cut* in black.

The effect of the raw cut positions as multiplicity, coincidence time and χ^2 anticut for $2\gamma n$ final states that are applied in the presort of EXPLOSCAR can be seen in Figure 4.1.

All kinematic cuts are essential for a clean event selection. All signals are already visible after the presort. The invariant mass spectra are also taken for estimating the remaining background contamination such that the *goodness* of the background suppression is best visible there. Besides reducing the background, the signal gets cleaner with every further kinematic cut. In $\pi^0 p$, for example, the FWHM of the invariant mass decreases from 21 MeV to 18 MeV from only preselection cuts to all background rejection cuts applied. It even gets down to 17 MeV when the carbon is subtracted at the end.

Besides removing unpolarised nucleons, carbon subtraction has another nice effect: it subtracts some background events itself. In the end, a low background signal of the meson and the recoil nucleon can be seen from the spectra.

Figures 4.21-4.26 show the different kinematic spectra for all reactions. The x -axis label indicates the kinematic type: $m_{\gamma\gamma}$ invariant mass of the meson, $\Delta\phi$ coplanarity between meson and recoil nucleon, Δm missing mass of the recoil nucleon, p_F absolute Fermi momentum of the initial nucleon, $p_F^{x,y}$ Fermi momentum in x - and y -direction of the initial nucleon, p_F^z Fermi moment in z -direction (beam direction) of the initial nucleon and $\Delta\theta$ polar angle difference between reconstructed and missing recoil nucleon. The $\eta \rightarrow 6\gamma$ decay channel reactions show an additional invariant mass spectrum of the π^0 mesons.

4.5. Background suppression

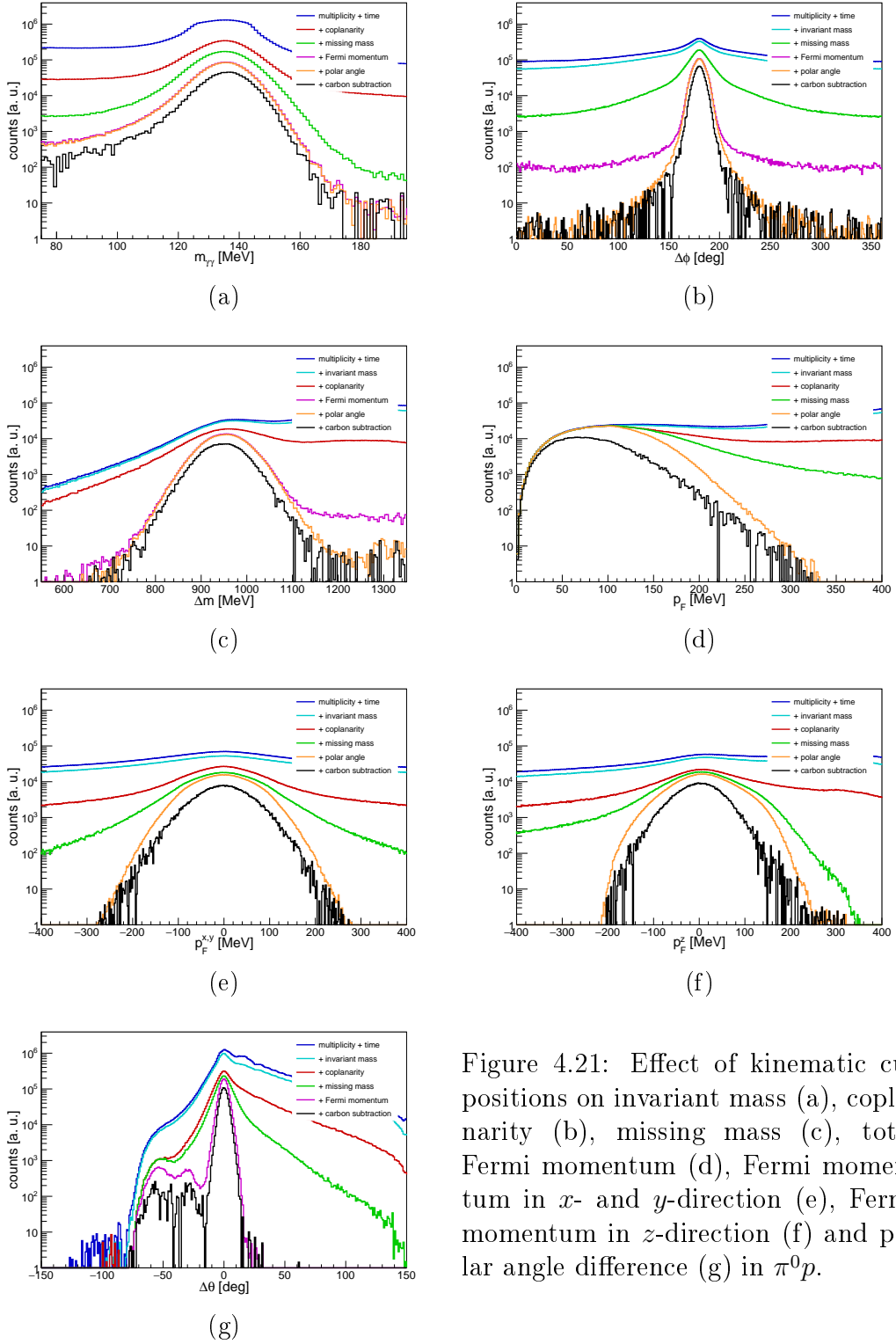


Figure 4.21: Effect of kinematic cut positions on invariant mass (a), coplanarity (b), missing mass (c), total Fermi momentum (d), Fermi momentum in x - and y -direction (e), Fermi momentum in z -direction (f) and polar angle difference (g) in $\pi^0 p$.

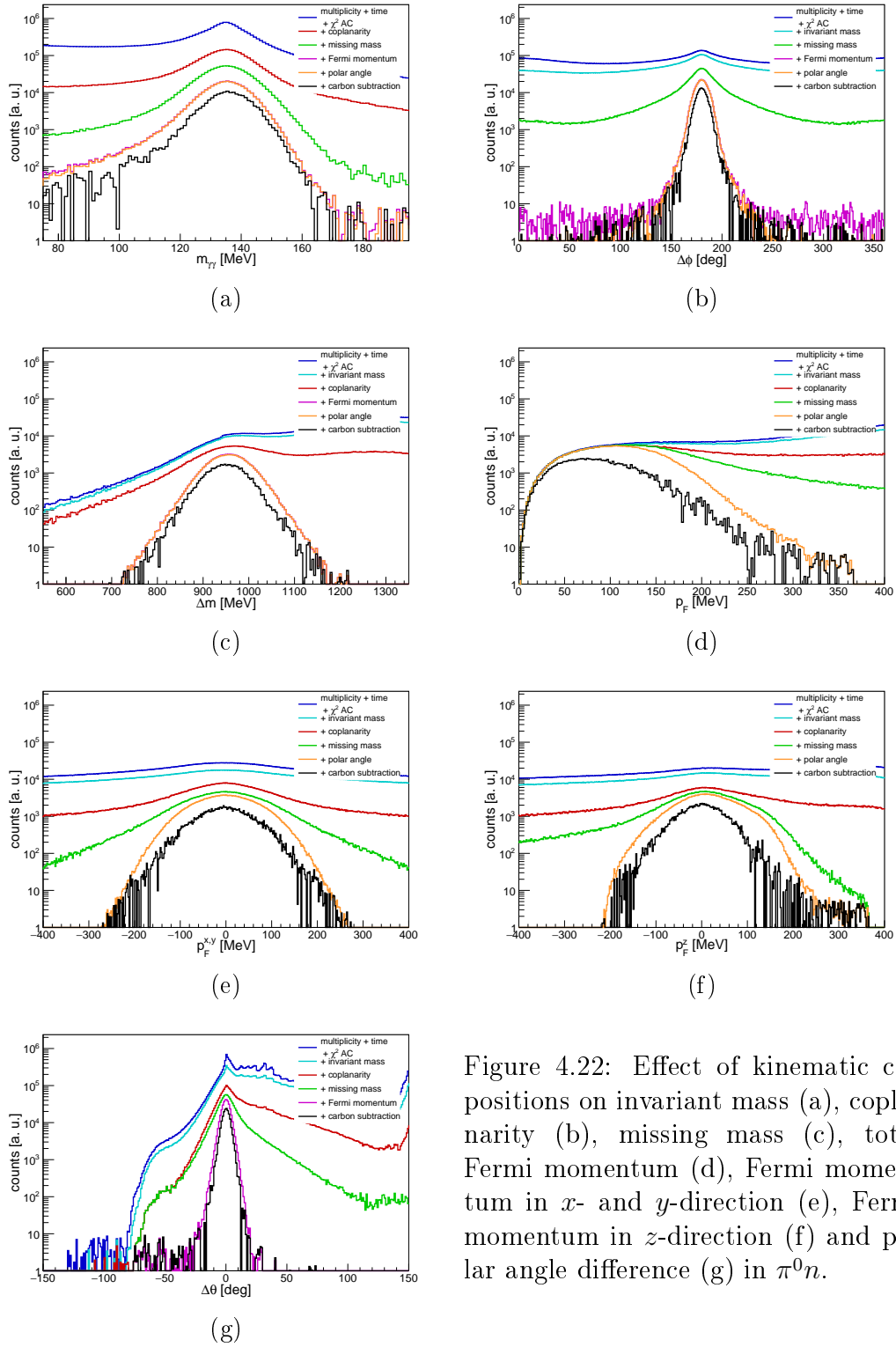


Figure 4.22: Effect of kinematic cut positions on invariant mass (a), coplanarity (b), missing mass (c), total Fermi momentum (d), Fermi momentum in x - and y -direction (e), Fermi momentum in z -direction (f) and polar angle difference (g) in $\pi^0 n$.

4.5. Background suppression

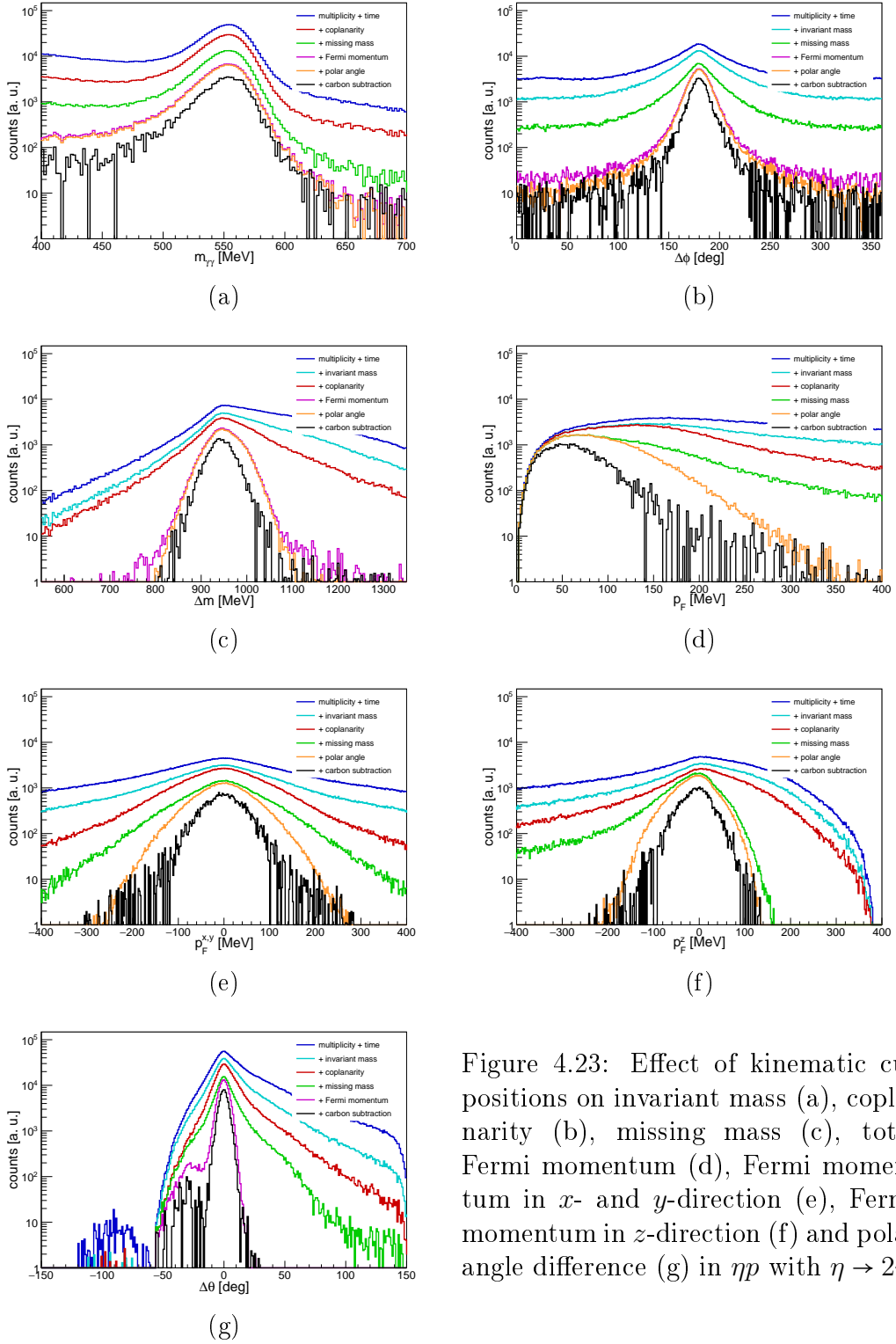


Figure 4.23: Effect of kinematic cut positions on invariant mass (a), coplanarity (b), missing mass (c), total Fermi momentum (d), Fermi momentum in x - and y -direction (e), Fermi momentum in z -direction (f) and polar angle difference (g) in ηp with $\eta \rightarrow 2\gamma$.

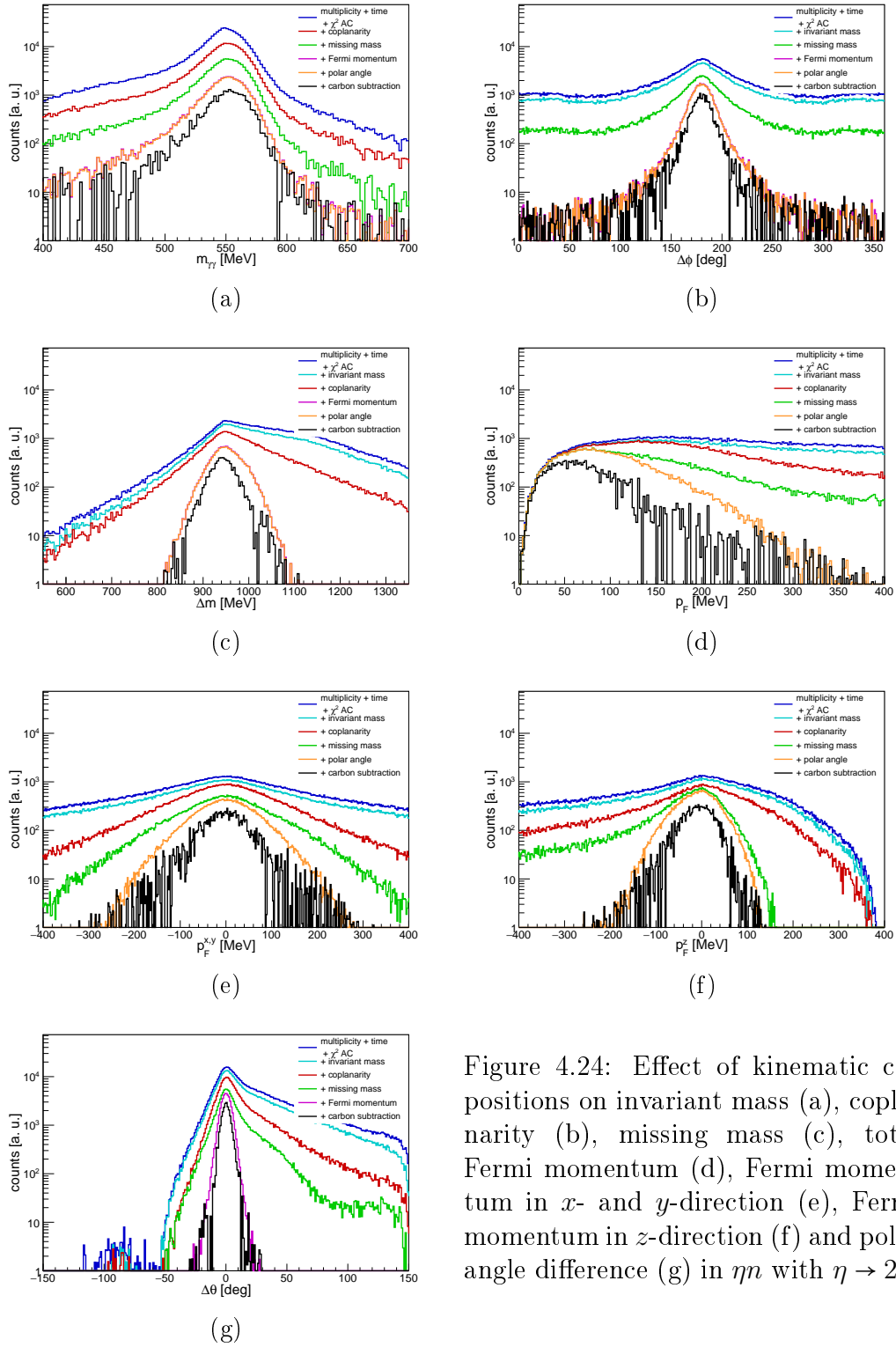


Figure 4.24: Effect of kinematic cut positions on invariant mass (a), coplanarity (b), missing mass (c), total Fermi momentum (d), Fermi momentum in x - and y -direction (e), Fermi momentum in z -direction (f) and polar angle difference (g) in $\eta\eta$ with $\eta \rightarrow 2\gamma$.

4.5. Background suppression

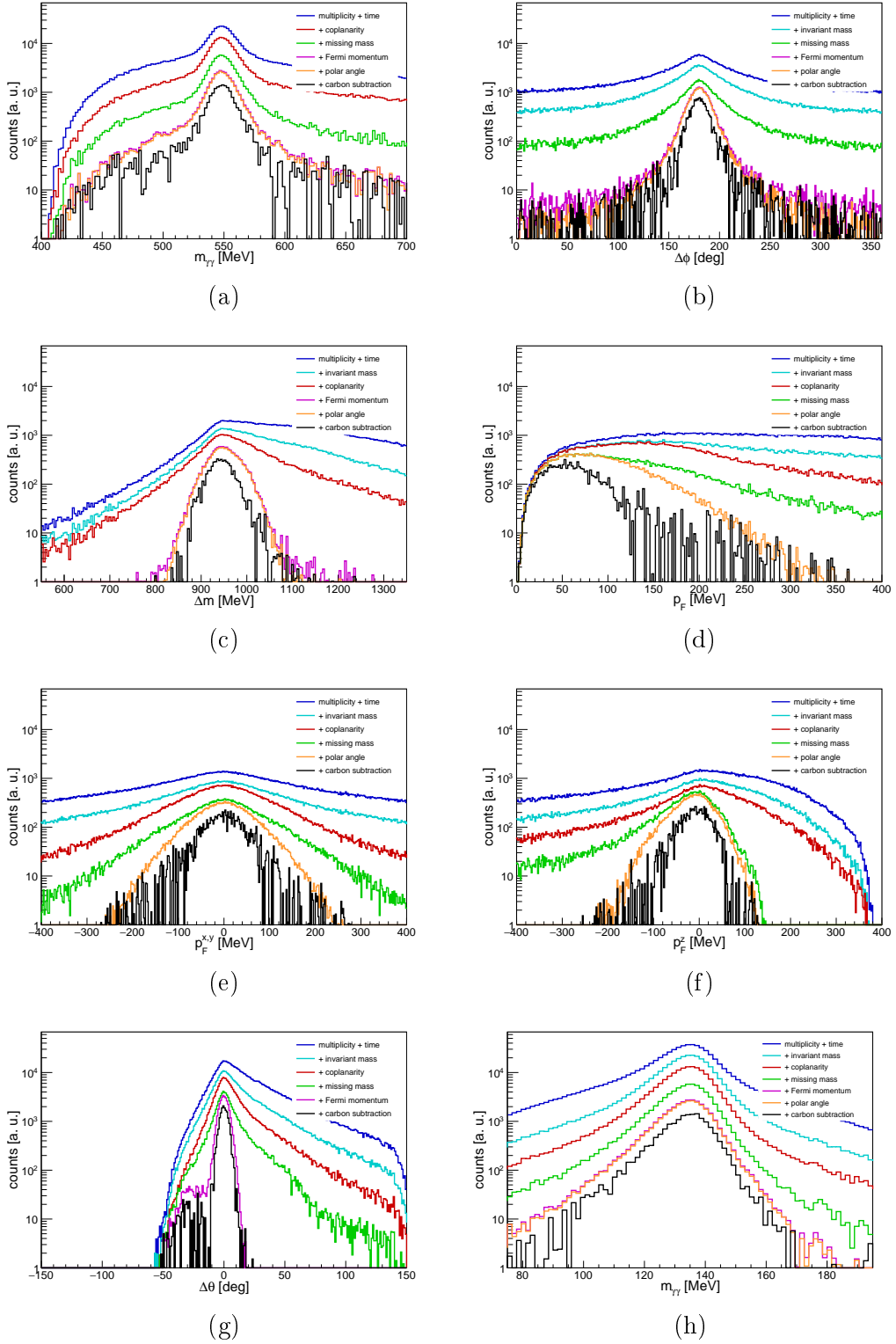


Figure 4.25: Effect of kinematic cut positions in ηp with $\eta \rightarrow 6\gamma$. Same labels as in Figure 4.23 with additional invariant mass of intermediate π^0 (h).

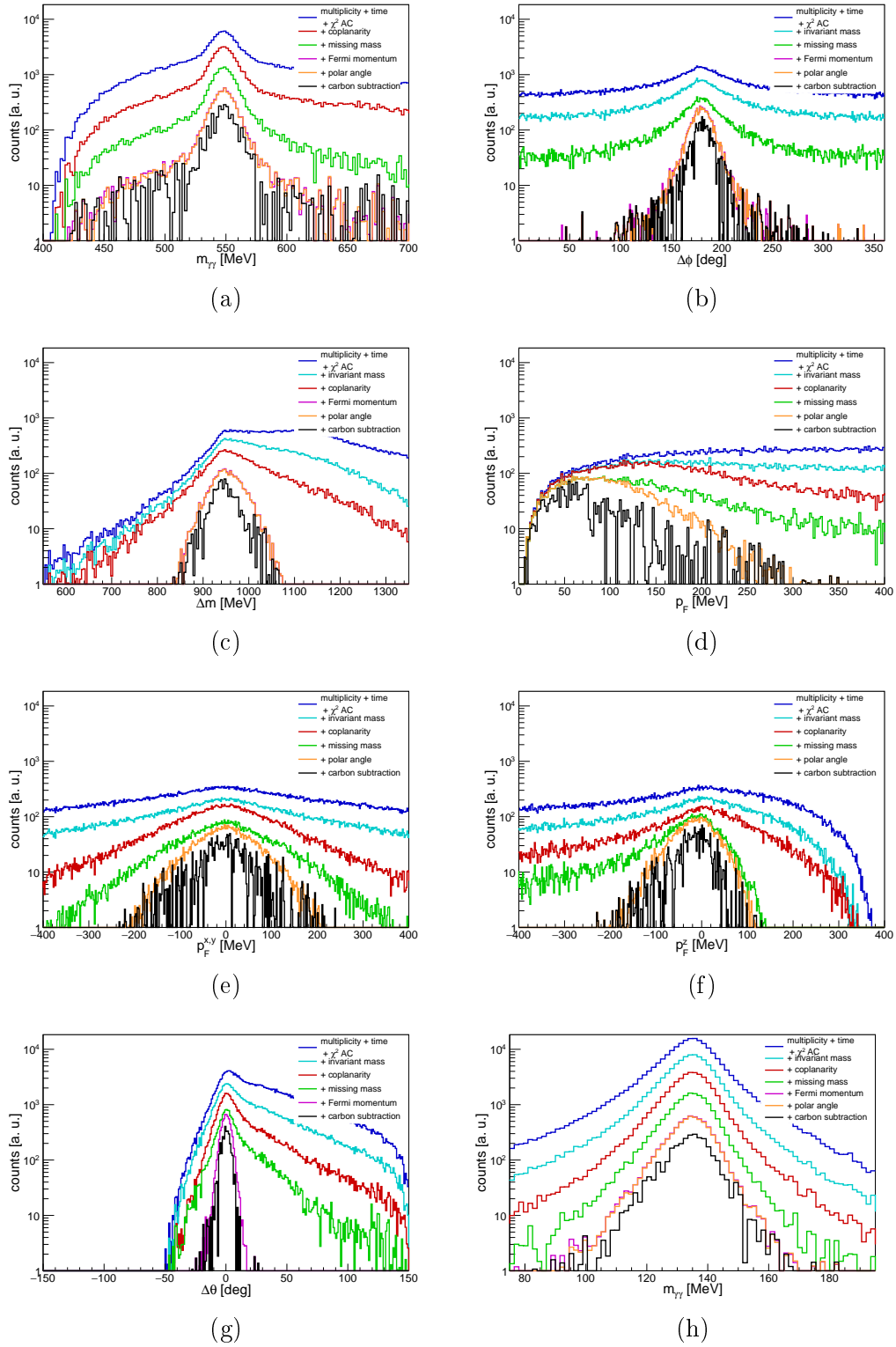


Figure 4.26: Effect of kinematic cut positions in ηn with $\eta \rightarrow 6\gamma$. Same labels as in Figure 4.23 with additional invariant mass of intermediate π^0 (h).

4.6 Remaining background contamination

The background contamination is estimated from the invariant mass as a final quality check. For all reactions, each E_γ and $\cos(\theta)$ dependent spectra are fitted with an extended fit function. This consists of a signal part that is equal to the invariant mass fit function in Equation 4.16 and an additional polynomial of degree 1 for $\pi^0 \rightarrow 2\gamma$ and $\eta \rightarrow 2\gamma$ or polynomial of degree 2 for $\eta \rightarrow 6\gamma$, respectively, as background term. The reason for the different treatments lies in the different kinematics. Due to different final states, different background terms may contribute to the contamination. For example, $3\pi^0$ phase space contribution may contribute to $\eta \rightarrow 6\gamma$ background contamination but not to the other decay channels.

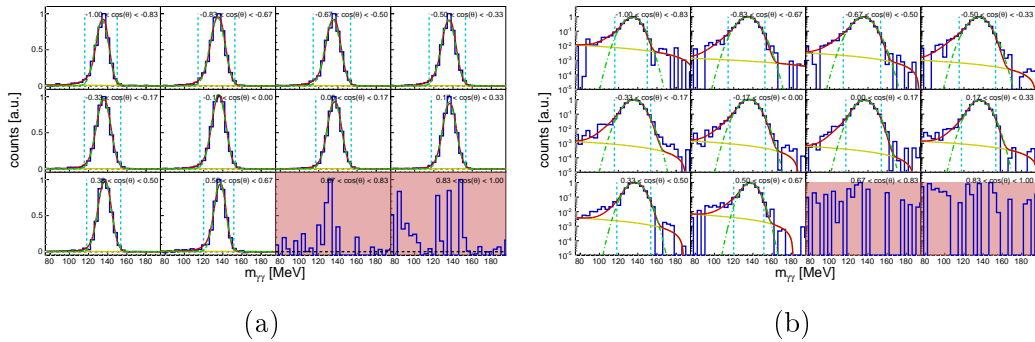


Figure 4.27: Invariant mass for background contamination estimation in π^0 for different $\cos(\theta)$ bins at a fixed energy of $E_\gamma = 760$ MeV. The same data is shown in a linear (a) and a logarithmic (b) scale. See text for more details.

The E_γ and $\cos(\theta)$ integrated total invariant mass is fitted with this function to confirm the chosen background polynomials with the full statistic. The ratio between the area of the background term and the total function within the 2.5σ is assumed to be the background contamination.

As usual, ηN with $\eta \rightarrow 6\gamma$ have fewer events than the others, such that the energy and angular dependence is hard to get. In the end, the data from both decay channels are merged and fitted together. Furthermore, the $\eta \rightarrow 2\gamma$ is expected to have more background contamination due to more possible misidentified events with three final state particles compared to the reaction with seven final state particles, where the single π^0 must be identified as well.

Figure 4.28 and 4.29 show the energy and angular integrated invariant mass

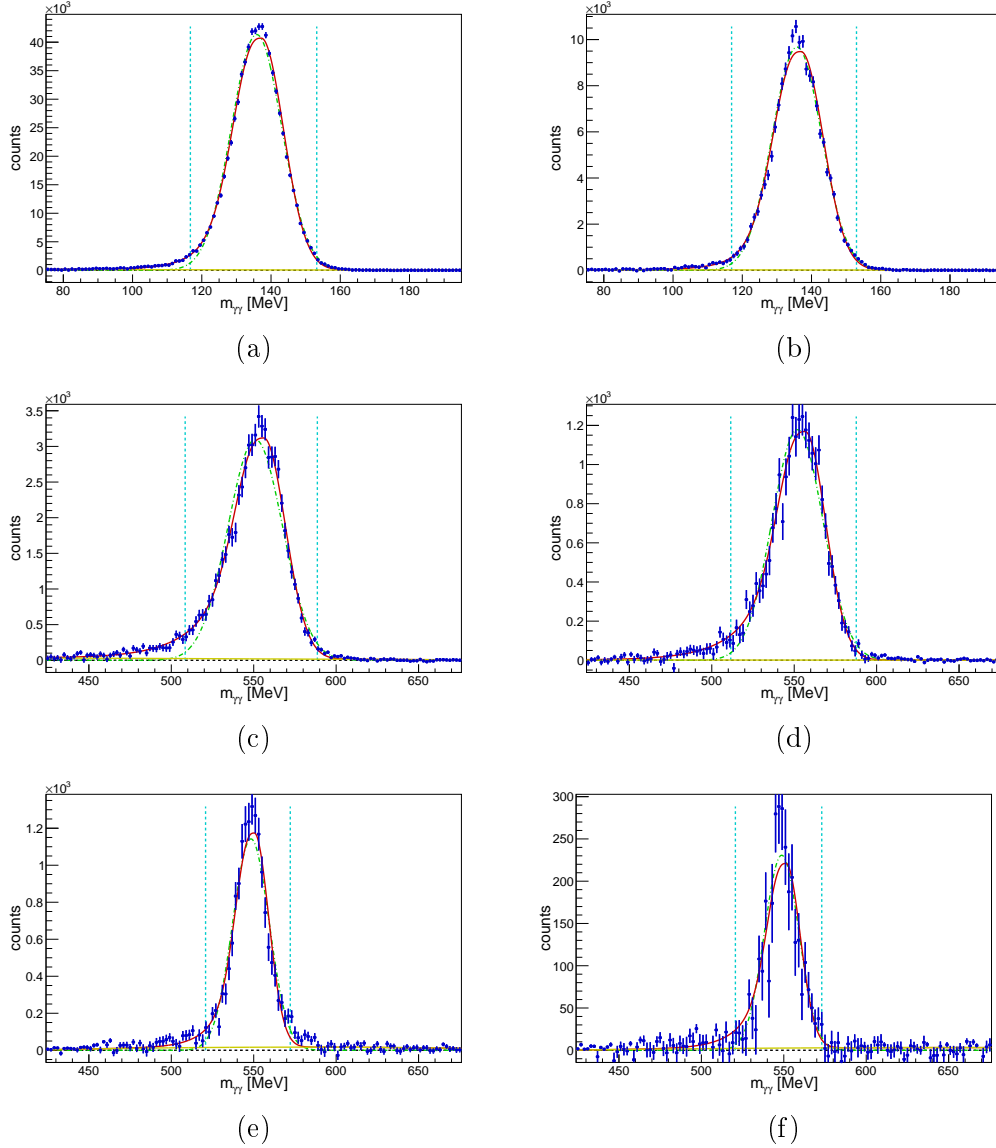


Figure 4.28: Total invariant mass with the total asymmetric Gaussian fit function and the linear (a-d) and quadratic (e-f) background term in $\pi^0 p$ (a), $\pi^0 n$ (b), ηp with $\eta \rightarrow 2\gamma$ (c), ηn with $\eta \rightarrow 2\gamma$ (d), ηp with $\eta \rightarrow 6\gamma$ (e) and ηn with $\eta \rightarrow 6\gamma$ (f). The y -axis is shown in a logarithmic scale. See text for more details.

spectra for all reactions with linear and logarithmic y -axis. Figure 4.27 shows an example of the $\cos(\theta)$ dependent invariant masses with the extended fit function in $\pi^0 p$ with a photon energy of $E_\gamma = 760$ MeV. The data are shown in blue, a Gaussian fit as a green dashed-dotted line, the used total asymmetry Gaussian fit including a background term as a red line, the background

4.6. Remaining background contamination

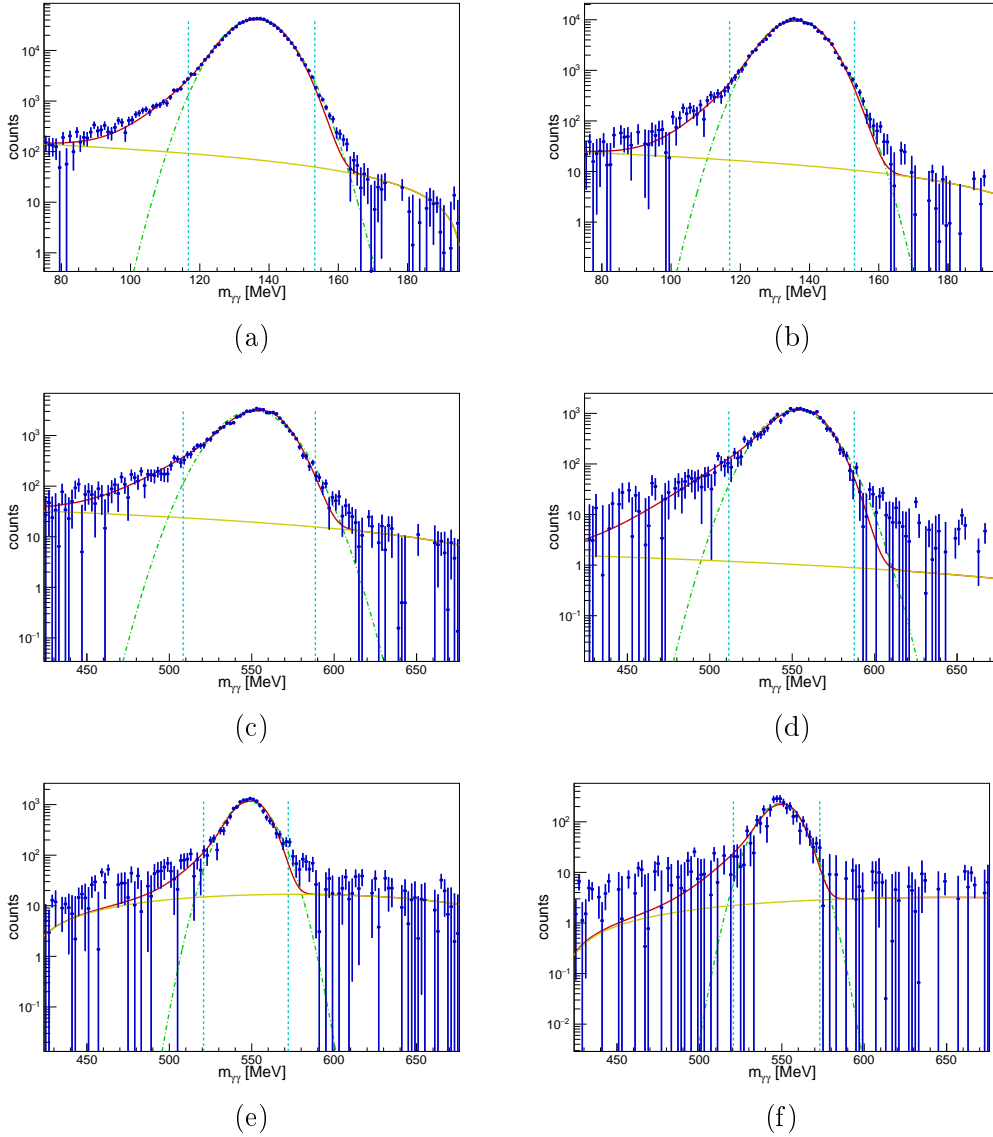


Figure 4.29: Total invariant mass with the total asymmetric Gaussian fit function and the linear (a-d) and quadratic (e-f) background term in $\pi^0 p$ (a), $\pi^0 n$ (b), ηp with $\eta \rightarrow 2\gamma$ (c), ηn with $\eta \rightarrow 2\gamma$ (d), ηp with $\eta \rightarrow 6\gamma$ (e) and ηn with $\eta \rightarrow 6\gamma$ (f). Please note the logarithmic scale on the y -axis. See text for more details.

contribution as a yellow line and the 2.5σ width positions as a cyan dotted line.

The Gaussian function can describe the peak as well as the adjusted Gaussian one. For values further away from the peak position, the adjusted Gaussian one is better suited for the description. However, the difference is only a

few per cent within the cut positions.

To get physically useful signals, at least 50 entries are required within an IM range from 100 MeV to 170 MeV for π^0 and 500 MeV to 600 MeV for η . The ones that do not meet these conditions are not fitted and their kinematic bins are coloured in red, as visible in Figure 4.27 for the two most forward angular bins.

The total estimated background contamination for the energy and angular integrated IM is found to be around 0.4% in $\pi^0 p$, 0.3% in $\pi^0 n$, 1.2% in ηp with $\eta \rightarrow 2\gamma$, 0.2% in ηn with $\eta \rightarrow 2\gamma$, 0.8% in ηp with $\eta \rightarrow 6\gamma$ and 1.4% in ηn with $\eta \rightarrow 6\gamma$. Although the largest contribution is estimated in ηn with $\eta \rightarrow 6\gamma$, the statistical uncertainty of the points is relatively large such that the value of 1.2% in ηp with $\eta \rightarrow 2\gamma$ is more reliable for the largest contribution. However, the individual energy- and angular-dependent fits result in a background contribution of mainly below 1%, for the most part even below 0.5%.

As seen in Section 4.5.1, the data are in excellent agreement with the MC simulation. The estimated background contribution from the adjusted asymmetric Gaussian fit function is assumed to be rather an overestimation. To treat a possible background contribution in a conservatively right way, a minimum of 0.5% is assumed for all used bins as systematic uncertainty in the end (Section 6.4.3).

Figure 4.30 shows the background contamination as a function of E_γ and $\cos(\theta)$ for all investigated reactions. Most bins have a background contamination of less than 0.5%. The bins with larger contamination are mainly found in regions with low event statistics, so the uncertainty of their value is also large. The missing bins have, as discussed earlier, fewer events than 50 such that no useful signal is found. They are dismissed in the final results.

4.6. Remaining background contamination

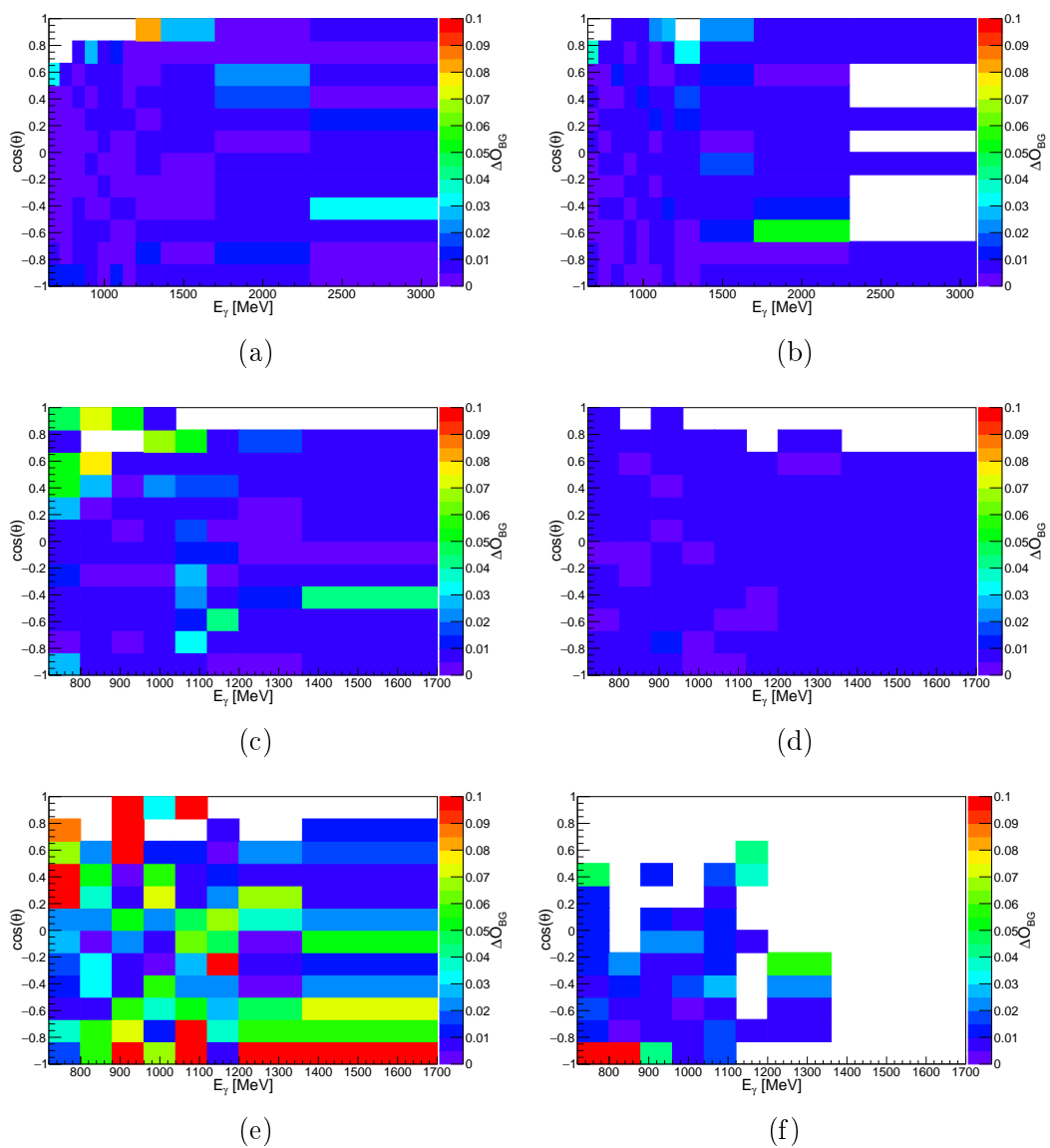


Figure 4.30: Background contamination in $\pi^0 p$ (a), $\pi^0 n$ (b), ηp with $\eta \rightarrow 2\gamma$ (c), ηn with $\eta \rightarrow 2\gamma$ (d), ηp with $\eta \rightarrow 6\gamma$ (e) and ηn with $\eta \rightarrow 6\gamma$ (f).

5 | Data analysis

Events of the investigated reactions are selected with a clean signal and low background contamination. Before polarisation observables can be extracted (Chapter 6), some more data analysis must be done.

The first Section 5.1 discusses the target surface densities that are directly correlated with the number of nucleons in the target materials.

The event yields depend on the data taking time, which must be considered for determining the observables. The photon flux, discussed in Section 5.2, provides this information.

Sections 5.3 and 5.4 discuss the determination of the polarisation degrees and the dilution factor, two necessary corrections. In a perfect experiment, there would be no need for these corrections. However, the photons and nucleons cannot be perfectly polarised, so the exact polarisation degrees must be known. The dilution factor must be known further to correct the number of reactions on polarised nucleons inside deuterium compared to unpolarised ones inside carbon (and oxygen).

Even though the events can be selected with a low background, some contributions from different final states may still remain and change the true observable values. This can be corrected to a certain extent, described in Section 5.5.

As already mentioned several times, the nucleons in this experiment are quasifree, i.e. bound in deuterium with a Fermi motion. The knowledge of the *true* centre of mass (CM) energy W is essential for removing these effects. Section 5.6 discusses this reconstruction process from the final state.

The chapter closes with a discussion of data merging methods in Section 5.7.

5.1 Target surface density

The target surface density is directly correlated with the number of reaction partners in the target material. Usually, the target stays the same during a beam time, so the target surface density is constant. For extracting experimental cross sections, the exact target surface density must be known for normalisation reasons (Equation 1.51). This value cancels out for polarisation asymmetries and observables and does not need to be known. However, since the experiment uses two targets - dButanol and carbon - it is important to know the ratio between the target surface densities between them. In that way, the carbon data can be rightfully subtracted from the dButanol data to get a pure deuterium signal for the kinematic cut positions (Section 4.5) and the determination of the dilution factor (Section 5.4) later on.

The target surface density is given by:

$$n_t = \frac{\rho_t l_t N_A f}{M_t}, \quad (5.1)$$

where ρ_t and l_t are the density and length of the target, f and M_t are the filling factor and molar mass of the target nucleons and $N_A = 6.022\,140\,857 \cdot 10^{23} \text{ mol}^{-1}$ [97] is the Avogadro constant. The filling factor is due to the shape of the used dButanol beads in the target cell. They are spherical and do not entirely fill the target cell (Figure 2.11b).

To get the ratio between the two targets, one needs to normalise them to the number of carbon nuclei inside the target molecules. The oxygen nuclei must also be considered, achieved by a relative $A^{2/3}$ term. The power of $2/3$ occurs from the fact that the cross sections of these nuclei with mass number A scale in such a way [269]. The number of carbon nuclei in dButanol is given by:

$$N^{C(dB)} = 4 + \left(\frac{M_O}{M_C}\right)^{2/3} = 5.211, \quad (5.2)$$

where $M_C = 12.011 \text{ g mol}^{-1}$ [318] and $M_O = 15.999 \text{ g mol}^{-1}$ [318] are the molar masses of carbon and oxygen. Note that the doping material is ignored here.

The target surface density of carbon nuclei inside dButanol respecting the

different behaviour of the oxygen nuclei is given by:

$$n_t^{C(dB)} = N^{C(dB)} \cdot n_t. \quad (5.3)$$

The experimental setup with the carbon foam target is the same as the dButanol one to have the same conditions, i.e. target container, helium, cryostat, etc. Therefore, the target surface density ratio can be directly calculated using the experimental parameters in Table 5.1. These values hold for both beam times: Oct2018 and Dec2021.

The density of the dButanol is measured in its fluid state of aggregation to be $(0.9200 \pm 0.0005) \text{ g cm}^{-3}$ at 25°C [319]. It melts at -89.99°C and therefore has another density in its solid state. A density of $(1.106 \pm 0.012) \text{ g cm}^{-3}$ at 77 K was measured [320] for dButanol in the past. Another measurement showed an increase in the density of butanol of $(14.72 \pm 1.24) \%$ at 4 K compared to room temperature [321], which should be very similar for dButanol. The mean value of both, $(1.106 \pm 0.012) \text{ g cm}^{-3}$ and $(0.9200 \pm 0.0005) \text{ g cm}^{-3} \cdot (1.1472 \pm 0.0124) = (1.055 \pm 0.012) \text{ g cm}^{-3}$, is taken with a relative error of 4% to ensure a rightful treatment. This results in a density of dButanol of $(1.08 \pm 0.04) \text{ g cm}^{-3}$. The other parameters are taken from [322].

material	dButanol	carbon
$\rho_t [\text{g cm}^{-3}]$	1.08 ± 0.04	0.5000 ± 0.0005
$l_t [\text{cm}]$	2.000 ± 0.005	2.040 ± 0.005
$M_t [\text{g mol}^{-1}]$	84.19	12.011
f	0.60 ± 0.05	1
N^C	5.211	1
$n_t [\text{barn}^{-1}]$	0.0094 ± 0.0009	0.05114 ± 0.00018
$n_t^C [\text{barn}^{-1}]$	0.0483 ± 0.0047	0.05114 ± 0.00018

Table 5.1: Parameters of the deuterated butanol and carbon target in both beam times.

By dividing the carbon nuclei target surface density of the dButanol and carbon target, a scaling factor c_t is found:

$$c_t = \frac{n_t^{C(dB)}}{n_t^C} = 0.94 \pm 0.09. \quad (5.4)$$

Particularly the filling factor has considerable uncertainty. A better knowledge of that or a direct measurement of it could increase the accuracy of future experiments.

5.2 Photon flux

It is crucial to know the photon flux to normalise the data from different experimental setups: dButanol and carbon targets or the different polarisation orientations. The flux is determined as a function of energy and time, i.e. run number. Especially the energy dependence is important due to the linearly polarised photons, which produce a *coherent enhancement* near the coherent edge.

Not all deflected electrons in the Tagger N_{e^-} belong to a photon that impinges the target. The main reasons are the used collimator that narrows the photon beam and the detection of random electron hits. The number of detected electrons must therefore be multiplied by the tagging efficiency ϵ_{tagg} to get the right photon flux:

$$N_{\gamma} = N_{e^-} \cdot \epsilon_{tagg}. \quad (5.5)$$

The tagging efficiency is like the electron and photon flux energy-dependent and determined as a function of the incident photon energy E_{γ} .

5.2.1 Electron flux

The electron flux cannot directly be taken from the number of hits in the Tagger since the energy distribution of the photons is strongly influenced by the trigger.

The number of tagged electrons N_{e^-} within the time window $\Delta t = \Delta t_1 + \Delta t_2$ is calculated by choosing the two windows outside the trigger window itself. Δt_1 goes from -450 ns to -50 ns and Δt_2 from 50 ns to 350 ns.

In the end, the number of tagged electrons within a time window of the total live time t_{live} is of interest. $N_{e^-}(\Delta t)$ must therefore be multiplied by a scaling factor c_{live} , that is given by the ratio between the number of coincident hits in neighbouring Tagger bars N_{scaler} during the total live time t_{live} and the coincident TDC hits in neighbouring tagger bars in the data N_{TDC} during the time window Δt .

The correct number of detected electrons - the electron flux - is so given by:

$$N_{e^-} = N_{e^-}(\Delta t) \cdot c_{live} = N_{e^-}(\Delta t) \cdot \frac{N_{scaler}(t_{live})}{N_{TDC}(\Delta t)}. \quad (5.6)$$

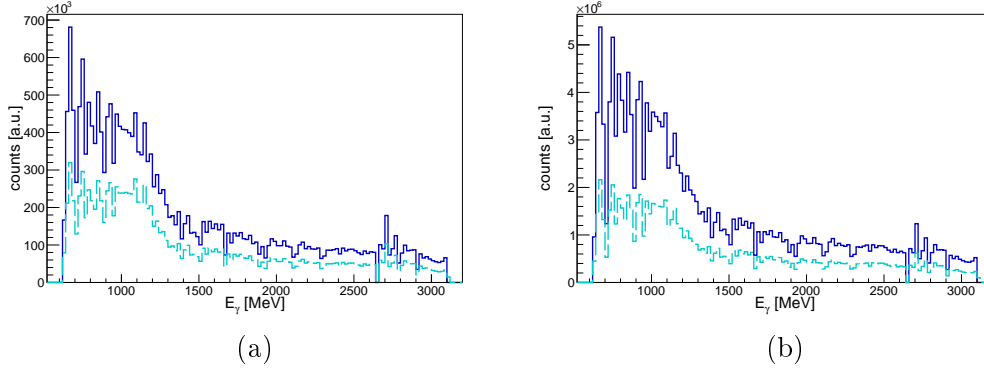


Figure 5.1: Photon flux without any corrections (dashed cyan) and with tagging efficiency and rate-independent GIM efficiency corrections (solid blue) in Oct2018 (a) and Dec2021 (b).

An additional correction should be applied in general: Cherenkov dead time correction. The Cherenkov detector works as a veto in the trigger system, influencing the time for data taking. By multiplying the dead time of a single Cherenkov hit Δt_{Chkv} with the Cherenkov trigger rate $N\dot{N}_{Chkv}$. The dead time is visible in the TDC spectrum and can be seen in Figure 5.2. It is $\Delta t_{chkv} = 86$ ns. This is true for both beam times, whereas the average Cherenkov rate differs. In Oct2018 it is given with $\dot{N}_{Chkv} = 1.34$ MHz, in Dec2021 with $\dot{N}_{Chkv} = 2.04$ MHz. Together, this results in a relative dead time of around $\Delta t_{Chkv}\dot{N}_{Chkv} = 11.5\%$ in Oct2018 and $\Delta t_{Chkv}\dot{N}_{Chkv} = 17.5\%$ in Dec2021.

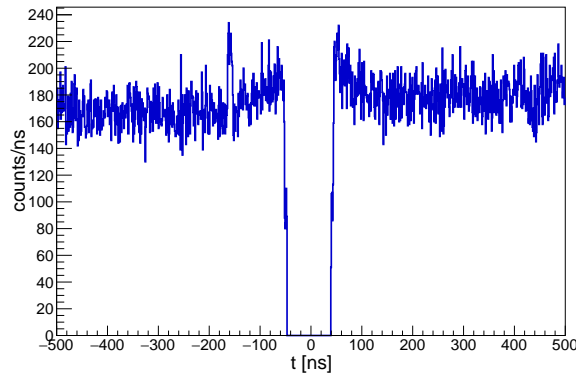


Figure 5.2: Cherenkov Time-to-Digital (TDC) spectrum in ns for run 203232 in Oct2018. All events where the Cherenkov holds as veto, i.e. $\text{taps2} \vee (\text{cf1} \wedge \text{taps1})$ are shown. The dead time is given as the width with no entries around $t = 0$ ns with $\Delta t_{Chkv} = 86$ ns.

Although this seems a lot, the Cherenkov veto signal is only included in around 10.2% of all trigger events, reducing its influence significantly. In all investigated reactions, the influence of the Cherenkov as a veto is even more suppressed. More than 99% of all final events are detected with the cf2 trigger.

Finally, the electron flux is given by:

$$N_{e^-} = N_{e^-}(\Delta t) \cdot c_{live} (1 - \Delta t_{Chkv} \dot{N}_{Chkv}). \quad (5.7)$$

5.2.2 Tagging efficiency

Some photons get lost on the way towards the target. The tagging efficiency is the ratio of detected photons to detected electrons.

During data-taking runs, the tagging efficiency is measured using the GIM and FluMo detectors at the end of the photon beam line (Section 2.2.7). The tagging efficiency is given by the number of coincidence hits in GIM and Tagger within a time window of $\Delta t = |t_{GIM} - t_{Tagg}| < 8$ ns (Figure 5.3) divided by the total number of detected hits in the Tagger. Furthermore, the rate-independent GIM efficiency must be considered as well to result in:

$$\epsilon_{tagg} = \frac{1}{\epsilon_{GIM}} \cdot \frac{N_{Tagg-GIM}}{N_{Tagg}}. \quad (5.8)$$

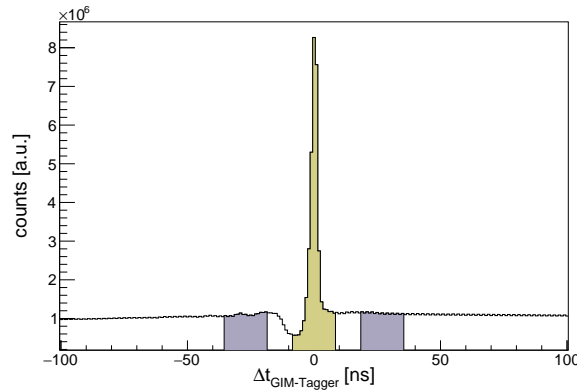


Figure 5.3: Coincidence time difference between GIM and tagging system in Oct2018. The yellow area show prompt hits within $\Delta t^P = [-8$ ns, 8 ns] and the violet areas show the sideband background windows $\Delta t^{SB1} = [-35$ ns, -19 ns] and $\Delta t^{SB2} = [19$ ns, 35 ns].

The coincidence hits in GIM and Tagger cannot directly be taken due

to random background hits. Similar to the random background subtraction of coincidence CB-Tagger and MT-Tagger hits (Section 4.4), the sideband subtraction method is used here, too. Therefore, $N_{Tagg-GIM}$ is given by the number of prompt events $N_{Tagg-GIM}^P$ minus sideband events $N_{Tagg-GIM}^{SB}$, scaled with $c_{P-SB} = \Delta t^P / \Delta t^{SB}$. The live time windows are given by the intervals $\Delta t^P = [-8 \text{ ns}, 8 \text{ ns}]$, $\Delta t^{SB1} = [-35 \text{ ns}, -19 \text{ ns}]$ and $\Delta t^{SB2} = [19 \text{ ns}, 35 \text{ ns}]$, resulting in:

$$\begin{aligned} N_{Tagg-GIM} &= N_{Tagg-GIM}^P - c_{P-SB} \cdot N_{Tagg-GIM}^{SB} \\ &= N_{Tagg-GIM}^P - \frac{\Delta t^P}{\Delta t^{SB}} \cdot N_{Tagg-GIM}^{SB}. \end{aligned} \quad (5.9)$$

The sideband time intervals are chosen in this way because the background slowly decreases towards larger distances from the signal peak and the dead time from the double pulse resolution of the GIM is $t_{DPR} = 12 \text{ ns}$, which is more dominant near the signal peak position.

The only term in Equation 5.8 that still needs to be determined is the GIM efficiency. For this, two methods can be used: First, one can calculate the losses due to dead time. Second, one can perform special low-rate runs (Section 2.5) with a rate below 300 kHz to determine the tagging efficiency. The latter is used in this experiment.

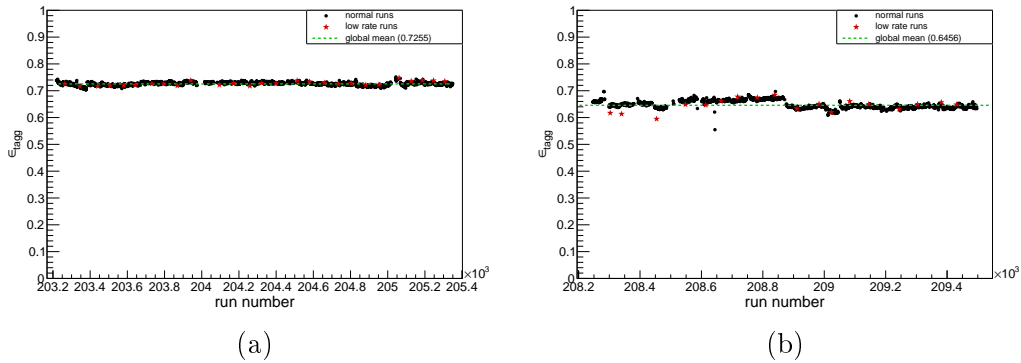


Figure 5.4: Tagging efficiency as a function of the run number or time, respectively, without the rate-independent GIM efficiency correction in Oct2018 (a) and Dec2021 (b).

The rate-independent GIM efficiency in low-rate runs ϵ_{GIM} is approximately 1. Due to detector threshold effects, this is only partially true for energies near the threshold itself. However, going towards higher energies, the

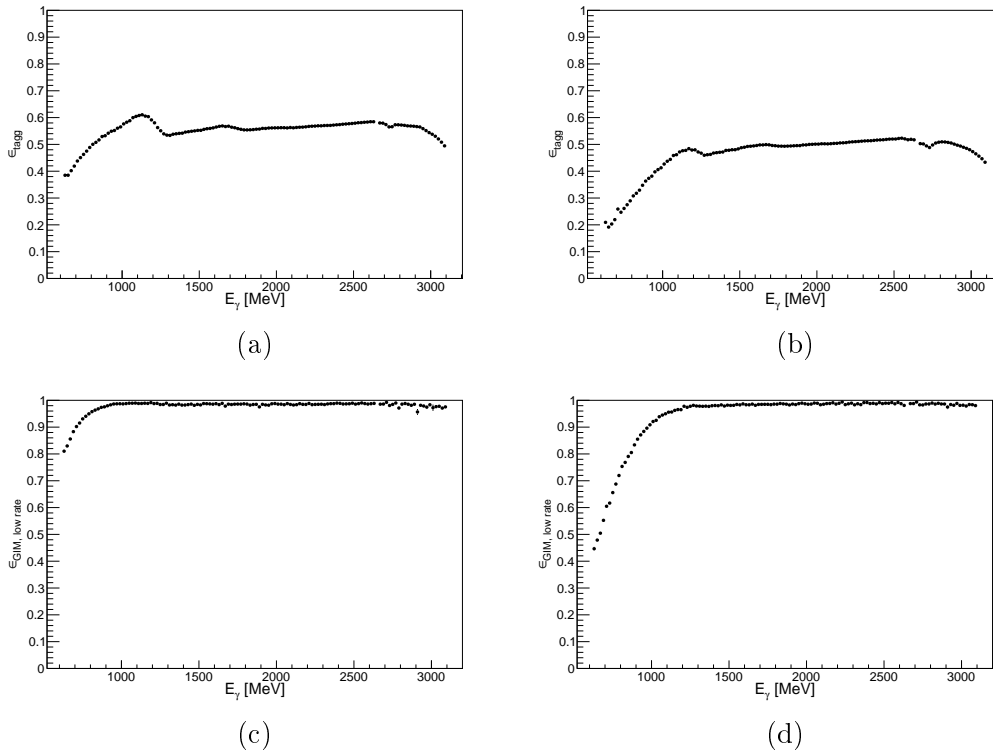


Figure 5.5: Tagging efficiency (a-b) and rate-independent GIM efficiency from low-rate runs (c-d) as a function of the photon energy E_γ in Oct2018 (left column) and Dec2021 (right column).

GIM efficiency asymptotically strives towards 1. The GIM efficiency as a function of the incident photon energy E_γ can be seen in Figure 5.5. The exact procedure for its determination can be found in [262]. This is the only step where the FluMo is used.

The tagging efficiency is strongly energy-dependent but may also fluctuate during a beam time, especially after the repolarisation breaks or after the changing of the target. Therefore, the tagging efficiency is calculated for every single run separately. The procedure is shortly described here.

First, the tagging efficiency is assumed to be approximately 1 for low-rate runs since the GIM efficiency is approximately 1 too. Of course, the spectra are corrected with the rate-independent GIM efficiencies.

Second, the tagging efficiency is calculated for every data-taking run resulting in a relative efficiency. To get absolute values, the relative efficiency is scaled to the absolute tagging efficiency from the low-rate runs with the help of the Simplex and Migrad algorithms from ROOT.

The calculation is performed by multiplying the scaled run-dependent tagging efficiency $\epsilon_{tagg}^{scaled}(t)$ by the energy mean of the low-rate runs $\bar{\epsilon}_{tagg}^{low\ rate}(E_\gamma)$ and dividing that by the global mean of the low-rate runs $\bar{\epsilon}_{tagg}^{low\ rate}$:

$$\epsilon_{tagg} = \epsilon_{tagg}(E_\gamma, t) = \frac{\bar{\epsilon}_{tagg}^{low\ rate}(E_\gamma)}{\bar{\epsilon}_{tagg}^{low\ rate}} \cdot \epsilon_{tagg}^{scaled}(t), \quad (5.10)$$

with

$$\bar{\epsilon}_{tagg}^{low\ rate}(E_\gamma) = \frac{1}{n_{E_\gamma}} \sum_{i=1}^{n_{E_\gamma}} \epsilon_{tagg, i}^{low\ rate}(E_\gamma), \quad (5.11)$$

$$\bar{\epsilon}_{tagg}^{low\ rate} = \frac{1}{n_{E_\gamma}} \sum_{i=1}^{n_{E_\gamma}} \epsilon_{tagg}^{low\ rate}(i). \quad (5.12)$$

See Figure 5.5 for the energy-dependent tagging efficiency. At low energies, the efficiency decreases due to detector threshold effects and the decrease of the rate-independent GIM efficiency. Furthermore, the tagging efficiency depends on the linear polarisation, which can be seen as an enhancement just before the coherent edge at 1200 MeV and to some extent also before the second coherent edge region at 1740 MeV. The missing point at 2650 MeV and the slightly different behaviour of the tagging efficiency afterwards are due to the tagging fibres that cover that region alone. Figure 5.4 shows the run-dependent tagging efficiency, which is equal to the time-dependent one. The values from the low-rate runs and the rightfully scaled values from the standard data runs are shown.

Due to the higher beam current, more electrons are detected in the Tagger with no corresponding photon, which results in a lower tagging efficiency, i.e. 0.65 compared to 0.73 for the global mean. Furthermore, the rate-independent GIM efficiency decreases stronger for low incoming photon energies in Dec2021 and the tagging efficiency is somewhat more stable over the time in Oct2018 compared to Dec2021. The latter results from the highly stable electron beam from ELSA in the first beam time, which fluctuated more in the second one.

Another approach to obtain the tagging efficiency would be the determination of the rate-dependent GIM efficiency with the help of the FluMo detector, which can be given by:

$$\epsilon_{GIM} = \epsilon_{FluMo} \cdot \frac{\dot{N}_{GIM}}{\dot{N}_{FluMo}}, \quad (5.13)$$

where ϵ_{FluMo} is the detection efficiency of the FluMo detector, which is rate-independent for low-rate runs ($\lesssim 300$ kHz), \dot{N}_{GIM} is the rate in GIM and \dot{N}_{FluMo} is the rate in FluMo. However, the rate-independent efficiency of the FluMo must be known and the calibration procedure needs to be performed for every beam electron energy separately.

5.3 Polarisation degrees

In a perfect experiment, one would reach polarisation degrees of 100 % for both: beam photons and target nucleons. However, this cannot be achieved in real experiments and the polarisation observables must be corrected correspondingly. The determination of the beam photon polarisation degree δ and the target nucleon polarisation degree Λ will be explained in the following.

5.3.1 Target nucleon polarisation

The polarisation degree of the target nucleons is measured with the NMR method [285,286] before and after each repolarisation when the target is moved out of the experimental position inside the CB. During the experiment, the target goes in frozen spin mode with very stable temperature and magnetic field conditions (Section 2.3). This is important because no NMR measurements can be performed during the data taking. Therefore, the target polarisation degree is interpolated between the two measurements with an exponential decay function to get a run-dependent target polarisation.

The interpolation function is given by:

$$\Lambda_{NMR}(t) = \Lambda_{NMR}(0) \cdot \exp\left(-\frac{t}{\tau}\right), \quad (5.14)$$

where $\Lambda_{NMR}(t)$ and $\Lambda_{NMR}(0)$ are the target polarisation degrees after time t and time $t = 0$, i.e. when the NMR measurement is done, and τ is the relaxation time. In Oct2018, target polarisation degrees of up to 75.3 % with relaxation times around 1100 h were reached. In Dec2021, the maximum was around 69.4 % with relaxation times around 800 h. The Λ_{NMR} values are provided by Runkel. Furthermore, the run-dependent target polarisation degrees for the Oct2018 beam time are calculated by Hartmann.

The measurement is calibrated at the beginning of the beam time at the thermal equilibrium ($B = 2.5$ T, $T \approx 1$ K) where the proton polarisation is given by:

$$\Lambda_{TE} = \tanh\left(\frac{\mu_p B}{k_B T}\right). \quad (5.15)$$

Here, $\mu_p = 1.4106 \cdot 10^{-26}$ J T⁻¹ [97] is the magnetic moment of the proton and

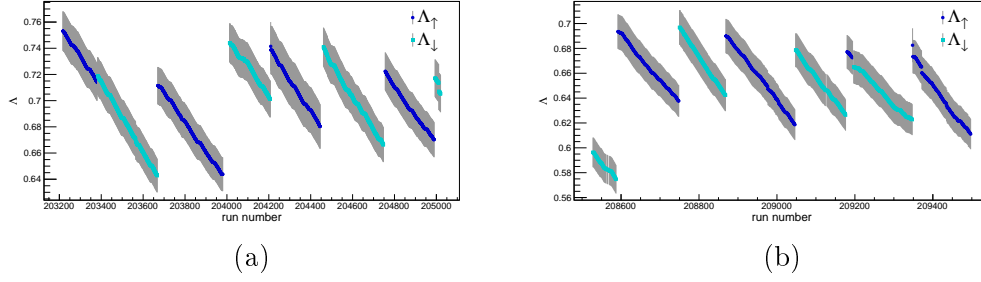


Figure 5.6: Target polarisation degrees Λ_{NMR} for both orientations with their 2.0% to 2.5% systematic uncertainties (see text) in Oct2018 (a) and Dec2021 (b). Note the different scaling.

$k_B = 1.3806 \cdot 10^{-23} \text{ JK}^{-1}$ [44] is the Boltzmann constant.

The main uncertainty from the calibration comes from the temperature measurement with a carbon resistor that is about 1% [323]. Additional uncertainty arises from the NMR measurement itself, resulting in an estimated systematic uncertainty of 2% [262]. For the runs between 02.11.2018 and 06.11.2018 (run numbers 204209 to 204445) in Oct2018, an additional uncertainty of 0.5% must be included because there was no NMR measurement at the end of the block.

Figure 5.6 shows the target polarisation values with the systematic uncertainty for both beam times. Different marker styles and colours indicate the two polarisation directions.

The measured target polarisation Λ_{NMR} is not yet equal to the nucleon polarisation such that the values must be corrected by $\gamma = 0.92616$ [281]:

$$\Lambda_N = \Lambda_{NMR} \cdot \gamma. \quad (5.16)$$

The origin of this lies in the D wave contribution in the wave function responsible for a quadrupole moment in the deuteron, which influences the polarisation measurements done with the NMR technique.

5.3.2 Beam photon polarisation

The calculation of linear beam photon polarisation degrees is more complex than that for the target nucleons. Linear polarisation is realised by coherent scattering on a diamond crystal. A detailed description can be found in [249].

Here, the method is summarised. The entire technique was developed by Livingston and can be found in [251].

In the first step, the relative intensity spectrum I_{rel} as a function of the incident photon energy E_γ of scattering on the diamond crystal with respect to an amorphous copper radiator is calculated (Figure 5.7a). To check the time stability, copper runs are performed every day.

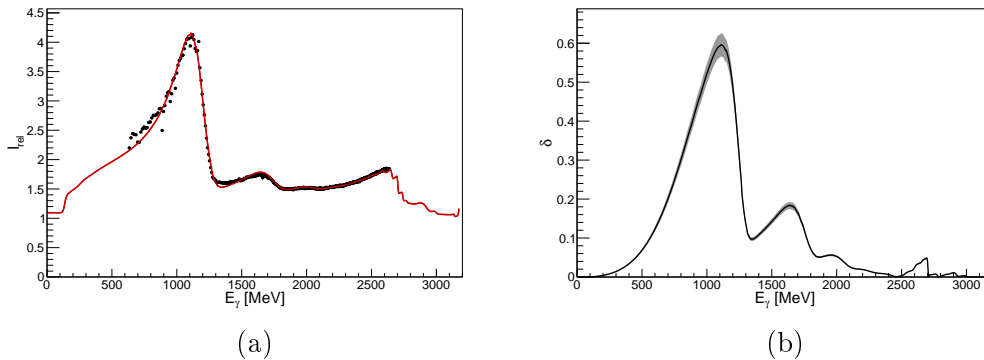


Figure 5.7: (a) Relative intensity spectrum (black points) with the ANB fit (red line). (b) Linear polarisation degree δ with the systematic uncertainty of 5% to 10%. Both figures show the negative crystal orientation of the 1st run block in Oct2018.

In the second step, the relative intensity spectra are fit with the **Analytic Bremsstrahlung's Calculation** (ANB) programme [324]. This programme analytically calculates the photon polarisation degree of the intensity spectra respecting interference terms from different grid vectors. The original programme [324] was further developed in the CBELSA/TAPS collaboration [249,325]. A detailed description can be found in [249].

The relative systematic uncertainty is estimated to be 5% from 960 MeV to 1310 MeV, 8% from 690 MeV to 960 MeV and from 1310 MeV to 1360 MeV and 10% from 650 MeV to 690 MeV. The estimation is based on the maximum difference between the data points and the ANB fit.

The calculated polarisation degrees can be seen in Figure 5.7. The good range for extracting beam polarisation-dependent observables (Σ , P , H) is defined as the range where the beam polarisation degree is larger than 10% excluding the second coherent edge, i.e. from 650 MeV to 1360 MeV.

The linear polarisation degrees are calculated by Afzal and Thiel. The Oct2018 beam time is split into four run sets and the two crystal orientations

($\pm 45^\circ$), for which relative intensities and polarisation degrees are calculated separately. This is due to slightly different coherent edge positions. The four run sets are defined by the run numbers, i.e. 203219–203943, 203933–204582, 204573–204804 and 204813–205955.

In the Dec2021 beam time, the coherent edge was not very stable. It drifted away up to 100 MeV, which had to be adjusted manually during the beam time. Therefore, determining the beam polarisation degrees is more sophisticated and only preliminary values are available when this work is written. A final determination of the beam asymmetry Σ_{but} , recoil asymmetry P and the beam-target double polarisation observable H is therefore not possible at this time.

Figure 5.7 shows an intensity spectrum with the ANB fit and the extracted beam photon polarisation degree with its systematic uncertainties in Oct2018. More spectra can be found in Appendix B.2. The preliminarily determined beam polarisation degrees based on the first few *good* runs, without walking coherent edge, can be found in Appendix B.2 as well.

dilution factor would be given by:

$$d_{mol} = \frac{10}{42} \approx 0.2381, \quad (5.18)$$

assuming that protons and neutrons are identified correctly.

However, this approximation cannot be used because of the event selection process. The applied kinematic cut positions (Section 4.5) dismiss events off polarised deuterium and unpolarised carbon and oxygen differently. The Fermi momentum distributions of both nuclei overlap but are still quite different (Figure 3.1). The average Fermi momentum of deuterium is around 70 MeV, that of carbon at twice that value with a different shape. Because the Fermi momentum is, on average, larger in carbon (and oxygen) than in deuterium (at least up to 260 MeV), the kinematic spectra get more diffuse. Thus, the applied coplanarity, missing mass and Fermi momentum cut positions dismiss more events off carbon (and oxygen) than off deuterium, which increases the dilution factor.

Additionally, there are final state interactions that cannot be described well enough, which further can differ for various reactions and nuclei.

The ratio between wanted and background reactions off carbon (and oxygen) are energy and angular sensitive. Therefore, an additional measurement with a carbon target of similar target surface density (Section 5.1) is conducted. In this way, the contribution from the carbon can be subtracted from the total signal afterwards. Oxygen atoms are therefore treated as carbon atoms due to simplifications and the similar Fermi momentum [272].

Calculated are the dilution factors with the photon flux normalised event yields $\hat{N} = N/N_\gamma$ that can replace the DCS $d\sigma/d\Omega$. For better readability, the DCS is replaced by the CS here:

$$d = \frac{\sigma_{dB} - \sigma_C}{\sigma_{dB}} = \frac{\hat{N}_{dB} - c_t \cdot \hat{N}_C}{\hat{N}_{dB}}, \quad (5.19)$$

where c_t is the ratio between dButanol and carbon target surface density, i.e. reaction partners, and all quantities except c_t are energy- and angular-dependent. The carbon data is taken directly after (Oct2018) or before (Dec2021) the dButanol beam times with the same experimental setup to reduce systematic uncertainties.

For simplicity, the data and MC simulation of ηp with $\eta \rightarrow 2\gamma$ from Oct2018 are shown as figure examples in the following. See Appendix B.3 for more figures.

5.4.1 Carbon scaling factor

The carbon scaling factor c_t is the ratio between the number of carbon (and oxygen) atoms inside the dButanol target and the ones in the carbon target.

An experimentally determined value of c_t is assumed to be more accurate than the theoretically calculated one from Section 5.1 because of the large systematic uncertainty and additional inhomogeneities in the dButanol target. Especially the filling factor is extremely experimental-dependent and has a significant uncertainty.

Due to the limited number of events that would result in substantial statistical uncertainties, the scaling factor c_t is determined globally and not energy- and angular-dependent. Possible fluctuations and dependencies are included in the systematic uncertainty.

The carbon scaling factor is calculated by:

$$c_t = \frac{\hat{N}_{dB}^{AC}}{\hat{N}_C^{AC}}, \quad (5.20)$$

where anticuts (AC) are applied to the normalised event yields. For these anticuts, the exact opposite in cut positions are determined compared to the background suppression cut positions in Section 4.4 to reject as many events on quasifree nucleons inside deuterium and keep as many events on bound nucleons inside carbon (and oxygen).

Therefore, a coplanarity anticut of $\Delta\phi = 180 \pm 2.5\sigma$, missing mass anticut of $\Delta m = m_N \pm 2.5\sigma$, as well as a Fermi momentum cut of $160 \text{ MeV} < p_F < 260 \text{ MeV}$ and the standard 2.5σ wide invariant mass cut are applied to extract the anticut event yields from Equation 5.20. The Fermi momentum cut is chosen to suppress as many deuterium reactions as possible. The ratio of the Fermi momentum of deuterium and carbon nuclei (Figure 3.1) is with 0.22–0.28 at its minimum in that region and dismisses over 70% of reactions off deuterium. The ordinary invariant mass cut ensures that no background reactions dominate in the event yields.

With the applied anticuts, the carbon scaling factor is found to be

$$c_t^{exp} = 0.89 \pm 0.01, \quad (5.21)$$

for the Oct2018. The error is statistical only. The systematical uncertainty of c_t is estimated to be 12% and is explained in more detail in the following sections. It can be seen that it is well within the theoretical value of 0.94 ± 0.09 from Section 5.1.

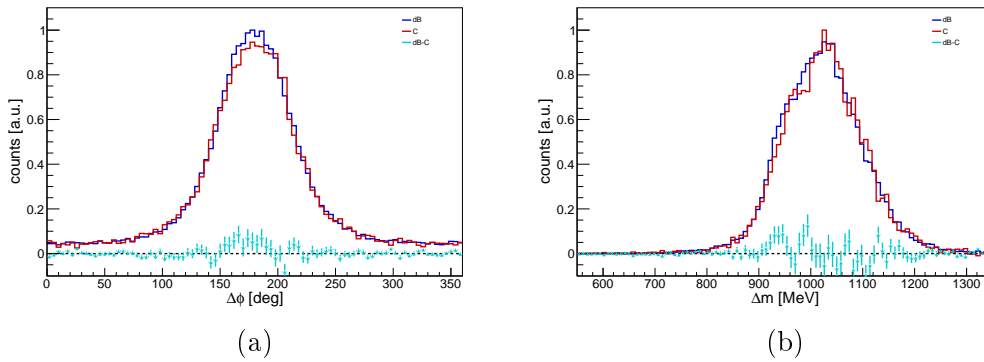


Figure 5.9: Coplanarity (a) and missing mass (b) of dButanol (blue) and carbon (red) data with applied anticuts (see text) in ηp with $\eta \rightarrow 2\gamma$ in Oct2018. The difference between them, i.e. remaining deuterium (cyan), is also shown. The scaling factor of $c_t = 0.89$ is applied for the carbon data.

The relative systematic uncertainty of the dilution factor $\Delta d^{rel} = \Delta d/d$ is given by the uncertainty of c_t that includes all differences between the target materials as well as possible E_γ and $\cos(\theta)$ dependence [262]:

$$\Delta d = \frac{\hat{N}_C}{\hat{N}_{dB}} \cdot \Delta c_t = (1 - d) \cdot \frac{\Delta c_t}{c_t}. \quad (5.22)$$

For large dilution factors, the systematic uncertainties in the target densities of the two materials are small. The statistical uncertainty, however, increases by increasing the dilution factor due to more stringent cut positions that throw more events away.

As discussed earlier, c_t may be energy- and angular-dependent. However, no larger dependency has been found such that the values of energy- and angular-dependent carbon scaling factors are all well within the systematic uncertainty of 12%. Figure 5.10 shows the energy- and angle-dependent factors in ηp with

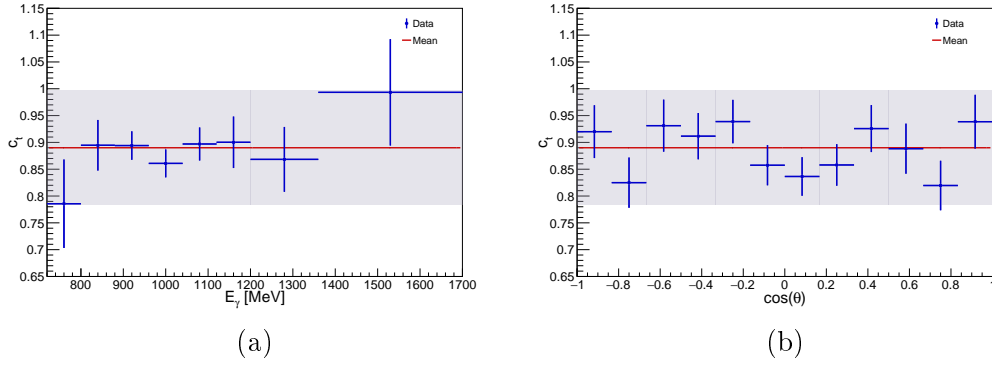


Figure 5.10: Carbon scaling factor c_t as a function of the incident photon energy E_γ (a) and $\cos(\theta)$ (b) in ηp with $\eta \rightarrow 2\gamma$ in Oct2018. The mean red line is shown at $c_t = 0.89$ and a 12% relative systematic uncertainty is shown as grey box.

$\eta \rightarrow 2\gamma$.

The scaling factor c_t should be a global variable for a beam time and, therefore, independent of the reaction. While the reaction ηn with $\eta \rightarrow 2\gamma$ results in the same value, the reactions with π^0 in the final state give a value of 0.95 ± 0.01 . As shown in Figure 5.11, the coplanarity and missing mass show an excess of carbon events, i.e. the deuterium reactions result in negative values. Since this makes no physical sense, it is assumed that the anticuts do not work as well as for the reactions with η . It is chosen to use the value of $c_t = 0.89 \pm 0.01$ as well. These spectra can also be seen in Figure 5.11. Furthermore, the remaining deuterium in the dButanol data leads to a too-high value for c_t such that the smaller value is more reasonable. It was also shown that final state interactions (FSI) play an important role in quasifree π^0 photoproduction [326], whereas they are negligible in quasifree η photoproduction [130, 269]. This might result in additional background not coming from the investigated reaction. The coplanarity and missing mass for $\pi^0 n$ and ηn with $\eta \rightarrow 2\gamma$ can be found in Appendix B.3.

As it can be seen in Figure 5.12, the extracted carbon scaling factor in the π^0 reactions is not only in agreement with the global value of $c_t = 0.89$ from the η reactions within the systematic uncertainty but also in agreement with the energy- and angle-dependent c_t values.

The investigation is also done for the Dec2021 beam time, resulting in a slightly smaller value. The coplanarity and missing mass spectra with the

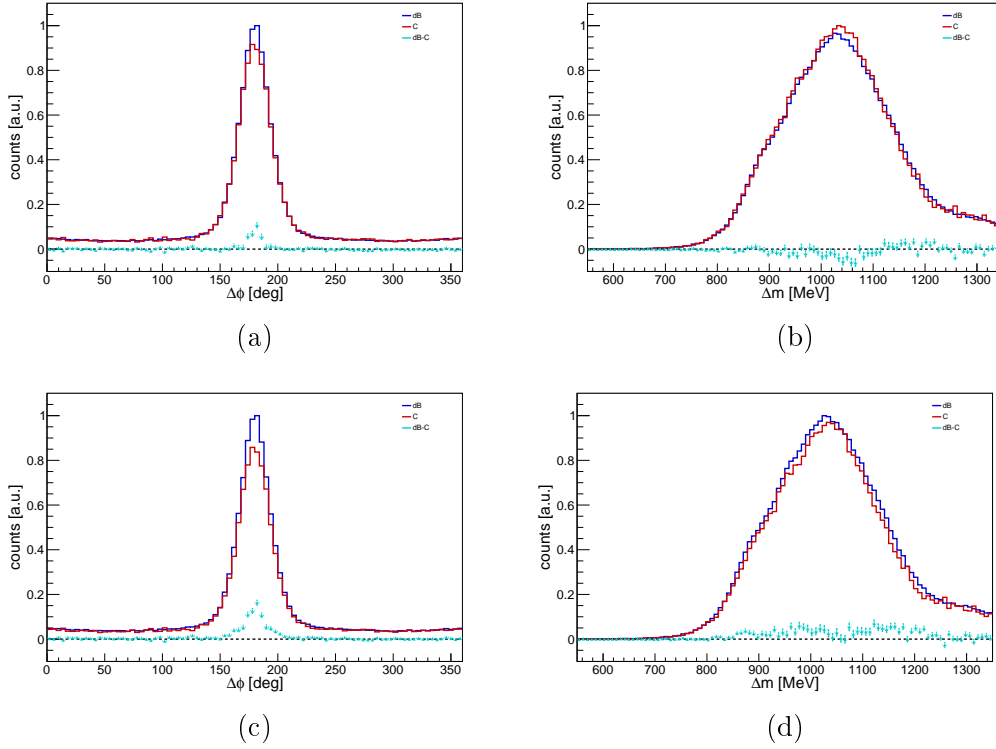


Figure 5.11: Coplanarity (left column) and missing mass (right column) of dBUTANOL (blue) and carbon (red) data with applied anticuts (see text) in $\pi^0 p$ in Oct2018. The difference between them, i.e. remaining deuterium (cyan), is also shown. Figures (a-b) are scaled with a factor of $c_t = 0.95$ and (c-d) are scaled with one of $c_t = 0.89$.

applied anticuts for the reaction ηp with $\eta \rightarrow 2\gamma$ in Dec2021 can be found in Appendix B.3.

In the end, the scaling factor is given by:

$$\begin{aligned}
 c_t &= c_t^{exp} = 0.89 \pm 0.01_{\text{stat}} \pm 0.11_{\text{syst}} && \text{for Oct2018} \\
 c_t &= c_t^{exp} = 0.85 \pm 0.01_{\text{stat}} \pm 0.11_{\text{syst}} && \text{for Dec2021.} \quad (5.23)
 \end{aligned}$$

5.4.2 Monte Carlo simulation

A raw cross-check of the estimated systematic uncertainty of the dilution factor constant is performed with a MC simulation. The dBUTANOL target material is a rather complicated molecule for simulations. It is therefore approximated by simulations of deuterium and carbon nuclei separately, considering

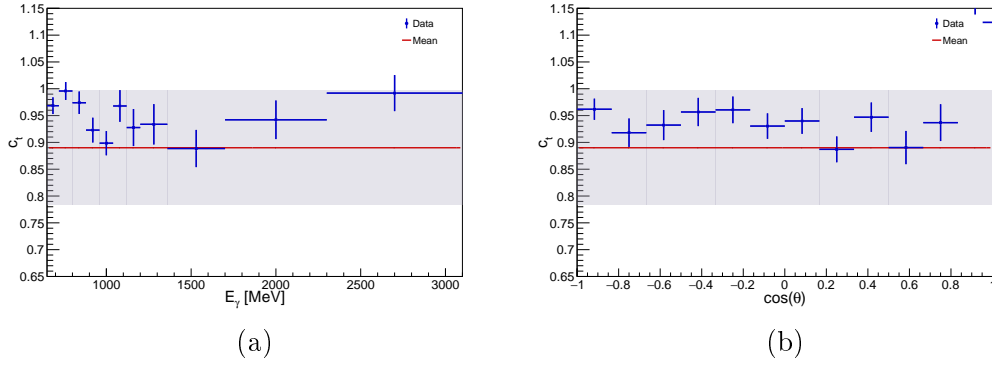


Figure 5.12: Carbon scaling factor c_t as a function of E_γ (a) and $\cos(\theta)$ (b) from the $\gamma p \rightarrow \pi^0 p$ reaction in the Oct2018 beam time. The mean red line is shown at $c_t = 0.89$ and a 12% relative systematic uncertainty is shown as grey box.

their different Fermi momenta distribution. Oxygen nuclei are treated as carbon ones since the Fermi momentum distribution is nearly identical for heavy nuclei, e.g. ^{12}C and ^{40}Ca [272]. The same number of events are generated, where a factor of 3.2 scales the carbon data due to the molecular structure of dButanol. The event yields can therefore be approximated by:

$$N_{dB} = N_D + 3.2 \cdot N_C. \quad (5.24)$$

The PDF of the Fermi momentum distribution of dButanol with the weighting from Equation 5.24 can be seen in Figure 5.13.

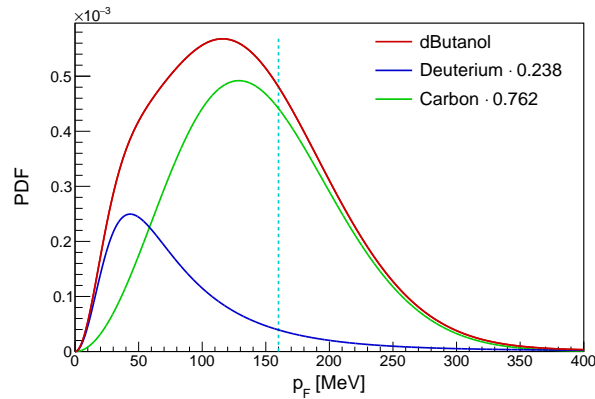


Figure 5.13: Probability density function (PDF) of the Fermi momentum distribution of deuterated butanol (dButanol) with their contribution of deuterium and carbon (Equation 5.24). Models taken from [299,300].

For the determination of c_t , anticuts are applied to remove as many reactions on deuterium as possible (Equation 5.20). However, there will be some remaining dilution of reactions on deuterium that cannot be cut away entirely due to the strongly overlapping Fermi momenta with carbon.

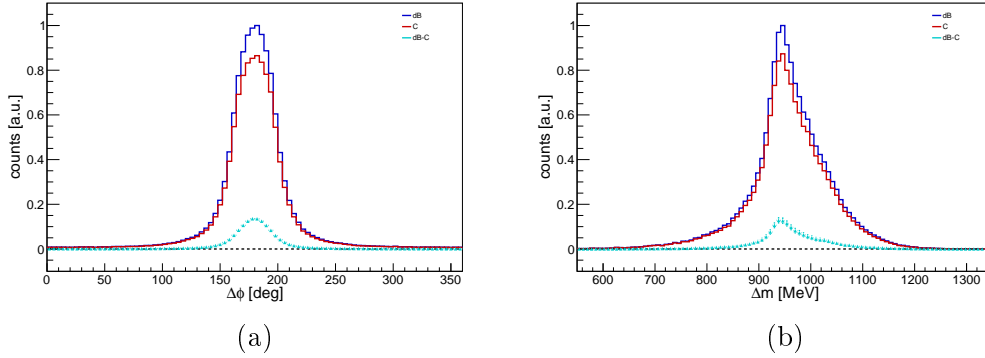


Figure 5.14: Coplanarity (a) and missing mass (b) of dBUTANOL (blue) and carbon (red) MC simulation data with applied anticuts in ηp with $\eta \rightarrow 2\gamma$. The difference between them, i.e. remaining deuterium (cyan), is also shown.

Figure 5.14 shows the MC simulation in ηp with $\eta \rightarrow 2\gamma$ of the constructed dBUTANOL simulation and the carbon simulation. It can be seen that outside the 2.5σ anticuts of the coplanarity (≈ 20 MeV) and missing mass spectra (≈ 100 MeV), the difference between both simulations is small and well within the estimated systematic uncertainty. Furthermore, the MC simulation shows that less than 12% deuterium remains in the dBUTANOL data. This confirms a proper treatment of the systematic uncertainty at this point.

5.4.3 Dependence on the Fermi momentum cut position

As expected, the dilution factor and the total number of events are found to be firmly Fermi momentum cut position dependent. Decreasing the cut-off value increases the dilution factor and decreases the number of remaining events.

Figure 5.15 shows the dilution factor and the total number of events as a function of the Fermi momentum cut position. The confidence level gives the percentage of remaining deuterium with this cut position based on the model (Equation 3.1). The values increase from 50% to 100% in 5% steps with additional values at 87.5% (finally used value) and 99%. The values are

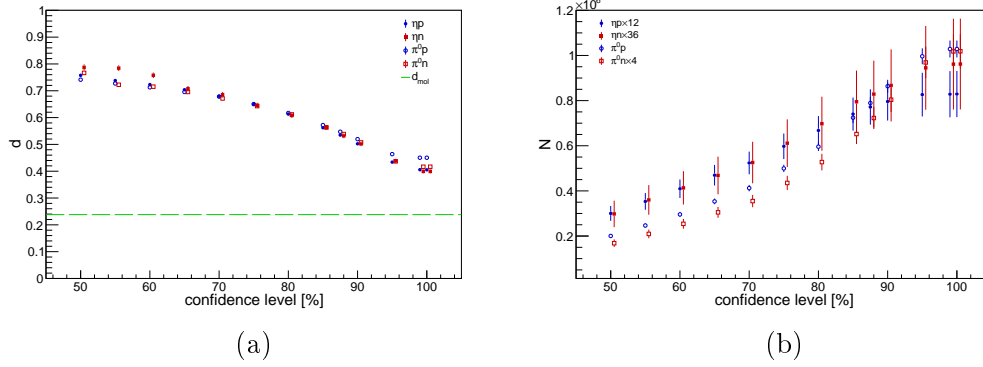


Figure 5.15: Average dilution factor d (a) and number of total events (b) as a function of the remaining deuterium with different Fermi momentum cut positions, i.e. confidence level. A value of 90 % corresponds to a Fermi momentum cut position of $p_F = 178$ MeV, meaning 10 % of the deuterium data are dismissed. The dashed green line in (a) correspond to the value $d_{mol} = 10/42$, which indicates the molecular/chemical dilution factor directly given by the structure of the deuterated butanol. Note the scaling for the different data sets in (b).

70 MeV, 77 MeV, 84 MeV, 92 MeV, 100 MeV, 112 MeV, 126 MeV, 147 MeV, 160 MeV, 178 MeV, 247 MeV, 533 MeV and no Fermi momentum cut.

With high Fermi momentum cut positions, not only does the carbon part increases, but also possible background contributions increase, e.g. final state interactions (FSI) in $\pi^0 N$.

The final cut position at $p_F < 160$ MeV is the compromise of dismissing carbon and other background, reducing the systematic uncertainty for the dilution factor and decreasing the statistical uncertainty of the dilution factor and the event yields.

5.4.4 Experimentally determined dilution factor

The dilution factor d is determined as a function of E_γ and $\cos(\theta)$ for every reaction separately and can be seen in Figure 5.16. A value of $c_t = 0.89 \pm 1_{\text{stat}} \pm 11_{\text{syst}}$ (Oct2018) and $c_t = 0.85 \pm 1_{\text{stat}} \pm 11_{\text{syst}}$ (Dec2021) is used as a scaling factor for the carbon data, as discussed in Section 5.4.1. As expected, the values for the reactions on the proton and neutron are very similar, as well as the values between Oct2018 and Dec2021.

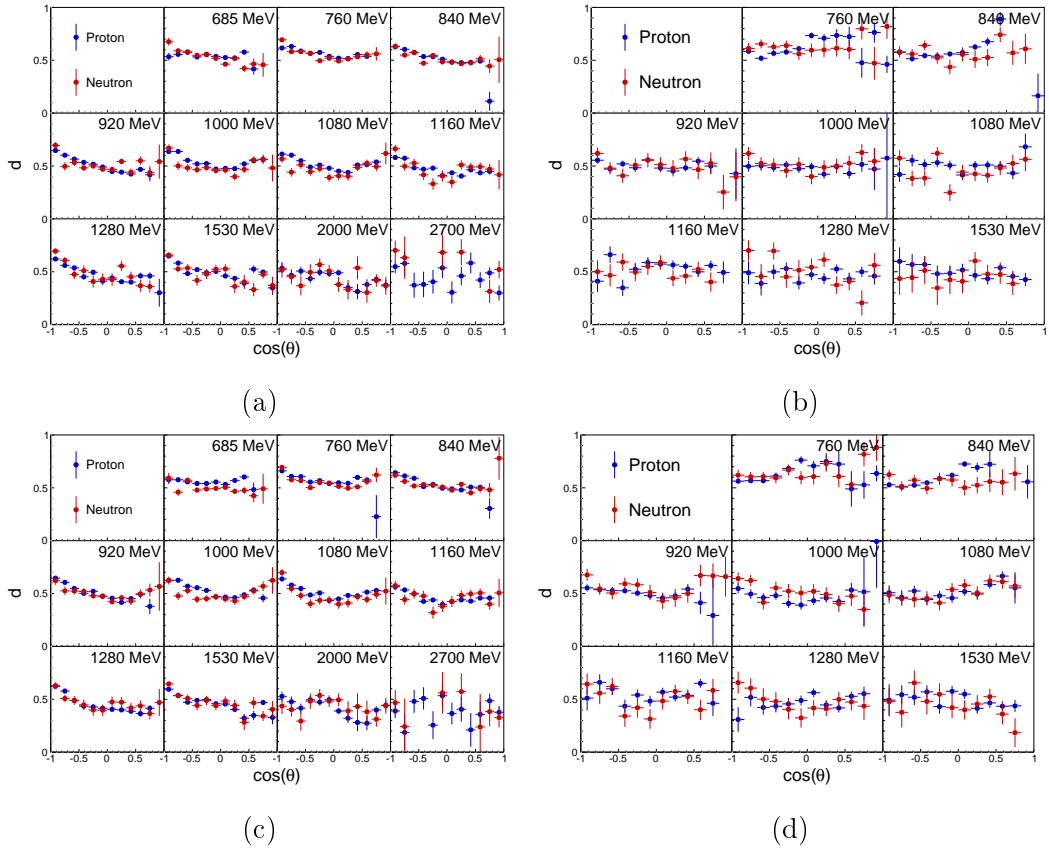


Figure 5.16: Dilution factor d in $\pi^0 N$ (a) and ηN (b) as a function of E_γ and $\cos(\theta)$ in Oct2018 (top row) and in Dec2021 (bottom row).

5.5 Background correction

All types of possible background reactions affect the observable values. Generally, the measured observable value O_{raw} must be corrected by an unknown background one O_{BG} with respect to the background ratio parameter δ_{BG} :

$$O_{raw} = (1 - \delta_{BG}) \cdot O + \delta_{BG} \cdot O_{BG}. \quad (5.25)$$

The background observable cannot be determined due to the low statistics.

However, the contribution δ_{BG} is rather small and it was shown [262, 288] that the systematic uncertainty coming from this is in the order of the background contamination or even smaller. Therefore, the energy- and angle-dependent background contribution (Figure 4.30) is taken for δ_{BG} . A corrected *real* observable value and its systematic uncertainty can be calculated by [288]:

$$O = \frac{O_{raw}}{1 - \delta_{BG}} \quad \Delta O_{syst, \delta_{BG}}^{abs} = \frac{1}{\sqrt{3}} \frac{\delta_{BG}}{1 - \delta_{BG}}. \quad (5.26)$$

The systematic uncertainty depends only on the background contribution and not on any observables anymore. The systematic uncertainty is a maximum estimation.

If the background is smaller than 0.5%, no correction is applied, but an additional systematic uncertainty of 0.5% is included, i.e. $\Delta O_{syst, \delta_{BG}}^{abs} = 0.0029$.

5.6 Reconstruction of the centre of mass energy from the final state

The centre of mass (CM) energy W can be calculated either from the initial or the final state. The first is the straightforward method and is usually used for photoproduction experiments with a free proton target. Like the dButanol target, they are cooled down such that the target nuclei have no momentum and the four-momentum is given by their masses.

Equation 1.23 shows W calculated from the initial γN state by assuming a target nucleon N at rest. This can be used as an estimation but is not generally suited for determining W . If results are given as a function of the incident photon energy E_γ , they are smeared out by the Fermi momentum distribution.

In this experiment, the polarised target nucleons are bound inside deuterium nuclei. The deuterium nuclei are at rest, whereas the quasifree nucleons inside deuterium experience Fermi motion (Section 3.1.3 and 4.5.5) that is not known in the beginning. However, it is possible to calculate the kinetic energy of the recoil nucleon [270,327] and, thus, the Fermi momentum of the nucleons in the initial state.

5.6.1 Kinematic reconstruction

The *true* CM energy W is given by the mass of the final state:

$$W = \sqrt{s} = m(mN), \quad (5.27)$$

where no Fermi momentum effects are present anymore. The calculation follows the participant-spectator model [328], saying that the participant target nucleon reacts with the incoming photon, whereas the second nucleon in deuterium acts as a spectator and is thus not involved in the reaction at all. The deuterium D is at rest with mass m_D , the participant nucleon P has energy E_P and Fermi momentum \vec{p}_F and the spectator nucleon S has energy E_S and

Fermi momentum $-\vec{p}_F$. Energy-momentum conservation leads to the relation:

$$p_D = p_P + p_S = \begin{pmatrix} m_D \\ 0 \end{pmatrix} = \begin{pmatrix} E_P \\ \vec{p}_F \end{pmatrix} + \begin{pmatrix} E_S \\ -\vec{p}_F \end{pmatrix}. \quad (5.28)$$

The energies are given by:

$$E_S = \sqrt{m_S^2 + \vec{p}_F^2} \quad E_P = m_D - E_S. \quad (5.29)$$

This model neglects the binding energy of deuterium $B_D = 2.2246 \text{ MeV}$ [329]. However, this value is relatively small compared with the photon energies and can be ignored.

The reaction can be described by:

$$\gamma D \rightarrow mnp, \quad (5.30)$$

where γ is the incident photon, D the deuterium, m the produced meson, n the neutron and p the proton. Depending on the investigated reaction, either n or p is the participant (recoil) nucleon and the other one is the spectator. Energy-momentum conservation of the reaction 5.30 leads to the relation:

$$\begin{pmatrix} E_\gamma \\ \vec{p}_\gamma \end{pmatrix} + \begin{pmatrix} m_D \\ 0 \end{pmatrix} = \begin{pmatrix} E_m \\ \vec{p}_m \end{pmatrix} + \begin{pmatrix} E_P \\ \vec{p}_P \end{pmatrix} + \begin{pmatrix} E_S \\ \vec{p}_S \end{pmatrix}, \quad (5.31)$$

where $\vec{p}_\gamma = (0, 0, E_\gamma)$ is the momentum of the incoming photon, $\vec{p}_{P,S}$ are the momenta of the (recoil) participant and spectator nucleon, respectively, and $E_{P,S}$ are their energies, defined in 5.29. The four-momentum of the participant can further be expressed in terms of its kinetic energy T_P :

$$E_P = T_P + m_P \quad \vec{p}_P = \vec{p}_F = \sqrt{T_P(T_P + 2m_P)} \cdot \begin{pmatrix} \sin(\theta_P) \cos(\phi_P) \\ \sin(\theta_P) \sin(\phi_P) \\ \cos(\theta_P) \end{pmatrix}, \quad (5.32)$$

where θ_P and ϕ_P are the polar and azimuthal angles of the participant (recoil) nucleon.

The measured quantities in this experiment are:

5.6. Reconstruction of the centre of mass energy from the final state

- initial state: $E_\gamma, \vec{p}_\gamma = (0, 0, E_\gamma)$,
- final state: $\theta_P, \phi_P, E_m, \theta_m, \phi_m$,

where the energy and angles of the meson are directly reconstructed from its detected decay products, the photons, i.e. $p_m = \sum_i p_{\gamma_i}$. After a clean event selection, the masses of the particles are known as well:

- initial state: m_D ,
- final state: m_P, m_S, m_m ,

where the mass of the meson m_m is calculated using Equation 3.18 and Equation 4.8. If, in addition, the kinetic energy of the participant recoil nucleon is known, its energy and momentum are known as well (Equation 5.32).

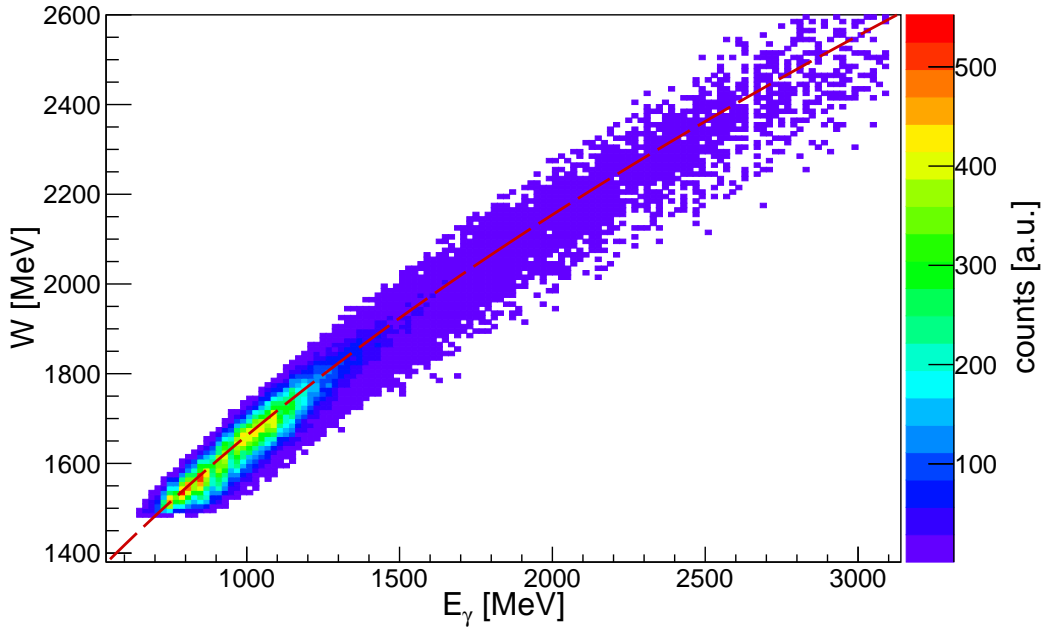


Figure 5.17: Final state reconstructed centre of mass energy $W = m(mN)$ as a function of the incident photon energy E_γ in ηn with $\eta \rightarrow 2\gamma$ in Oct2018. The Fermi momentum smearing is visible around the dashed red line, which shows the function 1.23, i.e. assuming the target nucleon is at rest with no Fermi motion.

Although the energy of the recoil nucleon is measured, that value has a large systematic uncertainty and it is not guaranteed that the nucleon deposits all

its kinetic energy in the detector. Therefore, it is favourable that the recoil nucleon's kinetic energy is determined differently.

Equation 5.31 must fulfil energy-momentum conservation and determines the kinetic energy of the participant recoil nucleon [327]:

$$T_P = \frac{-(bc - 2a^2m_P) + \sqrt{(bc - 2a^2m_P)^2 - c^2(b^2 - a^2)}}{2(b^2 - a^2)}, \quad (5.33)$$

with

$$\begin{aligned} a &= p_m^x \sin(\theta_P) \cos(\phi_P) + p_m^y \sin(\theta_P) \sin(\phi_P) + (p_m^z - E_\gamma) \cos(\theta_P) \\ b &= E_m - E_\gamma - m_D \\ c &= (E_m + m_P - E_\gamma - m_D)^2 - (m_S^2 + p_m^2 + E_\gamma^2 - 2E_\gamma p_m^z). \end{aligned} \quad (5.34)$$

As a result, the CM energy W is known from the mass of the final state. It is also possible to reconstruct W with the time-of-flight (TOF) method [270]. However, this is not used in this experiment.

5.6.2 Flux reconstruction

The determination of the photon flux as a function of the incoming photon beam energy E_γ has already been explained in Section 5.2. The photon flux as a function of W needs some additional modification due to the Fermi momentum of the target nucleons. Therefore, Equation 1.23 cannot be used to convert the flux values.

A specific photon energy corresponds to a broader distribution of W values and not one specifically. The integral of the distribution gives the number of photons for a specific energy.

Using the participant-spectator model again with Equation 5.29 and the photon beam in z -direction together with Equation 1.22 the CM energy can be extracted by:

$$W = \sqrt{m_D^2 + m_S^2 + 2E_\gamma(m_D - E_S) - 2m_DE_S - 2E_\gamma p_F^z}, \quad (5.35)$$

where E_S is given in Equation 5.29. For each E_γ bin $n = 10^6$ events are sampled with random isotropic Fermi momentum components satisfying the Fermi

5.6. Reconstruction of the centre of mass energy from the final state

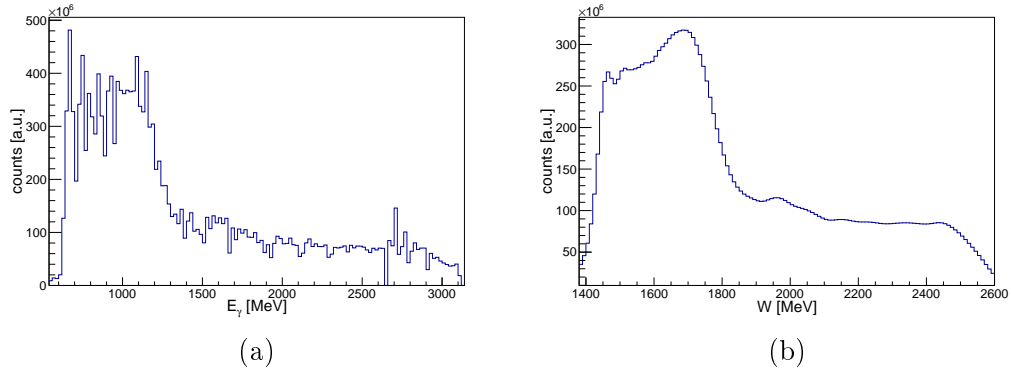


Figure 5.18: Photon flux as a function of the incoming photon energy E_γ (a) and the reconstructed centre of mass energy W in Oct2018.

momentum distribution of deuterium (Equation 3.1). Afterwards, the values are weighted by N_γ/n to ensure proper normalisation. This whole procedure also holds for nucleons in carbon (and oxygen). Only the Fermi momentum distribution function is different, as shown in Section 3.1.3. More details and the algorithm can be found in [270].

5.7 Data merging methods

5.7.1 Arithmetic Average

The arithmetic average, also called arithmetic mean or simple mean, for uncorrelated variables x and its error are given by:

$$x = \frac{1}{n} \sum_{i=1}^n x_i \quad \sigma_x = \frac{1}{\sqrt{n}} \sqrt{\sum_{i=1}^n \sigma_{x_i}^2}. \quad (5.36)$$

If the errors σ_{x_i} are all the same, i.e. σ_0 , Equation 5.36 simplifies to $\sigma_x = \sigma_0/\sqrt{n}$. When a mean is calculated and nothing particular is mentioned, the arithmetic average is taken.

5.7.2 Inverse-variance weighted average

Taking the variance or error, respectively, of a value into account for calculating an average, the inverse-variance weighted average is the best way to go. This minimises the variance and, therefore, the error. Again, it is assumed that the variables are uncorrelated and the distribution is similar to a Gaussian one. Calculating the average x of two values x_1 and x_2 with respect to their variances σ_{x_1} and σ_{x_2} it results in the formula:

$$x = \left(\frac{x_1}{\sigma_{x_1}^2} + \frac{x_2}{\sigma_{x_2}^2} \right) \left(\frac{1}{\sigma_{x_1}^2} + \frac{1}{\sigma_{x_2}^2} \right)^{-1} \quad \sigma_x = \left(\frac{1}{\sigma_{x_1}^2} + \frac{1}{\sigma_{x_2}^2} \right)^{-1/2}. \quad (5.37)$$

This can be generalised to n points:

$$x = \left(\sum_{i=1}^n \frac{x_i}{\sigma_{x_i}^2} \right) \left(\sum_{i=1}^n \frac{1}{\sigma_{x_i}^2} \right)^{-1} \quad \sigma_x = \left(\sum_{i=1}^n \frac{1}{\sigma_{x_i}^2} \right)^{-1/2}. \quad (5.38)$$

If all values have the same error, the inverse-variance weighted average and error are equal to the simple average and its error.

Within this work, an inverse-variance weighted average is used in multiple situations, e.g. merging the two decay channels from the η decay or merging the data from multiple beam times.

5.7.3 Linear weighted average

Another possibility for calculating a weighted average uses a linear weight factor w instead of an inverse-variance weight factor. The equation for the average x and its error σ is given by:

$$x = \left(\sum_{i=1}^n w_i x_i \right) \left(\sum_{i=1}^n w_i \right)^{-1} \quad \sigma = \sqrt{\sum_{i=1}^n w_i^2} \cdot \sigma_0. \quad (5.39)$$

Again, the variables must be independent. They also must all have the same variance σ_0^2 . Equation 5.39 can be generalised by interpreting w as a placeholder for any weight.

5.7.4 Average of overlapping bins

Data with different bin widths can be compared in several ways. Generally, the binning in E_γ and $\cos(\theta)$ is very different in different experiments.

On the one hand, the original data values of the nearest bin can be taken or the one with the largest bin overlaps. Alternatively, the data values can be adjusted by weighting the values, e.g. by the distance $l_{1,2}$ between the neighbouring bin centres and the new one with Equation 5.39 and $w_i = l_i$.

Another possible method of rebinning data was developed by Tom Jude [330] and is described in the following.

The method uses the overlap between the reference bins and the new ones. Instead of the usual rebinning, where only multiples of the original bin widths can be taken, every value can be chosen for the bin width.

The newly calculated bin value x is very similar to the general weighted average of Equation 5.39 with the overlapping fraction as weight $w_i = \delta_i = l_i/L_i$. Here, l_i is the overlap between the old bin i and the new bin and L_i is the bin width of the old one. The new bin value x and its error σ_x are given by [330]:

$$x = \left(\sum_{i=1}^n \delta_i x_i \right) \left(\sum_{i=1}^n \delta_i \right)^{-1} \quad \sigma_x = \sqrt{\sum_{i=1}^n \delta_i \sigma_{x_i}^2} \cdot \left(\sum_{i=1}^n \delta_i \right)^{-1} \quad (5.40)$$

Figure 5.19 shows an example of this rebinning method with three overlapping bins building a new one with large overlaps. The height of the bins

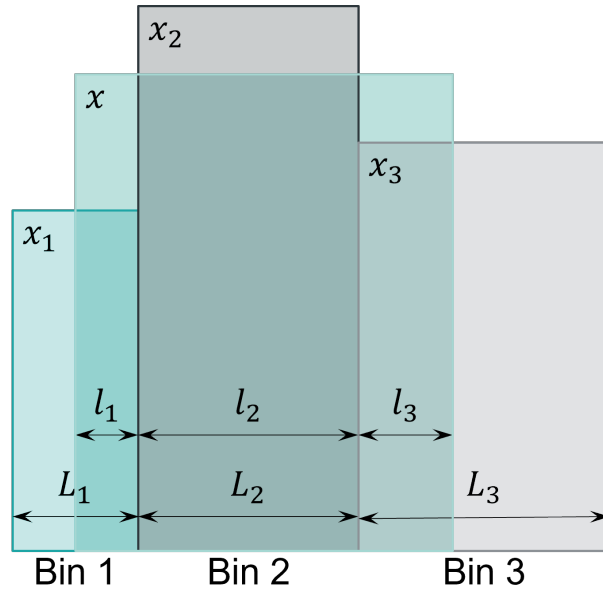


Figure 5.19: Rebinning of three bins 1, 2, 3 with widths $l_{1,2,3}$ and values $x_{1,2,3}$ into one new bin of width $l = l_1 + l_2 + l_3$, resulting in a new value x .

symbolises the values. The value and error of the new bin are given by

$$x = \delta_1 x_1 + \delta_2 x_2 + \delta_3 x_3 \quad \sigma_x = \sqrt{\delta_1^2 \sigma_{x_1}^2 + \delta_2^2 \sigma_{x_2}^2 + \delta_3^2 \sigma_{x_3}^2}. \quad (5.41)$$

In addition to adjusting the reference data to fit the here used energy bins, $\cos(\theta)$ bins can be rebinned in the same way with Equation 5.40.

More information can be found in [330].

6 | Extraction of polarisation observables

This chapter discusses the extraction of the polarisation observables. Therefore, two methods are used: ϕ binned asymmetry fitting method (Asym) and unbinned maximum likelihood estimation method (MLE).

The asymmetry method, described in Section 6.1, calculates energy and angular binned asymmetries as a function of the azimuthal angle of the meson in the CM frame ϕ and fits them with the corresponding functions.

The MLE method, described in Section 6.2, uses an event-based maximum likelihood fit for unbinned data. A probability density function is constructed and all single events are given as input for the fit.

After extracting the observables with the two methods, their values are compared in Section 6.3 to verify the correctness of both methods.

Section 6.4 discusses the systematic uncertainties that must be considered for a significant result.

Here, all polarisation observables will be shown without dilution factor correction for T , P and H (Section 5.4) if not mentioned otherwise. Furthermore, when η is mentioned without additional comment, the merged data from both decay channels are meant. The angles ϕ and θ are always the ones of the meson in the CM frame if not mentioned otherwise.

6.1 Binned asymmetry fitting method

As seen in Section 1.6.4 the different terms in the polarised DCS can be defined as asymmetries. Since the experimental environment is the same for all measurements, i. e. detection efficiency, branching ratio and target surface density, the DCS can be replaced by the flux normalised event yield $\hat{N} = N/N_\gamma$. Therefore, Equations 1.62-1.64 can be rewritten:

$$A_\Sigma(\phi) = \frac{1}{\delta} \frac{\hat{N}^\perp - \hat{N}^\parallel}{\hat{N}^\perp + \hat{N}^\parallel} = \Sigma \cos(2(\alpha - \phi)), \quad (6.1)$$

$$A_T(\phi) = \frac{1}{\Lambda} \frac{\hat{N}_\uparrow - \hat{N}_\downarrow}{\hat{N}_\uparrow + \hat{N}_\downarrow} = T \sin(\beta - \phi), \quad (6.2)$$

$$A_{PH}(\phi) = \frac{1}{\delta\Lambda} \frac{\hat{N}_\uparrow^\perp - \hat{N}_\downarrow^\perp - \hat{N}_\uparrow^\parallel + \hat{N}_\downarrow^\parallel}{\hat{N}_\uparrow^\perp + \hat{N}_\downarrow^\perp + \hat{N}_\uparrow^\parallel + \hat{N}_\downarrow^\parallel} = P \cos(2(\alpha - \phi)) \sin(\beta - \phi) + H \sin(2(\alpha - \phi)) \cos(\beta - \phi). \quad (6.3)$$

Again, δ and Λ are the polarisation degrees of the beam photon and target nucleon, α and β are the polarisation directions of the beam photon and target nucleon and the \perp / \parallel and \uparrow / \downarrow indicate the experimentally set polarisation direction.

For a perfect experiment, the polarisation degree of the beam photon and the target nucleon is the same for the different measurements, i.e. $\delta = \delta^\perp = \delta^\parallel$ and $\Lambda = \Lambda_\uparrow = \Lambda_\downarrow$. However, there are minor differences in the values of the corresponding measurements. It is better to weight the individual normalised event yields by the corresponding polarisation degrees, which results in the following formulas for the asymmetry [262]:

$$A_\Sigma(\phi) = \frac{\frac{1}{2} \left(\frac{\hat{N}^\perp}{\delta^\perp} - \frac{\hat{N}^\parallel}{\delta^\parallel} \right)}{\left(\frac{\hat{N}^\perp}{\delta^\perp} + \frac{\hat{N}^\parallel}{\delta^\parallel} \right) \left(\frac{1}{\delta^\perp} + \frac{1}{\delta^\parallel} \right)^{-1}} - \frac{1}{2} \left(\frac{1}{\delta^\perp} - \frac{1}{\delta^\parallel} \right), \quad (6.4)$$

$$A_T(\phi) = \frac{\frac{1}{2} \left(\frac{\hat{N}_\uparrow}{\Lambda_\uparrow} - \frac{\hat{N}_\downarrow}{\Lambda_\downarrow} \right)}{\left(\frac{\hat{N}_\uparrow}{\Lambda_\uparrow} + \frac{\hat{N}_\downarrow}{\Lambda_\downarrow} \right) \left(\frac{1}{\Lambda_\uparrow} + \frac{1}{\Lambda_\downarrow} \right)^{-1}} - \frac{1}{2} \left(\frac{1}{\Lambda_\uparrow} - \frac{1}{\Lambda_\downarrow} \right), \quad (6.5)$$

$$A_{PH}(\phi) = \frac{\frac{1}{4} \left(\frac{\hat{N}_{\uparrow}^{\perp}}{\delta_{\uparrow}^{\perp} \Lambda_{\uparrow}^{\perp}} - \frac{\hat{N}_{\downarrow}^{\perp}}{\delta_{\downarrow}^{\perp} \Lambda_{\downarrow}^{\perp}} - \frac{\hat{N}_{\uparrow}^{\parallel}}{\delta_{\uparrow}^{\parallel} \Lambda_{\uparrow}^{\parallel}} + \frac{\hat{N}_{\downarrow}^{\parallel}}{\delta_{\downarrow}^{\parallel} \Lambda_{\downarrow}^{\parallel}} \right)}{\left(\frac{\hat{N}_{\uparrow}^{\perp}}{\delta_{\uparrow}^{\perp} \Lambda_{\uparrow}^{\perp}} + \frac{\hat{N}_{\downarrow}^{\perp}}{\delta_{\downarrow}^{\perp} \Lambda_{\downarrow}^{\perp}} + \frac{\hat{N}_{\uparrow}^{\parallel}}{\delta_{\uparrow}^{\parallel} \Lambda_{\uparrow}^{\parallel}} + \frac{\hat{N}_{\downarrow}^{\parallel}}{\delta_{\downarrow}^{\parallel} \Lambda_{\downarrow}^{\parallel}} \right) \left(\frac{1}{\delta_{\uparrow}^{\perp} \Lambda_{\uparrow}^{\perp}} + \frac{1}{\delta_{\downarrow}^{\perp} \Lambda_{\downarrow}^{\perp}} + \frac{1}{\delta_{\uparrow}^{\parallel} \Lambda_{\uparrow}^{\parallel}} + \frac{1}{\delta_{\downarrow}^{\parallel} \Lambda_{\downarrow}^{\parallel}} \right)^{-1}} - \frac{A_{\Sigma}}{2} \left(\frac{1}{\Lambda_{\uparrow}} - \frac{1}{\Lambda_{\downarrow}} \right) - \frac{A_T}{2} \left(\frac{1}{\delta^{\perp}} - \frac{1}{\delta^{\parallel}} \right) + \frac{1}{4} \left(\frac{1}{\Lambda_{\uparrow}} - \frac{1}{\Lambda_{\downarrow}} \right) \left(\frac{1}{\delta^{\perp}} - \frac{1}{\delta^{\parallel}} \right), \quad (6.6)$$

where the asymmetries A_{Σ} and A_T within the PH asymmetry A_{PH} are calculated with an additional polarisation degree weighting:

$$\begin{aligned}
 \hat{N}^{\perp, \parallel} &= \left(\frac{\hat{N}_{\uparrow}^{\perp, \parallel}}{\Lambda_{\uparrow}^{\perp, \parallel}} + \frac{\hat{N}_{\downarrow}^{\perp, \parallel}}{\Lambda_{\downarrow}^{\perp, \parallel}} \right) \left(\frac{1}{\Lambda_{\uparrow}^{\perp, \parallel}} + \frac{1}{\Lambda_{\downarrow}^{\perp, \parallel}} \right)^{-1}, \\
 \hat{N}_{\uparrow, \downarrow} &= \left(\frac{\hat{N}_{\uparrow, \downarrow}^{\perp}}{\delta_{\uparrow, \downarrow}^{\perp}} + \frac{\hat{N}_{\uparrow, \downarrow}^{\parallel}}{\delta_{\uparrow, \downarrow}^{\parallel}} \right) \left(\frac{1}{\delta_{\uparrow, \downarrow}^{\perp}} + \frac{1}{\delta_{\uparrow, \downarrow}^{\parallel}} \right)^{-1}. \quad (6.7)
 \end{aligned}$$

The definitions from Equation 6.7 could also be used to calculate the beam and target asymmetry directly. However, this is not done here to be completely independent of the target polarisation for the beam asymmetry and the beam polarisation for the target asymmetry. However, it was checked that the results were consistently below the 0.1% level in Oct2018.

The observables are extracted by fitting the binned asymmetries in Equations 6.1-6.3 with the corresponding functions. 24 ϕ bins are chosen for $\pi^0 N$ and 12 for ηN . This is performed in R00T by minimising the χ^2 . To attain the right values, the observables T , P and H must be divided by the dilution factor afterwards.

Beam time	Oct2018		Oct2018	
	α [°]	β [°]	α [°]	β [°]
$\pi^0 p$	44.28 ± 0.35	90.66 ± 1.11	45.77 ± 0.35	87.81 ± 1.51
$\pi^0 n$	44.59 ± 0.39	83.46 ± 4.89	46.35 ± 0.41	76.33 ± 7.20
ηp	44.00 ± 1.00	89.92 ± 2.71	46.69 ± 1.00	84.75 ± 2.97
ηn	48.94 ± 1.51	-	46.07 ± 1.71	-
total	44.52 ± 0.25	90.25 ± 1.01	46.06 ± 0.25	86.82 ± 1.32

Table 6.1: Experimentally extracted beam and target polarisation direction values α and β from the energy and angular integrated total fits in Oct2018 and Dec2021. The fits can be found in Figure 6.1 and Appendix C.1, respectively.

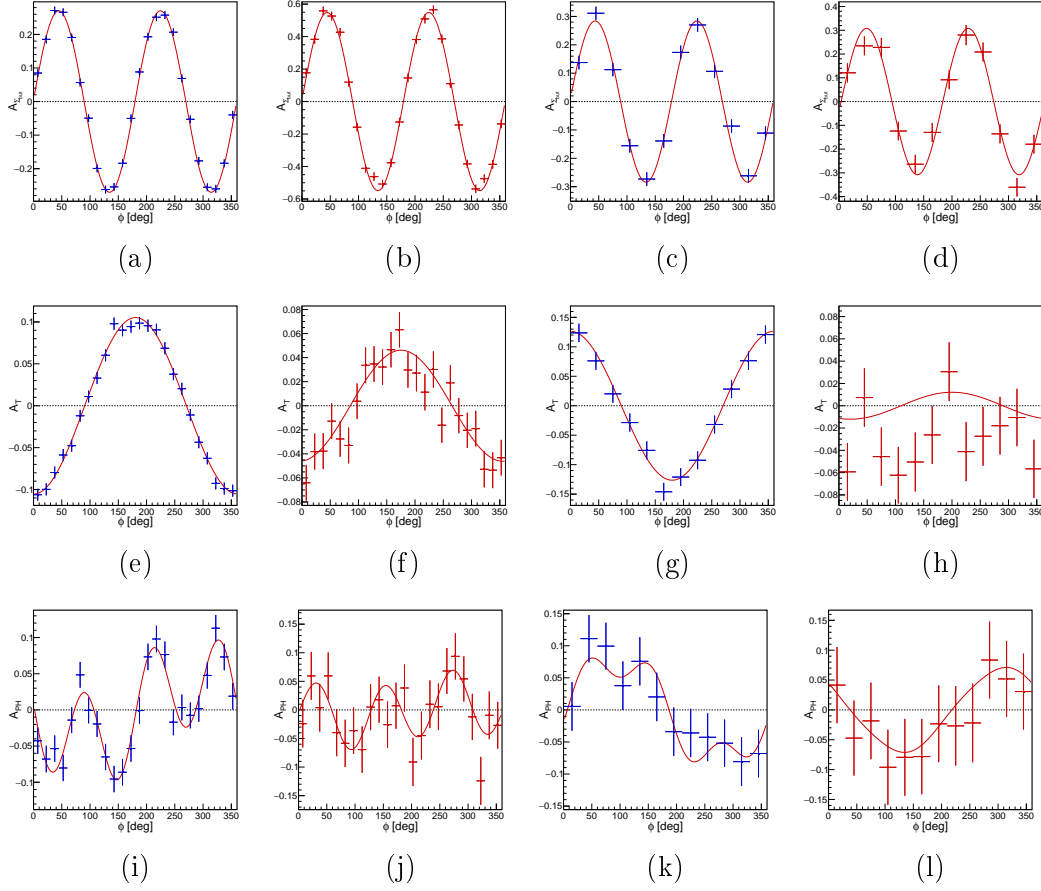


Figure 6.1: Beam asymmetry $A_{\Sigma_{but}}$ (top column), target asymmetry A_T (middle column) and beam-target asymmetry A_{PH} (bottom column) of E_γ and $\cos(\theta)$ integrated data in $\pi^0 p$ (1st row), $\pi^0 n$ (2nd row), ηp (3rd row) and ηn (4th row) in Oct2018. The asymmetries in Dec2021 can be found in Appendix C.1. Note the different scaling on the y-axis.

The polarisation directions of the beam α and target Λ are set to 45° and 90° , respectively, in the experiment. Experimental conditions can lead to a slight change in these values. Therefore, these polarisation directions are set as additional free parameters for the energy and angular integrated beam and target asymmetries. As inverse-variance weighted mean for all reactions except ηn for β , due to the disappearing signal, the values $\alpha = (44.52 \pm 0.25)^\circ$ and $\beta = (90.25 \pm 1.01)^\circ$ are found in Oct2018. In Dec2021 the values are determined to be $\alpha = (46.06 \pm 0.25)^\circ$ and $\beta = (86.82 \pm 1.32)^\circ$. See Table 6.1 for the individually found values.

Figure 6.1 shows the energy and angular merged asymmetry bins, where α

and β are free parameters in the beam and target asymmetry. However, for the E_γ and $\cos(\theta)$ dependent asymmetry fits, the α and β are fixed to the experimentally found values to reduce additional uncertainties correlated with low statistics.

The asymmetry is plotted as a function of the azimuthal angle ϕ for every E_γ and $\cos(\theta)$ bin separately and the observable values are extracted. For the beam and target asymmetry, the values are directly given by the amplitude of the fitting function, whereas P and H are extracted simultaneously from the PH asymmetry. Examples of energy- and angular-dependent asymmetry fits can be found in Appendix C.2. In contrast to the energy and angular merged one shown in Figure 6.1, their statistics are much lower. Otherwise, they look very alike.

It is important to mention that the measured beam asymmetry Σ_{but} is not equal to the physical beam asymmetry Σ . This is due to the dButanol target, where reactions off carbon and oxygen cannot be distinguished from the ones off deuterium. Depending on the nuclei where the reaction nucleon is bound, the beam asymmetry may differ. An additional background factor $\delta_{\Sigma,BG}$ must be introduced:

$$\Sigma = (1 - \delta_{\Sigma,BG}) \Sigma_{but} + \delta_{\Sigma,BG} \Sigma_{BG}. \quad (6.8)$$

Unfortunately, the factor $\delta_{\Sigma,BG}$ cannot be determined in this experiment such that all beam asymmetry results must be interpreted with respect to that, i.e. as Σ_{but} . Nevertheless, the background contribution is small (Section 4.5) and it is assumed that $\delta_{\Sigma,BG}$ is relatively small too. Therefore, the results should still be very similar to Σ and can be used to compare the here extracted observable values to the ones from other independent experiments.

Figures 6.2 and 6.3 show the extracted *raw* observable values for ηN . Remember, no dilution factor correction is applied here. The data from the two investigated decay channels and the combined data are shown. The latter combines the data from both decay channels for every ϕ dependent point and fits the asymmetry of the combined data. It is visible that the 2γ decay channel has significantly smaller error bars than the 6γ one. Nonetheless, the data agree well with each other. See Section 7.1 for a more detailed discussion.

The extracted observable values for $\pi^0 N$ and ηN can be seen in Figures 6.7-6.10, where they are also compared to those from the MLE method.

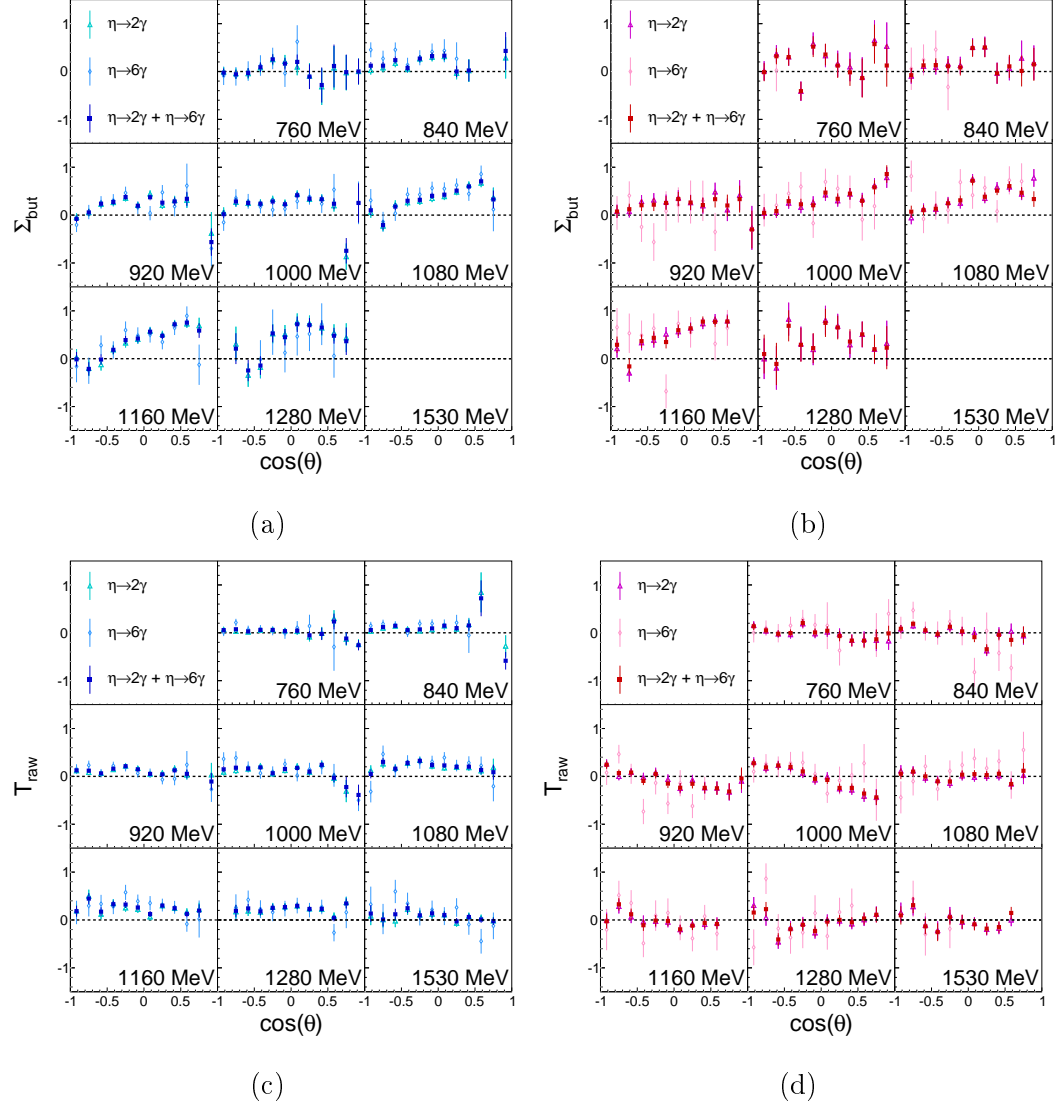


Figure 6.2: Beam asymmetry Σ_{but} (top row) and target asymmetry T (bottom row) as a function of $\cos(\theta)$ for fixed E_γ . The target asymmetry is not dilution factor corrected, indicated with *raw*. Shown are the values for the $\eta \rightarrow 2\gamma$ and $\eta \rightarrow 3\pi^0 \rightarrow 6\gamma$ decay channels as well as for the merged total η data in the reaction on the proton (left column) and the neutron (right column) in Oct2018.

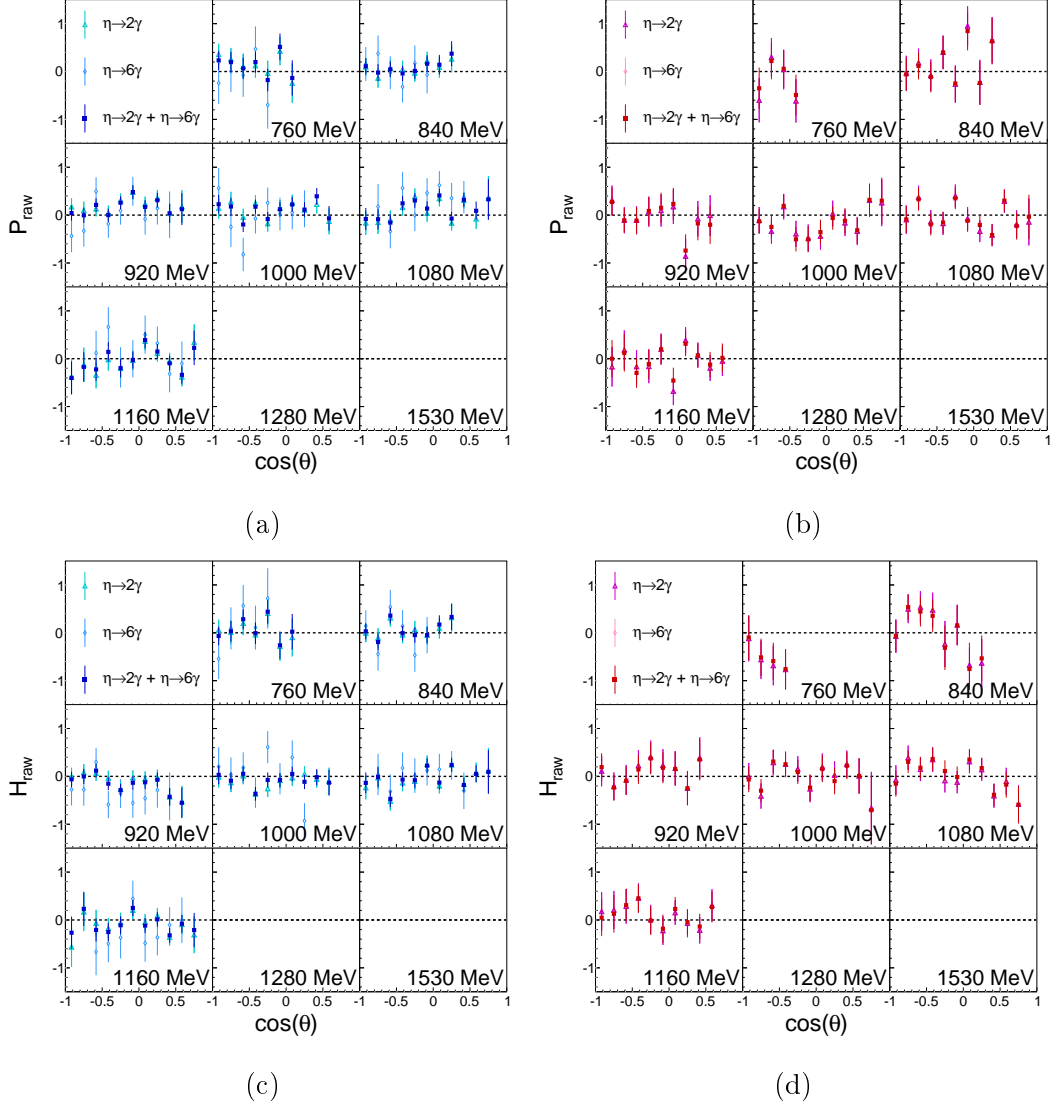


Figure 6.3: Recoil asymmetry P (top row) and beam-target observable H (bottom row) as a function of $\cos(\theta)$ for fixed E_γ . The observables are not dilution factor corrected, indicated with *raw*. Shown are the values for the $\eta \rightarrow 2\gamma$ and $\eta \rightarrow 3\pi^0 \rightarrow 6\gamma$ decay channels as well as for the merged total η data in the reaction on the proton (left column) and the neutron (right column) in Oct2018.

6.2 Unbinned maximum likelihood estimation method

The asymmetry method calculates binned asymmetries and fits them with the principle of least squares. Another approach can be used for extracting polarisation observables as well: event-based maximum likelihood estimation (MLE). Here, a data set (δ, Λ, ϕ) is given unbinned and the most probable values for the free parameters (Σ, T, P, H) of the probability density function (PDF) are obtained as a result. The values are still determined for each E_γ and $\cos(\theta)$ bin independently.

In the end, the likelihood function is rather complex, consisting of 32 free parameters. It can be difficult for the algorithm to converge and find a stable maximum or minimum, respectively. Therefore, the MLE method has problems with kinematic regions with very few events.

However, as shown before [262], the MLE method works well, is in excellent agreement with the asymmetry method and the statistical errors are smaller on average.

6.2.1 Probability density function

The likelihood function is built as a product of PDF that suits the experiment.

Here, the PDF normalised to 2π is given by the ratio of the polarised DCS (Equation 1.57) and the unpolarised one:

$$\begin{aligned}
 f(\Sigma, T, P, H; \delta, \Lambda, \phi) &= \left(\frac{d\sigma}{d\Omega}\right) \cdot \left(\frac{d\sigma}{d\Omega}\right)_0^{-1} \\
 &= 1 - \delta\Sigma \cos(2(\alpha - \phi)) + \Lambda T \sin(\beta - \phi) \\
 &\quad - \delta\Lambda P \cos(2(\alpha - \phi)) \sin(\beta - \phi) \\
 &\quad - \delta\Lambda H \sin(2(\alpha - \phi)) \cos(\beta - \phi). \tag{6.9}
 \end{aligned}$$

The PDF f depends on three quantities (δ, Λ, ϕ) and has four free parameters (Σ, T, P, H) . The normalisation to 2π instead of 1 is chosen for better readability. As long as a constant normalisation is included in all PDF, the

MLE results do not change. The proper probability is obtained by dividing the PDF by 2π .

The PDF from Equation 6.9 can also be written as a Fourier series with coefficients a_k and b_k that are independent of ϕ but contain the polarisation degrees and the four observables:

$$f = f(\Sigma, T, P, H; \delta, \Lambda, \phi) = 1 + \sum_{k=1}^3 a_k \sin(k\phi) + b_k \cos(k\phi). \quad (6.10)$$

The coefficients are given by:

$$\begin{aligned} a_1 &= -\Lambda T \cos(\beta) - 0.5\delta\Lambda(P - H)(\sin(2\alpha)\sin(\beta) + \cos(2\alpha)\cos(\beta)), \\ b_1 &= \Lambda T \sin(\beta) - 0.5\delta\Lambda(P - H)(\cos(2\alpha)\sin(\beta) - \sin(2\alpha)\cos(\beta)), \\ a_2 &= -\delta\Sigma \sin(2\alpha), \\ b_2 &= -\delta\Sigma \cos(2\alpha), \\ a_3 &= -0.5\delta\Lambda(P + H)(\sin(2\alpha)\sin(\beta) - \cos(2\alpha)\cos(\beta)), \\ b_3 &= -0.5\delta\Lambda(P + H)(\cos(2\alpha)\sin(\beta) + \sin(2\alpha)\cos(\beta)). \end{aligned} \quad (6.11)$$

In contrast to the asymmetry method, where possible unflat detector acceptance effects cancel out, they must be considered here. Therefore, a new PDF f_{DA} describing the detector acceptance must be included. Having no information about the exact form, the PDF can be written as a normalised Fourier series with coefficients c_k and d_k . It was shown [262] that only the first 6 coefficients can be considered, while all others can be ignored without losing information. The reason for this lies in the orthogonality of the sine and cosine terms. The detector acceptance PDF is given by:

$$f_{DA} = f_{DA}(c_1, d_1, \dots, c_6, d_6; \phi) = 1 + \sum_{k=1}^6 c_k \sin(k\phi) + d_k \cos(k\phi), \quad (6.12)$$

where coefficients $c_0 = 0$ and $d_0 = 1$ can be chosen without loss of generality in a way that they vanish. In the end f_{DA} depends on 12 free parameters: $c_1, d_1, \dots, c_6, d_6$.

The total PDF, including possible detector acceptance dependence, is a simple multiplication of f (Equation 6.10) with f_{DA} (Equation 6.12) and a

right normalisation factor \mathcal{N} :

$$\tilde{f} = \tilde{f}(\Sigma, T, P, H, c_1, d_1, \dots, c_6, d_6; \delta, \Lambda, \phi) = \frac{f \cdot f_{DA}}{\mathcal{N}}, \quad (6.13)$$

$$\mathcal{N} = \mathcal{N}(\Sigma, T, P, H, c_1, d_1, \dots, c_3, d_3; \delta, \Lambda, \phi) = 1 + \frac{1}{2} \cdot \sum_{k=1}^3 a_k c_k + b_k d_k. \quad (6.14)$$

To increase readability even more, the set of free model parameters is defined by:

$$\mathcal{O} \equiv \{\Sigma, T, P, H, c_1, d_1, \dots, c_6, d_6\}. \quad (6.15)$$

6.2.2 Likelihood function

The likelihood function \mathcal{L} is given as the joint probability of a data set with n events of the PDF. The maximum of the likelihood function returns the most probable free model parameters. The existence of a maximum requires two conditions: first, the parameter space must be compact and second, the likelihood function must be continuous [331]. Furthermore, the used algorithm must be able to find the global maximum for a rather complex function.

For the PDF \tilde{f} , the likelihood function is given by:

$$\mathcal{L}(\mathcal{O}) = \prod_{i=1}^n \tilde{f}(\mathcal{O}; \delta_i, \Lambda_i, \phi_i). \quad (6.16)$$

Computationally, it is a great effort to find the maximum for such a multi-dimensional hypersurface, which usually must be solved numerically. A more efficient method is minimising the negative logarithm of the likelihood function $-\ln(\mathcal{L})$. This method is also used here.

The errors for the free parameters can be found by searching for the smallest 1σ interval given by:

$$-\ln(\mathcal{L}) < -\ln(\mathcal{L}_{\max}) + 0.5. \quad (6.17)$$

The reason for this lies in the central limit theorem (CLT). If the number of events n tends to infinity, which can also be approximated by a large number, the likelihood function with N free parameters tends to a N dimension Gaussian function.

Besides possible detector asymmetry terms in the PDF, another complication occurs for unbinned events: the sideband subtraction method (Section

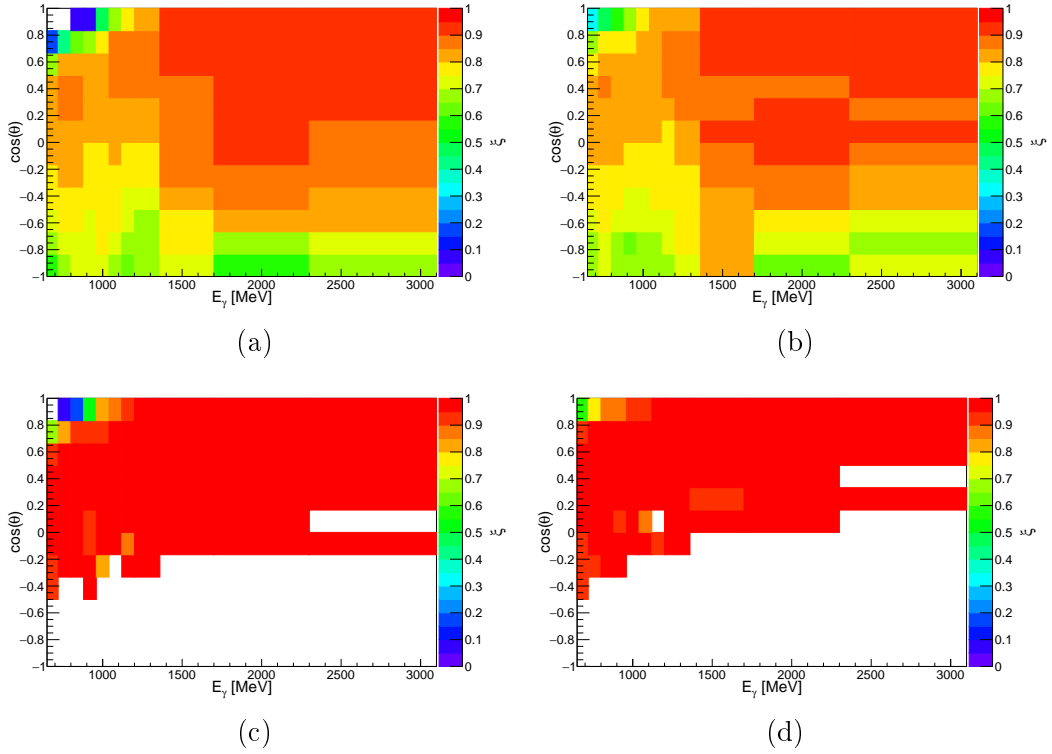


Figure 6.4: Signal to background ratio ξ as a function of E_γ and $\cos(\theta)$ for $\pi^0 p$ (left column) and $\pi^0 n$ (right column) in Oct2018. The first row shows the values for meson hits in CB, the second row for meson hits in MT.

4.4) is no more valid. Random background Tagger events must be handled differently. Assuming these events are truly random with no physical meaning, an additional PDF can be introduced: $\tilde{f}(\mathcal{O}^{BG})$. Here, \mathcal{O}^{BG} is a set of 16 new parameters, also defined by Equation 6.13 with the difference that all parameters are background parameters, i.e. $\mathcal{O}^{BG} \equiv \mathcal{O}^{BG}(\Sigma^{BG}, \dots, d_6^{BG})$.

All combined results in the likelihood function:

$$\mathcal{L}(\mathcal{O}, \mathcal{O}^{BG}) = \prod_{i=1}^n \left(\xi \cdot \tilde{f}(\mathcal{O}; \delta_i, \Lambda_i, \phi_i) + (1 - \xi) \cdot \tilde{f}(\mathcal{O}^{BG}; \delta_i, \Lambda_i, \phi_i) \right) \quad (6.18)$$

$$\cdot \prod_{j=1}^m \tilde{f}(\mathcal{O}^{BG}; \delta_j, \Lambda_j, \phi_j),$$

where n is the number of prompt signal hits, m is the number of random background (sideband) hits and ξ is the signal to background ratio directly

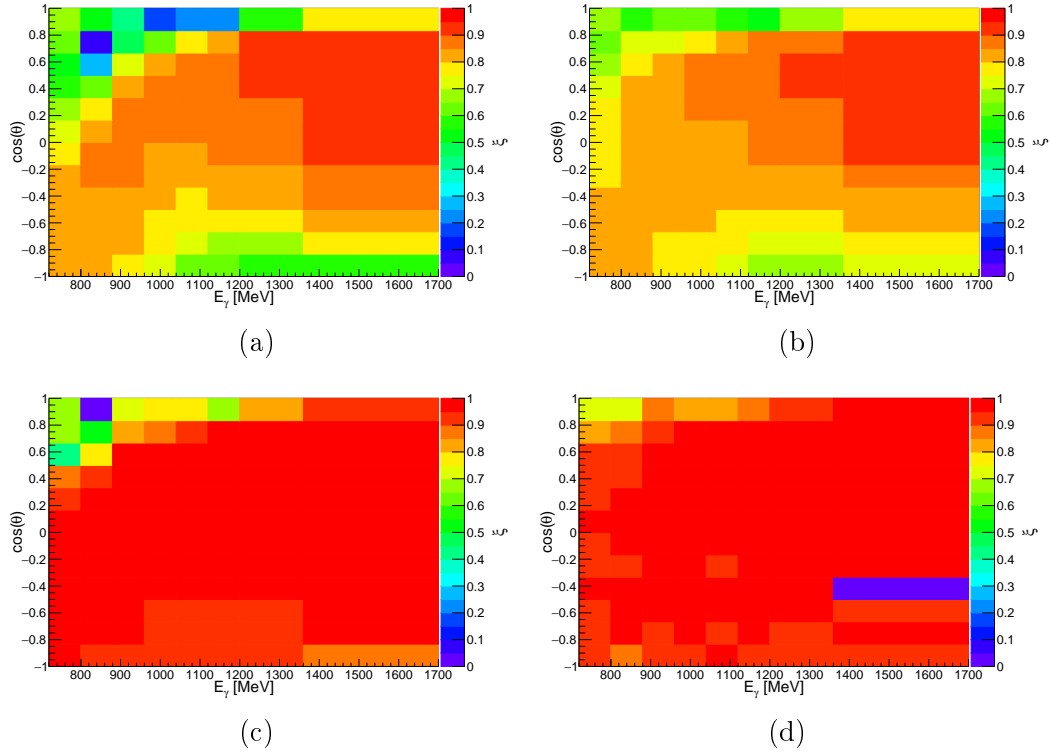


Figure 6.5: Signal to background ratio ξ as a function of E_γ and $\cos(\theta)$ for ηp (left column) and ηn (right column) in Oct2018. The first row shows the values for meson hits in CB, the second row for meson hits in MT.

given by the prompt and sideband time cuts. Explicitly ξ is given by:

$$\xi = \frac{N_P + w_{SB} \cdot N_{SB}}{N_P}, \quad (6.19)$$

where $N_{P,SB}$ are the events in the prompt and sideband time interval and w_{SB} is the ratio between the prompt and sideband time widths. These weights depend on the detector that provides the time information. For CB, it is $w_{SB} = -0.075$, for MT $w_{SB} = -0.0125$. See Section 4.4 for more information.

The signal strength ξ is E_γ and $\cos(\theta)$ dependent and can be seen in Figures 6.4 and 6.5. There are no ξ_{MT} values for $\pi^0 N$ in the very backward direction due to the small opening angle of the π^0 that peaks around 35° with more than 95% of all events below 55° , in contrast to η with an average opening angle around 125° . Moreover, there is almost no difference between the two nucleons. The ones from MT are more constant over the energy and angular range than the ones from CB.

6.2. Unbinned maximum likelihood estimation method

The average values for the signal to background ratios are $\bar{\xi}_{CB} = 0.72$ and $\bar{\xi}_{MT} = 0.93$ for $\pi^0 N$ and $\bar{\xi}_{CB} = 0.76$ and $\bar{\xi}_{MT} = 0.96$ for ηN .

The minimisation of $-\ln(\mathcal{L})$ is performed with the `Roofit` library of `ROOT`, where the `MINUIT` algorithm is used with the functions `MIGRAD` (finding minimum), `IMPROVE` (improving minimum), `HESSE` (finding symmetric errors) and `MINOS` (finding asymmetric errors as in Equation 6.17).

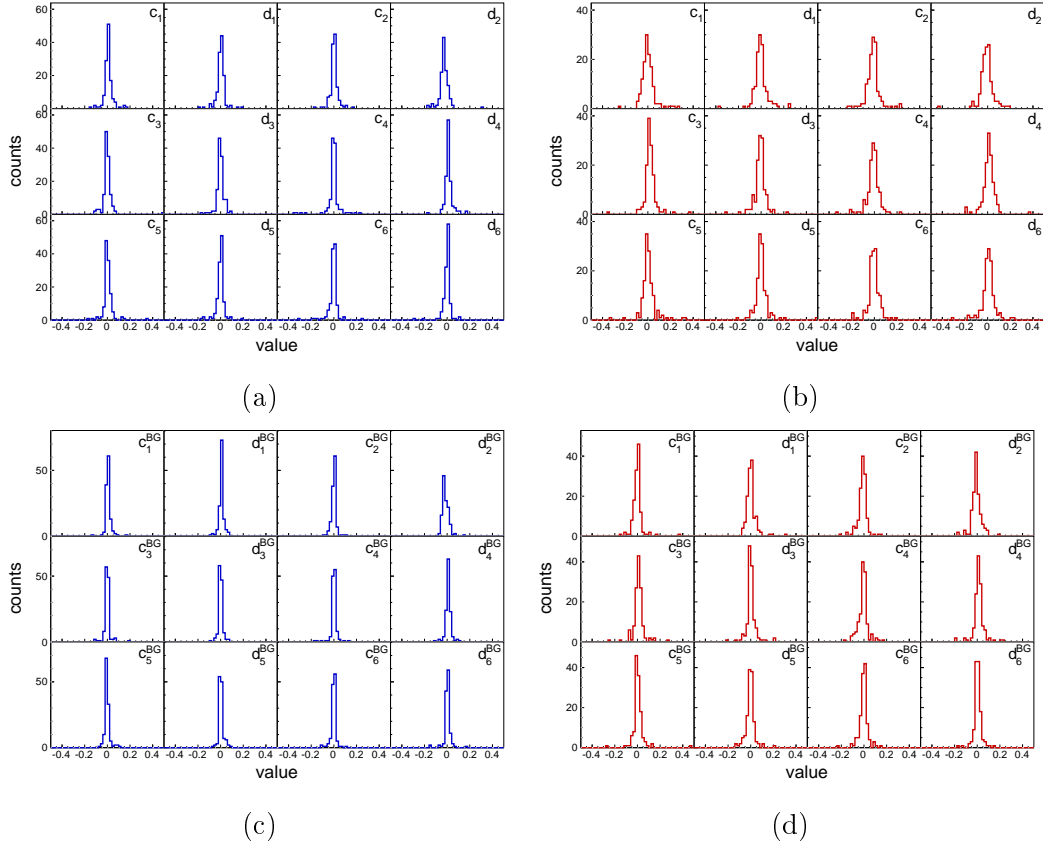


Figure 6.6: Detector acceptance parameters $c_1, d_1, \dots, c_6, d_6$ and background detector acceptance parameters $c_1^{BG}, d_1^{BG}, \dots, c_6^{BG}, d_6^{BG}$ in $\pi^0 p$ (left column) and $\pi^0 n$ (right column) in Oct2018.

The final likelihood function (Equation 6.18) consists of 32 free parameters: the four observables Σ, T, P, H , four background observables $\Sigma^{BG}, T^{BG}, P^{BG}, H^{BG}$, twelve detector acceptance parameters $c_1, d_1, \dots, c_6, d_6$ and twelve background detector acceptance parameters $c_1^{BG}, d_1^{BG}, \dots, c_6^{BG}, d_6^{BG}$.

Figure 6.6 shows the detector acceptance and background detector acceptance parameters for $\pi^0 N$. The values from all E_γ and $\cos(\theta)$ bins are filled in the histogram. All values peak around 0, indicating no strong ϕ dependence

in the detector acceptance. The observables do not change more than 1% compared to the extraction without including detector acceptance, which is far below the typical statistic and systematic uncertainties. The values for ηN can be found in Appendix C.3.

6.3 Comparison between the extraction methods

As discussed in the previous two sections, the polarisation observables are extracted using the asymmetry fitting method (Asym) and the maximum likelihood estimation method (MLE). Here, the observables and some more properties are compared between the two extraction methods.

6.3.1 Polarisation observables

The extracted observable values from both methods are shown in Figures 6.7-6.10. They are given as a function of $\cos(\theta)$ for fixed incident photon energies E_γ . The given angle θ is the polar angle of the meson in the CM frame, as usual.

The observables are given with the statistical uncertainties as error bars only and as *raw* value. T , P and H are not corrected for the dilution from unpolarised nucleons in carbon and oxygen nuclei (Equation 5.17). Whereas the statistical uncertainty coming from the correction of Σ_{but} is negligible, the one of the dilution factor will introduce additional statistical uncertainty of 2%. However, this would be added to both extraction methods' values so that their correction can be ignored here.

Both extraction methods work well and the results agree with each other. The smaller the statistical error bars are, the more identical the values. For some kinematic ranges with very few events, the statistical error bars increase and the difference between the extracted points become larger. The nearly perfect agreement is no surprise as the same data is taken as input for both methods, but it demonstrates the functioning of both methods. The observable values are strongly correlated with each other.

In kinematic regions with few events, one of both methods does not work, i.e. the fit or minimisation does not converge.

6.3.2 Statistical methods for comparison

Multiple statistical methods exist for a more qualitative comparison of the extracted values from the two methods than just looking at the points by eye.

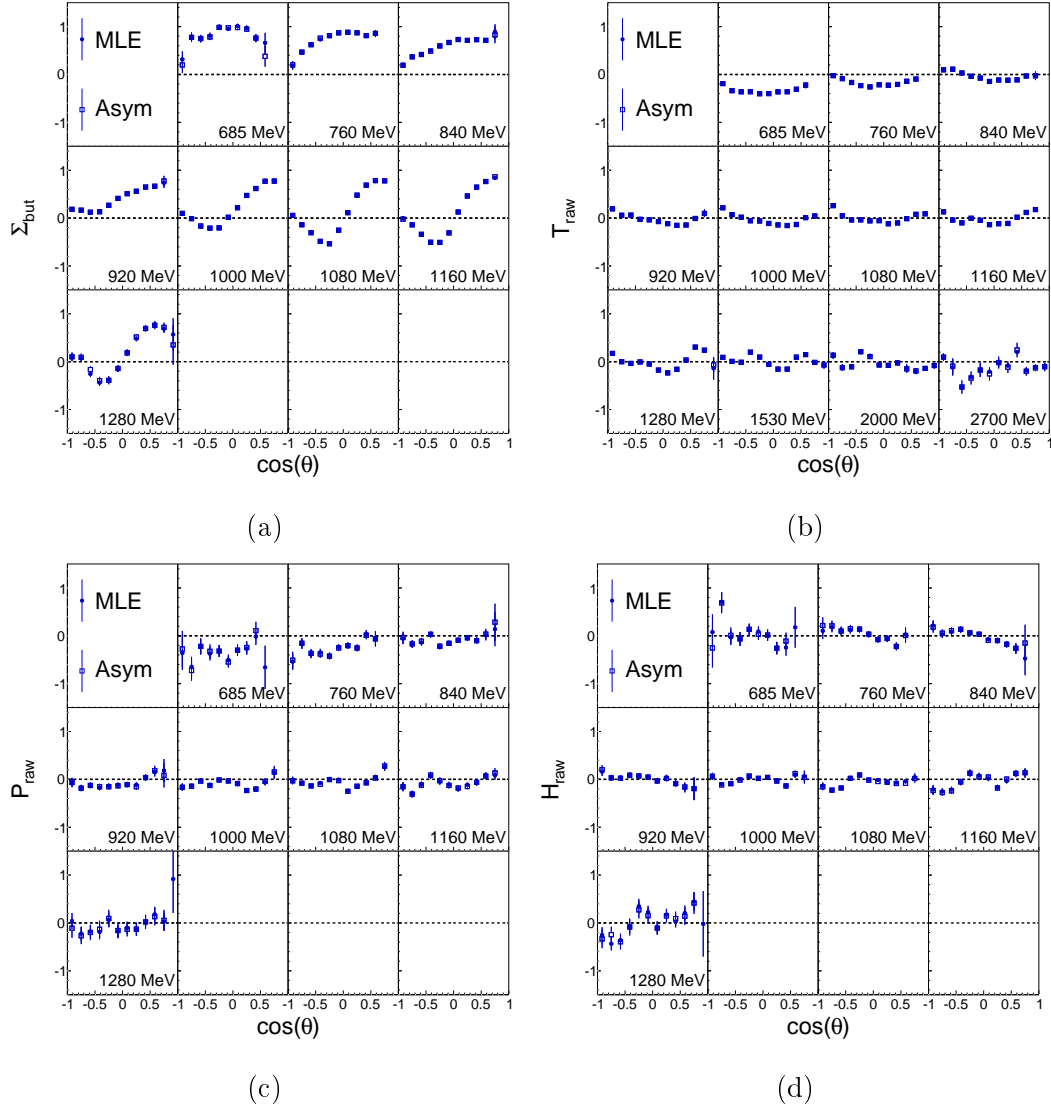


Figure 6.7: The four polarisation observables Σ_{but} , T , P and H in $\pi^0 p$. The observables are not dilution factor corrected, indicated with *raw*. The ones extracted from the maximum likelihood estimation method (MLE) are compared to the asymmetry fitting method (Asym) results in Oct2018.

Two are discussed here.

Simple difference

The straightforward method to compare two values is the simple difference:

$$\Delta O = O_{MLE} - O_{Asym}. \quad (6.20)$$

6.3. Comparison between the extraction methods

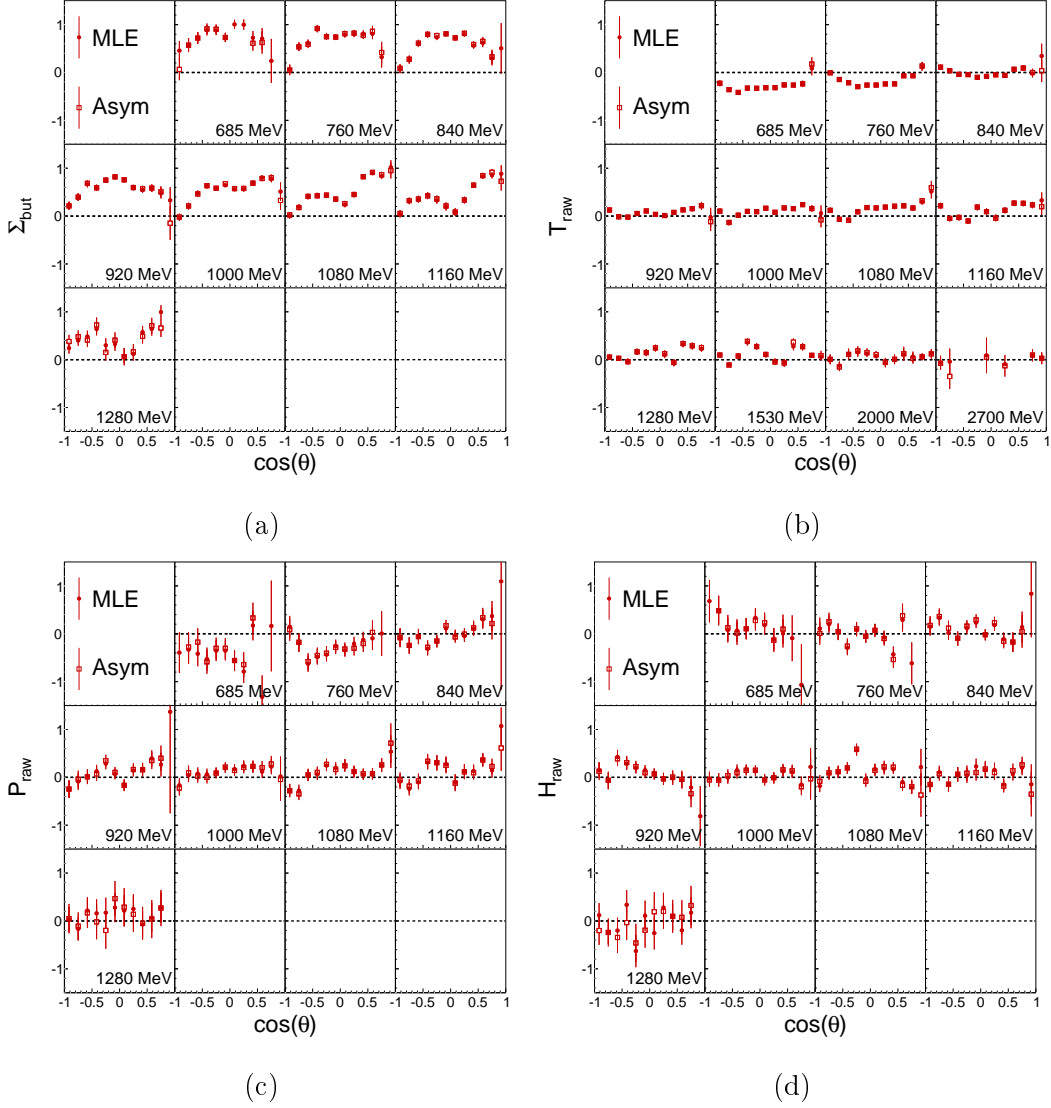


Figure 6.8: The four polarisation observables Σ_{but} , T , P and H in $\pi^0 n$. The observables are not dilution factor corrected, indicated with *raw*. The ones extracted from the maximum likelihood estimation method (MLE) are compared to the asymmetry fitting method (Asym) results in Oct2018.

If the mean values of the observables are shifted in one direction, it would indicate that one of the methods has systematic problems.

Figure 6.11 shows the simple difference of all observables merged for each reaction separately. All histograms are centred around 0 with a slight preference towards negative values. This indicates a possible systematic uncertainty between the two extraction methods. The mean from the reaction $\pi^0 n$, which is furthest away from 0, is with an absolute value of -0.007 ± 0.001 (Gaus-

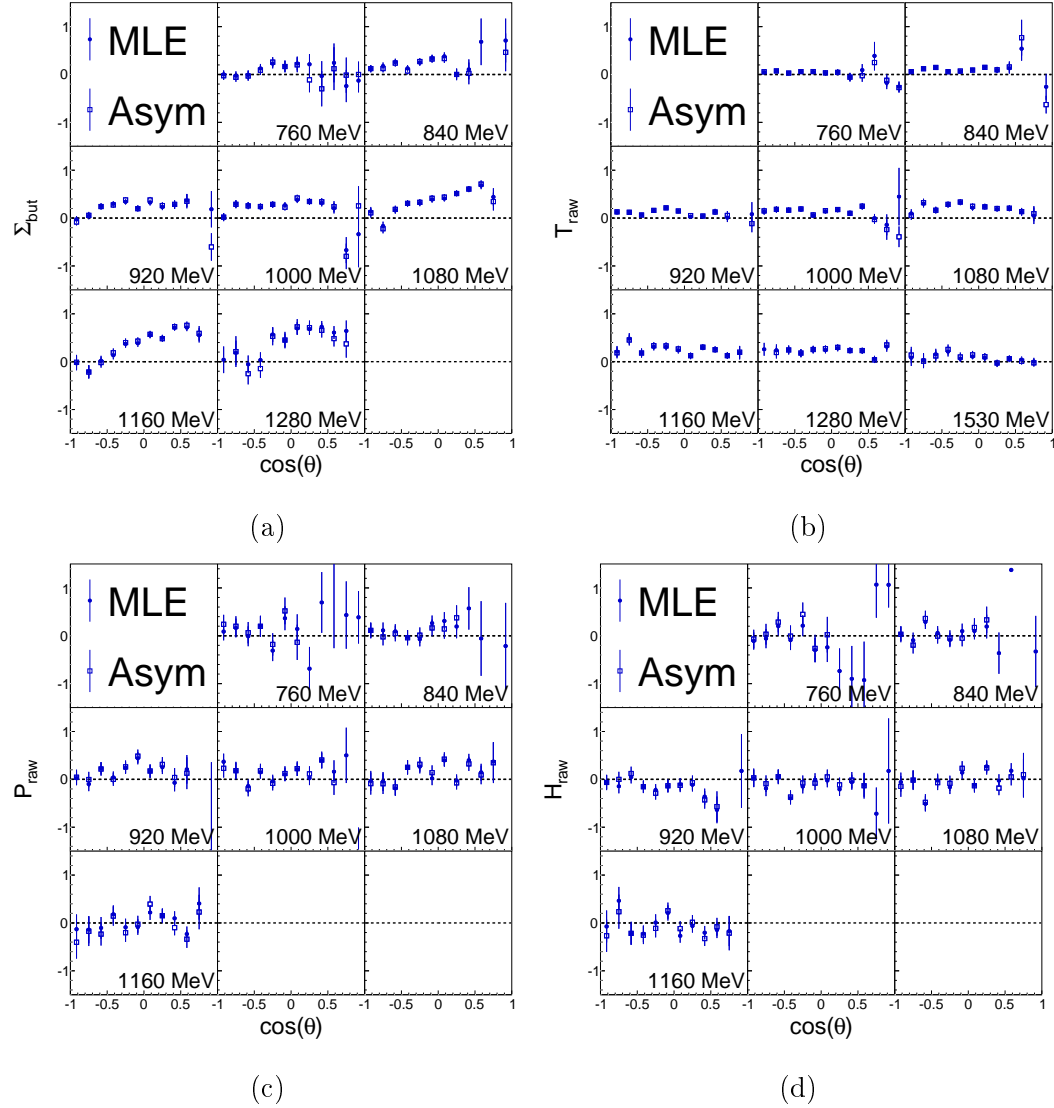


Figure 6.9: The four polarisation observables Σ_{but} , T , P and H in ηp . The observables are not dilution factor corrected, indicated with *raw*. The ones extracted from the maximum likelihood estimation method (MLE) are compared to the asymmetry fitting method (Asym) results in Oct2018.

sian fit) or -0.004 ± 0.003 (mean) still well within the systematic uncertainties. However, the MLE method is assumed to be more accurate due to its unbinned fit.

One can look at the single observables for every reaction (Appendix C.4.1) to check a systematic shift in one observable only. As for the total merged histogram, they are all very similar and in agreement with 0 or very close to it. For observable-reaction combinations with a low statistic and thus a small

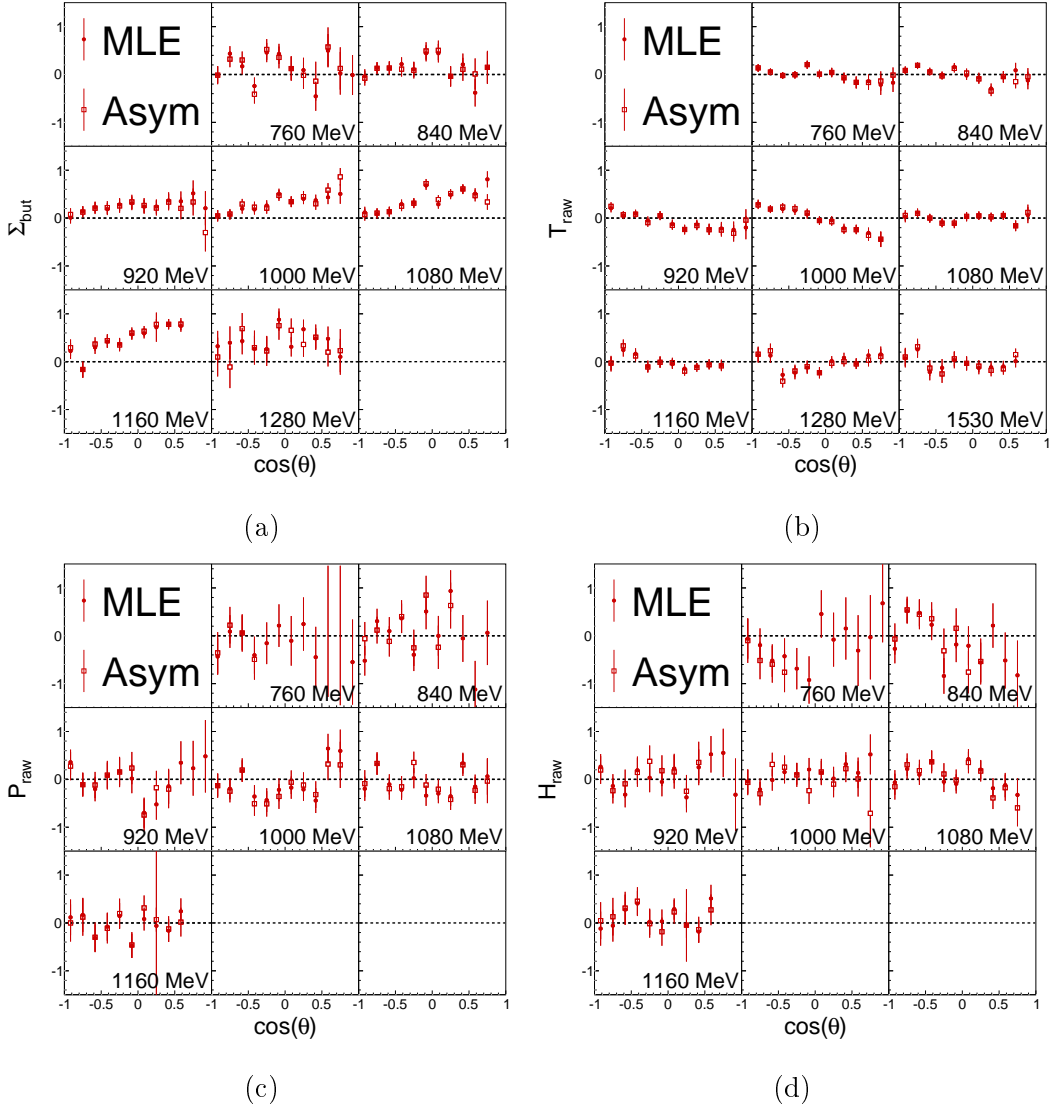


Figure 6.10: The four polarisation observables Σ_{but} , T , P and H in ηn . The observables are not dilution factor corrected, indicated with *raw*. The ones extracted from the maximum likelihood estimation method (MLE) are compared to the asymmetry fitting method (Asym) results in Oct2018.

number of total points, e.g. P and H in ηn , the comparison and interpretation are difficult.

Error normalised difference with maximum correlation

A more sophisticated comparison method looks at the differences normalised to the statistical uncertainties. As discussed in the previous section,

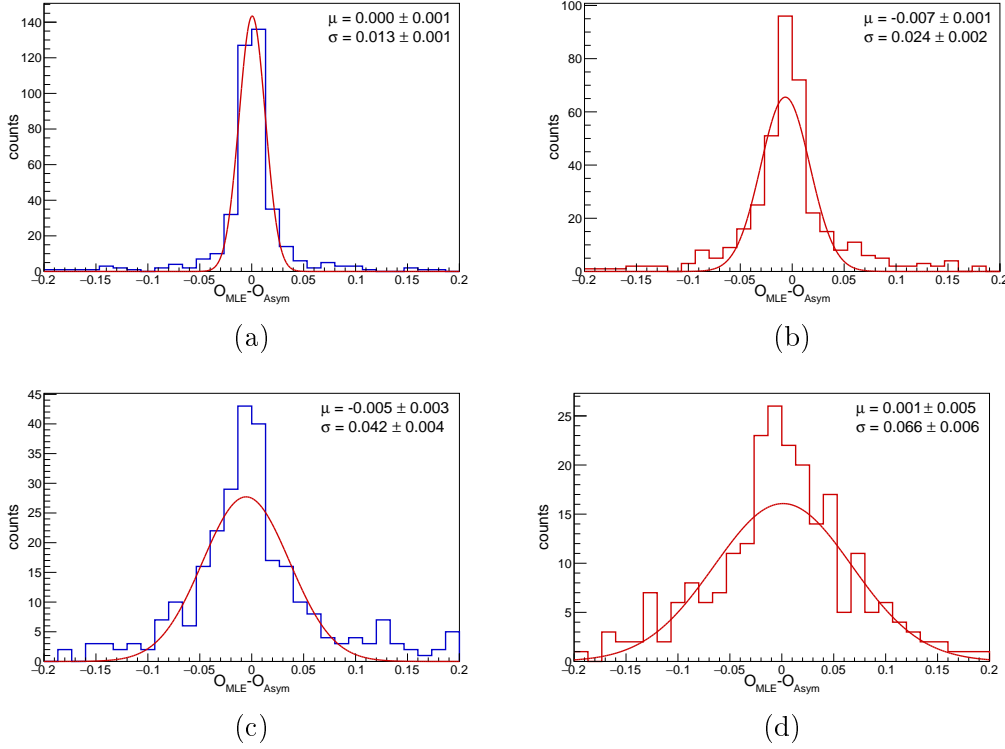


Figure 6.11: Simple difference $\Delta O = O_{MLE} - O_{Asym}$ of the observable values extracted from the two methods, i.e. maximum likelihood estimation method (MLE) and asymmetry fitting method (Asym) in Oct2018. The data from all observables are merged. Shown are all reactions: (a) $\pi^0 p$, (b) $\pi^0 n$, (c) ηp and (d) ηn .

the values are highly correlated, so this correlation should be considered. The formula is given by:

$$\frac{\Delta O}{\sigma_{\Delta O}} = \frac{O_{MLE} - O_{Asym}}{\sqrt{\sigma_{MLE}^2 + \sigma_{Asym}^2 - 2\rho\sigma_{MLE}\sigma_{Asym}}} \sim \mathcal{N}(0, 1), \quad (6.21)$$

where $O_{MLE,Asym}$ are the observable values from the MLE or asymmetry method, $\sigma_{MLE,Asym}$ is their statistical uncertainty and ρ is the correlation coefficient. If there is a perfect agreement between the two values, $\Delta O/\sigma_{\Delta O}$, will be a normal distribution $\mathcal{N}(0, 1)$ centred around 0 with standard deviation 1.

Unfortunately, the correlation ρ is unknown. A maximum correlation can be estimated by decomposing the uncertainty into a completely correlated and an uncorrelated part. The correlation is maximised if the smaller of both

6.3. Comparison between the extraction methods

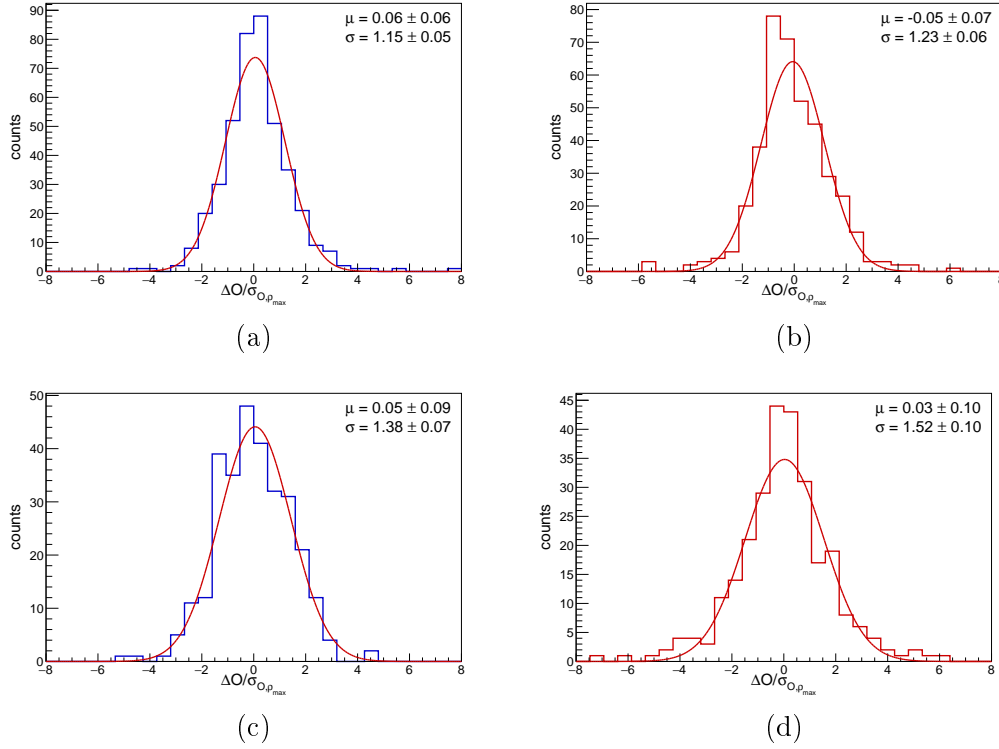


Figure 6.12: Difference of the observable values extracted from the two methods, i.e. maximum likelihood estimation method (MLE) and asymmetry fitting method (Asym), normalised to their statistical uncertainty with maximum correlation (Equations 6.21 and 6.22) in Oct2018. The data from all observables are merged. Shown are all reactions: (a) $\pi^0 p$, (b) $\pi^0 n$, (c) ηp and (d) ηn .

uncertainties is equal to the uncorrelated part, resulting in [262]:

$$\rho_{max} = \min \left\{ \frac{\sigma_{MLE}}{\sigma_{Asym}}, \frac{\sigma_{Asym}}{\sigma_{MLE}} \right\}. \quad (6.22)$$

An error normalised difference with a maximum correlation is rather an upper bound than the actual normalised difference. The uncorrelated part can be something other than 0 in general. However, as was shown in [288], it is not expected that the uncorrelated part is more than a few per cent.

Figure 6.12 shows the normalised difference with the maximum correlation. The mean values agree with 0 as seen for the absolute difference Section 6.3.2, leading to the conclusion that both methods deliver the same results.

The standard deviation is for all reactions larger than 1, indicating an uncorrelated part of more than 0. If the maximum correlation is reduced by

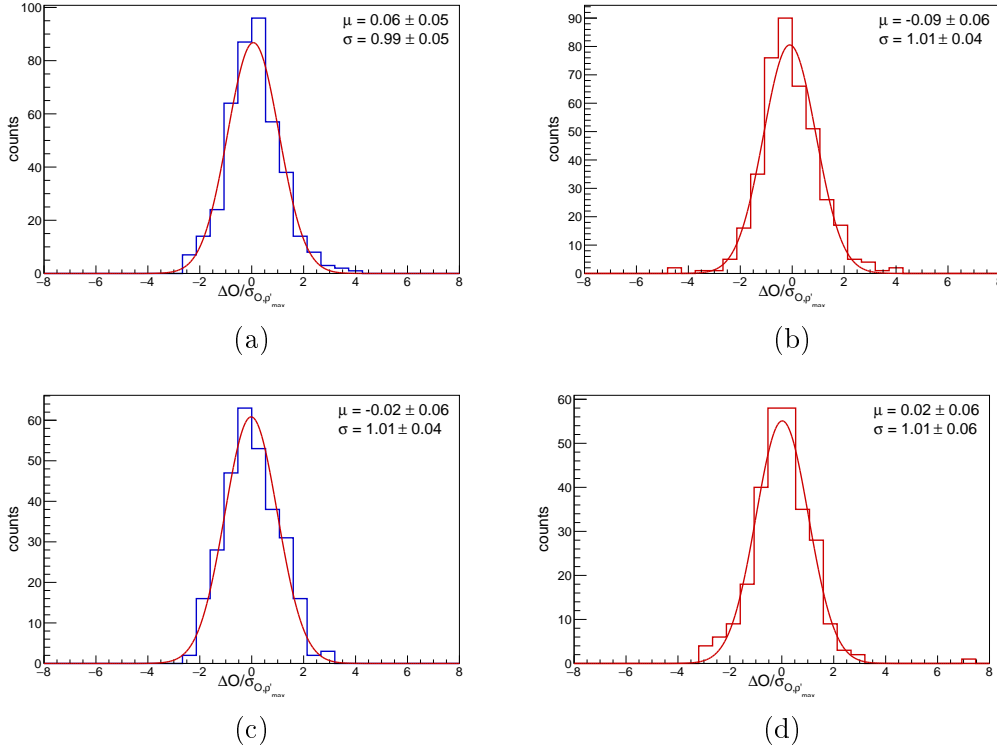


Figure 6.13: Difference of the observable values extracted from the two methods, i.e. maximum likelihood estimation method (MLE) and asymmetry fitting method (Asym), normalised to their statistical uncertainty with reduced maximum correlation (Equations 6.21 and 6.22) in Oct2018. The data from all observables are merged. Shown are all reactions: (a) π^0p , (b) π^0n , (c) ηp and (d) ηn . The reduction in the maximum correlation ρ is 0.3% in π^0p , 0.8% in π^0n , 2.8% in ηp and 5.2% in ηn .

0.3% (π^0p), 0.8% (π^0n), 2.8% (ηp) and 5.2% (ηn) the standard deviation is in perfect agreement with 1. This confirms an uncorrelated part of only a few per cent as claimed before.

Figure 6.13 shows the same as Figure 6.12 but with the reaction-dependent reduced maximum correlations. The value for the reduction is chosen to fit the width of 1 best.

See Appendix C.4.2 for the differences in the individual observable.

6.3.3 Statistical uncertainty

As claimed before, the average statistical uncertainty is smaller for observable values from the MLE method than the asymmetry method.

6.3. Comparison between the extraction methods

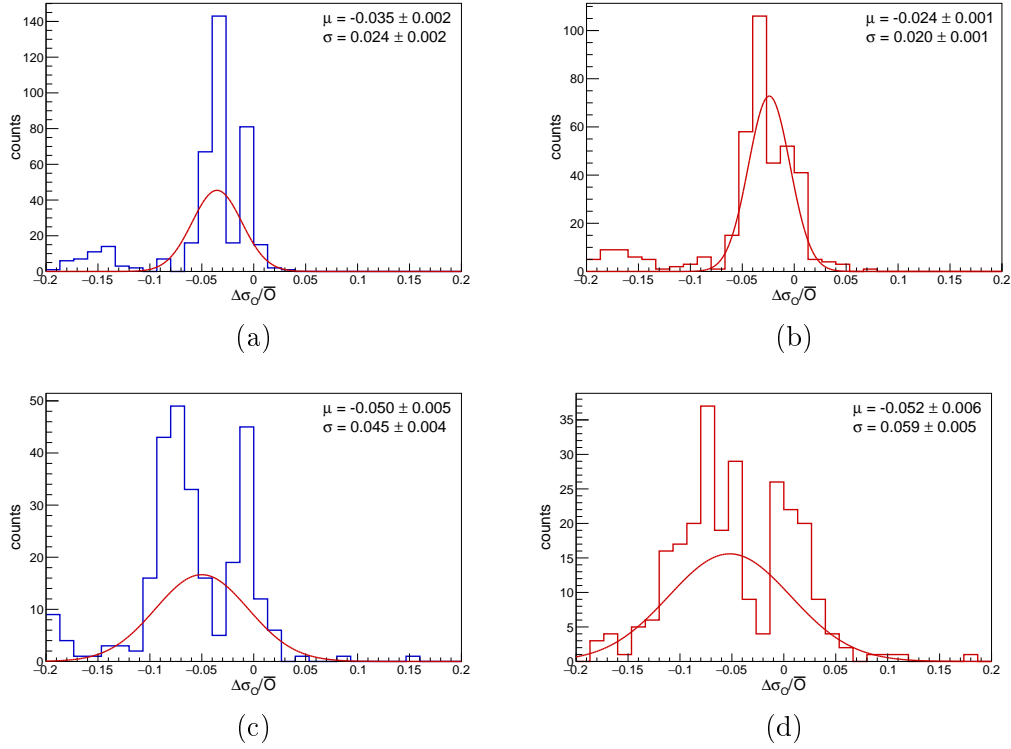


Figure 6.14: Relative difference of the statistical uncertainty between the maximum likelihood estimation method (MLE) and the asymmetry fitting method (Equation 6.23) from all observables combined in Oct2018. Shown are all reactions: (a) $\pi^0 p$, (b) $\pi^0 n$, (c) ηp and (d) ηn .

Figure 6.14 shows the relative difference between the statistical uncertainties, given by:

$$\frac{\Delta\sigma}{\bar{\sigma}} = 2 \frac{\sigma_{MLE} - \sigma_{Asym}}{\sigma_{MLE} + \sigma_{Asym}}, \quad (6.23)$$

where $\sigma_{MLE,Asym}$ are the statistical uncertainties coming from the observables extracted with the MLE and the asymmetry method. The merged data are from all four observables. To suppress outliers, only differences are taken where the relative statistical error σ_O/O is smaller than 1.

It is visible that the relative differences peak very close to 0 and that there are values on both sides, i.e. both methods have points with smaller statistical uncertainties. Nevertheless, the relative mean difference over all observables and reactions is $(-2.3 \pm 0.3)\%$, indicating smaller statistical uncertainties for MLE points.

Especially in the reactions on the proton, one might identify two peaks.

It is found that the relative uncertainty is much narrower around 0 for the T observable than for the other three. This may be due to the fitting function in the asymmetry, which is the most simple for T so that the uncertainties can be minimised best.

6.4 Systematic uncertainty

Most systematic uncertainties, i.e. detector efficiency, cut positions and branching ratio, can be omitted due to the definition of the polarisation observables. The DCS containing these uncertainties occur in the nominator and denominator in the same way (Equations 6.1-6.3).

However, systematic uncertainties need to be considered, which are discussed in the following.

6.4.1 Polarisation degrees

A major systematic uncertainty is due to the determination of the polarisation degrees. Their origin lies in the method that is used for the determination of the values themselves.

Target nucleon polarisation

As discussed in Section 5.3.1, the target polarisation degree Λ has a systematic uncertainty from the temperature and NMR measurements of $\Delta\Lambda_{T+NMR}^{rel} = \Delta\Lambda_{T+NMR}/\Lambda = 2\%$. In Oct2018, runs with a run number between 204209 and 204445 have a slightly larger one of 2.5%. The reason for this lies in the missing NMR measurement at the end of the run block. Weighting both values by the number of events, a systematic uncertainty of $\Delta\Lambda_{T+NMR}^{rel} = 2.2\%$ results.

The correction occurring from the D -wave contribution introduces an additional uncertainty of $\Delta\Lambda_{D-wave}^{rel} = \Delta\Lambda_{D-wave}/\Lambda = 1.8\%$.

Both these errors can be seen as uncorrelated. The combined uncertainty from the target polarisation degrees is therefore given by:

$$\begin{aligned} \Delta\Lambda^{rel} &= \sqrt{(\Delta\Lambda_{T+NMR}^{rel})^2 + (\Delta\Lambda_{D-wave}^{rel})^2} \\ &= \begin{cases} 2.9\%, & \text{in Oct2018} \\ 2.7\%, & \text{in Dec2021} \end{cases}. \end{aligned} \quad (6.24)$$

Beam photon polarisation

The systematic uncertainty from the beam polarisation degree δ is 5% for the incident photon energies $E_\gamma = 960\text{ MeV}$ to 1310 MeV , 8% for $E_\gamma = 690\text{ MeV}$ to 960 MeV and $E_\gamma = 1310\text{ MeV}$ to 1360 MeV and 10% for $E_\gamma = 650\text{ MeV}$ to 690 MeV Section 5.3.2). The estimation is based on the maximum difference between the data points and the ANB fit.

The systematic uncertainty from the beam polarisation degrees is therefore given by:

$$\Delta\delta^{rel} = \begin{cases} 10\%, & \text{if } 650\text{ MeV} < E_\gamma < 690\text{ MeV} \\ 8\%, & \text{if } 690\text{ MeV} < E_\gamma < 960\text{ MeV} \\ 5\%, & \text{if } 960\text{ MeV} < E_\gamma < 1310\text{ MeV} \\ 8\%, & 1310\text{ MeV} < E_\gamma < 1360\text{ MeV} \end{cases} . \quad (6.25)$$

Total polarisation

The beam asymmetry Σ and target asymmetry T only depend on one polarisation degree, whereas P and H depend on both. The determination of the linear and transverse polarisation is completely independent. Therefore, the total systematic uncertainty due to the polarisation can be calculated by Gaussian error propagation.

The relative systematic uncertainties for the individual observables are given by:

$$\Delta\Sigma_{pol}^{rel} = \Delta\delta^{rel}, \quad (6.26)$$

$$\Delta T_{pol}^{rel} = \Delta\Lambda^{rel}, \quad (6.27)$$

$$\Delta P_{pol}^{rel} = \Delta H_{pol}^{rel} = \sqrt{(\Delta\delta^{rel})^2 + (\Delta\Lambda^{rel})^2}, \quad (6.28)$$

where $\Delta\delta^{rel}$ and $\Delta\Lambda^{rel}$ values are given by Equations 6.25 and 6.24.

6.4.2 Dilution factor

As discussed in Section 5.4, the relative systematic uncertainty from the dilution factor $\Delta O_{df}^{rel} = \Delta d^{rel} = \Delta d/d$ can be calculated from the relative

systematic uncertainty of the relative target surface density scaling factor $\Delta c_t^{rel} = \Delta c_t / c_t = 12\%$ (Equation 5.22).

The uncertainty is energy- and angular-dependent and the values vary between 5% and 30%. The average relative systematic dilution factor uncertainty is around 13% over the complete kinematic range and all observables.

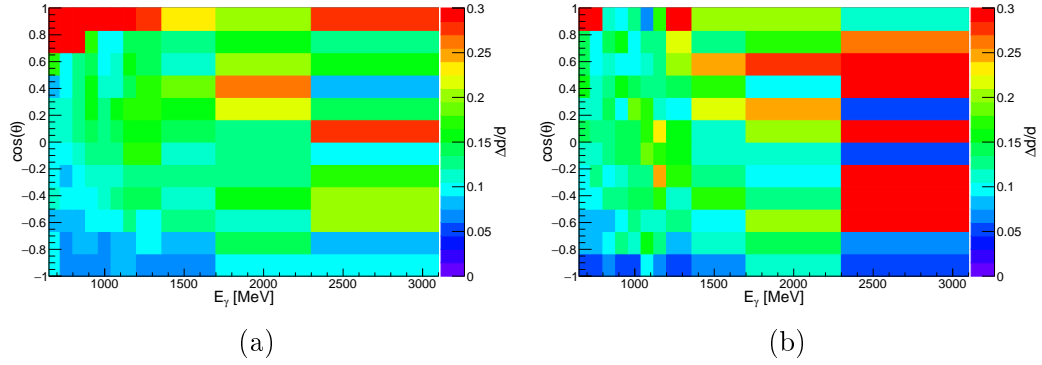


Figure 6.15: Relative systematic uncertainty of the dilution factor $\Delta d/d$ as a function of E_γ and $\cos(\theta)$ in $\pi^0 p$ (a) and $\pi^0 n$ (b) in Oct2018.

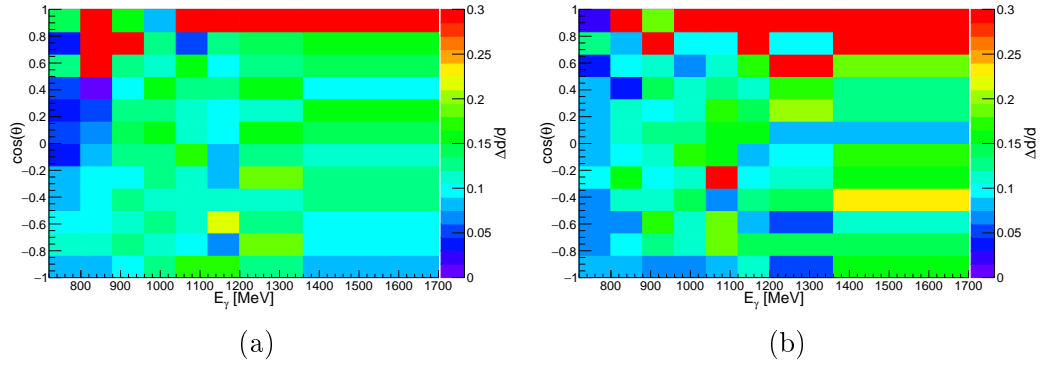


Figure 6.16: Relative systematic uncertainty of the dilution factor $\Delta d/d$ as a function of E_γ and $\cos(\theta)$ in ηp (a) and ηn (b) in Oct2018.

Figures 6.15 and 6.16 show the systematic uncertainty introduced from the dilution factor for the polarisation observables T , P and H as a function of E_γ in Oct2018. The values are very similar for all reactions. The ones from Dec2021 can be found in Appendix C.5.

6.4.3 Background contamination

Event yields used to determine the polarisation observables may contain background that originates from other reactions. The main background is assumed to be multi-meson photoproduction off nucleons where one or more particles were not detected or phase space background like direct $3\pi^0$ production in ηN with $\eta \rightarrow 6\gamma$. Also, final state interactions (FSI) are possible candidates for background in the data.

The complete Section 4.5 was about reducing background reactions while keeping as many good events as possible. However, some background events will still be a part of the final data. Everything is under control as long as this background is small and its contribution can be estimated.

Besides a correction factor for the measured observables, the absolute systematic uncertainty $\Delta O_{syst,\delta_{BG}}^{abs}$ coming from the background is given as well with Equation 5.26. A minimal possible contribution of $\delta_{BG} = 0.5\%$ is taken for all bins to be on the safe side, which results in a minimal absolute uncertainty of 0.0023.

As seen in Section 5.5, the error is directly connected to the background contamination found in Figure 4.30. Therefore, the resulting energy- and angular-dependent uncertainty is mostly below 0.5% such that this uncertainty has only a minor effect compared to the polarisation degree and the dilution factor.

6.4.4 Total systematic uncertainty

The total systematic uncertainty can be calculated with a Gaussian error propagation from the single uncertainties due to their uncorrelatedness.

A further relative systematic uncertainty is due to the polarisation planes α and β . Since this value is minimal and to a certain part included in the uncertainty of the polarisation degrees, this can be neglected.

The uncertainties from the polarisation degrees and the dilution factor are relative ones that need to be converted to absolute uncertainties. Ignoring the statistical uncertainty of the observable, one can multiply the relative uncertainties by the observables themselves. However, the statistical uncertainty σ_O needs to be considered for an appropriate treatment. Especially for small observable values with large statistical uncertainty, their systematic uncertainty

would be primarily underestimated otherwise.

The absolute systematic uncertainty of an observable O is given by the convolution of the relative error function and the normal distribution \mathcal{N} :

$$\Delta O_{syst}^{abs} = \int_{-5\sigma_O}^{5\sigma_O} \Delta O_{syst}^{rel} \cdot |O - x| \cdot \mathcal{N}(0, \sigma_O) dx. \quad (6.29)$$

The normal distribution $\mathcal{N}(0, \sigma_O)$ is further given by:

$$\mathcal{N}(0, \sigma_O) = \frac{1}{\sqrt{2\pi\sigma_O^2}} \exp\left(-\frac{x^2}{2\sigma_O^2}\right) \quad (6.30)$$

and depends on the integrated variable x .

Generally, the integral is made over the whole space. To ensure a proper treatment without introducing additional systematic uncertainties, it is sufficient to take a range of $\pm 5\sigma_O$, which is on the level of 0.5 ppm (parts per million).

The relative observable uncertainties are given by:

$$\Delta \Sigma_{syst}^{rel} = \Delta \Sigma_{pol}^{rel}, \quad (6.31)$$

$$\Delta T_{syst}^{rel} = \sqrt{(\Delta T_{pol}^{rel})^2 + (\Delta d^{rel})^2}, \quad (6.32)$$

$$\Delta P_{syst}^{rel} = \Delta H_{syst}^{rel} = \sqrt{(\Delta P_{pol}^{rel})^2 + (\Delta d^{rel})^2}, \quad (6.33)$$

where $\Delta P_{pol}^{rel} = \Delta H_{pol}^{rel}$.

In the end, the total uncertainty is given by:

$$\Delta O = \sqrt{(\Delta O_{pol}^{abs})^2 + (\Delta O_{df}^{abs})^2 + (\Delta O_{syst, \delta_{BG}}^{abs})^2}. \quad (6.34)$$

Table 6.2 gives an overview of the average values for the different systematic uncertainties in this experiment.

All E_γ and $\cos(\theta)$ dependent systematic uncertainties for the four polarisation observables Σ_{but} , T , P and H in all investigated reactions are shown in the final results as grey histograms in Section 7 and as numerical values in Appendix D.6 and D.7.

Figure 6.17 shows the comparison between systematic and statistical uncertainties. For each reaction, the data from all four polarisation observables are

	$\Delta\Sigma_{\text{syst}}$ [%]	ΔT_{syst} [%]	ΔP_{syst} [%]	ΔH_{syst} [%]
<i>Target pol.</i>	-		2.9	
<i>Beam pol.</i>	5.4	-		5.4
Total pol.	5.4	2.9		6.1
Dilution factor	-		12.5 – 13.8	
Background contr.			0.5 – 1.1	
Total	5.7 – 5.8	12.9 – 14.4	14.2 – 15.0	14.2 – 15.3

Table 6.2: Overview of the relative, average E_γ and $\cos(\theta)$ dependent systematic uncertainties in Oct2018. Some values depend on the kinematic range and the reaction, where no significant differences are observed. The values are all relative except the background contribution (but also given in %).

shown. The statistical uncertainty drives these data. Only for $\pi^0 p$ some points around the $\Delta O_{\text{syst}} = \Delta O_{\text{stat}}$ line can be seen, where the average statistical uncertainty increases from $\pi^0 p$ to $\pi^0 n$ to ηp to ηn . The points from the double polarisation P and H are shifted towards higher statistical uncertainties than those from Σ and T . The systematic uncertainty for the beam asymmetry is smaller than that for the other three observables. The origin of this lies in the systematic uncertainty of the dilution factor, dominating for T , P and H .

The comparison between systematic and statistical uncertainties for the combined results from both beam times merged can be found in Appendix C.4.3. Even though the linear polarisation degrees are not final, the figures show how small the statistical uncertainty will get. The values for T should be valid, though.

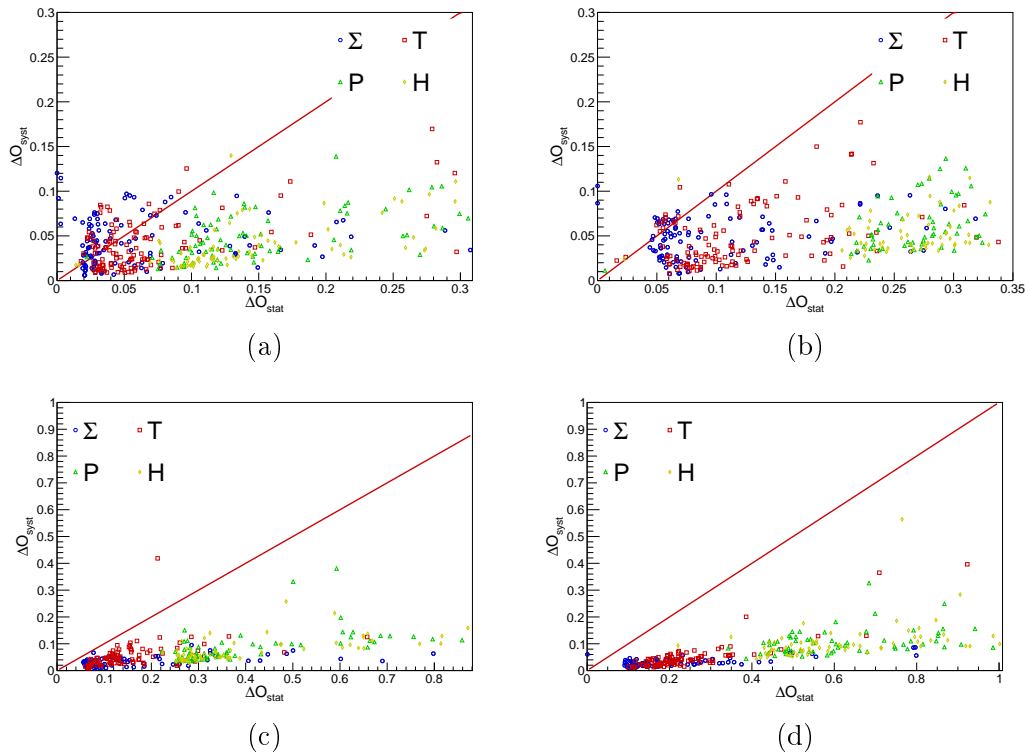


Figure 6.17: Comparison between systematic and statistical uncertainties in $\pi^0 p$ (a), $\pi^0 n$ (b), ηp (c) and ηn (d) in Oct2018. The red line indicates $\Delta O_{syst} = \Delta O_{stat}$.

7 | Results

The final results for the polarisation observables Σ_{but} , T , P and H in π^0 and η photoproduction off quasifree nucleons are shown and discussed in this chapter.

It starts with the two Sections 7.1 and 7.2 that compare the $\eta \rightarrow 2\gamma$ decay channel with the $\eta \rightarrow 3\pi^0 \rightarrow 6\gamma$ once more and the results from the two beam times, respectively.

The follow-up Sections 7.3, 7.4, 7.5 and 7.6 discuss the individual observables separately as a function of $\cos(\theta)$ for fixed incident photon energies E_γ and fixed CM energies W . Since the latter is reconstructed from the final state, no Fermi momentum smearing is visible anymore. Remember, θ is the polar angle of the meson in the CM system. The data will be compared to existing high statistical experiments and partial wave analyses (PWA). Section 7.3 also discusses how the results are presented in more detail.

As mentioned in the motivation, the observed narrow structure in ηn around $W = 1.68 \text{ GeV}$ is of particular interest. Section 7.8 provides a more detailed discussion about the structure.

To distinguish the reactions already with the naked eye, the photoproduction results on the proton are shown in blue and on the neutron in red.

Because the linear beam polarisation degrees could not be determined finally by the time this work is written, only preliminary results are possible for Σ_{but} , P and H . Therefore, the final results for these observables only use Oct2018 beam time data. Nevertheless, the target asymmetry T can be determined by taking the merged data from both beam times.

The numerical values can be found in data tables in Appendix D.6. These only include Oct2018 beam time data, whereas Appendix D.7 shows the data tables for the target asymmetry T of the merged full data from both beam times.

7.1 Comparison of η decay channels

Both η decay channels should give the same results. To ensure that the merging of both decay channels is physically valid, it is important to check if the analysis results in the same values for both decay channels.

Figures 6.2 and 6.3 already showed a direct comparison between the two decay channels. However, it is hard to state the quality of the agreement. A more scientific approach uses the normalised difference between the values given by:

$$\frac{\Delta O}{\Delta \sigma} = \frac{O_{\eta \rightarrow 2\gamma} - O_{\eta \rightarrow 6\gamma}}{\sqrt{\sigma_{\eta \rightarrow 2\gamma}^2 + \sigma_{\eta \rightarrow 6\gamma}^2}} \sim \mathcal{N}(0, 1), \quad (7.1)$$

where O are the observables, σ their error and $\mathcal{N}(0, 1)$ is the normal distribution with mean 0 and standard deviation 1. In contrast to Equation 6.21, there is no correlation factor ρ here since the two compared values are fully independent. The distribution should therefore end up in a normal distribution. Although the analysis is - ignoring the η reconstruction - nearly the same for both decay channels, the analysis takes very different events with different particles where no correlation is expected.

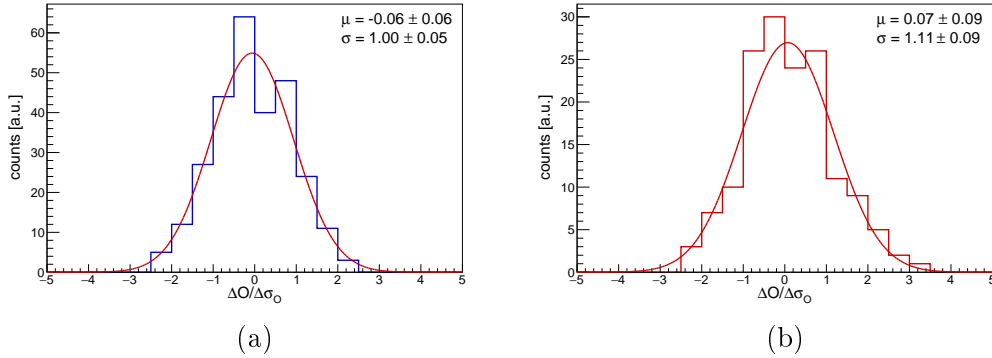


Figure 7.1: Error normalised difference (Equation 7.1) of all observables in the two decay channels of η on the proton (a) and the neutron (b) are shown together with a Gaussian fit function and its extracted mean μ and standard deviation σ .

Figure 7.1 shows the comparison between the two decay channels for proton and neutron. The data from all four observables are taken together.

The mean position is in perfect agreement with 0 for both reactions. No

systematic drive towards a decay channel is visible. The standard deviation is slightly too large for the neutron. Considering the low statistics in ηn with $\eta \rightarrow 6\gamma$, the reason may lie in statistical fluctuations.

The results, together with the visible agreement of both decay channels in Figures 6.2 and 6.3, show a good agreement for the results from both decay channels and both nucleons.

7.2 Comparison of beam times

The linear polarisation degrees could not finally be determined when this work was written. Therefore, observables that depend on the linear beam polarisation, i.e. Σ_{but} , P and H , cannot be determined finally. However, the target asymmetry T is independent of the linear beam polarisation degrees and can be extracted.

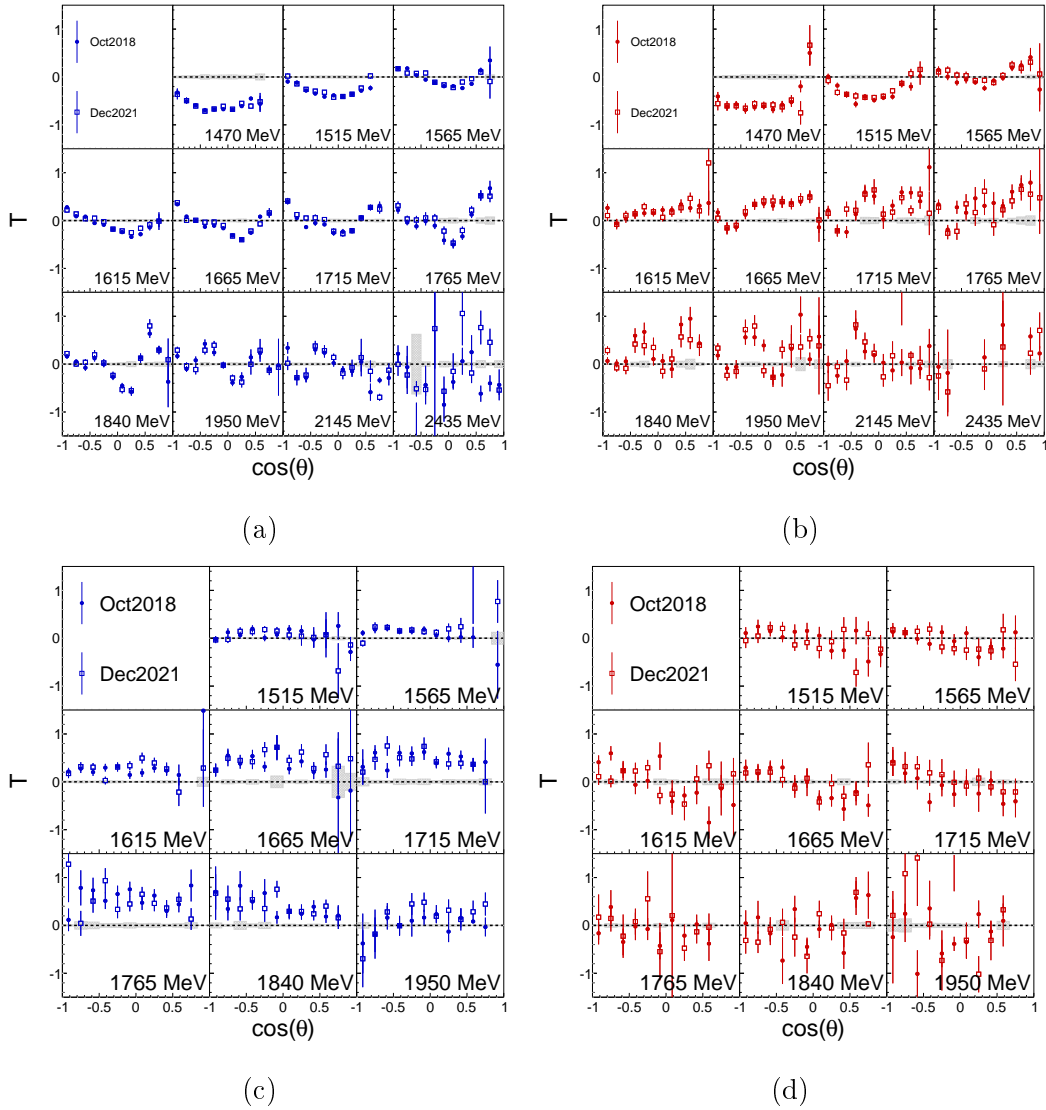


Figure 7.2: Target asymmetry T as a function of $\cos(\theta)$ for fixed centre of mass energies W in $\pi^0 p$ (a), $\pi^0 n$ (b), ηp (c) and ηn (d). Results from Oct2018 are compared to Dec2021 ones.

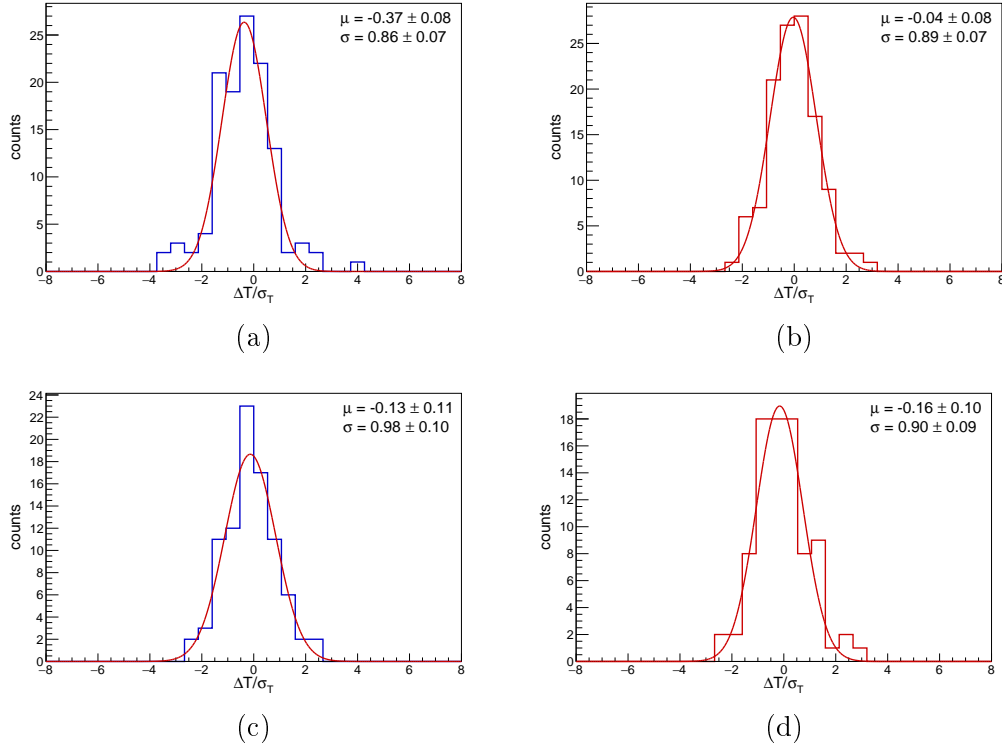


Figure 7.3: Error normalised difference $\Delta T/\sigma_T = (T_{Oct2018} - T_{Dec2021})/\sqrt{\sigma_{Oct2018}^2 + \sigma_{Dec2021}^2}$ between the target asymmetry values from Oct2018 and Dec2021 beam time in $\pi^0 p$ (a), $\pi^0 n$ (b), ηp (c) and ηn (d).

Figure 7.2 shows the target asymmetry T extracted from the Oct2018 beam time compared to the Dec2021 one. The data are in good agreement with each other. Their average difference is centred around 0 in all reactions except $\pi^0 p$, where a slight deviation is visible, i.e. Dec2021 data points are slightly smaller compared to Oct2018 ones. However, within the systematic uncertainty, they are still in excellent agreement.

Figure 7.3 shows the variance weighted difference between the target asymmetry results from both beam times. Since the experiments are independent of each other, this should result in a normal distribution $\mathcal{N}(0, 1)$, analogue to Equation 7.1 with Oct2018 and Dec2021 replacing $\eta \rightarrow 2\gamma$ and $\eta \rightarrow 6\gamma$. Except for $\pi^0 p$, they agree with a mean of 0 or are only slightly off. The same is true for the standard deviations that agree with 1 or very close to it. Looking at the absolute values, i.e. simple difference, in $\pi^0 p$, one finds a value of -0.010 ± 0.013 (Gaussian fit) and -0.013 ± 0.008 (mean) showing that the values

are still in agreement with each other. Including the systematic uncertainty, they firmly agree. Therefore, no further corrections or systematic uncertainties are included at this point.

Preliminary results for Σ_{but} , P and H in Dec2021 can be found in Appendix D.1. Although the linear beam polarisation degrees are not determined finally, the data's agreement is quite good over a large kinematic region. Furthermore, preliminary results from the merged data of both beam times can be found in Appendix D.1 as well. This should mainly illustrate the statistical uncertainty that is expected in the end. Even though the observable values from Dec2021 (except T) may still slightly change, the statistical uncertainty is not expected to be affected.

7.3 Beam asymmetry Σ_{but}

The following figures show the results for the beam asymmetry Σ_{but} in π^0 and η photoproduction on quasifree nucleons as a function of $\cos(\theta)$ for fixed incident photon energies E_γ (Figure 7.4) and fixed CM energies W (Figures 7.5-7.8).

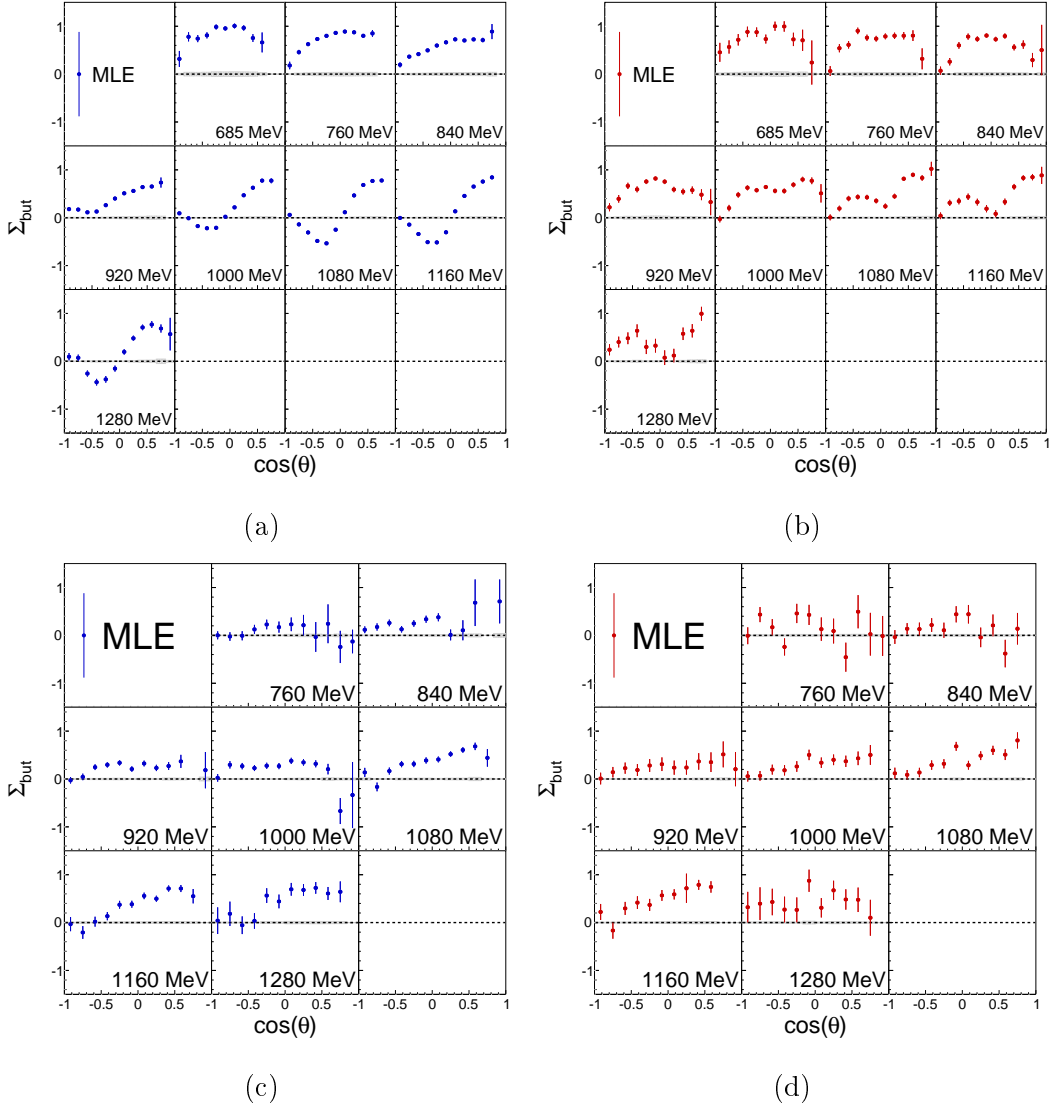


Figure 7.4: Beam asymmetry Σ_{but} as a function of $\cos(\theta)$ for fixed photon energies E_γ in the reactions $\gamma p \rightarrow \pi^0 p$ (a), $\gamma n \rightarrow \pi^0 n$ (b), $\gamma p \rightarrow \eta p$ (c) and $\gamma n \rightarrow \eta n$ (d).

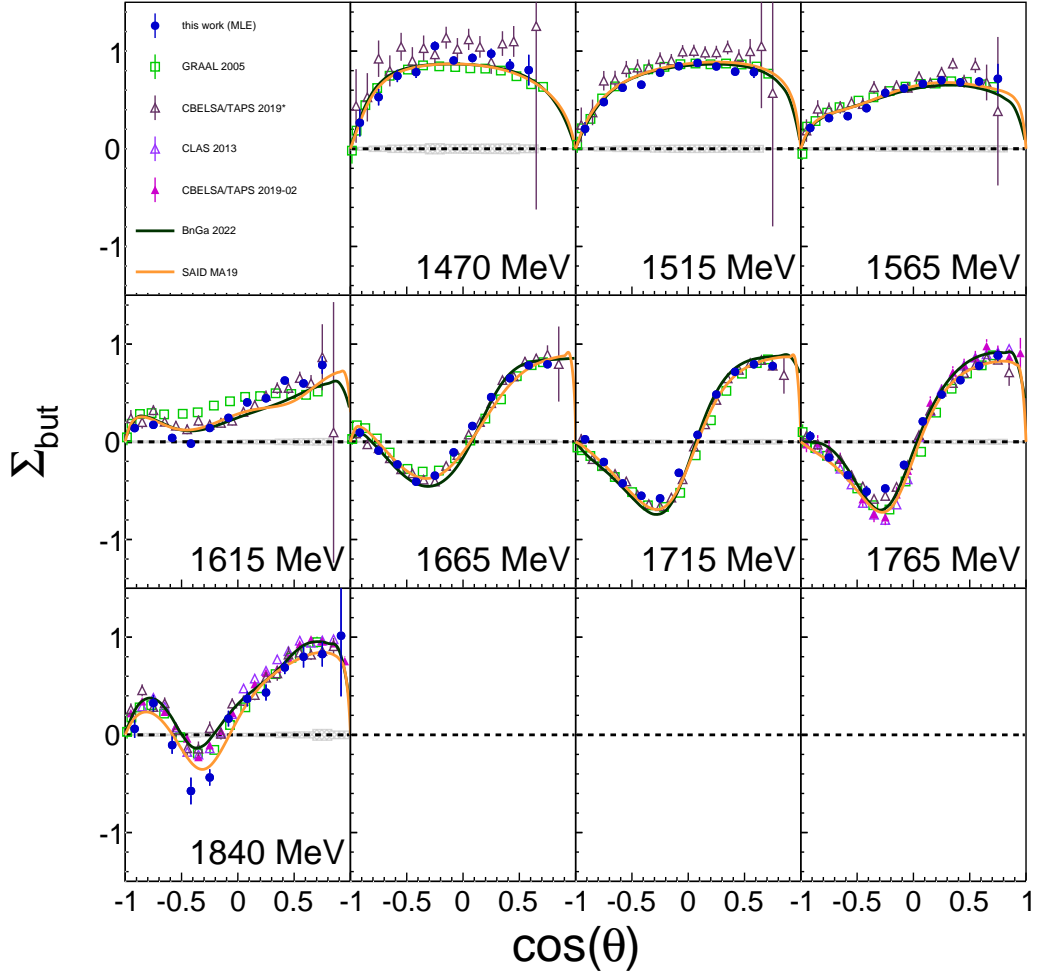


Figure 7.5: Beam asymmetry Σ_{but} as a function of $\cos(\theta)$ for fixed centre of mass energies W in the reaction $\gamma p \rightarrow \pi^0 p$. The data are compared with GRAAL 2005 [150], CLAS 2013 [149], CBELSA/TAPS 2019 [144] and CBELSA/TAPS 2019-02 [143] data and to BnGa 2022 [126] and SAID MA19 [121] partial wave analysis.

Shown are the data that were extracted with the MLE method. As discussed in Section 6.3.3, the statistical uncertainties are slightly smaller for the extracted polarisation observables than for the asymmetry one.

The error bars of the MLE points show the statistical uncertainty only, whereas the systematic uncertainty (Section 6.4) is shown as a grey histogram around the 0 line. The former is always larger than the latter, except for some energy bins in π^0 around high beam photon polarisation degrees (Section 5.3.2), i.e. around $W = 1665$ MeV ($E_\gamma = 1000$ MeV).

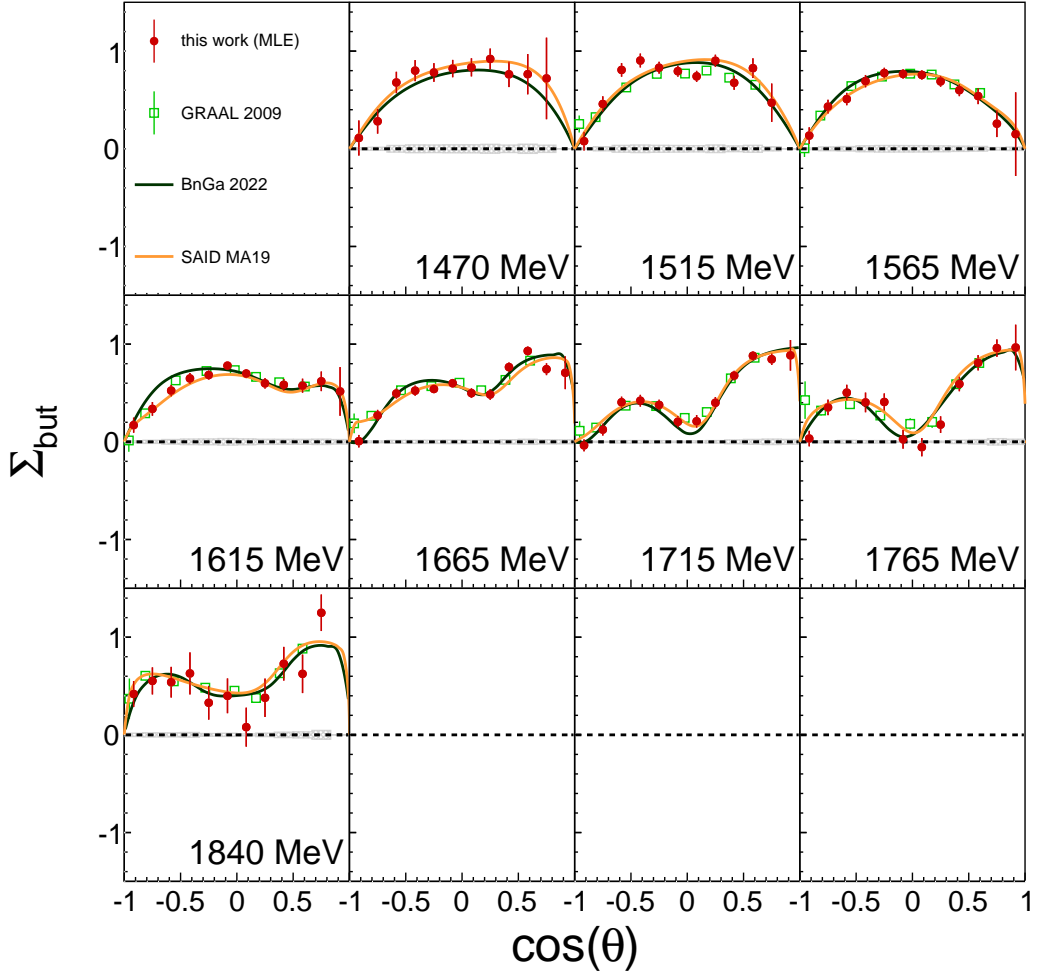


Figure 7.6: Beam asymmetry Σ_{but} as a function of $\cos(\theta)$ for fixed centre of mass energies W in the reaction $\gamma n \rightarrow \pi^0 n$. The data are compared with GRAAL 2009 [232] data and to BnGa 2022 [126] and SAID MA19 [121] partial wave analysis.

The beam asymmetry Σ_{but} is well suited to check if the analysis is working fine or if unexpected systematic uncertainties occur. Previous data exist for all reactions, and the PWA can describe these quite well. The results of this work are compared to previous data - all done on free protons - and PWA predictions in the results for fixed CM energies W . Here, the target material is dButanol with quasifree nucleons bound in deuterium. Also, remember that possible background reactions off carbon and oxygen cannot be distinguished from deuterium reactions and, therefore, cannot be subtracted. Σ_{but} is shown,

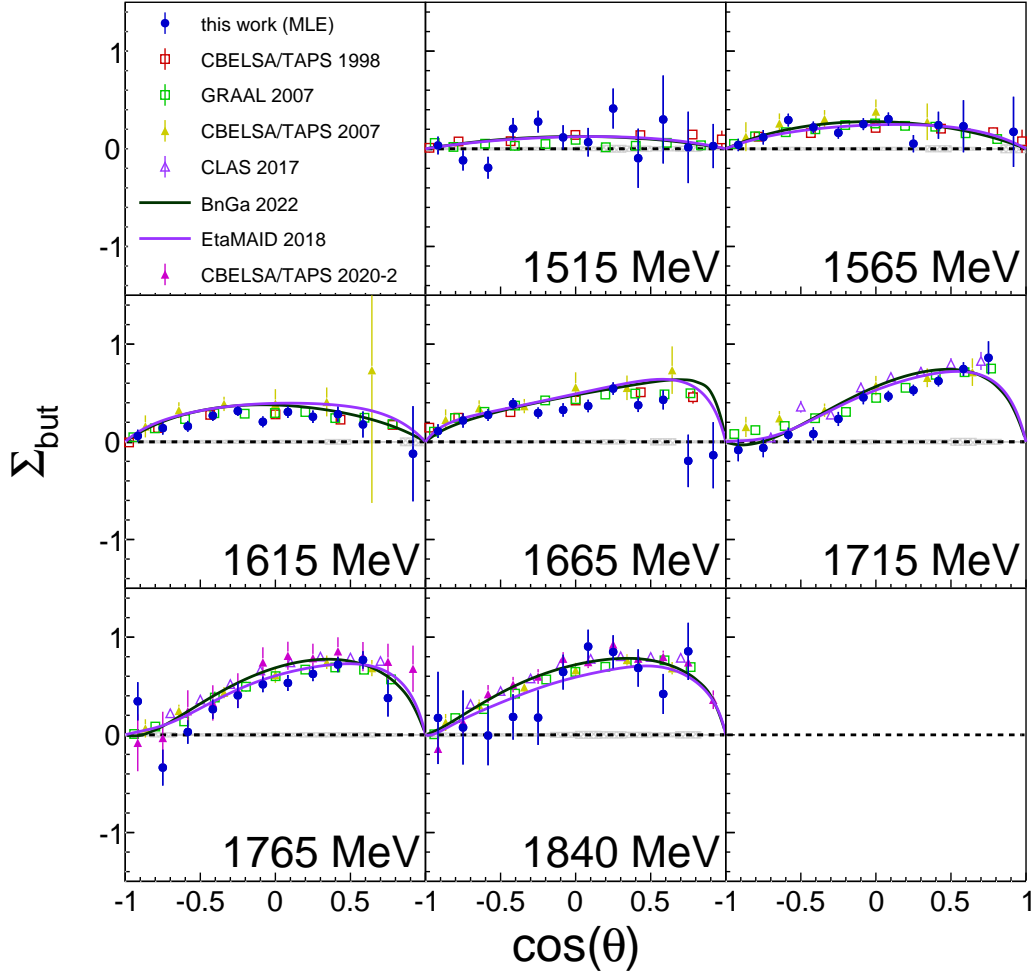


Figure 7.7: Beam asymmetry Σ_{but} as a function of $\cos(\theta)$ for fixed centre of mass energies W in the reaction $\gamma p \rightarrow \eta p$. The data are compared with CBELSA/TAPS 1998 [239], CBELSA/TAPS 2007 [234], GRAAL 2007 [238], CLAS 2017 [237] and CBELSA/TAPS 2020-2 [235] data and to BnGa 2022 [126] and EtaMAID 2018 [122] partial wave analysis.

which may still have background contributions.

The existing data from other experiments are adjusted to make the comparison easier. Whenever possible, previous results are adjusted with the overlapping bin average method (Section 5.7.4). Because the exact energy bin widths of the GRAAL data [150, 232, 238, 243] are unknown, their points are adjusted with the linear averaging method (Section 5.7.3). Their results are expected to be less exact, especially in kinematic regions where the observable changes strongly.

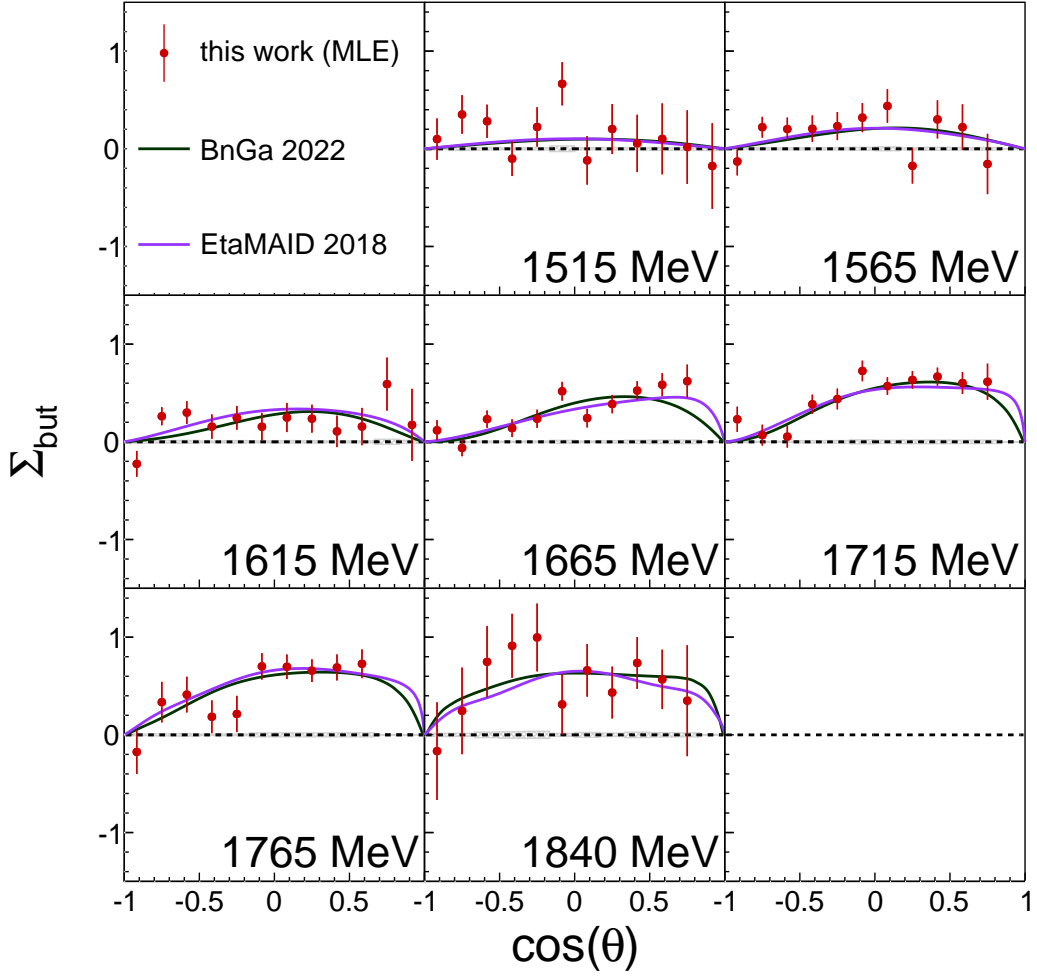


Figure 7.8: Beam asymmetry Σ_{but} as a function of $\cos(\theta)$ for fixed centre of mass energies W in the reaction $\gamma n \rightarrow \eta n$. The data are compared with GRAAL 2008 [243] data and to BnGa 2022 [126] and EtaMAID 2018 [122] partial wave analysis.

Data from $\pi^0 p$ are compared to previous data from GRAAL [150], CLAS [149] and two CBELSA/TAPS experiments [143,144]. The latter used the same accelerator and detector setup as this work does. Therefore, some systematic uncertainties might be the same. However, the target material was different and after the PED reconstruction with EXPLORA, different programmes with different methods were used.

It is essential to mention that the CBELSA/TAPS 2019 data in $\pi^0 p$ [144] are preliminary, i.e. not finalised and published. Because they are in a near-

to-finish state and cover an extensive kinematic range, they are shown as a comparison nevertheless.

The GRAAL data have the smallest uncertainties and measure the beam asymmetry with a completely different method. They are, therefore, excellent for an independent check. The data from this work perfectly agree with the two previous experiments. In some kinematic regions, the difference is more than one standard deviation away, but not unexpectedly many. The exception of the excellent agreement is the energy $W = 1615$ MeV, where especially the GRAAL data have a different shape. The fast-changing beam asymmetry can explain this in this region and the available GRAAL energies of $W = 1600$ MeV and $W = 1620$ MeV. Here, a wider energy binning of 50 MeV is used such that the data of this work average over a relatively large range.

Data from $\pi^0 n$ are compared to previous data from GRAAL [232] only. They agree with the one from this work in all kinematic regions. In contrast to $\pi^0 p$, the beam asymmetry does not change that fast around $W = 1615$ MeV such that the agreement also holds. This also confirms the assumption that the disagreement at this energy in $\pi^0 p$ is due to the fast-changing beam asymmetry.

Several high statistics measurements exist of the beam asymmetry in ηp . Three of the existing data were performed within the CBELSA/TAPS collaboration [234, 235, 239], i.e. using the same accelerator and similar detector setup. However, all these data were taken before the CB upgrade from QDC to SADC readout, unable to use the main spectrometer in the first level trigger system. Besides CBELSA/TAPS data, results from CLAS [237] and GRAAL [238] are shown for comparison. The data from this work are in agreement with all existing data. The statistical uncertainty, and therefore the fluctuations, are larger than for the compared data.

Also, ηn data are compared with GRAAL [243] and as for the other reactions, they agree with each other. The fluctuation is even larger than for ηp due to the lower statistics, but the structure is still clearly visible.

The data comparison with different PWA is also shown in Figures 7.5-7.8. BnGa [119] is the only model that is available for all four reactions, whereas SAID [121] is given for $\pi^0 N$ and EtaMAID [122] for ηN only. It is essential to mention that none of the models include any of the data from this work yet. As the shape of the beam asymmetry for $\pi^0 N$ and ηN has been known for quite some time, all three models agree over a large kinematic range with

each other and with the existing world data.

Because MAID 2021 is not finalised [120] and the previous MAID 2007 [127] is pretty old, ignoring the high statistics data from the last decade, the MAID model is not included in the figures for comparison. However, many kinematic regions look promising as well.

Comparing the proton with neutron data, the shape of the beam asymmetry is similar for the ηN final states but start to change significantly for $\pi^0 N$.

7.4 Target asymmetry T

Hereinafter, the results for the target asymmetry T in π^0 and η photo-production on quasifree nucleons are shown as a function of $\cos(\theta)$ for fixed incident photon energies E_γ (Figure 7.9) and fixed CM energies W (Figures 7.10-7.13). The results are shown for the merged full statistics data from both beam times. The results from Oct2018 alone can be found in Appendix D.2.

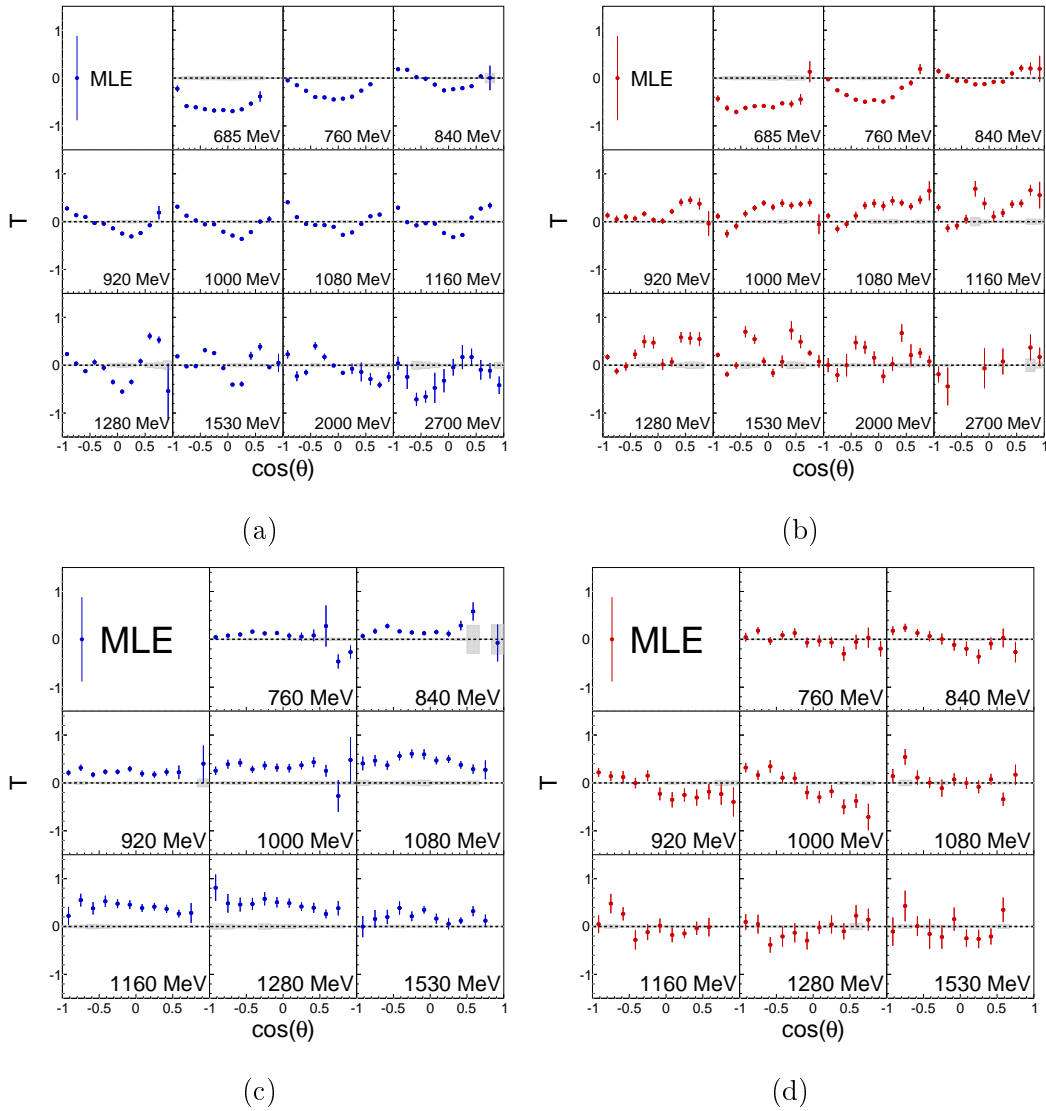


Figure 7.9: Target asymmetry T as a function of $\cos(\theta)$ for fixed photon energies E_γ in the reactions $\gamma p \rightarrow \pi^0 p$ (a), $\gamma n \rightarrow \pi^0 n$ (b), $\gamma p \rightarrow \eta p$ (c) and $\gamma n \rightarrow \eta n$ (d). The merged full data from both beam times are shown.

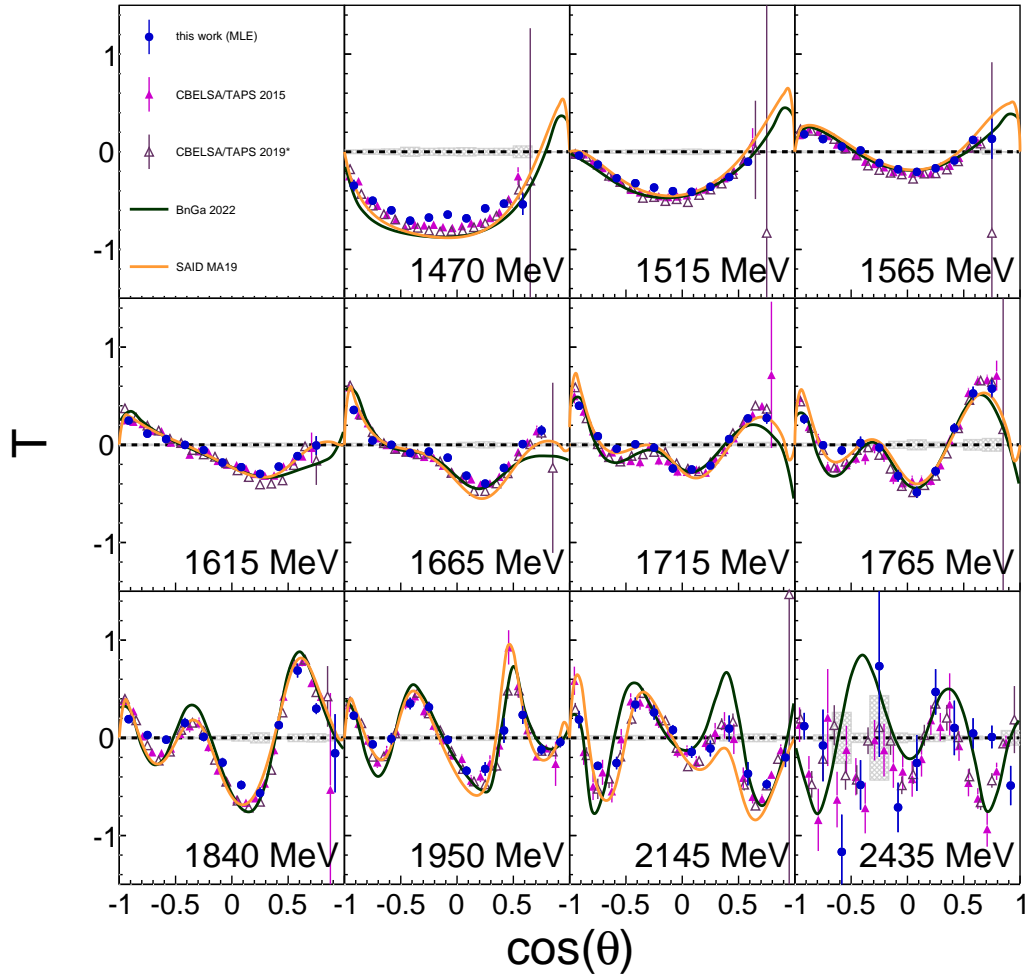


Figure 7.10: Target asymmetry T as a function of $\cos(\theta)$ for fixed centre of mass energies W in the reaction $\gamma p \rightarrow \pi^0 p$. The merged full data from both beam times are shown. The data are compared with CBELSA/TAPS 2015 [142] and CBELSA/TAPS 2019 [144] data and to BnGa 2022 [126] and SAID MA19 [121] partial wave analysis.

As for the beam asymmetry, the statistical uncertainties are larger than the systematic ones except for some kinematic ranges in $\pi^0 p$, e.g. $W = 1515$ MeV.

Besides comparison with previous data for the reactions on protons, it is the first time that results for the neutron are shown. The two reactions $\pi^0 p$ and ηp can verify if the analysis works fine for the target asymmetry.

As for all reference data except GRAAL, the ones shown here are adjusted with the energy overlapping bin average method (Section 5.7.3).

Reaction $\pi^0 p$ is compared to CBELSA/TAPS data from 2015 [142] and

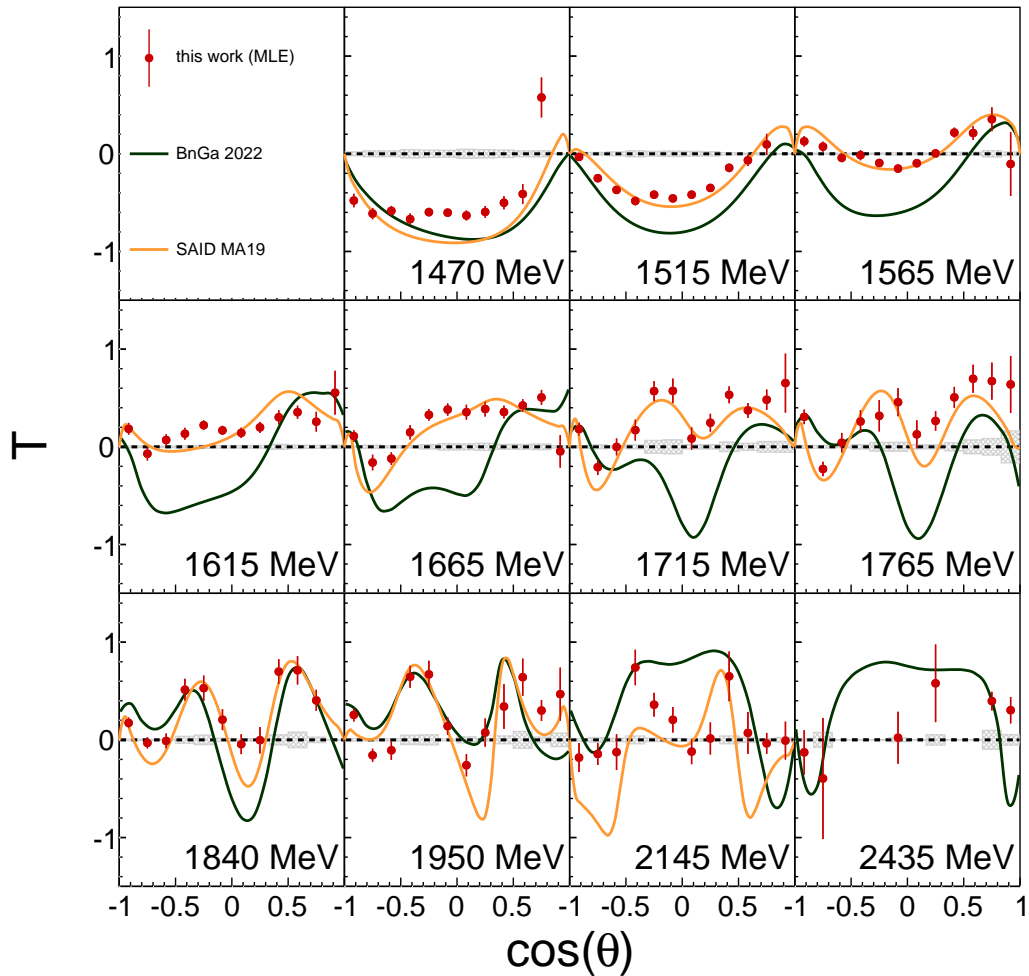


Figure 7.11: Target asymmetry T as a function of $\cos(\theta)$ for fixed centre of mass energies W in the reaction $\gamma n \rightarrow \pi^0 n$. The merged full data from both beam times are shown. The data are compared with BnGa 2022 [126] and SAID MA19 [121] partial wave analysis.

2019 [144] that used the Crystal Barrel/TAPS detector setup before the CB upgrade from QDC to SADC readout. Again, the CBELSA/TAPS 2019 data [144] are preliminary, i.e. not finalised and published. Because they are in a near-to-finish state and cover an extensive kinematic range, they are shown as a comparison nevertheless.

Over all kinematic ranges, the results are in excellent agreement with the previous ones. For the two lowest energies $W = 1470$ MeV and $W = 1515$ MeV a few points do not agree within 1σ with previous results around $\cos(\theta) = 0$.

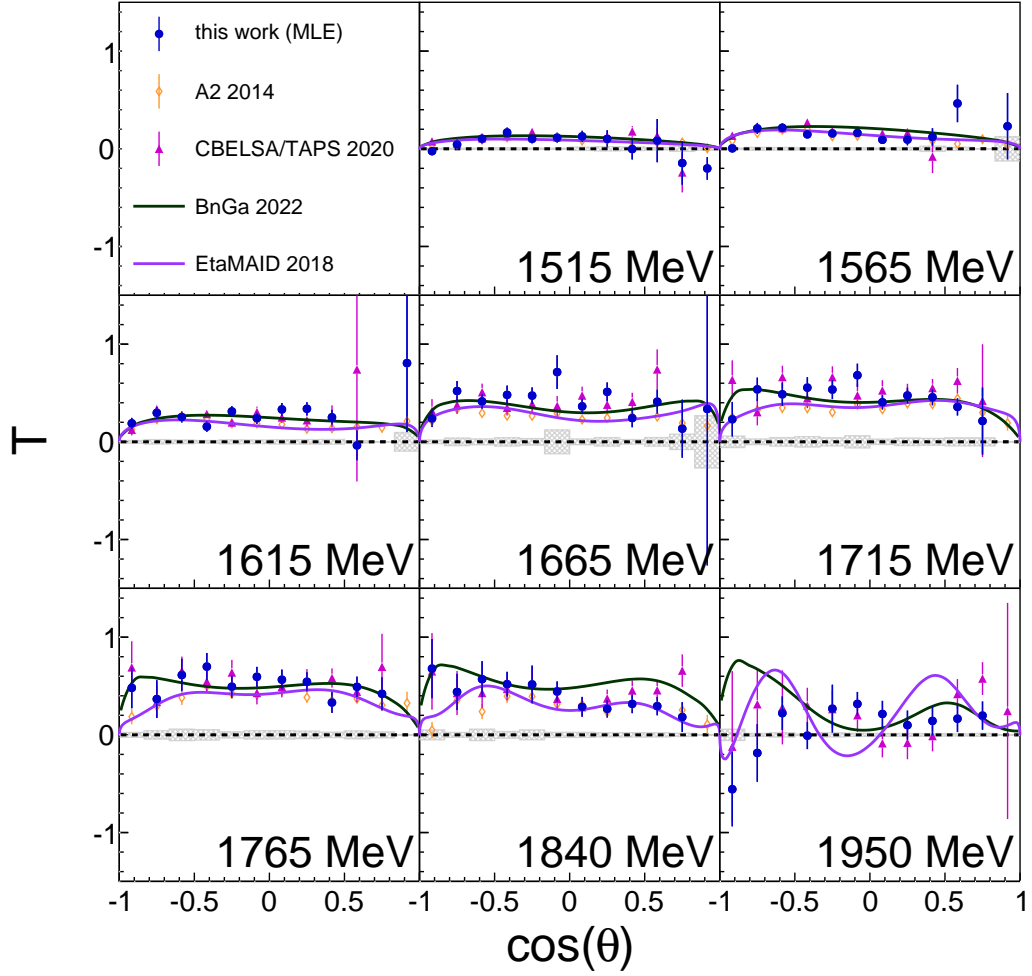


Figure 7.12: Target asymmetry T as a function of $\cos(\theta)$ for fixed centre of mass energies W in the reaction $\gamma p \rightarrow \eta p$. The merged full data from both beam times are shown. The data are compared with A2 2014 [236] and CBELSA/TAPS 2020 [119] data and to BnGa 2022 [126], BnGa 2022 (b) [332] and EtaMAID 2018 [122] partial wave analysis.

The photon tagging is not that stable at the beginning of that energy range around $E_\gamma = 650$ MeV, which could explain these fluctuations or they might be statistical fluctuations.

The results for ηp are compared to A2 [236] and CBELSA/TAPS [119] data, where former have the best statistics. The statistical uncertainty, and therefore the fluctuations, are larger than for $\pi^0 p$. Nevertheless, the agreement between the data of this work and the two other experiments is good. This is somewhat surprising since the CBELSA/TAPS data lie systematically higher

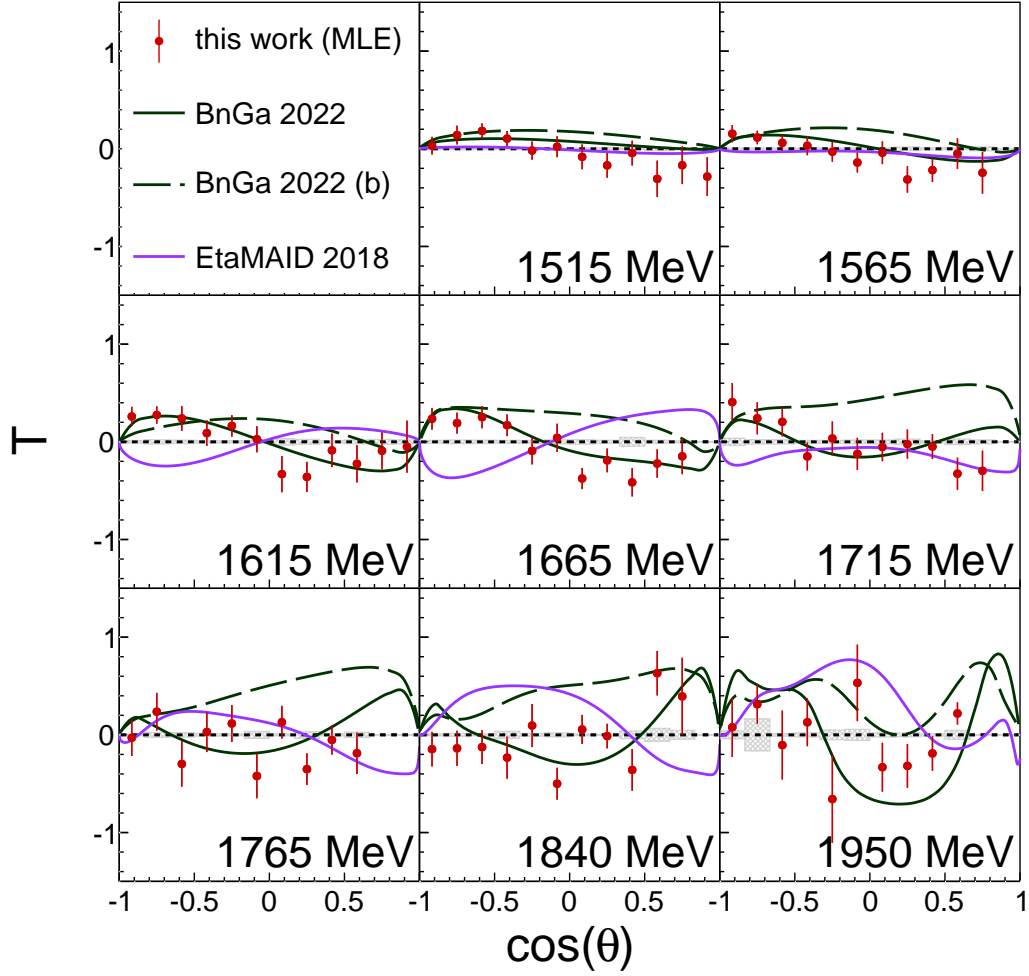


Figure 7.13: Target asymmetry T as a function of $\cos(\theta)$ for fixed centre of mass energies W in the reaction $\gamma n \rightarrow \eta n$. The merged full data from both beam times are shown. The data are compared with BnGa 2022 [126] and EtaMAID 2018 [122] partial wave analysis.

than the A2 one, by about 40% [262].

The difference between the target observable values normalised to the uncertainty can be seen in Figure 7.14. The explicitly calculated quantity is equal to Equation 6.21 without a correlation factor. Thereby, the data of this work is the first observable and the reference one is the second. The experiments are conducted independently such that no larger systematic drift towards one or another direction is expected. However, the T values from this work lie between the two existing ones. The average absolute difference is 0.08 ± 0.02 (Gaussian

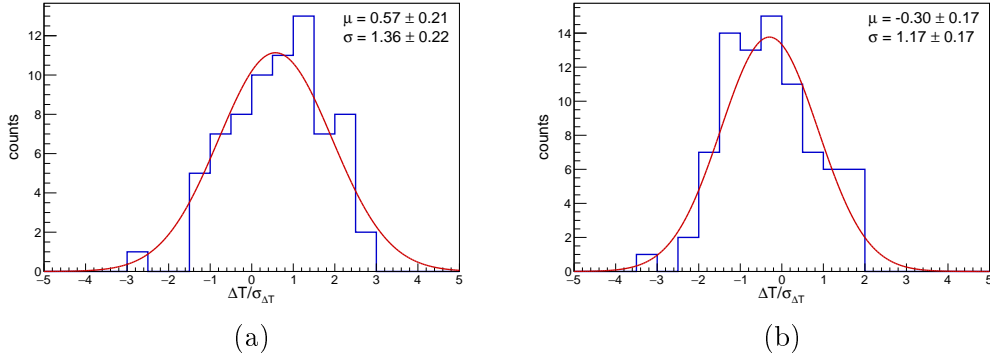


Figure 7.14: Difference between the T observable values from this work to the A2 data [236] (a) and CBELSA/TAPS data [119] (b) normalised to the uncertainty $\sigma_{\Delta T} = \sqrt{\sigma_1^2 - \sigma_2^2}$, where $\sigma_{1,2}$ are the uncertainties of this work (1) and the compared data (2), respectively.

fit) for the A2 data and -0.05 ± 0.02 (Gaussian fit) for the CBELSA/TAPS data. The first are about 18% lower and the latter about 15% higher than the data shown here.

The comparison of the data with the PWA and the PWA among each other do not agree as well as for the beam asymmetry. This indicates a lack of data for the PWA input to constrain resonance parameters. SAID [121] is in best agreement with $\pi^0 p$ and $\pi^0 n$ and can describe the data very well in large parts of the kinematic regions.

BnGa [119] describes $\pi^0 p$ as good as SAID but fails in $\pi^0 n$. Especially the backward region starting at 1565 MeV cannot be described. One possible explanation lies in the input data used for the PWA. SAID includes some more recent data of Σ in $\gamma n \rightarrow \pi^0 n$ from A2 [233] and E in $\gamma n \rightarrow p\pi^-$ from CLAS [333] that are excluded in BnGa yet. See [63] for an excellent overview of which data are included in which PWA.

Looking at ηp and ηn , BnGa is in much better agreement with the data. Especially the shape around 1665 MeV can almost be reproduced. The agreement in ηN and the disagreement in $\pi^0 n$ indicate a problem with Δ resonances and their treatment, where N^* resonances are included acceptably.

In ηn , a second BnGa 2022 model is shown, BnGa 2022 (b) [332], which describes the narrow structure around $W = 1.68$ GeV with an additional P_{11} resonance. On the other hand, the default BnGa 2022 solution describes the structure as interference between two S waves. See Section 7.8 for a detailed

discussion.

EtaMAID [122] could describe the beam asymmetry in ηp and ηn quite good also describes T in ηp quite good, with a remarkable agreement with the high statistics A2 data [236]. However, the PWA fails regarding the predictions of T in ηn . In the lower energy range, which is strongly influenced by the $N(1535)1/2^-$ resonance, EtaMAID has no difficulties for the description, but going towards the observed narrow structure around $W = 1665$ MeV the PWA predicts an entirely different shape. This indicates the importance of this experiment for solving the puzzle of that narrow structure. Section 7.8 discusses this narrow structure in great detail.

The target asymmetry T looks similar in the lower energy regime for both π^0 and η , where their shapes start to get very different for higher energies. Most different resonances and interferences between them play an essential role when going towards higher energies and regions where no single resonance dominates.

7.5 Recoil asymmetry P

This section shows the recoil asymmetry P in π^0 and η photoproduction on quasifree nucleons as a function of $\cos(\theta)$ for fixed incident photon energies E_γ (Figure 7.15) and fixed CM energies W (Figures 7.16-7.19).

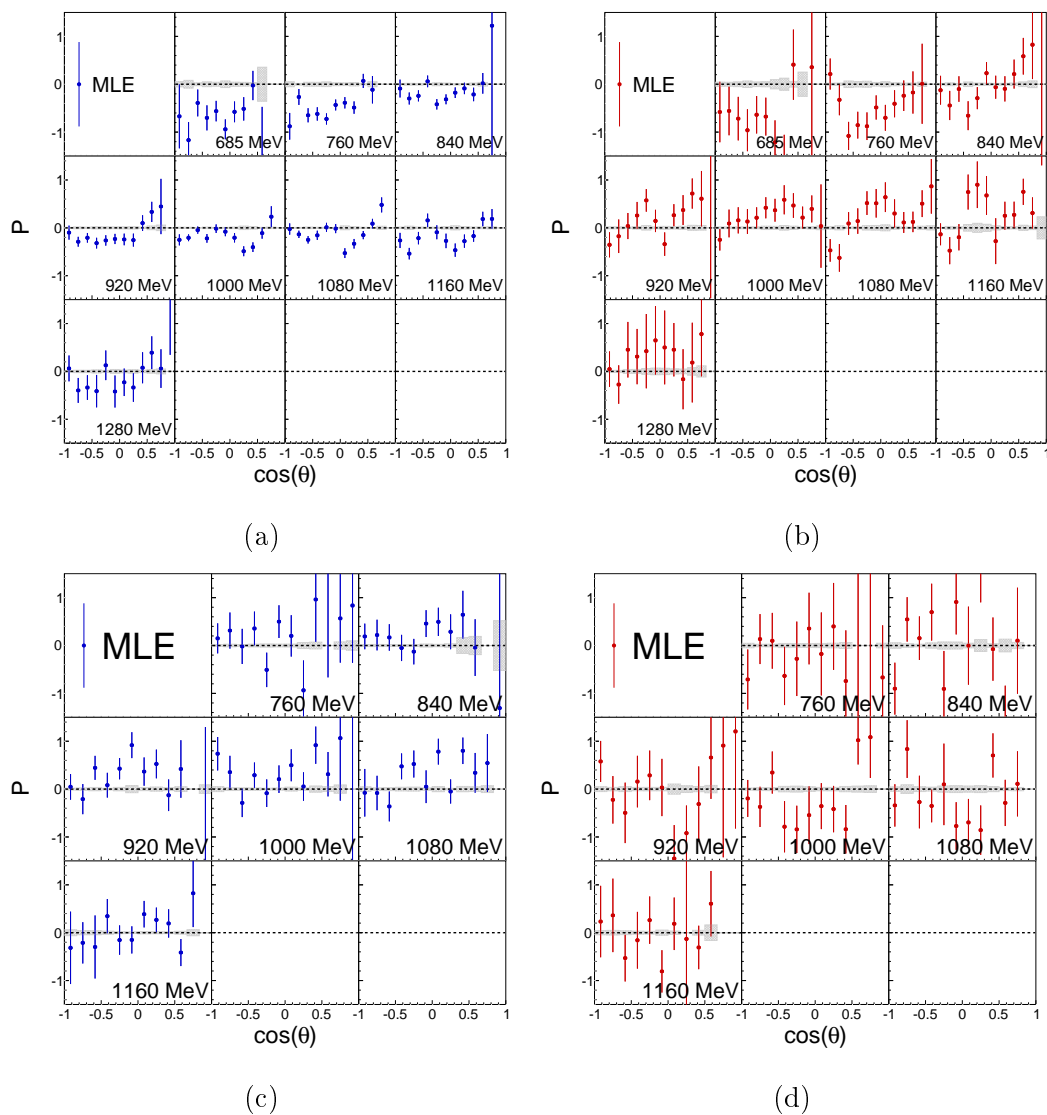


Figure 7.15: Recoil asymmetry P as a function of $\cos(\theta)$ for fixed photon energies E_γ in the reactions $\gamma p \rightarrow \pi^0 p$ (a), $\gamma n \rightarrow \pi^0 n$ (b), $\gamma p \rightarrow \eta p$ (c) and $\gamma n \rightarrow \eta n$ (d).

The recoil asymmetry P is not measured directly but extracted together with the \mathcal{BT} double polarisation observables H . By the design of this exper-

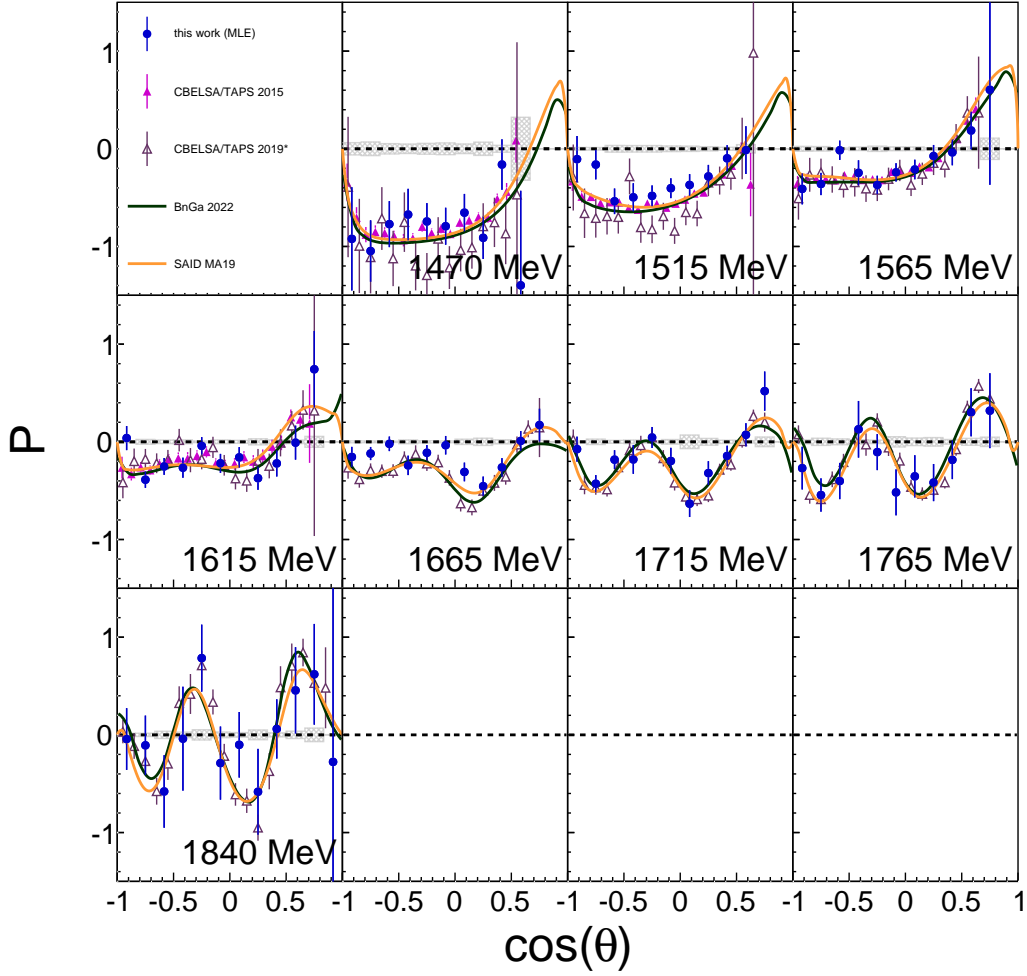


Figure 7.16: Recoil asymmetry P as a function of $\cos(\theta)$ for fixed centre of mass energies W in the reaction $\gamma p \rightarrow \pi^0 p$. The data are compared with CBELSA/TAPS 2015 [142] and CBELSA/TAPS 2019 [144] data and to BnGa 2022 [126] and SAID MA19 [121] partial wave analysis.

iment, P can only be extracted by measuring different beam and target polarisation orientations, resulting in around half the statistics of the normalised event yields in comparison to the other single polarisation observables Σ_{but} and T . This can be seen best in Equation 6.3 that shows the A_{PH} asymmetry that depends on both observables. The statistical uncertainties are expected to increase, which can be seen in the figures.

As for the target asymmetry T there are previous results for $\pi^0 p$ [142, 144] and ηp [119] from CBELSA/TAPS. These previous experiments were con-

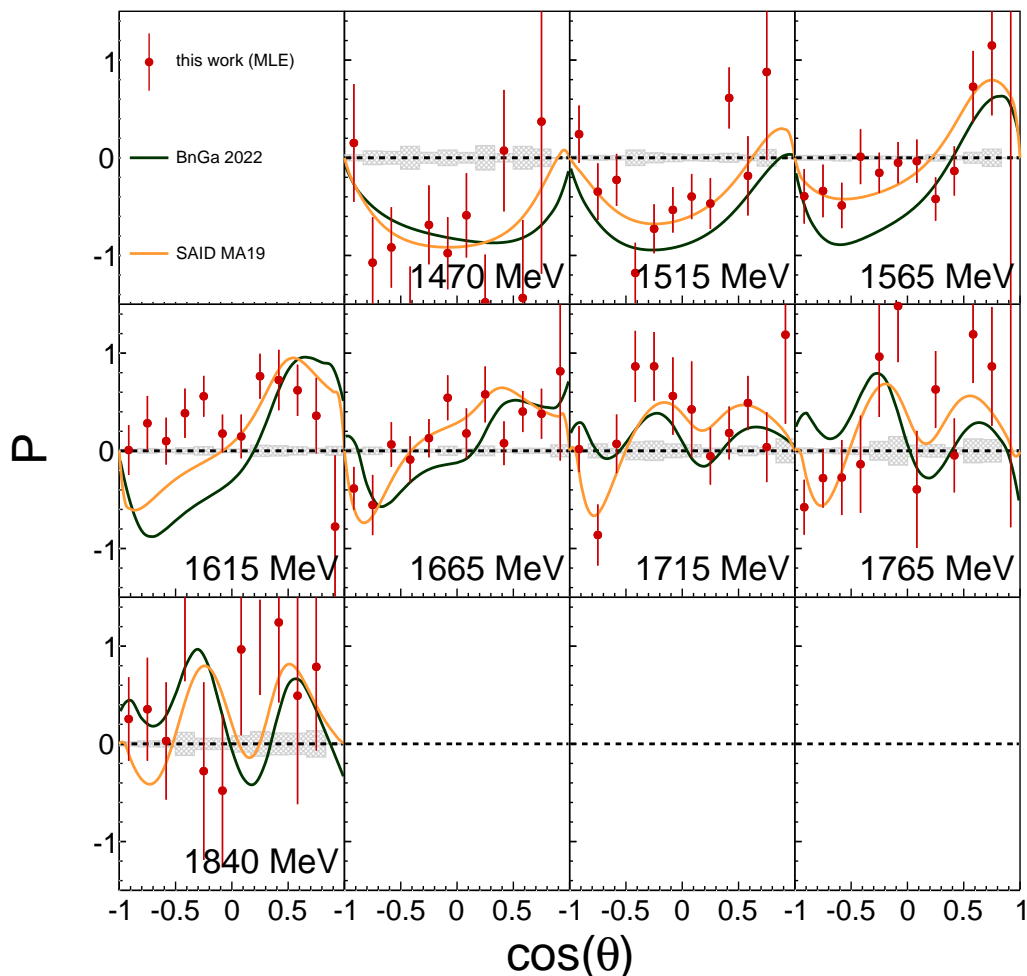


Figure 7.17: Recoil asymmetry P as a function of $\cos(\theta)$ for fixed centre of mass energies W in the reaction $\gamma n \rightarrow \pi^0 n$. The data are compared with BnGa 2022 [126] and SAID MA19 [121] partial wave analysis.

ducted with free proton targets (H-Butanol) that have some advantages: the dilution is easier to determine since free protons do not have any Fermi momentum and the background from misidentified protons or neutrons is strongly suppressed, such that the statistics can be increased significantly by looking at inclusive reactions too.

Nevertheless, the results are within the expected statistical fluctuations - especially for ηp - in agreement with previous data and can even increase the energy range. The $\pi^0 p$ reaction gives high statistics results, whereas the ones for ηp and $\pi^0 n$ do not have enough statistics to give quantitative statements.

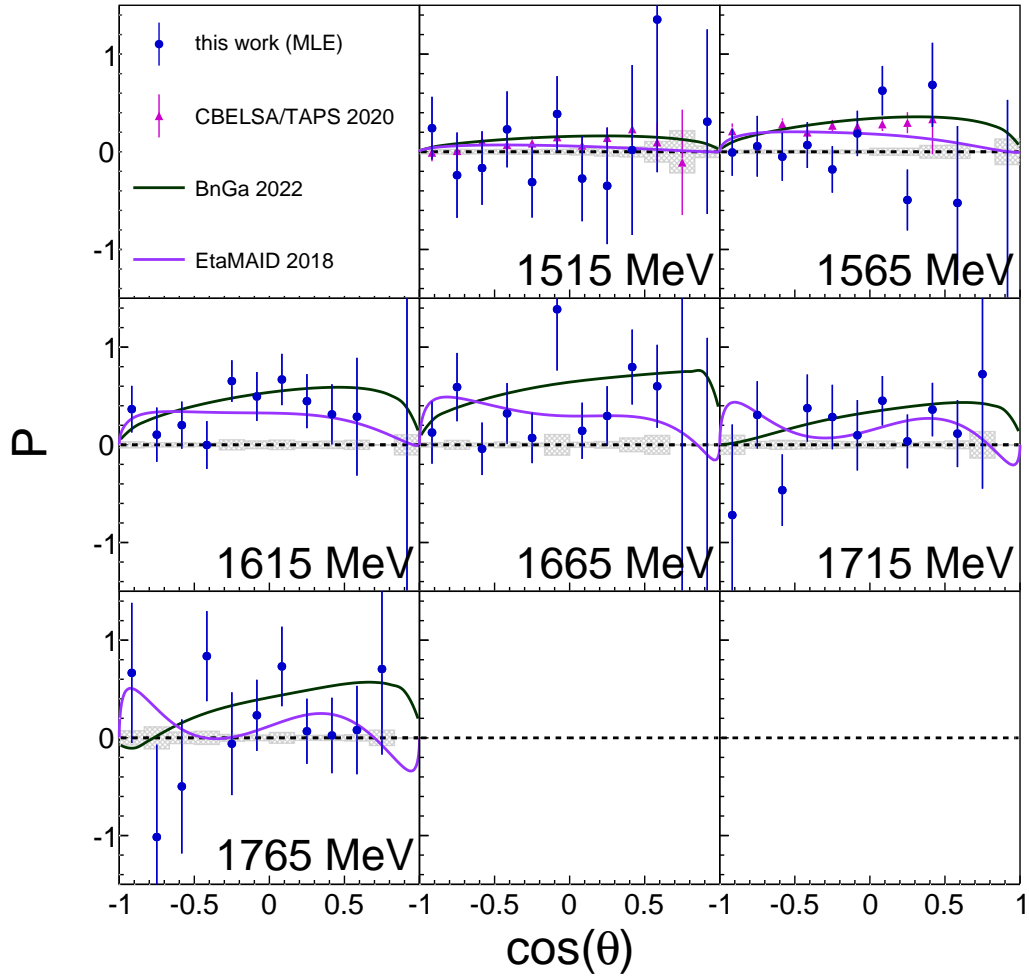


Figure 7.18: Recoil asymmetry P as a function of $\cos(\theta)$ for fixed centre of mass energies W in the reaction $\gamma p \rightarrow \eta p$. The data are compared with CBELSA/TAPS 2020 [119] data and to BnGa 2022 [126] and EtaMAID 2018 [122] partial wave analysis.

The reaction ηn is even worse. Only a tendency can be seen and even this is only visible in energy regions with the highest linear polarisation degrees, e.g. $W = 1665$ MeV.

Comparing the PWA with each other, the recoil asymmetry P gets more interesting. For $\pi^0 p$ both, BnGa [119] and SAID [121], describe the data quite well. The same is true in ηp and BnGa [119] and EtaMAID [122], where both PWA have different shapes but are rather close to each other. Within the uncertainties, both PWA can describe the data approximately.

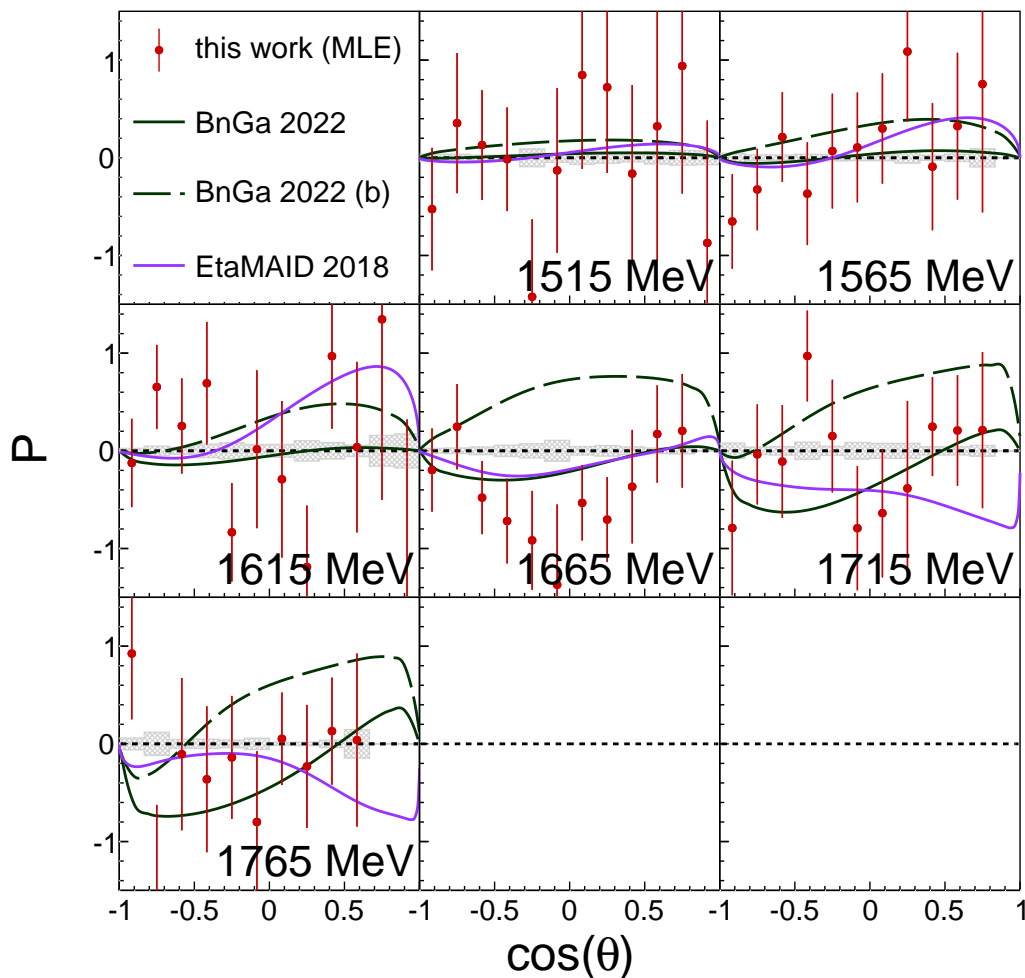


Figure 7.19: Recoil asymmetry P as a function of $\cos(\theta)$ for fixed centre of mass energies W in the reaction $\gamma n \rightarrow \eta n$. The data are compared with BnGa 2022 [126] and EtaMAID 2018 [122] partial wave analysis.

Of particular interest are $\pi^0 n$ and ηn , where the different PWA predict quite different structures towards higher energies, e.g. $W = 1665$ MeV. In $\pi^0 n$, SAID tends towards the right structure, whereas BnGa is far off for some energies. In ηn , the statistics are too low to make quantitative statements. However, the observable seems promising for testing the models as they differ very much at energies like $W = 1615$ MeV. However, EtaMAID and BnGa have the right sign at the energy of $W = 1665$ MeV, where a narrow structure has been observed.

7.6 Beam-target double polarisation observable

H

The results from the beam-target double polarisation observable H are given here in π^0 and η photoproduction on quasifree nucleons and shown as a function of $\cos(\theta)$ for fixed incident photon energies E_γ (Figure 7.20) and fixed CM energies W (Figures 7.21-7.24).

Like the P observable, H also depends on four different settings in this experiment, i.e. two beam and two target polarisation orientations. The statistical uncertainties are therefore expected to be of the same order.

Experiments with linearly polarised photons and transversely polarised nucleons are predestined as polarisation observable experiments since all three single polarisation observables and H can be extracted simultaneously. Hence, the same reference data from CBELSA/TAPS in π^0p [142, 144] and ηp [119] are available for H .

For π^0p , both reference data agree well with the ones from this work.

ηp also agrees with the reference data, although the statistics is worse for the existing energies. Towards higher energies, no previous data exist. The same is true for π^0n and ηn , where the first results for H are presented here.

The PWA comparison in π^0p looks very similar to the situation in P . Both PWA, BnGa [119] and SAID [121], describe the data quite well.

In π^0n , all PWA might explain the structures correctly since the statistical uncertainties are too large to make a quantitative statement. In contrast to T , where the two PWA make very different predictions, BnGa and SAID make similar predictions for H , analogue to P . If the statistics could be improved in future experiments, the agreement with PWA could be analysed more quantitatively and a preference for one PWA could be concluded. This would restrict the partial waves more and lead to more detailed information about their contributions.

In ηp , both PWA seems to have the right direction and none can be preferred. In ηn , a very different behaviour is visible, especially around $W = 1615$ MeV. However, the quality of the data does not allow a preference at this point.

7.6. Beam-target double polarisation observable H

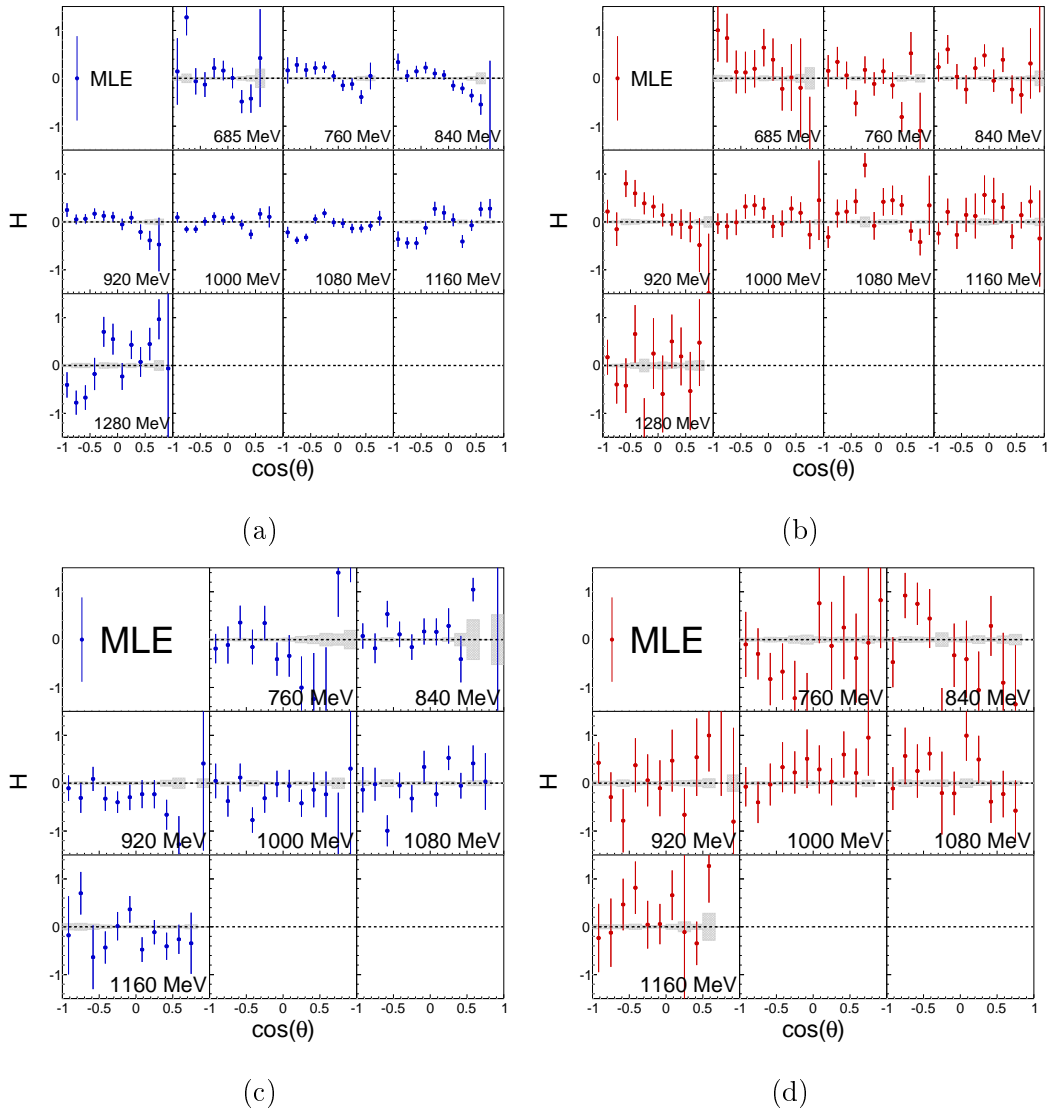


Figure 7.20: Beam-target double polarisation observable H as a function of $\cos(\theta)$ for fixed photon energies E_γ in the reactions $\gamma p \rightarrow \pi^0 p$ (a), $\gamma n \rightarrow \pi^0 n$ (b), $\gamma p \rightarrow \eta p$ (c) and $\gamma n \rightarrow \eta n$ (d).

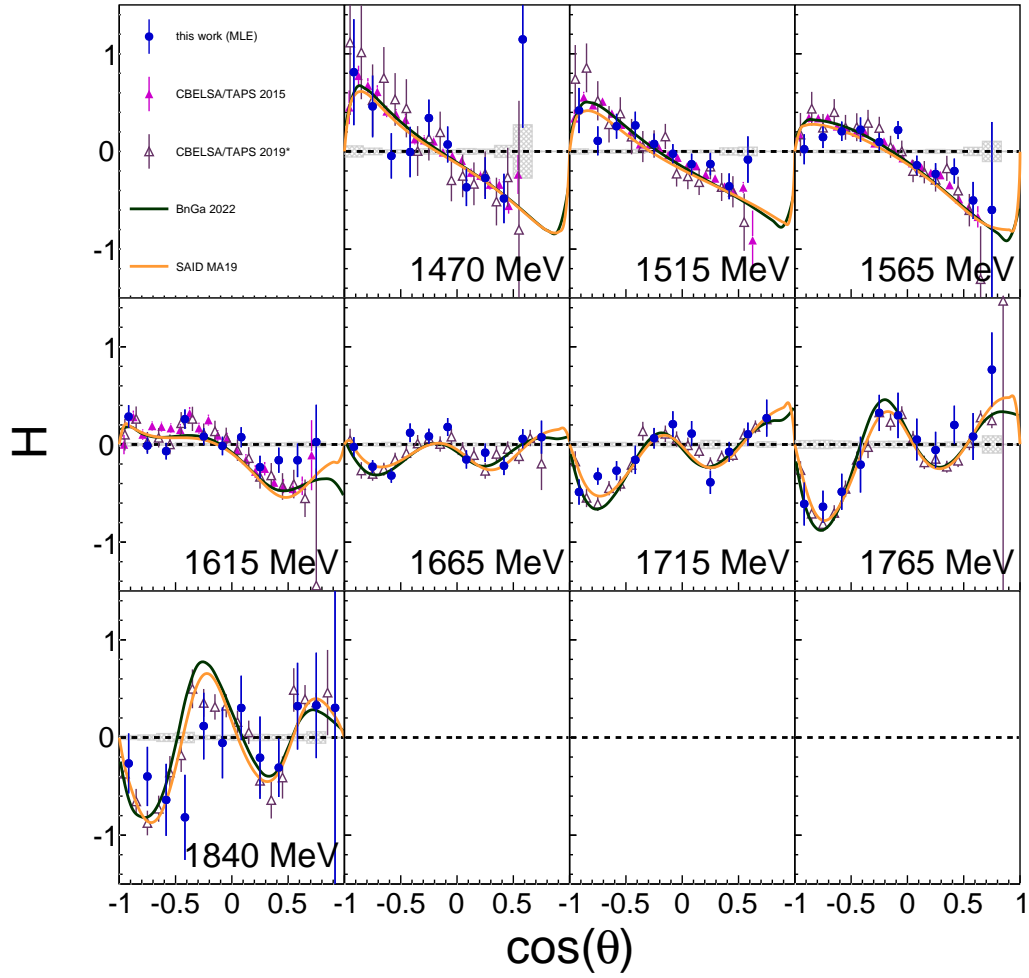


Figure 7.21: Beam-target double polarisation observable H as a function of $\cos(\theta)$ for fixed centre of mass energies W in the reaction $\gamma p \rightarrow \pi^0 p$. The data are compared with CBELSA/TAPS 2015 [142] and CBELSA/TAPS 2019 [144] data and to BnGa 2022 [126] and SAID MA19 [121] partial wave analysis.

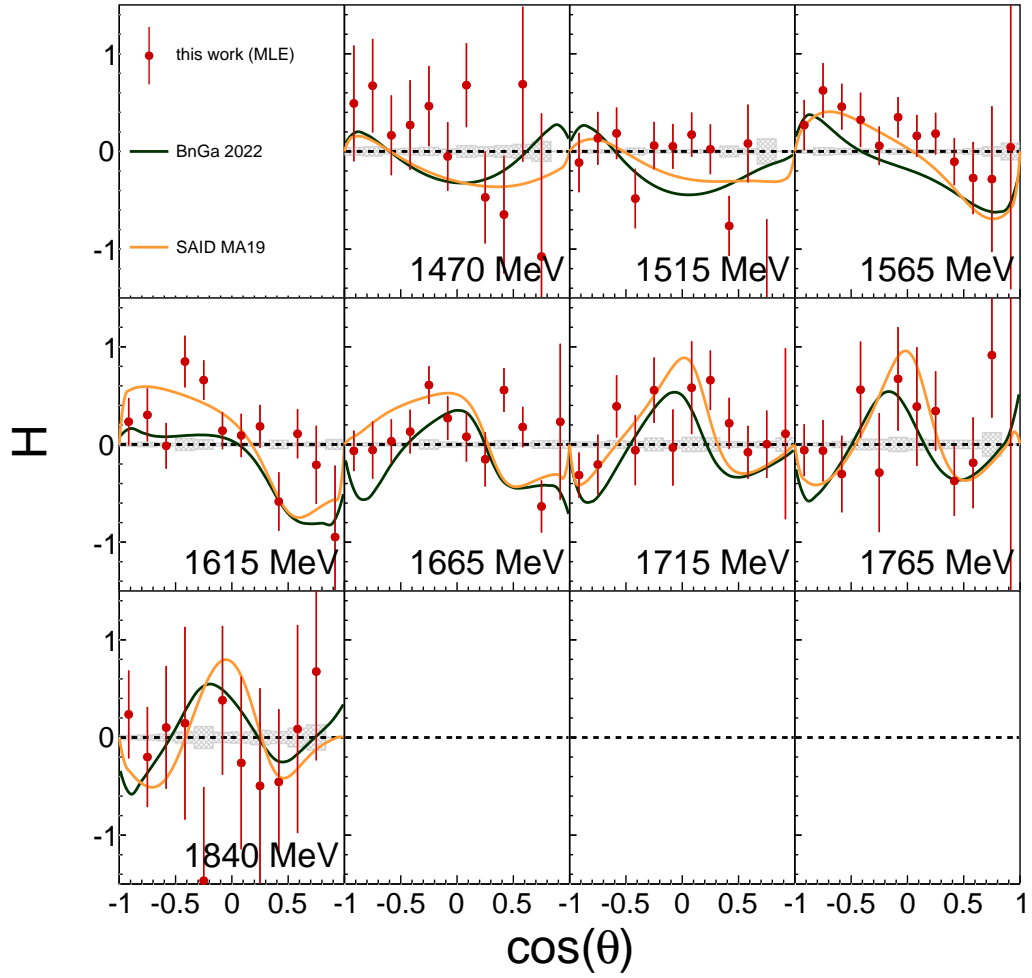


Figure 7.22: Beam-target double polarisation observable H as a function of $\cos(\theta)$ for fixed centre of mass energies W in the reaction $\gamma n \rightarrow \pi^0 n$. The data are compared with BnGa 2022 [126] and SAID MA19 [121] partial wave analysis.

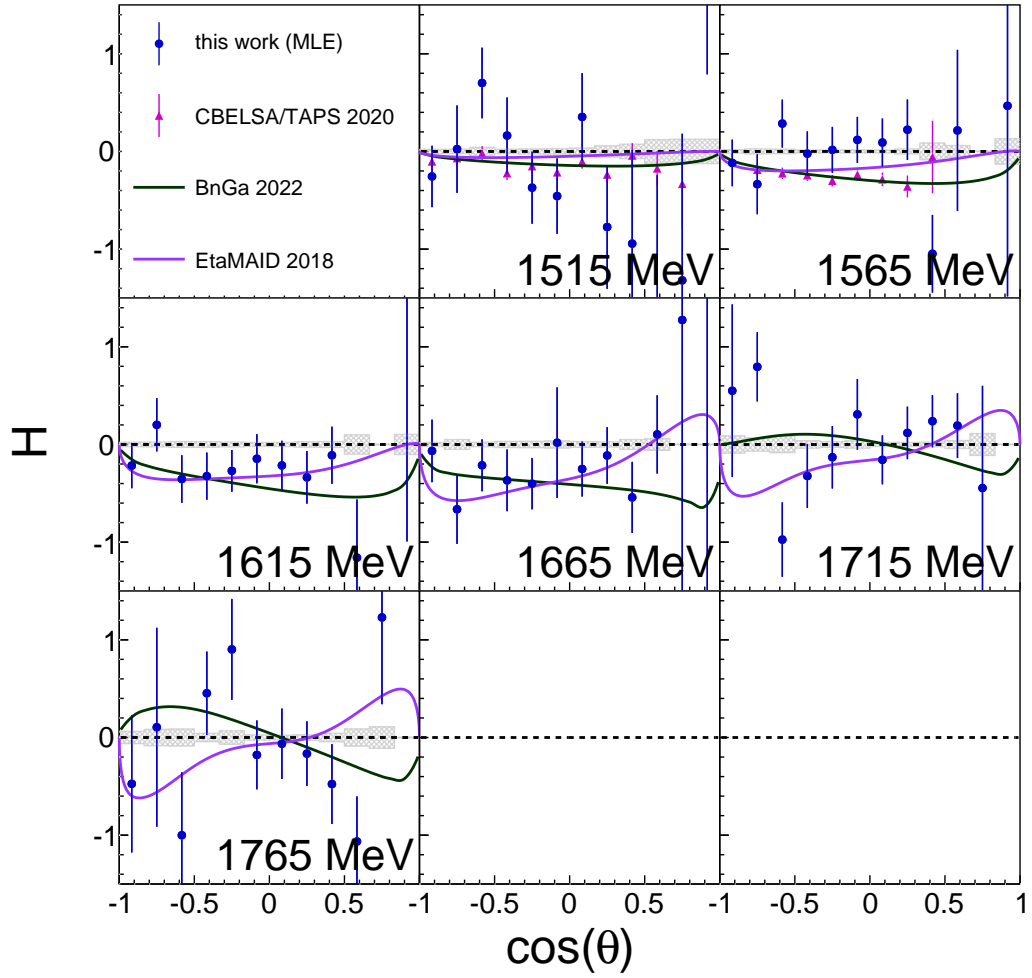


Figure 7.23: Beam-target double polarisation observable H as a function of $\cos(\theta)$ for fixed centre of mass energies W in the reaction $\gamma p \rightarrow \eta p$. The data are compared with CBELSA/TAPS 2020 [119] data and to BnGa 2022 [126] and EtaMAID 2018 [122] partial wave analysis.

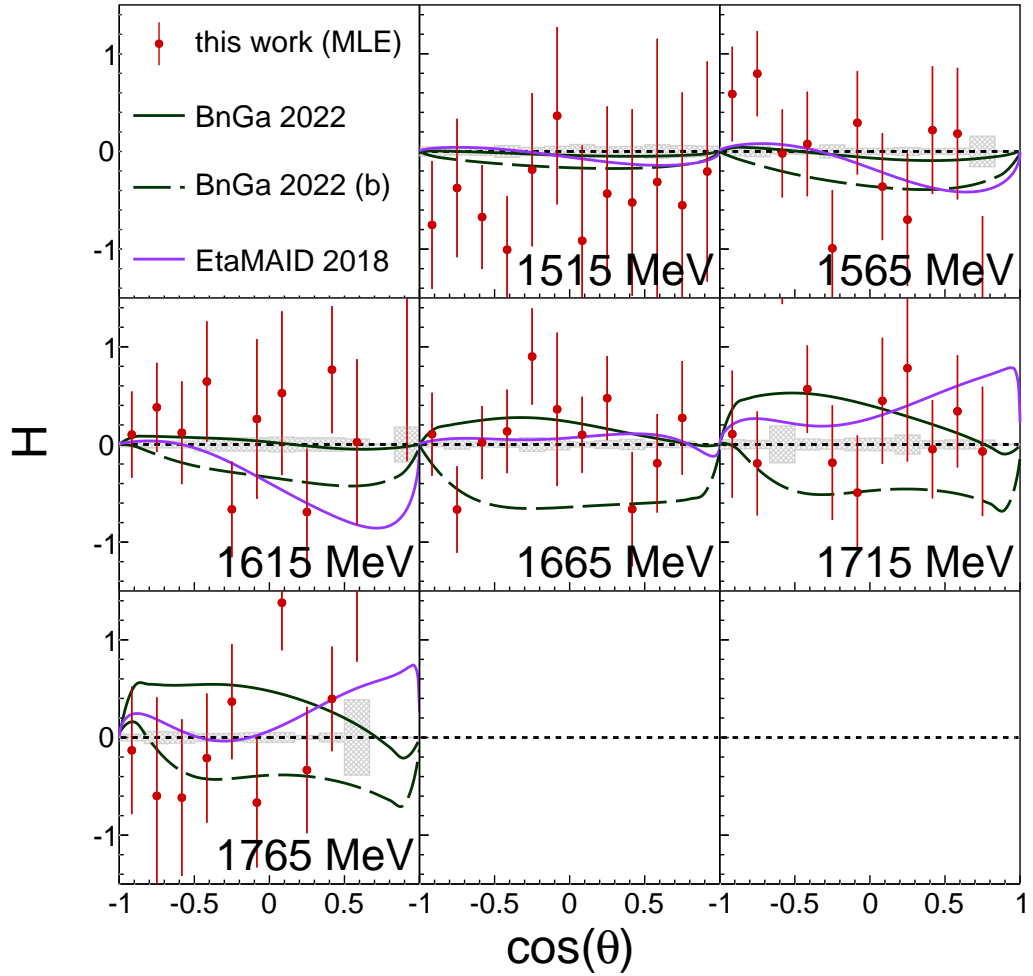


Figure 7.24: Beam-target double polarisation observable H as a function of $\cos(\theta)$ for fixed centre of mass energies W in the reaction $\gamma n \rightarrow \eta n$. The data are compared with BnGa 2022 [126] and EtaMAID 2018 [122] partial wave analysis.

7.7 Partial wave contributions

To connect the polarisation observable results to multipoles and, therefore, to partial wave contributions, they can be multiplied by the unpolarised DCS to get *profile functions*, as discussed in Sections 1.6.3 and 1.6.4. For minimising additional uncertainties, PWA data are used for the unpolarised DCS. BnGa 2019 [119] is chosen because this PWA is available for all investigated reactions.

Dividing the profile function by the phase space factor and the sine term results in an even more compact form for the observables in a truncated analysis. These reduced polarisation observables are obtained by explicitly calculating the observables based on Equation 1.55:

$$\tilde{\Sigma} = \check{\Sigma} \cdot \frac{p_m^*}{p_\gamma^*} \frac{1}{\sin^2(x)} = \sum_{l=2}^{2l_{max}} (A_{l_{max}})_l^{\check{\Sigma}}(W) P_l''(x), \quad (7.2)$$

$$\tilde{T} = \check{T} \cdot \frac{p_m^*}{p_\gamma^*} \frac{1}{\sin(x)} = \sum_{l=1}^{2l_{max}} (A_{l_{max}})_l^{\check{T}}(W) P_l'(x), \quad (7.3)$$

$$\tilde{P} = \check{P} \cdot \frac{p_m^*}{p_\gamma^*} \frac{1}{\sin(x)} = \sum_{l=1}^{2l_{max}} (A_{l_{max}})_l^{\check{P}}(W) P_l'(x), \quad (7.4)$$

$$\tilde{H} = \check{H} \cdot \frac{p_m^*}{p_\gamma^*} \frac{1}{\sin(x)} = \sum_{l=1}^{2l_{max}} (A_{l_{max}})_l^{\check{H}}(W) P_l'(x). \quad (7.5)$$

Truncating at a certain l_{max} provides details about the dominant partial wave contributions. With $l_{max} = 1$, only S and P waves contribute to the shape, where with $l_{max} = 2$ also D waves, $l_{max} = 3$ F waves and $l_{max} = 4$ G waves contribute to the shape of the Legendre polynomials.

Figures 7.25-7.28 show the same reduced polarisation observables with the corresponding Legendre fit functions truncated at $l_{max} = 1, 2, 3$ and 4. For T , the merged full data, including the statistics from both beam times, is shown. For the other observables, the results from Oct2018 are shown.

The truncation at $l_{max} = 1$ is insufficient for describing the data, whereas the data for the lower energy bins can nearly completely be described with $l_{max} = 2$ fits, i.e. S , P and D waves. Going towards higher energies, i.e. above $W = 1715$ MeV in $\pi^0 p$, at least $l_{max} = 3$ needs to be taken to describe the data adequately. It is also visible that with $l_{max} = 4$, all data structures can be described well, even for high energies. The statistical fluctuations get large in

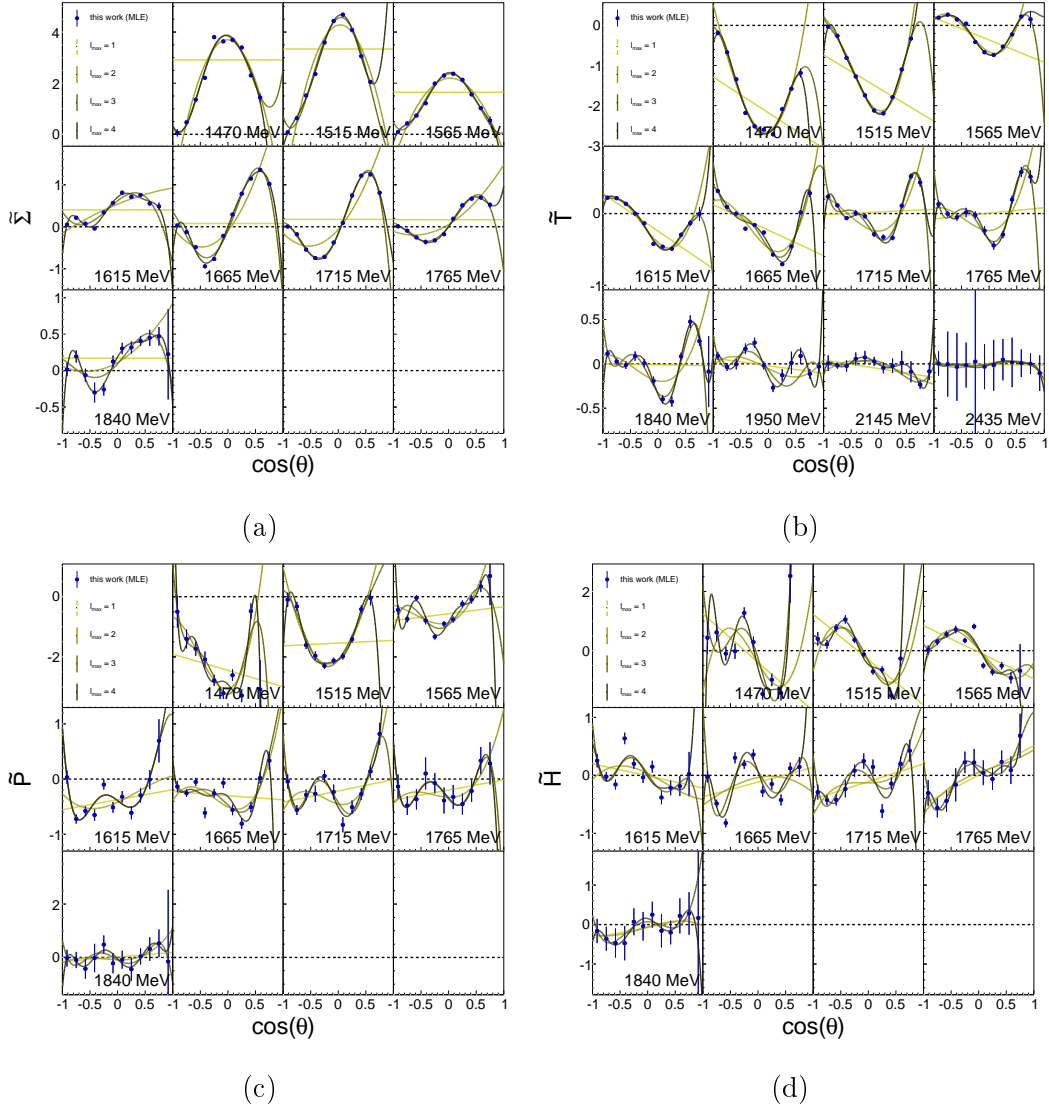


Figure 7.25: Reduced polarisation observables $\tilde{\Sigma}$ (a), \tilde{T} (b), \tilde{P} (c) and \tilde{H} as a function of $\cos(\theta)$ for fixed centre of mass energies W in the reaction $\gamma p \rightarrow \pi^0 p$. The fitted functions correspond to Legendre polynomials with a truncation at $l_{max} = 1, 2, 3, 4$. The darker the line, the higher the cut-off. Note the different scales of the y -axis.

some kinematic ranges in ηN , such that the Legendre fits are not that good or useful, respectively, anymore.

The χ^2 per degrees of freedoms (ndf), as well as the individual Legendre coefficients, can be found in Appendix D.3 and D.4.

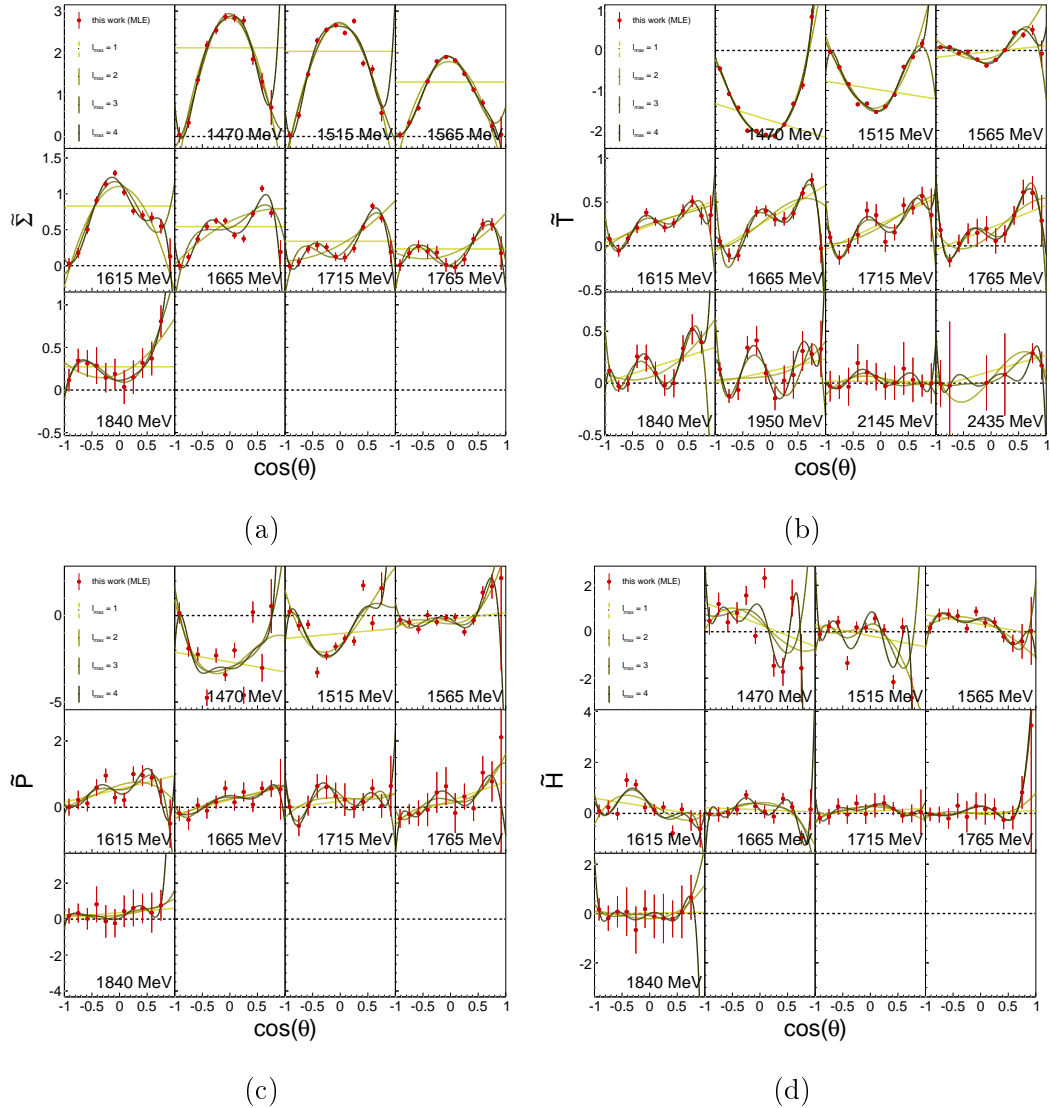


Figure 7.26: Reduced polarisation observables $\tilde{\Sigma}$ (a), \tilde{T} (b), \tilde{P} (c) and \tilde{H} as a function of $\cos(\theta)$ for fixed centre of mass energies W in the reaction $\gamma n \rightarrow \pi^0 n$. The fitted functions correspond to Legendre polynomials with a truncation at $l_{max} = 1, 2, 3, 4$. The darker the line, the higher the cut-off. Note the different scales of the y -axis.

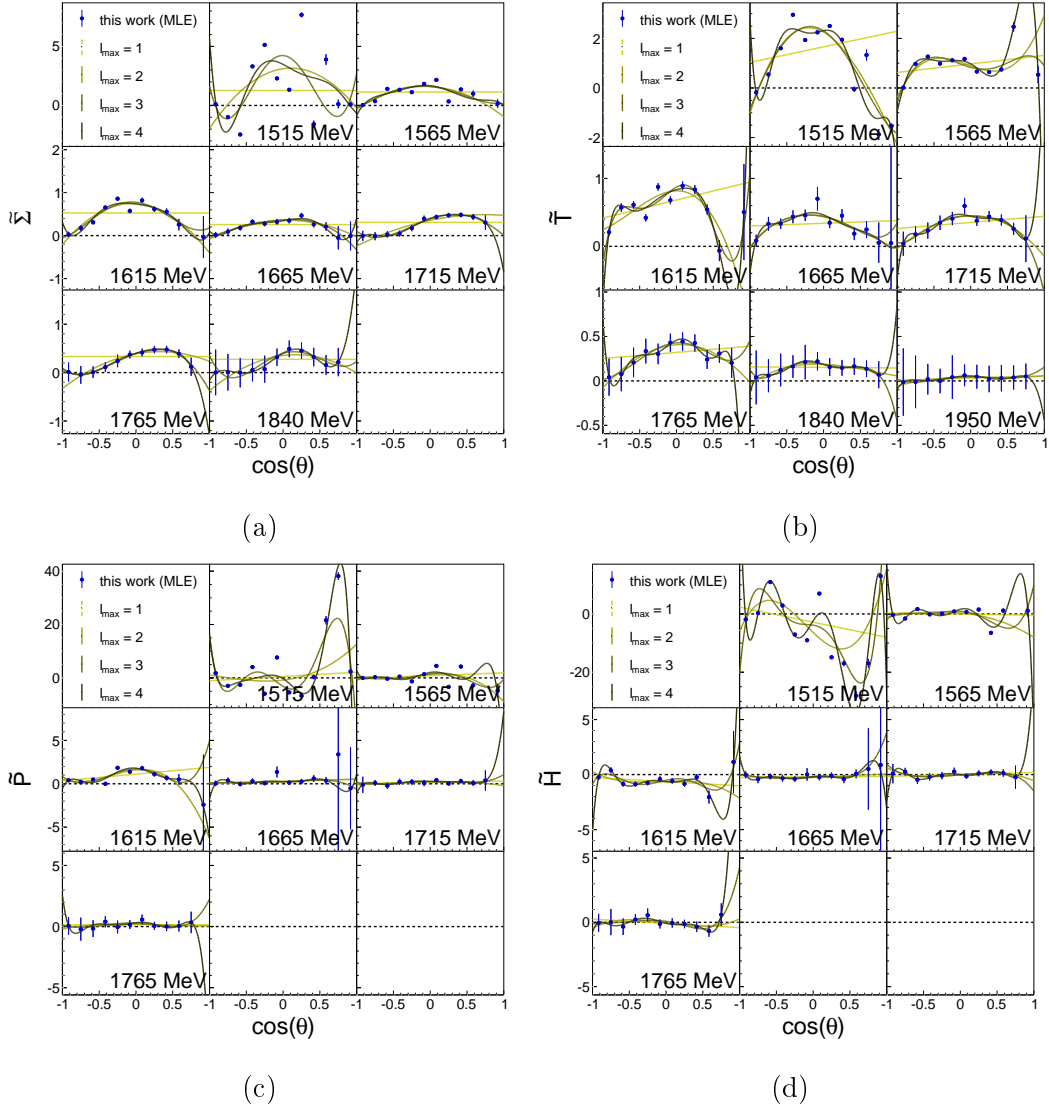


Figure 7.27: Reduced polarisation observables $\tilde{\Sigma}$ (a), \tilde{T} (b), \tilde{P} (c) and \tilde{H} as a function of $\cos(\theta)$ for fixed centre of mass energies W in the reaction $\gamma p \rightarrow \eta p$. The fitted functions correspond to Legendre polynomials with a truncation at $l_{max} = 1, 2, 3, 4$. The darker the line, the higher the cut-off. Note the different scales of the y -axis.

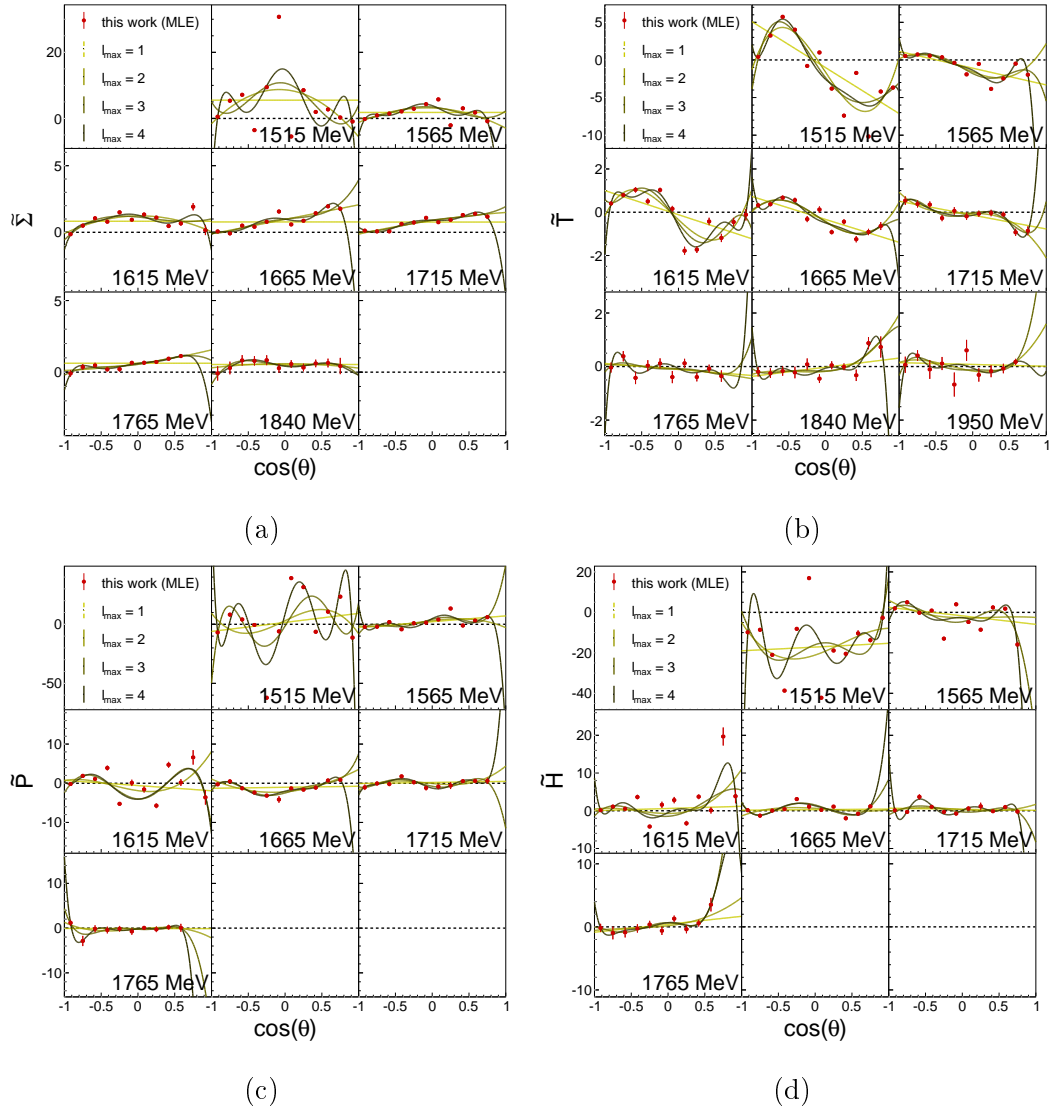


Figure 7.28: Reduced polarisation observables $\tilde{\Sigma}$ (a), \tilde{T} (b), \tilde{P} (c) and \tilde{H} as a function of $\cos(\theta)$ for fixed centre of mass energies W in the reaction $\gamma n \rightarrow \eta n$. The fitted functions correspond to Legendre polynomials with a truncation at $l_{max} = 1, 2, 3, 4$. The darker the line, the higher the cut-off. Note the different scales of the y-axis.

7.8 Narrow structure in ηn around $W = 1.68$ GeV

One of the main motivations for the chosen energy range is a more detailed analysis of the observed narrow structure around $W = 1.68$ GeV in ηn [122,140]. The 4th energy bin in the η reaction is with its value of $W = (1665 \pm 25)$ MeV exactly around that observed structure.

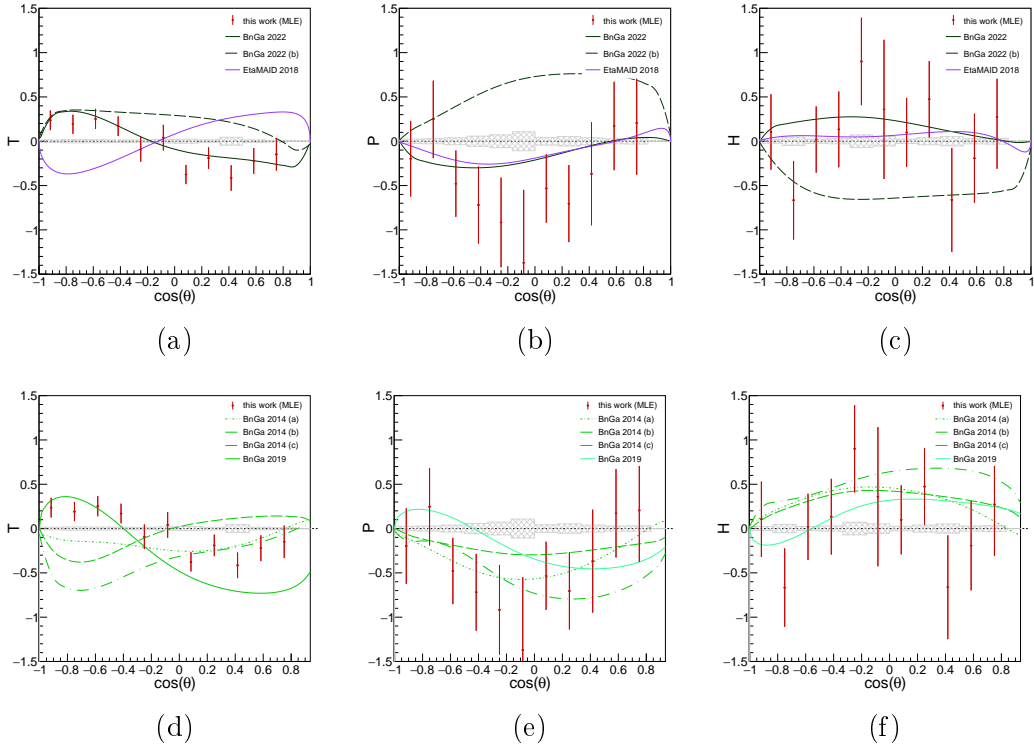


Figure 7.29: Polarisation observables T , P and H (from left to right) in ηn at a centre of mass energy of $W = 1665$ MeV. In the first row, the data are compared to BnGa 2022 with [332] and without [126] the introduction of a narrow P_{11} resonance as well as to EtaMAID 2018 [122]. In the second row, the data are compared to BnGa 2019 [119] and BnGa 2014 with and without additional narrow P_{11} resonance [133]. T shows the merged full data from both beam times, P and H only the one from Oct2018.

Figure 7.29 shows the data from ηn at $W = 1665$ MeV compared to different PWA. Again, T shows the merged full data from both beam times, whereas P and H show only the Oct2018 one. EtaMAID 2018 [122] and two BnGa 2022 [126,332] models can be seen in the upper row and BnGa 2019 model [119] together with three different BnGa 2014 models [334] can be seen in the lower

row. The data are the same in both rows. They are split to see the comparison to the PWA models better. BnGa 2022 is based on BnGa 2019, again based on BnGa 2014 (a).

The difference between the three BnGa 2014 PWA lies in the treatment of the observed narrow structure. Model (a) treats the structure as an interference of two S waves: $S_{11}(1535) 1/2^-$ and $S_{11}(1650) 1/2^-$. Models (b) and (c) both introduce an additional narrow $P_{11}(1685) 1/2^+$ resonance that couples to the S_{11} waves. There, the difference lies in the coupling. In (b), the P wave couples positively with the S wave, in (c) negatively. Two models exist because the PWA calculations result in two equally possible solutions for this situation.

As shown for the E observable and helicity-dependent cross sections [334], contributions with $J \geq 3/2$ were ruled out. Model (c) was ruled out as well due to a large discrepancy between the model and the data, where models (a) and (b) are concluded to be possible explanations. The preference was model (b) [334], where the deviation between model and data was the smallest, i.e. best χ^2/ndf .

PWA \ Observable	T	P	H	Total
EtaMAID 2018	8.82(5.61)	0.87(1.32)	0.81(1.16)	3.50(2.70)
BnGa 2022	0.73(1.13)	0.83(1.17)	0.80(0.90)	0.79(1.07)
BnGa 2022 (b)	4.65(4.65)	5.27(2.71)	2.81(2.10)	4.24(3.15)
BnGa 2019	1.79(2.17)	1.18(1.29)	0.71(0.99)	1.23(1.48)
BnGa 2014 (a)	3.18(2.87)	0.39(1.12)	0.98(1.04)	1.52(1.68)
BnGa 2014 (b)	7.12(4.91)	0.77(0.94)	0.96(1.08)	2.95(2.31)
BnGa 2014 (c)	11.51(5.48)	0.83(1.01)	1.60(1.24)	4.65(2.58)

Table 7.1: χ^2/ndf values for the comparison of the observables T , P and H from this work to different partial wave analysis models in the energy range $W = 1640 \text{ MeV} - 1690 \text{ MeV}$ ($W = 1590 \text{ MeV} - 1740 \text{ MeV}$). Models BnGa 2014 (b) and (c) [334] and BnGa 2022 (b) [332] include an additional narrow P_{11} resonance around the observed structure. T shows the merged full data from both beam times, P and H only the one from Oct2018.

The results in Figure 7.29 also disagree with model (c). Especially T indicates a different shape. Model (b) is closer to the data in T but still further away than model (a). In P and H , the statistical uncertainty of the data is too large to make quantitative statements. However, considering all three

observables, model (a) is preferred (see χ^2/ndf in Table 7.1).

BnGa 2019, which follows the S wave interference hypothesis, is in even better agreement than BnGa 2014 (a). EtaMAID 2018, on the other hand, seems to agree with P and H , but not in T . This PWA uses a different approach for treating the narrow structure: interference between the S wave and a dominant $P_{11}(1710)1/2^+$ wave [122].

A further comparison is conducted with the most recent BnGa 2022-02 - from now on called BnGa 2022 - solution [126] in Figure 7.29. In addition to the standard BnGa 2022 solution, one with an introduced $P_{11}(1680)$ resonance (BnGa 2022 (b) [332]) is shown. This model takes the phase of the state's coupling, mass and width from the fit to the DCS. As it can be found in Appendix D.5, the total CS can be described very well with both models, whereas the DCS has some problems around the observed structure as before the BnGa 2014 (b) [334]. In backward angles, the DCS of the model with the additional resonance is too small and in forward angles too high.

More quantitatively, the χ^2/ndf between the data here merged full data from both beam times for T and Oct2018 data for P and H , and PWA can be compared in the energy region from $W = 1600$ MeV to 1720 MeV. The DCS [132], beam asymmetry Σ [243] and helicity dependent DCS $d\sigma/d\Omega_{1/2,3/2}$ [334] of BnGa 2022 have one of 0.95, 2.39, 1.27 and 0.82 [332], whereas the same observables compared to BnGa 2022 (b) have values of 1.38, 3.68, 2.08 and 0.93 [332]. The values for T , P and H can be found in Table 7.1. It is remarkable how well the BnGa 2022 PWA agrees with the data in the complete range around the narrow structure, resulting in a χ^2/ndf value of 1.07. BnGa 2022 (b) with the narrow resonance, on the other hand, has even the wrong sign for T and P .

Taking the merged full data from both beam times, a χ^2/ndf of 0.73 (1.13) results for T in comparison to BnGa 2022 in the energy range of $W = 1640$ MeV – 1690 MeV ($W = 1590$ MeV – 1740 MeV). Whereas the comparison to BnGa 2022 (b) results in values of 4.65 (4.65), preferring a solution without an additional narrow P_{11} resonance even more.

All together allows the conclusion that the structure is probably produced from the interference of two S_{11} states, following the approach of BnGa instead of EtaMAID.

Figure 7.30 shows the reduced polarisation observables \tilde{T} , \tilde{P} and \tilde{H} in ηn

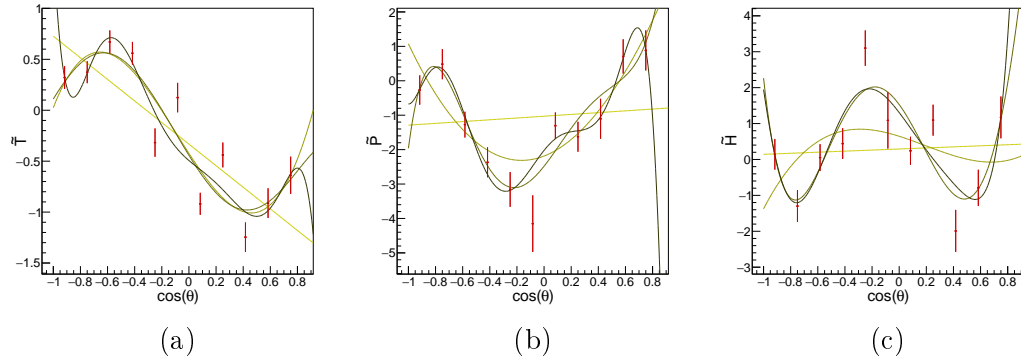


Figure 7.30: Reduced polarisation observables \tilde{T} , \tilde{P} and \tilde{H} (from left to right) in ηn at a centre of mass energy of $W = 1665$ MeV. T is shown with the merged full statistics of both beam times, whereas P and H are only shown from Oct2018. The fitted functions correspond to Legendre polynomials with a truncation at $l_{max} = 1, 2, 3$ and 4.

for the energy bin $W = 1665$ MeV. For \tilde{T} already $l_{max} = 1$, i.e. S and P waves, are enough to explain the main structure excluding the angular edges. In these regions, the structure can only be explained with $l_{max} = 4$, i.e. S, P, D, F and G waves. The situation gets different for \tilde{P} and \tilde{H} , where the values are scattered around the $l_{max} = 1$ line, but the structures need $l_{max} = 3$, i.e. S, P, D, F waves, for their description. Again, with $l_{max} = 4$, all data points can be described with great satisfaction.

8 | Conclusion and outlook

An experiment with linearly polarised beam photons and transversely polarised target nucleons was performed over two beam times in 2018 and 2021. With deuterated butanol as target material, reactions on protons and neutrons could be investigated. The setup enabled the simultaneous determination of the beam asymmetry Σ_{but} , target asymmetry T , recoil asymmetry P and beam-target double polarisation observable H . The reactions $\gamma p \rightarrow \pi^0 p$, $\gamma n \rightarrow \pi^0 n$, $\gamma p \rightarrow \eta p$ and $\gamma n \rightarrow \eta n$ were investigated with the meson decay channels $\pi^0 \rightarrow 2\gamma$, $\eta \rightarrow 2\gamma$ and $\eta \rightarrow 3\pi^0 \rightarrow 6\gamma$.

Different programmes were improved and written to analyse the raw experimental data. `EXPLORA` was expanded by including Fermi momentum smearing in Virtual Monte Carlo (VMC) simulations, a new interface between `EXPLORA` and `OSCAR` - `EXPLOSCAR` - was written and `OSCAR` with `libTOCB` was adapted and updated to the new experimental setup.

Particle reconstruction and background reduction worked well such that all investigated reactions could be extracted with a low background contamination of less than 1% on average. A challenge was the determination of reactions off unpolarised nucleons bound in carbon and oxygen, the dilution factor. The filling factor was not known well enough and new anticuts had to be introduced to determine the relative target surface densities. On average, the result was a relatively high systematic uncertainty of around 13%. Nevertheless, nearly all observables in all reactions are statistically driven, putting this uncertainty into perspective.

Since only exclusive reactions are investigated, the *true* centre of mass energy W of the system could be reconstructed from the final state, following the ideas of Werthmüller [270, 328] and Dieterle [327]. This allows a Fermi momentum independent determination of the observables.

On the experimental side, upgrading the Crystal Barrel with a new elec-

tronic by collaboration colleagues before this experiment was crucial. Neutrons could be detected in the first level trigger with good acceptance over the whole solid angle for the first time. Finalising the sampling ADC upgrade by collaboration colleagues before the second beam time further increased the trigger rate for this and all following experiments.

The existing results for Σ in all reactions and all four observables in $\pi^0 p$ and ηp are confirmed and partially expanded. Furthermore, this is the first experiment that showed results for T , P and H in $\pi^0 n$ and ηn . Even though the statistical uncertainties are rather large for the double polarisation observables, these data are crucial for clarifying the nucleon resonances in the range of $W = 1.5 \text{ GeV}$ to 2.5 GeV . Two different partial wave analyses (PWA) approaches were compared to the results. The deviation between PWA and data is significant in some kinematical ranges, especially on reactions off the neutron. This shows the importance of this experiment and the inclusion of the extracted results in PWA models.

The narrow structure in ηn around $W = 1.68 \text{ GeV}$ was investigated in more detail. The data favours a PWA solution with an interference of the resonances $S_{11}(1535)1/2^-$ and $S_{11}(1650)1/2^-$. A once and for all final statement, however, cannot be given with the available statistics.

The experiment enhances the world data of polarisation observables and makes a small step further towards the complete experiment. Some ideas about the origin of the narrow structure in ηn could be refuted and the interference of two S waves is concluded as the most probable interpretation.

A final evaluation of the second beam time will be important for making qualitative statements about the narrow structure in ηn and giving more stringent conditions for the PWA.

Appendices

A | Kinematic cut positions

A.1 Invariant mass cut positions

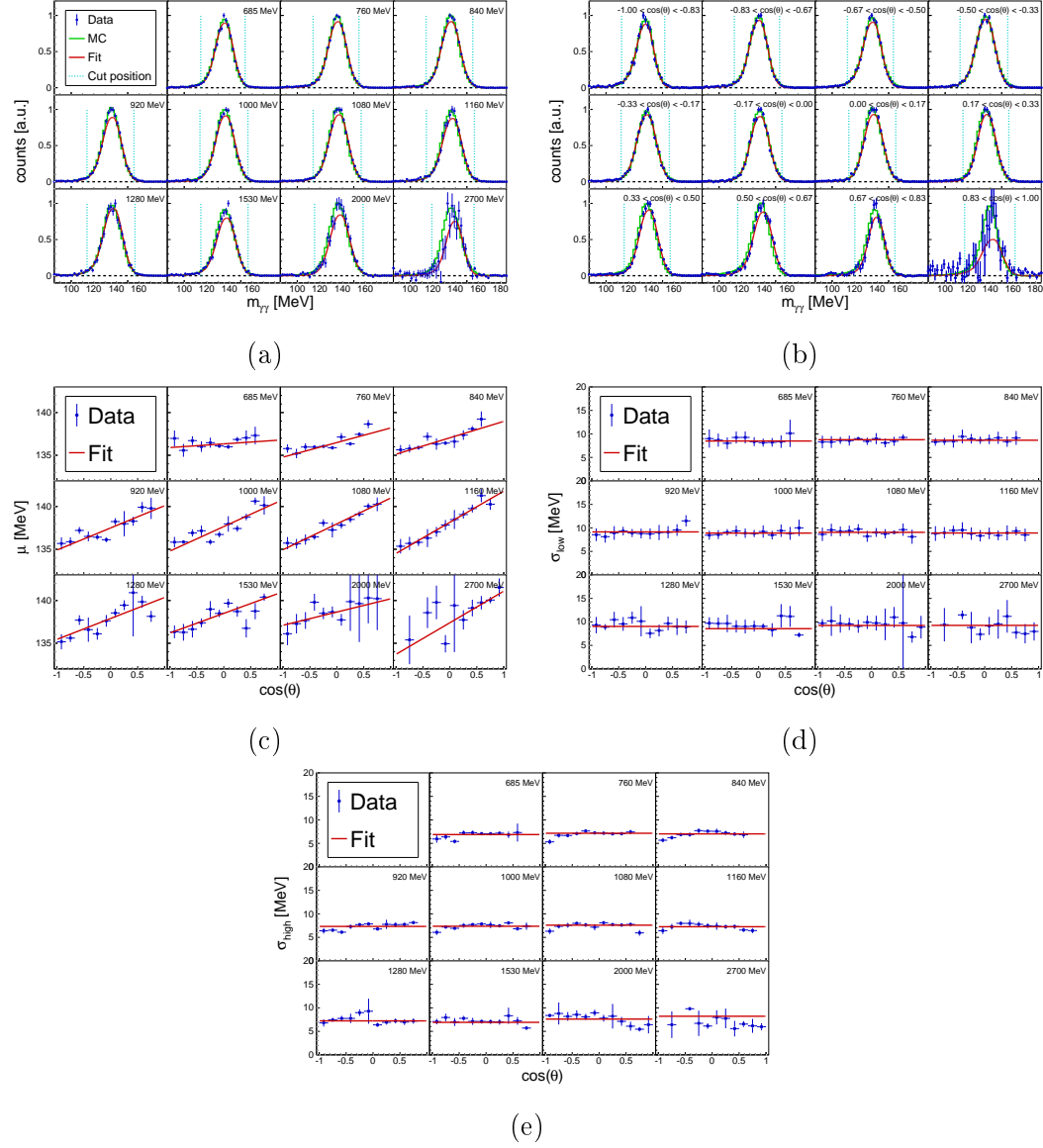


Figure A.1: Invariant mass cut positions as a function of the incident photon energy E_γ (a) and $\cos(\theta)$ (b) as well as the energy- and angular-dependent mean (c), sigma low (d) and sigma high (e) with their linear (c) and constant (d-e) fit functions in $\pi^0 p$.

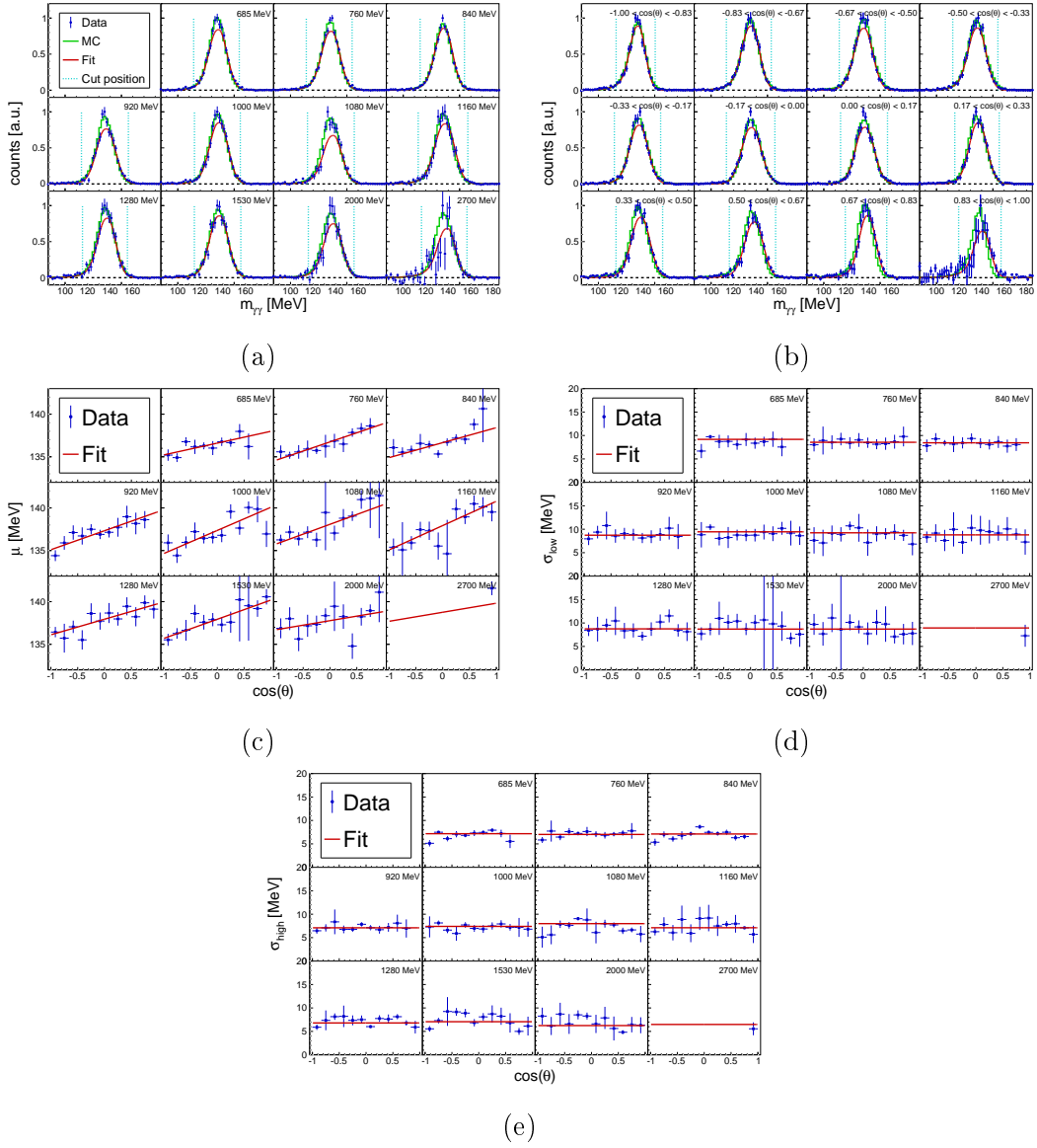


Figure A.2: Invariant mass cut positions as a function of the incident photon energy E_γ (a) and $\cos(\theta)$ (b) as well as the energy- and angular-dependent mean (c), sigma low (d) and sigma high (e) with their linear (c) and constant (d-e) fit functions in π^0n .

Appendix A. Kinematic cut positions

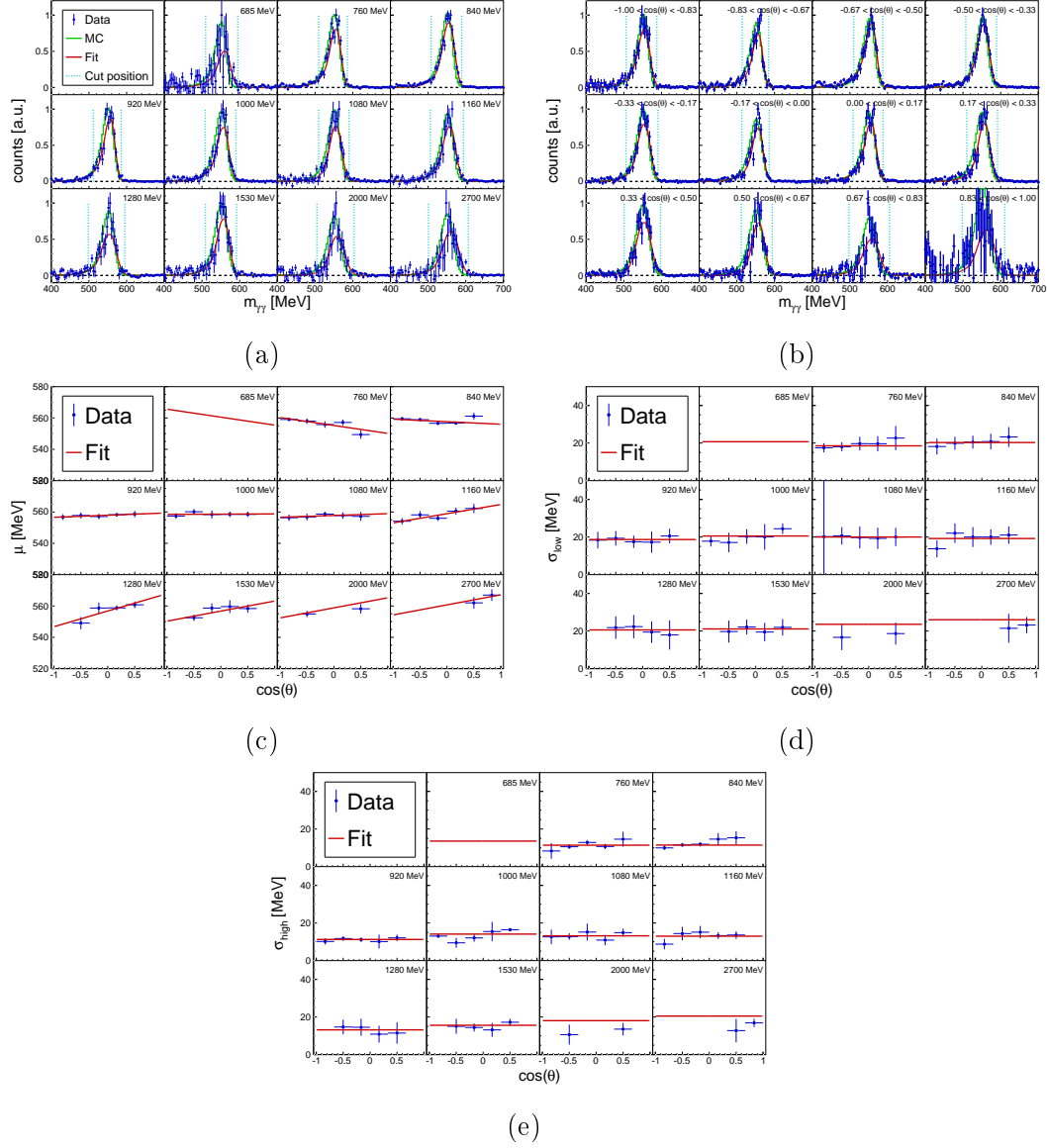


Figure A.3: Invariant mass cut positions as a function of the incident photon energy E_γ (a) and $\cos(\theta)$ (b) as well as the energy- and angular-dependent mean (c), sigma low (d) and sigma high (e) with their linear (c) and constant (d-e) fit functions in ηp with $\eta \rightarrow 2\gamma$.

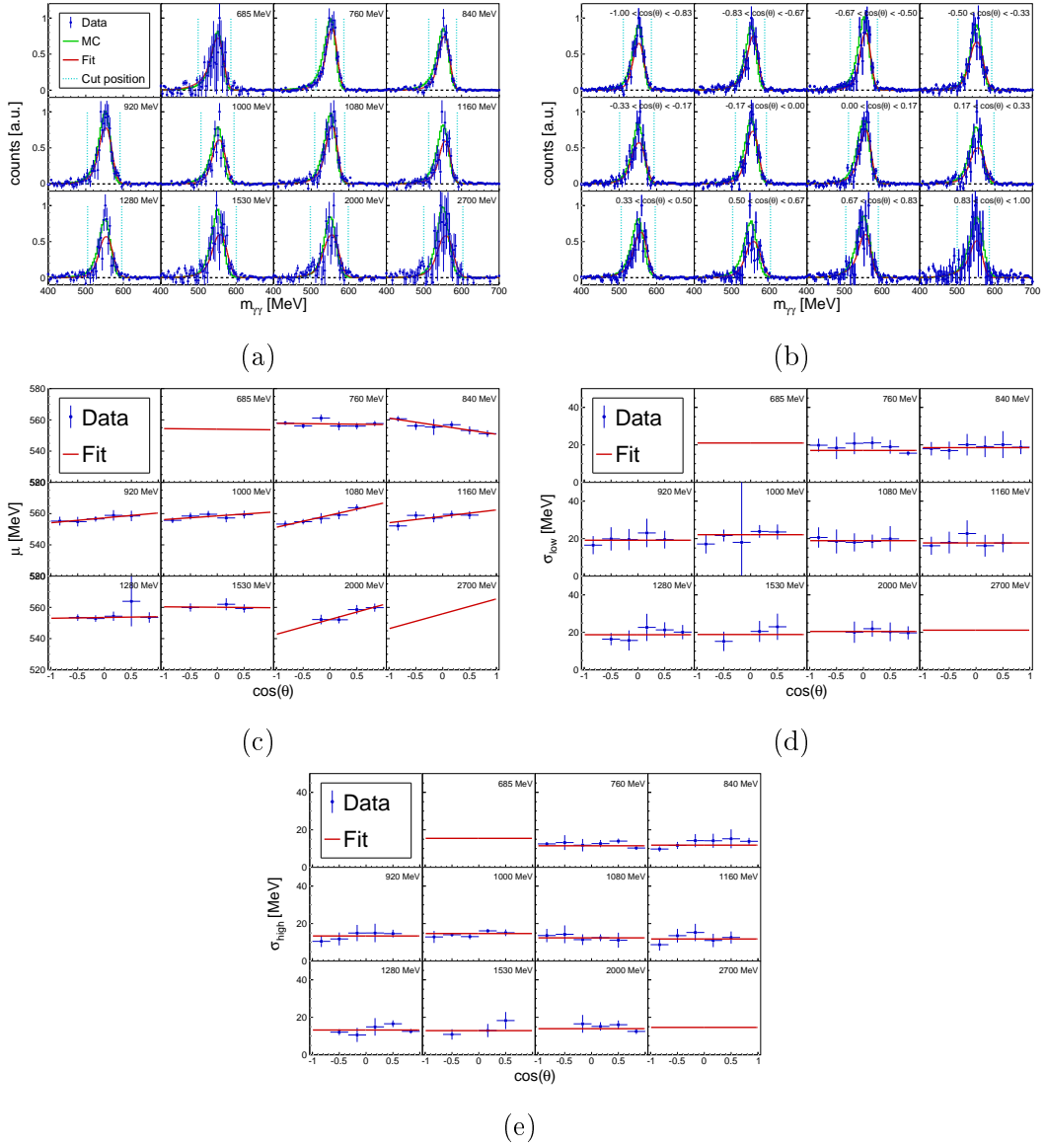


Figure A.4: Invariant mass cut positions as a function of the incident photon energy E_γ (a) and $\cos(\theta)$ (b) as well as the energy- and angular-dependent mean (c), sigma low (d) and sigma high (e) with their linear (c) and constant (d-e) fit functions in ηn with $\eta \rightarrow 2\gamma$

Appendix A. Kinematic cut positions

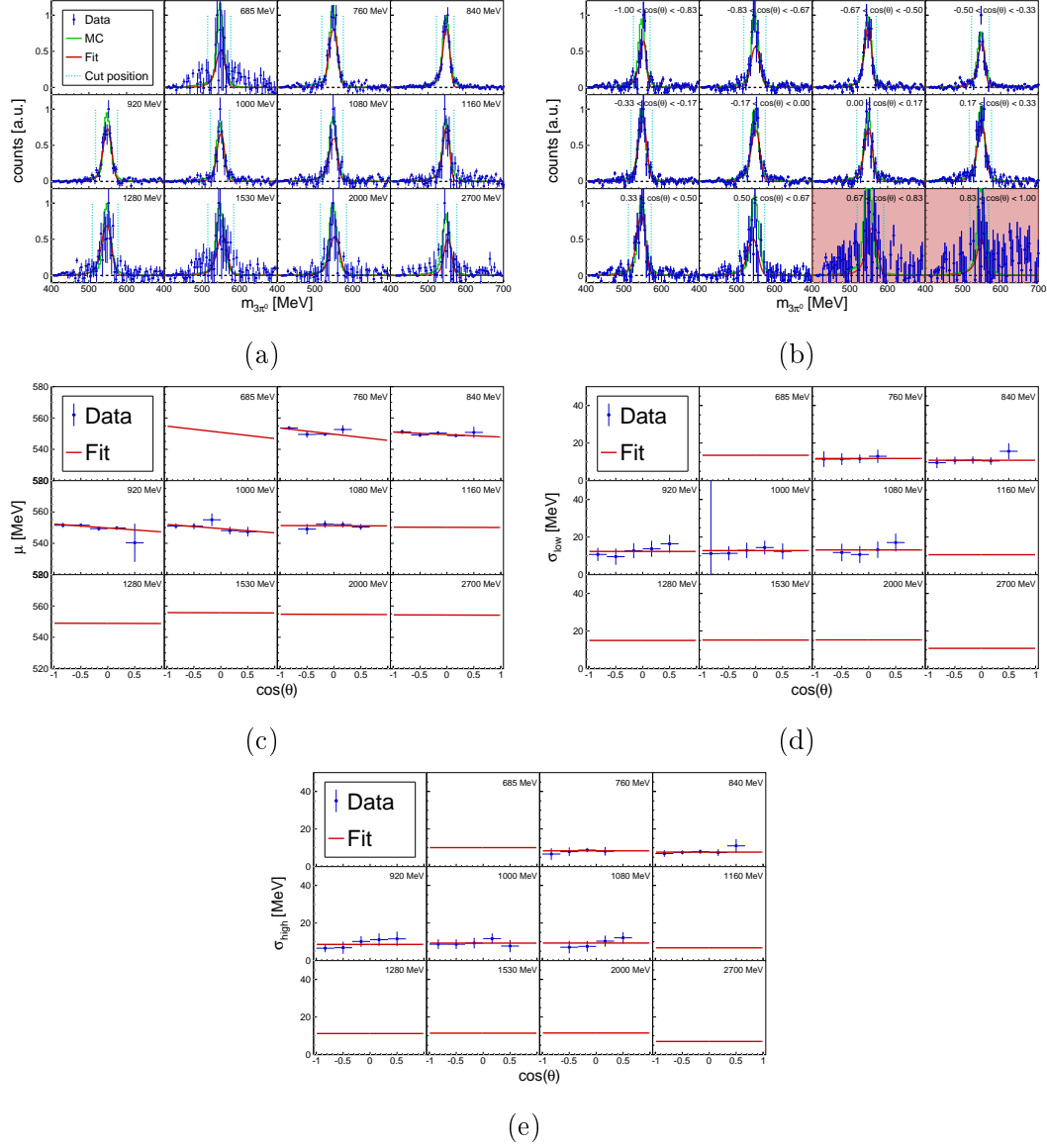


Figure A.5: Invariant mass cut positions as a function of the incident photon energy E_γ (a) and $\cos(\theta)$ (b) as well as the energy- and angular-dependent mean (c), sigma low (d) and sigma high (e) with their linear (c) and constant (d-e) fit functions in $\eta\pi$ with $\eta \rightarrow 6\gamma$.

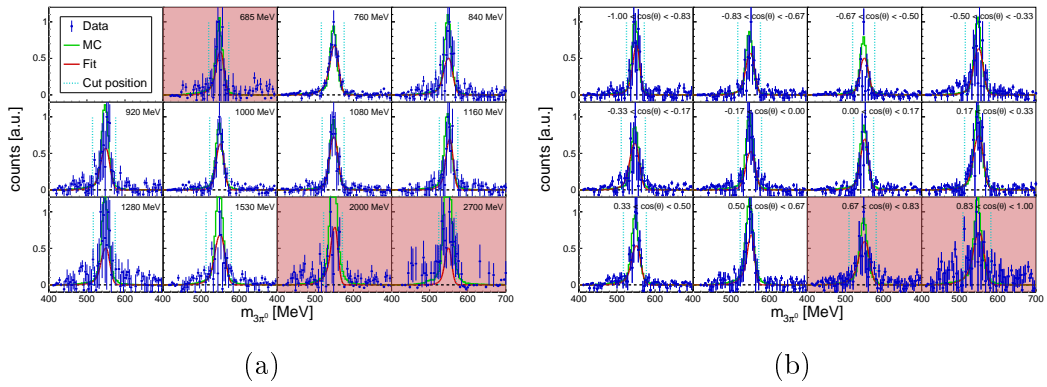


Figure A.6: Invariant mass cut positions as a function of the incident photon energy E_γ (a) and $\cos(\theta)$ (b) in ηn with $\eta \rightarrow 6\gamma$

A.2 Coplanarity cut positions

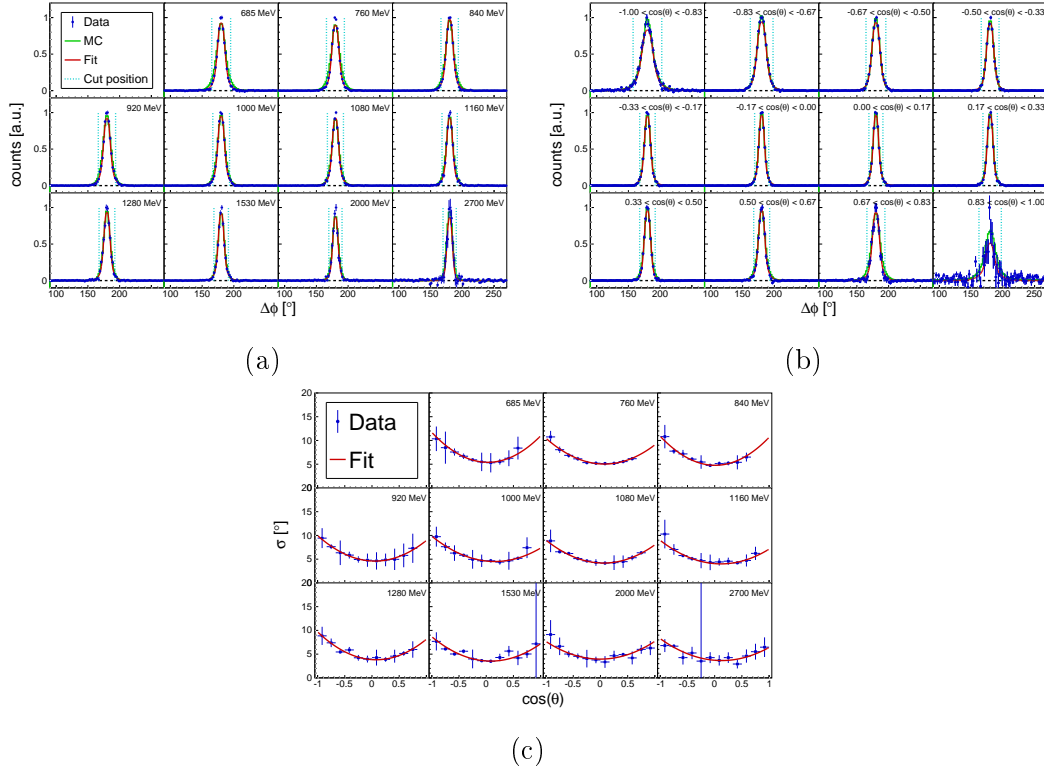


Figure A.7: Coplanarity cut positions as a function of the incident photon energy E_γ (a) and $\cos(\theta)$ (b) as well as the energy- and angular-dependent sigma (c) with its quadratic fit function in $\pi^0 p$.

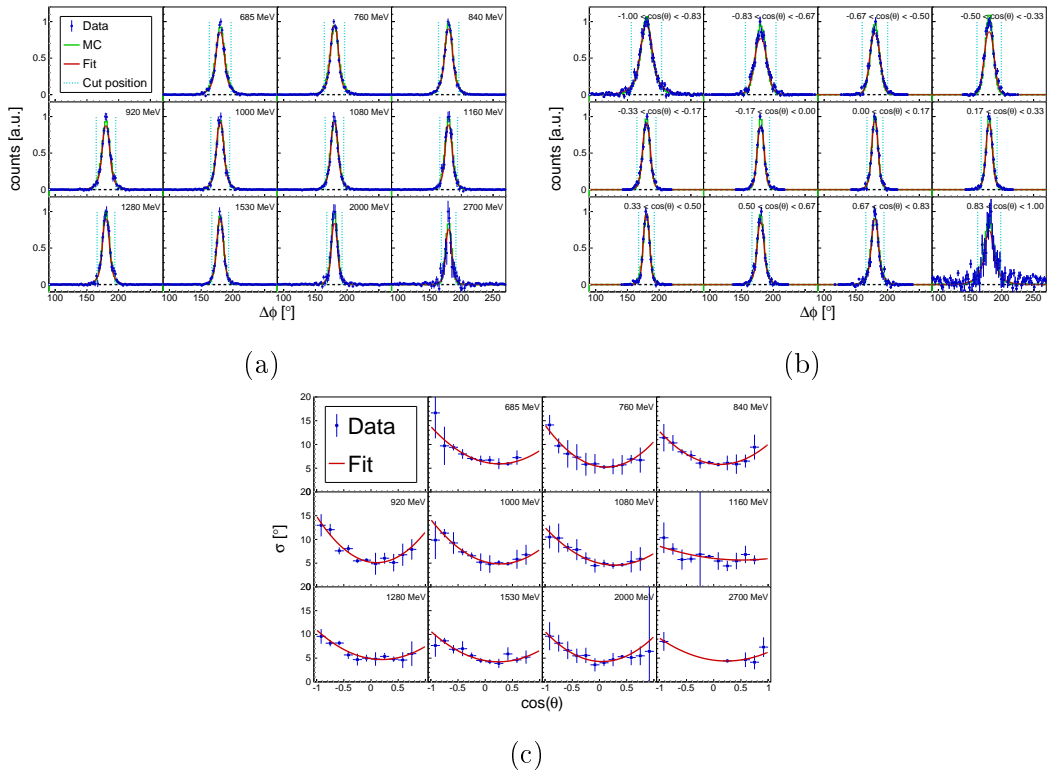


Figure A.8: Coplanarity cut positions as a function of the incident photon energy E_γ (a) and $\cos(\theta)$ (b) as well as the energy- and angular-dependent sigma with its quadratic fit function in $\pi^0 n$.

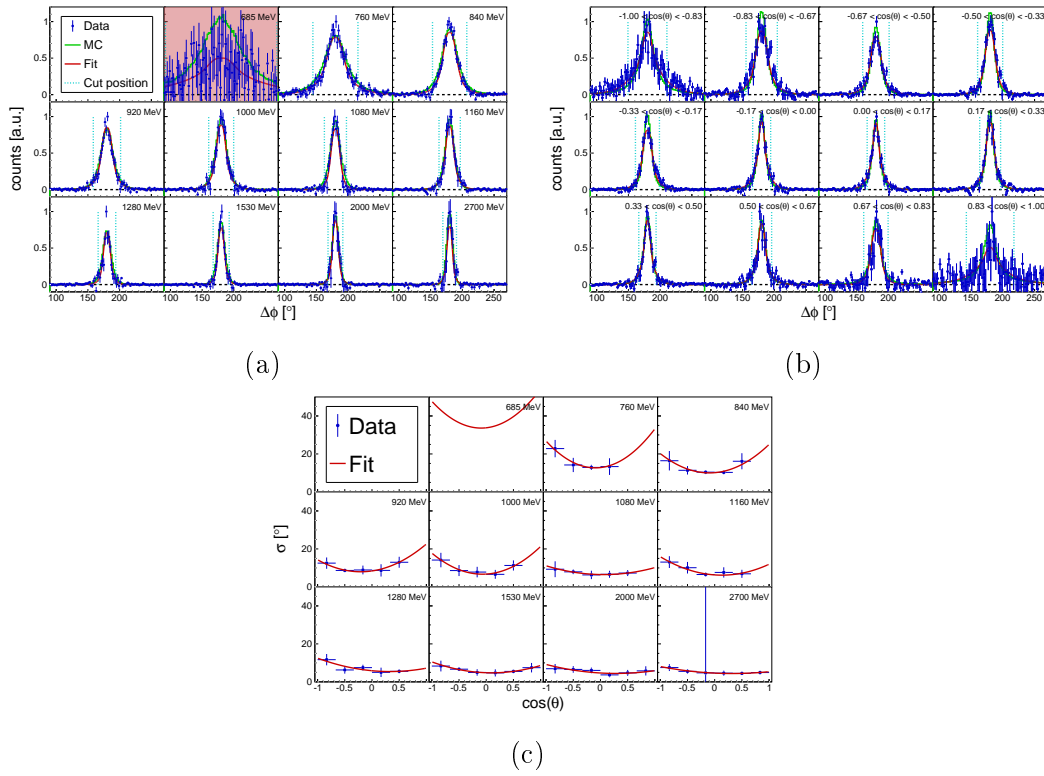


Figure A.9: Coplanarity cut positions as a function of the incident photon energy E_γ (a) and $\cos(\theta)$ (b) as well as the energy- and angular-dependent sigma (c) with its quadratic fit function in ηp with $\eta \rightarrow 2\gamma$.

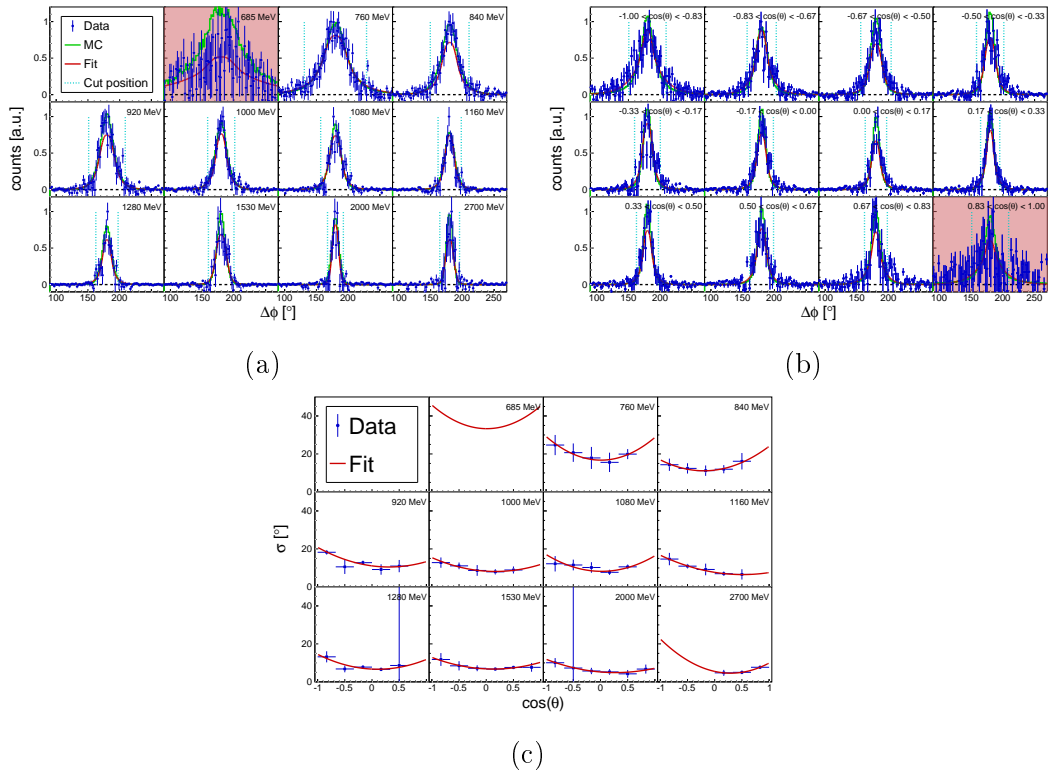


Figure A.10: Coplanarity cut positions as a function of the incident photon energy E_γ (a) and $\cos(\theta)$ (b) as well as the energy- and angular-dependent sigma (c) with its quadratic fit function in ηn with $\eta \rightarrow 2\gamma$

Appendix A. Kinematic cut positions

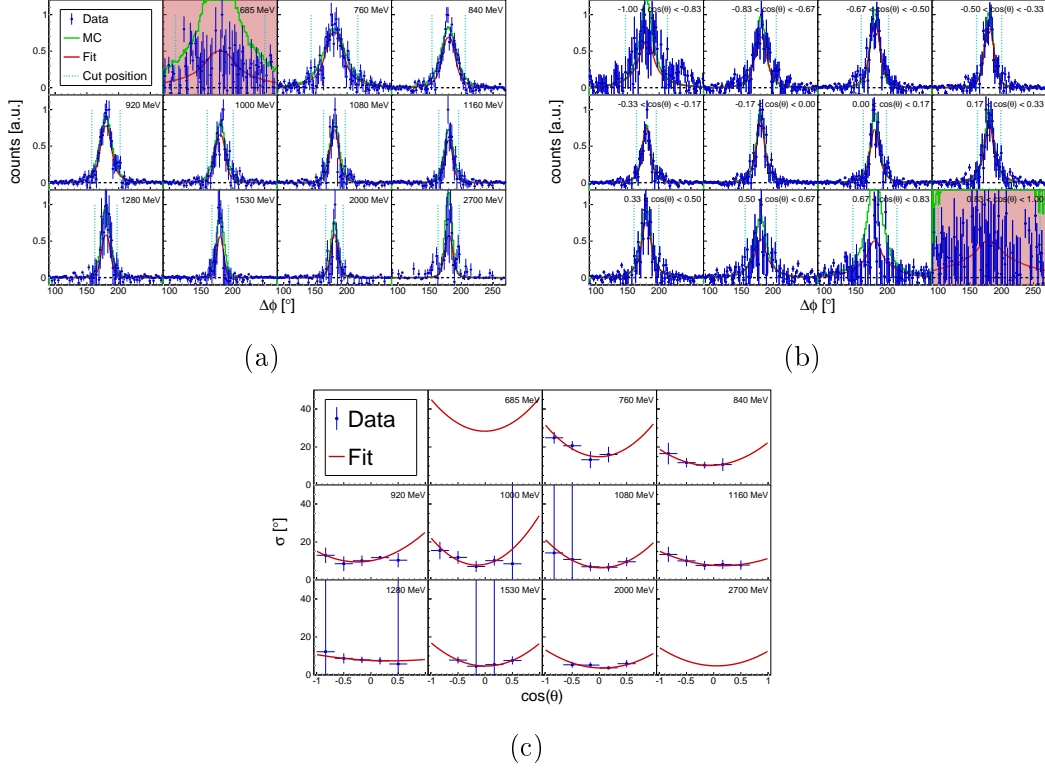


Figure A.11: Coplanarity cut positions as a function of the incident photon energy E_γ (a) and $\cos(\theta)$ (b) as well as the energy- and angular-dependent sigma (c) with its quadratic fit function in ηp with $\eta \rightarrow 6\gamma$.

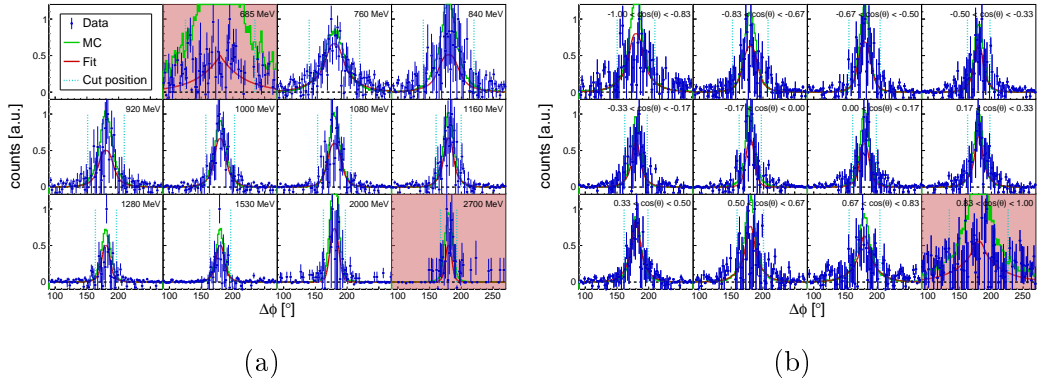


Figure A.12: Coplanarity cut positions as a function of the incident photon energy E_γ (a) and $\cos(\theta)$ (b) in ηn with $\eta \rightarrow 6\gamma$

A.3 Missing mass cut positions

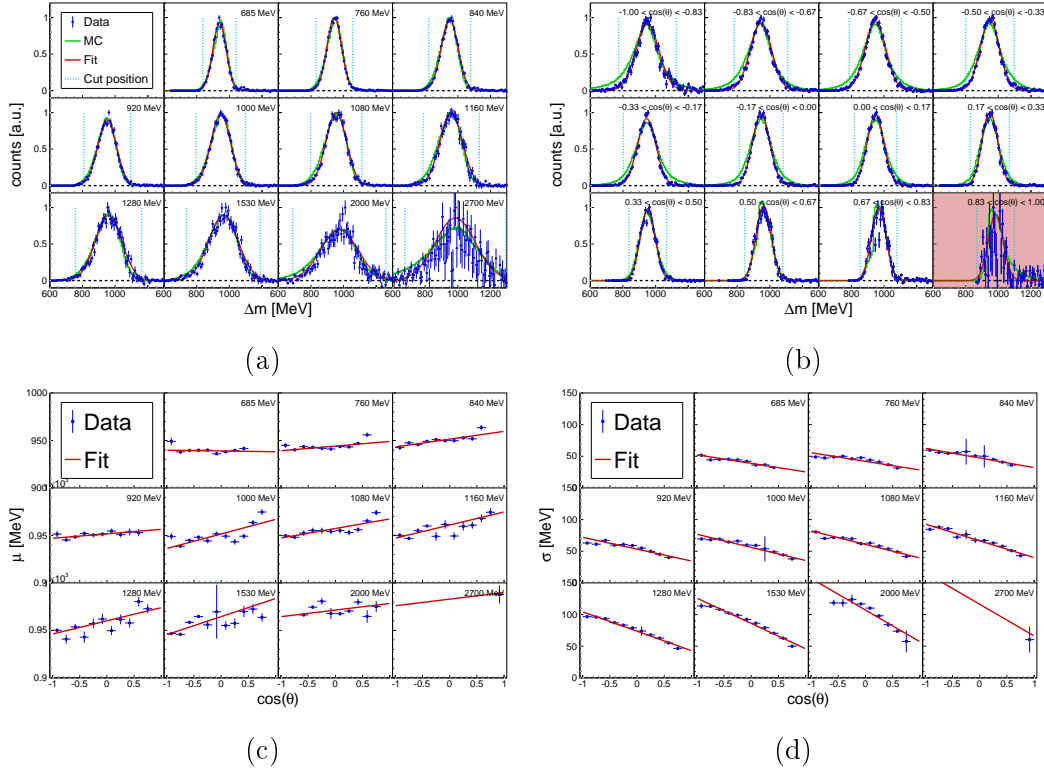


Figure A.13: Missing mass cut positions as a function of the incident photon energy E_γ (a) and $\cos(\theta)$ (b) as well as the energy- and angular-dependent mean (c) and sigma (d) with their linear fit functions in $\pi^0 p$.

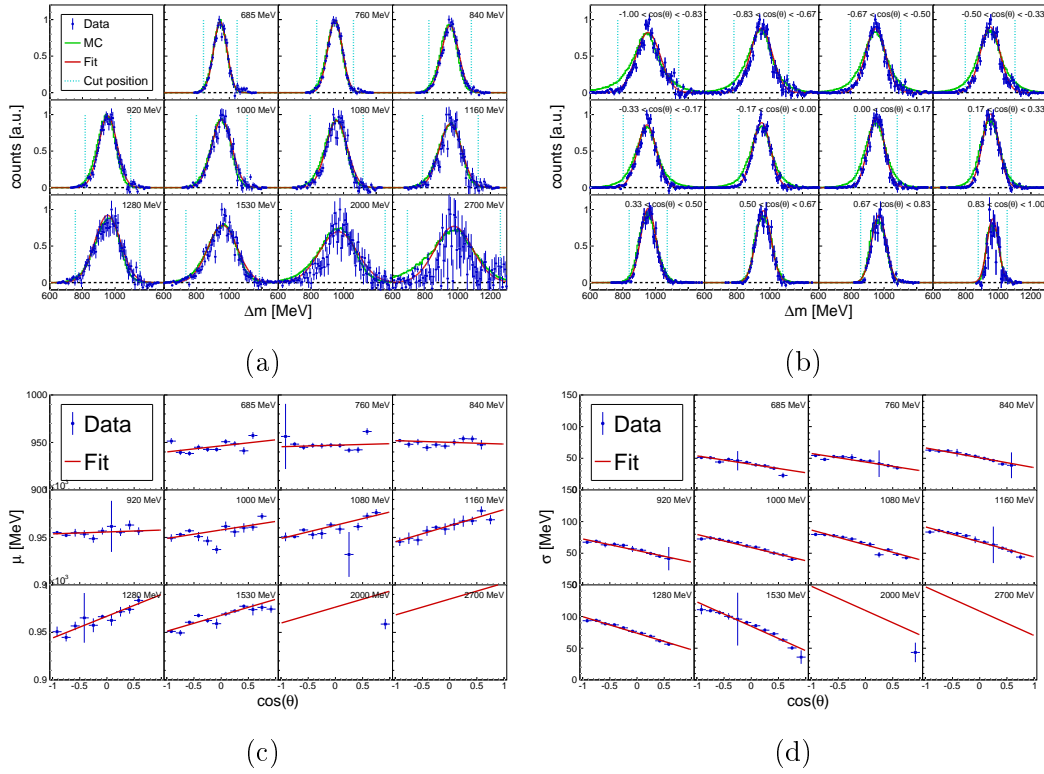


Figure A.14: Missing mass cut positions as a function of the incident photon energy E_γ (a) and $\cos(\theta)$ (b) as well as the energy- and angular-dependent mean (c) and sigma (d) with their linear fit functions in $\pi^0 n$.

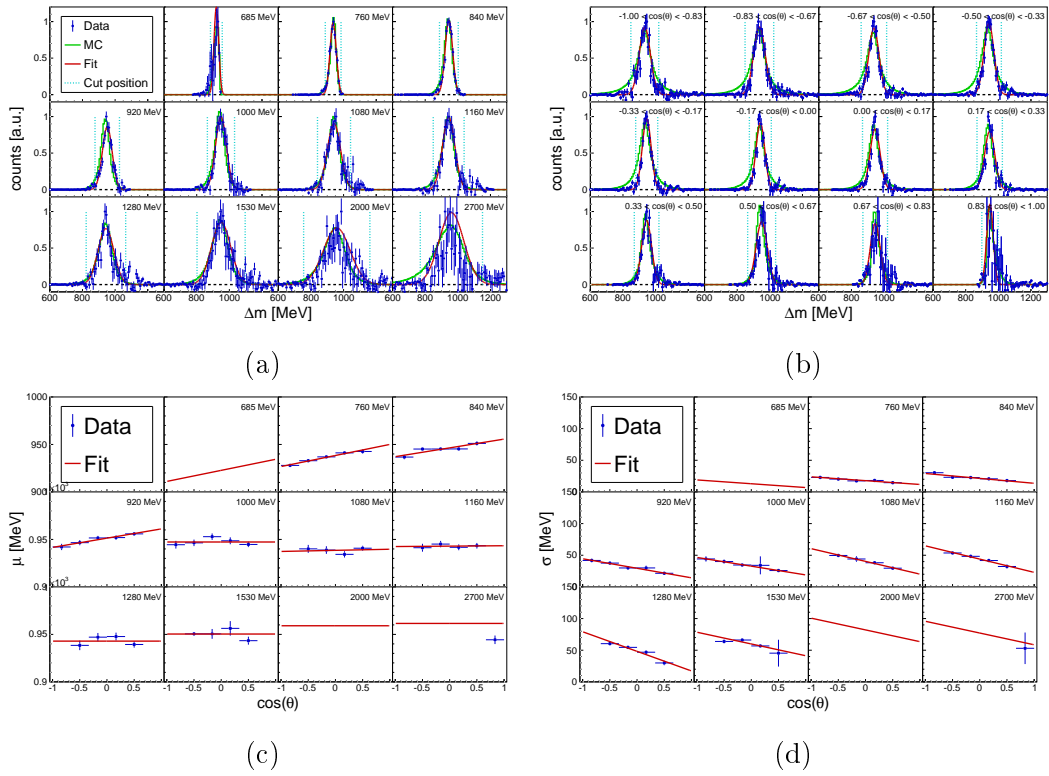


Figure A.15: Missing mass cut positions as a function of the incident photon energy E_γ (a) and $\cos(\theta)$ (b) as well as the energy- and angular-dependent mean (c) and sigma (d) with their linear fit functions in ηp with $\eta \rightarrow 2\gamma$.

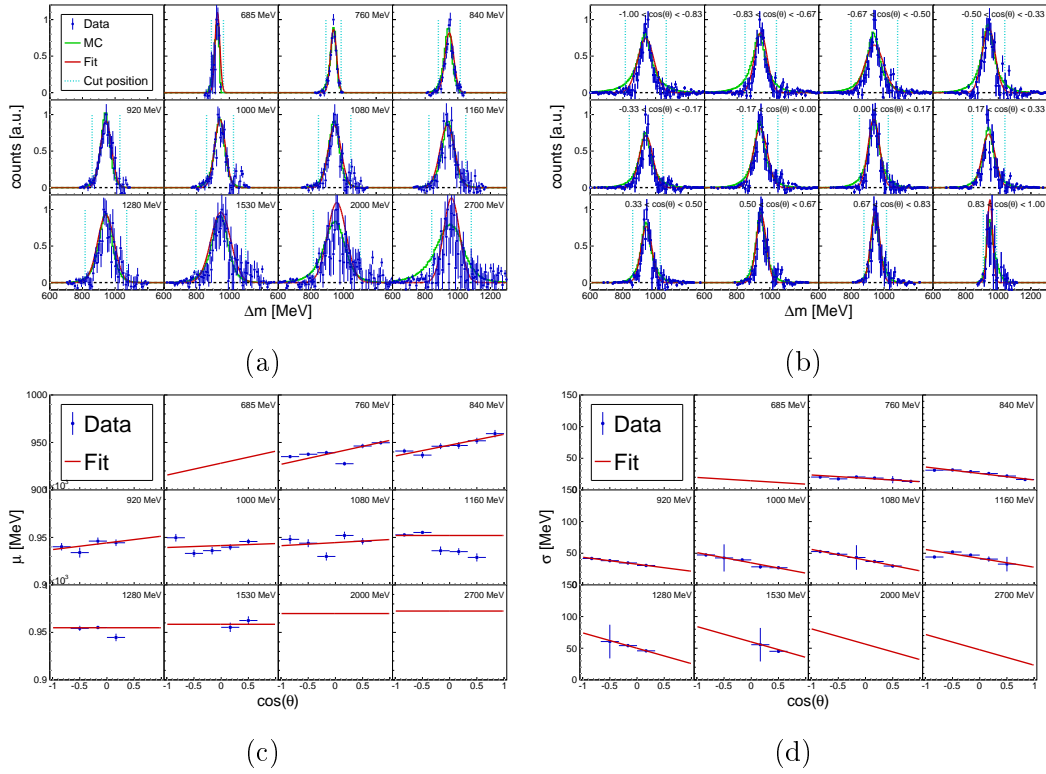


Figure A.16: Missing mass cut positions as a function of the incident photon energy E_γ (a) and $\cos(\theta)$ (b) as well as the energy- and angular-dependent mean (c) and sigma (d) with their linear fit functions in ηn with $\eta \rightarrow 2\gamma$

A.3. Missing mass cut positions

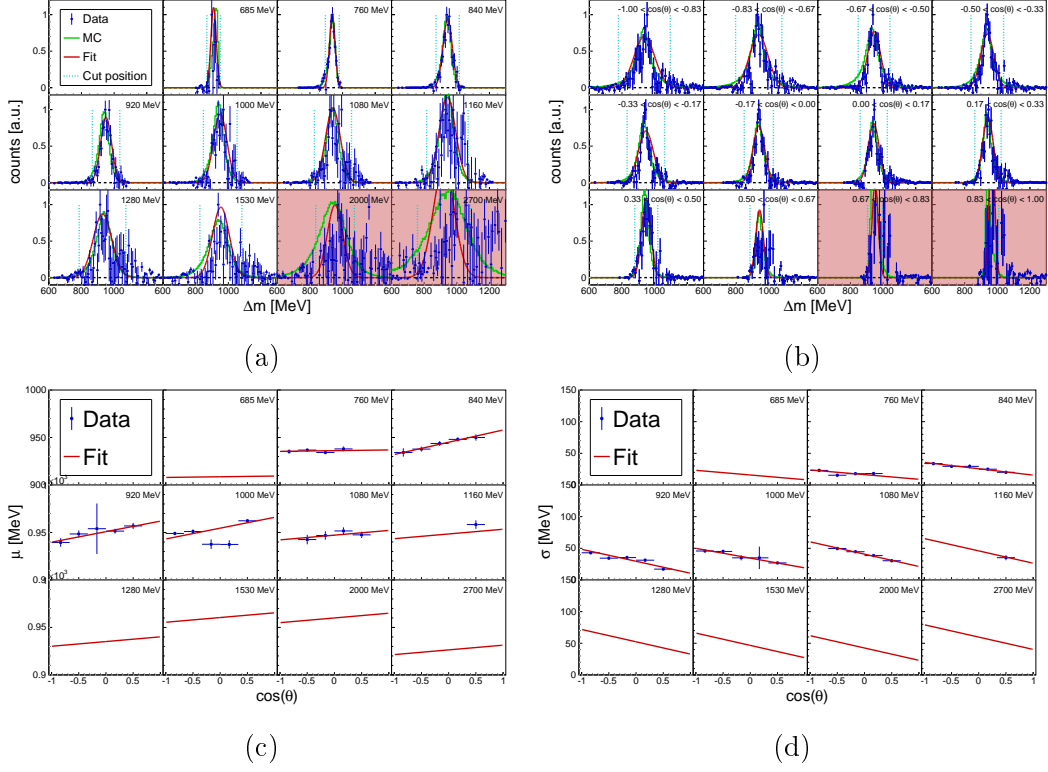


Figure A.17: Missing mass cut positions as a function of the incident photon energy E_γ (a) and $\cos(\theta)$ (b) as well as the energy- and angular-dependent mean (c) and sigma (d) with their linear fit functions in ηp with $\eta \rightarrow 6\gamma$.

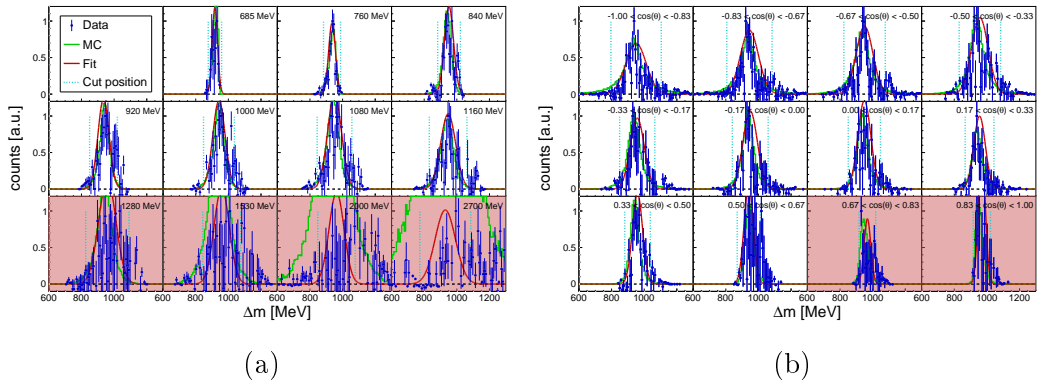


Figure A.18: Missing mass cut positions as a function of the incident photon energy E_γ (a) and $\cos(\theta)$ (b) in ηn with $\eta \rightarrow 6\gamma$

A.4 Fermi momentum cut positions

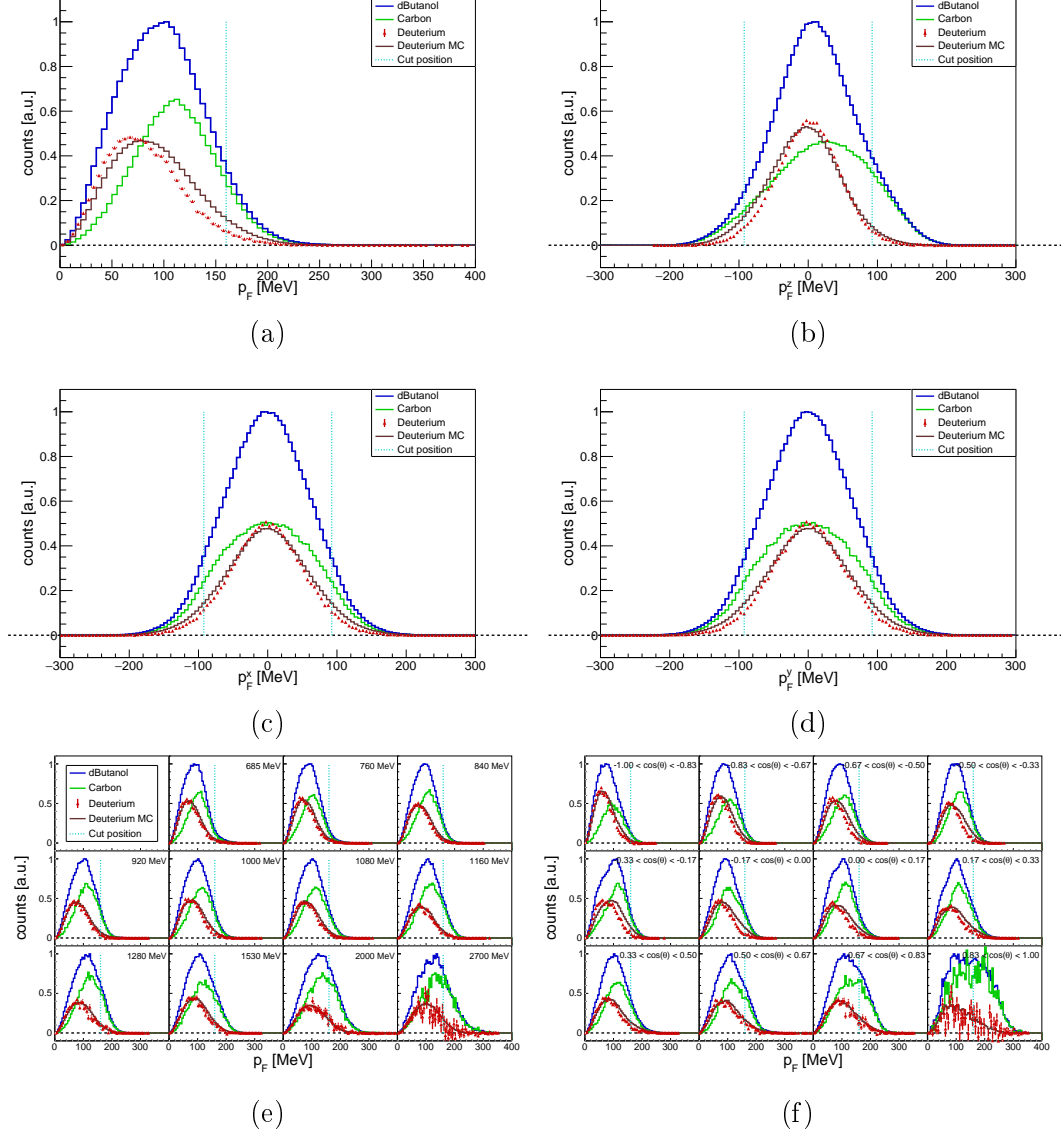


Figure A.19: Fermi momentum of the total Fermi momentum (a), the component Fermi momentum in x - (c), y - (d) and z -direction (b) and as a function of the incident photon energy E_γ (e) and $\cos(\theta)$ (f) in $\pi^0 p$.

A.4. Fermi momentum cut positions

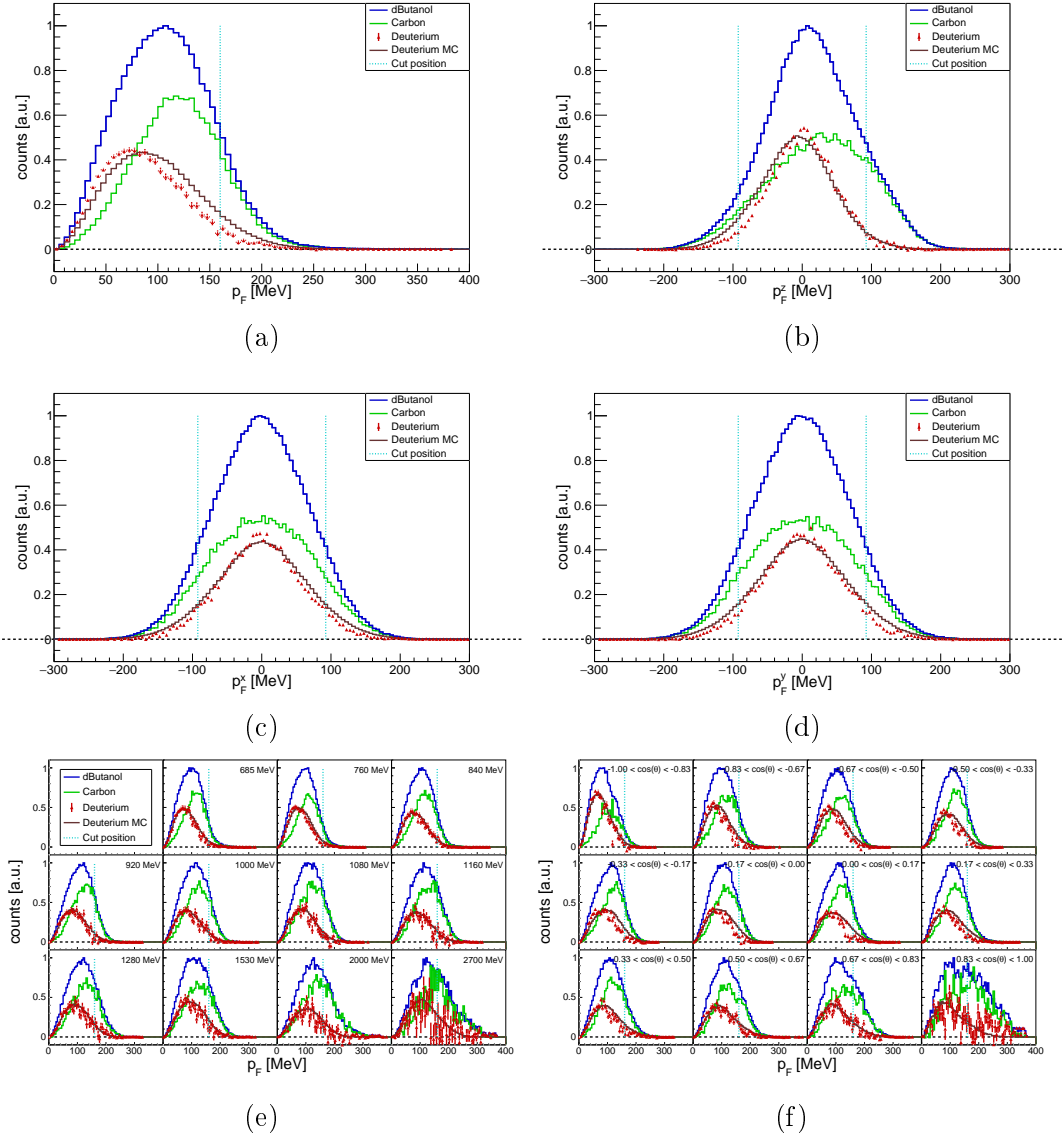


Figure A.20: Fermi momentum of the total Fermi momentum (a), the component Fermi momentum in x - (c), y - (d) and z -direction (b) and as a function of the incident photon energy E_γ (e) and $\cos(\theta)$ (f) in $\pi^0 n$.

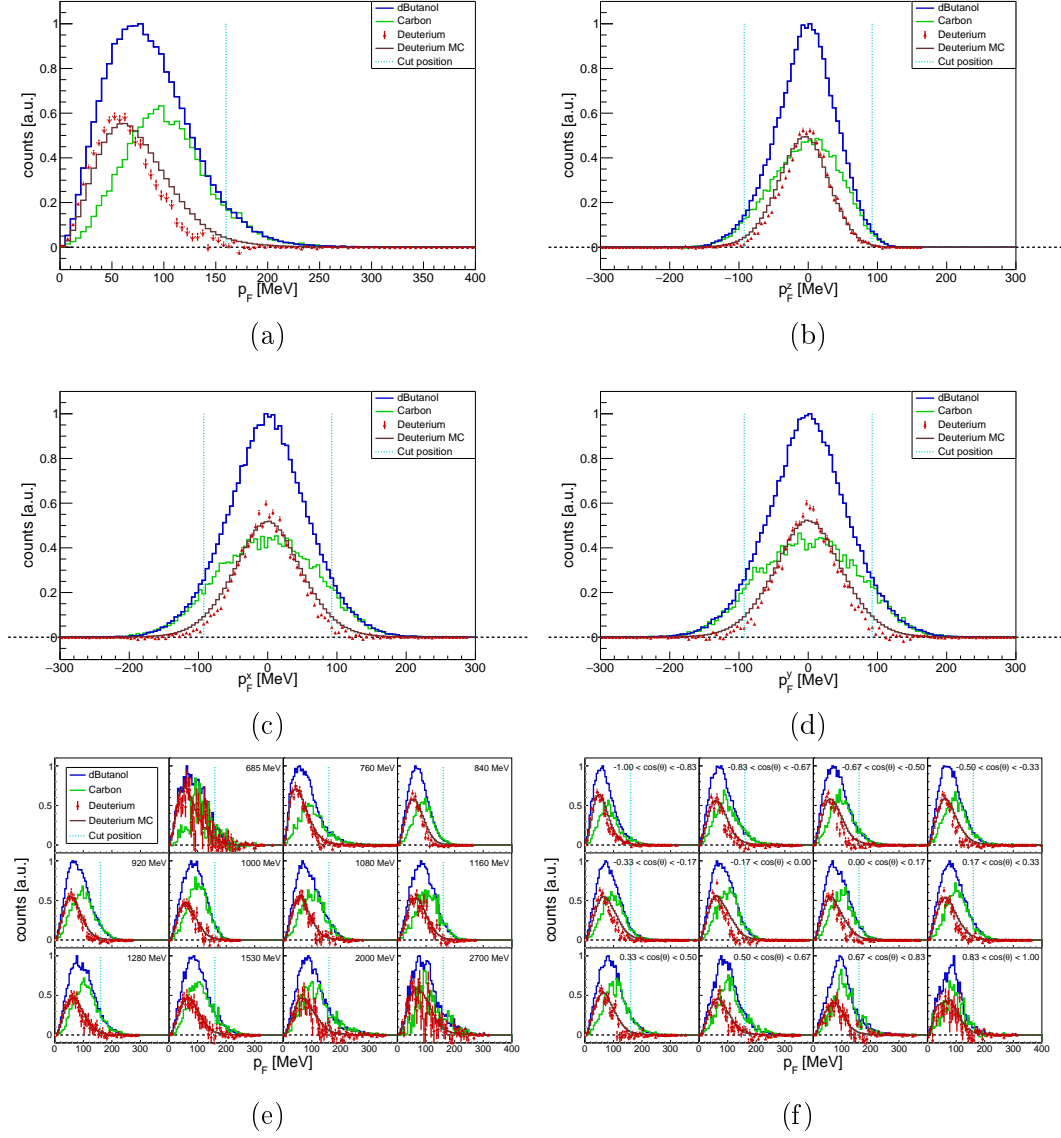


Figure A.21: Fermi momentum of the total Fermi momentum (a), the component Fermi momentum in x - (c), y - (d) and z -direction (b) and as a function of the incident photon energy E_γ (e) and $\cos(\theta)$ (f) in ηp with $\eta \rightarrow 2\gamma$.

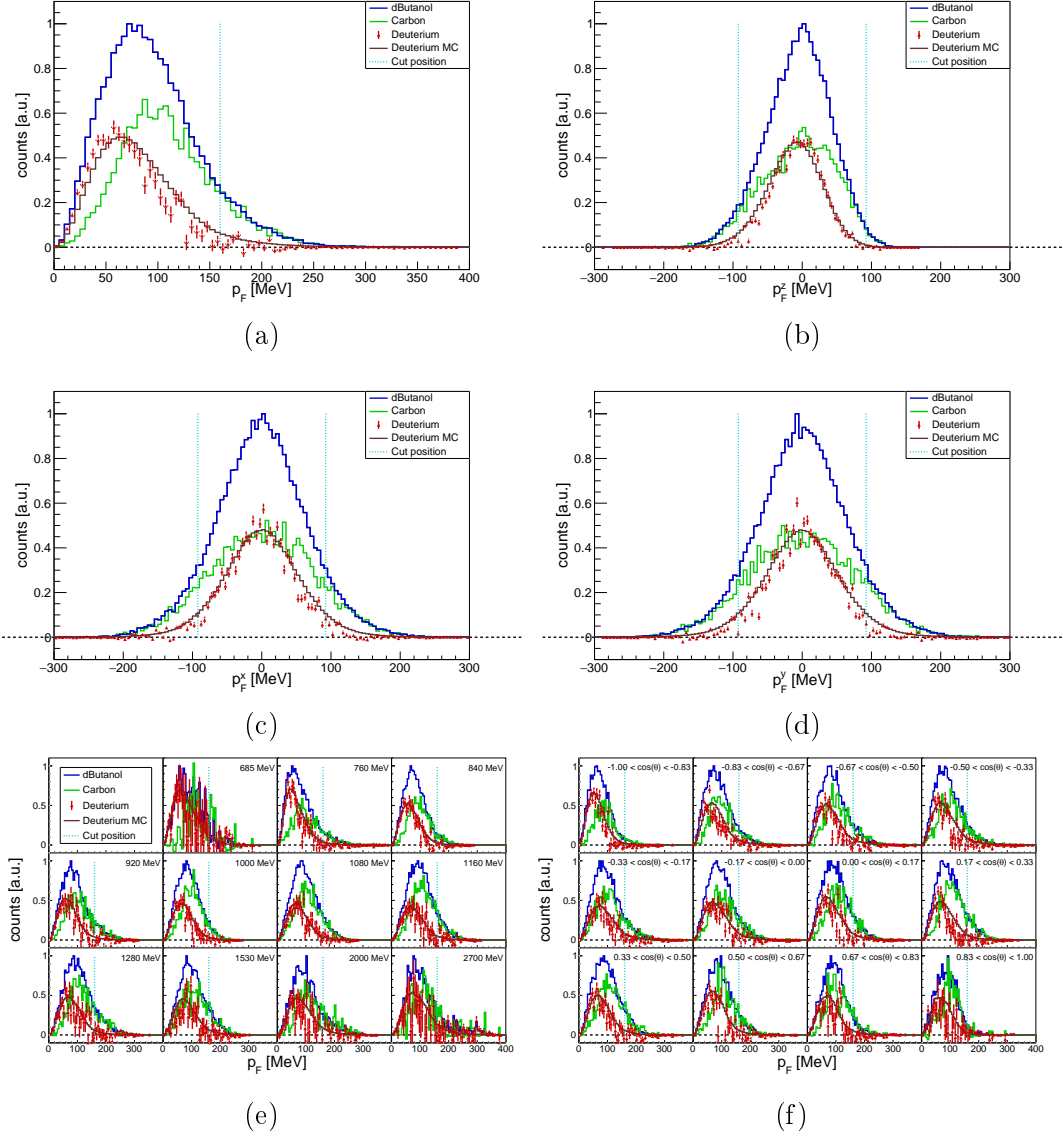


Figure A.22: Fermi momentum of the total Fermi momentum (a), the component Fermi momentum in x - (c), y - (d) and z -direction (b) and as a function of the incident photon energy E_γ (e) and $\cos(\theta)$ (f) in ηn with $\eta \rightarrow 2\gamma$.

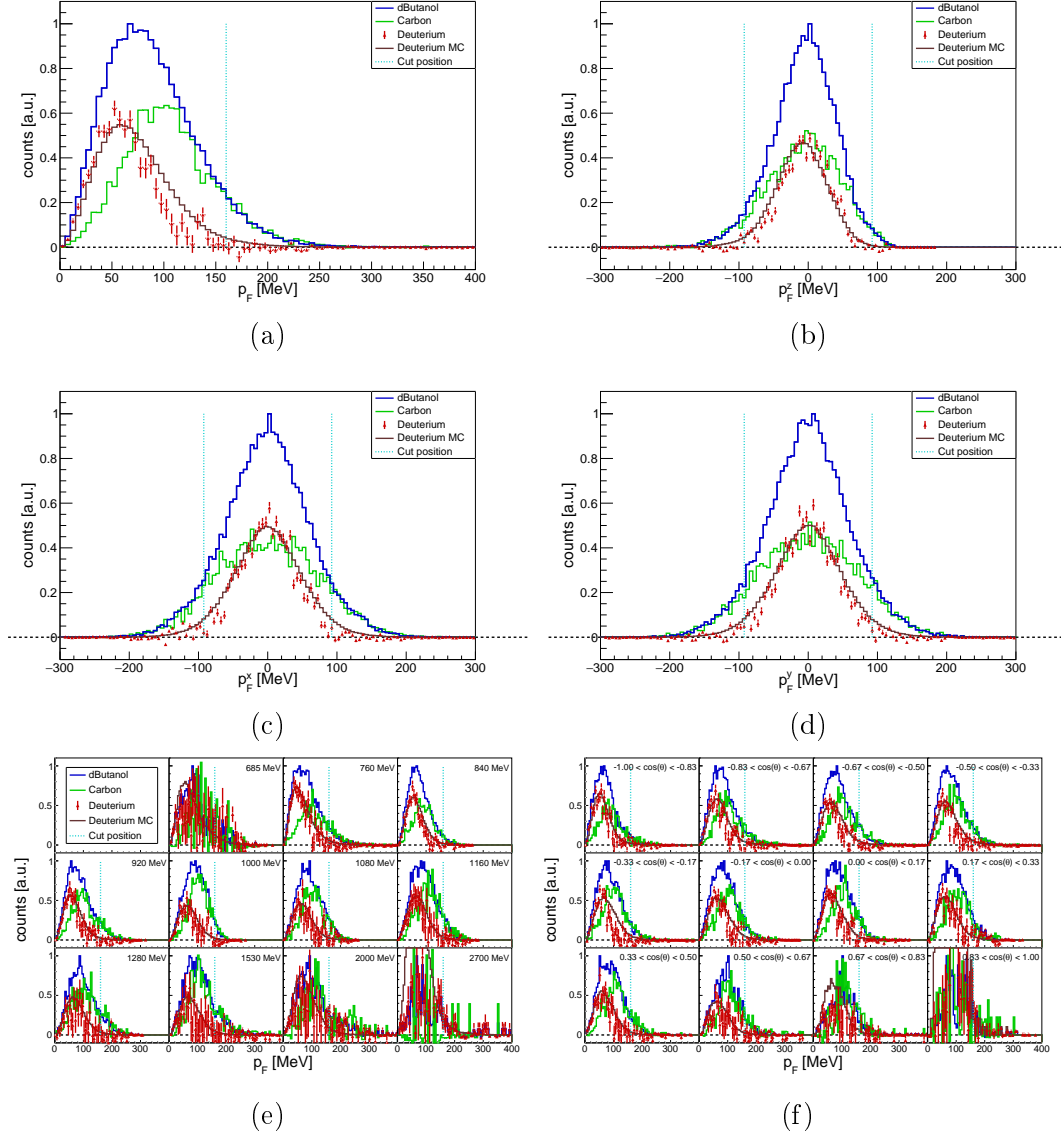


Figure A.23: Fermi momentum of the total Fermi momentum (a), the component Fermi momentum in x - (c), y - (d) and z -direction (b) and as a function of the incident photon energy E_γ (e) and $\cos(\theta)$ (f) in ηp with $\eta \rightarrow 6\gamma$.

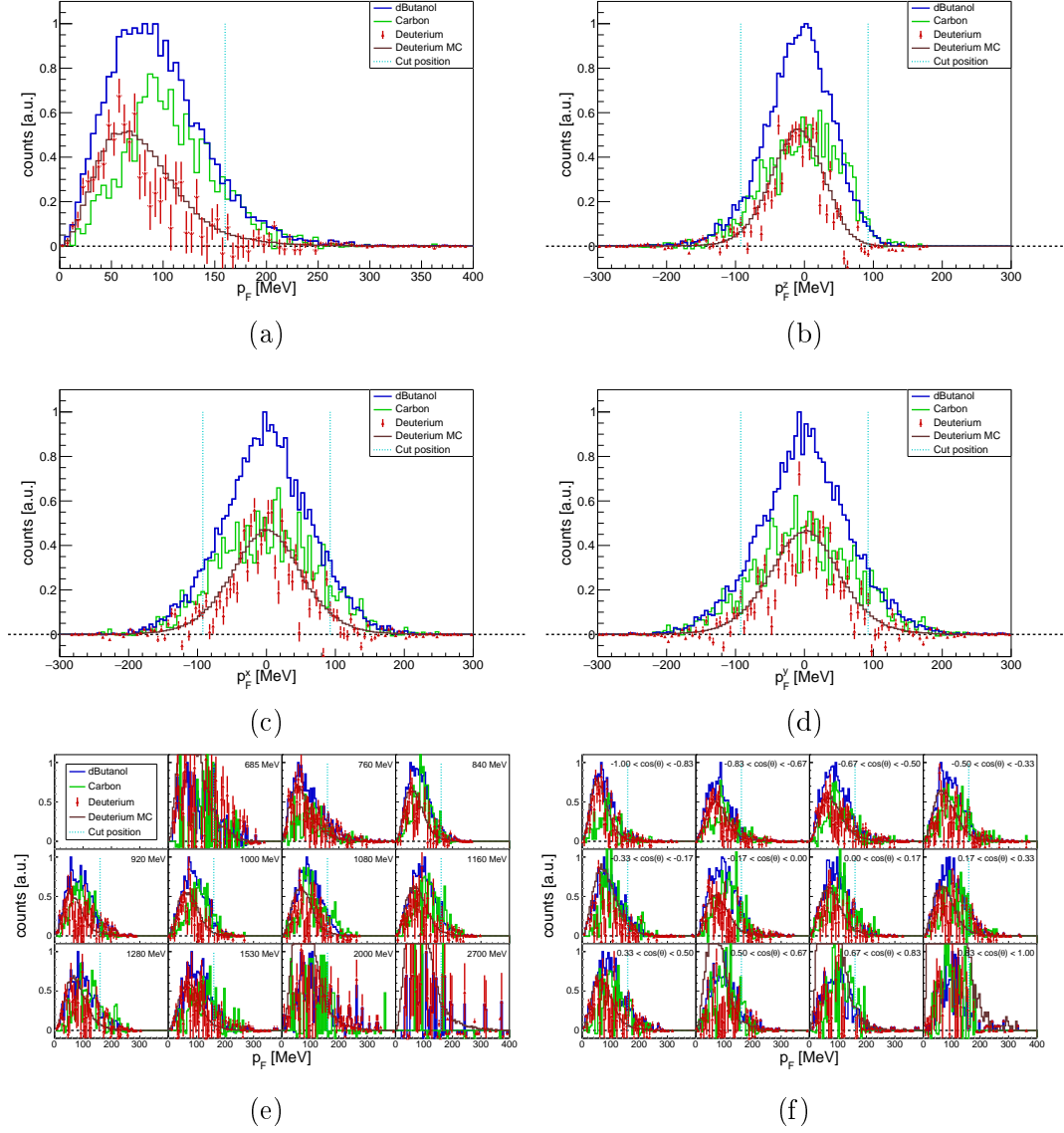


Figure A.24: Fermi momentum of the total Fermi momentum (a), the component Fermi momentum in x - (c), y - (d) and z -direction (b) and as a function of the incident photon energy E_γ (e) and $\cos(\theta)$ (f) in ηn with $\eta \rightarrow 6\gamma$.

A.5 Polar angle difference cut positions

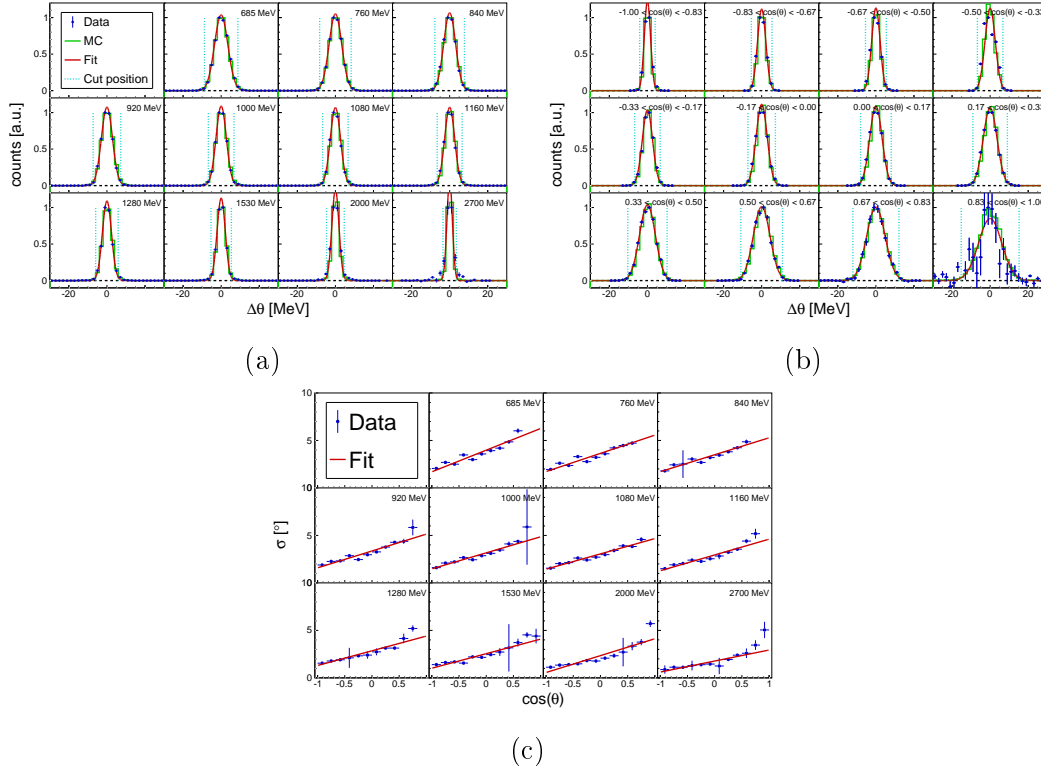


Figure A.25: Polar angle difference cut positions as a function of the incident photon energy E_γ (a) and $\cos(\theta)$ (b) as well as the energy- and angular-dependent sigma (c) with its linear fit function in $\pi^0 p$.

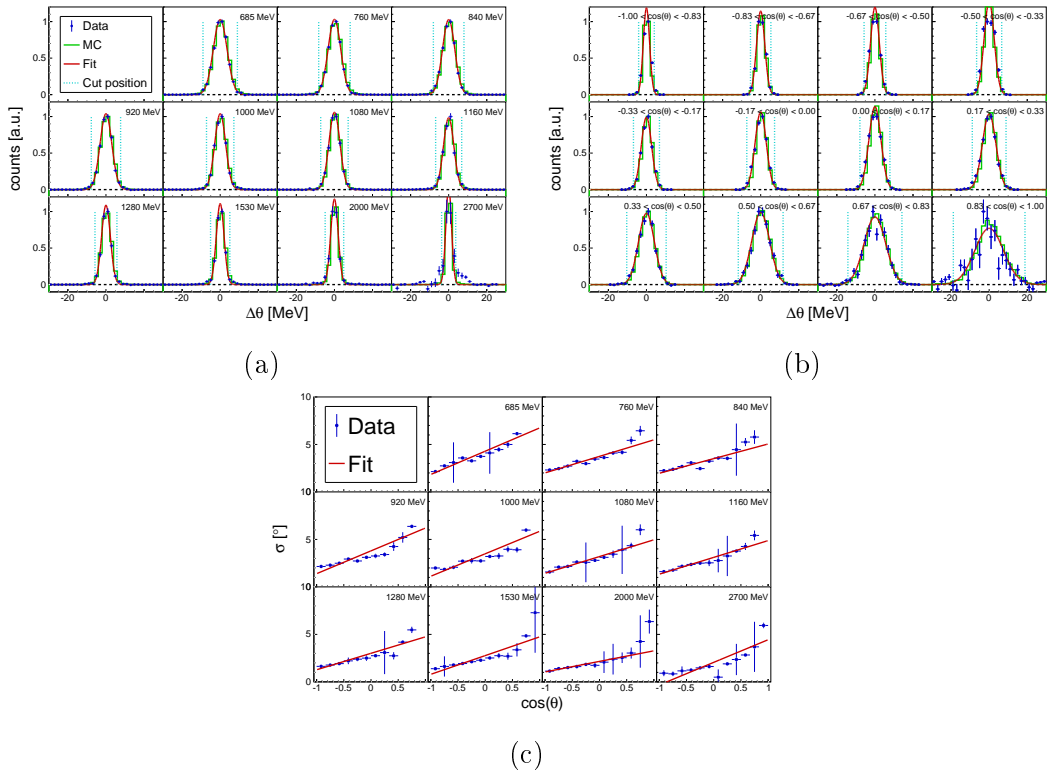


Figure A.26: Polar angle difference cut positions as a function of the incident photon energy E_γ (a) and $\cos(\theta)$ (b) as well as the energy- and angular-dependent sigma (c) with its linear fit function in $\pi^0 n$.

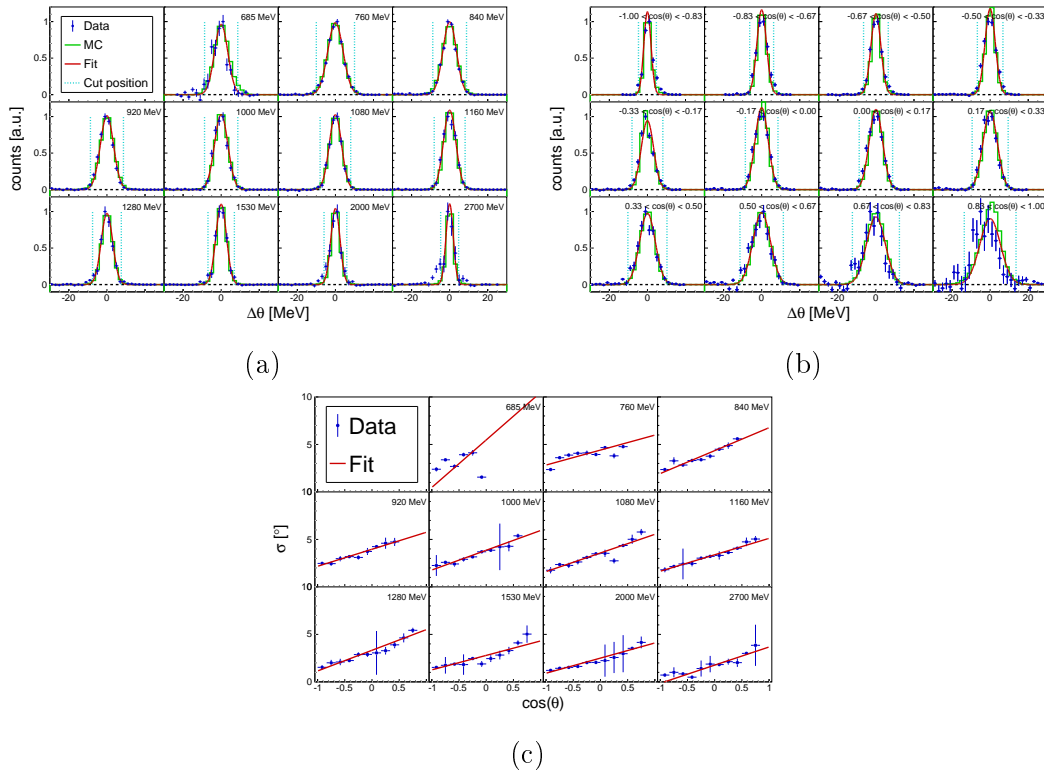


Figure A.27: Polar angle difference cut positions as a function of the incident photon energy E_γ (a) and $\cos(\theta)$ (b) as well as the energy- and angular-dependent sigma (c) with its linear fit function in ηp with $\eta \rightarrow 2\gamma$.

A.5. Polar angle difference cut positions

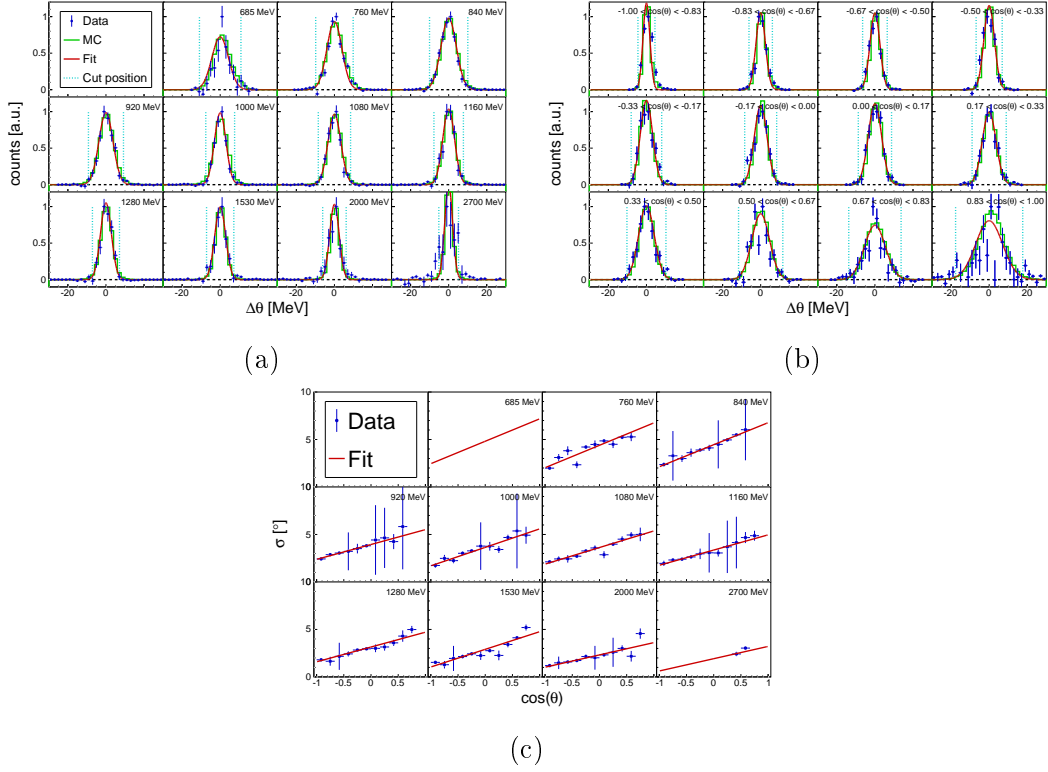


Figure A.28: Polar angle difference cut positions as a function of the incident photon energy E_γ (a) and $\cos(\theta)$ (b) as well as the energy- and angular-dependent sigma (c) with its linear fit function in $\eta\eta$ with $\eta \rightarrow 6\gamma$.

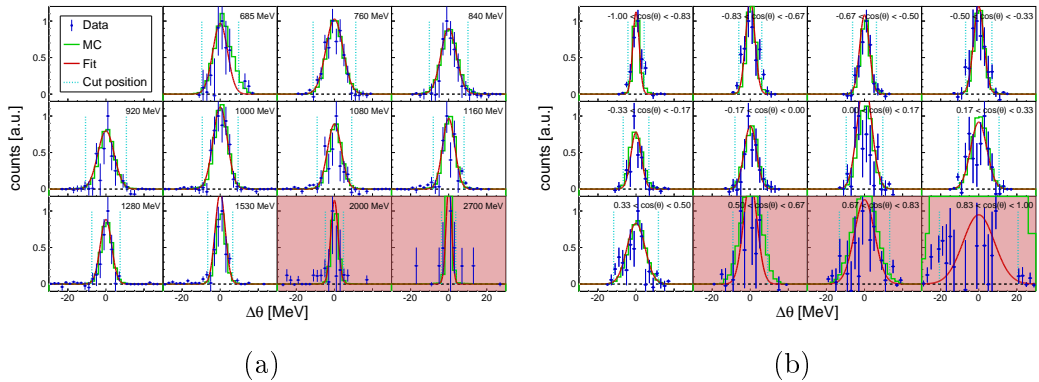


Figure A.29: Polar angle difference cut positions as a function of the incident photon energy E_γ (a) and $\cos(\theta)$ (b) in $\eta\eta$ with $\eta \rightarrow 6\gamma$.

B | Data analysis

B.1 Cherenkov radiation for CO₂

Cherenkov light is emitted if the phase velocity of the electric-charged particle v is faster than the speed of light in that medium, i.e.:

$$v \geq \frac{c}{n} \quad (\text{B.1})$$

must be fulfilled. Here, n is the refractive index of the medium and c is the speed of light. This leads to a condition for the half-opening angle θ of the Cherenkov light cone:

$$\cos(\theta) = \frac{1}{n\beta}, \quad (\text{B.2})$$

where $\beta = v/c$.

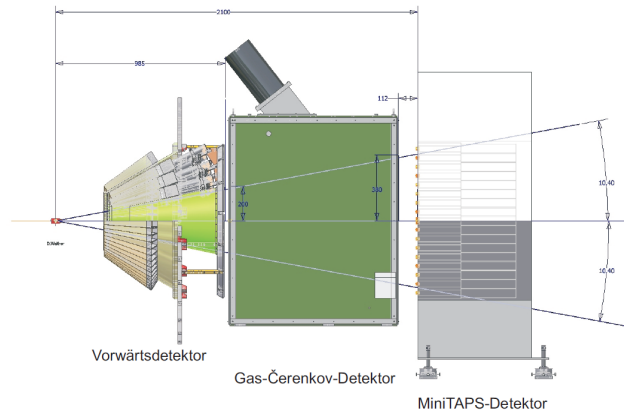


Figure B.1: Kinematic conditions for Cherenkov radiation, where c is the light velocity, n the refractive index, t the time and $\beta = v/c$ the velocity in terms of the light velocity. Figure taken from [335]

The threshold velocity v_{thr} is given for the equal sign in equation (B.1),

leading to:

$$v_{thr} = \frac{c}{n} \quad \Leftrightarrow \quad \beta_{thr} = \frac{1}{n}, \quad (\text{B.3})$$

which is equivalent with a threshold angle $\theta_{thr} = 0$.

In terms of the relativistic kinetic energy that is given by:

$$E_{kin} = \gamma mc^2 \quad (\text{B.4})$$

with the Lorentz factor $\gamma = (1 - \beta)^{-1}$ and the mass m of the particle, the threshold is given by:

$$E_{kin}^{thr} = \frac{mc^2}{\sqrt{1 - \beta_{thr}}} = \frac{mc^2}{\sqrt{1 - \frac{1}{n^2}}}. \quad (\text{B.5})$$

If the refractive index is $n = 1.00045$, like it is for CO_2 under standard conditions [276, 277], the threshold energy for an electron or positron is given by 17.4 MeV.

B.2 Linear beam photon polarisation degrees

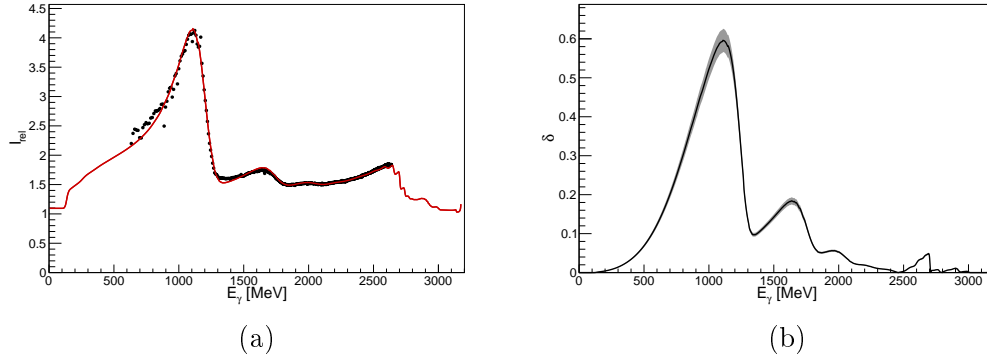


Figure B.2: Relative intensity spectrum with the ANB fit (a) and linear polarisation degree δ with error range (b) for negative crystal orientation and run numbers 203219 to 203943 in Oct2018.

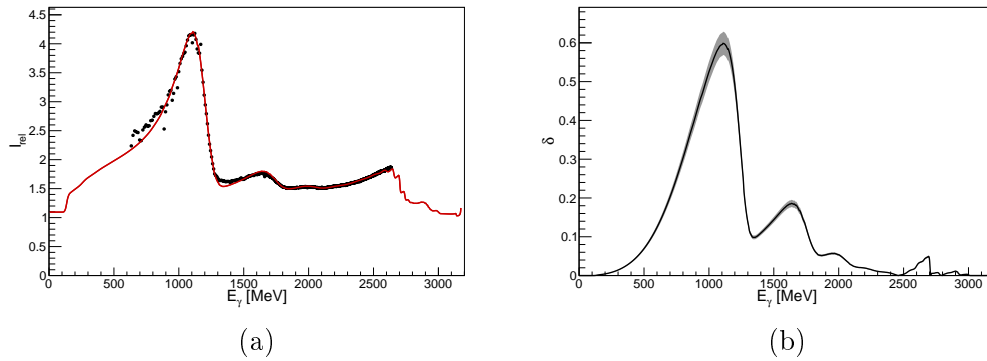


Figure B.3: Relative intensity spectrum with the ANB fit (a) and linear polarisation degree δ with error range (b) for positive crystal orientation and run numbers 203219 to 203943 in Oct2018.

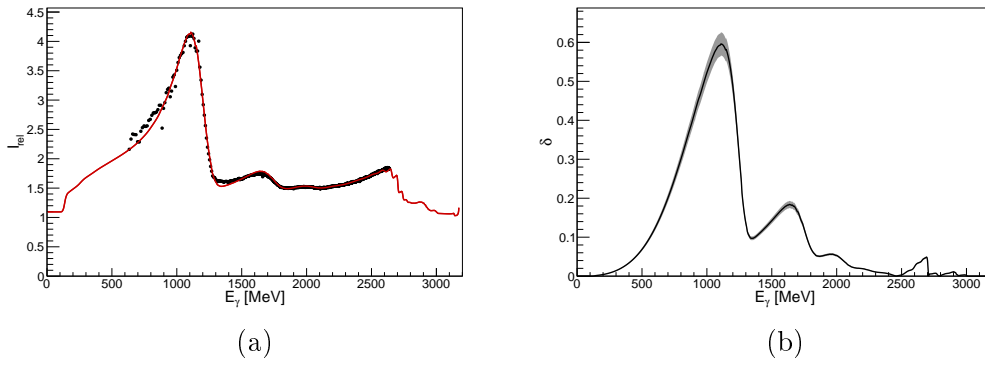


Figure B.4: Relative intensity spectrum with the ANB fit (a) and linear polarisation degree δ with error range (b) for negative crystal orientation and run numbers 203933 to 204582 in Oct2018.

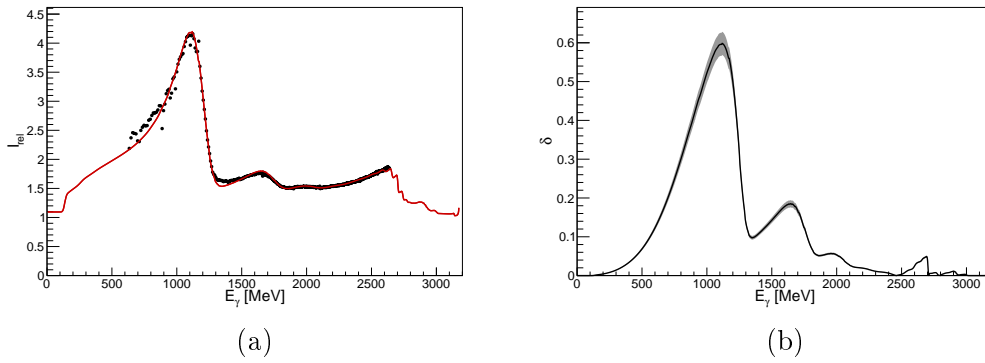


Figure B.5: Relative intensity spectrum with the ANB fit (a) and linear polarisation degree δ with error range (b) for positive crystal orientation and run numbers 203933 to 204582 in Oct2018.

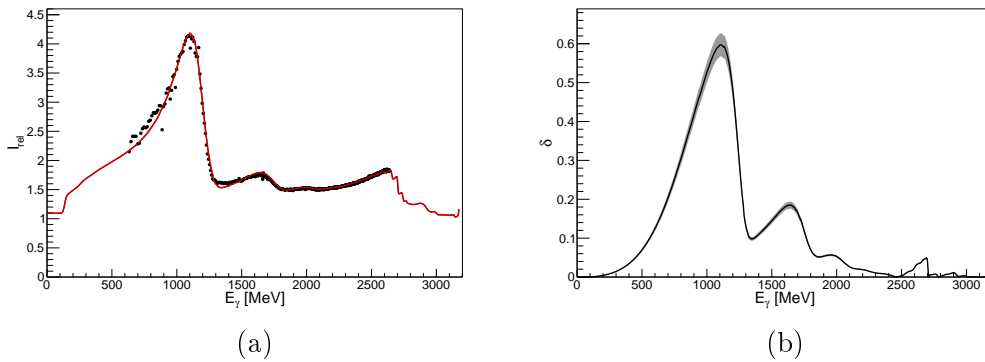


Figure B.6: Relative intensity spectrum with the ANB fit (a) and linear polarisation degree δ with error range (b) for negative crystal orientation and run numbers 204573 to 204813 in Oct2018.

B.2. Linear beam photon polarisation degrees

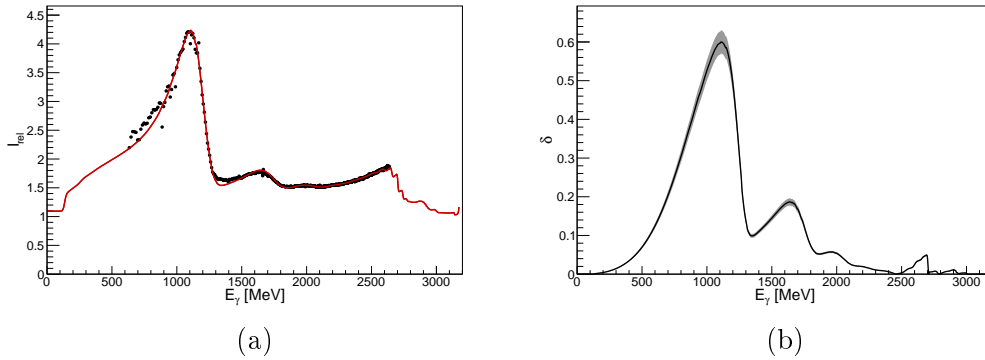


Figure B.7: Relative intensity spectrum with the ANB fit (a) and linear polarisation degree δ with error range (b) for positive crystal orientation and run numbers 204573 to 204813 in Oct2018.

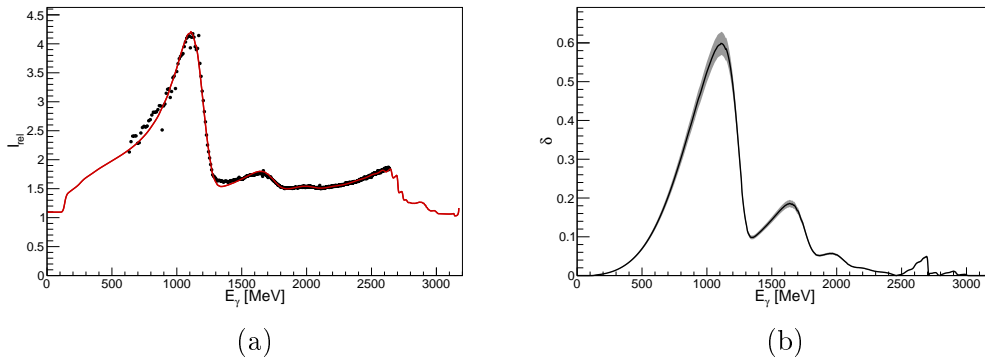


Figure B.8: Relative intensity spectrum with the ANB fit (a) and linear polarisation degree δ with error range (b) for negative crystal orientation and run numbers 204804 to 205955 in Oct2018.

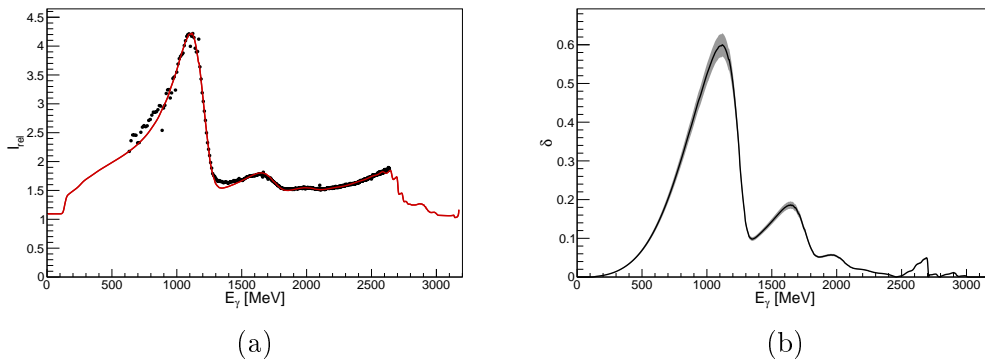


Figure B.9: Relative intensity spectrum with the ANB fit (a) and linear polarisation degree δ with error range (b) for positive crystal orientation and run numbers 204804 to 205955 in Oct2018.

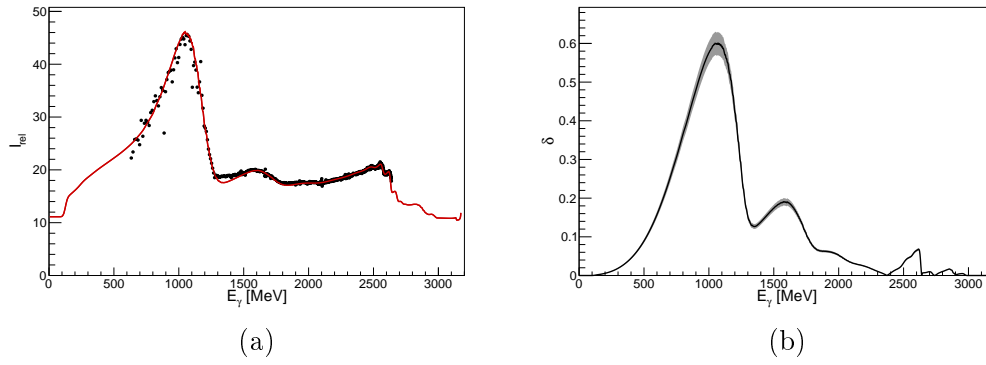


Figure B.10: Preliminary relative intensity spectrum with the ANB fit (a) and linear polarisation degree δ with error range (b) for negative crystal orientation in Dec2021.

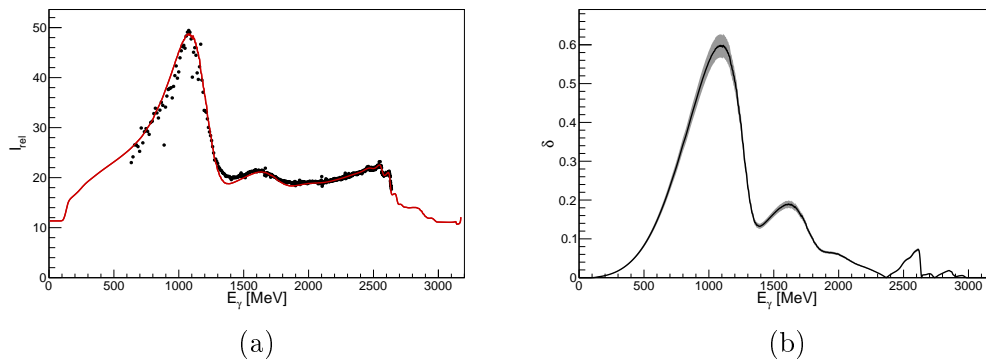


Figure B.11: Preliminary relative intensity spectrum with the ANB fit (a) and linear polarisation degree δ with error range (b) for positive crystal orientation in Dec2021.

B.3 Carbon scaling factor

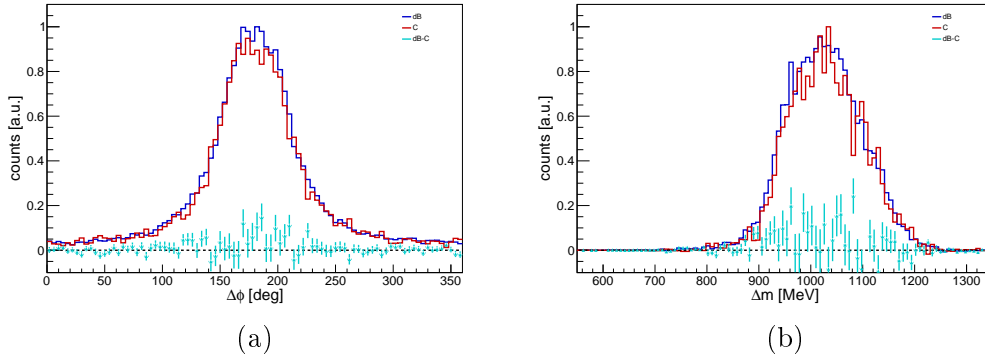


Figure B.12: Coplanarity (a) and missing mass (b) spectra of the dButanol and carbon data with applied anticuts. The difference between them, i.e. remaining deuterium reactions, is also shown. The scaling factor of $c_t = 0.89$ is applied for the carbon data. The data show ηn with $\eta \rightarrow 2\gamma$ in Oct2018.

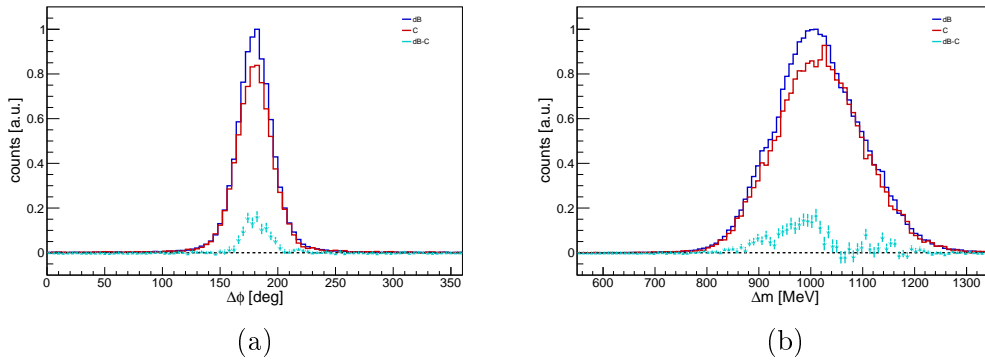


Figure B.13: Coplanarity (a) and missing mass (b) spectra of the dButanol and carbon data with applied anticuts. The difference between them, i.e. remaining deuterium reactions, is also shown. The scaling factor of $c_t = 0.89$ is applied for the carbon data. The data show $\pi^0 n$ in Oct2018.

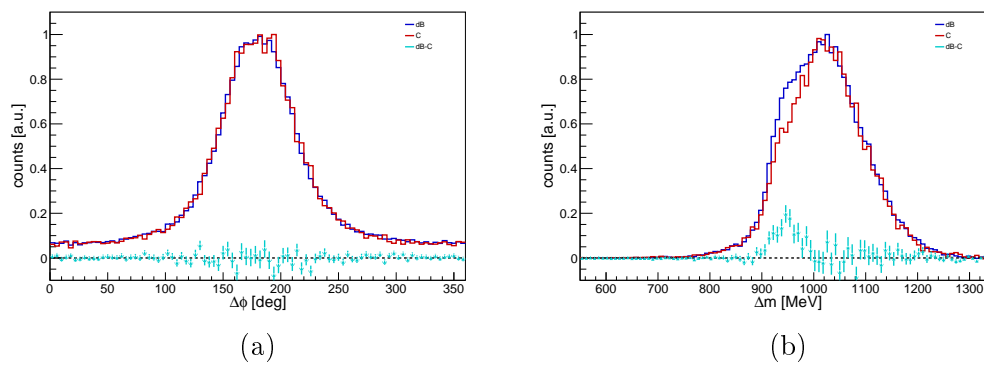


Figure B.14: Coplanarity (a) and missing mass (b) spectra of the dButanol and carbon data with applied anticuts. The difference between them, i.e. remaining deuterium reactions, is also shown. The scaling factor of $c_t = 0.85$ is applied for the carbon data. The data show ηp with $\eta \rightarrow 2\gamma$ in Dec2021.

C | Extraction of polarisation observables

C.1 Integrated asymmetries in Dec2021

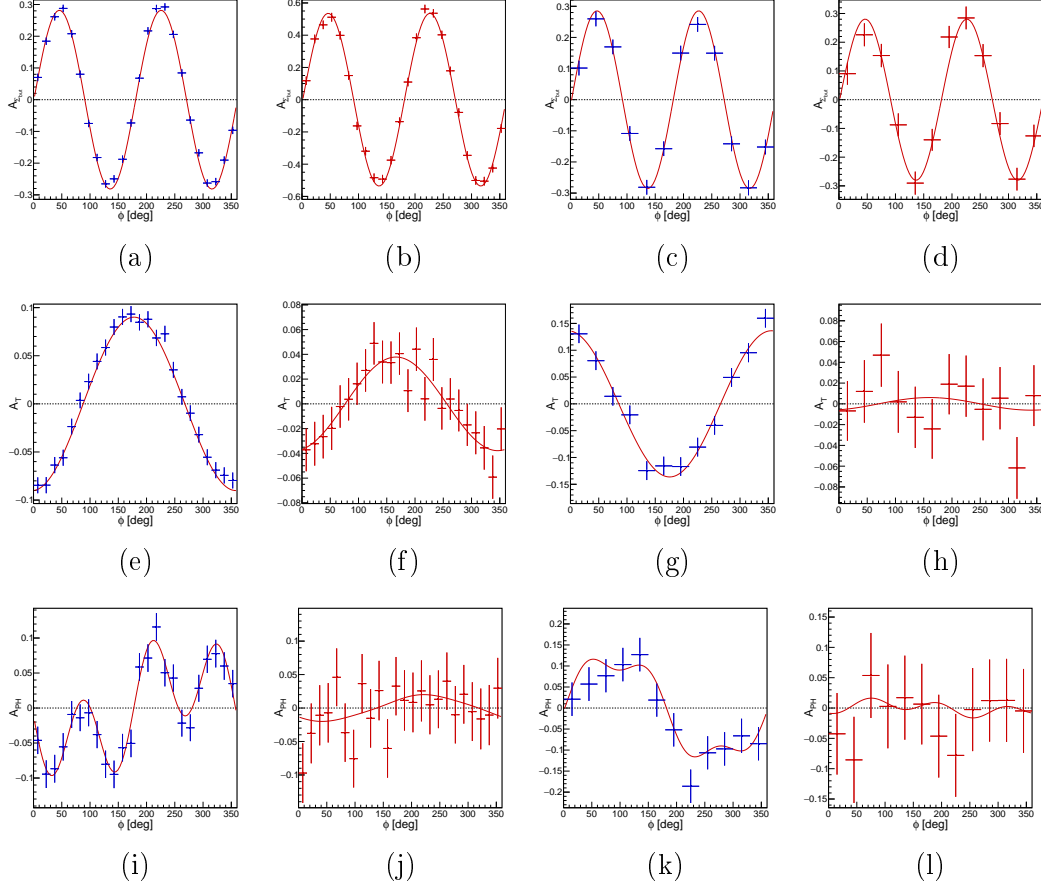


Figure C.1: Beam asymmetry $A_{\Sigma_{but}}$ (top column), target asymmetry A_T (middle column) and beam-target asymmetry A_{PH} (bottom column) of E_γ and $\cos(\theta)$ integrated data in $\pi^0 p$ (1st row), $\pi^0 n$ (2nd row), ηp (3rd row) and ηn (4th row) in Dec2021.

C.2 Asymmetry Fitting

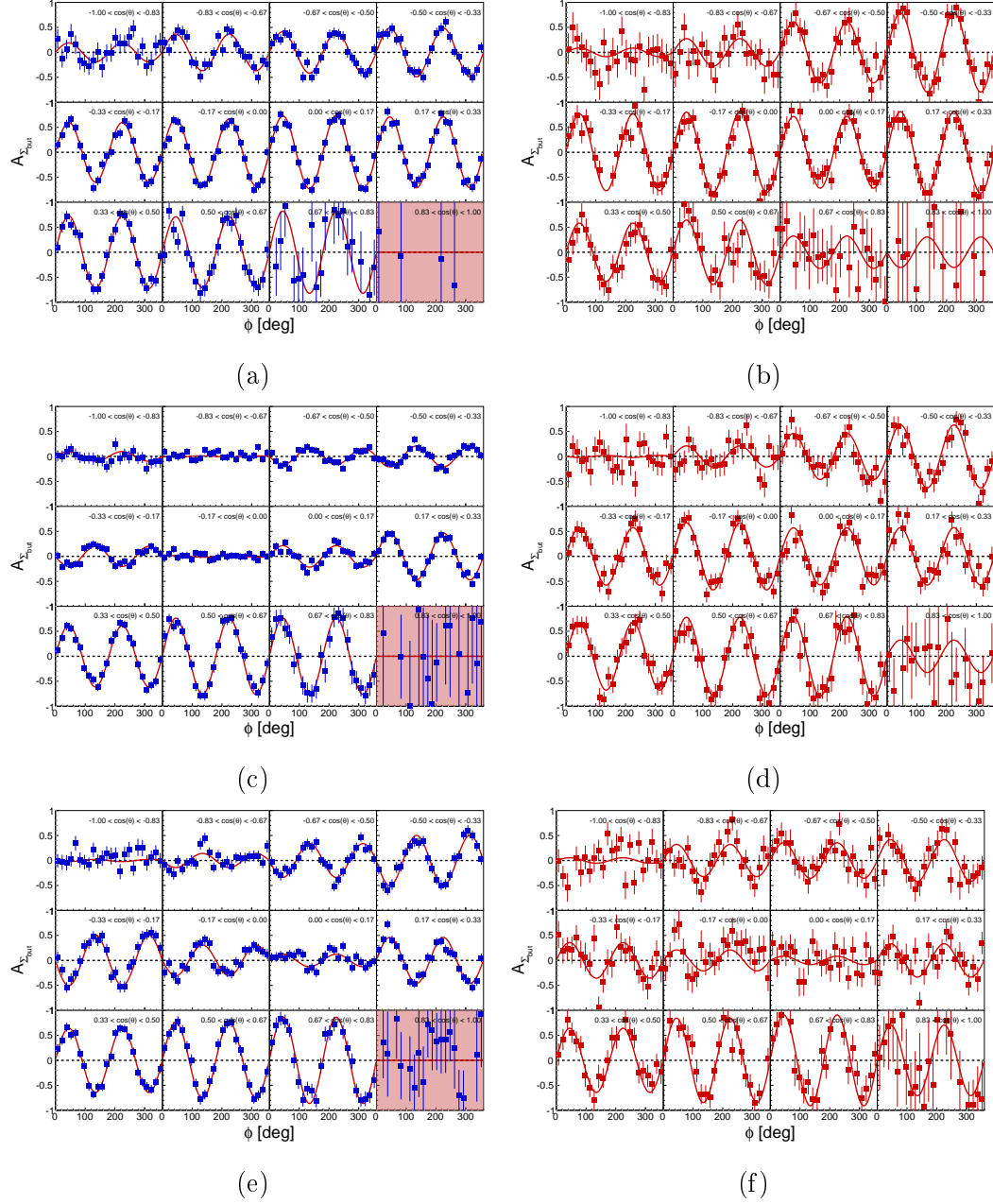
C.2.1 Beam asymmetry $A_{\Sigma_{but}}$


Figure C.2: ϕ -dependent beam asymmetries $A_{\Sigma_{but}}$ with their fit functions (Equation 6.1) for fixed $\cos(\theta)$ and fixed incident photon energies $E_\gamma = 840$ MeV (a-b), 1000 MeV (c-d) and 1160 MeV (e-f) in $\pi^0 p$ (left column) and $\pi^0 n$ (right column).

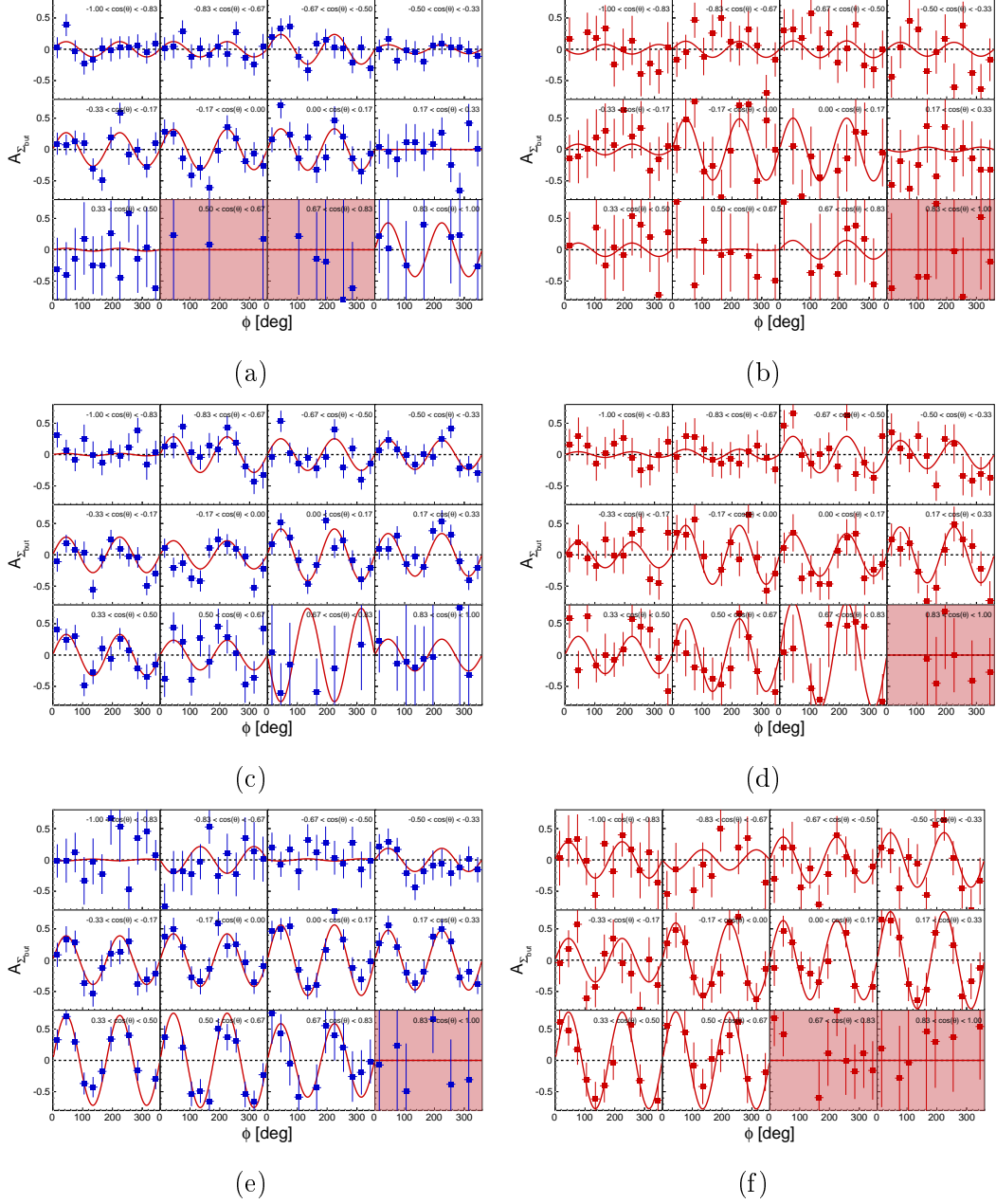


Figure C.3: ϕ -dependent beam asymmetries $A_{\Sigma_{but}}$ with their fit functions (Equation 6.1) for fixed $\cos(\theta)$ and fixed incident photon energies $E_\gamma = 840$ MeV (a-b), 1000 MeV (c-d) and 1160 MeV (e-f) in ηp (left column) and ηn (right column) with merged decay channels.

Appendix C. Extraction of polarisation observables

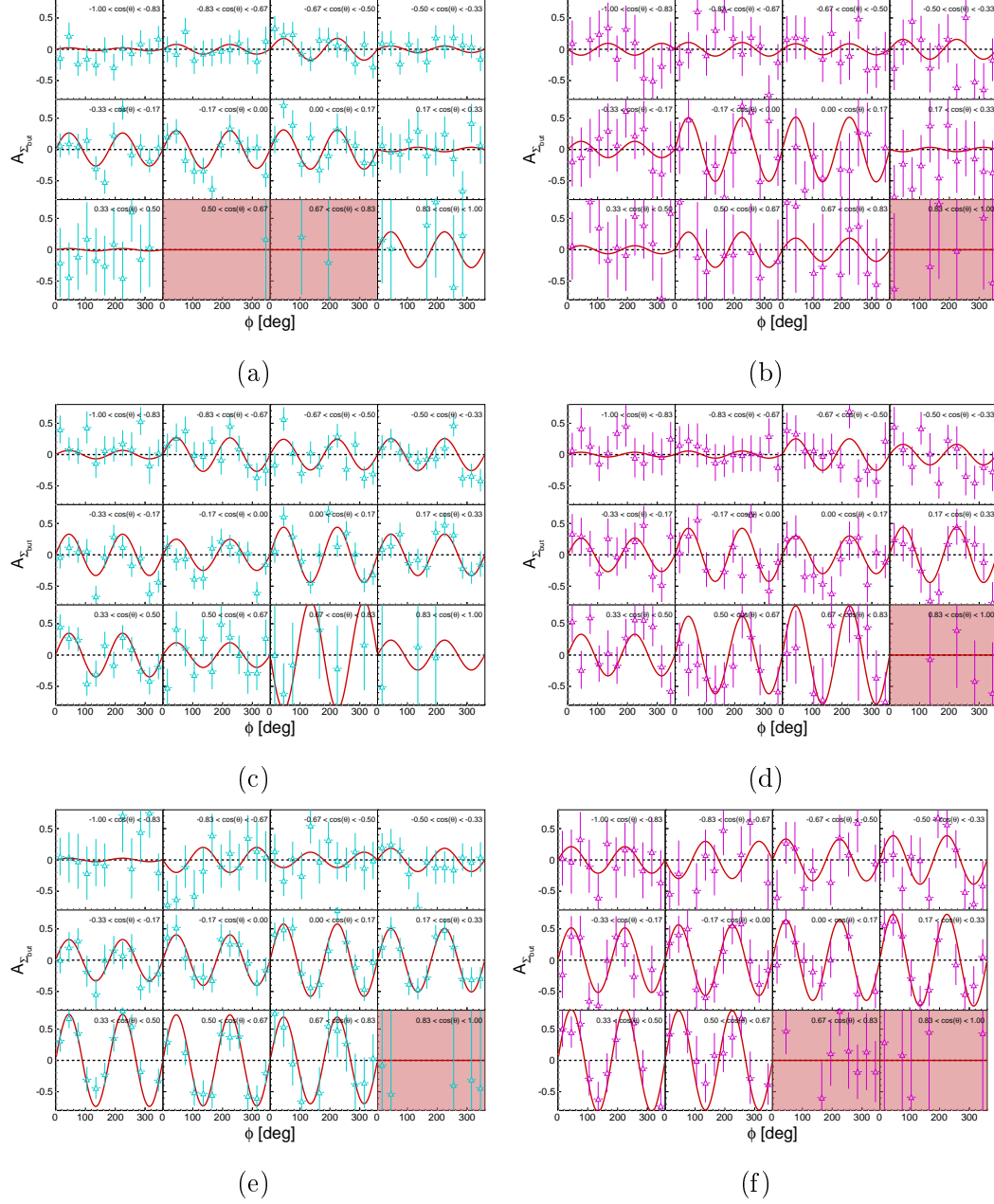


Figure C.4: ϕ -dependent beam asymmetries $A_{\Sigma_{but}}$ with their fit functions (Equation 6.1) for fixed $\cos(\theta)$ and fixed incident photon energies $E_\gamma = 840$ MeV (a-b), 1000 MeV (c-d) and 1160 MeV (e-f) in ηp (left column) and ηn (right column) with $\eta \rightarrow 2\gamma$.

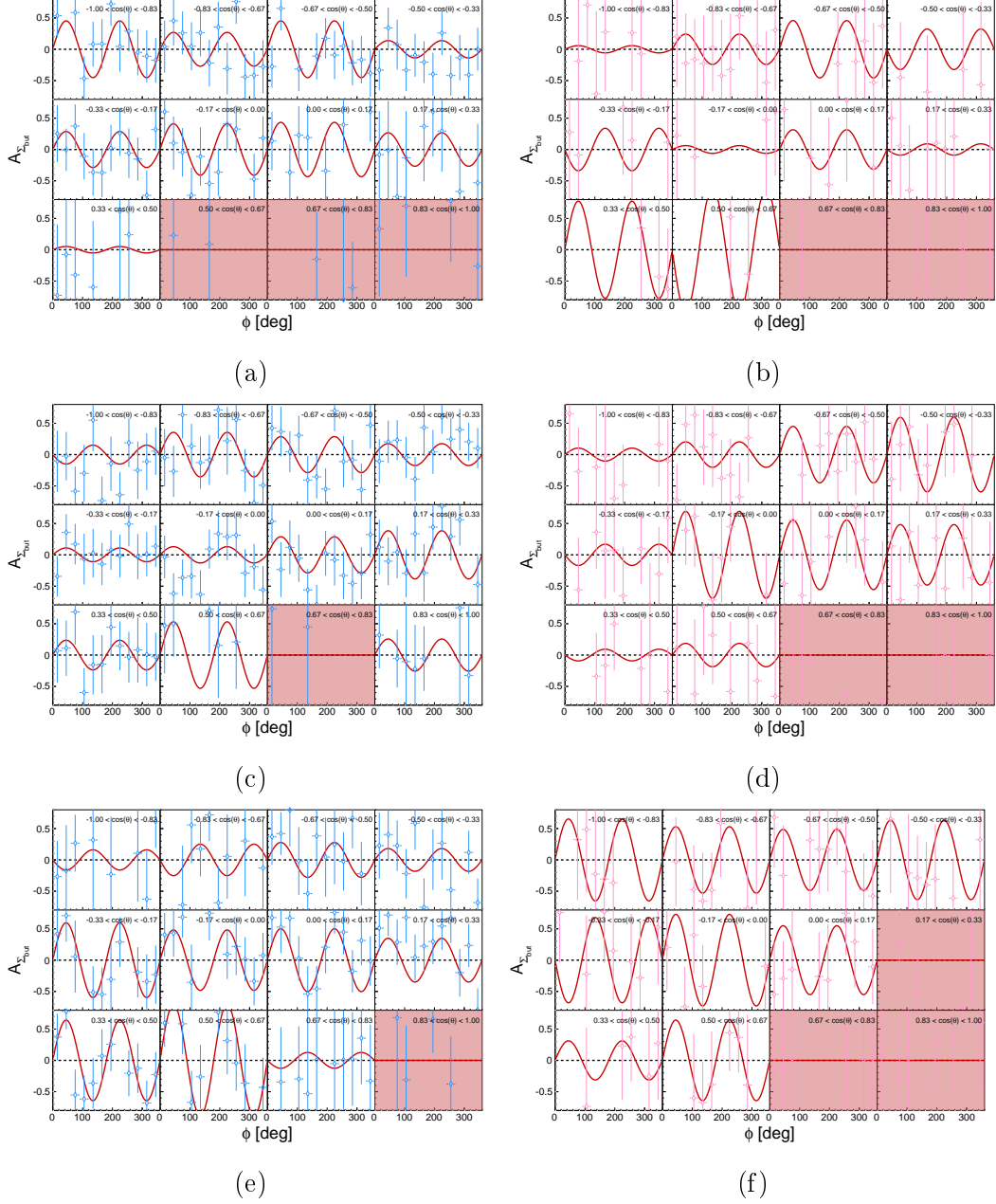


Figure C.5: ϕ -dependent beam asymmetries $A_{\Sigma_{but}}$ with their fit functions (Equation 6.1) for fixed $\cos(\theta)$ and fixed incident photon energies $E_\gamma = 840$ MeV (a-b), 1000 MeV (c-d) and 1160 MeV (e-f) in ηp (left column) and ηn (right column) with $\eta \rightarrow 6\gamma$.

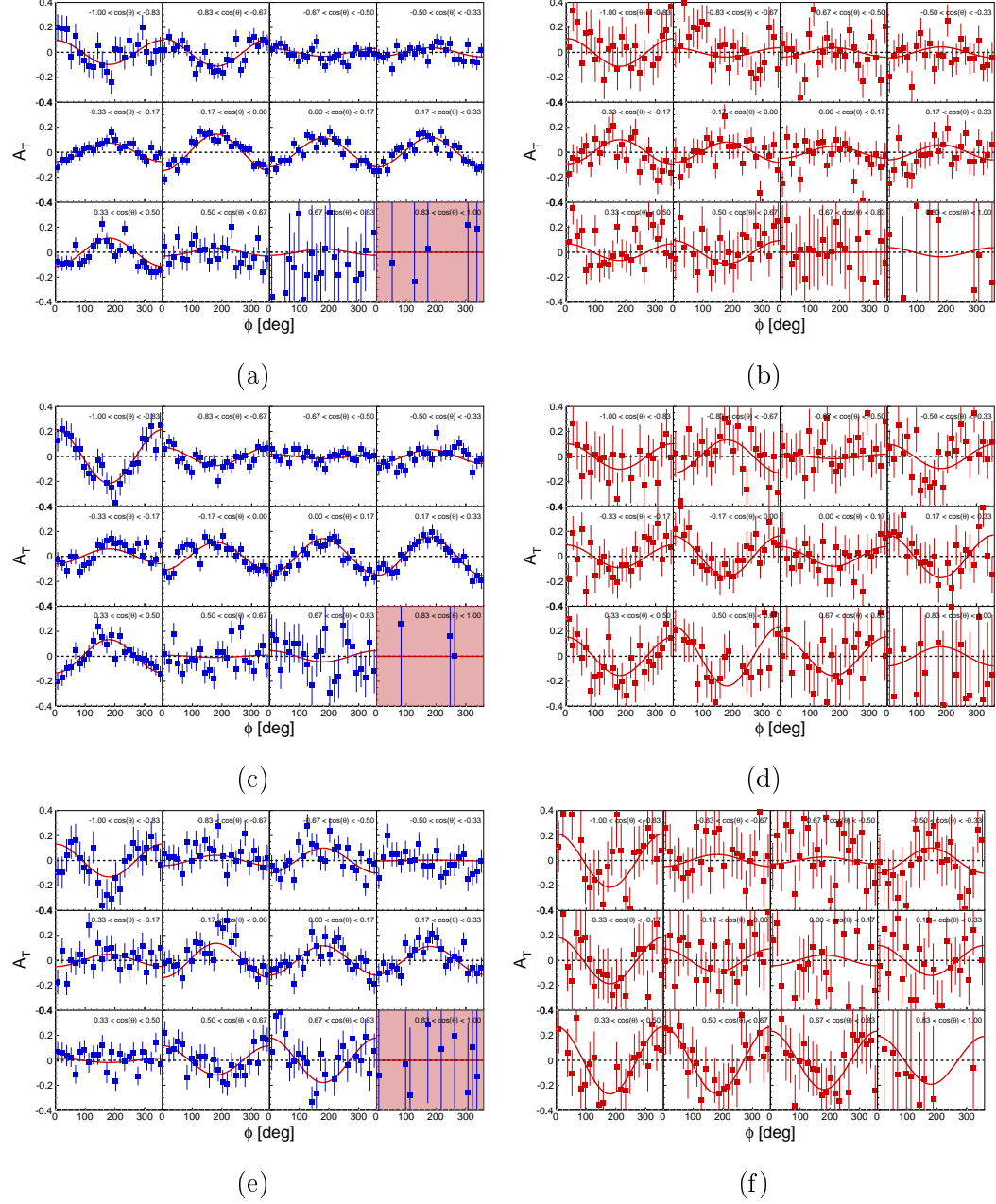
C.2.2 Target asymmetry A_T


Figure C.6: ϕ -dependent target asymmetries A_T with their fit functions (Equation 6.2) for fixed $\cos(\theta)$ and fixed incident photon energies $E_\gamma = 840$ MeV (a-b), 1000 MeV (c-d) and 1160 MeV (e-f) in $\pi^0 p$ (left column) and $\pi^0 n$ (right column).

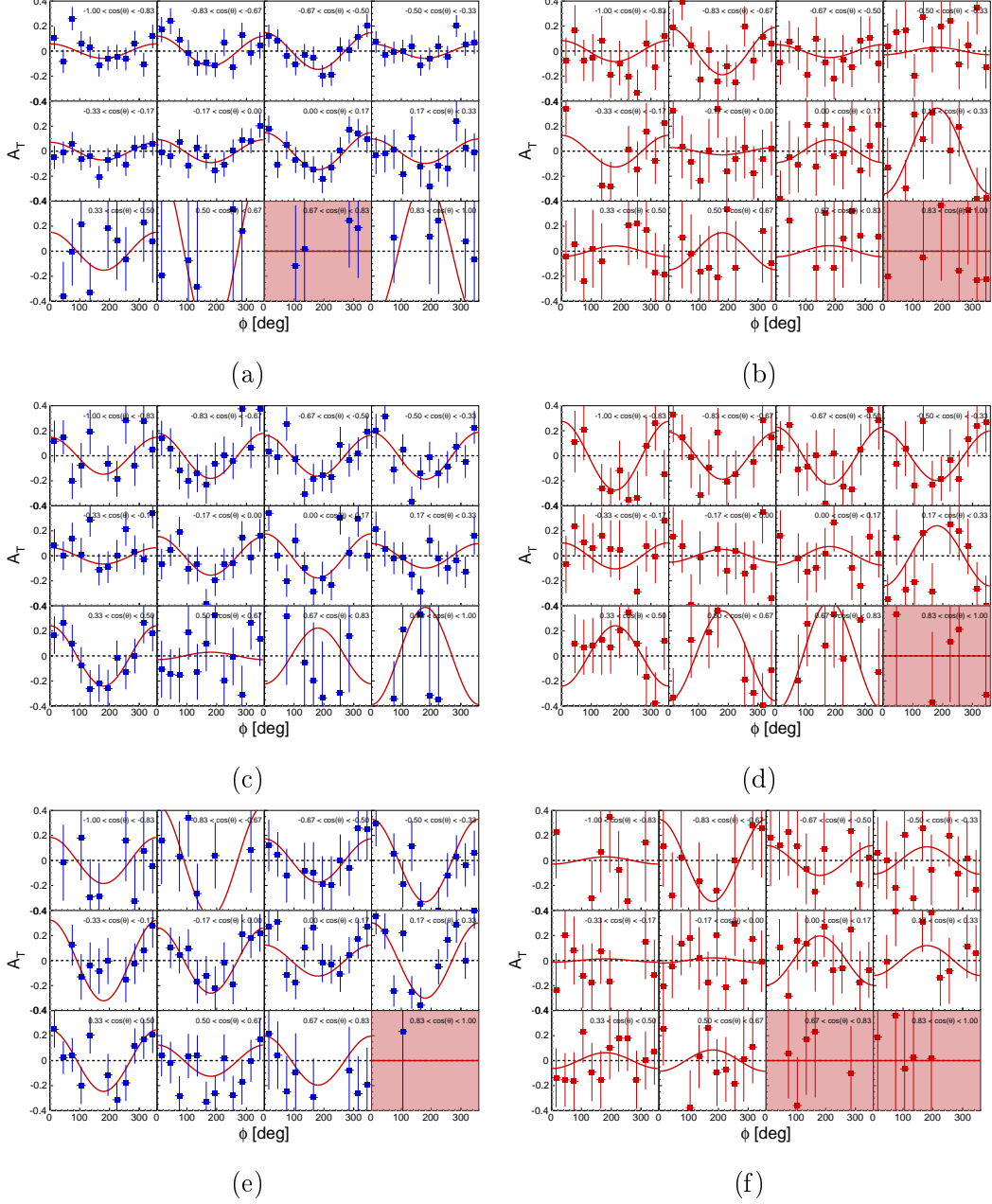


Figure C.7: ϕ -dependent target asymmetries A_T with their fit functions (Equation 6.2) for fixed $\cos(\theta)$ and fixed incident photon energies $E_\gamma = 840$ MeV (a-b), 1000 MeV (c-d) and 1160 MeV (e-f) in ηp (left column) and ηn (right column) with merged decay channels.

Appendix C. Extraction of polarisation observables

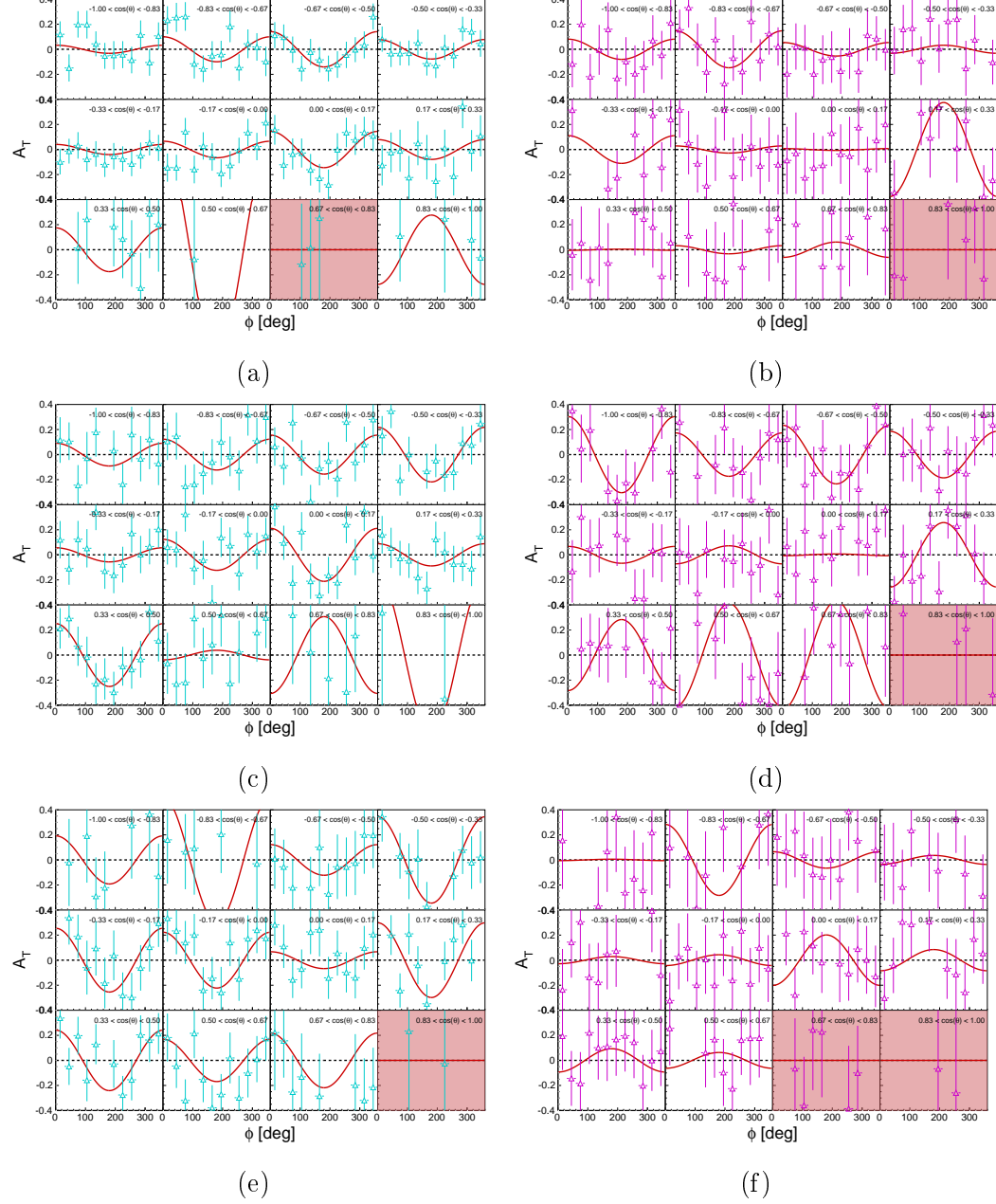


Figure C.8: ϕ -dependent target asymmetries A_T with their fit functions (Equation 6.2) for fixed $\cos(\theta)$ and fixed incident photon energies $E_\gamma = 840$ MeV (a-b), 1000 MeV (c-d) and 1160 MeV (e-f) in ηp (left column) and ηn (right column) with $\eta \rightarrow 2\gamma$.

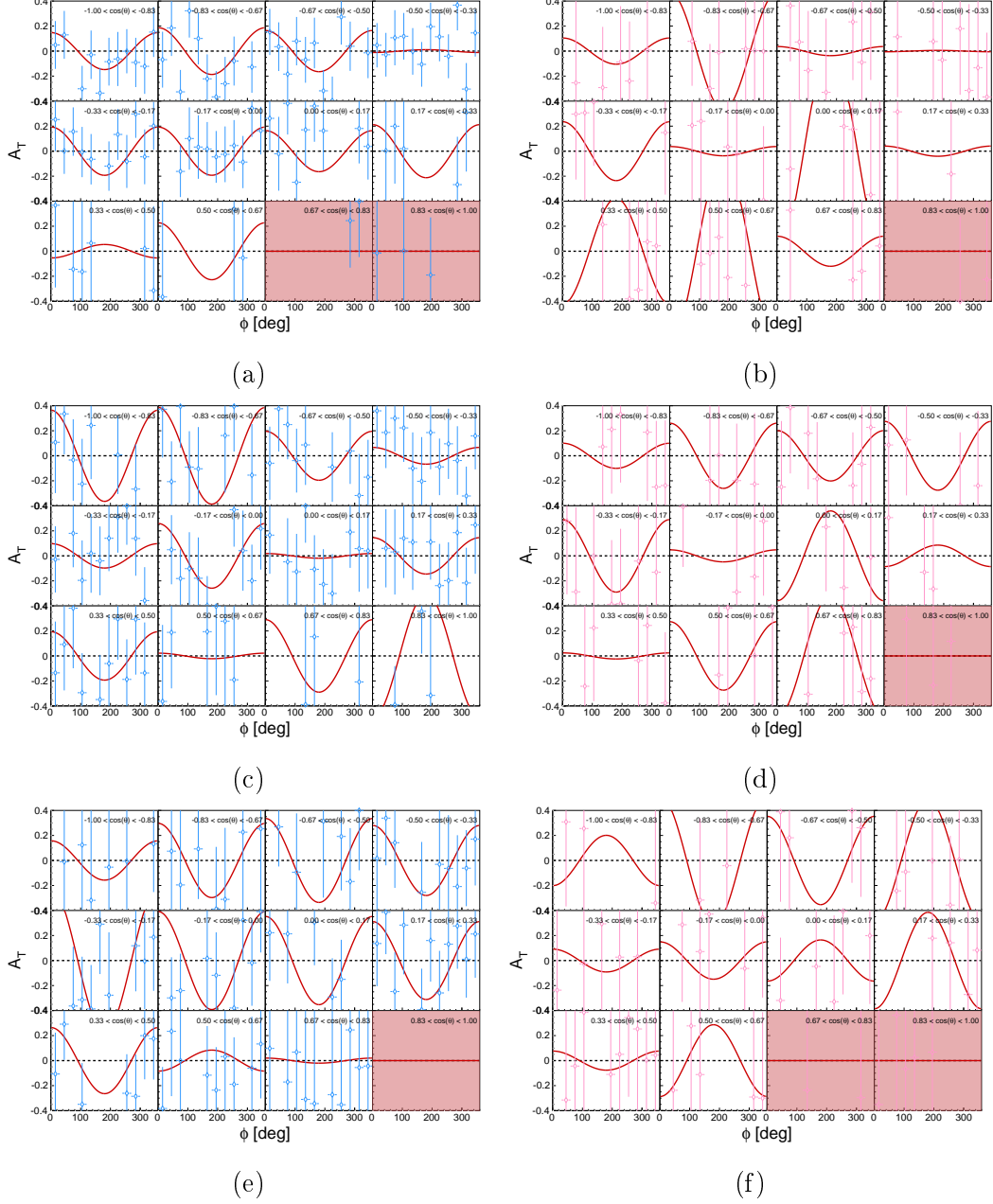


Figure C.9: ϕ -dependent target asymmetries A_T with their fit functions (Equation 6.2) for fixed $\cos(\theta)$ and fixed incident photon energies $E_\gamma = 840$ MeV (a-b), 1000 MeV (c-d) and 1160 MeV (e-f) in ηp (left column) and ηn (right column) with $\eta \rightarrow 6\gamma$.

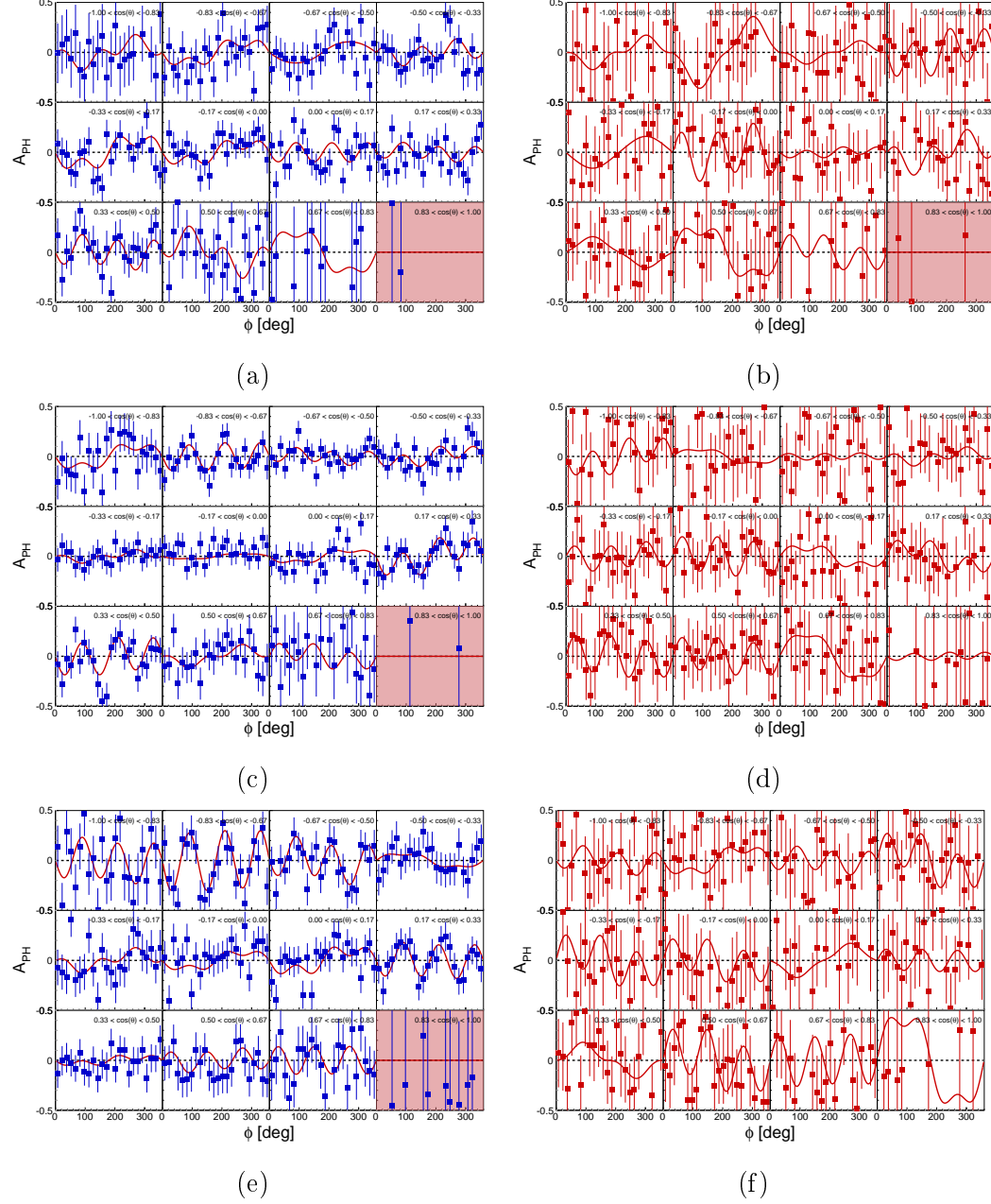
C.2.3 Beam-target asymmetry A_{PH}


Figure C.10: ϕ -dependent beam-target asymmetries A_{PH} with their fit functions (Equation 6.3) for fixed $\cos(\theta)$ and fixed incident photon energies $E_\gamma = 840$ MeV (a-b), 1000 MeV (c-d) and 1160 MeV (e-f) in $\pi^0 p$ (left column) and $\pi^0 n$ (right column).

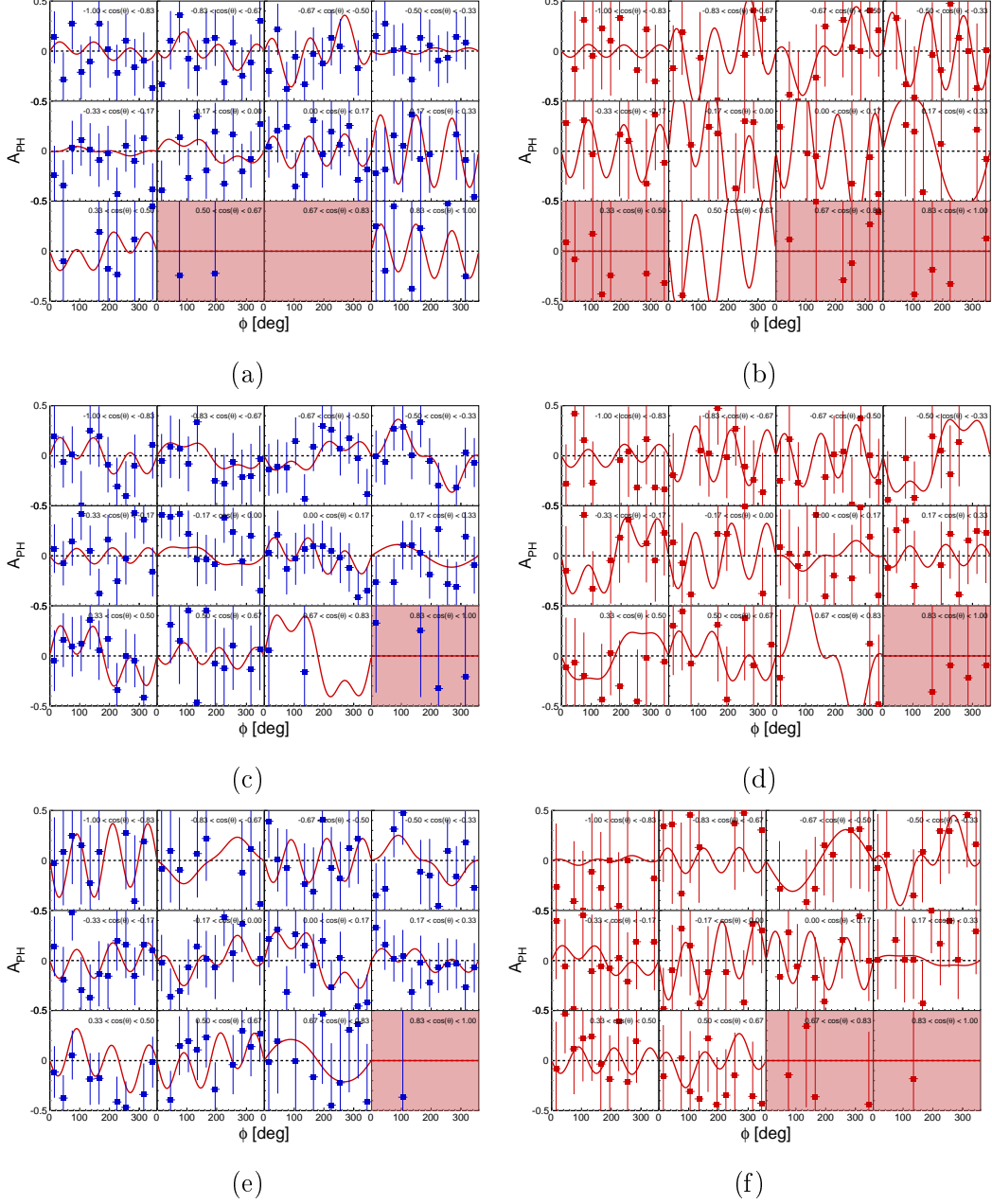


Figure C.11: ϕ -dependent beam-target asymmetries A_{PH} with their fit functions (Equation 6.3) for fixed $\cos(\theta)$ and fixed incident photon energies $E_\gamma = 840$ MeV (a-b), 1000 MeV (c-d) and 1160 MeV (e-f) in ηp (left column) and ηn (right column) with merged decay channels.

Appendix C. Extraction of polarisation observables

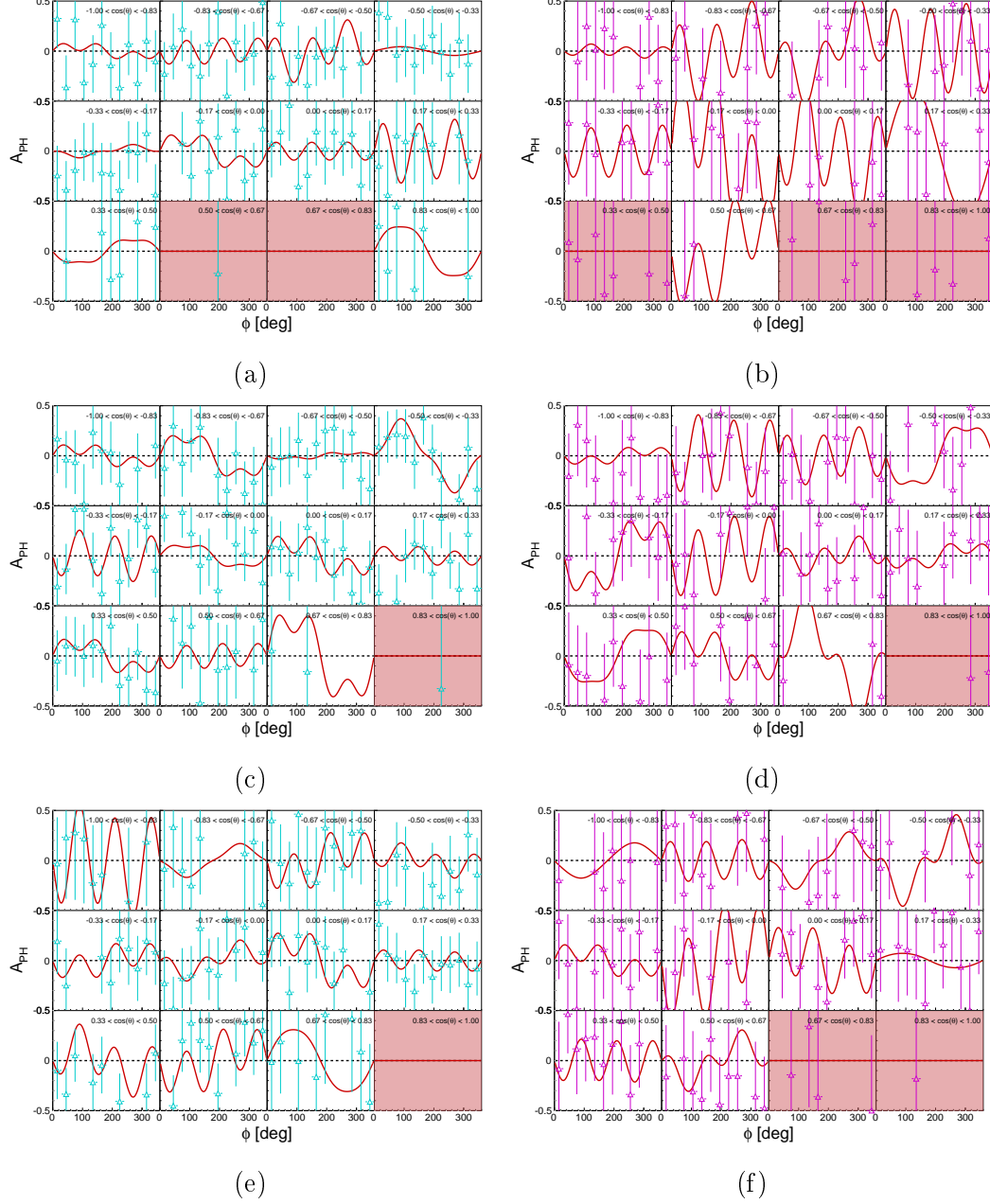


Figure C.12: ϕ -dependent beam-target asymmetries A_{PH} with their fit functions (Equation 6.3) for fixed $\cos(\theta)$ and fixed incident photon energies $E_\gamma = 840$ MeV (a-b), 1000 MeV (c-d) and 1160 MeV (e-f) in ηp (left column) and ηn (right column) with $\eta \rightarrow 2\gamma$.

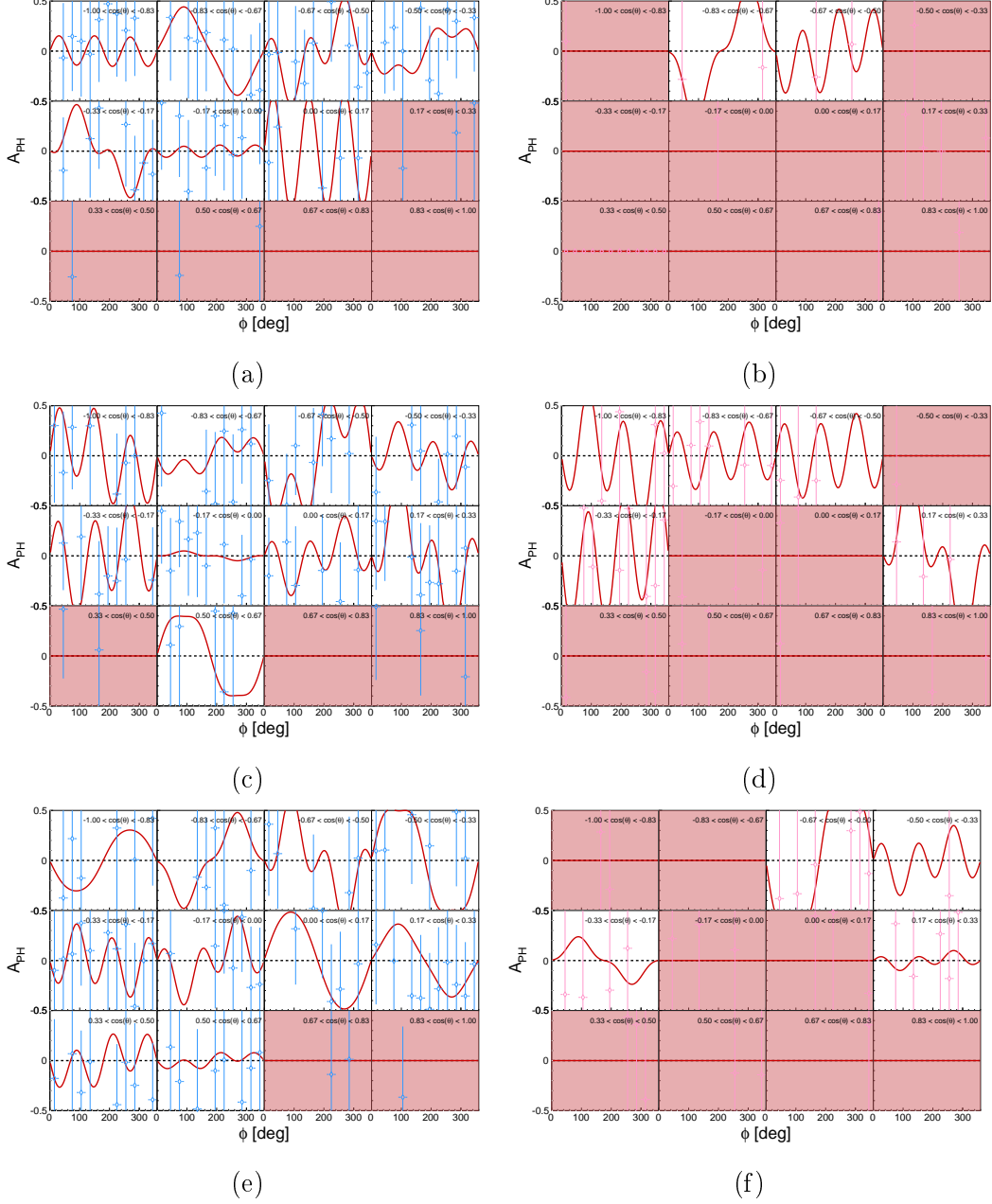


Figure C.13: ϕ -dependent beam-target asymmetries A_{PH} with their fit functions (Equation 6.3) for fixed $\cos(\theta)$ and fixed incident photon energies $E_\gamma = 840$ MeV (a-b), 1000 MeV (c-d) and 1160 MeV (e-f) in ηp (left column) and ηn (right column) with $\eta \rightarrow 6\gamma$.

C.3 Detector acceptance from the maximum likelihood estimation in ηN

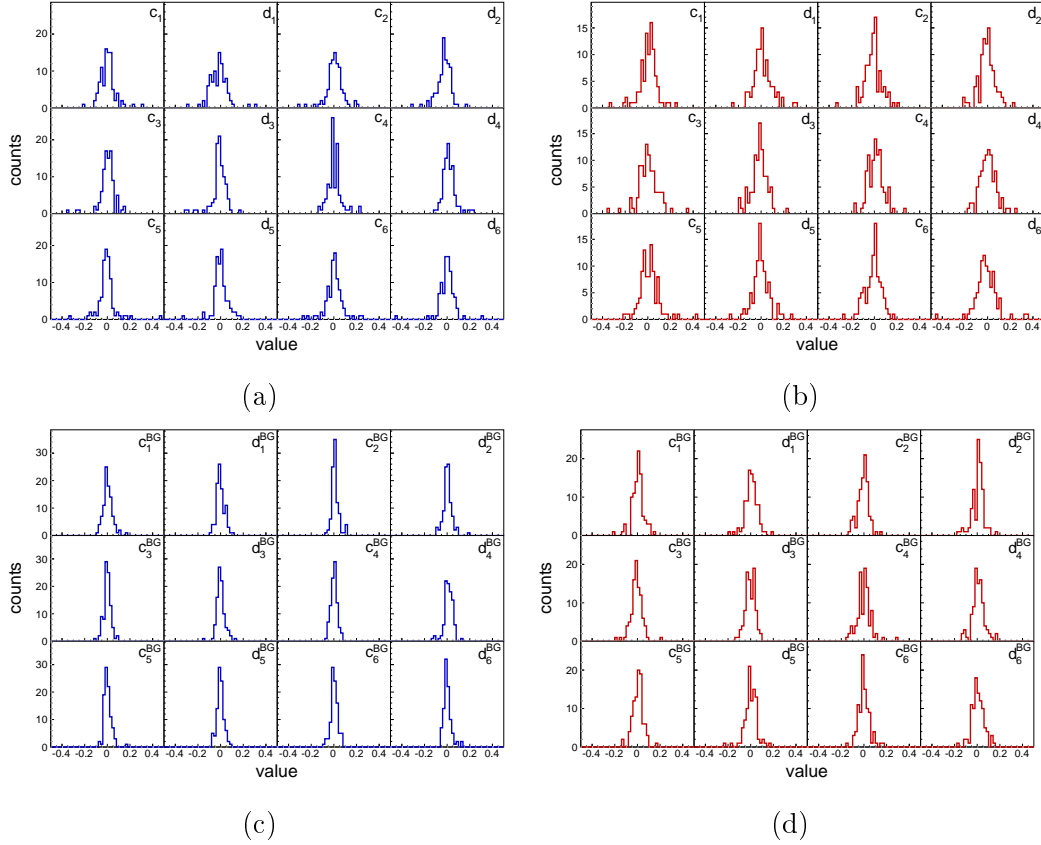


Figure C.14: Detector acceptance parameters $c_1, d_1, \dots, c_6, d_6$ and background detector acceptance parameters $c_1^{BG}, d_1^{BG}, \dots, c_6^{BG}, d_6^{BG}$ in ηp (left column) and ηn (right column) in Oct2018.

C.4 Comparison between extraction methods

C.4.1 Simple difference

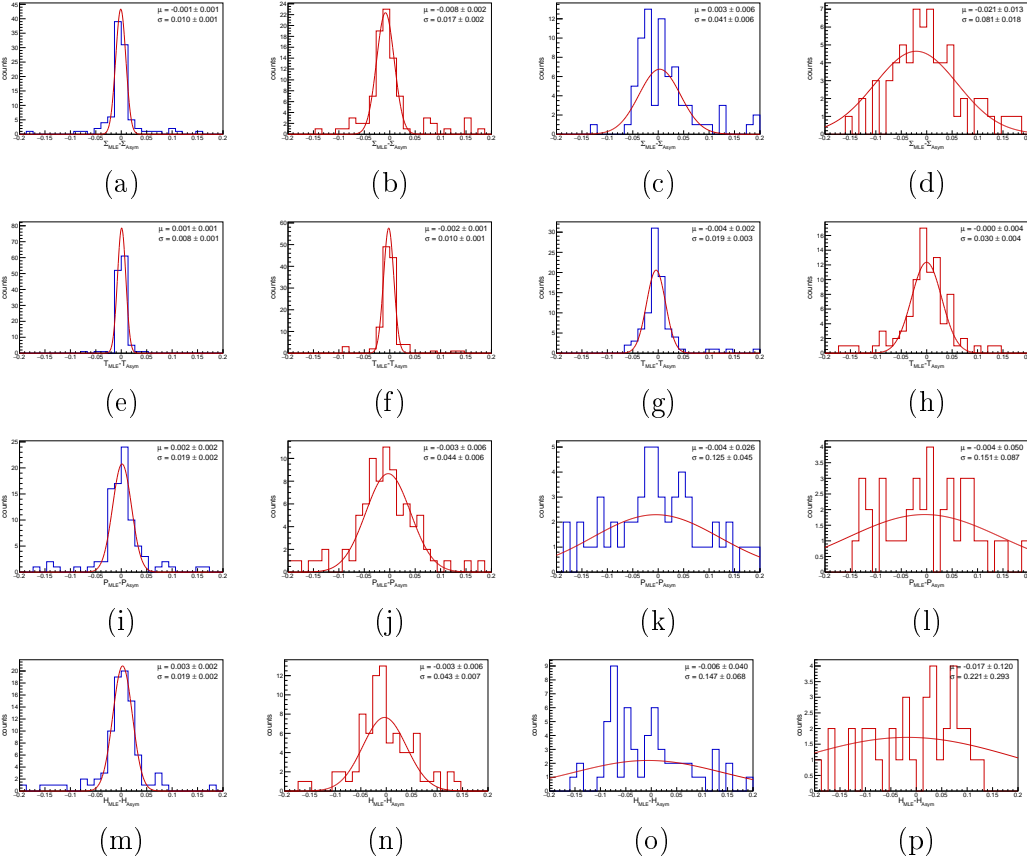


Figure C.15: Simple difference $\Delta O = O_{MLE} - O_{Asym}$ of the polarisation observables extracted from the two methods, i.e. maximum likelihood method (MLE) and asymmetry fitting method (Asym), with a Gaussian fit function in Oct2018. The data from Σ_{but} (a-d), T (e-h), P (i-l) and H (m-p) in $\pi^0 p$ (1st column), $\pi^0 n$ (2nd column), ηp (3rd column) and ηn (4th column) are shown. The Gaussian fit function's mean μ and standard deviation σ are given as numerical values.

C.4.2 Error normalised difference with maximum correlation

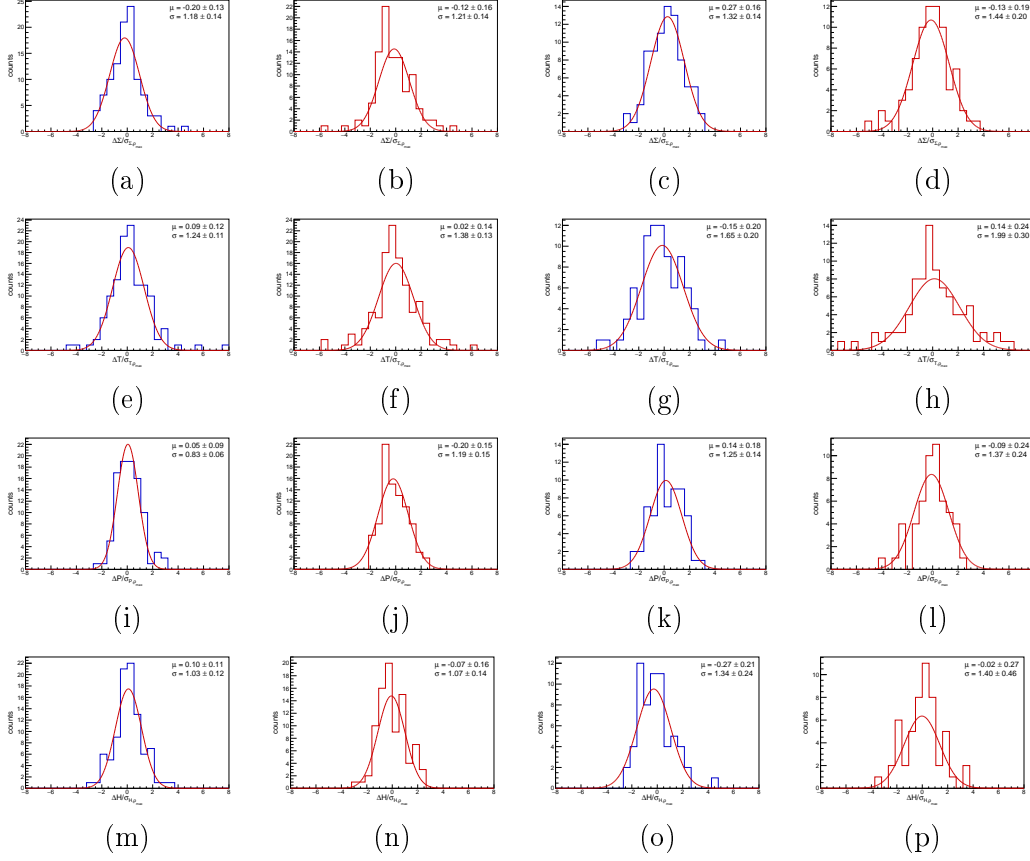


Figure C.16: Error normalised difference (Equation 6.21) with maximum correlation of the polarisation observables extracted from the two methods, i.e. maximum likelihood method (MLE) and asymmetry fitting method (Asym), with a Gaussian fit function in Oct2018. The data from Σ_{but} (a-d), T (e-h), P (i-l) and H (m-p) in $\pi^0 p$ (1st column), $\pi^0 n$ (2nd column), ηp (3rd column) and ηn (4th column) are shown. The Gaussian fit function's mean μ and standard deviation σ are given as numerical values.

C.4.3 Systematic and statistical uncertainty in merged beam time data

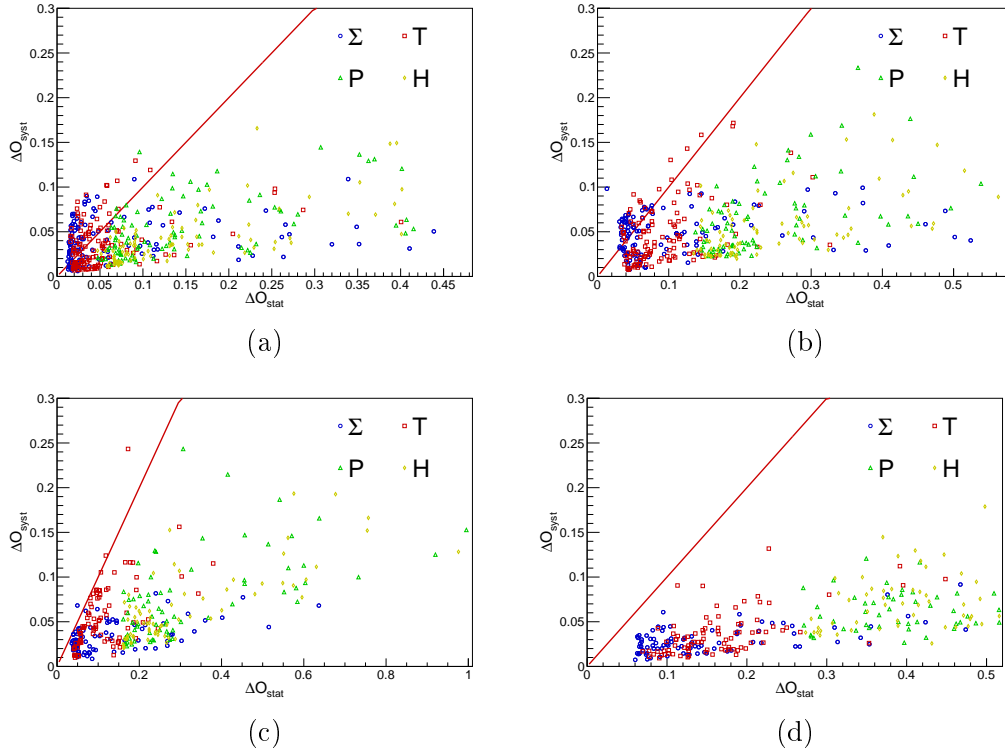


Figure C.17: Comparison between systematic and statistical uncertainties in $\pi^0 p$ (a), $\pi^0 n$ (b), ηp (c) and ηn (d) with the data of both beam times, i.e. Oct2018 and Dec2021 merged. The red line indicates $\Delta O_{syst} = \Delta O_{stat}$.

C.5 Systematic uncertainty of the dilution factor in Dec2021

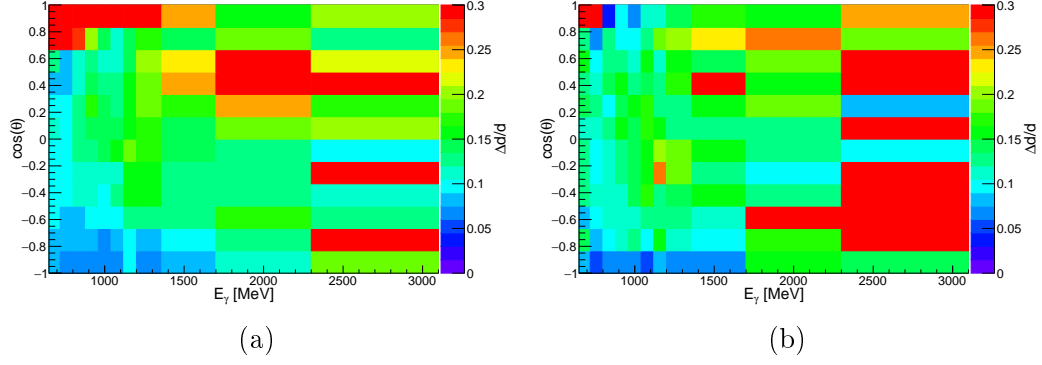


Figure C.18: Relative systematic uncertainty of the dilution factor $\Delta d/d$ as a function of E_γ and $\cos(\theta)$ in $\pi^0 p$ (a) and $\pi^0 n$ (b) in Dec2021.

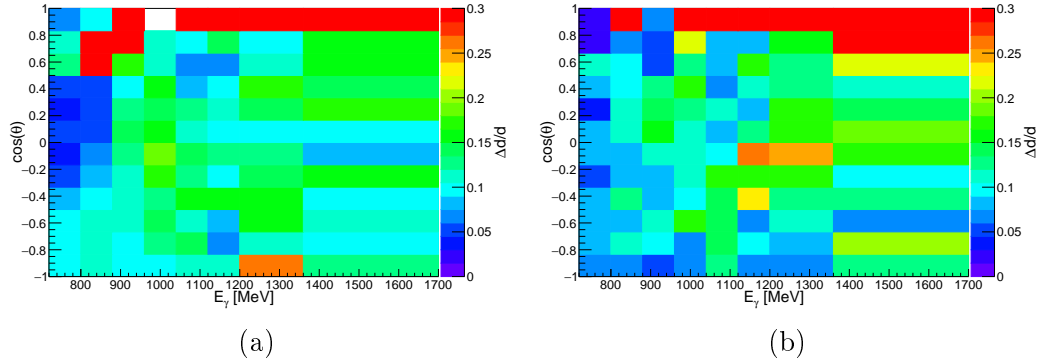


Figure C.19: Relative systematic uncertainty of the dilution factor $\Delta d/d$ as a function of E_γ and $\cos(\theta)$ in ηp (a) and ηn (b) in Dec2021.

D | Results

D.1 Preliminary results from Dec2021

D.1.1 Comparison of beam times with preliminary data

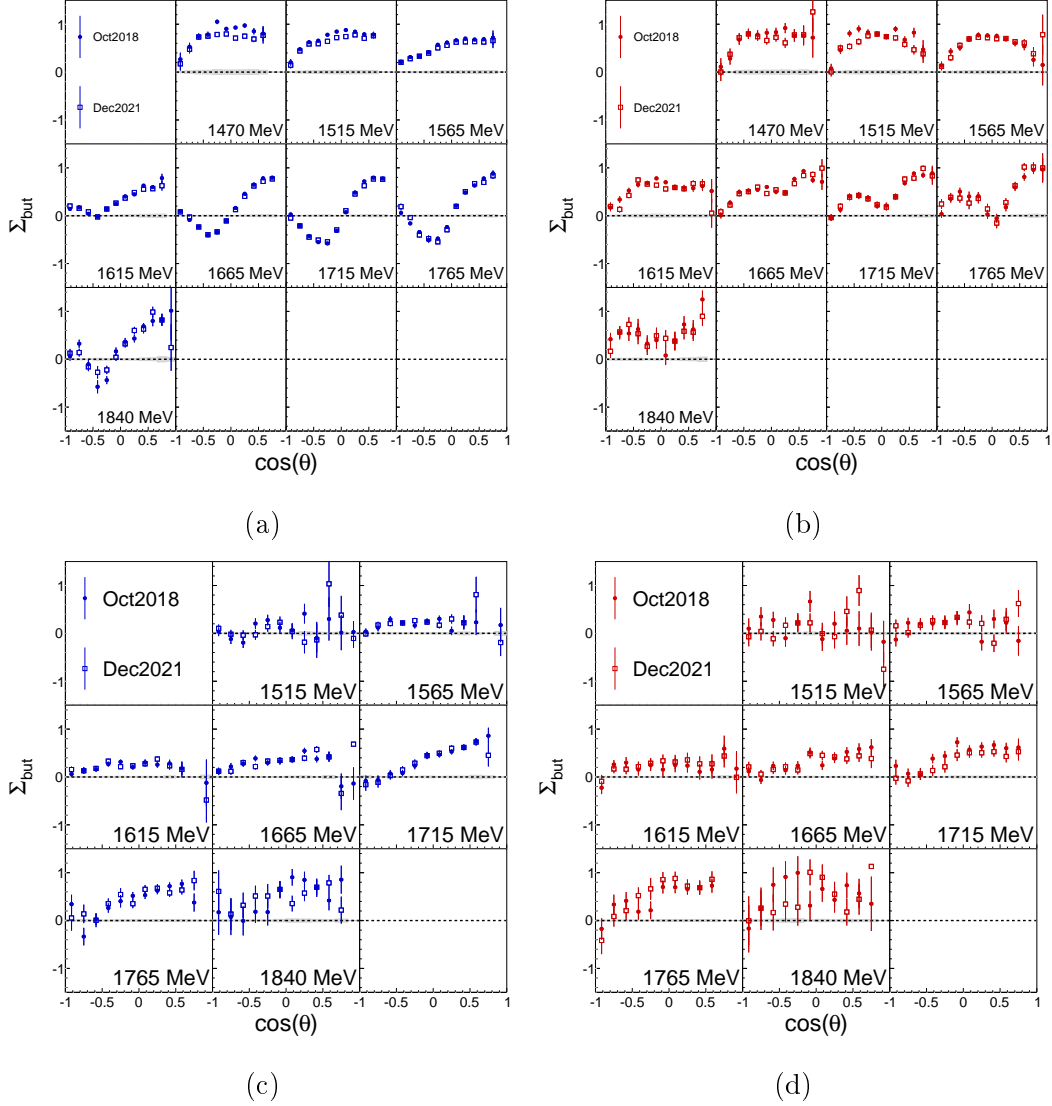


Figure D.1: Preliminary beam asymmetry Σ_{but} as a function of $\cos(\theta)$ for fixed centre of mass energies W in $\pi^0 p$ (a), $\pi^0 n$ (b), ηp (c) and ηn (d). Results from Oct2018 are compared to Dec2021 ones.

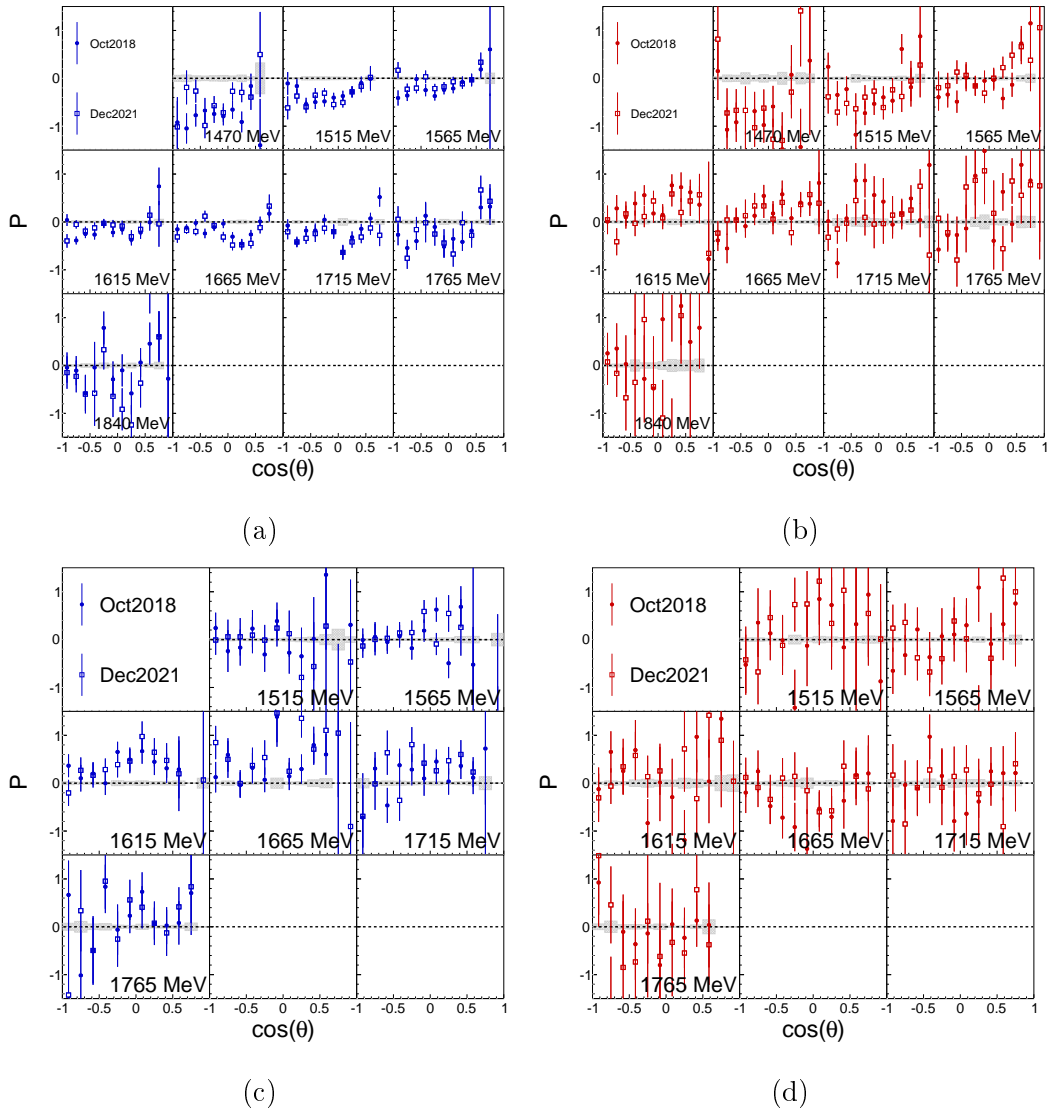


Figure D.2: Preliminary recoil asymmetry P as a function of $\cos(\theta)$ for fixed centre of mass energies W in $\pi^0 p$ (a), $\pi^0 n$ (b), ηp (c) and ηn (d). Results from Oct2018 are compared to Dec2021 ones.

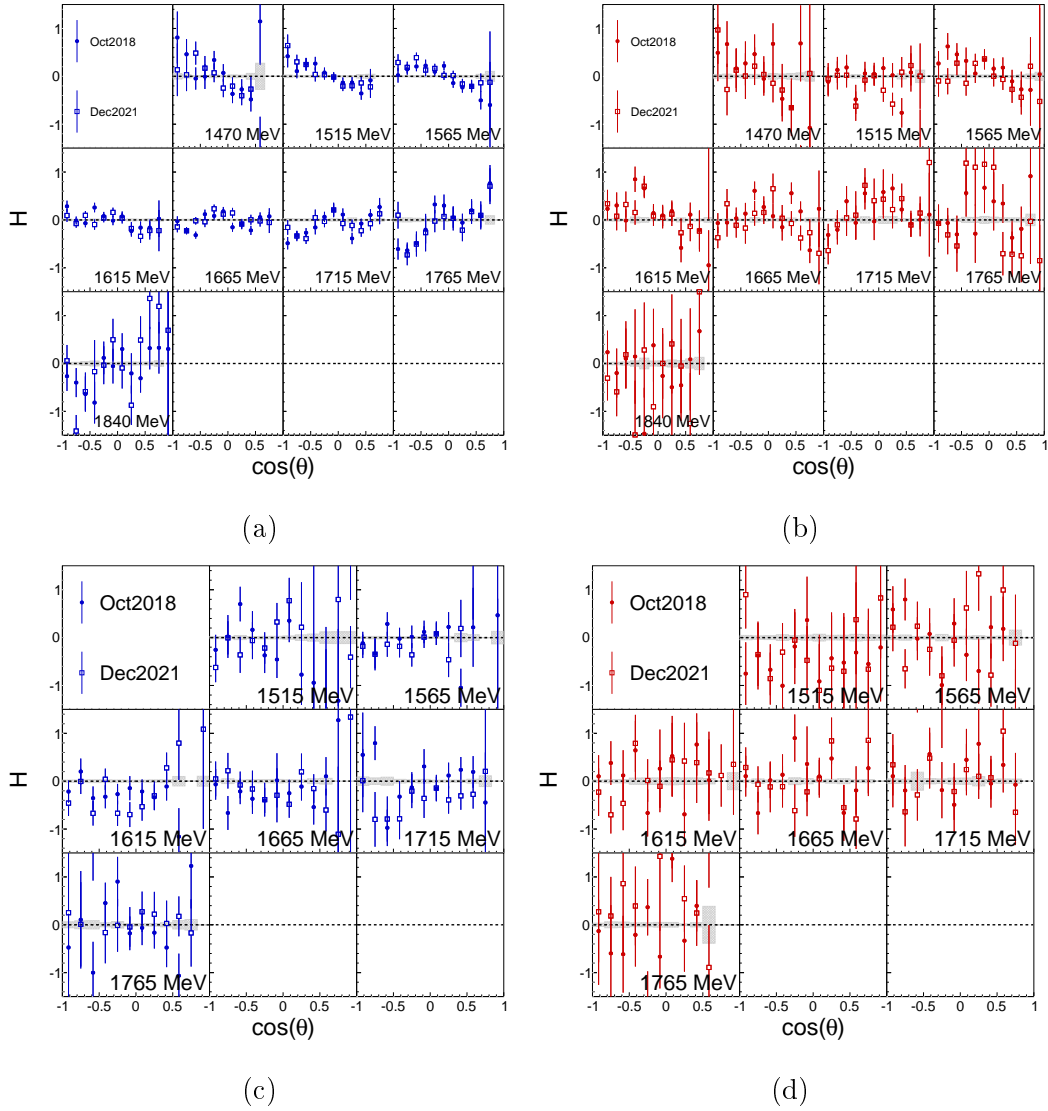


Figure D.3: Preliminary beam-target asymmetry H as a function of $\cos(\theta)$ for fixed centre of mass energies W in $\pi^0 p$ (a), $\pi^0 n$ (b), ηp (c) and ηn (d). Results from Oct2018 are compared to Dec2021 ones.

D.1.2 Results with merged preliminary data

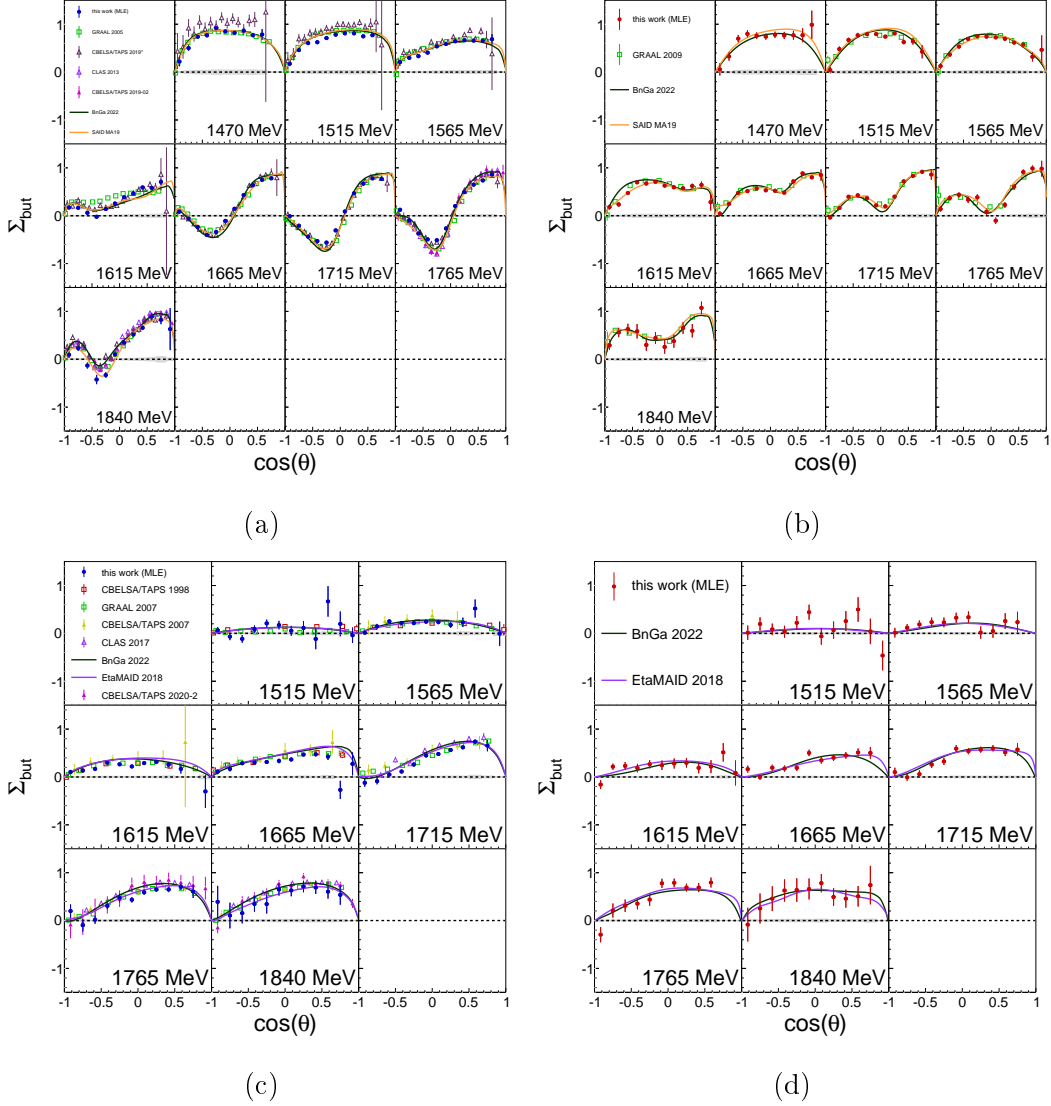


Figure D.4: Beam asymmetry Σ_{but} as a function of $\cos(\theta)$ for fixed centre of mass energies W in $\pi^0 p$ (a), $\pi^0 n$ (b), ηp (c) and ηn (d). Results with the full statistics is shown, i.e. merged from both beam times with preliminary Dec2021 results.

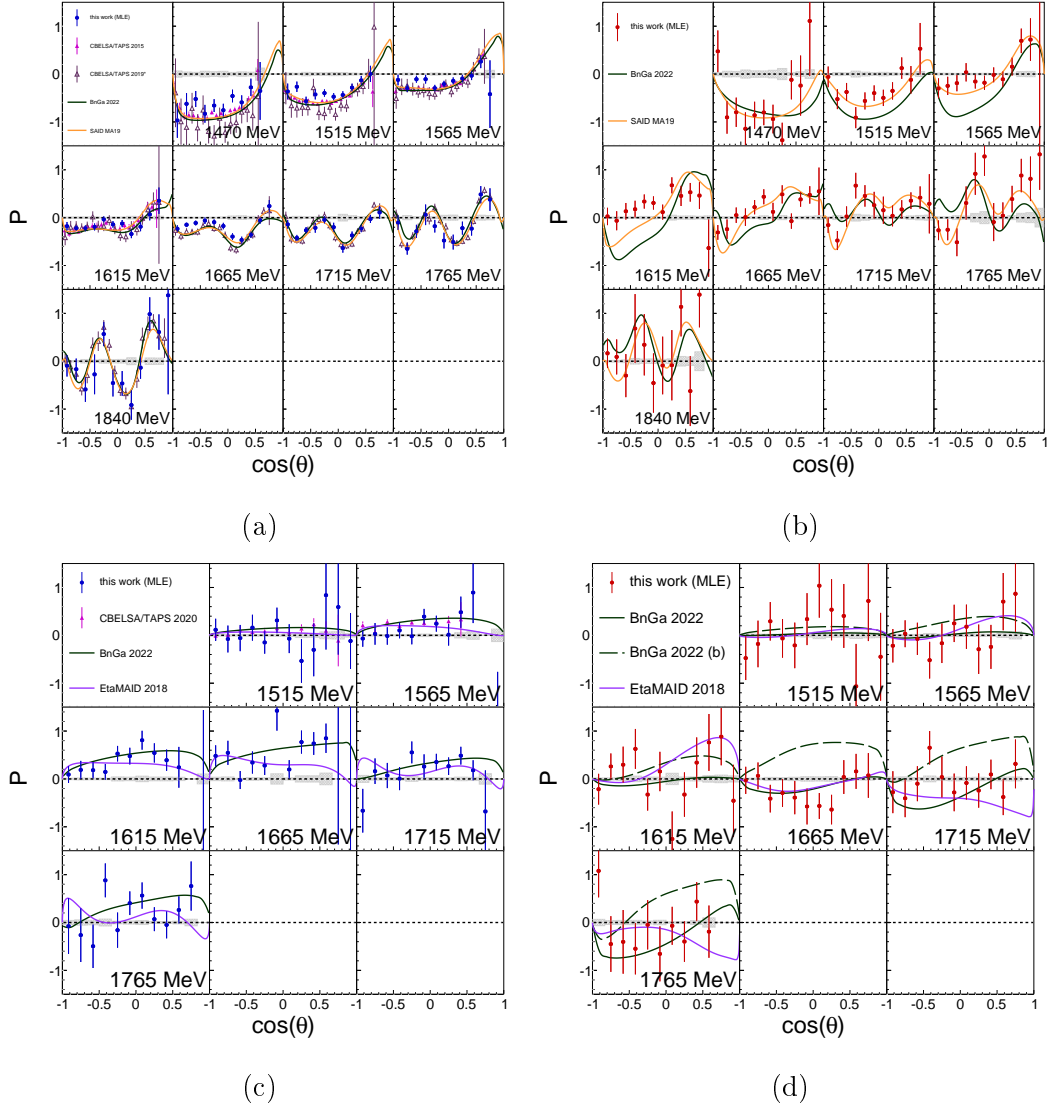


Figure D.5: Recoil asymmetry P as a function of $\cos(\theta)$ for fixed centre of mass energies W in $\pi^0 p$ (a), $\pi^0 n$ (b), ηp (c) and ηn (d). Results with the full statistics is shown, i.e. merged from both beam times with preliminary Dec2021 results.

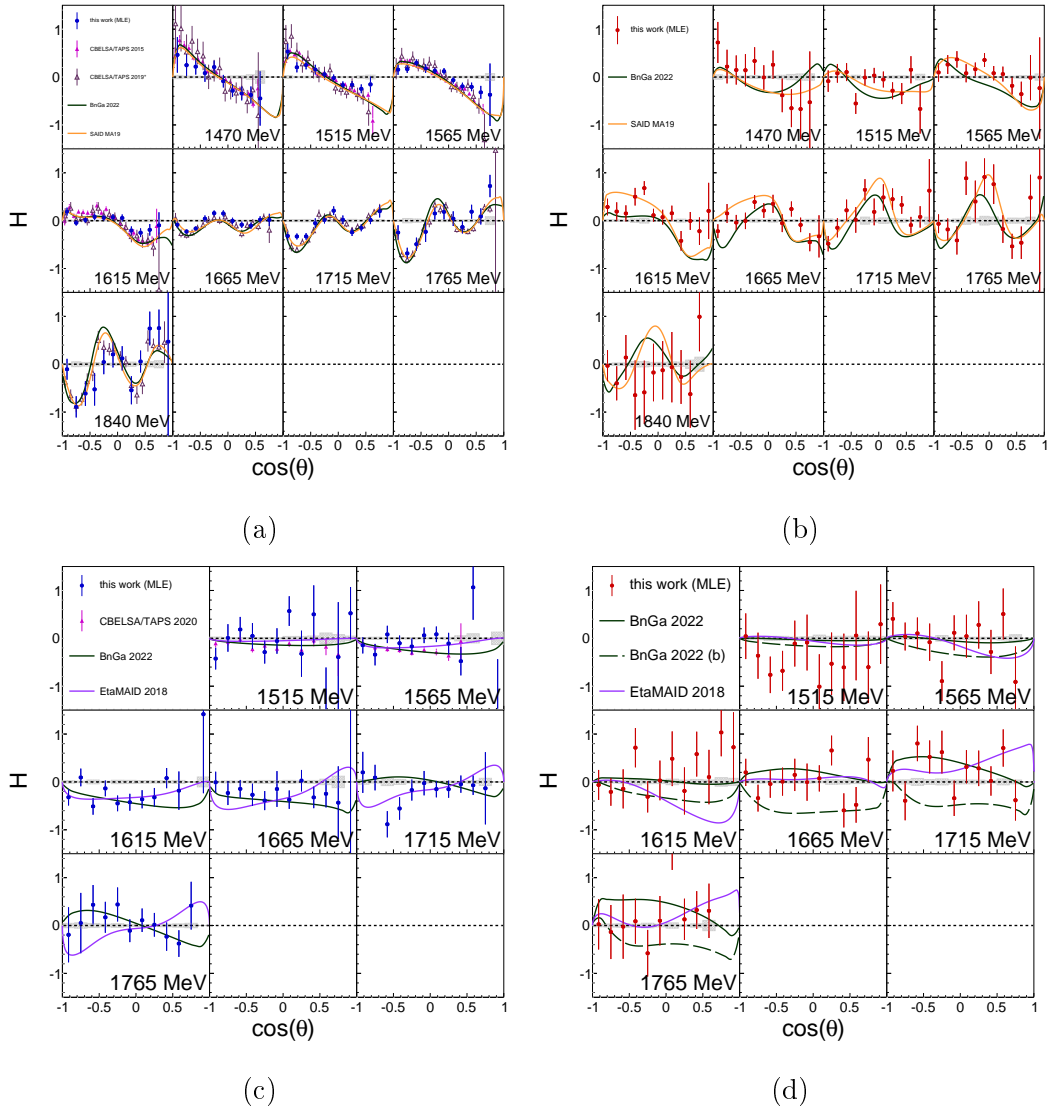


Figure D.6: Beam-target double polarisation observable H as a function of $\cos(\theta)$ for fixed centre of mass energies W in $\pi^0 p$ (a), $\pi^0 n$ (b), ηp (c) and ηn (d). Results with the full statistics is shown, i.e. merged from both beam times with preliminary Dec2021 results.

D.2 Target asymmetry T from Oct2018

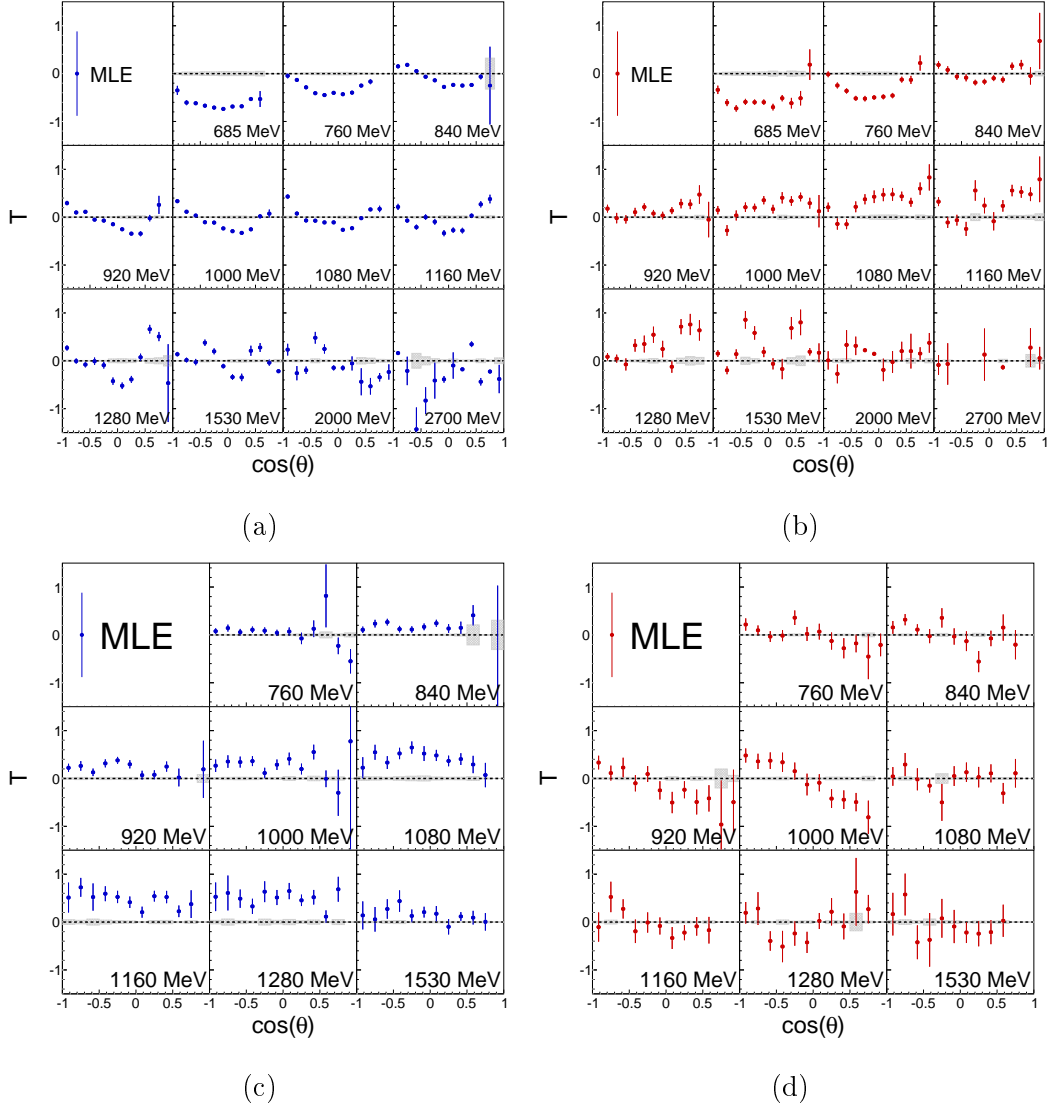


Figure D.7: Target asymmetry T as a function of $\cos(\theta)$ for fixed photon energies E_γ in the reactions $\gamma p \rightarrow \pi^0 p$ (a), $\gamma n \rightarrow \pi^0 n$ (b), $\gamma p \rightarrow \eta p$ (c) and $\gamma n \rightarrow \eta n$ (d). Results from Oct2018 are shown.

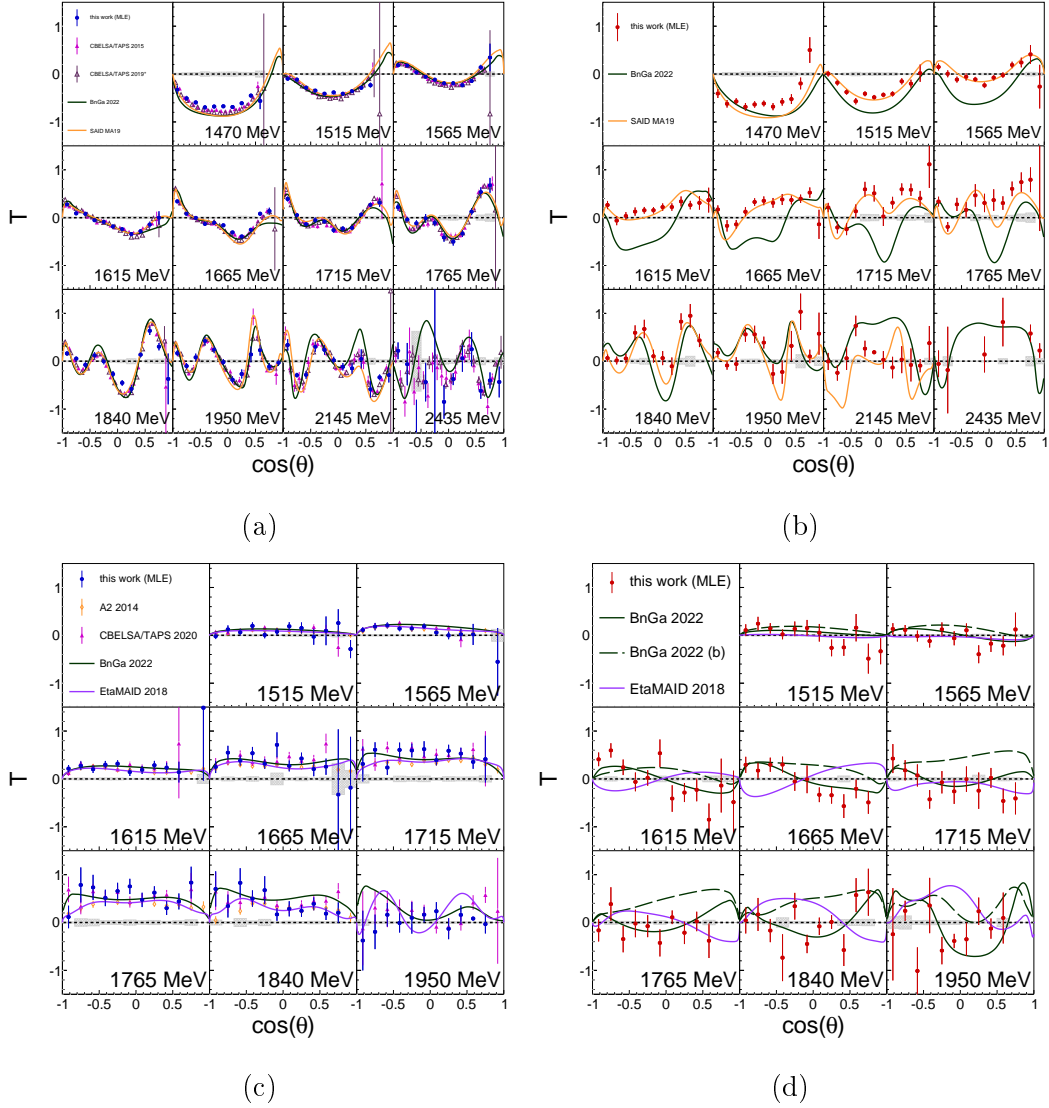


Figure D.8: Target asymmetry T as a function of $\cos(\theta)$ for fixed centre of mass energies W in $\pi^0 p$ (a), $\pi^0 n$ (b), ηp (c) and ηn (d). Results from Oct2018 are shown. Please see the captions of Figures 7.10-7.13 for details about the references from compared data and partial wave analyses.

D.3 χ^2/ndf from Legendre polynomial fits

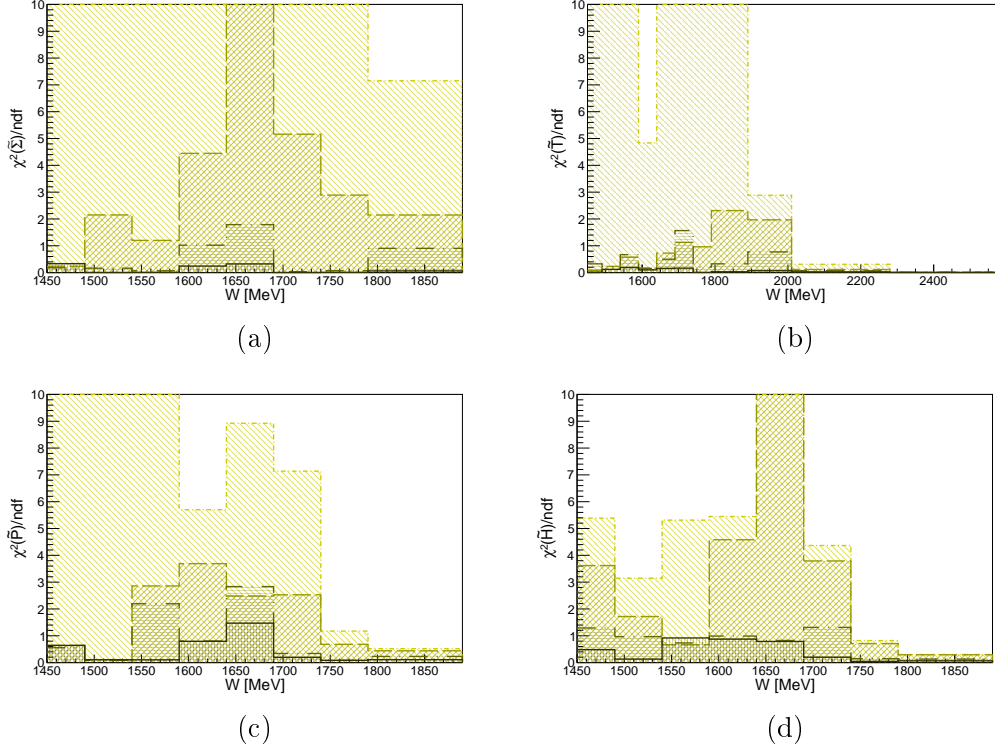


Figure D.9: χ^2/ndf from the Legendre polynomial fits to the reduced polarisation observables $\tilde{\Sigma}$ (a), \tilde{T} (b), \tilde{P} (c) and \tilde{H} as a function of $\cos(\theta)$ for fixed centre of mass energies W in $\pi^0 p$ in Oct2018. The fitted functions correspond to Legendre polynomials with a truncation at 1, 2, 3 and 4. The darker the colour, the higher the cut-off.

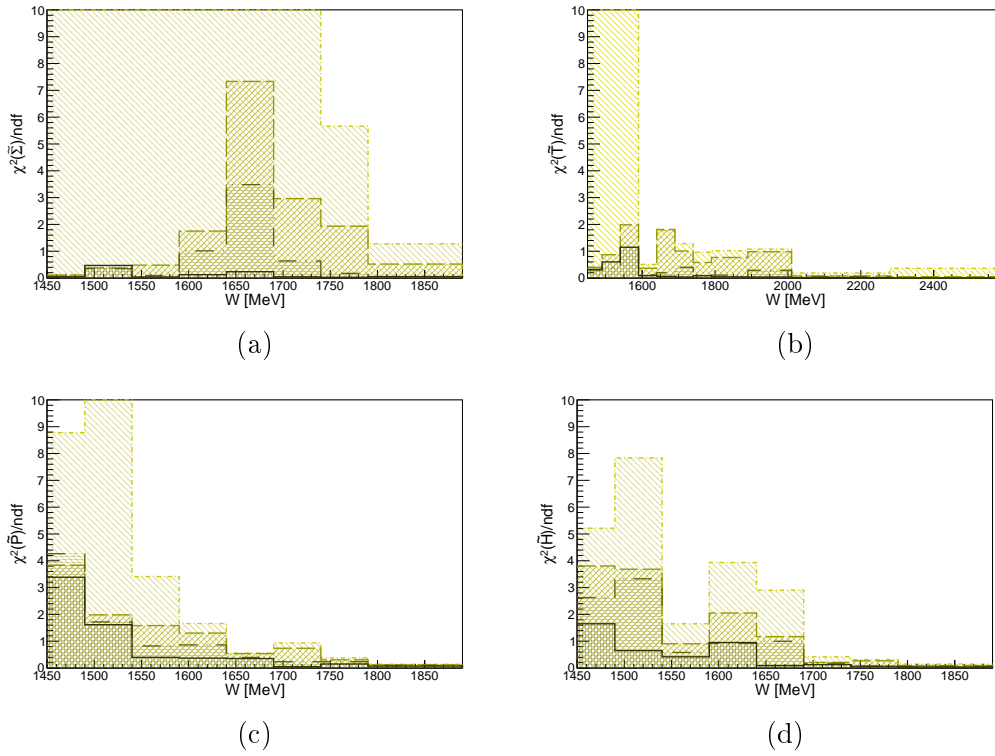


Figure D.10: χ^2/ndf from the Legendre polynomial fits to the reduced polarisation observables $\tilde{\Sigma}$ (a), \tilde{T} (b), \tilde{P} (c) and \tilde{H} as a function of $\cos(\theta)$ for fixed centre of mass energies W in $\pi^0 n$ in Oct2018. The fitted functions correspond to Legendre polynomials with a truncation at 1, 2, 3 and 4. The darker the colour, the higher the cut-off.

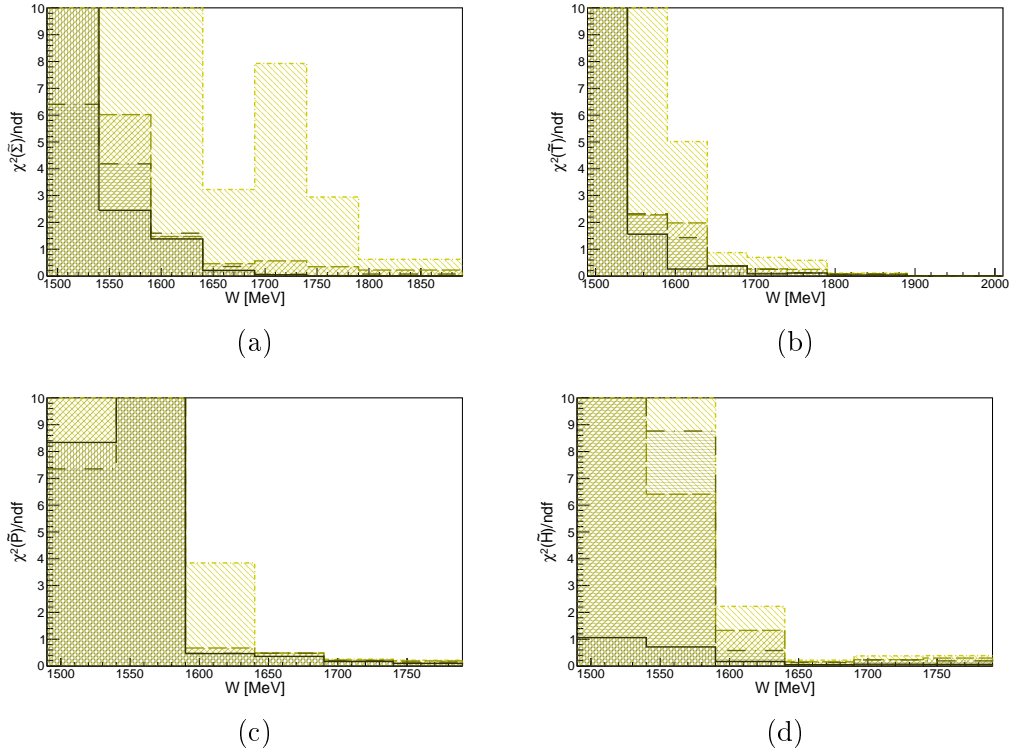


Figure D.11: χ^2/ndf from the Legendre polynomial fits to the reduced polarisation observables $\tilde{\Sigma}$ (a), \tilde{T} (b), \tilde{P} (c) and \tilde{H} as a function of $\cos(\theta)$ for fixed centre of mass energies W in ηp in Oct2018. The fitted functions correspond to Legendre polynomials with a truncation at 1, 2, 3 and 4. The darker the colour, the higher the cut-off.

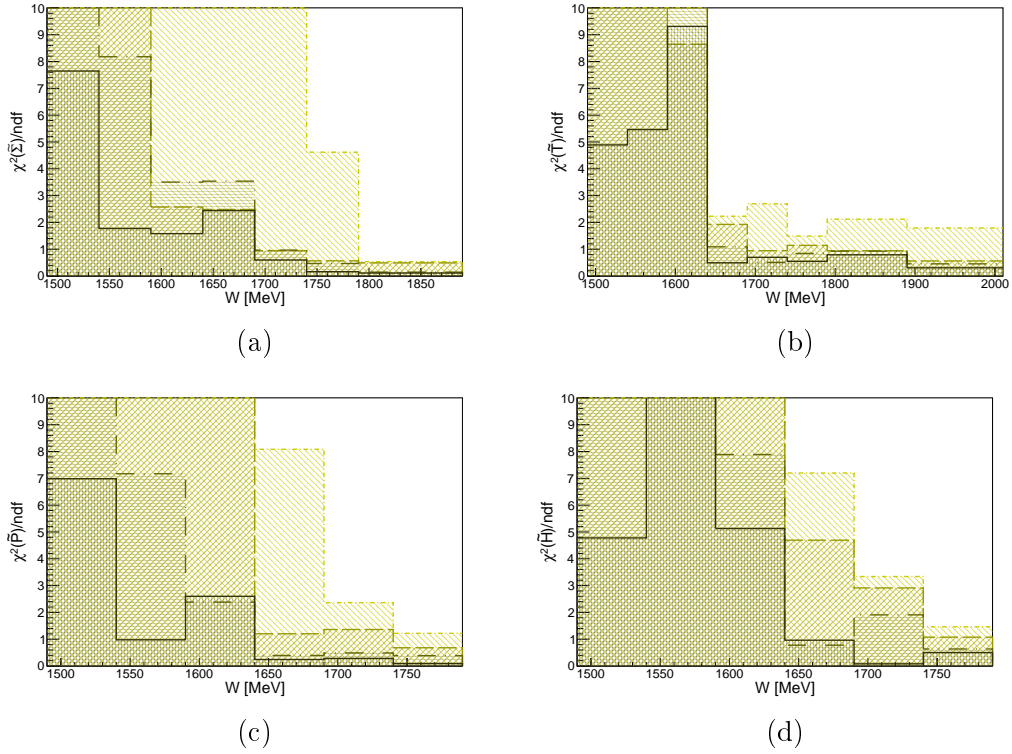


Figure D.12: χ^2/ndf from the Legendre polynomial fits to the reduced polarisation observables $\tilde{\Sigma}$ (a), \tilde{T} (b), \tilde{P} (c) and \tilde{H} as a function of $\cos(\theta)$ for fixed centre of mass energies W in ηm in Oct2018. The fitted functions correspond to Legendre polynomials with a truncation at 1, 2, 3 and 4. The darker the colour, the higher the cut-off.

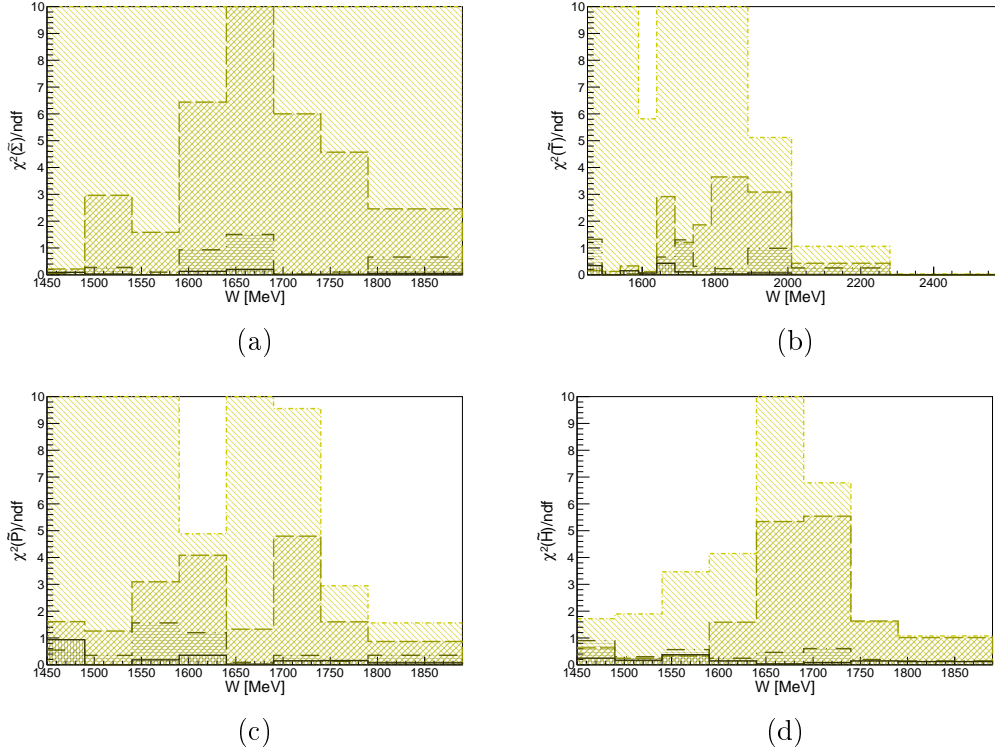


Figure D.13: χ^2/ndf from the Legendre polynomial fits to the reduced polarisation observable \bar{T} as a function of $\cos(\theta)$ for fixed centre of mass energies W in $\pi^0 p$ (a), $\pi^0 n$ (b), ηp (c) and ηn (d). The data is shown for the merged full data from both beam times. The fitted functions correspond to Legendre polynomials with a truncation at 1, 2, 3 and 4. The darker the colour, the higher the cut-off.

D.4 Legendre coefficients

D.4.1 $\gamma p \rightarrow \pi^0 p$

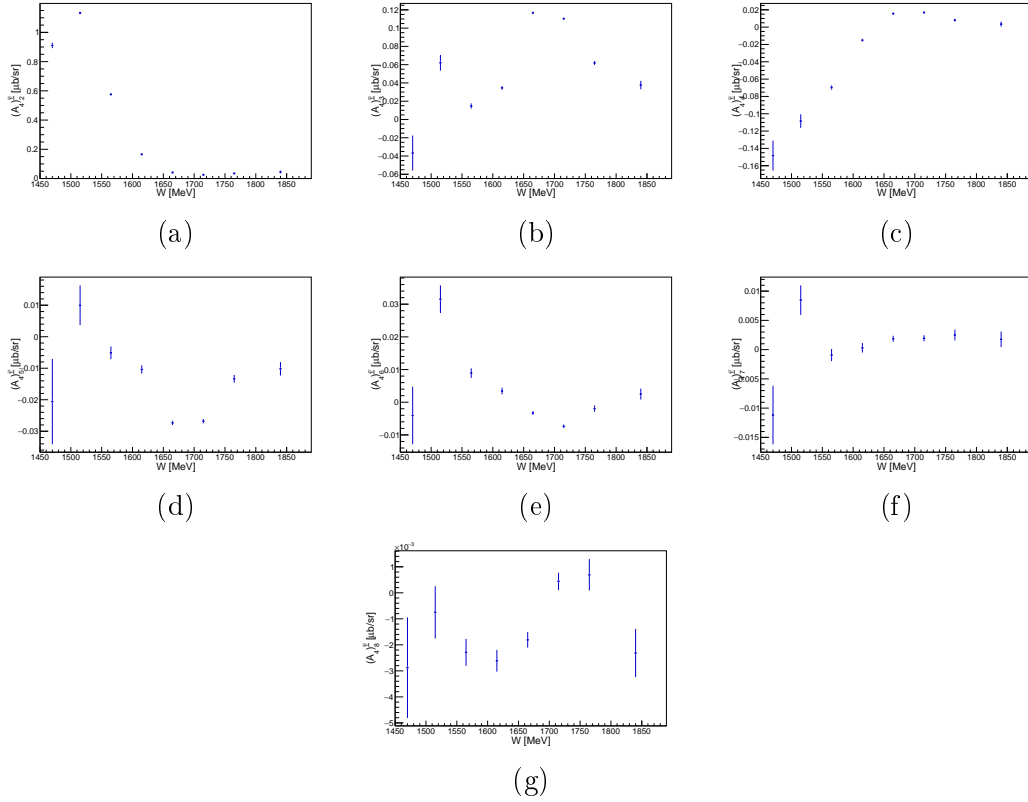


Figure D.14: Legendre coefficients $(A_{l_{max}}^{\Sigma})_{\tilde{l}}$ in $\pi^0 p$ in Oct2018.

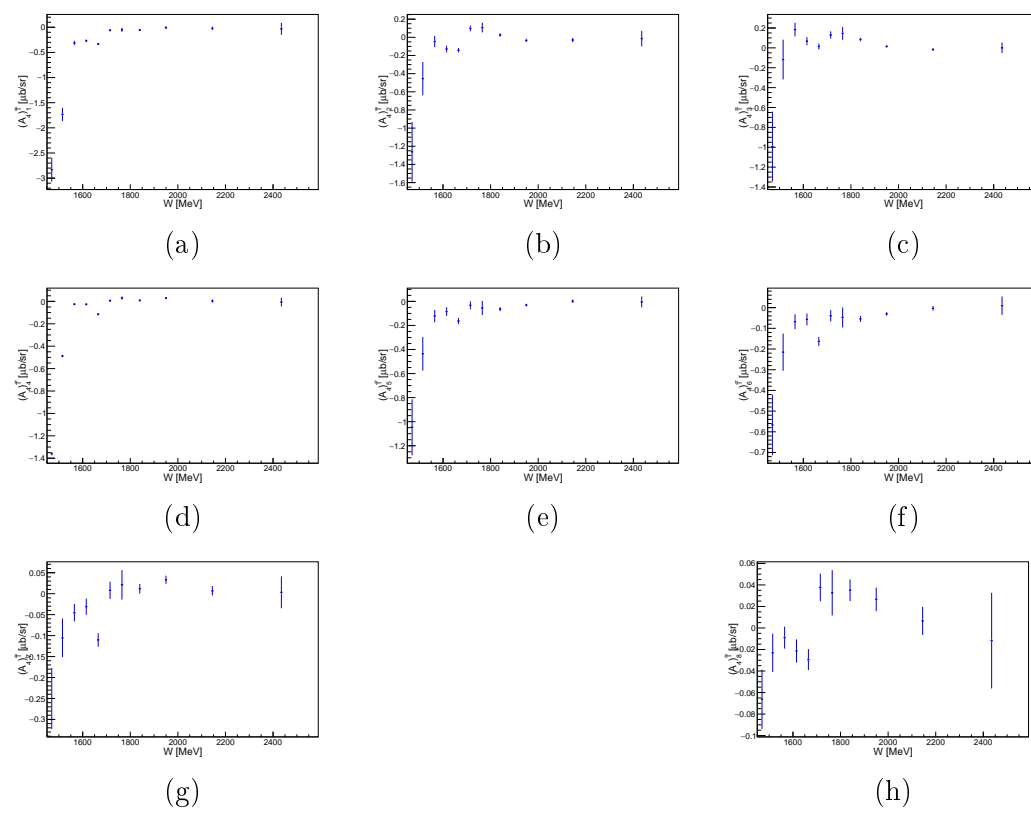


Figure D.15: Legendre coefficients $(A_{l_{max}}^T)_l$ in $\pi^0 p$ in Oct2018.

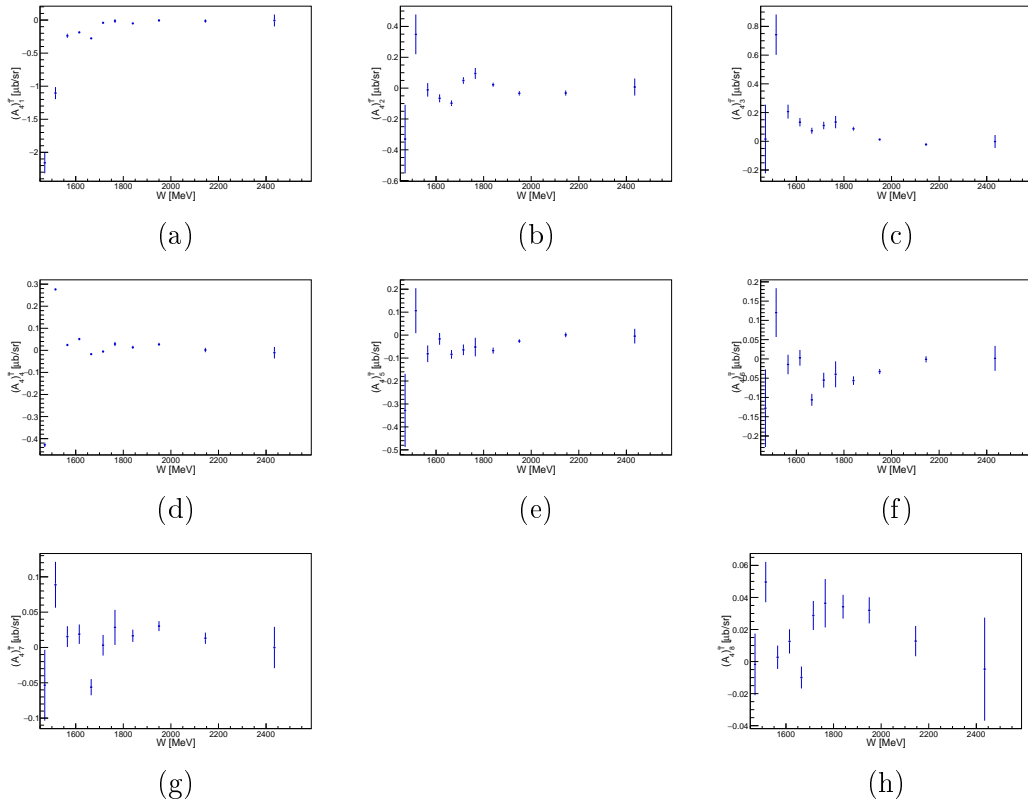


Figure D.16: Legendre coefficients $(A_{l_{max}}^T)$ in $\pi^0 p$ from the merged full data from both beam times.

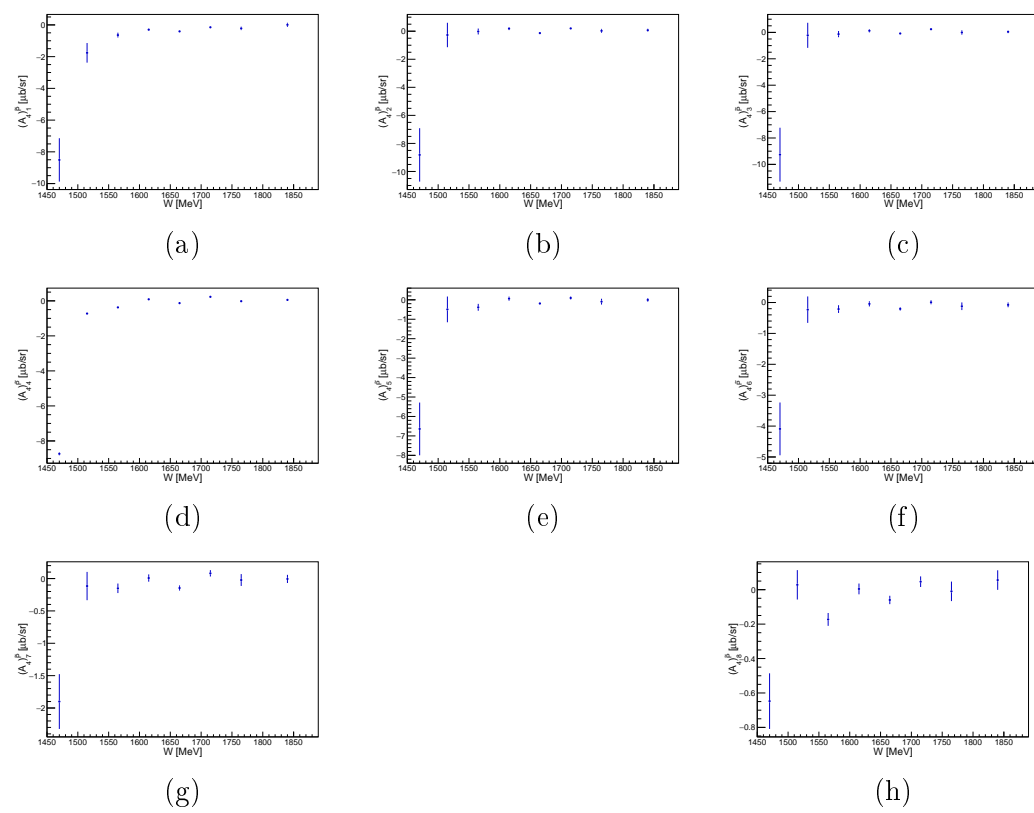


Figure D.17: Legendre coefficients $(A_{l_{max}}^P)$ in $\pi^0 p$ in Oct2018.

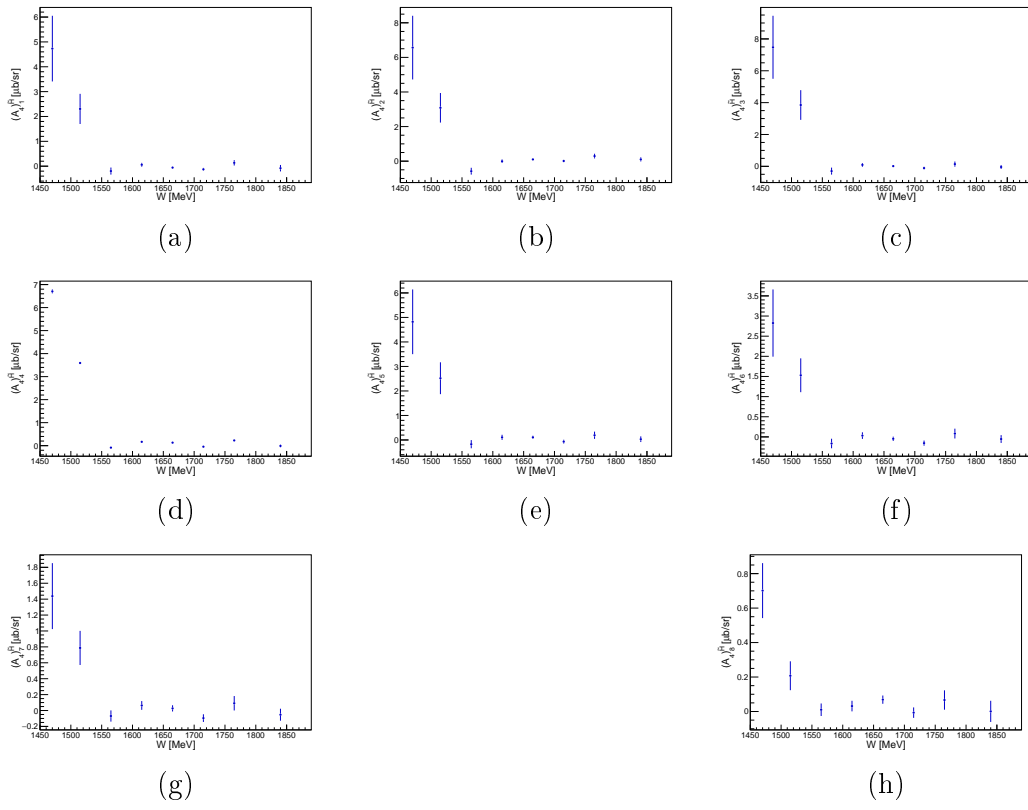


Figure D.18: Legendre coefficients $(A_{l_{max}}^H)_l$ in $\pi^0 p$ in Oct2018.

D.4.2 $\gamma n \rightarrow \pi^0 n$

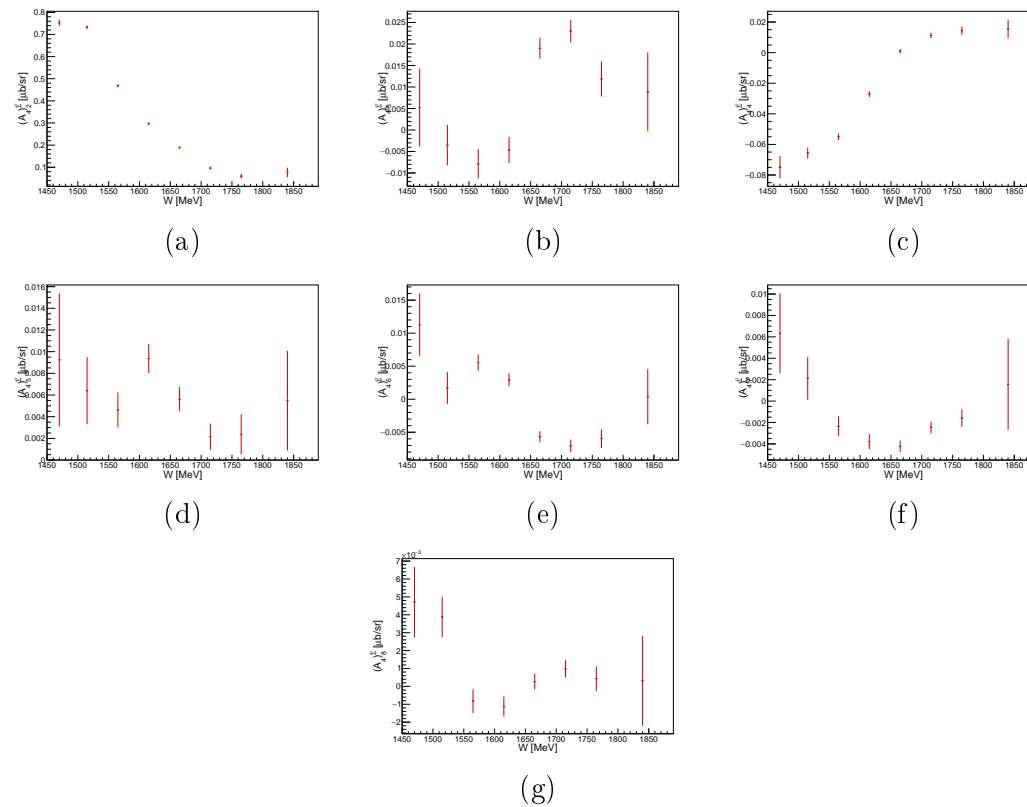


Figure D.19: Legendre coefficients $(A_{l_{max}})_l^{\Sigma}$ in $\pi^0 n$ in Oct2018.

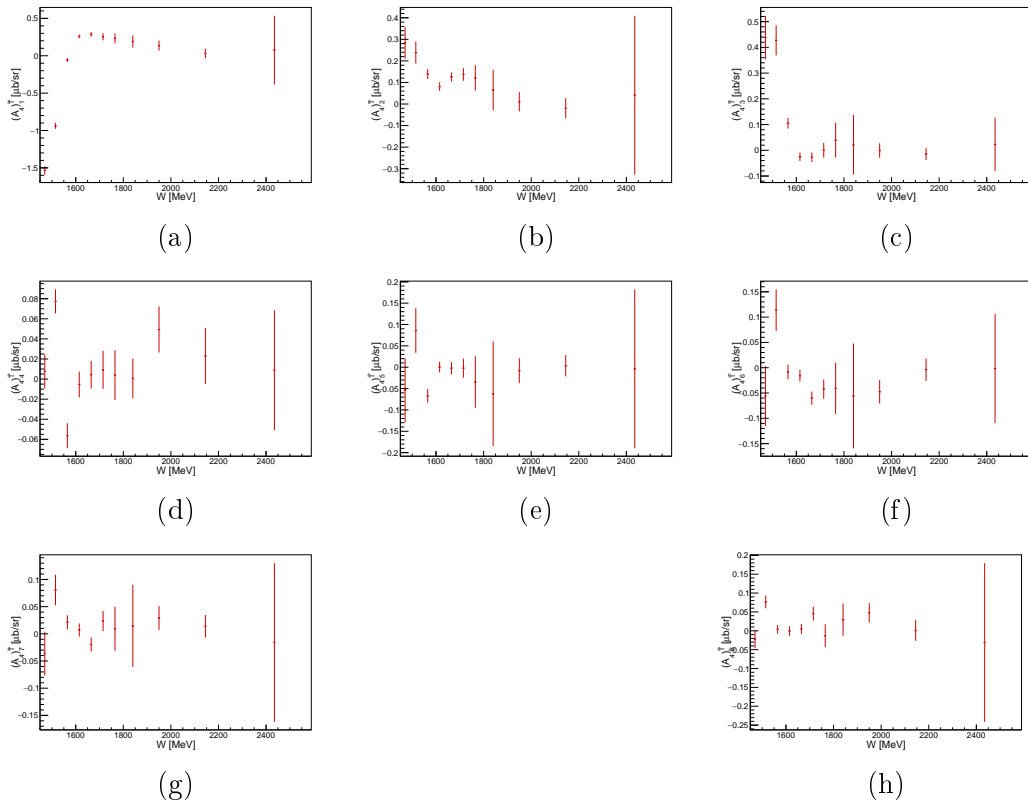


Figure D.20: Legendre coefficients $(A_{l_{max}}^T)_l$ in $\pi^0 n$ in Oct2018.

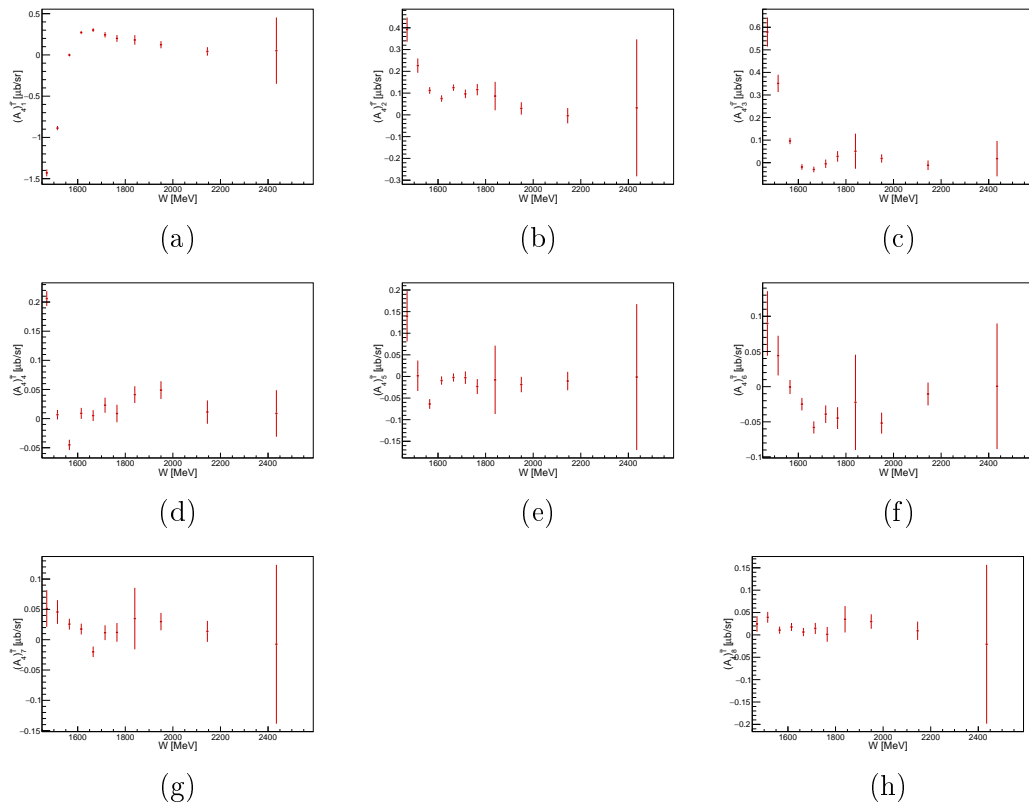


Figure D.21: Legendre coefficients $(A_{l_{max}})^T$ in $\pi^0 n$ from the merged full data from both beam times.

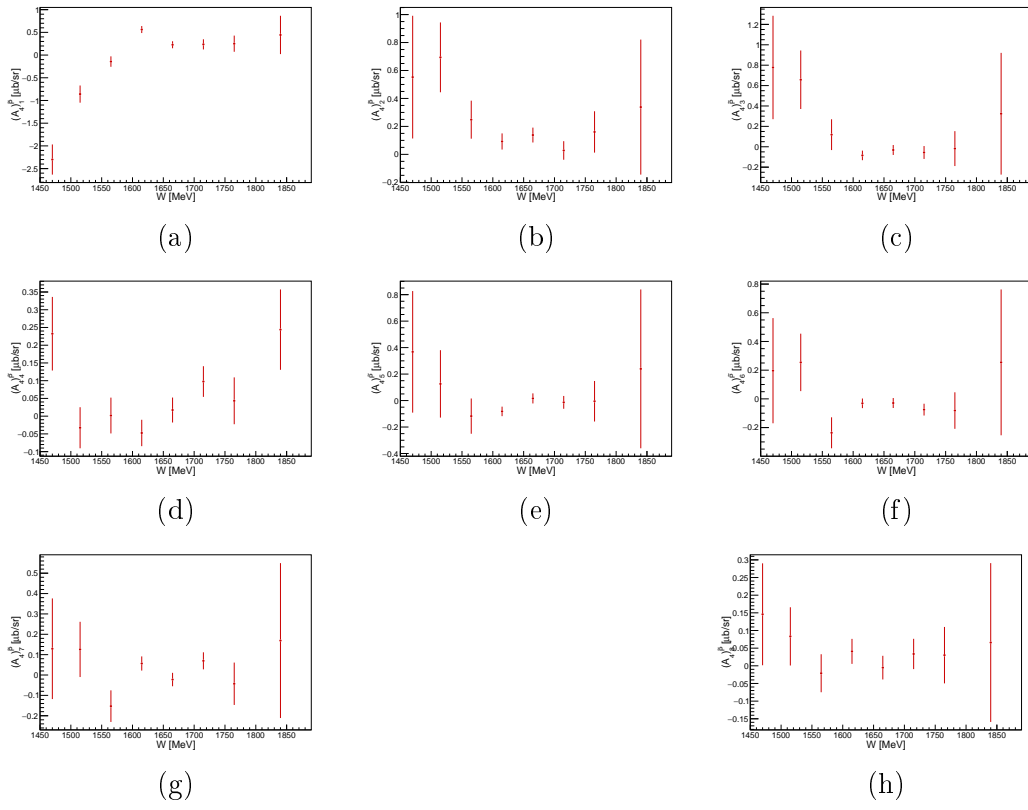


Figure D.22: Legendre coefficients $(A_{l_{max}}^P)_l$ in $\pi^0 n$ in Oct2018.

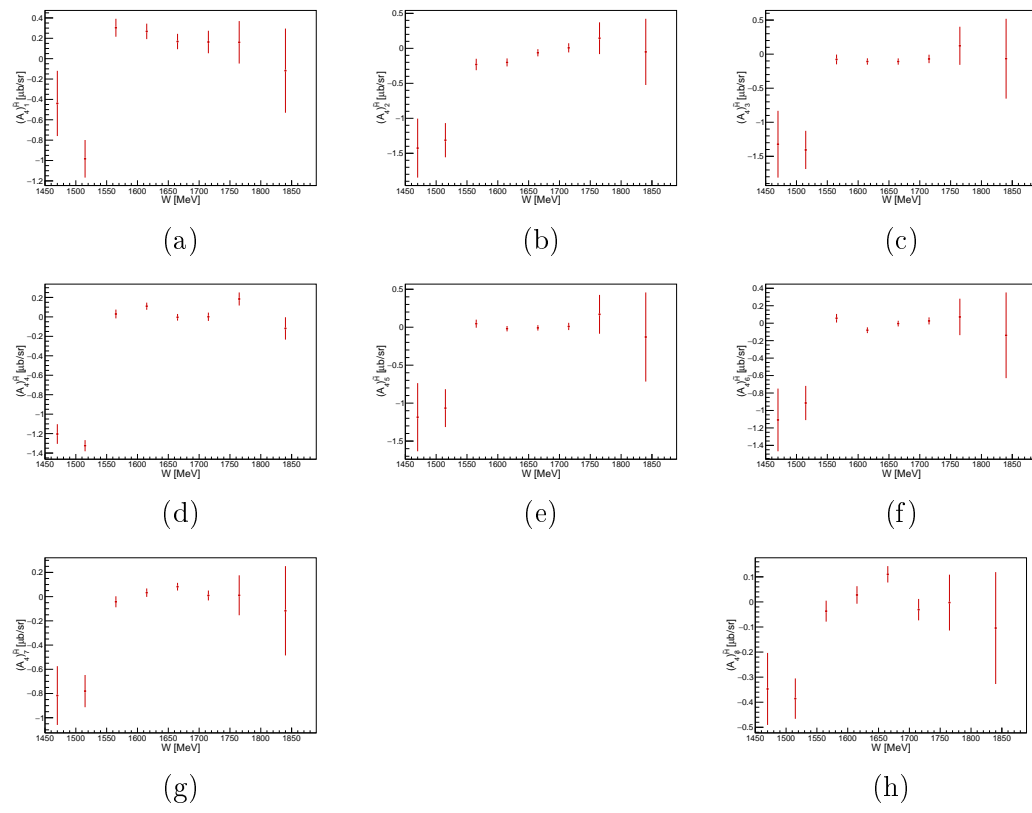


Figure D.23: Legendre coefficients $(A_{l_{max}}^H)_l$ in $\pi^0 n$ in Oct2018.

D.4.3 $\gamma p \rightarrow \eta p$

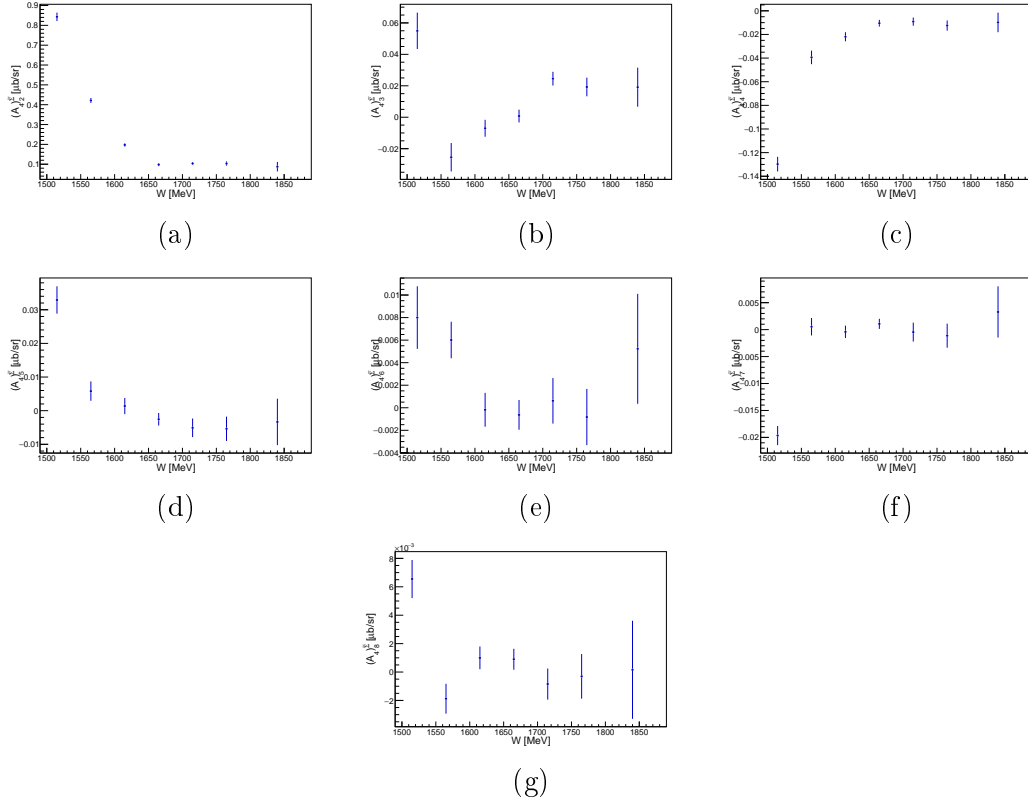


Figure D.24: Legendre coefficients $(A_{l,max})_l^{\hat{\Sigma}}$ in ηp in Oct2018.

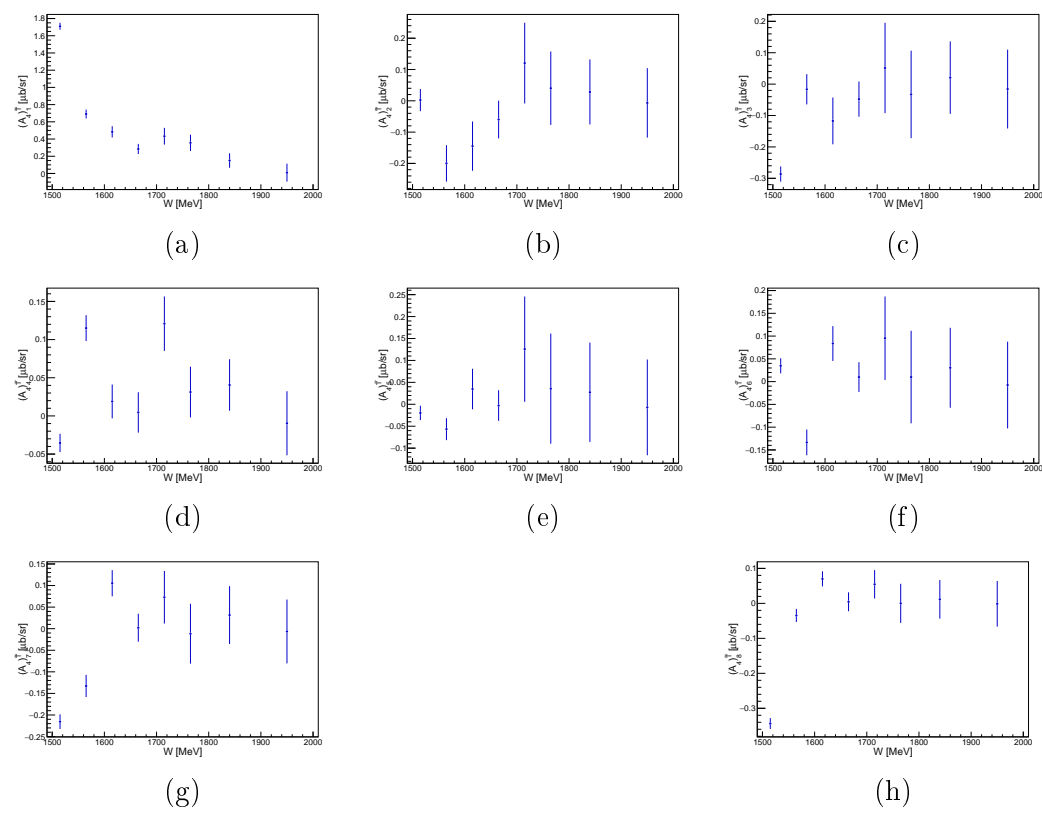


Figure D.25: Legendre coefficients $(A_{l,max})_l^T$ in ηp in Oct2018.

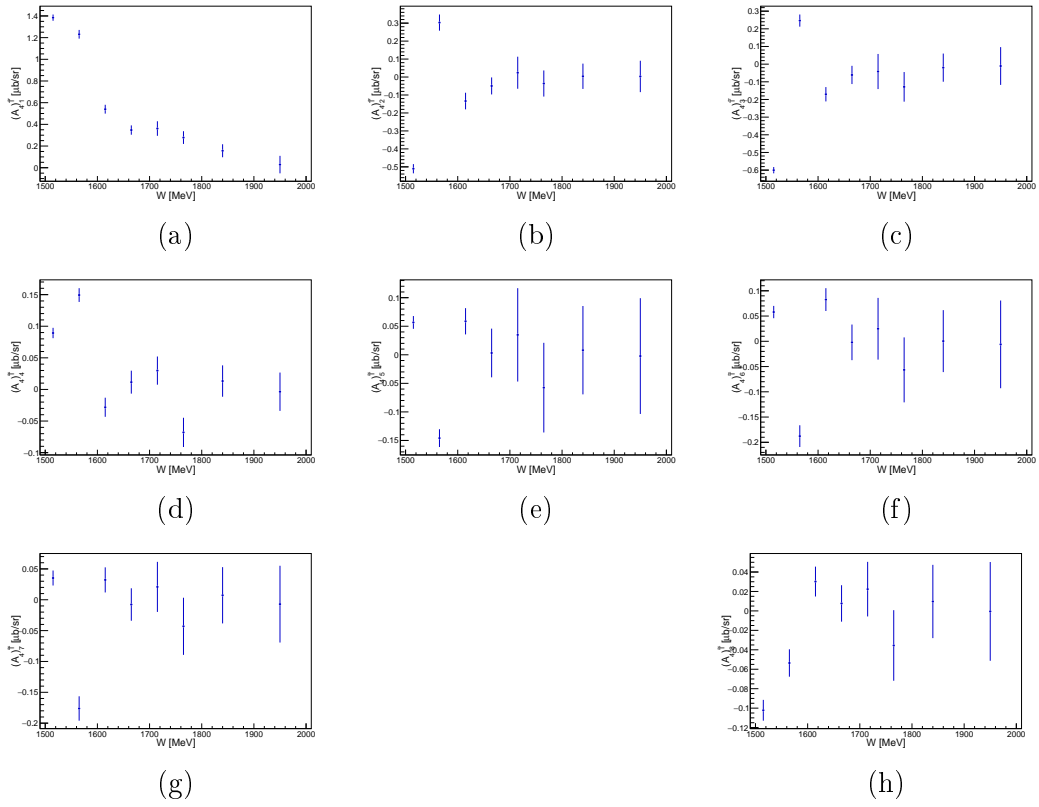


Figure D.26: Legendre coefficients $(A_{l_{max}}^T)$ in ηp from the merged full data from both beam times.

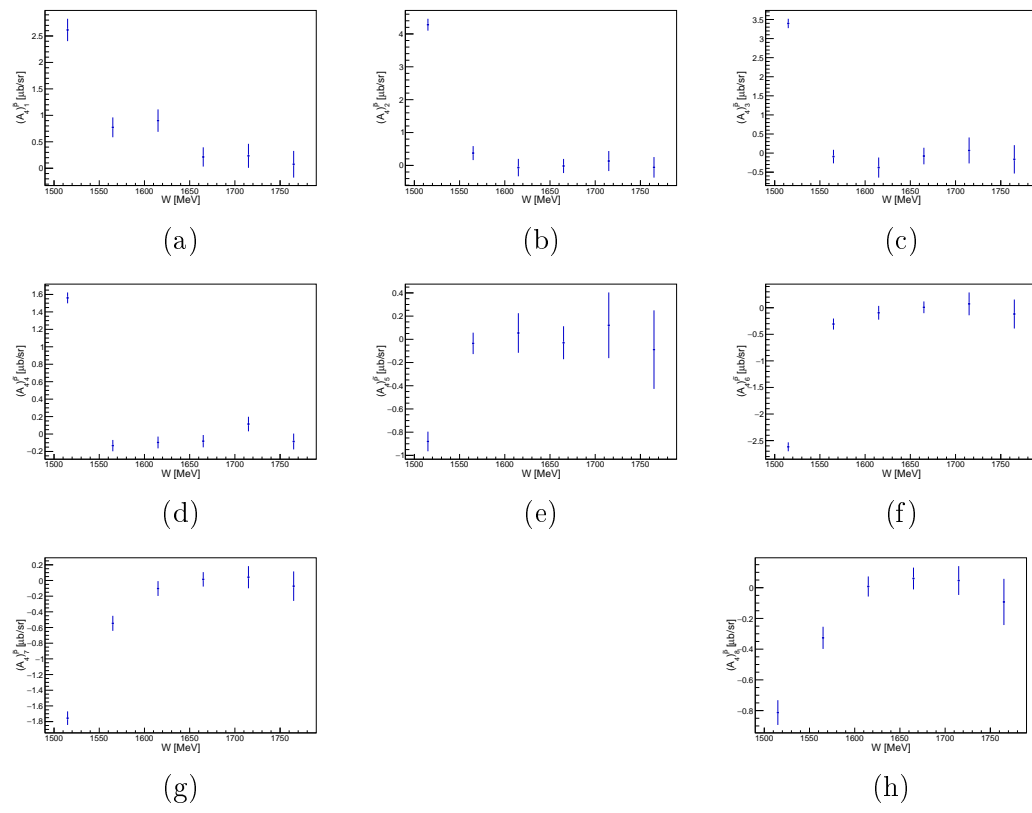


Figure D.27: Legendre coefficients $(A_{l,max})_l^{\tilde{P}}$ in ηp in Oct2018.

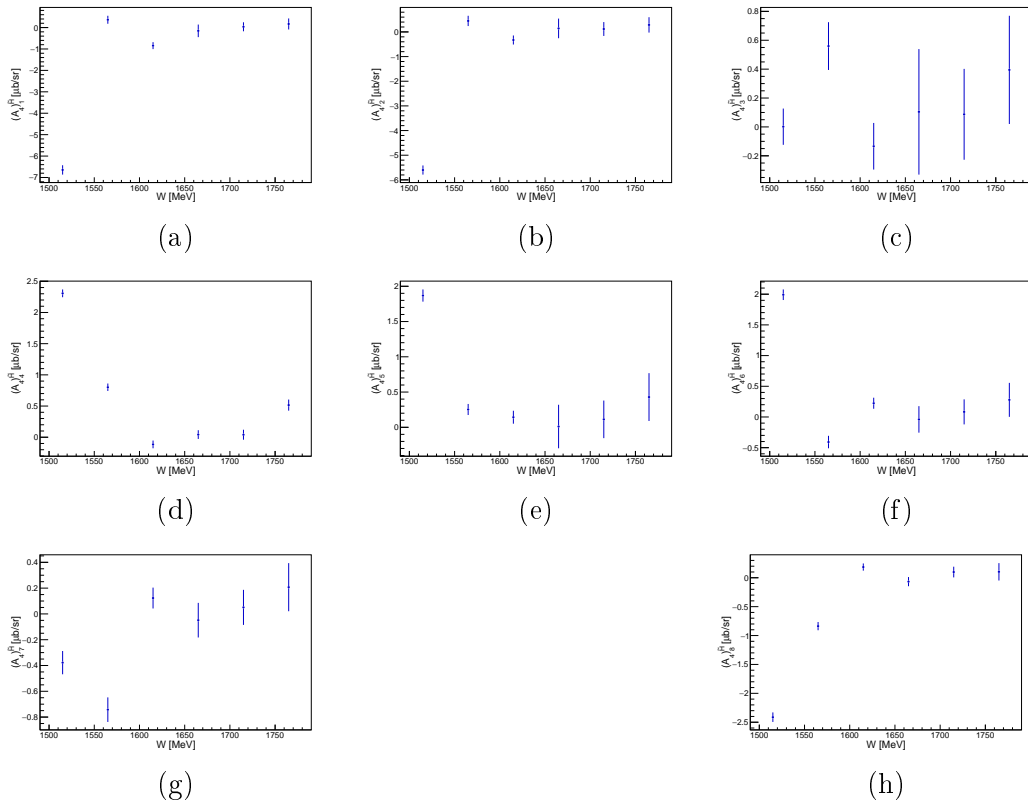


Figure D.28: Legendre coefficients $(A_{l,max})_l^{\tilde{H}}$ in $\eta\pi$ in Oct 2018.

D.4.4 $\gamma n \rightarrow \eta n$

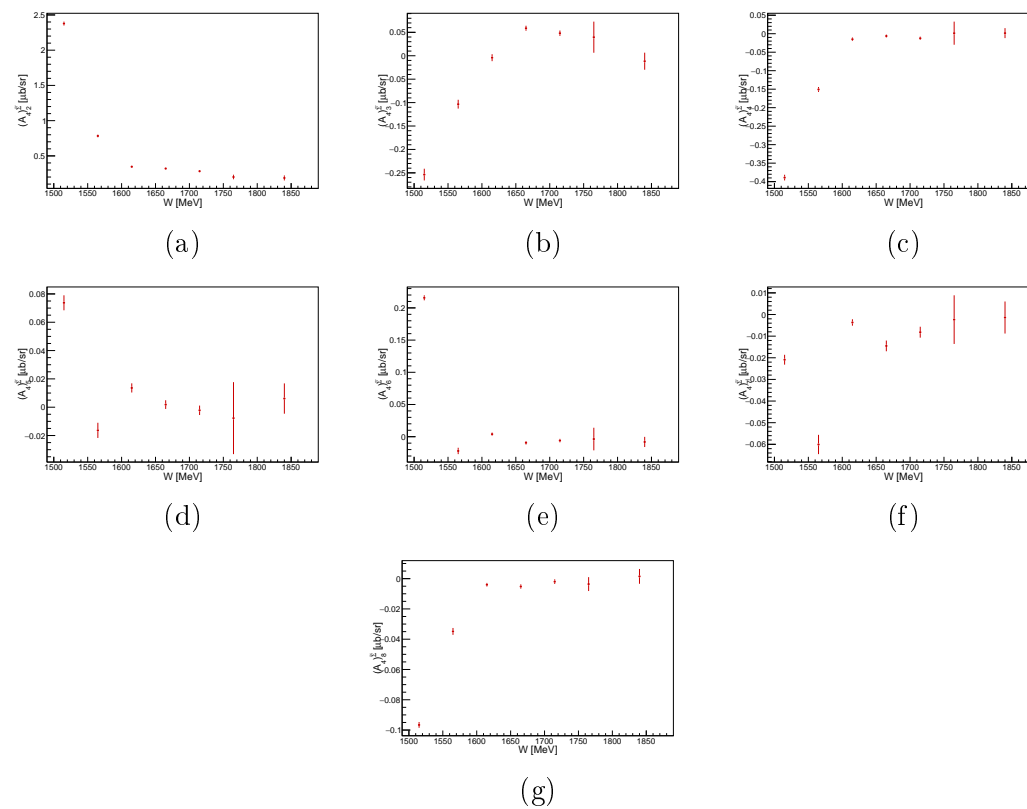


Figure D.29: Legendre coefficients $(A_{l_{max}})_l^{\tilde{\Sigma}}$ in ηn in Oct2018.

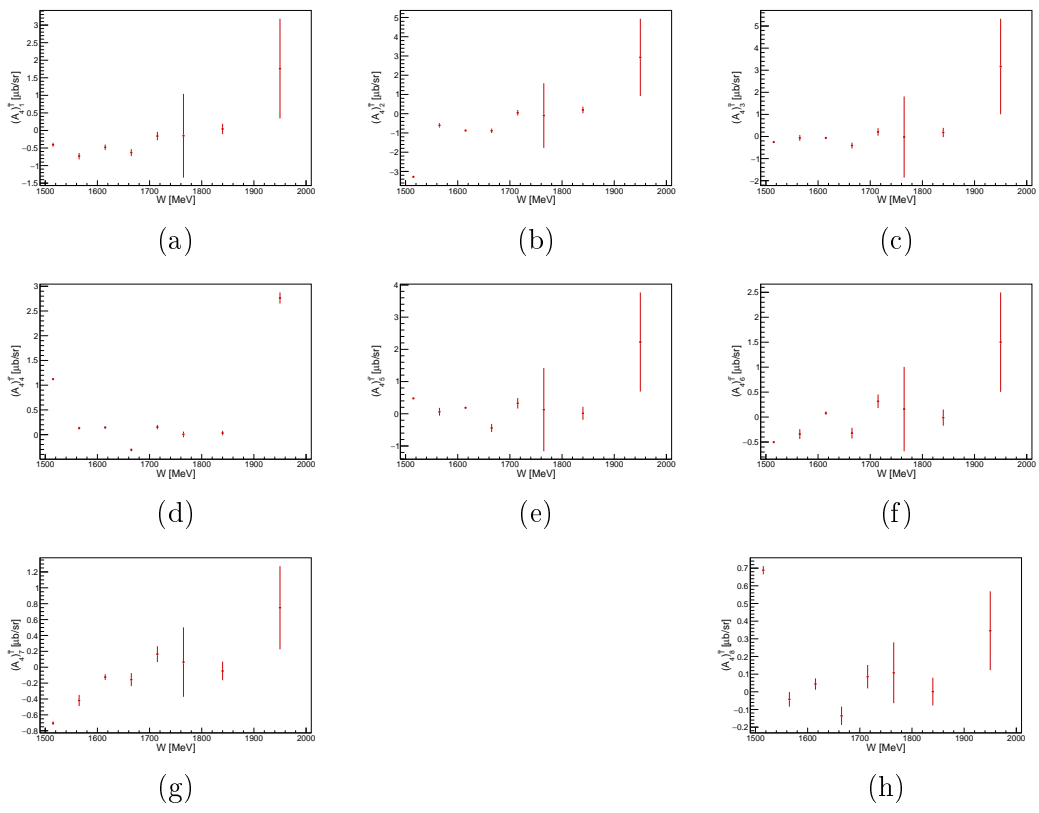


Figure D.30: Legendre coefficients $(A_{l_{max}}^T)_l$ in $\eta\eta$ in Oct2018.

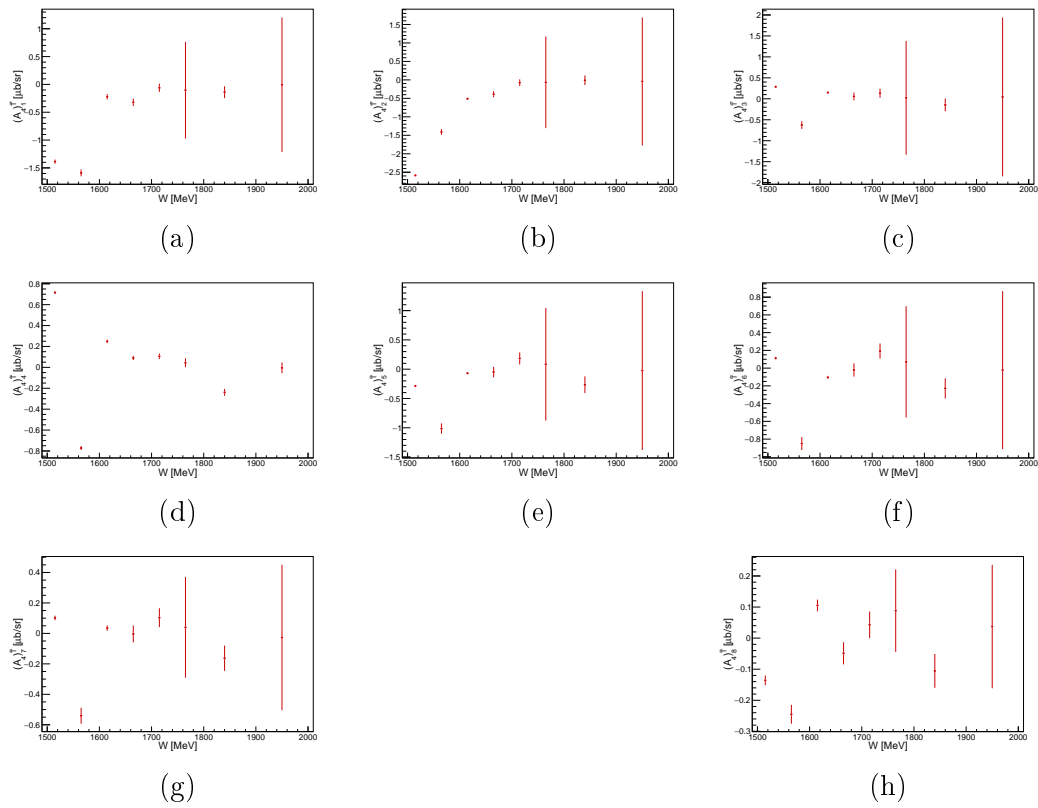


Figure D.31: Legendre coefficients $(A_{l_{max}}^T)_l$ in ηn from the merged full data from both beam times.

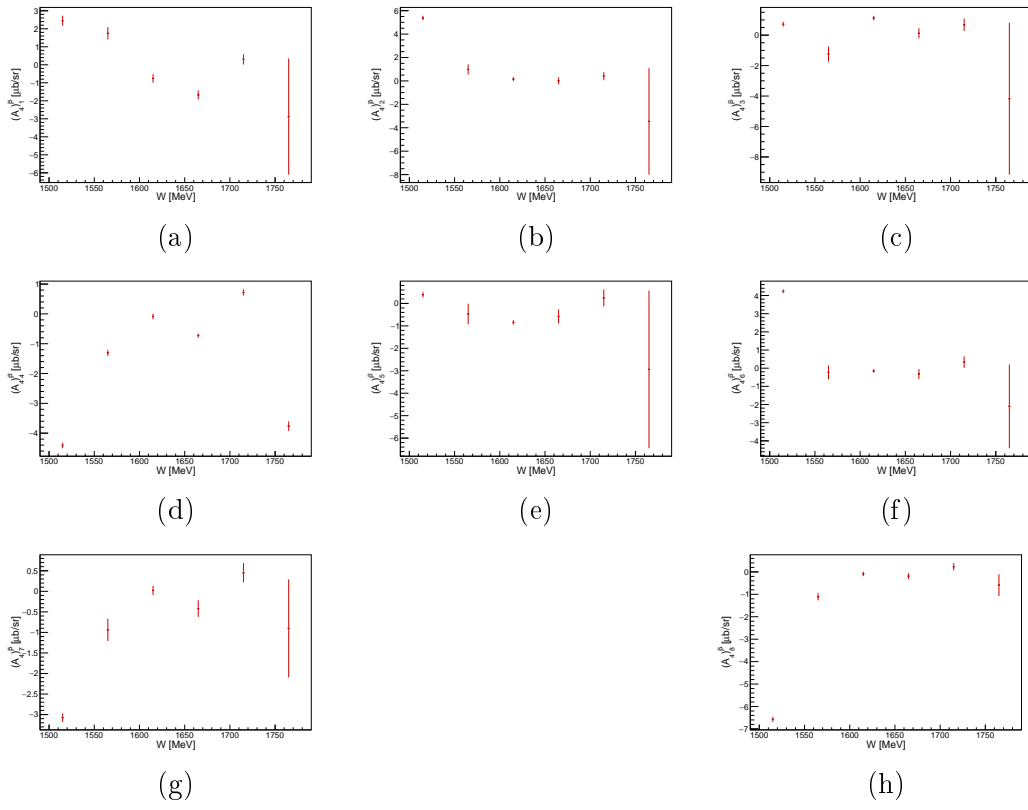


Figure D.32: Legendre coefficients $(A_{l_{max}})^{\tilde{P}}$ in $\eta\eta$ in Oct2018.

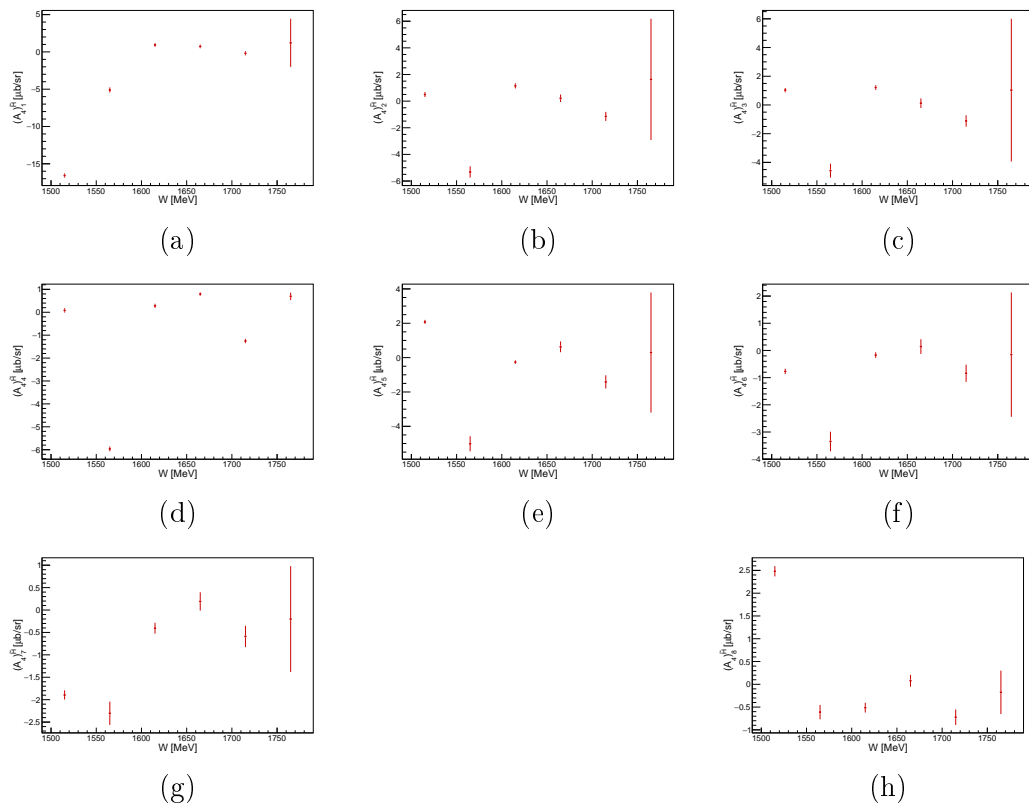


Figure D.33: Legendre coefficients $(A_{l_{max}}^{\tilde{H}})_l$ in ηn in Oct2018.

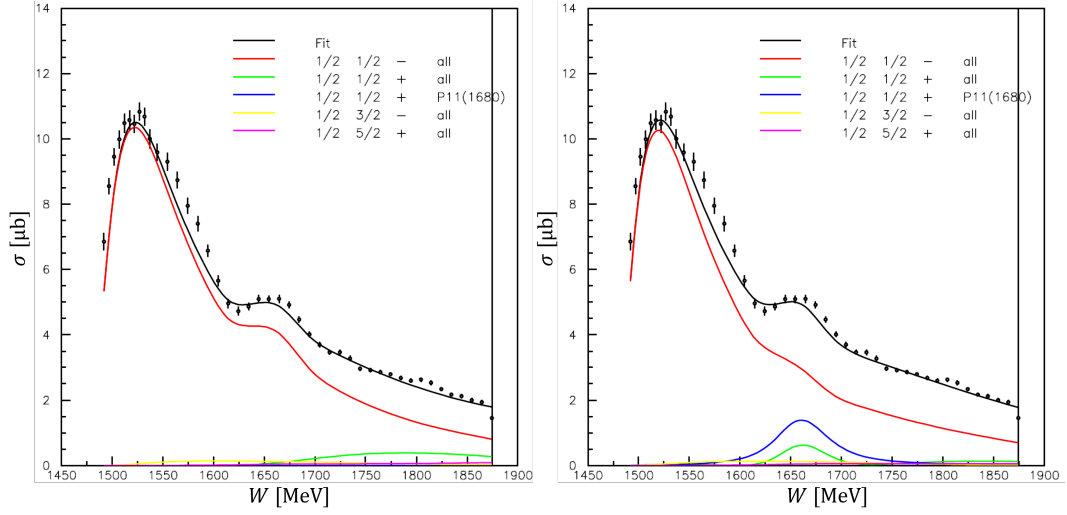
D.5 BnGa 2022-02 predictions in ηn


Figure D.34: Total CS as a function of W in $\gamma n \rightarrow \eta n$. The standard BnGa 2022-02 [126] (left) prediction is compared to a BnGa 2022-02 one with an additional $P_{11}(1680)$ resonance (b) [332]. The fitted data are from [132].

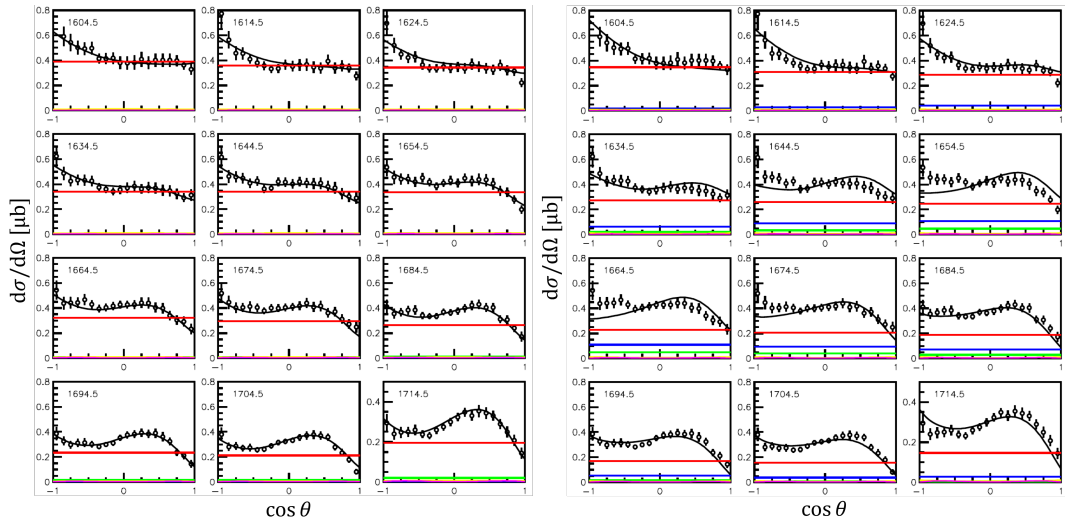


Figure D.35: DCS as a function of $\cos(\theta)$ for fixed W in $\gamma n \rightarrow \eta n$. The standard BnGa 2022-02 [126] (left) prediction is compared to a BnGa 2022-02 one with an additional $P_{11}(1680)$ resonance (b) [332]. The fitted data are from [132].

D.6 Data tables (Oct2018 data)

D.6.1 $\gamma p \rightarrow \pi^0 p$

E_γ [MeV]	$\cos(\theta)$	Σ_{but}	$\Delta\Sigma_{but}^{stat}$	$\Delta\Sigma_{but}^{syst}$	E_γ [MeV]	$\cos(\theta)$	Σ_{but}	$\Delta\Sigma_{but}^{stat}$	$\Delta\Sigma_{but}^{syst}$
1470	-0.917	0.2666	0.1398	0.0299	1515	-0.917	0.2045	0.0693	0.0214
	-0.750	0.5287	0.0845	0.0539		-0.750	0.4783	0.0436	0.0433
	-0.583	0.7456	0.0630	0.0739		-0.583	0.6253	0.0345	0.0550
	-0.417	0.7850	0.0602	0.0776		-0.417	0.6559	0.0348	0.0575
	-0.250	1.0515	0.0490	0.1022		-0.250	0.7794	0.0279	0.0674
	-0.083	0.9033	0.0454	0.0885		-0.083	0.8459	0.0254	0.0727
	0.083	0.9300	0.0456	0.0909		0.083	0.8783	0.0254	0.0753
	0.250	0.9729	0.0523	0.0949		0.250	0.8436	0.0280	0.0725
	0.417	0.8528	0.0661	0.0978		0.417	0.7901	0.0328	0.0682
0.583	0.8055	0.1570	0.0794	0.583	0.7842	0.0585	0.0677		
1565	-0.917	0.2140	0.0484	0.0221	1615	-0.917	0.1409	0.0370	0.0161
	-0.750	0.3147	0.0317	0.0302		-0.750	0.1742	0.0240	0.0187
	-0.583	0.3344	0.0274	0.0317		-0.583	0.0397	0.0222	0.0082
	-0.417	0.4158	0.0298	0.0383		-0.417	-0.0182	0.0245	0.0069
	-0.250	0.5708	0.0247	0.0507		-0.250	0.1423	0.0230	0.0162
	-0.083	0.6178	0.0225	0.0544		-0.083	0.2449	0.0218	0.0242
	0.083	0.6648	0.0229	0.0582		0.083	0.4040	0.0227	0.0367
	0.250	0.7004	0.0253	0.0610		0.250	0.4460	0.0260	0.0400
	0.417	0.6804	0.0297	0.0594		0.417	0.6274	0.0293	0.0543
0.583	0.6877	0.0463	0.0600	0.583	0.5980	0.0396	0.0627		
0.750	0.7170	0.1527	0.0624	0.750	0.7859	0.0893	0.0668		
1665	-0.917	0.0938	0.0303	0.0097	1715	-0.917	0.0262	0.0339	0.0067
	-0.750	-0.0897	0.0186	0.0095		-0.750	-0.2068	0.0228	0.0153
	-0.583	-0.2316	0.0176	0.0166		-0.583	-0.4264	0.0214	0.0263
	-0.417	-0.4080	0.0207	0.0254		-0.417	-0.5524	0.0273	0.0326
	-0.250	-0.3462	0.0192	0.0223		-0.250	-0.5795	0.0221	0.0340
	-0.083	-0.1083	0.0192	0.0104		-0.083	-0.3175	0.0229	0.0209
	0.083	0.1618	0.0198	0.0131		0.083	0.0709	0.0223	0.0085
	0.250	0.4572	0.0202	0.0279		0.250	0.4843	0.0204	0.0292
	0.417	0.6503	0.0202	0.0375		0.417	0.7166	0.0195	0.0408
0.583	0.7819	0.0230	0.0444	0.583	0.7941	0.0228	0.0456		
0.750	0.7943	0.0396	0.0447	0.750	0.7756	0.0359	0.0438		

D.6. Data tables (Oct2018 data)

E_γ [MeV]	$\cos(\theta)$	Σ_{but}	$\Delta\Sigma_{but}^{stat}$	$\Delta\Sigma_{but}^{syst}$	E_γ [MeV]	$\cos(\theta)$	Σ_{but}	$\Delta\Sigma_{but}^{stat}$	$\Delta\Sigma_{but}^{syst}$
1765	-0.917	0.0573	0.0531	0.0082	1840	-0.917	0.0616	0.0923	0.0132
	-0.750	-0.1613	0.0423	0.0131		-0.750	0.3252	0.0843	0.0274
	-0.583	-0.3418	0.0413	0.0221		-0.583	-0.1049	0.0888	0.0129
	-0.417	-0.5090	0.0581	0.0304		-0.417	-0.5745	0.1367	0.0445
	-0.250	-0.4778	0.0389	0.0289		-0.250	-0.4362	0.0837	0.0350
	-0.083	-0.2361	0.0394	0.0168		-0.083	0.1663	0.0804	0.0165
	0.083	0.2085	0.0370	0.0154		0.083	0.3682	0.0773	0.0303
	0.250	0.4844	0.0339	0.0292		0.250	0.4336	0.0820	0.0353
	0.417	0.6315	0.0340	0.0366		0.417	0.6898	0.0677	0.0525
	0.583	0.7778	0.0412	0.0439		0.583	0.8000	0.1105	0.0601
	0.750	0.8844	0.0596	0.0492		0.750	0.8267	0.1272	0.1097
						0.917	1.0150	0.6204	0.0767

E_γ [MeV]	$\cos(\theta)$	T	ΔT^{stat}	ΔT^{syst}	E_γ [MeV]	$\cos(\theta)$	T	ΔT^{stat}	ΔT^{syst}
1470	-0.917	-0.3269	0.0863	0.0356	1515	-0.917	-0.0957	0.0487	0.0122
	-0.750	-0.5077	0.0514	0.0503		-0.750	-0.1176	0.0304	0.0139
	-0.583	-0.5923	0.0387	0.0579		-0.583	-0.2837	0.0269	0.0309
	-0.417	-0.6954	0.0476	0.0902		-0.417	-0.3470	0.0310	0.0428
	-0.250	-0.6787	0.0336	0.0708		-0.250	-0.4116	0.0222	0.0430
	-0.083	-0.6732	0.0330	0.0792		-0.083	-0.3841	0.0215	0.0434
	0.083	-0.6884	0.0347	0.0844		0.083	-0.4123	0.0240	0.0542
	0.250	-0.6094	0.0363	0.0708		0.250	-0.3561	0.0248	0.0446
	0.417	-0.4504	0.0434	0.0629		0.417	-0.2862	0.0286	0.0351
	0.583	-0.5625	0.1698	0.1242		0.583	-0.2324	0.0515	0.0303
1565	-0.917	0.1846	0.0419	0.0171	1615	-0.917	0.2777	0.0423	0.0239
	-0.750	0.1795	0.0303	0.0198		-0.750	0.0905	0.0280	0.0119
	-0.583	0.0358	0.0262	0.0082		-0.583	0.0806	0.0291	0.0129
	-0.417	-0.0554	0.0350	0.0118		-0.417	-0.0524	0.0362	0.0112
	-0.250	-0.1192	0.0244	0.0159		-0.250	-0.0885	0.0293	0.0135
	-0.083	-0.1920	0.0252	0.0259		-0.083	-0.1847	0.0332	0.0284
	0.083	-0.1926	0.0271	0.0280		0.083	-0.2415	0.0363	0.0375
	0.250	-0.2324	0.0305	0.0343		0.250	-0.3418	0.0409	0.0495
	0.417	-0.1440	0.0355	0.0227		0.417	-0.2849	0.0470	0.0413
	0.583	0.1400	0.0528	0.0203		0.583	-0.1440	0.0607	0.0330
	0.750	0.3458	0.2897	0.0871		0.750	-0.0014	0.1346	0.0171

Appendix D. Results

E_γ [MeV]	$\cos(\theta)$	T	ΔT^{stat}	ΔT^{syst}	E_γ [MeV]	$\cos(\theta)$	T	ΔT^{stat}	ΔT^{syst}
1665	-0.917	0.3402	0.0410	0.0300	1715	-0.917	0.3912	0.0539	0.0410
	-0.750	0.0831	0.0261	0.0120		-0.750	0.0519	0.0354	0.0102
	-0.583	-0.0062	0.0290	0.0077		-0.583	-0.1365	0.0396	0.0224
	-0.417	-0.1298	0.0399	0.0234		-0.417	-0.0509	0.0587	0.0159
	-0.250	-0.1074	0.0308	0.0166		-0.250	-0.0809	0.0455	0.0168
	-0.083	-0.1600	0.0373	0.0293		-0.083	-0.2610	0.0562	0.0576
	0.083	-0.3094	0.0385	0.0502		0.083	-0.2307	0.0553	0.0530
	0.250	-0.3939	0.0405	0.0619		0.250	-0.2140	0.0509	0.0477
	0.417	-0.2547	0.0388	0.0388		0.417	0.0628	0.0439	0.0158
	0.583	0.0812	0.0412	0.0146		0.583	0.2654	0.0514	0.0470
0.750	0.1381	0.0696	0.0196	0.750	0.3111	0.0851	0.0571		
1765	-0.917	0.2195	0.0748	0.0293	1840	-0.917	0.1621	0.0515	0.0190
	-0.750	-0.0402	0.0576	0.0108		-0.750	0.0534	0.0490	0.0101
	-0.583	-0.1197	0.0648	0.0204		-0.583	-0.0755	0.0627	0.0143
	-0.417	-0.0125	0.0880	0.0158		-0.417	0.1226	0.0670	0.0167
	-0.250	-0.1075	0.0700	0.0206		-0.250	-0.0019	0.0628	0.0103
	-0.083	-0.4138	0.0890	0.0904		-0.083	-0.2684	0.0644	0.0418
	0.083	-0.5013	0.0822	0.1047		0.083	-0.4520	0.0597	0.0605
	0.250	-0.3315	0.0716	0.0657		0.250	-0.5772	0.0838	0.1044
	0.417	0.1247	0.0728	0.0291		0.417	0.1368	0.0551	0.0224
	0.583	0.5342	0.0999	0.1086		0.583	0.6362	0.0881	0.0701
0.750	0.6749	0.1557	0.1510	0.750	0.3041	0.0774	0.0851		
					0.917	-0.3693	0.5306	0.0898	
1950	-0.917	0.1677	0.0617	0.0179	2145	-0.917	0.3401	0.1216	0.0411
	-0.750	-0.1008	0.0628	0.0146		-0.750	-0.2915	0.0487	0.0464
	-0.583	0.0806	0.0792	0.0162		-0.583	-0.2847	0.0829	0.0379
	-0.417	0.4244	0.0924	0.0682		-0.417	0.3037	0.1060	0.0453
	-0.250	0.2428	0.0745	0.0323		-0.250	0.2389	0.1013	0.0338
	-0.083	-0.0178	0.0634	0.0126		-0.083	0.0211	0.0722	0.0122
	0.083	-0.3879	0.0710	0.0585		0.083	-0.1160	0.0773	0.0191
	0.250	-0.2663	0.0947	0.0440		0.250	-0.1488	0.1187	0.0397
	0.417	0.1419	0.1664	0.0344		0.417	0.0461	0.2014	0.0733
	0.583	0.2310	0.1148	0.0298		0.583	-0.5863	0.1790	0.1207
0.750	-0.1123	0.0758	0.0312	0.750	-0.3368	0.0599	0.0563		
0.917	-0.0288	0.0681	0.0333	0.917	-0.2887	0.1551	0.0572		

D.6. Data tables (Oct2018 data)

E_γ [MeV]	$\cos(\theta)$	T	ΔT^{stat}	ΔT^{syst}	E_γ [MeV]	$\cos(\theta)$	T	ΔT^{stat}	ΔT^{syst}
2435	-0.917	0.2179	0.1754	0.0352					
	-0.750	-0.0609	0.4427	0.0699					
	-0.583	-2.7120	1.9069	1.2479					
	-0.417	-0.4358	0.4033	0.0949					
	-0.250	-1.7892	6.9663	0.0050					
	-0.083	-0.8492	0.3542	0.1162					
	0.083	-0.3729	0.1257	0.0869					
	0.250	0.0600	0.2808	0.0391					
	0.417	0.2500	0.3547	0.0645					
	0.583	-0.6172	0.1682	0.1479					
	0.750	-0.4012	0.1677	0.0578					
	0.917	-0.4334	0.3221	0.1406					

E_γ [MeV]	$\cos(\theta)$	P	ΔP^{stat}	ΔP^{syst}	E_γ [MeV]	$\cos(\theta)$	P	ΔP^{stat}	ΔP^{syst}
1470	-0.917	-0.9219	0.5286	0.1254	1515	-0.917	-0.1063	0.2371	0.0277
	-0.750	-1.0465	0.3149	0.1395		-0.750	-0.1617	0.1515	0.0259
	-0.583	-0.7715	0.2354	0.1057		-0.583	-0.5376	0.1310	0.0689
	-0.417	-0.6734	0.2638	0.0966		-0.417	-0.4967	0.1442	0.0665
	-0.250	-0.7442	0.1881	0.1110		-0.250	-0.4818	0.1068	0.0665
	-0.083	-0.7928	0.1894	0.1201		-0.083	-0.4035	0.1015	0.0576
	0.083	-0.6539	0.1918	0.0983		0.083	-0.3700	0.1108	0.0540
	0.250	-0.9112	0.2169	0.1357		0.250	-0.2828	0.1178	0.0430
	0.417	-0.1613	0.2583	0.0706		0.417	-0.0977	0.1343	0.0305
	0.583	-1.3979	0.9681	0.6451		0.583	-0.0133	0.2447	0.0845
1565	-0.917	-0.4104	0.1587	0.0499	1615	-0.917	0.0384	0.1233	0.0157
	-0.750	-0.3602	0.1140	0.0455		-0.750	-0.3876	0.0835	0.0487
	-0.583	-0.0151	0.0989	0.0143		-0.583	-0.2518	0.0863	0.0356
	-0.417	-0.2460	0.1283	0.0354		-0.417	-0.2648	0.1030	0.0395
	-0.250	-0.3702	0.0942	0.0535		-0.250	-0.0406	0.0891	0.0159
	-0.083	-0.2413	0.0937	0.0393		-0.083	-0.2205	0.0970	0.0378
	0.083	-0.2120	0.1004	0.0369		0.083	-0.1592	0.1052	0.0303
	0.250	-0.0747	0.1139	0.0214		0.250	-0.3720	0.1190	0.0620
	0.417	-0.0367	0.1320	0.0207		0.417	-0.2208	0.1342	0.0387
	0.583	0.1874	0.1929	0.0397		0.583	-0.0084	0.1741	0.0357
	0.750	0.6043	0.9728	0.2180		0.750	0.7427	0.3919	0.1111

Appendix D. Results

E_γ [MeV]	$\cos(\theta)$	P	ΔP^{stat}	ΔP^{syst}	E_γ [MeV]	$\cos(\theta)$	P	ΔP^{stat}	ΔP^{syst}
1665	-0.917	-0.1547	0.1031	0.0193	1715	-0.917	-0.0750	0.1282	0.0175
	-0.750	-0.1198	0.0671	0.0178		-0.750	-0.4290	0.0885	0.0554
	-0.583	-0.0205	0.0745	0.0125		-0.583	-0.1823	0.0964	0.0301
	-0.417	-0.2411	0.0994	0.0382		-0.417	-0.1803	0.1472	0.0361
	-0.250	-0.1120	0.0786	0.0226		-0.250	0.0443	0.1075	0.0220
	-0.083	-0.0347	0.0946	0.0177		-0.083	-0.1958	0.1346	0.0467
	0.083	-0.3084	0.0957	0.0538		0.083	-0.6332	0.1364	0.1388
	0.250	-0.4542	0.0987	0.0740		0.250	-0.3200	0.1218	0.0696
	0.417	-0.2622	0.0953	0.0417		0.417	-0.1445	0.1048	0.0331
	0.583	0.0092	0.1015	0.0156		0.583	0.0719	0.1187	0.0255
0.750	0.1717	0.1677	0.0287	0.750	0.5190	0.2008	0.0983		
1765	-0.917	-0.2693	0.2184	0.0404	1840	-0.917	-0.0427	0.3161	0.0328
	-0.750	-0.5446	0.1706	0.0735		-0.750	-0.1073	0.3046	0.0330
	-0.583	-0.4014	0.1855	0.0597		-0.583	-0.5795	0.3716	0.0739
	-0.417	0.1284	0.2899	0.0437		-0.417	-0.0390	0.5319	0.0561
	-0.250	-0.1052	0.1845	0.0348		-0.250	0.7855	0.3431	0.1049
	-0.083	-0.5175	0.2352	0.1051		-0.083	-0.2890	0.3744	0.0578
	0.083	-0.3534	0.2162	0.0768		0.083	-0.1017	0.3357	0.0466
	0.250	-0.4171	0.1902	0.0875		0.250	-0.5825	0.4393	0.0997
	0.417	-0.1843	0.1973	0.0484		0.417	0.0607	0.3033	0.0408
	0.583	0.3023	0.2463	0.0711		0.583	0.4553	0.4422	0.0751
0.750	0.3189	0.3835	0.0952	0.750	0.6200	0.5156	0.1385		
					0.917	-0.2766	2.6895	0.0050	

E_γ [MeV]	$\cos(\theta)$	H	ΔH^{stat}	ΔH^{syst}	E_γ [MeV]	$\cos(\theta)$	H	ΔH^{stat}	ΔH^{syst}
1470	-0.917	0.8111	0.5424	0.1131	1515	-0.917	0.4190	0.2313	0.0515
	-0.750	0.4613	0.3163	0.0669		-0.750	0.1083	0.1485	0.0219
	-0.583	-0.0455	0.2317	0.0296		-0.583	0.2578	0.1276	0.0359
	-0.417	-0.0060	0.2581	0.0330		-0.417	0.2663	0.1406	0.0384
	-0.250	0.3415	0.1890	0.0544		-0.250	0.0768	0.1060	0.0185
	-0.083	0.0713	0.1841	0.0279		-0.083	-0.0239	0.0990	0.0156
	0.083	-0.3673	0.1922	0.0580		0.083	-0.1311	0.1085	0.0239
	0.250	-0.2729	0.2140	0.0471		0.250	-0.1292	0.1155	0.0244
	0.417	-0.4816	0.2529	0.1216		0.417	-0.3572	0.1323	0.0728
	0.583	1.1471	0.9064	0.5460		0.583	-0.0831	0.2374	0.0866

D.6. Data tables (Oct2018 data)

E_γ [MeV]	$\cos(\theta)$	H	ΔH^{stat}	ΔH^{syst}	E_γ [MeV]	$\cos(\theta)$	H	ΔH^{stat}	ΔH^{syst}
1565	-0.917	0.0223	0.1535	0.0185	1615	-0.917	0.2852	0.1170	0.0347
	-0.750	0.1466	0.1119	0.0226		-0.750	-0.0121	0.0823	0.0125
	-0.583	0.2062	0.0995	0.0291		-0.583	-0.0685	0.0851	0.0158
	-0.417	0.2227	0.1256	0.0326		-0.417	0.2590	0.0993	0.0388
	-0.250	0.0958	0.0914	0.0194		-0.250	0.0804	0.0868	0.0185
	-0.083	0.2189	0.0922	0.0362		-0.083	-0.0154	0.0949	0.0164
	0.083	-0.1413	0.0983	0.0271		0.083	0.0741	0.1029	0.0207
	0.250	-0.2310	0.1103	0.0397		0.250	-0.2322	0.1165	0.0408
	0.417	-0.2010	0.1281	0.0347		0.417	-0.1613	0.1287	0.0309
	0.583	-0.5018	0.1897	0.0838		0.583	-0.1621	0.1721	0.0436
0.750	-0.5990	0.9006	0.2066	0.750	0.0246	0.3820	0.0481		
1665	-0.917	-0.0248	0.1001	0.0123	1715	-0.917	-0.4870	0.1293	0.0560
	-0.750	-0.2272	0.0665	0.0288		-0.750	-0.3254	0.0868	0.0432
	-0.583	-0.3181	0.0738	0.0437		-0.583	-0.2680	0.0976	0.0415
	-0.417	0.1194	0.0957	0.0228		-0.417	-0.1572	0.1454	0.0333
	-0.250	0.0830	0.0783	0.0192		-0.250	0.0637	0.1055	0.0232
	-0.083	0.1787	0.0921	0.0334		-0.083	0.2078	0.1322	0.0487
	0.083	-0.1535	0.0931	0.0299		0.083	0.1113	0.1288	0.0344
	0.250	-0.0837	0.0953	0.0208		0.250	-0.3874	0.1190	0.0831
	0.417	-0.2184	0.0949	0.0356		0.417	-0.0756	0.1022	0.0240
	0.583	0.0575	0.0992	0.0170		0.583	0.1038	0.1202	0.0287
0.750	0.0744	0.1694	0.0227	0.750	0.2696	0.1893	0.0557		
1765	-0.917	-0.6086	0.2211	0.0789	1840	-0.917	-0.2655	0.3071	0.0405
	-0.750	-0.6372	0.1641	0.0851		-0.750	-0.3988	0.3033	0.0512
	-0.583	-0.4841	0.1847	0.0707		-0.583	-0.6383	0.3688	0.0799
	-0.417	-0.2064	0.2855	0.0484		-0.417	-0.8175	0.4356	0.1044
	-0.250	0.3229	0.1853	0.0625		-0.250	0.1172	0.3413	0.0415
	-0.083	0.2974	0.2324	0.0665		-0.083	-0.0552	0.3624	0.0453
	0.083	0.0502	0.2142	0.0398		0.083	0.3025	0.3301	0.0595
	0.250	-0.0561	0.1860	0.0355		0.250	-0.2064	0.4209	0.0625
	0.417	0.1995	0.1976	0.0504		0.417	-0.3083	0.3004	0.0566
	0.583	0.0816	0.2397	0.0457		0.583	0.3209	0.4440	0.0641
0.750	0.7660	0.3808	0.1765	0.750	0.3287	0.5397	0.1170		
					0.917	0.3038	3.8717	0.0050	

D.6.2 $\gamma n \rightarrow \pi^0 n$

E_γ [MeV]	$\cos(\theta)$	Σ_{but}	$\Delta\Sigma_{but}^{stat}$	$\Delta\Sigma_{but}^{syst}$	E_γ [MeV]	$\cos(\theta)$	Σ_{but}	$\Delta\Sigma_{but}^{stat}$	$\Delta\Sigma_{but}^{syst}$
1470	-0.917	0.1104	0.1796	0.0208	1515	-0.917	0.0779	0.0953	0.0130
	-0.750	0.2814	0.1261	0.0313		-0.750	0.4586	0.0787	0.0417
	-0.583	0.6789	0.1095	0.0682		-0.583	0.8076	0.0694	0.0696
	-0.417	0.8003	0.1078	0.0795		-0.417	0.9039	0.0710	0.0773
	-0.250	0.7811	0.0954	0.0778		-0.250	0.8301	0.0608	0.0714
	-0.083	0.8213	0.0888	0.0815		-0.083	0.7944	0.0558	0.0685
	0.083	0.8338	0.0926	0.0827		0.083	0.7415	0.0565	0.0643
	0.250	0.9199	0.1064	0.0907		0.250	0.9012	0.0619	0.0771
	0.417	0.7624	0.1305	0.0760		0.417	0.6759	0.0718	0.0591
	0.583	0.7637	0.2062	0.0931		0.583	0.8254	0.1009	0.0710
0.750	0.7203	0.4175	0.0734	0.750	0.4718	0.1962	0.0428		
1565	-0.917	0.1351	0.0847	0.0161	1615	-0.917	0.1706	0.0772	0.0186
	-0.750	0.4318	0.0703	0.0395		-0.750	0.3373	0.0701	0.0318
	-0.583	0.5093	0.0634	0.0457		-0.583	0.5242	0.0591	0.0467
	-0.417	0.6926	0.0631	0.0604		-0.417	0.6485	0.0560	0.0570
	-0.250	0.7756	0.0538	0.0670		-0.250	0.6839	0.0479	0.0594
	-0.083	0.7665	0.0486	0.0663		-0.083	0.7795	0.0435	0.0670
	0.083	0.7560	0.0489	0.0655		0.083	0.6985	0.0462	0.0605
	0.250	0.6900	0.0539	0.0602		0.250	0.5987	0.0534	0.0526
	0.417	0.6000	0.0611	0.0539		0.417	0.5834	0.0605	0.0514
	0.583	0.5396	0.0824	0.0482		0.583	0.5748	0.0717	0.0507
0.750	0.2571	0.1370	0.0258	0.750	0.6195	0.1003	0.0542		
0.917	0.1498	0.4283	0.0340	0.917	0.5159	0.2492	0.0463		

D.6. Data tables (Oct2018 data)

E_γ [MeV]	$\cos(\theta)$	Σ_{but}	$\Delta\Sigma_{but}^{stat}$	$\Delta\Sigma_{but}^{syst}$	E_γ [MeV]	$\cos(\theta)$	Σ_{but}	$\Delta\Sigma_{but}^{stat}$	$\Delta\Sigma_{but}^{syst}$
1665	-0.917	0.0065	0.0639	0.0076	1715	-0.917	-0.0362	0.0610	0.0079
	-0.750	0.2705	0.0568	0.0185		-0.750	0.1250	0.0606	0.0113
	-0.583	0.4948	0.0515	0.0297		-0.583	0.4049	0.0575	0.0252
	-0.417	0.5238	0.0517	0.0312		-0.417	0.4210	0.0600	0.0260
	-0.250	0.5413	0.0443	0.0321		-0.250	0.3776	0.0537	0.0239
	-0.083	0.5996	0.0442	0.0350		-0.083	0.2056	0.0593	0.0153
	0.083	0.4986	0.0500	0.0299		0.083	0.2098	0.0643	0.0189
	0.250	0.4846	0.0539	0.0328		0.250	0.4001	0.0583	0.0254
	0.417	0.7648	0.0488	0.0432		0.417	0.6780	0.0490	0.0389
	0.583	0.9302	0.0471	0.0515		0.583	0.8809	0.0469	0.0490
	0.750	0.7433	0.0606	0.0422		0.750	0.8453	0.0588	0.0561
	0.917	0.7071	0.1677	0.0404		0.917	0.8857	0.1567	0.0493
1765	-0.917	0.0334	0.0796	0.0085	1840	-0.917	0.4190	0.1323	0.0336
	-0.750	0.3525	0.0794	0.0226		-0.750	0.5524	0.1384	0.0428
	-0.583	0.5037	0.0805	0.0311		-0.583	0.5392	0.1570	0.0419
	-0.417	0.4034	0.1007	0.0252		-0.417	0.6290	0.2152	0.0480
	-0.250	0.4080	0.0872	0.0254		-0.250	0.3287	0.1726	0.0277
	-0.083	0.0256	0.0956	0.0097		-0.083	0.3996	0.1779	0.0324
	0.083	-0.0547	0.0936	0.0094		0.083	0.0790	0.1995	0.0185
	0.250	0.1761	0.0849	0.0139		0.250	0.3798	0.1965	0.0353
	0.417	0.5922	0.0743	0.0346		0.417	0.7283	0.1724	0.0548
	0.583	0.8093	0.0781	0.0455		0.583	0.6247	0.1969	0.0618
	0.750	0.9594	0.0888	0.0651		0.750	1.2499	0.1868	0.0905
	0.917	0.9655	0.2338	0.0533					
E_γ [MeV]	$\cos(\theta)$	T	ΔT^{stat}	ΔT^{syst}	E_γ [MeV]	$\cos(\theta)$	T	ΔT^{stat}	ΔT^{syst}
1470	-0.917	-0.4067	0.0935	0.0336	1515	-0.917	0.0081	0.0592	0.0077
	-0.750	-0.6214	0.0783	0.0606		-0.750	-0.1796	0.0589	0.0205
	-0.583	-0.5718	0.0674	0.0575		-0.583	-0.3763	0.0554	0.0400
	-0.417	-0.6861	0.0807	0.0869		-0.417	-0.5667	0.0664	0.0712
	-0.250	-0.6349	0.0663	0.0794		-0.250	-0.4112	0.0517	0.0484
	-0.083	-0.6149	0.0608	0.0721		-0.083	-0.4853	0.0491	0.0586
	0.083	-0.6816	0.0743	0.0986		0.083	-0.4339	0.0484	0.0512
	0.250	-0.5798	0.0797	0.0809		0.250	-0.4132	0.0540	0.0511
	0.417	-0.5233	0.1023	0.0797		0.417	-0.1518	0.0635	0.0231
	0.583	-0.1964	0.1228	0.0417		0.583	-0.2010	0.0839	0.0257
	0.750	0.5014	0.2689	0.0549		0.750	0.0186	0.1810	0.0249

Appendix D. Results

E_γ [MeV]	$\cos(\theta)$	T	ΔT^{stat}	ΔT^{syst}	E_γ [MeV]	$\cos(\theta)$	T	ΔT^{stat}	ΔT^{syst}
1565	-0.917	0.1477	0.0715	0.0148	1615	-0.917	0.2637	0.0852	0.0231
	-0.750	0.0055	0.0722	0.0105		-0.750	-0.0616	0.0962	0.0144
	-0.583	-0.1157	0.0621	0.0150		-0.583	0.0342	0.0812	0.0122
	-0.417	-0.0572	0.0764	0.0146		-0.417	0.1263	0.0864	0.0216
	-0.250	-0.1128	0.0535	0.0153		-0.250	0.1535	0.0698	0.0226
	-0.083	-0.2356	0.0573	0.0329		-0.083	0.1540	0.0668	0.0234
	0.083	-0.0762	0.0586	0.0152		0.083	0.2204	0.0769	0.0359
	0.250	-0.0221	0.0578	0.0103		0.250	0.2217	0.0769	0.0303
	0.417	0.1905	0.0678	0.0259		0.417	0.3380	0.1049	0.0562
	0.583	0.2418	0.1010	0.0340		0.583	0.2623	0.0888	0.0261
	0.750	0.4109	0.1954	0.0744		0.750	0.3093	0.1416	0.0343
0.917	-0.2624	0.4561	0.0518	0.917	0.3665	0.2589	0.0244		
1665	-0.917	0.1712	0.0857	0.0177	1715	-0.917	0.2116	0.0968	0.0254
	-0.750	-0.1710	0.1197	0.0364		-0.750	-0.2055	0.1223	0.0385
	-0.583	-0.1403	0.0921	0.0228		-0.583	-0.2405	0.1252	0.0464
	-0.417	0.1230	0.0954	0.0221		-0.417	0.1330	0.1426	0.0364
	-0.250	0.3272	0.0786	0.0441		-0.250	0.5919	0.1565	0.1351
	-0.083	0.3516	0.0919	0.0605		-0.083	0.5085	0.1712	0.1275
	0.083	0.3089	0.1022	0.0543		0.083	0.0229	0.1965	0.0545
	0.250	0.3792	0.1152	0.0716		0.250	0.3118	0.1232	0.0544
	0.417	0.3695	0.0914	0.0513		0.417	0.5919	0.1240	0.1080
	0.583	0.3943	0.0874	0.0478		0.583	0.5821	0.1282	0.1100
	0.750	0.5227	0.1087	0.0595		0.750	0.4019	0.1570	0.0929
0.917	-0.1396	0.3046	0.0410	0.917	1.1146	0.4938	0.1859		
1765	-0.917	0.3354	0.1018	0.0302	1840	-0.917	0.0663	0.0760	0.0104
	-0.750	-0.1919	0.1006	0.0232		-0.750	0.0160	0.0814	0.0113
	-0.583	0.2771	0.1369	0.0452		-0.583	0.0579	0.1016	0.0140
	-0.417	0.1626	0.1638	0.0341		-0.417	0.5945	0.1555	0.0814
	-0.250	0.4651	0.2350	0.1260		-0.250	0.6741	0.1924	0.1221
	-0.083	0.3071	0.1917	0.0649		-0.083	0.1051	0.1348	0.0227
	0.083	0.3670	0.2258	0.0935		0.083	0.0657	0.1471	0.0231
	0.250	0.3047	0.1421	0.0460		0.250	-0.1053	0.1841	0.0376
	0.417	0.6022	0.1522	0.0970		0.417	0.8275	0.1742	0.1221
	0.583	0.7418	0.2033	0.1504		0.583	0.9497	0.2463	0.2061
	0.750	0.7918	0.2580	0.1957		0.750	0.4342	0.1378	0.0596
0.917	1.8963	2.1755	0.0050						

D.6. Data tables (Oct2018 data)

E_γ [MeV]	$\cos(\theta)$	T	ΔT^{stat}	ΔT^{syst}	E_γ [MeV]	$\cos(\theta)$	T	ΔT^{stat}	ΔT^{syst}
1950	-0.917	0.1800	0.0945	0.0191	2145	-0.917	-0.0045	0.1785	0.0173
	-0.750	-0.0881	0.0888	0.0169		-0.750	-0.2422	0.1632	0.0579
	-0.583	-0.0579	0.1433	0.0232		-0.583	0.0613	0.2435	0.0343
	-0.417	0.5613	0.1552	0.0828		-0.417	0.7377	0.2140	0.0798
	-0.250	0.5611	0.1809	0.0873		-0.250	0.2635	0.1654	0.0275
	-0.083	0.3896	0.1243	0.0456		-0.083	0.1878	0.0207	0.0280
	0.083	-0.2652	0.2116	0.0673		0.083	0.0287	0.1840	0.0259
	0.250	-0.2248	0.2452	0.0508		0.250	-0.1318	0.2245	0.0309
	0.417	0.3206	0.3121	0.0838		0.417	0.0332	0.2823	0.0308
	0.583	1.0334	0.3795	0.2738		0.583	-0.0773	0.3454	0.0785
0.750	0.1010	0.1407	0.0341	0.750	-0.0920	0.1384	0.0317		
0.917	0.5753	0.4395	0.1766	0.917	0.3780	0.3584	0.1234		
2435	-0.917	-0.0535	0.2785	0.0305					
	-0.750	-0.1837	0.9045	0.1896					
	-0.083	0.1411	0.3747	0.0251					
	0.250	0.8182	0.5073	0.0941					
	0.750	0.5789	0.1853	0.1173					
0.917	0.2235	0.1516	0.0302						

E_γ [MeV]	$\cos(\theta)$	P	ΔP^{stat}	ΔP^{syst}	E_γ [MeV]	$\cos(\theta)$	P	ΔP^{stat}	ΔP^{syst}
1470	-0.917	0.1516	0.6029	0.0627	1515	-0.917	0.2414	0.2943	0.0365
	-0.750	-1.0734	0.4651	0.1390		-0.750	-0.3469	0.2899	0.0481
	-0.583	-0.9175	0.4117	0.1285		-0.583	-0.2260	0.2662	0.0400
	-0.417	-1.5853	0.4718	0.2323		-0.417	-1.1787	0.3091	0.1575
	-0.250	-0.6866	0.4039	0.1100		-0.250	-0.7269	0.2508	0.1022
	-0.083	-0.9764	0.3691	0.1576		-0.083	-0.5331	0.2324	0.0777
	0.083	-0.5889	0.4318	0.1070		0.083	-0.3967	0.2315	0.0604
	0.250	-1.4794	0.4888	0.2495		0.250	-0.4679	0.2609	0.0702
	0.417	0.0731	0.6218	0.0832		0.417	0.6127	0.3127	0.0902
	0.583	-1.4353	0.7985	0.2309		0.583	-0.1847	0.4058	0.0561
0.750	0.3706	1.5572	0.1779	0.750	0.8783	0.9021	0.1696		

Appendix D. Results

E_γ [MeV]	$\cos(\theta)$	P	ΔP^{stat}	ΔP^{syst}	E_γ [MeV]	$\cos(\theta)$	P	ΔP^{stat}	ΔP^{syst}
1565	-0.917	-0.3940	0.2795	0.0479	1615	-0.917	0.0077	0.2547	0.0299
	-0.750	-0.3392	0.2692	0.0464		-0.750	0.2819	0.2801	0.0464
	-0.583	-0.4878	0.2324	0.0643		-0.583	0.0995	0.2399	0.0322
	-0.417	0.0110	0.2808	0.0338		-0.417	0.3849	0.2520	0.0599
	-0.250	-0.1538	0.2065	0.0335		-0.250	0.5585	0.2090	0.0842
	-0.083	-0.0507	0.2118	0.0297		-0.083	0.1764	0.1940	0.0360
	0.083	-0.0347	0.2218	0.0306		0.083	0.1474	0.2239	0.0363
	0.250	-0.4215	0.2227	0.0660		0.250	0.7637	0.2304	0.1136
	0.417	-0.1347	0.2519	0.0387		0.417	0.7249	0.3094	0.1036
	0.583	0.7278	0.3663	0.1106		0.583	0.6194	0.2625	0.0826
	0.750	1.1496	0.7150	0.1753		0.750	0.3594	0.3877	0.0530
0.917	2.8427	5.3437	0.0050	0.917	-0.7758	0.7316	0.0885		
1665	-0.917	-0.3855	0.2209	0.0487	1715	-0.917	0.0168	0.2356	0.0310
	-0.750	-0.5547	0.3081	0.0749		-0.750	-0.8617	0.3129	0.1425
	-0.583	0.0649	0.2282	0.0300		-0.583	0.0714	0.3006	0.0496
	-0.417	-0.0893	0.2388	0.0331		-0.417	0.8640	0.3642	0.1810
	-0.250	0.1289	0.1955	0.0329		-0.250	0.8649	0.3516	0.1972
	-0.083	0.5433	0.2303	0.0927		-0.083	0.5609	0.3959	0.1393
	0.083	0.1781	0.2563	0.0467		0.083	0.4237	0.4916	0.1240
	0.250	0.5775	0.2862	0.0989		0.250	-0.0544	0.2913	0.0528
	0.417	0.0776	0.2242	0.0308		0.417	0.1828	0.2709	0.0550
	0.583	0.4023	0.2102	0.0540		0.583	0.4897	0.2775	0.0983
	0.750	0.3798	0.2562	0.0505		0.750	0.0375	0.3578	0.0676
0.917	0.8141	0.9134	0.1207	0.917	1.1889	0.9122	0.2431		
1765	-0.917	-0.5773	0.2813	0.0575	1840	-0.917	0.2544	0.4278	0.0432
	-0.750	-0.2797	0.3020	0.0437		-0.750	0.3542	0.5273	0.0608
	-0.583	-0.2731	0.3844	0.0598		-0.583	0.0298	0.6007	0.0644
	-0.417	-0.1374	0.4980	0.0739		-0.417	1.6362	0.9948	0.2353
	-0.250	0.9641	0.6180	0.1901		-0.250	-0.2791	0.9091	0.1145
	-0.083	1.4825	0.5745	0.2914		-0.083	-0.4787	0.7846	0.1129
	0.083	-0.3950	0.5992	0.1155		0.083	0.9666	0.8798	0.1674
	0.250	0.6285	0.3935	0.1270		0.250	1.5192	1.0187	0.2517
	0.417	-0.0468	0.3787	0.0623		0.417	1.2431	0.8194	0.2224
	0.583	1.1923	0.4981	0.2434		0.583	0.4931	1.1108	0.2163
	0.750	0.8641	0.6081	0.2289		0.750	0.7886	0.8570	0.2695
0.917	4.6746	5.4572	0.0050						

D.6. Data tables (Oct2018 data)

E_γ [MeV]	$\cos(\theta)$	H	ΔH^{stat}	ΔH^{syst}	E_γ [MeV]	$\cos(\theta)$	H	ΔH^{stat}	ΔH^{syst}
1470	-0.917	0.4914	0.5927	0.0779	1515	-0.917	-0.1138	0.3041	0.0314
	-0.750	0.6733	0.4789	0.0931		-0.750	0.1342	0.2710	0.0325
	-0.583	0.1650	0.4089	0.0523		-0.583	0.1850	0.2644	0.0370
	-0.417	0.2704	0.4589	0.0664		-0.417	-0.4825	0.3045	0.0693
	-0.250	0.4641	0.4108	0.0824		-0.250	0.0599	0.2431	0.0317
	-0.083	-0.0511	0.3525	0.0494		-0.083	0.0523	0.2298	0.0306
	0.083	0.6780	0.4301	0.1194		0.083	0.1720	0.2263	0.0365
	0.250	-0.4702	0.4714	0.0957		0.250	0.0221	0.2548	0.0330
	0.417	-0.6463	0.6022	0.1198		0.417	-0.7620	0.3072	0.1102
	0.583	0.6880	0.7937	0.1448		0.583	0.0814	0.3991	0.0516
0.750	-1.0763	1.4658	0.2041	0.750	-1.5743	0.8807	0.2591		
1565	-0.917	0.2691	0.2589	0.0370	1615	-0.917	0.2327	0.2433	0.0389
	-0.750	0.6247	0.2797	0.0760		-0.750	0.3025	0.2718	0.0477
	-0.583	0.4581	0.2348	0.0609		-0.583	-0.0138	0.2344	0.0295
	-0.417	0.3231	0.2787	0.0509		-0.417	0.8489	0.2646	0.1215
	-0.250	0.0579	0.1972	0.0274		-0.250	0.6586	0.2038	0.0984
	-0.083	0.3502	0.2070	0.0558		-0.083	0.1417	0.1909	0.0328
	0.083	0.1597	0.2149	0.0360		0.083	0.0928	0.2220	0.0329
	0.250	0.1820	0.2140	0.0378		0.250	0.1854	0.2194	0.0383
	0.417	-0.1047	0.2409	0.0360		0.417	-0.5844	0.3005	0.0851
	0.583	-0.2723	0.3699	0.0584		0.583	0.1096	0.2515	0.0324
0.750	-0.2837	0.7468	0.0970	0.750	-0.2087	0.4009	0.0451		
0.917	0.0435	1.4545	0.1723	0.917	-0.9477	0.7318	0.1008		
1665	-0.917	-0.0656	0.2074	0.0243	1715	-0.917	-0.3140	0.2316	0.0509
	-0.750	-0.0566	0.2937	0.0346		-0.750	-0.2055	0.3063	0.0524
	-0.583	0.0324	0.2259	0.0290		-0.583	0.3901	0.3186	0.0817
	-0.417	0.1316	0.2237	0.0338		-0.417	-0.0592	0.3585	0.0639
	-0.250	0.6084	0.1933	0.0951		-0.250	0.5548	0.3354	0.1311
	-0.083	0.2690	0.2238	0.0523		-0.083	-0.0316	0.3898	0.0761
	0.083	0.0797	0.2547	0.0402		0.083	0.5811	0.4749	0.1463
	0.250	-0.1519	0.2781	0.0480		0.250	0.6577	0.3045	0.1380
	0.417	0.5572	0.2239	0.0809		0.417	0.2169	0.2606	0.0573
	0.583	0.1784	0.2070	0.0319		0.583	-0.0801	0.2713	0.0473
0.750	-0.6346	0.2675	0.0782	0.750	0.0024	0.3446	0.0653		
0.917	0.2324	0.7986	0.0818	0.917	0.1097	0.8749	0.1367		

Appendix D. Results

E_γ [MeV]	$\cos(\theta)$	H	ΔH^{stat}	ΔH^{syst}	E_γ [MeV]	$\cos(\theta)$	H	ΔH^{stat}	ΔH^{syst}
1765	-0.917	-0.0583	0.2659	0.0246	1840	-0.917	0.2361	0.4500	0.0439
	-0.750	-0.0638	0.3145	0.0344		-0.750	-0.1998	0.5127	0.0529
	-0.583	-0.3028	0.3920	0.0627		-0.583	0.1025	0.6277	0.0678
	-0.417	0.5609	0.4929	0.1092		-0.417	0.1459	0.9866	0.1142
	-0.250	-0.2880	0.6097	0.1054		-0.250	-1.4659	0.9590	0.2240
	-0.083	0.6716	0.5298	0.1449		-0.083	0.3807	0.7621	0.1047
	0.083	0.3880	0.6076	0.1159		0.083	-0.2604	0.8835	0.1154
	0.250	0.3422	0.4066	0.0866		0.250	-0.4951	0.9994	0.1462
	0.417	-0.3733	0.3582	0.0856		0.417	-0.4553	0.7462	0.1235
	0.583	-0.1876	0.4654	0.0850		0.583	0.0867	1.0654	0.1921
	0.750	0.9138	0.6396	0.2408		0.750	0.6751	0.9092	0.2591
	0.917	7.6286	16.0313	0.0050					

D.6.3 $\gamma p \rightarrow \eta p$

E_γ [MeV]	$\cos(\theta)$	Σ_{but}	$\Delta \Sigma_{but}^{stat}$	$\Delta \Sigma_{but}^{syst}$	E_γ [MeV]	$\cos(\theta)$	Σ_{but}	$\Delta \Sigma_{but}^{stat}$	$\Delta \Sigma_{but}^{syst}$
1515	-0.917	0.0338	0.0911	0.0134	1565	-0.917	0.0392	0.0634	0.0146
	-0.750	-0.1185	0.1040	0.0155		-0.750	0.1180	0.0740	0.0147
	-0.583	-0.1940	0.1120	0.0208		-0.583	0.2938	0.0656	0.0304
	-0.417	0.2056	0.1100	0.0247		-0.417	0.2188	0.0599	0.0225
	-0.250	0.2779	0.1120	0.0281		-0.250	0.1635	0.0595	0.0181
	-0.083	0.1165	0.1249	0.0162		-0.083	0.2522	0.0610	0.0252
	0.083	0.0672	0.1465	0.0362		0.083	0.3031	0.0683	0.0292
	0.250	0.4121	0.2048	0.0686		0.250	0.0522	0.0881	0.0259
	0.417	-0.0967	0.3030	0.0528		0.417	0.2410	0.1386	0.0610
	0.583	0.3002	0.4504	0.0411		0.583	0.2307	0.2665	0.0280
	0.750	0.0143	0.3656	0.0520		0.917	0.1738	0.3592	0.0306
	0.917	0.0283	0.2262	0.0196					

D.6. Data tables (Oct2018 data)

E_γ [MeV]	$\cos(\theta)$	Σ_{but}	$\Delta\Sigma_{but}^{stat}$	$\Delta\Sigma_{but}^{syst}$	E_γ [MeV]	$\cos(\theta)$	Σ_{but}	$\Delta\Sigma_{but}^{stat}$	$\Delta\Sigma_{but}^{syst}$
1615	-0.917	0.0607	0.0636	0.0186	1665	-0.917	0.1100	0.0702	0.0107
	-0.750	0.1401	0.0661	0.0212		-0.750	0.2187	0.0737	0.0165
	-0.583	0.1590	0.0555	0.0175		-0.583	0.2749	0.0608	0.0194
	-0.417	0.2675	0.0535	0.0260		-0.417	0.3879	0.0600	0.0244
	-0.250	0.3153	0.0509	0.0301		-0.250	0.2953	0.0570	0.0198
	-0.083	0.2048	0.0558	0.0238		-0.083	0.3264	0.0689	0.0234
	0.083	0.3060	0.0612	0.0290		0.083	0.3671	0.0642	0.0321
	0.250	0.2569	0.0640	0.0252		0.250	0.5453	0.0638	0.0433
	0.417	0.2825	0.0782	0.0457		0.417	0.3751	0.0702	0.0238
	0.583	0.1777	0.1331	0.0198		0.583	0.4303	0.0988	0.0632
0.917	-0.1219	0.4872	0.0365	0.750	-0.1950	0.2686	0.0184		
				0.917	-0.1371	0.3384	0.0196		
1715	-0.917	-0.0840	0.1150	0.0507	1765	-0.917	0.3433	0.1961	0.0233
	-0.750	-0.0625	0.0949	0.0149		-0.750	-0.3350	0.1842	0.0426
	-0.583	0.0716	0.0744	0.0174		-0.583	0.0293	0.1207	0.0100
	-0.417	0.0802	0.0684	0.0215		-0.417	0.2625	0.0986	0.0215
	-0.250	0.2340	0.0722	0.0258		-0.250	0.4043	0.1301	0.0313
	-0.083	0.4548	0.0702	0.0376		-0.083	0.5168	0.0802	0.0353
	0.083	0.4652	0.0570	0.0283		0.083	0.5313	0.0817	0.0316
	0.250	0.5281	0.0562	0.0342		0.250	0.6237	0.0739	0.0413
	0.417	0.6230	0.0557	0.0362		0.417	0.7192	0.0776	0.0410
	0.583	0.7450	0.0699	0.0698		0.583	0.7669	0.0899	0.0433
0.750	0.8604	0.1686	0.0480	0.750	0.3765	0.1889	0.0240		
1840	-0.917	0.1734	0.4721	0.0355					
	-0.750	0.0754	0.3791	0.0292					
	-0.583	-0.0068	0.3044	0.0224					
	-0.417	0.1836	0.2328	0.0216					
	-0.250	0.1765	0.2795	0.0233					
	-0.083	0.6432	0.1796	0.0497					
	0.083	0.9039	0.1728	0.0695					
	0.250	0.8495	0.1703	0.0635					
	0.417	0.6844	0.1914	0.0521					
	0.583	0.4189	0.2049	0.0392					
0.750	0.8549	0.2926	0.0639						

Appendix D. Results

E_γ [MeV]	$\cos(\theta)$	T	ΔT^{stat}	ΔT^{syst}	E_γ [MeV]	$\cos(\theta)$	T	ΔT^{stat}	ΔT^{syst}
1515	-0.917	-0.0166	0.0608	0.0111	1565	-0.917	0.1105	0.0591	0.0200
	-0.750	0.1246	0.0827	0.0200		-0.750	0.1821	0.0775	0.0261
	-0.583	0.0651	0.0697	0.0105		-0.583	0.2069	0.0618	0.0259
	-0.417	0.1967	0.0727	0.0242		-0.417	0.1437	0.0579	0.0192
	-0.250	0.0085	0.0698	0.0095		-0.250	0.1430	0.0598	0.0198
	-0.083	0.0755	0.0736	0.0103		-0.083	0.1877	0.0602	0.0227
	0.083	0.1894	0.0846	0.0363		0.083	0.0592	0.0660	0.0113
	0.250	0.1522	0.1164	0.0440		0.250	-0.0005	0.0809	0.0245
	0.417	-0.0280	0.1684	0.0398		0.417	0.0224	0.1177	0.0471
	0.583	0.0942	0.3002	0.0295		0.583	0.0189	0.2199	0.0150
	0.750	0.2573	0.2884	0.0665		0.917	-0.5534	0.7071	0.1862
0.917	-0.2865	0.1893	0.0383						
1615	-0.917	0.2149	0.0762	0.0321	1665	-0.917	0.2503	0.1271	0.0382
	-0.750	0.2754	0.0913	0.0422		-0.750	0.5492	0.1430	0.0816
	-0.583	0.2028	0.0775	0.0302		-0.583	0.3816	0.1078	0.0547
	-0.417	0.2959	0.0799	0.0452		-0.417	0.5373	0.1308	0.0943
	-0.250	0.3174	0.0711	0.0407		-0.250	0.3158	0.1062	0.0461
	-0.083	0.1445	0.0825	0.0266		-0.083	0.7119	0.2618	0.2434
	0.083	0.1888	0.0857	0.0268		0.083	0.2721	0.1141	0.0487
	0.250	0.2859	0.0911	0.0388		0.250	0.4264	0.1222	0.0748
	0.417	0.2345	0.1055	0.0468		0.417	0.2070	0.1502	0.0419
	0.583	0.1426	0.2173	0.0325		0.583	0.2557	0.1700	0.0717
	0.917	1.4861	1.5238	0.3382		0.750	-0.3250	1.3612	0.6516
				0.917	-0.1814	1.0612	0.3534		
1715	-0.917	0.3123	0.3663	0.1707	1765	-0.917	0.1161	0.2353	0.0247
	-0.750	0.6093	0.1566	0.0630		-0.750	0.7844	0.3668	0.1561
	-0.583	0.2377	0.1560	0.0501		-0.583	0.7340	0.2624	0.1386
	-0.417	0.6056	0.1531	0.1140		-0.417	0.5138	0.1716	0.0767
	-0.250	0.5943	0.1446	0.0921		-0.250	0.6555	0.1746	0.0805
	-0.083	0.6225	0.1651	0.1155		-0.083	0.7542	0.1593	0.1071
	0.083	0.3897	0.1076	0.0524		0.083	0.4727	0.1499	0.0720
	0.250	0.5872	0.1267	0.0933		0.250	0.6237	0.1336	0.0861
	0.417	0.5293	0.1234	0.0804		0.417	0.3018	0.1451	0.0502
	0.583	0.3557	0.1444	0.0824		0.583	0.4405	0.1665	0.0726
	0.750	0.4129	0.4907	0.1280		0.750	0.8336	0.3327	0.1142

D.6. Data tables (Oct2018 data)

E_γ [MeV]	$\cos(\theta)$	T	ΔT^{stat}	ΔT^{syst}	E_γ [MeV]	$\cos(\theta)$	T	ΔT^{stat}	ΔT^{syst}
1840	-0.917	0.7011	0.3688	0.1027	1950	-0.917	-0.3769	0.6237	0.1166
	-0.750	0.3446	0.2391	0.0422		-0.750	-0.1953	0.3609	0.0330
	-0.583	0.8284	0.3063	0.1665		-0.583	0.1616	0.2464	0.0442
	-0.417	0.4992	0.1719	0.0657		-0.417	-0.0094	0.1994	0.0160
	-0.250	0.6757	0.2922	0.1293		-0.250	0.0977	0.3304	0.0404
	-0.083	0.1689	0.1328	0.0245		-0.083	0.1636	0.1640	0.0211
	0.083	0.2863	0.1584	0.0532		0.083	0.2356	0.1895	0.0324
	0.250	0.2428	0.1235	0.0376		0.250	-0.1299	0.2185	0.0374
	0.417	0.3905	0.1358	0.0534		0.417	0.1593	0.1977	0.0312
	0.583	0.1846	0.1321	0.0317		0.583	0.0826	0.0160	0.0129
0.750	0.2051	0.2170	0.0385	0.750	-0.0329	0.1955	0.0238		

E_γ [MeV]	$\cos(\theta)$	P	ΔP^{stat}	ΔP^{syst}	E_γ [MeV]	$\cos(\theta)$	P	ΔP^{stat}	ΔP^{syst}
1515	-0.917	0.2413	0.3217	0.0435	1565	-0.917	-0.0068	0.2386	0.0329
	-0.750	-0.2396	0.4371	0.0497		-0.750	0.0570	0.3106	0.0360
	-0.583	-0.1664	0.3766	0.0417		-0.583	-0.0505	0.2465	0.0322
	-0.417	0.2295	0.3890	0.0478		-0.417	0.0689	0.2343	0.0301
	-0.250	-0.3106	0.3628	0.0469		-0.250	-0.1805	0.2379	0.0363
	-0.083	0.3872	0.3871	0.0499		-0.083	0.1881	0.2320	0.0346
	0.083	-0.2741	0.4372	0.0651		0.083	0.6259	0.2528	0.0722
	0.250	-0.3482	0.5969	0.0877		0.250	-0.4936	0.3120	0.0723
	0.417	0.0181	0.8700	0.1045		0.417	0.6848	0.4311	0.1296
	0.583	1.3537	1.5627	0.2107		0.583	-0.5237	0.7879	0.1353
0.750	2.9706	1.4463	0.4332	0.917	-2.0792	2.6104	0.0050		
0.917	0.3082	0.9449	0.1173						
1615	-0.917	0.3651	0.2388	0.0615	1665	-0.917	0.1259	0.3185	0.0435
	-0.750	0.1039	0.2776	0.0432		-0.750	0.5910	0.3498	0.0905
	-0.583	0.2015	0.2412	0.0426		-0.583	-0.0406	0.2687	0.0363
	-0.417	-0.0020	0.2450	0.0343		-0.417	0.3214	0.3111	0.0577
	-0.250	0.6526	0.2130	0.1024		-0.250	0.0708	0.2585	0.0360
	-0.083	0.4950	0.2503	0.0793		-0.083	1.3873	0.6264	0.2109
	0.083	0.6689	0.2628	0.0966		0.083	0.1437	0.2878	0.0514
	0.250	0.4470	0.2767	0.0675		0.250	0.2955	0.3049	0.0673
	0.417	0.3117	0.3080	0.0759		0.417	0.7964	0.3834	0.1399
	0.583	0.2879	0.6029	0.0928		0.583	0.5993	0.4247	0.1916
0.917	-3.8491	5.7683	0.0050	0.750	8.5240	18.6010	0.0050		
				0.917	-3.6309	4.7261	0.0050		

Appendix D. Results

E_γ [MeV]	$\cos(\theta)$	P	ΔP^{stat}	ΔP^{syst}	E_γ [MeV]	$\cos(\theta)$	P	ΔP^{stat}	ΔP^{syst}
1715	-0.917	-0.7194	0.9276	0.1954	1765	-0.917	0.6654	0.7170	0.1461
	-0.750	0.3059	0.3449	0.0698		-0.750	-1.0154	0.9471	0.2249
	-0.583	-0.4644	0.3667	0.0922		-0.583	-0.4975	0.6863	0.1171
	-0.417	0.3752	0.3444	0.0840		-0.417	0.8365	0.4611	0.1345
	-0.250	0.2845	0.3300	0.0702		-0.250	-0.0599	0.5261	0.0694
	-0.083	0.0978	0.3603	0.0617		-0.083	0.2307	0.3640	0.0568
	0.083	0.4516	0.2530	0.0759		0.083	0.7311	0.4072	0.1102
	0.250	0.0352	0.2753	0.0410		0.250	0.0674	0.3337	0.0507
	0.417	0.3610	0.2737	0.0606		0.417	0.0244	0.3863	0.0531
	0.583	0.1149	0.3430	0.0791		0.583	0.0800	0.4525	0.0637
	0.750	0.7235	1.1721	0.2715		0.750	0.7048	0.8760	0.1568

E_γ [MeV]	$\cos(\theta)$	H	ΔH^{stat}	ΔH^{syst}	E_γ [MeV]	$\cos(\theta)$	H	ΔH^{stat}	ΔH^{syst}
1515	-0.917	-0.2562	0.3146	0.0440	1565	-0.917	-0.1176	0.2387	0.0357
	-0.750	0.0237	0.4476	0.0450		-0.750	-0.3355	0.3074	0.0516
	-0.583	0.7009	0.3617	0.0839		-0.583	0.2853	0.2453	0.0466
	-0.417	0.1626	0.3901	0.0451		-0.417	-0.0223	0.2273	0.0285
	-0.250	-0.3707	0.3695	0.0514		-0.250	0.0159	0.2353	0.0294
	-0.083	-0.4573	0.3866	0.0550		-0.083	0.1184	0.2356	0.0307
	0.083	0.3533	0.4484	0.0696		0.083	0.0911	0.2458	0.0275
	0.250	-0.7736	0.6331	0.1148		0.250	0.2226	0.3094	0.0514
	0.417	-0.9436	0.9602	0.1476		0.417	-1.0476	0.3975	0.1726
	0.583	-1.7617	1.5182	0.2421		0.583	0.2148	0.8252	0.1213
	0.750	-1.3199	1.5008	0.2494		0.917	0.4668	1.9515	0.4234
	0.917	1.7025	0.9137	0.2491					

1615	-0.917	-0.2161	0.2322	0.0463	1665	-0.917	-0.0659	0.3204	0.0417
	-0.750	0.2012	0.2723	0.0484		-0.750	-0.6635	0.3544	0.1001
	-0.583	-0.3540	0.2442	0.0594		-0.583	-0.2134	0.2660	0.0448
	-0.417	-0.3245	0.2416	0.0567		-0.417	-0.3673	0.3162	0.0628
	-0.250	-0.2704	0.2138	0.0487		-0.250	-0.4018	0.2624	0.0653
	-0.083	-0.1458	0.2520	0.0412		-0.083	0.0181	0.5662	0.0732
	0.083	-0.2148	0.2528	0.0420		0.083	-0.2507	0.2825	0.0588
	0.250	-0.3371	0.2691	0.0545		0.250	-0.1128	0.2905	0.0526
	0.417	-0.1106	0.2930	0.0598		0.417	-0.5418	0.3638	0.0998
	0.583	-1.1588	0.5956	0.1972		0.583	0.1029	0.4004	0.1203
	0.917	1.8292	2.8219	0.0050		0.750	1.2743	3.7051	0.0050
						0.917	6.0320	12.2189	0.0050

D.6. Data tables (Oct2018 data)

E_γ [MeV]	$\cos(\theta)$	H	ΔH^{stat}	ΔH^{syst}	E_γ [MeV]	$\cos(\theta)$	H	ΔH^{stat}	ΔH^{syst}
1715	-0.917	0.5499	0.8837	0.1772	1765	-0.917	-0.4743	0.7029	0.1254
	-0.750	0.7948	0.3541	0.1363		-0.750	0.1049	1.0184	0.1668
	-0.583	-0.9741	0.3811	0.1673		-0.583	-1.0006	0.6452	0.1742
	-0.417	-0.3230	0.3277	0.0770		-0.417	0.4533	0.4268	0.0851
	-0.250	-0.1308	0.3200	0.0577		-0.250	0.9021	0.5167	0.1379
	-0.083	0.3083	0.3619	0.0757		-0.083	-0.1781	0.3527	0.0526
	0.083	-0.1571	0.2504	0.0417		0.083	-0.0640	0.3608	0.0464
	0.250	0.1185	0.2689	0.0431		0.250	-0.1652	0.3311	0.0544
	0.417	0.2380	0.2674	0.0473		0.417	-0.4765	0.4085	0.0868
	0.583	0.1932	0.3312	0.0822		0.583	-1.0644	0.4618	0.1760
	0.750	-0.4461	1.0468	0.2239		0.750	1.2293	0.8886	0.2204

D.6.4 $\gamma n \rightarrow \eta n$

E_γ [MeV]	$\cos(\theta)$	Σ_{but}	$\Delta \Sigma_{but}^{stat}$	$\Delta \Sigma_{but}^{syst}$	E_γ [MeV]	$\cos(\theta)$	Σ_{but}	$\Delta \Sigma_{but}^{stat}$	$\Delta \Sigma_{but}^{syst}$
1515	-0.917	0.0992	0.2115	0.0200	1565	-0.917	-0.1302	0.1419	0.0176
	-0.750	0.3512	0.1976	0.0336		-0.750	0.2209	0.1061	0.0228
	-0.583	0.2814	0.1704	0.0281		-0.583	0.2019	0.1180	0.0215
	-0.417	-0.1009	0.1780	0.0181		-0.417	0.2053	0.1355	0.0220
	-0.250	0.2234	0.2022	0.0251		-0.250	0.2322	0.1435	0.0241
	-0.083	0.6657	0.2214	0.0583		-0.083	0.3193	0.1488	0.0307
	0.083	-0.1186	0.2483	0.0226		0.083	0.4383	0.1724	0.0401
	0.250	0.2025	0.2552	0.0262		0.250	-0.1747	0.1809	0.0216
	0.417	0.0552	0.2937	0.0241		0.417	0.3008	0.1953	0.0299
	0.583	0.1018	0.3630	0.0291		0.583	0.2213	0.2335	0.0261
	0.750	0.0173	0.3765	0.0291		0.750	-0.1555	0.3084	0.0271
	0.917	-0.1765	0.4381	0.0352					

Appendix D. Results

E_γ [MeV]	$\cos(\theta)$	Σ_{but}	$\Delta\Sigma_{but}^{stat}$	$\Delta\Sigma_{but}^{syst}$	E_γ [MeV]	$\cos(\theta)$	Σ_{but}	$\Delta\Sigma_{but}^{stat}$	$\Delta\Sigma_{but}^{syst}$
1615	-0.917	-0.2252	0.1323	0.0258	1665	-0.917	0.1177	0.1044	0.0116
	-0.750	0.2618	0.0925	0.0258		-0.750	-0.0623	0.0852	0.0093
	-0.583	0.2994	0.1162	0.0288		-0.583	0.2319	0.0887	0.0166
	-0.417	0.1554	0.1248	0.0184		-0.417	0.1400	0.0911	0.0122
	-0.250	0.2459	0.1219	0.0247		-0.250	0.2364	0.0930	0.0168
	-0.083	0.1546	0.1412	0.0188		-0.083	0.5175	0.0965	0.0309
	0.083	0.2488	0.1493	0.0252		0.083	0.2429	0.0956	0.0172
	0.250	0.2370	0.1431	0.0243		0.250	0.3865	0.0938	0.0243
	0.417	0.1072	0.1610	0.0174		0.417	0.5243	0.0964	0.0312
	0.583	0.1564	0.1909	0.0210		0.583	0.5845	0.1182	0.0342
	0.750	0.5910	0.2717	0.0522		0.750	0.6203	0.1704	0.0360
0.917	0.1737	0.3687	0.0309						
1715	-0.917	0.2309	0.1291	0.0167	1765	-0.917	-0.1747	0.2250	0.0166
	-0.750	0.0688	0.1065	0.0101		-0.750	0.3350	0.2077	0.0222
	-0.583	0.0532	0.1122	0.0106		-0.583	0.4120	0.1826	0.0257
	-0.417	0.3842	0.0990	0.0242		-0.417	0.1852	0.1674	0.0154
	-0.250	0.4385	0.1065	0.0269		-0.250	0.2140	0.1856	0.0168
	-0.083	0.7258	0.1053	0.0413		-0.083	0.7011	0.1353	0.0401
	0.083	0.5705	0.0900	0.0335		0.083	0.6970	0.1257	0.0399
	0.250	0.6345	0.0891	0.0367		0.250	0.6576	0.1161	0.0394
	0.417	0.6678	0.0922	0.0384		0.417	0.6901	0.1331	0.0399
	0.583	0.6018	0.1122	0.0351		0.583	0.7277	0.1472	0.0414
	0.750	0.6152	0.1851	0.0358					
1840	-0.917	-0.1664	0.4996	0.0338					
	-0.750	0.2457	0.4434	0.0328					
	-0.583	0.7475	0.3663	0.0567					
	-0.417	0.9120	0.3276	0.0675					
	-0.250	0.9972	0.3473	0.0732					
	-0.083	0.3121	0.3096	0.0298					
	0.083	0.6607	0.2696	0.0503					
	0.250	0.4333	0.2658	0.0354					
	0.417	0.7363	0.2653	0.0554					
	0.583	0.5679	0.3043	0.0443					
	0.750	0.3500	0.5682	0.0417					

D.6. Data tables (Oct2018 data)

E_γ [MeV]	$\cos(\theta)$	T	ΔT^{stat}	ΔT^{syst}	E_γ [MeV]	$\cos(\theta)$	T	ΔT^{stat}	ΔT^{syst}
1515	-0.917	0.1077	0.1238	0.0124	1565	-0.917	0.1331	0.1214	0.0161
	-0.750	0.2441	0.1430	0.0263		-0.750	0.1128	0.1031	0.0177
	-0.583	0.1467	0.1082	0.0155		-0.583	-0.0150	0.1134	0.0143
	-0.417	0.0202	0.1023	0.0094		-0.417	-0.1194	0.1343	0.0198
	-0.250	0.1357	0.1534	0.0218		-0.250	0.1246	0.1457	0.0225
	-0.083	0.1537	0.1680	0.0236		-0.083	-0.0609	0.1471	0.0163
	0.083	0.0540	0.1837	0.0207		0.083	0.1059	0.1429	0.0148
	0.250	-0.2622	0.1748	0.0268		0.250	-0.3948	0.1873	0.0452
	0.417	-0.2523	0.1756	0.0211		0.417	-0.1748	0.1720	0.0196
	0.583	0.1595	0.2860	0.0322		0.583	-0.2175	0.2009	0.0205
0.750	-0.4866	0.3121	0.0439	0.750	0.1234	0.3502	0.0419		
0.917	-0.3328	0.2714	0.0233						
1615	-0.917	0.4095	0.1428	0.0394	1665	-0.917	0.2942	0.1684	0.0371
	-0.750	0.5961	0.1499	0.0867		-0.750	0.1740	0.1676	0.0375
	-0.583	0.2432	0.1624	0.0345		-0.583	0.2968	0.1479	0.0393
	-0.417	-0.0618	0.1959	0.0305		-0.417	0.2999	0.1657	0.0481
	-0.250	0.0207	0.1620	0.0191		-0.250	-0.0536	0.1954	0.0317
	-0.083	0.5366	0.2878	0.1172		-0.083	-0.0077	0.2902	0.0735
	0.083	-0.4098	0.2772	0.0825		0.083	-0.3312	0.1534	0.0406
	0.250	-0.2852	0.1975	0.0414		0.250	-0.3408	0.1752	0.0508
	0.417	-0.2278	0.2392	0.0414		0.417	-0.5682	0.2485	0.1219
	0.583	-0.8506	0.3362	0.1200		0.583	-0.2069	0.1981	0.0315
0.750	-0.1390	0.5622	0.1211	0.750	-0.4904	0.2384	0.0415		
0.917	-0.4844	0.6558	0.1069						
1715	-0.917	0.4253	0.3031	0.0794	1765	-0.917	-0.1638	0.2325	0.0173
	-0.750	0.1795	0.2132	0.0394		-0.750	0.3850	0.3521	0.0777
	-0.583	0.0727	0.2307	0.0390		-0.583	-0.3458	0.2767	0.0513
	-0.417	-0.4269	0.1950	0.0607		-0.417	-0.0202	0.2872	0.0348
	-0.250	-0.0696	0.2335	0.0391		-0.250	-0.0761	0.2298	0.0191
	-0.083	-0.2600	0.2622	0.0619		-0.083	-0.4262	0.2829	0.0735
	0.083	-0.0049	0.2664	0.0605		0.083	0.1093	0.1423	0.0172
	0.250	-0.2457	0.3798	0.1557		0.250	-0.2135	0.2363	0.0522
	0.417	0.0216	0.2077	0.0332		0.417	0.0221	0.2034	0.0223
	0.583	-0.4606	0.2577	0.0776		0.583	-0.3811	0.3608	0.0933
0.750	-0.4073	0.3332	0.0519						

Appendix D. Results

E_γ [MeV]	$\cos(\theta)$	T	ΔT^{stat}	ΔT^{syst}	E_γ [MeV]	$\cos(\theta)$	T	ΔT^{stat}	ΔT^{syst}
1840	-0.917	0.0433	0.2720	0.0215	1950	-0.917	-0.2454	0.9647	0.2448
	-0.750	0.1686	0.3445	0.0491		-0.750	0.2430	0.2115	0.2743
	-0.583	-0.1680	0.2426	0.0230		-0.583	-1.0122	0.4933	0.0782
	-0.417	-0.7350	0.4894	0.1971		-0.417	0.3553	0.5777	0.0921
	-0.250	0.3403	0.2788	0.0467		-0.250	-0.5869	0.2863	0.0849
	-0.083	-0.4480	0.1920	0.0361		-0.083	-0.3857	0.1489	0.0784
	0.083	-0.0795	0.1824	0.0188		0.083	-0.3496	0.3491	0.0494
	0.250	0.0109	0.1439	0.0110		0.250	0.2349	0.2861	0.0353
	0.417	-0.5755	0.3334	0.1225		0.417	-0.1271	0.2116	0.0203
	0.583	0.5729	0.3549	0.1233		0.583	0.0939	0.5323	0.1718
	0.750	0.6323	0.4913	0.1314					

D.6. Data tables (Oct2018 data)

E_γ [MeV]	$\cos(\theta)$	P	ΔP^{stat}	ΔP^{syst}	E_γ [MeV]	$\cos(\theta)$	P	ΔP^{stat}	ΔP^{syst}
1515	-0.917	-0.5256	0.6277	0.0748	1565	-0.917	-0.6517	0.4843	0.0917
	-0.750	0.3547	0.7174	0.0721		-0.750	-0.3245	0.4176	0.0595
	-0.583	0.1304	0.5619	0.0538		-0.583	0.2124	0.4593	0.0568
	-0.417	-0.0150	0.5305	0.0527		-0.417	-0.3673	0.5261	0.0712
	-0.250	-1.4231	0.7939	0.1823		-0.250	0.0689	0.5875	0.0644
	-0.083	-0.1291	0.8432	0.0919		-0.083	0.1059	0.5623	0.0599
	0.083	0.8471	0.9612	0.1344		0.083	0.2998	0.5644	0.0603
	0.250	0.7218	0.8771	0.1115		0.250	1.0875	0.7171	0.1098
	0.417	-0.1620	0.9063	0.0862		0.417	-0.0912	0.6509	0.0519
	0.583	0.3222	1.3695	0.1288		0.583	0.3235	0.7523	0.0749
0.750	0.9400	1.3072	0.1495	0.750	0.7544	1.3136	0.1864		
0.917	-0.8715	1.2536	0.1422						
1615	-0.917	-0.1239	0.4525	0.0492	1665	-0.917	-0.1970	0.4264	0.0495
	-0.750	0.6538	0.4313	0.0948		-0.750	0.2470	0.4369	0.0577
	-0.583	0.2541	0.4877	0.0718		-0.583	-0.4789	0.3743	0.0783
	-0.417	0.6915	0.6284	0.1380		-0.417	-0.7190	0.4344	0.1149
	-0.250	-0.8342	0.5038	0.1649		-0.250	-0.9165	0.5059	0.1451
	-0.083	0.0163	0.8086	0.1290		-0.083	-1.3712	0.8225	0.2139
	0.083	-0.2915	0.8021	0.1302		0.083	-0.5330	0.3852	0.0869
	0.250	-1.1893	0.6291	0.2068		0.250	-0.7040	0.4348	0.1076
	0.417	0.9686	0.7424	0.1678		0.417	-0.3672	0.5815	0.0795
	0.583	0.0377	0.8733	0.1157		0.583	0.1720	0.4990	0.0574
0.750	1.3462	1.8485	0.3139	0.750	0.2047	0.5821	0.0630		
0.917	-1.5490	1.8710	0.3483						
1715	-0.917	-0.7897	0.6897	0.1572	1765	-0.917	0.9245	0.6738	0.1198
	-0.750	-0.0365	0.5126	0.0759		-0.750	-1.7663	1.1413	0.2372
	-0.583	-0.1095	0.5779	0.0867		-0.583	-0.1058	0.7800	0.0889
	-0.417	0.9708	0.4649	0.1763		-0.417	-0.3629	0.7470	0.0954
	-0.250	0.1512	0.5772	0.0923		-0.250	-0.1390	0.6300	0.0777
	-0.083	-0.7923	0.6351	0.1702		-0.083	-0.8000	0.7254	0.1151
	0.083	-0.6384	0.6569	0.1529		0.083	0.0527	0.4743	0.0306
	0.250	-0.3842	0.8946	0.1526		0.250	-0.2312	0.6303	0.0359
	0.417	0.2477	0.5068	0.0847		0.417	0.1302	0.5485	0.0757
	0.583	0.2083	0.5656	0.0843		0.583	0.0388	0.8872	0.2931
0.750	0.2119	0.7993	0.1103						

Appendix D. Results

E_γ [MeV]	$\cos(\theta)$	H	ΔH^{stat}	ΔH^{syst}	E_γ [MeV]	$\cos(\theta)$	H	ΔH^{stat}	ΔH^{syst}
1515	-0.917	-0.7525	0.6548	0.0923	1565	-0.917	0.5877	0.4853	0.0854
	-0.750	-0.3743	0.7092	0.0723		-0.750	0.7964	0.4365	0.1077
	-0.583	-0.6716	0.5325	0.0818		-0.583	-0.0208	0.4509	0.0511
	-0.417	-1.0058	0.5505	0.1199		-0.417	0.0765	0.5352	0.0601
	-0.250	-0.1864	0.7847	0.0839		-0.250	-0.9919	0.5961	0.1327
	-0.083	0.3655	0.9079	0.1049		-0.083	0.2933	0.5290	0.0634
	0.083	-0.9142	0.9765	0.1407		0.083	-0.3600	0.5484	0.0621
	0.250	-0.4322	0.8932	0.0965		0.250	-0.6986	0.6797	0.0799
	0.417	-0.5224	0.9555	0.1015		0.417	0.2180	0.6540	0.0542
	0.583	-0.3124	1.4660	0.1369		0.583	0.1823	0.6734	0.0644
	0.750	-0.5511	1.1552	0.1187		0.750	-1.9809	1.3202	0.3119
0.917	-0.2056	1.1272	0.1068						
1615	-0.917	0.1014	0.4416	0.0478	1665	-0.917	0.1049	0.4257	0.0464
	-0.750	0.3800	0.4562	0.0690		-0.750	-0.6660	0.4433	0.0954
	-0.583	0.1203	0.5268	0.0704		-0.583	0.0193	0.3741	0.0476
	-0.417	0.6442	0.6168	0.1313		-0.417	0.1340	0.4277	0.0584
	-0.250	-0.6644	0.4904	0.1367		-0.250	0.9003	0.4936	0.1425
	-0.083	0.2609	0.8180	0.1368		-0.083	0.3595	0.7855	0.1079
	0.083	0.5252	0.8385	0.1512		0.083	0.0988	0.3900	0.0518
	0.250	-0.6922	0.6512	0.1372		0.250	0.4739	0.4317	0.0806
	0.417	0.7659	0.6510	0.1375		0.417	-0.6622	0.5856	0.1043
	0.583	0.0229	0.8502	0.1128		0.583	-0.1925	0.5044	0.0586
	0.750	4.0103	2.3884	0.0050		0.750	0.2719	0.5823	0.0655
0.917	1.6570	1.8296	0.3559						
1715	-0.917	0.1052	0.6508	0.0964	1765	-0.917	-0.1315	0.6533	0.0675
	-0.750	-0.1942	0.5318	0.0832		-0.750	-0.5974	1.0084	0.1248
	-0.583	2.1461	0.7092	0.3761		-0.583	-0.6155	0.8025	0.1145
	-0.417	0.5664	0.4477	0.1120		-0.417	-0.2108	0.6615	0.0803
	-0.250	-0.1866	0.5870	0.0951		-0.250	0.3669	0.5893	0.0838
	-0.083	-0.4930	0.5852	0.1252		-0.083	-0.6661	0.6641	0.1000
	0.083	0.4466	0.6459	0.1294		0.083	1.3802	0.4881	0.0977
	0.250	0.7808	0.9564	0.1954		0.250	-0.3327	0.6471	0.0385
	0.417	-0.0491	0.5029	0.0761		0.417	0.3954	0.5357	0.0897
	0.583	0.3398	0.5746	0.0933		0.583	1.8468	1.0713	0.7710
	0.750	-0.0714	0.6622	0.0898					

D.7 Data tables (T in merged full data)

D.7.1 $\gamma p \rightarrow \pi^0 p$

E_γ [MeV]	$\cos(\theta)$	T	ΔT^{stat}	ΔT^{syst}	E_γ [MeV]	$\cos(\theta)$	T	ΔT^{stat}	ΔT^{syst}
1470	-0.917	-0.3458	0.0595	0.0374	1515	-0.917	-0.0377	0.0339	0.0081
	-0.750	-0.5007	0.0368	0.0497		-0.750	-0.1305	0.0217	0.0149
	-0.583	-0.5994	0.0278	0.0585		-0.583	-0.2710	0.0192	0.0298
	-0.417	-0.7051	0.0338	0.0913		-0.417	-0.3218	0.0223	0.0401
	-0.250	-0.6737	0.0241	0.0703		-0.250	-0.3660	0.0157	0.0388
	-0.083	-0.6430	0.0233	0.0759		-0.083	-0.4033	0.0157	0.0453
	0.083	-0.6814	0.0239	0.0836		0.083	-0.4102	0.0168	0.0540
	0.250	-0.5797	0.0245	0.0676		0.250	-0.3582	0.0175	0.0448
	0.417	-0.5308	0.0312	0.0696		0.417	-0.2584	0.0199	0.0322
0.583	-0.5385	0.1085	0.1191	0.583	-0.1020	0.0352	0.0161		
1565	-0.917	0.1789	0.0298	0.0167	1615	-0.917	0.2488	0.0300	0.0219
	-0.750	0.1305	0.0215	0.0158		-0.750	0.1145	0.0198	0.0137
	-0.583	0.0547	0.0190	0.0096		-0.583	0.0591	0.0205	0.0108
	-0.417	0.0136	0.0248	0.0077		-0.417	-0.0009	0.0254	0.0073
	-0.250	-0.1150	0.0177	0.0155		-0.250	-0.0548	0.0206	0.0103
	-0.083	-0.1791	0.0182	0.0245		-0.083	-0.1819	0.0234	0.0280
	0.083	-0.2063	0.0196	0.0297		0.083	-0.2291	0.0258	0.0359
	0.250	-0.1685	0.0212	0.0262		0.250	-0.2981	0.0298	0.0438
	0.417	-0.0890	0.0246	0.0159		0.417	-0.2232	0.0330	0.0335
0.583	0.1216	0.0375	0.0183	0.583	-0.1157	0.0426	0.0288		
0.750	0.1326	0.2047	0.0476	0.750	-0.0065	0.0960	0.0137		
1665	-0.917	0.3568	0.0293	0.0312	1715	-0.917	0.3998	0.0378	0.0418
	-0.750	0.0432	0.0185	0.0087		-0.750	0.0877	0.0253	0.0134
	-0.583	-0.0005	0.0203	0.0069		-0.583	-0.0409	0.0276	0.0104
	-0.417	-0.0828	0.0283	0.0167		-0.417	0.0048	0.0406	0.0106
	-0.250	-0.0696	0.0221	0.0125		-0.250	-0.0295	0.0318	0.0101
	-0.083	-0.1316	0.0264	0.0249		-0.083	-0.2418	0.0385	0.0537
	0.083	-0.3158	0.0274	0.0511		0.083	-0.2525	0.0391	0.0575
	0.250	-0.3970	0.0284	0.0623		0.250	-0.2128	0.0336	0.0475
	0.417	-0.2366	0.0270	0.0364		0.417	0.0584	0.0316	0.0147
0.583	0.0074	0.0296	0.0080	0.583	0.2698	0.0367	0.0476		
0.750	0.1463	0.0528	0.0204	0.750	0.2749	0.0583	0.0511		

Appendix D. Results

E_γ [MeV]	$\cos(\theta)$	T	ΔT^{stat}	ΔT^{syst}	E_γ [MeV]	$\cos(\theta)$	T	ΔT^{stat}	ΔT^{syst}
1765	-0.917	0.2652	0.0523	0.0344	1840	-0.917	0.1912	0.0367	0.0210
	-0.750	-0.0042	0.0409	0.0083		-0.750	0.0287	0.0357	0.0081
	-0.583	-0.0571	0.0479	0.0129		-0.583	-0.0185	0.0439	0.0093
	-0.417	0.0192	0.0652	0.0132		-0.417	0.1525	0.0524	0.0194
	-0.250	-0.0280	0.0497	0.0114		-0.250	0.0109	0.0465	0.0090
	-0.083	-0.3165	0.0609	0.0703		-0.083	-0.2526	0.0481	0.0397
	0.083	-0.4862	0.0583	0.1017		0.083	-0.4830	0.0465	0.0643
	0.250	-0.2697	0.0506	0.0544		0.250	-0.5644	0.0576	0.1021
	0.417	0.1680	0.0538	0.0367		0.417	0.1302	0.0421	0.0216
	0.583	0.5259	0.0701	0.1070		0.583	0.6890	0.0714	0.0755
0.750	0.5755	0.0913	0.1295	0.750	0.2986	0.0554	0.0838		
					0.917	-0.1578	0.4005	0.0609	
1950	-0.917	0.2279	0.0454	0.0225	2145	-0.917	0.1875	0.0886	0.0262
	-0.750	-0.0666	0.0444	0.0114		-0.750	-0.2867	0.0335	0.0457
	-0.583	-0.0090	0.0598	0.0108		-0.583	-0.2578	0.0639	0.0348
	-0.417	0.3518	0.0599	0.0574		-0.417	0.3413	0.0715	0.0503
	-0.250	0.3133	0.0565	0.0402		-0.250	0.2600	0.0745	0.0362
	-0.083	-0.0197	0.0451	0.0107		-0.083	0.0810	0.0510	0.0150
	0.083	-0.3372	0.0482	0.0515		0.083	-0.1442	0.0613	0.0220
	0.250	-0.3183	0.0696	0.0515		0.250	-0.1086	0.0814	0.0294
	0.417	0.0752	0.1264	0.0245		0.417	0.0952	0.1338	0.0611
	0.583	0.2353	0.0926	0.0301		0.583	-0.3668	0.1196	0.0774
0.750	-0.1194	0.0550	0.0308	0.750	-0.4759	0.0499	0.0775		
0.917	-0.0442	0.0532	0.0320	0.917	-0.2006	0.0986	0.0411		
2435	-0.917	0.1196	0.1363	0.0240					
	-0.750	-0.0777	0.3671	0.0595					
	-0.583	-1.1672	0.3815	0.5209					
	-0.417	-0.4816	0.2533	0.0937					
	-0.250	0.7339	0.9297	0.8646					
	-0.083	-0.7121	0.2537	0.0981					
	0.083	-0.2569	0.2865	0.0744					
	0.250	0.4702	0.2329	0.0756					
	0.417	0.1018	0.2791	0.0453					
	0.583	0.0453	0.1556	0.0350					
0.750	0.0090	0.1163	0.0172						
0.917	-0.4881	0.2012	0.1492						

D.7.2 $\gamma n \rightarrow \pi^0 n$

E_γ [MeV]	$\cos(\theta)$	T	ΔT^{stat}	ΔT^{syst}	E_γ [MeV]	$\cos(\theta)$	T	ΔT^{stat}	ΔT^{syst}
1470	-0.917	-0.4785	0.0690	0.0386	1515	-0.917	-0.0314	0.0436	0.0075
	-0.750	-0.6121	0.0579	0.0598		-0.750	-0.2501	0.0427	0.0266
	-0.583	-0.5840	0.0506	0.0586		-0.583	-0.3698	0.0392	0.0394
	-0.417	-0.6691	0.0591	0.0849		-0.417	-0.4826	0.0467	0.0614
	-0.250	-0.5976	0.0460	0.0750		-0.250	-0.4185	0.0369	0.0492
	-0.083	-0.6025	0.0441	0.0708		-0.083	-0.4566	0.0339	0.0554
	0.083	-0.6317	0.0506	0.0918		0.083	-0.4184	0.0355	0.0495
	0.250	-0.5952	0.0605	0.0830		0.250	-0.3497	0.0369	0.0440
	0.417	-0.5013	0.0668	0.0766		0.417	-0.1437	0.0456	0.0221
	0.583	-0.4115	0.1020	0.0611		0.583	-0.0666	0.0591	0.0126
0.750	0.5766	0.2045	0.0616	0.750	0.0959	0.1090	0.0213		
1565	-0.917	0.1276	0.0534	0.0134	1615	-0.917	0.1846	0.0602	0.0177
	-0.750	0.0732	0.0511	0.0122		-0.750	-0.0708	0.0683	0.0133
	-0.583	-0.0416	0.0453	0.0093		-0.583	0.0699	0.0584	0.0128
	-0.417	-0.0142	0.0520	0.0103		-0.417	0.1337	0.0608	0.0217
	-0.250	-0.0941	0.0379	0.0136		-0.250	0.2212	0.0499	0.0303
	-0.083	-0.1514	0.0397	0.0230		-0.083	0.1681	0.0473	0.0251
	0.083	-0.0968	0.0411	0.0172		0.083	0.1430	0.0535	0.0251
	0.250	0.0037	0.0422	0.0086		0.250	0.1990	0.0559	0.0277
	0.417	0.2172	0.0509	0.0284		0.417	0.3023	0.0718	0.0508
	0.583	0.2123	0.0705	0.0304		0.583	0.3543	0.0669	0.0335
0.750	0.3534	0.1219	0.0643	0.750	0.2573	0.1011	0.0293		
0.917	-0.1046	0.3263	0.0353	0.917	0.5541	0.2243	0.0330		

Appendix D. Results

E_γ [MeV]	$\cos(\theta)$	T	ΔT^{stat}	ΔT^{syst}	E_γ [MeV]	$\cos(\theta)$	T	ΔT^{stat}	ΔT^{syst}
1665	-0.917	0.1095	0.0595	0.0132	1715	-0.917	0.1811	0.0668	0.0224
	-0.750	-0.1607	0.0799	0.0334		-0.750	-0.2086	0.0800	0.0383
	-0.583	-0.1202	0.0648	0.0199		-0.583	-0.0007	0.0866	0.0168
	-0.417	0.1485	0.0732	0.0245		-0.417	0.1706	0.1070	0.0395
	-0.250	0.3278	0.0601	0.0442		-0.250	0.5703	0.1026	0.1304
	-0.083	0.3816	0.0635	0.0652		-0.083	0.5731	0.1259	0.1430
	0.083	0.3549	0.0763	0.0616		0.083	0.0850	0.1150	0.0419
	0.250	0.3871	0.0768	0.0727		0.250	0.2466	0.0912	0.0440
	0.417	0.3563	0.0649	0.0497		0.417	0.5326	0.0865	0.0977
	0.583	0.4232	0.0646	0.0509		0.583	0.3730	0.0758	0.0723
	0.750	0.5059	0.0769	0.0577		0.750	0.4822	0.1040	0.1082
0.917	-0.0463	0.1667	0.0236	0.917	0.6524	0.3022	0.1110		
1765	-0.917	0.3067	0.0748	0.0281	1840	-0.917	0.1737	0.0550	0.0165
	-0.750	-0.2266	0.0736	0.0263		-0.750	-0.0312	0.0565	0.0099
	-0.583	0.0421	0.1003	0.0179		-0.583	-0.0109	0.0761	0.0109
	-0.417	0.2594	0.1157	0.0448		-0.417	0.5137	0.1117	0.0710
	-0.250	0.3176	0.1605	0.0876		-0.250	0.5294	0.1292	0.0970
	-0.083	0.4569	0.1436	0.0910		-0.083	0.2071	0.1073	0.0317
	0.083	0.1276	0.1441	0.0419		0.083	-0.0445	0.1014	0.0178
	0.250	0.2651	0.1008	0.0405		0.250	-0.0036	0.1352	0.0268
	0.417	0.5064	0.1075	0.0824		0.417	0.6987	0.1266	0.1038
	0.583	0.6972	0.1439	0.1417		0.583	0.7122	0.1457	0.1584
	0.750	0.6725	0.1898	0.1681		0.750	0.4040	0.1086	0.0558
0.917	0.6390	0.2917	0.3268						
1950	-0.917	0.2561	0.0682	0.0249	2145	-0.917	-0.1818	0.1477	0.0221
	-0.750	-0.1574	0.0665	0.0222		-0.750	-0.1449	0.1125	0.0461
	-0.583	-0.1067	0.0979	0.0227		-0.583	-0.1259	0.1826	0.0356
	-0.417	0.6462	0.1133	0.0946		-0.417	0.7411	0.1817	0.0802
	-0.250	0.6702	0.1401	0.1021		-0.250	0.3602	0.1217	0.0349
	-0.083	0.1402	0.0896	0.0201		-0.083	0.2054	0.1311	0.0310
	0.083	-0.2599	0.1136	0.0617		0.083	-0.1199	0.1290	0.0253
	0.250	0.0747	0.1445	0.0269		0.250	0.0141	0.1647	0.0213
	0.417	0.3412	0.2287	0.0802		0.417	0.6502	0.2547	0.0791
	0.583	0.6413	0.1907	0.1717		0.583	0.0710	0.2145	0.0519
	0.750	0.3007	0.1068	0.0579		0.750	-0.0356	0.1066	0.0229
0.917	0.4682	0.2715	0.1383	0.917	-0.0074	0.1942	0.0475		

D.7. Data tables (T in merged full data)

E_γ [MeV]	$\cos(\theta)$	T	ΔT^{stat}	ΔT^{syst}	E_γ [MeV]	$\cos(\theta)$	T	ΔT^{stat}	ΔT^{syst}
2435	-0.917	-0.1280	0.2267	0.0284					
	-0.750	-0.3953	0.6199	0.1534					
	-0.083	0.0218	0.2661	0.0184					
	0.250	0.5790	0.3976	0.0690					
	0.750	0.3968	0.0955	0.0820					
	0.917	0.3036	0.1349	0.0380					

D.7.3 $\gamma p \rightarrow \eta p$

E_γ [MeV]	$\cos(\theta)$	T	ΔT^{stat}	ΔT^{syst}	E_γ [MeV]	$\cos(\theta)$	T	ΔT^{stat}	ΔT^{syst}
1515	-0.917	-0.0241	0.0438	0.0099	1565	-0.917	0.0047	0.0423	0.0123
	-0.750	0.0436	0.0529	0.0115		-0.750	0.2083	0.0567	0.0291
	-0.583	0.1029	0.0508	0.0123		-0.583	0.2153	0.0457	0.0261
	-0.417	0.1667	0.0505	0.0215		-0.417	0.1479	0.0409	0.0196
	-0.250	0.1016	0.0454	0.0124		-0.250	0.1572	0.0428	0.0212
	-0.083	0.1137	0.0508	0.0119		-0.083	0.1615	0.0416	0.0202
	0.083	0.1264	0.0582	0.0335		0.083	0.0925	0.0437	0.0130
	0.250	0.1012	0.0886	0.0429		0.250	0.0943	0.0587	0.0266
	0.417	-0.0028	0.1067	0.0353		0.417	0.1204	0.0897	0.0533
	0.583	0.0834	0.2211	0.0226		0.583	0.4641	0.1915	0.0314
	0.750	-0.1464	0.2219	0.0526		0.917	0.2311	0.3401	0.0875
	0.917	-0.2011	0.1158	0.0279					
1615	-0.917	0.1890	0.0564	0.0277	1665	-0.917	0.2389	0.0875	0.0364
	-0.750	0.2965	0.0621	0.0448		-0.750	0.5204	0.1024	0.0773
	-0.583	0.2537	0.0554	0.0365		-0.583	0.4137	0.0759	0.0599
	-0.417	0.1562	0.0535	0.0262		-0.417	0.4806	0.0955	0.0849
	-0.250	0.3111	0.0543	0.0397		-0.250	0.4732	0.0839	0.0665
	-0.083	0.2418	0.0581	0.0371		-0.083	0.7138	0.1727	0.2433
	0.083	0.3316	0.0652	0.0432		0.083	0.3631	0.0783	0.0578
	0.250	0.3384	0.0666	0.0450		0.250	0.5115	0.0965	0.0858
	0.417	0.2511	0.0761	0.0475		0.417	0.2433	0.0941	0.0462
	0.583	-0.0361	0.1529	0.0214		0.583	0.4109	0.1243	0.0874
	0.917	0.8059	0.7061	0.1752		0.750	0.1348	0.2973	0.1562
						0.917	0.3361	1.6015	0.5347

Appendix D. Results

E_γ [MeV]	$\cos(\theta)$	T	ΔT^{stat}	ΔT^{syst}	E_γ [MeV]	$\cos(\theta)$	T	ΔT^{stat}	ΔT^{syst}
1715	-0.917	0.2309	0.1777	0.1164	1765	-0.917	0.4813	0.2090	0.0493
	-0.750	0.5371	0.1202	0.0575		-0.750	0.3667	0.1928	0.0856
	-0.583	0.4864	0.1197	0.0857		-0.583	0.6127	0.1660	0.1165
	-0.417	0.5547	0.1067	0.1053		-0.417	0.6988	0.1395	0.1052
	-0.250	0.5350	0.0971	0.0825		-0.250	0.4932	0.1161	0.0625
	-0.083	0.6815	0.1186	0.1240		-0.083	0.5945	0.1017	0.0852
	0.083	0.4048	0.0737	0.0543		0.083	0.5646	0.1038	0.0850
	0.250	0.4742	0.0812	0.0765		0.250	0.5434	0.0982	0.0761
	0.417	0.4555	0.0814	0.0699		0.417	0.3313	0.1062	0.0543
	0.583	0.3578	0.0882	0.0814		0.583	0.4917	0.1047	0.0804
0.750	0.2130	0.3435	0.0815	0.750	0.4202	0.1693	0.0600		
1840	-0.917	0.6783	0.3030	0.1007	1950	-0.917	-0.5568	0.3797	0.1152
	-0.750	0.4396	0.1858	0.0492		-0.750	-0.1854	0.2952	0.0288
	-0.583	0.5700	0.1846	0.1162		-0.583	0.2219	0.1722	0.0428
	-0.417	0.5189	0.1267	0.0681		-0.417	-0.0080	0.1377	0.0126
	-0.250	0.5163	0.1934	0.0997		-0.250	0.2680	0.2455	0.0425
	-0.083	0.4440	0.1029	0.0519		-0.083	0.3169	0.1224	0.0306
	0.083	0.2871	0.1016	0.0509		0.083	0.2140	0.1342	0.0286
	0.250	0.2664	0.0894	0.0405		0.250	0.0991	0.1496	0.0279
	0.417	0.3170	0.0947	0.0443		0.417	0.1429	0.1483	0.0265
	0.583	0.2941	0.0937	0.0421		0.583	0.1656	0.1368	0.0222
0.750	0.1822	0.1520	0.0322	0.750	0.1972	0.1445	0.0297		

D.7.4 $\gamma n \rightarrow \eta n$

E_γ [MeV]	$\cos(\theta)$	T	ΔT^{stat}	ΔT^{syst}	E_γ [MeV]	$\cos(\theta)$	T	ΔT^{stat}	ΔT^{syst}
1515	-0.917	0.0318	0.0904	0.0092	1565	-0.917	0.1545	0.0881	0.0167
	-0.750	0.1408	0.0963	0.0176		-0.750	0.1154	0.0695	0.0168
	-0.583	0.1832	0.0776	0.0174		-0.583	0.0614	0.0833	0.0135
	-0.417	0.1044	0.0778	0.0109		-0.417	0.0313	0.0973	0.0132
	-0.250	-0.0183	0.0933	0.0126		-0.250	-0.0297	0.1020	0.0145
	-0.083	0.0214	0.1074	0.0137		-0.083	-0.1406	0.1022	0.0182
	0.083	-0.0825	0.1273	0.0175		0.083	-0.0401	0.1168	0.0117
	0.250	-0.1698	0.1264	0.0200		0.250	-0.3140	0.1354	0.0369
	0.417	-0.0440	0.1274	0.0116		0.417	-0.2188	0.1218	0.0210
	0.583	-0.3073	0.1859	0.0376		0.583	-0.0492	0.1570	0.0133
0.750	-0.1687	0.1926	0.0212	0.750	-0.2452	0.2144	0.0388		
0.917	-0.2845	0.1986	0.0201						
1615	-0.917	0.2595	0.0993	0.0275	1665	-0.917	0.2360	0.1113	0.0305
	-0.750	0.2750	0.0886	0.0427		-0.750	0.1916	0.1079	0.0367
	-0.583	0.2396	0.1258	0.0333		-0.583	0.2521	0.1135	0.0340
	-0.417	0.0891	0.1304	0.0248		-0.417	0.1699	0.1113	0.0299
	-0.250	0.1632	0.1100	0.0234		-0.250	-0.0922	0.1392	0.0272
	-0.083	0.0263	0.1333	0.0274		-0.083	0.0411	0.1447	0.0405
	0.083	-0.3307	0.1858	0.0660		0.083	-0.3756	0.1084	0.0452
	0.250	-0.3591	0.1539	0.0489		0.250	-0.1901	0.1220	0.0311
	0.417	-0.0874	0.1715	0.0257		0.417	-0.4148	0.1448	0.0901
	0.583	-0.2252	0.1905	0.0384		0.583	-0.2219	0.1457	0.0307
0.750	-0.0917	0.1893	0.0473	0.750	-0.1484	0.1832	0.0191		
0.917	-0.0496	0.2669	0.0384						

Appendix D. Results

E_γ [MeV]	$\cos(\theta)$	T	ΔT^{stat}	ΔT^{syst}	E_γ [MeV]	$\cos(\theta)$	T	ΔT^{stat}	ΔT^{syst}
1715	-0.917	0.4060	0.1967	0.0730	1765	-0.917	-0.0297	0.1865	0.0131
	-0.750	0.2409	0.1640	0.0431		-0.750	0.2372	0.1929	0.0481
	-0.583	0.2047	0.1477	0.0426		-0.583	-0.2975	0.2329	0.0446
	-0.417	-0.1496	0.1433	0.0273		-0.417	0.0289	0.2051	0.0264
	-0.250	0.0343	0.1738	0.0298		-0.250	0.1164	0.1886	0.0180
	-0.083	-0.1235	0.1648	0.0362		-0.083	-0.4211	0.2279	0.0711
	0.083	-0.0531	0.1455	0.0373		0.083	0.1293	0.1682	0.0194
	0.250	-0.0236	0.1492	0.0549		0.250	-0.3511	0.1623	0.0678
	0.417	-0.0485	0.1269	0.0233		0.417	-0.0521	0.1503	0.0187
	0.583	-0.3260	0.1644	0.0560		0.583	-0.1877	0.2128	0.0521
0.750	-0.2971	0.2069	0.0379						
1840	-0.917	-0.1465	0.1772	0.0190	1950	-0.917	0.0769	0.3029	0.0803
	-0.750	-0.1380	0.1802	0.0314		-0.750	0.3131	0.1991	0.3280
	-0.583	-0.1254	0.1734	0.0179		-0.583	-0.1047	0.3529	0.0261
	-0.417	-0.2329	0.2163	0.0720		-0.417	0.1288	0.2447	0.0404
	-0.250	0.0955	0.2206	0.0266		-0.250	-0.6575	0.4485	0.0977
	-0.083	-0.5000	0.1637	0.0396		-0.083	0.5324	0.3916	0.1122
	0.083	0.0554	0.1487	0.0160		0.083	-0.3312	0.2498	0.0434
	0.250	-0.0123	0.1259	0.0103		0.250	-0.3176	0.2239	0.0386
	0.417	-0.3587	0.2137	0.0785		0.417	-0.1901	0.1775	0.0217
	0.583	0.6311	0.2274	0.1318		0.583	0.2189	0.1132	0.0906
0.750	0.3938	0.3956	0.0908						

References

- [1] B. Pullman, *The Atom in the History of Human Thought*, Oxford University Press (1998).
- [2] H. Cohen and C. Lefebvre, *Handbook of Categorization in Cognitive Science*, Elsevier Science (2017).
- [3] A. Pyle, *Atoms and Atomism*, The Belknap Press of Harvard University Press (2010).
- [4] J. Dalton, *III. On the absorption of gases by water and other liquids*, *Philos. Mag.* 24 (93), 15 (1806).
- [5] R. Brown, *The miscellaneous botanical works of Robert Brown*, vol. 1, Ray Society (1866).
- [6] W. Prout, *On the Relation between the Specific Gravities of Bodies in their Gaseous State and the Weights of their Atoms*, *Ann. Philos.* 6, 321 (1815).
- [7] I. Falconer, *Corpuscles to Electrons in J. Buchwald and A. Warwick (eds) Histories of the Electron*, MIT Press (2001).
- [8] A. Einstein, *Zur Elektrodynamik bewegter Körper (In German)*, *Ann. Phy.* 322 (10), 891 (1905).
- [9] E. Rutherford and J. Nuttall, *LVII. Scattering of α particles by gases*, *Philos. Mag.* 26 (154), 702 (1913).
- [10] N. Bohr, *On the Constitution of Atoms and Molecules*, *Philos. Mag.* 26, 1 (1913).

References

- [11] F. Soddy, *The Radio-Elements and the Periodic Law*, Nature 91, 57 (1913).
- [12] E. Rutherford, *Collision of α particles with light atoms, IV: An anomalous effect in nitrogen*, Philos. Mag. 26, 581 (1919).
- [13] E. Rutherford, *Nuclear Constitution of Atoms*, Proc. R. Soc. A 97, 374 (1920).
- [14] J. Chadwick, *Possible Existence of a Neutron*, Nature 129, 312 (1932).
- [15] H. Yukawa, *On the Interaction of Elementary Particles. I*, Proc. Phys.-Math. Soc. Jpn. 17, 48 (1935).
- [16] J. C. Street and E. C. Stevenson, *New Evidence for the Existence of a Particle of Mass Intermediate Between the Proton and Electron*, Phys. Rev. 52, 1003 (1937).
- [17] G. P. S. Occhialini and C. F. Powell, *Nuclear disintegrations produced by slow charged particles of small mass*, Nature 159, 186 (1947).
- [18] C. M. G. Lattes, G. P. S. Occhialini and C. F. Powell, *Observations on the Tracks of Slow Mesons in Photographic Emulsions**, Nature 160, 453 (1947).
- [19] G. D. Rochester and C. C. Butler, *Evidence for the Existence of New Unstable Elementary Particles*, Nature 160, 855 (1947).
- [20] C. N. Yang and R. L. Mills, *Conservation of Isotopic Spin and Isotopic Gauge Invariance*, Phys. Rev. 96, 191 (1954).
- [21] O. Chamberlain et al., *Observation of Antiprotons*, Phys. Rev. 100, 947 (1955).
- [22] C. L. Cowan et al., *Detection of the Free Neutrino: a Confirmation*, Science 124 (3212), 103 (1956).
- [23] NobelPrize.org, *The Nobel Prize in Physics 1965* (2018), URL <https://www.nobelprize.org/prizes/physics/1965/summary/> (visited on 07.12.2022).

-
- [24] M. E. Peskin and D. V. Schröder, *An Introduction to Quantum Field Theory*, Westview (1995).
- [25] T. Lancaster and S. Blundell, *Quantum Field Theory for the Gifted Amateur*, Oxford University Press (2014).
- [26] M. Gell-Mann, *The symmetry group of vector and axial vector currents*, Phys. Phys. Fiz. 1, 63 (1964).
- [27] G. Zweig, *An SU_3 model for strong interaction symmetry and its breaking; Version 1*, Tech. Rep. CERN-TH-401, CERN, Geneva (1964).
- [28] F. Englert and R. Brout, *Broken Symmetry and the Mass of Gauge Vector Mesons*, Phys. Rev. Lett. 13, 321 (1964).
- [29] P. W. Higgs, *Broken Symmetries and the Masses of Gauge Bosons*, Phys. Rev. Lett. 13, 508 (1964).
- [30] G. S. Guralnik, C. R. Hagen and T. W. B. Kibble, *Global Conservation Laws and Massless Particles*, Phys. Rev. Lett. 13, 585 (1964).
- [31] S. Weinberg, *A Model of Leptons*, Phys. Rev. Lett. 19, 1264 (1967).
- [32] A. Salam, *Weak and Electromagnetic Interactions*, Conf. Proc. C680519, 367 (1968).
- [33] E. D. Bloom et al., *High-Energy Inelastic $e-p$ Scattering at 6° and 10°* , Phys. Rev. Lett. 23, 930 (1969).
- [34] F. J. Hasert et al., *Search for elastic muon-neutrino electron scattering*, Phys. Lett. B 46 (1), 121 (1973).
- [35] F. J. Hasert et al., *Observation of neutrino-like interactions without muon or electron in the gargamelle neutrino experiment*, Phys. Lett. B 46 (1), 138 (1973).
- [36] T. Y. Cao, *Conceptual Developments of 20th Century Field Theories*, Cambridge University Press (1998).
- [37] G. Aad et al., *Observation of a new particle in the search for the Standard Model Higgs boson with the ATLAS detector at the LHC*, Phys. Lett. B 716 (1), 1 (2012).

- [38] S. Chatrchyan et al., *Observation of a new boson at a mass of 125 GeV with the CMS experiment at the LHC*, Phys. Lett. B 716 (1), 30 (2012).
- [39] N. Science, *Dark Energy, Dark Matter* (2021), URL <https://science.nasa.gov/astrophysics/focus-areas/what-is-dark-energy> (visited on 07.12.2022).
- [40] N. Aghanim et al., *Planck 2018 results*, Astron. Astrophys. 641, A6 (2020).
- [41] W. Pauli, *The Connection Between Spin and Statistics*, Phys. Rev. 58, 716 (1940).
- [42] M. Fierz, *Über die relativistische Theorie kräftefreier Teilchen mit beliebigem Spin (In German)*, Helv. Phys. Acta 12, 3 (1939).
- [43] J. Schwinger, *The Theory of Quantized Fields. I*, Phys. Rev. 82, 914 (1951).
- [44] R. L. Workman et al. (Particle Data Group), *Review of Particle Physics*, Prog. Theor. Exp. Phys. 2022 (8), 083C01 (2022).
- [45] A. Einstein, *Die Grundlage der allgemeinen Relativitätstheorie (In German)*, Ann. Phys. 354 (7), 769 (1916).
- [46] P. Achard et al., *Measurement of the running of the electromagnetic coupling at large momentum-transfer at LEP*, Phys. Lett. B 623 (1), 26 (2005).
- [47] D. J. Gross and F. Wilczek, *Ultraviolet Behavior of Non-Abelian Gauge Theories*, Phys. Rev. Lett. 30, 1343 (1973).
- [48] H. D. Politzer, *Reliable Perturbative Results for Strong Interactions?*, Phys. Rev. Lett. 30, 1346 (1973).
- [49] S. L. Glashow, *The renormalizability of vector meson interactions*, Nucl. Phys. 10, 107 (1959).
- [50] S.-K. Choi et al. (Belle Collaboration), *Observation of a Narrow Charmoniumlike State in Exclusive $B^\pm \rightarrow K^\pm \pi^+ \pi^- J/\psi$ Decays*, Phys. Rev. Lett. 91, 262001 (2003).

-
- [51] R. Aaij et al. (LHCb Collaboration), *Observation of $J/\psi\phi$ Structures Consistent with Exotic States from Amplitude Analysis of $B^+ \rightarrow J/\psi\phi K^+$ Decays*, Phys. Rev. Lett. 118, 022003 (2017).
- [52] R. Aaij et al. (LHCb Collaboration), *Amplitude analysis of $B^+ \rightarrow J/\psi\phi K^+$ decays*, Phys. Rev. D 95, 012002 (2017).
- [53] R. Aaij et al. (LHCb Collaboration), *Observation of structure in the $J\psi$ -pair mass spectrum*, Science Bulletin 65 (23), 1983 (2020).
- [54] R. Aaij et al. (LHCb Collaboration), *Observation of $J/\psi p$ Resonances Consistent with Pentaquark States in $\Lambda_b^0 \rightarrow J/\psi K^- p$ Decays*, Phys. Rev. Lett. 115, 072001 (2015).
- [55] R. Aaij et al. (LHCb Collaboration), *Observation of a Narrow Pentaquark State, $P_c(4312)^+$, and of the Two-Peak Structure of the $P_c(4450)^+$* , Phys. Rev. Lett. 122, 222001 (2019).
- [56] N. H. Christ et al. (RBC and UKQCD Collaborations), *η and η' Mesons from Lattice QCD*, Phys. Rev. Lett. 105, 241601 (2010).
- [57] W. Heisenberg, *Über den Bau der Atomkerne. I (In German)*, Z. Phys. 77 (1), 1 (1932).
- [58] E. Wigner, *On the Consequences of the Symmetry of the Nuclear Hamiltonian on the Spectroscopy of Nuclei*, Phys. Rev. 51, 106 (1937).
- [59] T. Nakano and K. Nishijima, *Charge Independence for V -particles**, Prog. Theor. Phys. 10 (5), 581 (1953).
- [60] M. Gell-Mann, *The interpretation of the new particles as displaced charge multiplets*, Nuovo Cim. 4 (2), 848 (1956).
- [61] B. Povh et al., *Teilchen und Kerne, 9. Auflage (In German)*, Springer-Verlag (2014).
- [62] W. Bartel et al., *Electroproduction of pions near the $\Delta(1236)$ isobar and the form factor $G_M^*(q^2)$ of the $(\gamma N \Delta)$ -vertex*, Phys. Lett. B 28 (2), 148 (1968).

- [63] A. Thiel, F. Afzal and Y. Wunderlich, *Light Baryon Spectroscopy*, Progress in Particle and Nucl. Phys. 125, 103949 (2022).
- [64] K. Nakamura et al. (Particle Data Group), *Review of Particle Physics*, J. Phys. G 37 (7A), 075021 (2010).
- [65] S. Schumann et al. (A2 Collaboration), *Radiative π^0 photoproduction on protons in the $\Delta^+(1232)$ region*, Eur. Phys. J. A 43 (3), 269 (2010).
- [66] O. Bartholomy et al. (CBELSA/TAPS Collaboration), *Neutral-Pion Photoproduction off Protons in the Energy Range $0.3 \text{ GeV} < E_\gamma < 3 \text{ GeV}$* , Phys. Rev. Lett. 94, 012003 (2005).
- [67] E. F. McNicoll et al. (A2 Collaboration), *Experimental study of the $\gamma p \rightarrow \eta p$ reaction with the Crystal Ball detector at the Mainz Microtron (MAMI-C)*, Phys. Rev. C 82, 035208 (2010).
- [68] V. Crede et al. (CBELSA/TAPS Collaboration), *Photoproduction of η and η' mesons off protons*, Phys. Rev. C 80, 055202 (2009).
- [69] V. Crede et al. (CBELSA/TAPS Collaboration), *Photoproduction of η Mesons off Protons for $0.75 \text{ GeV} < E_\gamma < 3 \text{ GeV}$* , Phys. Rev. Lett. 94, 012004 (2005).
- [70] A. Braghieri et al., *Total cross section measurement for the three double pion photoproduction channels on the proton*, Phys. Lett. B 363 (1), 46 (1995).
- [71] C. Wu et al., *Photoproduction of ρ mesons and Δ -baryons in the reaction $\gamma p \rightarrow p\pi^+\pi^-$ at energies up to $\sqrt{s} = 2.6 \text{ GeV}$* , Eur. Phys. J. A 23 (2), 317 (2005).
- [72] W. Struczinski et al., *Study of photoproduction on hydrogen in a streamer chamber with tagged photons for $1.6 \text{ GeV} < E_\gamma < 6.3 \text{ GeV}$ Topological and reaction cross sections*, Nucl. Phys. B 108 (1), 45 (1976).
- [73] U. Thoma et al., *N^* and Δ^* decays into $N\pi^0\pi^0$* , Phys. Lett. B 659 (1), 87 (2008).

-
- [74] V. Sokhoyan et al. (CBELSA/TAPS Collaboration), *High-statistics study of the reaction $\gamma p \rightarrow p 2\pi^0$* , The European Physical Journal A 51 (8), 95 (2015).
- [75] R. Machleidt and D. Entem, *Chiral effective field theory and nuclear forces*, Phys. Rep. 503 (1), 1 (2011).
- [76] G. Eichmann and C. S. Fischer, *Baryon Structure and Reactions from Dyson–Schwinger Equations*, Few-Body Syst. 60 (1), 2 (2018).
- [77] G. F. de T eramond and S. J. Brodsky, *Hadronic Spectrum of a Holographic Dual of QCD*, Phys. Rev. Lett. 94, 201601 (2005).
- [78] N. Isgur and J. Paton, *Flux-tube model for hadrons in QCD*, Phys. Rev. D 31, 2910 (1985).
- [79] S. Capstick and W. Roberts, *Quark models of baryon masses and decays*, Progress in Particle and Nucl. Phys. 45, S241 (2000).
- [80] U. L oring, B. Metsch and H. R. Petry, *The light-baryon spectrum in a relativistic quark model with instanton-induced quark forces*, Eur. Phys. J. A 10 (4), 395 (2001).
- [81] M. Ronniger and B. C. Metsch, *Effects of a spin-flavour-dependent interaction on the baryon mass spectrum*, Eur. Phys. J. A 47 (12), 162 (2011).
- [82] Y. Nambu, *Quasi-Particles and Gauge Invariance in the Theory of Superconductivity*, Phys. Rev. 117, 648 (1960).
- [83] J. Goldstone, *Field theories with « Superconductor » solutions*, Nuovo Cim. 19 (1), 154 (1961).
- [84] E. Epelbaum, H.-W. Hammer and U.-G. Meißner, *Modern theory of nuclear forces*, Rev. Mod. Phys. 81, 1773 (2009).
- [85] J. Gasser and H. Leutwyler, *Chiral perturbation theory to one loop*, Annals of Physics 158 (1), 142 (1984).
- [86] J. Gasser and H. Leutwyler, *Chiral perturbation theory: Expansions in the mass of the strange quark*, Nucl. Phys. B 250 (1), 465 (1985).

- [87] G. 't Hooft, *Computation of the quantum effects due to a four-dimensional pseudoparticle*, Phys. Rev. D 14, 3432 (1976).
- [88] B. Metsch, *Quark models**, Eur. Phys. J. A 35 (3), 275 (2008).
- [89] A. Bazavov et al., *Nonperturbative QCD simulations with 2+1 flavors of improved staggered quarks*, Rev. Mod. Phys. 82, 1349 (2010).
- [90] R. G. Edwards et al., *Excited state baryon spectroscopy from lattice QCD*, Phys. Rev. D 84 (7) (2011).
- [91] T. Khan, D. Richards and F. Winter, *Positive-parity baryon spectrum and the role of hybrid baryons*, Phys. Rev. D 104, 034503 (2021).
- [92] F. Frommberger, *The Electron Stretcher Accelerator* (2019), URL https://www-elsa.physik.uni-bonn.de/elsa-facility_en.html (visited on 07.12.2022).
- [93] I. for Nuclear Physics at Johannes Gutenberg Universität Mainz, *The Mainz Microtron*, URL <https://www.blogs.uni-mainz.de/fb08-nuclear-physics/accelerators-mami-mesa/the-mainz-microtron/> (visited on 07.12.2022).
- [94] E. Chudakov et al., *The newly upgraded Jefferson Lab CEBAF accelerator opens door to strong force studies* (2017), URL https://www.jlab.org/research/rhl_firstresult (visited on 07.12.2022).
- [95] B. Krusche and S. Schadmand, *Study of nonstrange baryon resonances with meson photoproduction*, Prog. Part. Nucl. Phys. 51, 399 (2003).
- [96] H. Minkowski, *Raum und Zeit (In German)*, Presentation at 80. Nuatrforscher-Versammlung zu Köln (1908), URL [https://de.wikisource.org/wiki/Raum_und_Zeit_\(Minkowski\)](https://de.wikisource.org/wiki/Raum_und_Zeit_(Minkowski)) (visited on 07.12.2022).
- [97] E. Tiesinga et al., *The 2018 CODATA Recommended Values of the Fundamental Physical Constants (Web Version 8.1)* (2020), URL <http://physics.nist.gov/constants> (visited on 07.12.2022).
- [98] D. Dreschel and L. Tiator, *Threshold pion photoproduction on nucleons*, J. Phys. G 18 (3), 449 (1992).

-
- [99] G. Knochlein, D. Drechsel and L. Tiator, *Photoproduction and electroproduction of eta mesons*, Z. Phys. A352, 327 (1995).
- [100] S. Minami, *An Invariance Theorem for Cross Sections of Meson-Nucleon Scattering*, Prog. Theor. Phys. 11 (2), 213 (1954).
- [101] R. L. Walker, *Phenomenological Analysis of Single-Pion Photoproduction*, Phys. Rev. 182, 1729 (1969).
- [102] M. Benmerrouche, N. C. Mukhopadhyay and J. F. Zhang, *Effective Lagrangian approach to the theory of η photoproduction in the $N^*(1535)$ region*, Phys. Rev. D 51, 3237 (1995).
- [103] G. F. Chew et al., *Relativistic Dispersion Relation Approach to Photomeson Production*, Phys. Rev. 106, 1345 (1957).
- [104] K. M. Watson, *The Hypothesis of Charge Independence for Nuclear Phenomena*, Phys. Rev. 85, 852 (1952).
- [105] I. S. Barker, A. Donnachie and J. K. Storrow, *Complete experiments in pseudoscalar photoproduction*, Nucl. Phys. B 95 (2), 347 (1975).
- [106] G. Keaton and R. Workman, *Amplitude ambiguities in pseudoscalar meson photoproduction*, Phys. Rev. C 53, 1434 (1996).
- [107] W.-T. Chiang and F. Tabakin, *Completeness rules for spin observables in pseudoscalar meson photoproduction*, Phys. Rev. C 55, 2054 (1997).
- [108] Y. Wunderlich, R. Beck and L. Tiator, *The complete-experiment problem of photoproduction of pseudoscalar mesons in a truncated partial-wave analysis*, Phys. Rev. C 89, 055203 (2014).
- [109] Y. Wunderlich et al., *Determining the dominant partial wave contributions from angular distributions of single- and double-polarization observables in pseudoscalar meson photoproduction*, Eur. Phys. J. A 53 (5), 86 (2017).
- [110] A. M. Sandorfi et al., *Calculations of Polarization Observables in Pseudoscalar Meson Photo-production Reactions* (2010), URL <https://doi.org/10.48550/arXiv.0912.3505> (visited on 07.12.2022).

- [111] W. J. Briscoe et al., *George Washington University Partial Wave Analysis*, URL <http://gwdac.phys.gwu.edu> (visited on 07.12.2022).
- [112] A. V. Anisovich et al., *Bonn-Gatchina Partial Wave Analysis*, URL <https://pwa.hiskp.uni-bonn.de> (visited on 07.12.2022).
- [113] L. Tiator et al., *MAID Partial Wave Analysis*, URL <https://maid.kph.uni-mainz.de> (visited on 07.12.2022).
- [114] D. Rönchen et al., *Coupled-channel dynamics in the reactions $\pi N \rightarrow \pi N$, ηN , $K\Lambda$, $K\Sigma$* , Eur. Phys. J. A 49 (4), 44 (2013).
- [115] V. Shklyar, H. Lenske and U. Mosel, *Giessen coupled-channel model for pion- and photon-induced reactions*, AIP Conf. Proc. 1432 (1), 349 (2012).
- [116] G. Breit and E. Wigner, *Capture of Slow Neutrons*, Phys. Rev. 49, 519 (1936).
- [117] S. U. Chung et al., *Partial wave analysis in K-matrix formalism*, Ann. Phys. 507 (5), 404 (1995).
- [118] R. L. Workman et al., *Updated SAID analysis of pion photoproduction data*, Phys. Rev. C 85, 025201 (2012).
- [119] J. Müller et al. (CBELSA/TAPS Collaboration), *New data on $\vec{\gamma}\vec{p} \rightarrow \eta p$ with polarized photons and protons and their implications for $N^* \rightarrow N\eta$ decays*, Phys. Lett. B 803, 135323 (2020).
- [120] V. Kashevarov, Private communication (2022).
- [121] W. J. Briscoe et al. (A2 Collaboration), *Cross section for $\gamma n \rightarrow \pi^0 n$ measured at the Mainz A2 experiment*, Phys. Rev. C 100, 065205 (2019).
- [122] L. Tiator et al., *Eta and etaprime photoproduction on the nucleon with the isobar model EtaMAID2018*, Eur. Phys. J. A 54 (12), 210 (2018).
- [123] R. L. Workman et al., *Unified Chew-Mandelstam SAID analysis of pion photoproduction data*, Phys. Rev. C 86, 015202 (2012).

-
- [124] A. V. Anisovich et al., *The impact of new polarization data from Bonn, Mainz and Jefferson Laboratory on $\gamma p \rightarrow \pi N$ multipoles*, Eur. Phys. J. A 52 (9), 284 (2016).
- [125] A. V. Anisovich et al., *Properties of baryon resonances from a multi-channel partial wave analysis*, Eur. Phys. J. A 48 (2), 15 (2012).
- [126] T. Seifen et al. (CBELSA/TAPS Collaboration), *Polarization observables in double neutral pion photoproduction*, Preprint (2022), URL <https://arxiv.org/abs/2207.01981>.
- [127] D. Drechsel, S. S. Kamalov and L. Tiator, *Unitary isobar model – MAID2007*, Eur. Phys. J. A 34 (1), 69 (2007).
- [128] V. Kuznetsov et al., *Evidence for a narrow structure at $W \sim 1.68$ GeV in η photoproduction off the neutron*, Phys. Lett. B 647 (1), 23 (2007).
- [129] F. Miyahara et al., *Narrow Resonance at $E_\gamma = 1020$ MeV in the $D(\gamma, \eta)pn$ Reaction*, Prog. Theor. Phys. Suppl. 168, 90 (2007).
- [130] I. Jaegle et al. (CBELSA/TAPS Collaboration), *Quasi-free photoproduction of η -mesons off the deuteron*, Eur. Phys. J. A 47 (8), 89 (2011).
- [131] I. Jaegle et al. (CBELSA/TAPS Collaboration), *Quasifree Photoproduction of η Mesons off the Neutron*, Phys. Rev. Lett. 100, 252002 (2008).
- [132] D. Werthmüller et al. (A2 Collaboration), *Narrow Structure in the Excitation Function of η Photoproduction off the Neutron*, Phys. Rev. Lett. 111, 232001 (2013).
- [133] L. Witthauer et al. (A2 Collaboration), *Insight into the Narrow Structure in η Photoproduction on the Neutron from Helicity-Dependent Cross Sections*, Phys. Rev. Lett. 117, 132502 (2016).
- [134] A. Fix, L. Tiator and M. V. Polyakov, *Photoproduction of η -mesons on the deuteron above $S_{11}(1535)$ in the presence of a narrow $P_{11}(1670)$ -resonance*, Eur. Phys. J. A 32 (3), 311 (2007).
- [135] M. Shrestha and D. M. Manley, *Multichannel parametrization of πN scattering amplitudes and extraction of resonance parameters*, Phys. Rev. C 86, 055203 (2012).

- [136] M. Döring and K. Nakayama, *On the cross section ratio σ_n/σ_p in η photoproduction*, Phys. Lett. B 683 (2), 145 (2010).
- [137] V. Shklyar, H. Lenske and U. Mosel, *η photoproduction in the resonance energy region*, Phys. Lett. B 650 (2), 172 (2007).
- [138] R. Shyam and O. Scholten, *Photoproduction of η mesons within a coupled-channels K -matrix approach*, Phys. Rev. C 78, 065201 (2008).
- [139] A. V. Anisovich et al., *Interference phenomena in the $J^P = 1/2^-$ wave in η photoproduction*, Eur. Phys. J. A 51 (6), 72 (2015).
- [140] L. Witthauer et al. (A2 Collaboration), *Helicity-dependent cross sections and double-polarization observable E in η photoproduction from quasifree protons and neutrons*, Phys. Rev. C 95, 055201 (2017).
- [141] J.-M. Suh, S.-H. Kim and H.-C. Kim, *Effects of nucleon resonances on η photoproduction off the neutron reexamined*, Phys. Rev. D 99, 074010 (2019).
- [142] J. Hartmann et al., *The polarization observables T , P , and H and their impact on $\gamma p \rightarrow p\pi^0$ multipoles*, Phys. Lett. B 748, 212 (2015).
- [143] F. N. Afzal, *Measurement of the beam and helicity asymmetries in the reactions $\gamma p \rightarrow p\pi^0$ and $\gamma p \rightarrow p\eta$* , Ph.D. thesis, Rheinische Friedrich-Wilhelms-Universität Bonn (2019).
- [144] N. Stausberg, *Time Calibration and Target Asymmetry Determination for Single Meson-Photoproduction at the CBELSA/TAPS Experiment*, Master's thesis, Rheinische Friedrich-Wilhelms-Universität Bonn (2019).
- [145] N. Muramatsu et al. (LEPS2/BGOegg Collaboration), *Measurement of neutral pion photoproduction off the proton with the large acceptance electromagnetic calorimeter BGOegg*, Phys. Rev. C 100, 055202 (2019).
- [146] S. Schumann et al. (A2 Collaboration), *Threshold π^0 photoproduction on transverse polarised protons at MAMI*, Phys. Lett. B 750, 252 (2015).

-
- [147] S. Gardner et al. (A2 Collaboration), *Photon asymmetry measurements of $\vec{\gamma}p \rightarrow \pi^0 p$ for $E_\gamma = 320 - 650$ MeV*, Eur. Phys. J. A 52 (11), 333 (2016).
- [148] J. R. M. Annand et al. (A2 Collaboration), *T and F asymmetries in π^0 photoproduction on the proton*, Phys. Rev. C 93, 055209 (2016).
- [149] M. Dugger et al. (CLAS Collaboration), *Beam asymmetry Σ for π^+ and π^0 photoproduction on the proton for photon energies from 1.102 to 1.862 GeV*, Phys. Rev. C 88, 065203 (2013).
- [150] O. Bartalini et al. (GRAAL Collaboration), *Measurement of π photoproduction on the proton from 550 to 1500 MeV at GRAAL*, Eur. Phys. J. A 26 (3), 399 (2005).
- [151] D. Hornidge et al. (A2 Collaboration), *Accurate Test of Chiral Dynamics in the $\vec{\gamma} p \rightarrow \pi^0 p$ Reaction*, Phys. Rev. Lett. 111, 062004 (2013).
- [152] A. Schmidt et al., *Test of Low-Energy Theorems for ${}^1H(\vec{\gamma}, \pi^0){}^1H$ in the Threshold Region*, Phys. Rev. Lett. 87, 232501 (2001).
- [153] G. Blanpied et al. (LEPS Collaboration), *$\vec{N} \Delta$ transition and proton polarizabilities from measurements of $p(\vec{\gamma}, \gamma)$, $p(\vec{\gamma}, \pi^0)$, and $p(\vec{\gamma}, \pi^+)$* , Phys. Rev. C 64, 025203 (2001).
- [154] R. Beck, *Experiments with photons at MAMI*, Eur. Phys. J. A 28 (1), 173 (2006).
- [155] R. Beck et al., *Measurement of the $E2/M1$ Ratio in the $N \rightarrow \Delta$ Transition using the reaction $p(\vec{\gamma}, p)\pi^0$* , Phys. Rev. Lett. 78, 606 (1997).
- [156] G. Barbiellini et al., *Photoproduction of π^0 on Protons by Polarized γ Rays*, Phys. Rev. 184, 1402 (1969).
- [157] G. Blanpied et al., *$p(\gamma \rightarrow \pi^0)$ reaction and the $E2$ excitation of the Δ* , Phys. Rev. Lett. 69, 1880 (1992).
- [158] V. B. Ganenko et al., *Asymmetry Angular Distributions for $\gamma p \rightarrow p\pi^0$ Events Initiated by 250–650 MeV Polarized Photons*, Sov. J. Nucl. Phys. 23, 162 (1976).

- [159] G. Bologna et al., *Asymmetry in single π^0 photoproduction by polarized γ -rays on protons*, Report number LNF-70-39 (1970), URL http://www.lnf.infn.it/sis/preprint/getfilepdf.php?filename=LNF_70_039.pdf (visited on 07.12.2022).
- [160] G. Knies et al., *Measurement of asymmetries in polarized $\gamma N \rightarrow \pi N$, with E_γ from 600 to 900 MeV*, Phys. Rev. D 10, 2778 (1974).
- [161] M. Sumihama et al., *Backward-angle photoproduction of π^0 mesons on the proton at $E_\gamma = 1.5 - 2.4$ GeV*, Phys. Lett. B 657 (1), 32 (2007).
- [162] F. V. Adamian et al., *Measurement of the cross section asymmetry of the reaction $\gamma \vec{p} \pi^0 p$ in the resonance energy region $E_\gamma = 0.5 - 1.1$ GeV*, Phys. Rev. C 63, 054606 (2001).
- [163] D. Elsner et al., *Linearly polarised photon beams at ELSA and measurement of the beam asymmetry in π^0 photoproduction off the proton*, Eur. Phys. J. A 39 (3), 373 (2009).
- [164] N. Sparks et al. (CBELSA/TAPS Collaboration), *Measurement of the beam asymmetry Σ in the forward direction for $\vec{\gamma} p \rightarrow p \pi^0$* , Phys. Rev. C 81, 065210 (2010).
- [165] P. Bussey et al., *A measurement of the beam asymmetry parameter Σ for neutral pion photoproduction in the energy range 1.2–2.8 GeV*, Nucl. Phys. B 104 (2), 253 (1976).
- [166] V. G. Gorbenko et al., *Angular distribution of the cross section asymmetry in the $\gamma p \rightarrow p \pi^0$ reaction for polarized photons at 280 and 480 MeV*, Tech. rep., Kharkov Institute of Physics and Technology, USSR, KFTI-77-9 (1977).
- [167] D. J. Drickey and R. F. Mozley, *Neutral Meson Production with Polarized X Rays*, Phys. Rev. 136, B543 (1964).
- [168] V. G. Gorbenko et al., *Study of the asymmetry for the $\gamma p \rightarrow p \pi^0$ reaction cross sections by coincidence technique*, Tech. rep., Kharkov Institute of Physics and Technology, USSR, KFTI-77-9 (1977).

-
- [169] R. W. Zdarko and E. B. Dally, *Asymmetry measurements for π^0 and π^+ photoproduction by linearly polarized γ -rays in the energy range (400÷900) MeV*, Nuovo Cim. A 10 (1), 10 (1972).
- [170] R. O. Avakyan, A. Avetisyan and A. S. Bagdasaryan, *Measurements of the asymmetry in the $\gamma p \rightarrow p\pi^0$ cross section in the resonance region*, Sov. J. Nucl. Phys. 38 (5), 721 (1983).
- [171] R. O. Avakian et al., *Measurement of the asymmetry of the reaction $\gamma p \rightarrow p\pi^0$ cross-section for pion production angles in C.M.S. $65^\circ - 80^\circ$ in the resonance energy range*, Tech. rep., Yerevan Physics Institute (1983).
- [172] R. O. Avakyan, E. Avakyan and A. Avetisyan, *Measurement of asymmetry in the π^0 -meson photoproduction cross section for the pion emission angle of 40 and 50 deg in cms in the resonance region (In Russian)*, Yad. Fiz. 29 (5), 1212 (1979).
- [173] R. O. Avakyan et al., *Angular dependence of the asymmetry of the cross section for the reaction $\gamma p \rightarrow p\pi^0$ in the resonance region*, Sov. J. Nucl. Phys. 40 (4), 588 (1984).
- [174] R. O. Avakyan, E. Avakyan and A. Avetisyan, *Measurement of asymmetry in photoproduction of π^0 meson in the resonance region (In Russian)*, Yad. Fiz. 26 (5), 1014 (1977).
- [175] L. Abramyan et al., *Asymmetry of the cross section of the reaction $\gamma P \rightarrow P\pi^0$ In the energy interval 0.9 – 1.65 GeV at $\theta_{\pi^0}^{cms} = 110^\circ$* , J. Exp. Theor. Phys. 23, 375 (1976).
- [176] L. Abrahamian et al., *π^0 and π^+ production with polarized photons in the energy range 1–2 GeV*, Phys. Lett. B 48 (5), 463 (1974).
- [177] J. Alspector et al., *π^\pm and π^0 Production by Polarized Photons in the Resonance Region*, Phys. Rev. Lett. 28, 1403 (1972).
- [178] D. Bellenger et al., *Photoproduction of π^0 With Plane Polarized 3-GeV Photons*, Phys. Rev. Lett. 23, 540 (1969).

- [179] A. Belyaev et al., *Experimental studies of the Σ , T , P polarization parameters and the $\gamma p \rightarrow p\pi^0$ reaction multipole analysis in the first resonance region*, Nucl. Phys. B 213 (2), 201 (1983).
- [180] V. G. Gorbenko, A. I. Derebchinskij and Y. Zhebrovskij, *Measurement of recoil proton polarization in the $\gamma p \rightarrow \pi^0 p$ reaction with polarized photons at energies of 360, 400, 450, 500 MeV (In Russian)*, Yad. Fiz. 27 (5), 1204 (1978).
- [181] P. Bussey et al., *Polarisation parameters in neutral pion photoproduction*, Nucl. Phys. B 154 (3), 492 (1979).
- [182] V. G. Gorbenko et al., *Measurement of proton recoil polarization for $\gamma p \rightarrow p\pi^0$ on linear polarized photon beams in the first πN - resonance range (In Russian)*, Tech. rep., Kharkov Institute of Physics and Technology, KFTI-77-9 (1977).
- [183] K. S. Agababian et al., *Measurement of Polarization Parameters Σ , T , and P in π^0 Photoproduction at $E_\gamma = 0.9 - 1.35$ GeV (In Russian)*, Sov. J. Nucl. Phys. 50, 834 (1989).
- [184] A. Bock et al., *Measurement of the Target Asymmetry of η and π^0 Photoproduction on the Proton*, Phys. Rev. Lett. 81, 534 (1998).
- [185] H. Herr et al., *Forward photoproduction of neutral pions on polarized protons in the third resonance region*, Nucl. Phys. B 125 (2), 157 (1977).
- [186] M. Fukushima et al., *Measurement of polarized target asymmetry on $\gamma p \rightarrow \pi^0 p$ below 1 GeV*, Nucl. Phys. B 136 (2), 189 (1978).
- [187] P. Feller et al., *The measurement of polarized target asymmetry in $\gamma p \rightarrow \pi^0 p$ between 0.4 and 1.0 GeV around 100°* , Nucl. Phys. B 110 (4), 397 (1976).
- [188] P. Booth et al., *The polarised target asymmetry for neutral pion photoproduction from protons in the photon energy range 0.7 - 1.45 GeV*, Nucl. Phys. B 121 (1), 45 (1977).

-
- [189] M. M. Asaturyan et al., *Polarization parameters Σ , T , and P for the reaction $\gamma p \rightarrow p\pi^0$ in the energy interval 0.9 – 1.5 GeV at $\theta_{\pi^0}^{c.m.} = 120^\circ$* , Nucl. Phys. B 44, 341 (1986).
- [190] V. Gobenko et al., *Polarization of protons from the reaction $\gamma + p \rightarrow \pi^0 + p$ on a linearly polarized photon beam*, J. Exp. Theor. Phys. 19 (5), 340 (1974).
- [191] K. Althoff et al., *Measurement of the angular dependence of the polarization of the recoil protons from the photoproduction of neutral pions on hydrogen at proton energies between 240 and 420 MeV*, Phys. Lett. B 26 (11), 677 (1968).
- [192] K. H. Althoff et al., *Measurement of the polarization of the recoil proton from the photoproduction of neutral pions on hydrogen in the region of the first resonance. I*, Z. Phys. 194 (2), 135 (1966).
- [193] P. Bluem, DARES conference (1969).
- [194] D. Trines, *Messung der Polarisation der Rückstoßprotonen aus der Reaktion $\gamma + p \rightarrow p + \pi^0$ im Gebiet der zweiten Resonanz bei kleinen Pion-Schwerpunkts winkeln (In German)*, Ph.D. thesis, Physikalisches Institut der Universität Bonn (1972).
- [195] S. Kato et al., *Recoil proton polarization of neutral pion photoproduction from protons in the energy range between 400 MeV and 1142 MeV*, Nucl. Phys. B 168 (1), 1 (1980).
- [196] A. Bratashevskij et al., *Polarization of recoil protons from the reaction $\gamma p \rightarrow \pi^0 p$ in the proton energy range 450–800 MeV*, Nucl. Phys. B 166 (3), 525 (1980).
- [197] S. Hayakawa et al., *Polarization of Recoil Protons from Neutral Pion Photoproduction*, J. Phys. Soc. Jpn. 25 (2), 307 (1968).
- [198] J. O. Maloy et al., *Polarization of the Recoil Proton from π^0 Photoproduction in Hydrogen*, Phys. Rev. 139, B733 (1965).
- [199] A. S. Bratashevsky et al., *Measurements of polarization of secondary protons in the $\gamma p \rightarrow p\pi^0$ reaction at $\theta_\pi = 150^\circ$ CMS within the range of*

- $E_\gamma = 0.45 - 0.7 \text{ GeV}$ (In Russian), Ukr. Fiz. Zh. (Russ. Ed.) 31, 1306 (1986).
- [200] V. G. Gorbenko et al., *Measurement of longitudinal component of proton polarization in the reaction $\gamma + p \rightarrow \pi^0 + p$ on linearly-polarized photons*, J. Exp. Theor. Phys. 22 (5), 186 (1975).
- [201] D. E. Lundquist et al., *Polarization of Recoil Protons from Neutral Pion Photoproduction*, Phys. Rev. 168, 1527 (1968).
- [202] P. C. Stein, *Polarization of Recoil Protons from the Photoproduction of π^0 Mesons from Hydrogen*, Phys. Rev. Lett. 2, 473 (1959).
- [203] R. Querzoli, G. Salvini and A. Silverman, *The polarization of the proton from the process $\gamma + p \rightarrow p + \pi^0$ in the region of the higher resonances*, Nuovo Cim. 19 (1), 53 (1961).
- [204] R. O. Avakian et al., *Measurement of proton polarization in the reaction $\gamma p \rightarrow p\pi^0$ at an angle $\theta_{\pi^0}^* = 80^\circ$ in a linearly polarized photon beam*, Sov. J. Nucl. Phys. 48, 1030 (1988).
- [205] K. Wijesooriya et al., *Polarization measurements in neutral pion photoproduction*, Phys. Rev. C 66, 034614 (2002).
- [206] M. Prentice et al., *The recoil proton polarization in the reaction $\gamma p \rightarrow \pi^0 p$ in the third resonance region*, Nucl. Phys. B 41 (2), 353 (1972).
- [207] W. Luo et al. (GEP-III and GEP2 γ Collaborations), *Polarization Components in π^0 Photoproduction at Photon Energies up to 5.6 GeV*, Phys. Rev. Lett. 108, 222004 (2012).
- [208] K. H. Althoff et al., *Measurement of the angular distribution of the polarization of the recoil proton from the photoproduction of neutral pions on hydrogen at a photon energy of 360 MeV. II*, Z. Phys. 194 (2), 144 (1966).
- [209] P. Bluem, *Report PI-1-105*, Tech. rep., Universität Bonn Physikalisches Institut (1970).

-
- [210] A. S. Bratashevskij et al., *Measurement of proton polarization from the $\gamma p \rightarrow p\pi^0$ reaction at $\theta_\pi = 110^\circ$ cms in the range of the second and third resonances (In Russian)*, *Yad. Fiz.* 42 (3), 658 (1985).
- [211] A. A. Zybalov et al., *Angular dependence of polarization of secondary protons from the $\gamma p \rightarrow \pi^0 p$ reaction at photon energy 650 and 700 MeV (In Russian)*, *Yad. Fiz.* 28 (1), 105 (1978).
- [212] A. I. Derebchinskij, A. A. Zybalov and O. G. Kononov, *Polarization of secondary protons in the $\gamma + p \rightarrow \pi^0 + p$ reaction at $E_\gamma = 536 - 640$ MeV*, *Zh. Eksp. Teor. Fiz.* 70 (2), 423 (1976).
- [213] A. S. Bratashevsky et al., *Polarization of the recoil protons in $\gamma p \rightarrow p\pi^0$ reaction for $E_\gamma = 0.65 - 1.4$ GeV at $\theta_\pi = 70^\circ$ CM (In Russian)*, *Yad. Fiz.* 35, 56 (1982).
- [214] N. Tanaka et al., *Recoil-Proton Polarization in Neutral-Pion Photoproduction Between 1000 and 1800 MeV*, *Phys. Rev. D* 8, 1 (1973).
- [215] P. Blüm et al., *Angular dependence of the polarization of the recoil proton from the reaction $\gamma p \rightarrow \pi^0 p$ in the region of the second resonance*, *Z. Phys. A* 277 (3), 311 (1976).
- [216] L. Bertanza et al., *Measurement of the polarization of the recoil proton in $\gamma + p \rightarrow p + \pi^0$ using a propane-ethane bubble chamber*, *Nuovo Cim.* 24 (4), 734 (1962).
- [217] R. O. Avakyan, O. Avakyan and A. Avetisyan, *Measurement of polarization of recoil protons in π^0 photoproduction for $\theta_{\pi^0}^* = 60^\circ$ in the resonance region (In Russian)*, *Sov. J. Nucl. Phys.* 37 (2), 199 (1983).
- [218] E. D. Bloom et al., *Recoil-Proton Polarization in π^0 Photoproduction*, *Phys. Rev. Lett.* 19, 671 (1967).
- [219] N. V. Goncharov et al., *Polarization of protons in the $\gamma + p \rightarrow \pi^0 + p$ reaction by 692-1028 MeV photons at an angle of 90° in the CMS (In Russian)*, *Zh. Eksp. Teor. Fiz.* 64 (2), 401 (1973).

- [220] S. Kabe et al., *Polarization of recoil protons from proton Compton scattering in the region of the second πN resonance*, Nucl. Phys. B 50 (1), 17 (1972).
- [221] J. R. Kenemuth and P. C. Stein, *Polarization of the Proton from the $\gamma + n \rightarrow p + \pi^-$ Reaction*, Phys. Rev. 129, 2259 (1963).
- [222] A. S. Bratashevskij et al., *Recoil proton polarization from $\gamma + p \rightarrow p + \pi^0$ reaction in the photon energy range from 800 to 1300 MeV and for the angle $\theta_\pi^* = 60^\circ$ (In Russian)*, Yad. Fiz. 33 (4), 1020 (1981).
- [223] A. S. Bratashevskij et al., *Polarization of recoil protons in the $\gamma p \rightarrow p\pi^0$ reaction for the angle $\theta_\pi = 80^\circ$ at the energy of $E_\gamma = 0.7 - 1.4$ GeV (In Russian)*, Yad. Fiz. 38 (8), 390 (1983).
- [224] A. S. Bratashevskij et al., *Polarization of protons in the reaction $\gamma p \rightarrow p\pi^0$ at an angle of $\theta_\pi = 120^\circ$ in CMS at the third maximum of total cross section (In Russian)*, Yad. Fiz. 46 (4), 1095 (1987).
- [225] R. O. Avakyan et al., *Measurement of P_x , P_y , P_z components of the proton's polarization vector in the reaction $\gamma p \rightarrow p\pi^0$ for linearly polarized photons*, Sov. J. Nucl. Phys. 53 (3), 448 (1991).
- [226] P. Blüm, R. Brockmann and W. Mohr, *Angular dependence of the polarization of the recoil proton from the reaction $\gamma p \rightarrow \pi^0 p$ in the region of the third resonance*, Z. Phys. A 278 (3), 275 (1976).
- [227] A. S. Bratashevskij, A. A. Zybalov and S. P. Karasev, *Measurement of proton polarization from the $\gamma p \rightarrow p\pi^0$ reaction in the third resonance (In Russian)*, Yad. Fiz. 41 (6), 1515 (1985).
- [228] R. O. Avakyan, E. O. Avakyan and A. E. Avetisyan, *Measurement of proton polarization in π^0 photoproduction at $\theta_{\pi^0}^* = 70^\circ$ in a linearly polarized photon beam (In Russian)*, Yad. Fiz. 46, 1445 (1987).
- [229] A. I. Derebchinskij et al., *Polarization of the secondary protons for the $\gamma + p \rightarrow \pi^0 + p$ reaction in the third resonance region (In Russian)*, Zh. Eksp. Teor. Fiz. 66 (1), 68 (1974).

-
- [230] P. Booth, *Daresbury Nucl. Phys. Laboratory Annual Report*, Tech. rep., Daresbury Laboratory (1977).
- [231] P. Bussey et al., *Measurements of the double polarisation parameters G and H in neutral pion photoproduction*, Nucl. Phys. B 159 (3), 383 (1979).
- [232] R. Di Salvo et al. (GRAAL Collaboration), *Measurement of Σ beam asymmetry in π^0 photoproduction off the neutron in the second and third resonances region**, Eur. Phys. J. A 42 (2), 151 (2009).
- [233] C. Mullen et al. (A2 Collaboration), *Single π^0 production off neutrons bound in deuteron with linearly polarized photons*, Eur. Phys. J. A 57 (6), 205 (2021).
- [234] D. Elsner et al. (CBELSA/TAPS Collaboration), *Measurement of the beam asymmetry in η photoproduction off the proton*, Eur. Phys. J. A 33 (2), 147 (2007).
- [235] F. Afzal et al. (CBELSA/TAPS Collaboration), *Observation of the η' Cusp in the New Precise Beam Asymmetry Σ Data for $\gamma p \rightarrow p\eta$* , Phys. Rev. Lett. 125, 152002 (2020).
- [236] C. S. Akondi et al. (A2 Collaboration), *Measurement of the Transverse Target and Beam-Target Asymmetries in η Meson Photoproduction at MAMI*, Phys. Rev. Lett. 113, 102001 (2014).
- [237] P. Collins et al. (CLAS Collaboration), *Photon beam asymmetry Σ for η and η' photoproduction from the proton*, Phys. Lett. B 771, 213 (2017).
- [238] O. Bartalini et al. (GRAAL Collaboration), *Measurement of η photoproduction on the proton from threshold to 1500 MeV*, Eur. Phys. J. A 33 (2), 169 (2007).
- [239] J. Ajaka et al., *New Measurement of Σ Beam Asymmetry for η Meson Photoproduction on the Proton*, Phys. Rev. Lett. 81, 1797 (1998).
- [240] H. A. Vartapetyan and S. E. Piliposyan, *Measurements of cross section asymmetry by polarized photons and models of η meson photoproduc-*

- tion in the energy range $E_\gamma = 1-2$ GeV (In Russian)*, Tech. rep., Yerevan Physics Institute, USSR, EFI-415(22)-80 (1980).
- [241] C. A. Heusch et al., *Recoil Proton Polarization in Eta Photoproduction*, Phys. Rev. Lett. 25, 1381 (1970).
- [242] M. Hongoh et al., *Differential cross-section and recoil proton polarization of η -meson photoproduction at 890 MeV*, Lett. Nuovo Cim. 2 (6), 317 (1971).
- [243] A. Fantini et al. (GRAAL Collaboration), *First measurement of the Σ beam asymmetry in η photoproduction on the neutron*, Phys. Rev. C 78, 015203 (2008).
- [244] F. Frommberger, *Electron accelerator ELSA* (2021), URL https://www-elsa.physik.uni-bonn.de/elsa_en.html (visited on 07.12.2022).
- [245] W. Hillert, *Erzeugung eines Nutzstrahls spinpolarisierter Elektronen an der Beschleunigeranlage ELSA (In German)*, Habilitation, Rheinische Friedrich-Wilhelms-Universität Bonn (2000).
- [246] H. Schmieden et al., *BGO-OD Experiment*, URL <https://bgo-od.physik.uni-bonn.de/> (visited on 07.12.2022).
- [247] K. Fornet-Ponse, *Die Photonenmarkierungsanlage für das Crystal-Barrel/TAPS-Experiment an ELSA (In German)*, Ph.D. thesis, Rheinische Friedrich-Wilhelms-Universität Bonn (2009).
- [248] A. Fösel, *Entwicklung und Bau des Innendetektors für das Crystal Barrel Experiment an ELSA/Bonn (In German)*, Ph.D. thesis, Friedrich-Alexander-Universität Erlangen-Nürnberg (2000).
- [249] H. Eberhardt, *Bestimmung von Polarisationsobservablen in der π^0 und ω Photoproduktion am Proton mit dem CBELSA/TAPS-Experiment (In German)*, Ph.D. thesis, Rheinische Friedrich-Wilhelms-Universität Bonn (2012).

-
- [250] S. Kammer, *Strahlpolarimetrie am CBELSA/TAPS Experiment (In German)*, Ph.D. thesis, Rheinische Friedrich-Wilhelms-Universität Bonn (2010).
- [251] K. Livingston, *The Stonehenge technique. A method for aligning coherent bremsstrahlung radiators*, Nucl. Instrum. Methods Phys. Res., Sec. A 603 (3), 205 (2009).
- [252] E. Blucher et al., *Tests of cesium iodide crystals for an electromagnetic calorimeter*, Nucl. Instrum. Methods Phys. Res., Sec. A 249 (2), 201 (1986).
- [253] A. Thiel, *Bestimmung der Doppelpolarisationsobservablen G in π^0 -Photoproduktion (In German)*, Ph.D. thesis, Rheinische Friedrich-Wilhelms-Universität Bonn (2012).
- [254] E. Aker et al. (Crystal Barrel Collaboration), *The crystal barrel spectrometer at LEAR*, Nucl. Instrum. Methods Phys. Res., Sec. A 321 (1), 69 (1992).
- [255] C. Honisch et al., *The new APD Based Readout of the Crystal Barrel Calorimeter - An Overview*, Publication in preparation.
- [256] C. Honisch, *Design, Aufbau und Test einer neuen Ausleseelektronik für das Crystal-Barrel-Kalorimeter (In German)*, Ph.D. thesis, Rheinische Friedrich-Wilhelms-Universität Bonn (2015).
- [257] M. Urban, *Design eines neuen Lichtpulsersystems sowie Aufbau und Inbetriebnahme der neuen APD Auslese für das Crystal-Barrel-Kalorimeter (In German)*, Ph.D. thesis, Rheinische Friedrich-Wilhelms-Universität Bonn (2018).
- [258] J. Müllers, *An FPGA-based Sampling ADC for the Crystal Barrel Calorimeter*, Ph.D. thesis, Rheinische Friedrich-Wilhelms-Universität Bonn (2019).
- [259] C. Funke, *Analyse der Triggerfähigkeiten zur Selektion hadronischer Ereignisse und Entwicklung eines Hochgeschwindigkeits-Triggers für den Vorwärtskonus des Crystal-Barrel-Detektors (In German)*, Ph.D. thesis, Rheinische Friedrich-Wilhelms-Universität Bonn (2008).

- [260] C. Wendel, *Design und Aufbau eines Szintillationsdetektors zur Identifizierung geladener Teilchen im Crystal-Barrel-Vorwärtsdetektor (In German)*, Ph.D. thesis, Rheinische Friedrich-Wilhelms-Universität Bonn (2008).
- [261] G. Suft et al., *A scintillating fibre detector for the Crystal Barrel experiment at ELSA*, Nucl. Instrum. Methods Phys. Res., Sec. A 538 (1), 416 (2005).
- [262] J. Hartmann, *Measurement of Double Polarization Observables in the Reactions $\gamma p \rightarrow p\pi^0$ and $\gamma p \rightarrow p\eta$ with the Crystal Barrel/TAPS Experiment at ELSA*, Ph.D. thesis, Rheinische Friedrich-Wilhelms-Universität Bonn (2017).
- [263] M. Grüner, *Modifikation und Test des Innendetektors für das Crystal Barrel Experiment (In German)*, Master's thesis, Rheinische Friedrich-Wilhelms-Universität Bonn (2006).
- [264] M. Gottschall, *Bestimmung der Doppelpolarisationsobservablen E für die Reaktion $\gamma p \rightarrow p\pi^0$ am CBELSA/TAPS-Experiment (In German)*, Ph.D. thesis, Rheinische Friedrich-Wilhelms-Universität Bonn (2013).
- [265] R. Novotny, *The BaF₂ photon spectrometer TAPS*, IEEE Trans. Nucl. Sci. 38 (2), 379 (1991).
- [266] A. Gabler et al., *Response of TAPS to monochromatic photons with energies between 45 and 790 MeV*, Nucl. Instrum. Methods Phys. Res., Sec. A 346 (1), 168 (1994).
- [267] P. Drexler, *Entwicklung und Aufbau der neuen TAPS-Elektronik (In German)*, Ph.D. thesis, Justus-Liebig-Universität Giessen (2004).
- [268] J. Hartmann, *Zeitkalibrierung und Photonenflussbestimmung für das Crystal-Barrel-Experiment an ELSA (In German)*, Master's thesis, Rheinische Friedrich-Wilhelms-Universität Bonn (2008).
- [269] Witthauer, L. and others (A2 Collaboration), *Quasi-free photoproduction of η -mesons off ^3He nuclei*, Eur. Phys. J. A 49 (12), 154 (2013).

-
- [270] D. Werthmüller, *Experimental study of nucleon resonance contributions to η -photoproduction on the neutron*, Ph.D. thesis, Universität Basel (2014).
- [271] L. Witthauer, *Measurement of cross sections and polarisation observables in η photoproduction from neutrons and protons bound in light nuclei*, Ph.D. thesis, Universität Basel (2015).
- [272] M. Dieterle, *Measurement of polarization observables in π^0 and $\pi^0\pi^0$ photoproduction from protons and neutrons at MAMI and ELSA*, Ph.D. thesis, Universität Basel (2016).
- [273] W. McGehee, *The Gamma Intensity Monitor at the Crystal-Barrel-Experiment*, Bachelor's thesis, Massachusetts Institute Of Technology (2008).
- [274] J. Dielmann, *Entwicklung, Aufbau und Test eines Detektors zur Bestimmung des Photonenflusses an der Bonner Photonenmarkierungsanlage (In German)*, Master's thesis, Rheinische Friedrich-Wilhelms-Universität Bonn (2008).
- [275] D. Kaiser, *Aufbau und Test des Gas-Cerenkov-Detektors für den Crystal-Barrel-Aufbau an ELSA (In German)*, Master's thesis, Rheinische Friedrich-Wilhelms-Universität Bonn (2007).
- [276] A. Bideau-Mehu et al., *Interferometric determination of the refractive index of carbon dioxide in the ultraviolet region*, Opt. Commun. 9 (4), 432 (1973).
- [277] M. Polyanskiy, *Optical constants of CO_2 (Carbon dioxide)* (2020), URL <https://refractiveindex.info/?shelf=main&book=CO2&page=Bideau-Mehu> (visited on 07.12.2022).
- [278] M. Schiemann, *Polarisationsmessungen an mit Trityl-Radikalen dotiertem D-Butanol (In German)*, Master's thesis, Ruhr-Universität Bochum (2006).
- [279] S. Runkel, *The Polarized Target at the CBELSA/TAPS Experiment*, The 12th International Workshop on the Physics of Excited Nucleons (2019).

- [280] S. Goertz, *The dynamic nuclear polarization process*, Nucl. Instrum. Methods Phys. Res., Sec. A 526 (1), 28, Proceedings of the ninth International Workshop on Polarized Solid Targets and Techniques (2004).
- [281] O. A. Rondon, *Corrections to nucleon spin structure asymmetries measured on nuclear polarized targets*, Phys. Rev. C 60, 035201 (1999).
- [282] C. Rohlof, *Entwicklung polarisierter Targets zur Messung der Gerasimov-Drell-Hearn-Summenregel an ELSA (In German)*, Ph.D. thesis, Rheinische Friedrich-Wilhelms-Universität Bonn (2003).
- [283] C. Bradtke et al., *A new frozen-spin target for 4π particle detection*, Nucl. Instrum. Methods Phys. Res., Sec. A 436 (3), 430 (1999).
- [284] A. Thomas, *Polarised targets for 4π detectors at MAMI*, Eur. Phys. J. Special Topics 198 (1), 171 (2011).
- [285] G. Reicherz, *Kontroll- und NMR-System eines polarisierten Festkörpertargets (In German)*, Ph.D. thesis, Rheinische Friedrich-Wilhelms-Universität Bonn (1994).
- [286] G. Reicherz et al., *The Bonn polarized target NMR-system*, Nucl. Instrum. Methods Phys. Res., Sec. A 356 (1), 74, Proceedings of the Seventh International Workshop on Polarized Target Materials and Techniques (1995).
- [287] M. Grüner, *Messung der Doppelpolarisationsobservable G in der Reaktion $\gamma p \rightarrow p\eta$ mit dem Crystal-Barrel/TAPS-Experiment an ELSA (In German)*, Ph.D. thesis, Rheinische Friedrich-Wilhelms-Universität Bonn (2016).
- [288] T. Seifen, *Messung von Polarisationsobservablen in der $2\pi^0$ -Photoproduktion mit dem Crystal-Barrel/TAPS-Experiment (In German)*, Ph.D. thesis, Rheinische Friedrich-Wilhelms-Universität Bonn (2021).
- [289] A. Winnebeck, *Entwicklung und Implementierung eines universellen, FPGA basierten Triggermoduls für das Crystal-Barrel-Experiment an ELSA (In German)*, Master's thesis, Rheinische Friedrich-Wilhelms-Universität Bonn (2006).

-
- [290] P. Hoffmeister, *Das Datenerfassungssystem für das Crystal-Barrel/TAPS-Experiment an ELSA (In German)*, Ph.D. thesis, Rheinische Friedrich-Wilhelms-Universität Bonn (2019).
- [291] R. Brun and F. Rademakers, *ROOT — An object oriented data analysis framework*, Nucl. Instrum. Methods Phys. Res., Sec. A 389 (1), 81, New Computing Techniques in Physics Research V. See <https://github.com/root-project/root> for the official repository for ROOT. (1997).
- [292] ROOT, *ROOT: analyzing petabytes of data, scientifically*, URL <https://root.cern.ch> (visited on 07.12.2022).
- [293] F. Kalischewski, *Entwicklung eines neuen Datenakquisitionssystems für das CB-ELSA-Experiment (In German)*, Ph.D. thesis, Rheinische Friedrich-Wilhelms-Universität Bonn (2004).
- [294] D. Piontek, *Entwicklung eines Online-Monitors für das Crystal-Barrel-Experiment an ELSA (In German)*, Master's thesis, Rheinische Friedrich-Wilhelms-Universität Bonn (2007).
- [295] R. Schmitz, *Simulationen zum Nachweis geladener Teilchen für das Crystal-Barrel-Experiment an ELSA (In German)*, Master's thesis, Rheinische Friedrich-Wilhelms-Universität Bonn (2008).
- [296] F. Kalischewski, *Development of a new simulation for the CBELSA/TAPS experiment using Virtual Monte Carlo*, Master's thesis, Rheinische Friedrich-Wilhelms-Universität Bonn (2011).
- [297] S. Agostinelli et al., *Geant4—a simulation toolkit*, Nucl. Instrum. Methods Phys. Res., Sec. A 506 (3), 250 (2003).
- [298] J. Allison et al., *Geant4 developments and applications*, IEEE Trans. Nucl. Sci. 53 (1), 270 (2006).
- [299] M. Lacombe et al., *Parametrization of the deuteron wave function of the Paris N-N potential*, Phys. Lett. B 101 (3), 139 (1981).
- [300] K. Nakamura et al., *The reaction $^{12}\text{C}(e, e'p)$ at 700 MeV and DWIA analysis*, Nucl. Phys. A 268 (3), 381 (1976).

- [301] T. Seifen, *Verbesserung der Rekonstruktion und Entwicklung eines First-Level-Triggerschemas für das Crystal-Barrel-Kalorimeter (In German)*, Master's thesis, Rheinische Friedrich-Wilhelms-Universität Bonn (2009).
- [302] J. Junkersfeld, *Kalibration des Crystal-Barrel-ELSA Detektors mit Hilfe der Reaktion $\gamma p \rightarrow p\pi^0$ (In German)*, Master's thesis, Rheinische Friedrich-Wilhelms-Universität Bonn (2000).
- [303] J. Müller, *Bestimmung einer Energiekorrekturfunktion für das Kalorimeter des Crystal-Barrel-Experiments an ELSA (In German)*, Master's thesis, Rheinische Friedrich-Wilhelms-Universität Bonn (2007).
- [304] J. Müller, *Bestimmung der Doppelpolarisationsobservablen E in der Reaktion $\gamma p \rightarrow p\eta$ am CBELSA/TAPS-Experiment (In German)*, Ph.D. thesis, Friedrich-Wilhelms-Universität Bonn (2017).
- [305] R. Castelijns, *Photoproduction of strange mesons and hyperons on the proton*, Ph.D. thesis, Rijksuniversiteit Groningen (2006).
- [306] T. Dahlke, *Bestimmung einer winkelabhängigen Energiekorrekturfunktion für das TAPS-Kalorimeter des Crystal-Barrel/TAPS-Experimentes an ELSA (In German)*, Master's thesis, Rheinische Friedrich-Wilhelms-Universität Bonn (2008).
- [307] S. Böse, *Modifikation und Test des Lichtpulsersystems für den Crystal Barrel Aufbau an ELSA (In German)*, Master's thesis, Rheinische Friedrich-Wilhelms-Universität Bonn (2006).
- [308] N. Davis, Private communication (2021).
- [309] B. Salisbury, Private communication (2021).
- [310] H. Bethe, *Zur Theorie des Durchgangs schneller Korpuskularstrahlen durch Materie*, Ann. Phys. 397 (3), 325 (1930).
- [311] F. Bloch, *Zur Bremsung rasch bewegter Teilchen beim Durchgang durch Materie*, Ann. Phys. 408 (3), 285 (1933).
- [312] S. Eidelman et al. (Particle Data Group), *Review of Particle Physics*, Phys. Lett. B 592, 1+ (2004).

-
- [313] P. D. Group, *Atomic and nuclear properties of barium fluoride (BaF₂)* (2020), URL https://pdg.lbl.gov/2020/AtomicNuclearProperties/HTML/barium_fluoride.html (visited on 07.12.2022).
- [314] L. Gottardi, *Test and improvement of the calibration mechanisms of the MiniTAPS detector*, Master's thesis, Rheinische Friedrich-Wilhelms-Universität Bonn (2019).
- [315] V. Hejny, *Photoproduktion von η -Mesonen an Helium 4*, Ph.D. thesis, Justus-Liebig-Universität Giessen (1998).
- [316] M. Pfeiffer, *Photoproduction of η mesons from ^3He* , Ph.D. thesis, Justus-Liebig-Universität Giessen (2002).
- [317] T. Matulewicz et al., *Response of BaF₂ detectors to photons of 3–50 MeV energy*, Nucl. Instrum. Methods Phys. Res., Sec. A 289 (1), 194 (1990).
- [318] NIST, *NIST Chemistry WebBook* (2021), URL <https://doi.org/10.18434/T4D303> (visited on 07.12.2022).
- [319] M. KGaA, *1-Butanol-d₁₀* (2021), URL <https://www.sigmaaldrich.com/CH/de/product/ALDRICH/302996> (visited on 07.12.2022).
- [320] S. Bültmann et al., *Properties of the deuterated target material used by the SMC*, Nucl. Instrum. Methods Phys. Res., Sec. A 356 (1), 102, Proceedings of the Seventh International Workshop on Polarized Target Materials and Techniques (1995).
- [321] S. Robinson et al., *Density Measurement of Solid Butanol by γ -ray Attenuation*, In W. Meyer, E. Steffens and W. Thiel (eds.), *High Energy Spin Physics*. Springer Berlin Heidelberg, Berlin, Heidelberg, 385–387 (1991).
- [322] S. Runkel, Private communication (2020).
- [323] C. Rohlof and H. Dutz, *Effective densities and polarizations of the targets for the GDH-experiments at MAMI and ELSA*, Nucl. Instrum. Methods Phys. Res., Sec. A 526 (1), 126, Proceedings of the ninth International Workshop on Polarized Solid Targets and Techniques (2004).

- [324] F. A. Natter et al., *Monte Carlo simulation and analytical calculation of coherent bremsstrahlung and its polarisation*, Nucl. Instrum. Methods Phys. Res., Sect. B 211 (4), 465 (2003).
- [325] D. Elsner, *Untersuchung kleiner Partialwellenbeiträge in der Nähe dominierender Resonanzzustände des Protons mit linear polarisierten Photonen (In German)*, Ph.D. thesis, Rheinische Friedrich-Wilhelms-Universität Bonn (2006).
- [326] M. Dieterle et al. (A2 Collaboration), *Photoproduction of π^0 mesons off protons and neutrons in the second and third nucleon resonance regions*, Phys. Rev. C 97, 065205 (2018).
- [327] M. Dieterle, *Comparison of the Experimental Resolution in Case of Using a 1.76 or 4.76 cm LD_2 Target*, Master project thesis (2009), URL https://jazz.physik.unibas.ch/site/publications/project/project_dieterle.pdf (visited on 07.12.2022).
- [328] D. Werthmüller, *Photoproduction of η' Mesons off the Deuteron near Threshold*, Master's thesis, Universität Basel (2007).
- [329] National Nuclear Data Center (NNDC) at Brookhaven National Laboratory, *Ground and isomeric state information for 2_1H* , URL <https://www.nndc.bnl.gov/nudat3/> (visited on 07.12.2022).
- [330] T. Jude, *Strangeness photoproduction off the proton at threshold energies*, Ph.D. thesis, The University of Edinburgh (2010).
- [331] C. Gourieroux and A. Monfort, *Statistics and Econometric Models*, Cambridge University Press (1995).
- [332] A. Sarantsev and K. Nikonov, Private communication (2022).
- [333] D. Ho et al. (CLAS Collaboration), *Beam-Target Helicity Asymmetry for $\vec{\gamma}\vec{n}\rightarrow\pi^-p$ in the N^* Resonance Region*, Phys. Rev. Lett. 118, 242002 (2017).
- [334] L. Witthauer et al. (A2 Collaboration), *Insight into the Narrow Structure in η Photoproduction on the Neutron from Helicity-Dependent Cross Sections*, Phys. Rev. Lett. 117, 132502 (2016).

- [335] A. Horvath, *Cherenkov* (2006), URL <https://commons.wikimedia.org/wiki/File:Cherenkov.svg> (visited on 07.12.2022).

Curriculum Vitae

Personal details

Name Nicolas Martin Jermann
Date of birth 25 June 1994
Place of birth Zurich, Switzerland

Education

2019–2023 PhD in Physics, University of Basel
2017–2019 M Sc in Physics, University of Basel
 Master’s thesis: Coherent and quasifree η -Photoproduction off ${}^4\text{He}$
2014–2017 B Sc in Physics, University of Basel
2010–2013 Grammar school, Regionales Gymnasium Laufental-Thierstein
 Profile A: Applications of Mathematics and Physics

Positions

2022–2023 Computer manager
2022 Co-Lecturer: Hadron structure with electromagnetic interaction
2020–2022 Proseminar assistant: Nuclear and Particle Physics
2019–2023 Physic’s lab assistant: Beginner’s Lab I & II
2019–2023 Physic’s lab assistant: Advanced Lab I & II
2019–2023 Teaching assistant: Introduction to Nuclear and Particle Physics
2018 Teaching assistant: Mathematical Methods I
2018 Teaching assistant: Introduction to Physics II

Awards

Best poster award, Gordon Research Conference on Photonuclear Reactions, Holderness, NH, USA, 2022.

Publications

1. C. Mullen et al. (A2 Collaboration), *Single π^0 production off neutrons bound in deuteron with linearly polarized photons*, Eur. Phys. J. A 57 (6), 205 (2021).

Conference Contributions

1. N. Jermann, *Experimental study of polarization observables in π^0 and η photoproduction off quasifree nucleons*, Invited talk, Gordon Research Conference on Photonuclear Reactions, Holderness, NH, USA, 2022.
2. N. Jermann, *Experimental study of polarization observables in π^0 and η photoproduction off quasifree nucleons*, Poster, Gordon Research Conference on Photonuclear Reactions, Holderness, NH, USA, 2022.
3. N. Jermann, *Experimental study of polarization observables in π^0 and η photoproduction off quasifree nucleons*, Talk, 2022 Frontiers and Careers in Nuclear and Hadronic Physics, Cambridge, MA, USA, 2022.
4. N. Jermann, *Polarisation observables Σ , T , P and H in π^0 and η photoproduction off quasifree nucleons*, Talk, 4th Jagiellonian Symposium on Advances in Particles Physics and Medicine, Krakow, Poland, 2022.
5. N. Jermann, *Polarisation observables Σ , T , P , and H in π^0 and η photoproduction off quasifree nucleons*, Group report, DPG Spring Meeting, "Mainz", Germany, 2022.
6. N. Jermann, *Results from TAPS Test-Beamtime*, Talk, A2 Collaboration Meeting, Mainz, Germany, 2021.
7. N. Jermann, *Status of TAPS after its maintenance in 2019/2020*, Talk, A2 Collaboration Meeting, Mainz, Germany, 2020.
8. N. Jermann, *First steps towards T , P , and H observables for quasifree η -photoproduction off deuterium*, Talk, A2 Collaboration Meeting, Mainz, Germany, 2020.
9. N. Jermann, *First Steps for the Analysis of polarisation Observables for the measurement with the deuterated Butanol Target*, Talk, CBELSA/TAPS Collaboration Meeting, Bonn, Germany, 2019.
10. N. Jermann, *Coherent and quasifree η -Photoproduction off ^4He* , Talk, A2 Collaboration Meeting, Mainz, Germany, 2019.

